STRUCTURAL ANALYSIS OF LARGE SCALE DARRIEUS TYPE VERTICAL AXIS WIND TURBINES WITH MONITORING AND CONTROL

Lin Jinghua

Ph.D

The Hong Kong Polytechnic University

2017

The Hong Kong Polytechnic University

Department of Civil and Environmental Engineering

STRUCTURAL ANALYSIS OF LARGE SCALE DARRIEUS TYPE VERTICAL AXIS WIND TURBINES WITH MONITORING AND CONTROL

Lin Jinghua

A thesis submitted in partial fulfillment of the requirements for

the Degree of **Doctor of Philosophy**

May 2016

CERTIFICATE OF ORIGINALITY

I hereby declare that this thesis is my own work and that, to the best of my knowledge and belief, it reproduces no material previously published or written, nor material that has been accepted for the award of any other degree or diploma, except where due acknowledgement has been made in the text.

_______________(Signed)

_______________(Name of student)

To my family

for their love and support

ABSTRACT

Compared with horizontal axis wind turbines (HAWT), vertical axis wind turbines (VAWT) have the primary advantages of insensitivity to wind direction and turbulent wind, a simpler structure, less fatigue loading, and easy maintenance. As a result, a renewed interest in VAWTs has been seen in recent years and there is a trend worldwide in building large-scale VAWTs. Nevertheless, VAWTs were not pursued after brief development and failing in the 1980s, which resulted in a lack of design experience of large-scale VAWTs. Furthermore, VAWTs suffer the disadvantages of low power coefficient and difficulties in self-start and shut-down. Hence, great research efforts are urgently required to make VAWTs workable. In this regard, this thesis is devoted to a systematic and novel study of large-scale VAWTs, which includes the determination of wind loads on all the components of the VAWT using computational fluid dynamics (CFD) simulation, the finite element modelling and model updating of laminated composite blades, the fatigue and ultimate strength analyses of blades and other components of the VAWT, the pitch control systems for four states of the VAWT, the structural health monitoring (SHM) of the VAWT, and the concept of the smart VAWT.

To conduct fatigue and ultimate strength analyses, dynamic loads on the whole VAWT must be determined. A practical method of wind load simulation for VAWTs is proposed in this study based on the strip analysis method and the 2D shear stress transport (SST) $k-\omega$ model. The validity of 2D SST $k-\omega$ model for VAWTs is assessed by comparing simulation results with those obtained by 2.5D large eddy simulation (LES). The influences of the tower, arms and turbulent inflow on the aerodynamic forces of the blades are further studied. The results show that the wind pressure and aerodynamic forces simulated by the 2D SST $k-\omega$ model match well

with those obtained by 2.5D LES. The influences of the mean wind speed profile, turbulence, and interaction of all the components can be included in the proposed method at an acceptable computation cost. The influence of the tower is unapparent while the influence of the arms is obvious. The tangential force, and thus the power coefficient, is reduced due to the existence of the arms. The turbulent inflow wind speed causes fluctuation in the wind loads.

In addition to wind loads, a precise finite element (FE) model is also needed for the structural analysis. The blades of modern wind turbines are made of laminated composite materials. In this thesis, an FE model of blades is established using laminated shell elements and a micromechanics-based model updating method is proposed to update the laminar elastic constants of the FE model. Analyses of sensitivity and uncertainty are conducted to determine the parameters of micromechanics models to be updated. Static bending tests are conducted and the measured data are used to update the models. The results show that by applying micromechanics models to the process of updating laminar elastic constants, direct identification of these constants can be avoided. In addition, the number of updating parameters can be reduced. It is found that the fiber volume fraction is the most influential parameter with the largest uncertainty for both unidirectional fiber reinforced plastic (UD FRP) and plain weave fiber reinforced plastic (PW FRP). After updating the fiber volume fractions for UP FRP and PW FRP based on the measured strains and displacements, both the calculated local strains and the global displacement match well with the measured data.

A framework for the fatigue and ultimate strength analyses of composite blades is proposed. First, a refined FE model of a laminated composite straight blade is established. Based on the FE model, fatigue analyses are conducted and the influences of the ultimate tensile and compressive strains, damping ratio and fundamental frequency on fatigue damage are studied. Ultimate strength analysis at the extreme wind speed is also conducted and the influence of wind direction on the response of blade is considered. The results show that for the specific composite straight blade considered, the locations at the supports and the mid-span of the blade have larger fatigue damage than other positions of the blade. The positions subjected to compressive cyclic loads have the larger fatigue damage than those subjected to tensile cyclic loads. The fatigue damage is sensitive to the damping ratio and fundamental frequency. The critical locations of strength failure are near the supports. The largest interlaminar shear stresses occur near the supports while the largest interlaminar normal stresses occur at the leading edge, not in the support section.

A framework for fatigue and ultimate strength analyses of other components of VAWTs is also proposed. A FE model of the VAWT is established by beam elements. The rotating frame method is used to eliminate the rigid motion of the VAWT. Based on the FE model, fatigue and ultimate strength analyses are then conducted. The results show that the largest fatigue damage occurs at the root of the main arms. The fatigue critical location of the tower is at the bottom. It is found that larger fatigue damage occurs in the leeward side of the tower. For the rotor, the strength failure critical locations are the roots of main arm and the shaft. Assuming that the direction of the extreme wind speed is at the azimuth angle of 0^o, the dangerous azimuth angles of the main arm are 60^o and 240^o; the dangerous azimuth angles of the shaft are 30^o, 150^o and 270^o. For the tower, the fatigue critical location is at the bottom and in the leeward side and the dangerous azimuth angles are 30^o, 150^o and 270^o.

Field tests of a straight-bladed VAWT are conducted to validate the proposed frameworks for the fatigue and ultimate strength analyses of VAWTs. The power spectrum densities (PSDs) of the measured responses are calculated under different conditions. Natural frequencies are determined from the peaks of the normalized PSDs of measured responses. The FE model of the VAWT is updated by the identified natural frequencies. By comparing the simulated responses with the corresponding measured data in the frequency domain, it is found that these two results match well with each other. Therefore, the proposed frameworks are validated to some extent.

The pitch control system for large-scale VAWTs is proposed. The operation of VAWTs can be divided into four states: start-up above the cut-in wind speed, operation under the rated wind speed, operation above the rated wind speed, and shut-down over the cut-out wind speed. To improve the power generation, self-starting and shut-down performance of straight-bladed VAWTs, two pitch control algorithms ,the fixed pitch (in one revolution) and the variable pitch (in one revolution), are studied for the four states using the double multiple streamtube theory (DMST). It is found that the sinusoidal pitch algorithm produces better control results than the fixed pitch algorithm. Based on these studies, a pitch control system is defined. Two sets of data acquisition and processing devices are used, one for the rotating parts and the other for the stationary parts.

Furthermore, based on the results of fatigue and ultimate strength analyses, a SHM system is proposed for the VAWT. Anemometers are installed to monitor the wind condition; a tachometer is installed to monitor the rotational speed and the azimuth angle; strains gauges are installed at the critical locations of fatigue and ultimate strength failure to monitor the local deformations; accelerometers are installed to monitor global deformations; and load cells are installed to monitor the service loads. Similar to the control system, two sets of data acquisition and processing devices are used. Synthesizing the SHM system, control system and power supply, a smart VAWT concept is defined. Such a smart VAWT has self-sensing, self-inspecting, self-control and self-power capabilities.

LIST OF PUBLICATIONS

Journal Papers

Lin J.H., Xu Y.L, Zhu S.Y. “Modelling and model updating of laminate composite blades for a vertical axis wind turbine” *Wind Energy*. (*under reviewed*)

Lin J.H., Leung K.K., Xu Y.L., Zhu S.Y., Zhan S. “Field measurement and model updating of a large-scale straight-bladed vertical axis wind turbine” *Renewable Energy*. (*under reviewed*)

Lin J.H., Xu Y.L., Xia Y. “Structural Analysis of Large-Scale Vertical Axis Wind Turbines I: Wind Load Simulation” (*submitted*)

Lin J.H., Xu Y.L., Xia Y. “Structural Analysis of Large-Scale Vertical Axis Wind Turbines II: Fatigue and Ultimate Strength Analyses” (*submitted*)

Lin J.H., Xu Y.L. “Structural health monitoring and control of straight-bladed VAWTs” (*to be submitted*)

Conference Papers

Lin J.H., Xu Y.L. “Fatigue Life Analysis of an H-type Darrieus VAWT Blade under Turbulent Wind” , The 2nd International Symposium on Life-Cycle Performance of Bridges and Structures, 18-20 December 2015, Changsha, China

Lin J.H., Xu Y.L., Zhu S.Y. “FE Modeling of VAWT Blades and Model Updating Using a Micromechanics Approach”, The 2nd International Symposium on Life-Cycle Performance of Bridges and Structures, 18-20 December 2015, Changsha, China

Lin J.H., Xu Y.L., Zhu S.Y. and Xia Y. “A Hybrid Identification Method of Wind Pressure on Straight Blade of Vertical Axis Wind Turbine”, Proceedings of the 6th

International Conference on Structural Health Monitoring of Intelligent Infrastructure, 9-11 December 2013, Hong Kong

Lin J.H., Xu Y.L., Zhu S.Y. and Xia Y. Distributed Load Identification for Vertical Wind Turbine Straight Blade[C]. The 12th International Symposium on Structural Engineering, 2012.

Xu, Y. L., Zhang, J., Xia, Y., Li, J., & **Lin, J. H.** "Damage Detection and Reliability Assessment of Building Structures Using Stochastic Approaches." The 6th International Workshop on Advanced Smart Materials and Smart Structures Technology. 25-26 July 2011, Dalian, China.

ACKNOWLEDGEMENTS

First, I would like to express my sincere gratitude to my chief supervisor, Prof. You-Lin Xu, for giving me the opportunity to pursue my Ph.D. study in The Hong Kong Polytechnic University, which is a definitely a great challenge and achievement in my life. I deeply appreciate his expert guidance, extensive discussion, excellent training, continuous care and support throughout the course of my study in five years. Under Prof. Xu's five-year supervision and inspiration, I have a better understand of my own research work and learn a lot from his conscientious and positive attitude towards research.

I would like to express my profound appreciation to Mr. Sheng Zhan and my co-supervisors, Dr. Yong Xia and Dr. Song-ye Zhu, for their continuous care and encouragement. Their positive attitude and extraordinary experience in research inspired me. I also give my thanks to Dr. Chao Li, Dr. Wan-ai Li, Dr. Yi Han and Dr. Xian-rong Cen for their helps in CFD simulation and ANSYS. I would also like to express my special appreciation to my master degree supervisor, Prof. Ming-hui Fu. His encouragement and guidance are important to me.

I wish to particularly thank the committee members, Prof. Kwok-Fai Chung from our department, Dr. Suren Chen from Colorado State University, and Prof. Chun-Man Chan from the Hong Kong University of Science and Technology, for their valuable and insightful comments to my thesis and taking their time to attend my oral examination.

My thanks also go to former and current members of Prof. Xu's research groups, and friends in PolyU, Dr. Zhi-wei Chen, Dr. Liang Hu, Dr. Peng Zhang, Dr. Hong-wen Xia, Dr. Xiao-hua Zhang, Dr. Bin Wang, Dr. Wen-feng Huang, Dr. Qing Huang, Dr. Jia-zhan Su, Dr. Xiao-liang Meng, Dr. Xiang Xiao, Dr. Jia He, Dr. Wen-ai Shen, Dr. Jin-hua Li, Dr. Yue Zheng, Dr. Feng-yang Wang, Mr. Chao-dong Zhang, Miss. Yi-xin Peng, Mr.

Jian-fu Lin, Mr. Rong-pan Hu, Mr. Bin Sun, Mr. Zi-lu Wang, Dr. Meng-shi Zhang, Dr.Wen-yu He, Dr. Can-xing Qiu, Mr. Wei-qiang Feng, Dr. Yao-peng Liu, Dr. Man Fong, Dr. Si-wei Liu, Mr. Bo Li, Mr. Huan-jian Mo, Mr. Wen-feng Chen, Mr. Yi-qun Tang, Dr. Ke-lang Lu, Dr. Qiong-guan Xiao and Dr. Bing Zhang for their warm support and assistance.

Getting through my Ph.D. study required more than academic support, and I have many people to thank for accompanying me over the past five years. I also express my gratitude and appreciation for their friendship.

Finally and most importantly, I am deeply grateful to my parents and my girlfriend for their unconditional love and support.

TABLE OF CONTENTS

LIST OF FIGURES

LIST OF TABLES

LIST OF NOTATIONS

α	angle of attack (AOA)
α_r	AOA with zero-pitch
β	pitch angle
β_u	undulation angle of PW FRP
ε	strain
ε_A	strain range of a strain cycle with zero-mean
$\varepsilon_{\max}$	maximum strain in a strain cycle
$\varepsilon_{\min}$	minimum strain in a strain cycle
ε_r	strain range of a strain cycle
ε_t	ultimate tension strain
ε_c	ultimate compression strain
$\bar{\varepsilon}$	mean strain of a strain cycle
ϕ	angel between relative wind speed and the rotor plane of HAWT
λ	tip speed ratio
$\gamma_{xy}, \gamma_{yz}, \gamma_{zx}$	shear strain
θ	azimuth angle

θ_b	braid angle of PW FRP
ρ	density of air
σ	normal stress or standard deviation
$\sigma_1, \sigma_2, \sigma_3$	the 1st, 2nd and 3rd principle stress
σ_u	the standard deviation of longitudinal turbulence
σ_v	von Mises stress
$\sigma_x, \sigma_y, \sigma_z$	normal stress
$\sigma_{x,\mathrm{C1}}, \sigma_{x,\mathrm{C2}}$	normal stress at node C1 and C2 in Section C
$\sigma_{x,\mathrm{hA}}, \sigma_{x,\mathrm{hB}}$	normal stress due to horizontal bending at node A2 in Section A and node B2 in Section B
$\sigma_{x,\mathrm{vA}}, \sigma_{x,\mathrm{vB}}$	normal stress due to vertical bending at node A1 in Section A and node B1 in Section B
$\sigma_{Z_o,\mathrm{D1}}, \sigma_{Z_o,\mathrm{D2}}$	normal stress at node D1 and D2 in Section D
$\tau_{xy}, \tau_{yz}, \tau_{zx}$	shear stress
v	the kinematic viscosity
ν_f	Poisson's ratio of fiber
ν_m	Poisson's ratio of matrix
ν_{yx}	Poisson's ratio of FRP
ω	rotational speed

$\boldsymbol{\Omega}$	spin matrix
A_0, A, A_1	area of the actuator disk in the momentum theory
$\boldsymbol{B}$	geometric matrix
$\boldsymbol{C}$, $\boldsymbol{C}_k$	stiffness matrix of sub cell of RVE of PW FRP; or damping matrix
$\bar{\boldsymbol{C}}$	stiffness matrix of RVE of PW FRP
$\boldsymbol{C}_{\mathrm{C}}$	additional damping matrix due to the Coriolis force
C_d	the drag coefficient
C_l	the lift coefficient
C_M	the moment coefficient
C_n	the normal force coefficient
C_t	the tangential force coefficient
C_p	power coefficient
$C_{p,\max}$	the maximum power coefficient
Coh	the corresponding coherence function
D	drag force or fatigue damage
$\boldsymbol{D}_C$	material matrix of concrete
$\boldsymbol{D}_S$	material matrix of steel

E_f	Young's modulus of fiber
E_m	Young's modulus of matrix
E_x, E_y, E_z	Young's modulus of FRP
$\boldsymbol{F}_C$	Coriolis' force vector
F_{cen}	centrifugal force
F_{Cor}	Coriolis' force
F_d	aerodynamic drag of blade in the downwind side
$\bar{F}_d$	streamwise force exerted by the downwind actuator disk
$\boldsymbol{F}_E$	centrifugal force vector
$\boldsymbol{F}_E^{'}$	constant component of the centrifugal force
$\boldsymbol{F}_G$	gravity force vector
F_n	normal force
F_t	tangential force
F_u	aerodynamic drag of blade in the upwind side
$\bar{F}_u$	streamwise force exerted by the upwind actuator disk
$\boldsymbol{F}_W$	wind load vector
F_X,F_Y,F_Z	force component

G_f	shear modulus of fiber
G_m	shear modulus of matrix
G_{xy}, G_{yz}, G_{zx}	shear modulus of FRP
$\boldsymbol{H}(f)$	Cholesky decomposition of cross-spectral density matrix
$H_{jm}(f)$	an element of $\boldsymbol{H}(f)$
$\mathrm{Im}\left[H_{jm}(f)\right]$	the image part of the complex function $H_{jm}(f)$
$\mathrm{Re}\left[H_{jm}(f)\right]$	the real part of the complex function $H_{jm}(f)$
$I(z)$	the turbulence intensity
I_{ref}	the respected turbulence intensity at a mean wind speed of 15 m/s
J_2	the second deviatoric stress invariant
$\boldsymbol{K}$	stiffness matrix
L	lift force
L_c	the coherence scale parameter
L_u	the integral length scale of longitudinal turbulence
$\boldsymbol{M}$	mass matrix
N	number of blades or the number of cycle to failure
P	Tsai-Wu strength index or power

P_{max}	maximum Tsai-Wu strength index
P_i	probability of wind speed bin i
R	strain or stress ratio
$\boldsymbol{S}$, $\boldsymbol{S}_k$	flexibility matrix of sub cell of RVE of FRP; or soften matrix due to rotation
$\overline{\boldsymbol{S}}$	flexibility matrix of RVE of FRP
$\boldsymbol{S}(f)$	the cross-spectral density function
$V^{'}(z)$	the gust wind speed at height z
V_{o}, u, u_1	wind speed
V_{∞}	the wind speed in the far upstream
V_d	wind speed in the downwind rotor of VAWT
V_e	wind speed inside the rotor of VAWT
V_{e50}	the extreme wind speed with a recurrence period of 50 years
V_f	fiber volume fraction
$V_{f,\mathrm{UD}}$	fiber volume fraction of UD FRP
$V_{f,\mathrm{PW}}$	fiber volume fraction of PW FRP
V_m	matrix volume fraction
V_{hub}	mean wind speed at the hub height

V_r	relative wind speed
V_{ref}	the reference wind speed depending on the wind turbine class
V_u	wind speed in the upwind rotor of VAWT
V_w	wind speed in the far wake of VAWT
M	aerodynamic torque of HAWT or aerodynamic moment on airfoil
R	radius of rotor
Re	Reynolds number
$S(f,z)$	the power spectrum of longitudinal turbulent wind at height z
T	trust of HAWT or aerodynamic torque of VAWT
a, a_u, a_d, a'	induction factor
c	chord length of blade
d_{bend}	measured displacement in static bending tests
f	frequency of wind speed
Δf	frequency increment
f_{up}	the upper cutoff frequency
g_v	peak factor in the theory of equivalent static wind loads
p, p_o	wind pressure

Δp	wind pressure drop
p_d	pressure in front of the downstream actuator in DMST
Δp_d	pressure drop of the downstream actuator in DMST
p_N	normal force of HAWT blade
p_T	tangential force of HAWT blade
p_u	pressure in front of the upstream actuator in DMST
Δp_u	pressure drop of the upstream actuator in DMST
Δt	time step
$\boldsymbol{u}$	displacement vector
$\dot{\boldsymbol{u}}$	velocity vector
$\ddot{\boldsymbol{u}}$	acceleration vector
u_θ	induced tangential wind velocity
z	the height above the ground
Δz	the distance between the two heights
z_{hub}	the hub height

LIST OF ABBREVIATIONS

AOA	angle of attack
BEM	blade element momentum theory
CFD	vomputational fluid dynamics
CFRP	carbon fiber reinforced plastic
CLT	classic laminate theory
DMST	double multiple streamtube theory
DNS	direct numerical simulation of turbulence
DOF	degree of freedom
EOG	extreme operation gust
EDC	extreme direction change
ECD	extreme coherent gust with direction change
ETM	extreme turbulence model
EWM	extreme wind speed model
EWS	extreme wind shear
FBG	optical fiber bragg grating
FE	finite element

FRP	fiber reinforced plastic
FSDT	first order shear deformation theory
GFRP	glass fiber reinforced plastic
HAWT	horizontal axis wind turbine
HHCL	the Hill-Hashin-Chrestensen-Lo model
HSDT	higher-order shear deformation theory
LES	large eddy simulation
LVDT	linear variable differential transformer
MBS	multibody system
NTM	normal turbulence model
NWP	normal wind profile model
PSD	power spectrum density
PW FRP	plain weave fiber reinforced plastic
RANS	reynolds-averaged Navier–Stokes equations
RVE	representative volume element
SHM	structural health monitoring
SST	shear stress transport

UD FRP	unidirectional fiber reinforced plastic
UPS	uninterruptible power system
VAWT	vertical axis wind turbine
WF	woven fabric

CHAPTER 1

INTRODUCTION

1.1 Research Motivation

Renewable energy, especially wind energy, attracts the growing interest of the world nowadays. In order to better take advantage of wind power, wind turbines have undergone considerable development in the recent decades. There are two kinds of wind turbines, horizontal axis wind turbines (HAWTs) and vertical axis wind turbines (VAWTs). VAWTs can be further classified as lift-type and drag-type. HAWTs are the mainstream at present due to their higher power efficiency. Drag-type VAWTs are low efficient and thus they are seldom applied in large-scale wind turbines. Lift-type VAWTs had a brief development in 1980s and they were then gradually out of sight in 1990s after a series of faults and accidents (Gipe, 2009). To pursue larger power capacity, the diameter of HAWTs has grown up to 120m (IEA, 2013). However, the growth in tower height and rotor diameter of HAWTs meets many challenges, and very often the cost is increased more rapidly than the increasing of power capacities. Some researchers then turn to VAWTs because VAWTs have simpler structure than HAWTs, do not suffer from the serious fatigue problem, and hence have the potential of application in larger scale wind turbines. A renewed interest in VAWTs has been seen in recent years, and there is a trend worldwide in building large-scale VAWTs.

Wind turbines are often built in areas of harsh environment. During operation, large cyclic stresses in wind turbine blades will be produced by time-varying wind loads, and the number of cycles will be in the order of 10^8 to 10^9 over a 20 to 30 years life time. Besides fatigue loads, a wind turbine is also subjected to ultimate loads in the extreme wind condition. The collapses of wind turbines due to failures of blades are reported in many references (Gipe, 2005). Therefore, to improve the design of the wind turbines, the fatigue and ultimate strength analyses are required and the critical locations of fatigue and ultimate strength failure need to be figured out. Researchers have made a great effort on this study for HAWTs (Ciang et al., 2008; Kirikera et al., 2008; Rumsey & Paquette, 2008). However, the analyses for VAWTs, especially straight-bladed VAWTs, are rare. This is because after a brief development in 1970s-1980s, VAWTs were out of sight. Due to the lack of case studies and tests, the studies of the critical locations of fatigue and ultimate strength failure for VAWTs, including blades and other components, are nearly absent.

To conduct the fatigue and ultimate strength analyses, the operational loads in different conditions should be obtained first, among which wind loads are the key components for wind turbines. For VAWTs, a few tools have been proposed to estimate wind loads, which include double multiple streamtube theory (DMST), vortex model, and computational fluid dynamics (CFD) simulation (Paraschivoiu, 2002). DMST is the simplest and most widely-used method. However, DMST cannot consider the influence of the arms and tower on the wind loads acting on the blades. Moreover, this method can only get aerodynamic forces rather than wind pressures on the blades. Although the vortex model can consider the influences of other components and obtain wind pressures, the computational cost is much higher than DMST, and the accuracy of this method is less than CFD. Many researchers now simplify a VAWT as a planar structure and conducted 2D or 2.5D CFD simulation to compute the aerodynamic forces on VAWTs (Almohammadi et al., 2013; Amet et al., 2009; Castelli et al., 2011; Danao et al., 2014; Ferreira et al., 2007; Hassan et al., 2015; Ismail & Vijayaraghavan, 2015; Lanzafame et al., 2013; Li et al., 2013; Mcintosh et al., 2008; Nini et al., 2014; Scheurich & Brown, 2013; Wang et al., 2010; Wekesa et al., 2015). Nevertheless, wind speed along the height of a VAWT is not uniform, which does not match 2D or 2.5D simulation. Furthermore, the computational cost of CFD turbulence modeling for a 3D VAWT is extremely high (Elkhoury et al., 2015; Nini et al., 2014; Siddiqui et al., 2015).

Therefore, almost all researchers adopt the steady inflow boundary when they study wind loads on a VAWT, and the influence of turbulent inflow on wind loads is less investigated. For HAWTs, this problem has been studied for years (Burton et al., 2001). A basic method is to use the blade element momentum theory (BEM) and the Taylor's frozen hypothesis to calculate the aerodynamic forces. Empirical dynamic inflow models were also proposed in this regard (Snel et al., 1995). However, these methods are for HAWTs only, while the aerodynamics of VAWTs is quite different from HAWTs. There are no enough studies to verify the applicability of these methods for VAWTs. As a result, the performance of a VAWT in unsteady wind conditions attract many attentions in recent years (Danao et al., 2013; Danao et al., 2014; Mcintosh et al., 2007, 2008; Scheurich & Brown, 2013; Wekesa et al., 2015). However, only simple sinusoidal variation wind speeds are considered in these studies, which is quite different from real atmospheric turbulent inflow. Therefore, a practical and efficient simulation method is needed to accurately and efficiently estimate the wind loads on the VAWT with the consideration of the influence of all structural components, the mean wind profile and the turbulence.

For wind turbines, blades are the most costly and important components and it is therefore worth paying special attention to the analysis and design of blades. Nowadays, fiber-reinforced plastics (FRP) laminated materials are widely used in making wind turbine blades (Burton et al., 2001). FRP is composed of fiber (glass or carbon) and matrix (resin). There are different textile structures that fiber and matrix can be combined together, such as unidirectional FRP (UD FRP) and plain woven FRP (PW FRP). A laminate is composed of multiple layers (plies) of FRP and adjacent layers are usually bonded together by latex. Hence, there exist many interfaces in an FRP laminate. Under different load cases, such as extreme and normal operation loading cases, ultimate strength and fatigue failures may take place in these interfaces (Jones, 1975). According to the first-ply failure criteria (Gohari et al., 2015; Reddy & Pandey, 1987), when one ply of a laminate failure, the laminate is considered out of work. Therefore, the stress or strain analysis at the ply level is important and necessary.

To obtain accurate laminar stresses and strains, precise elastic constants at each ply are necessary. Usually, the laminar elastic constants of FRP are unknown. Even though the certified values are given, there exist unavoidable uncertainties due to large manufacturing tolerances unlike the single-constituent material, such as glass fiber and resin which have less uncertainties of the certified values. Therefore, the model updating or calibration techniques are needed. (Behmanesh et al., 2015; Brownjohn & Xia, 2000; Friswell & Mottershead, 1995; Jaishi & Ren, 2005). Many researchers were devoted themselves to the approaches of identifying the elastic constants of composite, (Avril et al., 2008; Cunha & Piranda, 1999; Cugnoni et al., 2007; De Wilde et al., 1984; Deobald & Gibson, 1988; Genovese et al., 2004; Gras et al., 2013; Grédiac & Paris, 1996; Larsson, 1997; Lecompte et al., 2007; Mishra & Chakraborty, 2015; Mishra & Chakraborty, 2015; Moussu & Nivoit, 1993; Molimard et al., 2005; Rahmani et al., 2013; Schwaar et al., 2012; Van Buren et al., 2013). However, most of the methods can only identify the elastic constants of laminated composite rather than laminar properties. Although some researchers indeed identified laminar or even constituent properties (A. Mishra & S. Chakraborty, 2015; A. K. Mishra & S. Chakraborty, 2015), there are too many elastic constants to be identified. With the increasing layer number of a laminate, the number of parameters will increase dramatically. It is thus difficult to identify the laminar elastic constants directly. Therefore, a practical method is required to update the laminar elastic constants of laminated composite blades.

Usually, a wind turbine is established in an uninhabited area and exposed to various environmental effects, such as typhoons, earthquake and collisions. Inspection and maintenance must be carried out regularly. Hence, enormous cost and effort are required (Ciang et al., 2008; Fingersh et al., 2006; Walford, 2006). From 1989 to 2006, about 64,000 incidents were reported from 1,500 onshore wind turbines, which were counted by the Institute for Solar Energy Technology (ISET). Hence, the installation of structural health monitoring (SHM) system on wind turbines has become a trend to monitor wind condition, to ensure the functionality and safety during long-term service and to reduce the cost of maintenance and inspection. SHM has been widely applied in

HAWTs. However, the reports on the SHM system for VAWTs are rare and the sensor placement of SHM systems is lack of guidance. The method to establish a SHM system for VAWTs needs to be studied.

Besides SHM systems, control systems are also widely applied in wind turbines. Compared with HAWTs, the disadvantages of VAWTs are difficulties in start-up and shut-down and the lower power coefficient. In 1980s, the interest was focused on the Phi-type VAWT without the ability of pitch regulation (Paraschivoiu, 2002; Sutherland et al., 2012) and the straight-bladed VAWTs, which have the potential in pitch regulation, were not the mainstream. Hence the pitch control VAWTs were seldom studied in those years (Lazauskas, 1992; Vandenberghe and Dick, 1986). A pitch variation system has the possibilities of bettering the start-up process, improving the power coefficient below the rated wind speed, maintaining the output power at the rated value above the rated wind speed and assisting the shut-down process in high wind. However, for straight-bladed VAWTs, most of the previous literatures only focus improving the power coefficient (Hwang et al., 2005; Hwang et al., 2006; Kosaku et al., 2002; Liu et al., 2015; Paraschivoiu et al., 2009; Zhang et al., 2015).

Generally, large-scale wind turbines need both the SHM system and the control system. Both of the systems require sensors and data acquisition and signal transmission systems. However, the primary objectives of these two systems are different, the two systems are often treated separately. But a separate approach is not practical and cost-effective. Hence, it is necessary to synthesize the SHM and control systems together (He et al., 2014; Xu et al., 2015). Moreover, the power supply is important factors for the design of both the SHM and control systems (Huston, 2010). Batteries are often used in the devices of SHM and control system but recharging or replacing batteries brings about difficulties for wind turbines which are usually located in uninhabited area. Power from the electric grid is a good choice but it will be cut off in the extreme event, such as hurricane or earthquake; but the SHM or control systems are valuable and cannot be absent in these cases. Researchers have proposed many solutions to these problem, such as developing lower-power consumption sensors (Lin et al., 2015) and energy harvesting methods (Chalasani & Conrad, 2008; Shen et al., 2012; Stanton et al., 2010; Zhu et al., 2012). However, it is special that a VAWT itself is an energy harvesting machine. It is promising that the systems of power generation, SHM and control can be synthesized together to form smart wind turbines and extensive researches should be performed in this area.

In view of the problems outlined, this thesis is devoted to a systematic and novel study of large-scale VAWTs, which includes the determination of wind loads on all the components of the VAWT using computational fluid dynamics (CFD) simulation, the finite element modelling and model updating of laminated composite blades, the fatigue and ultimate strength analyses of blades and other components of the VAWT, the pitch control systems for four states of the VAWT, the structural health monitoring (SHM) of the VAWT, and the concept of the smart VAWT.

1.2 Research Objectives

This thesis focuses on the fatigue and ultimate strength analyses of large-scale VAWTs with monitoring and control. The major objectives are as follows:

1. Propose a method for determining wind loads, including wind pressures and aerodynamic forces, on the whole VAWT. This method can consider the influences of the existences of arms and tower, the variation of mean wind speed along the height of the VAWT, and the turbulence. Simulate the wind loads in different operation and wind speed conditions. Evaluate the influences of the existence of the tower, arms and turbulent inflow on aerodynamic forces on the blades.

2. Establish a FE model of composite blade using laminate shell elements so that the laminar stresses can be obtained. Propose a laminar elastic constants updating method

using micromechanics models. Conduct sensitivity studies to determine the parameters of the micromechanics models to be identified. Identify these parameters by static tests.

3. Propose a fatigue and ultimate strength analysis framework for blades. Figure out the fatigue-critical locations of blades. Evaluate the influences of turbulence and mean wind on fatigue life. Study the influences of material strengths, damping ratio, modal frequencies and wind speed distribution (Weibull model parameters) on fatigue life. Figure out the failure-critical locations and the locations with large inter-laminar stresses and study the influence of the wind direction on the stress of the blade.

4. Propose a framework for fatigue and ultimate strength analysis of a VAWT except its blades. Establish a FE model of VAWT by beam elements. Propose a two-step calculation method to obtain the responses of rotor and tower based on the rotating frame. Figure out the fatigue critical locations of the VAWT in operation conditions and the failure-critical locations in the extreme wind conditions.

5. Conduct the field measurement for a straight-bladed VAWT. Evaluate the rotational speed, wind speed, and the natural frequencies of the VAWT. Update the FE model by natural frequencies. Validate the proposed fatigue and ultimate strength analysis framework by comparing the measured responses with those of simulation in the frequency domain.

6. Study the pitch control algorithms for straight-bladed VAWTs based on the double multiple streamtube method (DMST) and propose a pitch control system. Propose an SHM system for the straight-bladed VAWT based on the results of fatigue and ultimate strength analyses. Propose a concept of smart VAWT by synthesizing the SHM, control and power supply systems.

1.3 Assumptions and Limitations

The development of fatigue and ultimate strength analysis methods and the applications of SHM and control technologies to large-scale VAWTs in this thesis are subjected to the following assumptions and limitations:

1. The wind load simulation method is based on the strip analysis and 2D simulation; hence the 3D effect is ignored. Accordingly, the vertical components of wind speed and wind loads are ignored.

2. Although the turbulence is considered in the inflow in the CFD simulation, only the vertical correlation is considered and the inflow wind speed is identical at the same height.

3. It is assumed that the along wind component of turbulence in the inflow wind speed is larger than the lateral and vertical components, so that only the along wind turbulence is considered in the inflow wind speed of the CFD simulation.

4. It is assumed that VAWTs operate at the constant speed, so that the process of startup and shutdown are not considered in the wind load simulation and the fatigue analysis.

5. It is assumed that the material properties of fiber and matrix, such as glass and polyester resin, are already known and the uncertainties in the elastic constants of fiber and matrix can be ignored so that only the fiber volume fractions are needed to be updated.

6. It is assumed that the deformation of arms which support the blade is small so that the blade can be studied solely in the rotating reference frame.

7. It is assumed that the tower is axially symmetric so that the dynamic calculation can be conducted in the rotating reference frame to eliminate the rigid motion and the rotation of the tower in this frame can be ignored.

8. It is assumed that the wind field will not change quickly when pitch angle changes so that the quasi-steady assumption is still valid. In this assumption, DMST is used to calculate the aerodynamic force when pitch changes.

1.4 Outline of the Thesis

This thesis covers a variety of research topics to achieve the aforementioned objectives. It is divided into 9 chapters and is organized as follows:

Chapter 1 introduces the motivation for this study and states its objectives, assumptions and limitations.

Chapter 2 contains a literature review on relevant topics. The types and development histories of wind turbines are reviewed first. The wind load simulation methods of wind turbines are then discussed. The fatigue analysis and the ultimate strength analysis are also reviewed in brief in this chapter.

Chapter 3 presents a method for determining wind loads, including wind pressures and aerodynamic forces, on the whole VAWT. Based on the strip analysis method and 2D CFD simulation, the influences of the existence of arms and tower on the aerodynamic forces and wind pressures on the blades, the variation of mean wind speed along the height of the VAWT, and the effects of the turbulent wind are all considered by this method. The influences of the existence of the tower, arms and turbulent inflow on aerodynamic forces of the blades are further evaluated.

Chapter 4 establishes a FE modeling scheme of composite blades so that the laminar stresses can be obtained. Then micromechanics models are applied in the identification of laminar elastic constants. Sensitivity studies are carried out to determine the parameters of the micromechanics models to be identified. To identify these parameters, static tests are conducted. Based on the measured responses and the FE model of the static tests, the chosen parameters of the micromechanics models are updated by the pattern search algorithm. The proposed method is verified by the measured data which are not used in the updating procedure.

Chapter 5 proposes a fatigue and ultimate strength analysis framework for composite blades. In the fatigue analysis, fatigue-critical locations are figured out. The influences of turbulence and mean wind on fatigue life are specified. Parametric analyses are also conducted to study the influences of material strengths, damping ratio, modal frequencies and wind speed distribution (Weibull model parameters) on fatigue life. For the ultimate strength analysis, the influence of the wind direction on the stress of the blade is considered and the failure-critical locations and the locations with large inter-laminar stresses are also figured out.

Chapter 6 proposes a framework for fatigue and ultimate strength analysis of VAWTs except blades is proposed. The rotating frame method is used for analyzing fatigue damage and ultimate strength of all components of the VAWT except for blades and tower. The responses of the tower are then obtained by a two-step calculation method. Based on this two-step calculation method, the fatigue analysis of the whole turbine in the normal wind conditions and the ultimate strength analysis in the extreme wind conditions are conducted. The fatigue critical locations of the VAWT in operation conditions and the failure-critical locations in the extreme wind conditions are figured out.

Chapter 7 analyzes the field measurement results for a straight-bladed VAWT to update the FE model in Chapter 5 and validate the frameworks proposed in Chapter 5 and

Chapter 6. Using the measured data, the natural frequencies of the VAWT are identified and the model updating is then conducted for the FE model. Finally, the measured results are used to compare with the corresponding simulated responses in the frequency domain.

Chapter 8 compares two pitch control algorithms for straight-bladed VAWTs in different operational states based on DMST and establishes a pitch control system. Then an SHM system for VAWTs is proposed based on the works of Chapter 5 and Chapter 6. Finally, by synthesizing the SHM, control and power supply systems for a VAWT, the concept of smart VAWTs is given.

Chapter 9 summarizes the contributions, findings and conclusions of this study. Limitations of this study are also discussed and some recommendations for future study are provided.

CHAPTER 2

LITERATURE REVIEW

2.1 Energy Harvesting and Wind Power

With the advancement of science and technology in the few decades, human society develops in an unprecedented speed. Not only the world population increased from 2,521 million in 1950 to 7052 million in 2012, but also the consumption of energy increased from 1.0 TWh in 1950 to 23,537 TWh in 2012. The constituents of the energy were varying all the time. In 1950, the energies were mainly composed of coal, petroleum and natural gas which are fuel resources and non-renewable. However, these traditional non-renewable energy resources are limited. The growing demanding on the limited resources would lead to the energy crisis. On the other hand, these traditional energy resources have serious impacts on the environment. Besides the global warming due to the emission of carbon dioxides by burning fuel resources, the fine particulate matter (PM2.5) also cause serious health problems (Hoek, et al. 2013).

Nuclear power is one of the alternatives to fuel resources. The nuclear power increases from 25.7 TWh in 1965 to 2,536.8 TWh in 2014. However, there is always a social debate about the nuclear power. Some people insist that the nuclear power is safe and can efficiently reduce carbon emissions while some people argue that nuclear plants pose threats to people and the environment. The fact is that in the Three Mile Island accident in1979, no deaths were reported at that time but cancer or leukemia, have been found in follow up studies of this accident; the Chernobyl accident in1986 caused a predicted eventual total death toll from 4000 to 25,000 due to latent cancers deaths. The Fukushima Daiichi nuclear disaster in 2011 has not caused any radiation related deaths but the predicted eventual total death toll is from 0 to 1000. Moreover, the fuel that nuclear power plants use for nuclear fission is uranium and uranium is a non-renewable resource.

Therefore, safe renewable energy attracts many attentions. Renewable energies include hydropower, wind power, solar photovoltaic (PV), geothermal, biomass, etc.. Hydropower has been applied for years. The global hydropower capacity is up to 1,064 GW in 2015 and 3,885 TWh is generated. Hydropower does not pollute the water or the air. However, hydropower facilities can have large environmental impacts by changing the environment and affecting land use, homes, and natural habitats in the dam area. Most hydroelectric power plants have a dam and a reservoir. These structures may obstruct fish migration and affect their populations. Operating a hydroelectric power plant may also change the water temperature and the river's flow. There are still social debates about the influences of these changes on the environment. Reservoirs may cover people's homes, important natural areas, agricultural land, and archeological sites. So building dams usually require relocating people.

In this regard, other renewable energy, especially wind power, increases very quickly in these years. The consumption of the renewable power except hydropower increases from 228.8 TWh in year 2000 to 1400 TWh in year 2014 (BP, 2016). The capacity of these renewable energy reaches 785 GW in 2015, of which 433 GW is produced by wind power (Sawin et al, 2016). Compared with other energies, there are many advantages of wind power. It is clean, and wind-generated electricity does not pollute the air, water or soil. It also does not create acid rain, radioactive waste, or generate CO_2 emissions which contribute to global warming. Additionally, wind power does not consume the large amounts of water needed by other energy sources, such as nuclear power and fuel. It is renewable. Unlike fossil fuels, the kinetic energy of wind comes from the solar radiation which is unlimited. It is compatible with other land uses. The direct impact area (both temporary and permanently disturbed land) is about 1 ± 0.7 hectare/MW (Hand et al., 2009), while the establishment of a dam may significantly change the land use, such as the Three Gorges Dam (Zhang et al., 2009). The vast majority of land remains free to use in other ways, including ranching, farming, mineral development, hunting, recreation, and many other activities. It promotes national security and energy independence. Wind energy is homegrown. It cannot be embargoed, and because the wind is free, it is not subject to the dramatic price volatility of fossil fuels. Wind-generated electricity diversifies our energy supply, reduces our dependence on foreign fuels, and reduces the flow of our energy dollars to potentially hostile governments, which increases our national security. It is fast to install. Large utility-scale wind power plants can be built in less than one year. By contrast, most other large power plants take years to construct.

The market of wind power is huge and growing quickly. Take China for example, wind-generated electricity was just over a 100 TWh in 2012, accounting for 2% of the country's total electricity output, while wind power generation reached 186.3 TWh in 2015, accounting for 3.3% of total electricity generation (Sawyer and Rave, 2016). The generated wind power almost double in 3 years. The future market of wind power can be seen from the 13th Five-Year Plan of Chinese government, which includes an objective for non-fossil renewable energy consumption to reach 15% by 2020 and 20% by 2030; for wind power, the target is to reach cumulative installed capacity of 250 GW by 2020 (Jiang et al., 2015).

2.2 Wind Turbines

2.2.1 Wind turbines types

A wind turbine is a device that converts kinetic energy from wind into electrical power. Wind turbines can be divided into horizontal axis wind turbines (HAWTs) and vertical axis wind turbines (VAWTs) according to the direction of the axis of rotation. A HAWT has a set of blades that rotate about an axis, the direction of which is horizontal, while a VAWT has a set of blades that rotate about an axis, the direction of which is vertical.

According to the position of the rotor in operation, HAWTs can be further divided into the upwind type and the downwind type, as shown in Fig. 2.1. Upwind HAWTs have the rotor facing the wind. The basic advantage of upwind designs is that one avoids the wind shade behind the tower, while the basic drawback of upwind designs is that the rotor needs to be made rather inflexible and placed at some distance from the tower to avoid the collision between blades and tower, because blades will bend at high wind speeds and get close to the tower. Additionally, an upwind machine needs a yaw system to keep the rotor facing the wind. Downwind HAWTs have the rotor placed on the lee side of the tower. For small HAWTs, one advantage of this type is that they do not need a yaw system but for large HAWTs, a yaw system is still necessary. The main advantage of the downwind type is that the rotor can be more flexible and thus lighter. When blades bend at high wind speeds, they just get away from the tower other than get close. The basic drawback is the fluctuation of blades due to the rotor passing through the wind shade of the tower. This may give more fatigue loads on the turbine than upwind HAWTs.

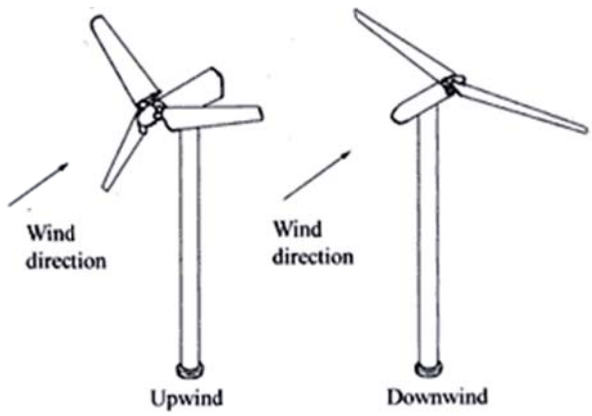

Fig. 2.1 Upwind type and downwind type HAWT

VAWTs consist of two major types, the Darrieus rotor and Savonius rotor. The Darrieus wind turbine is a VAWT that rotates around a central axis due to the lift force of blades, whereas a Savonius rotor rotates due to the drag force of blades. According to the configuration of the blade, there are three shapes of Darrieus

VAWTs: the H-type (straight-bladed), the Phi-type (or eggbeater type) and the helical (twisted) type as shown in Fig. 2.2. For Savonius VAWTs, the traditional configuration is shown in Fig. 2.3(a) and a newly developed Savonius has a twisted blade as shown in Fig. 2.3(b). There is also a new type of VAWT which is a mixture of the Darrieus and Savonius designs shown in Fig. 2.3(c).

(a) (b) (c)

Fig. 2.2 Darrieus VAWTs. (a) H type; (b) eggbeater type; (c) helical type.

(a)

(b)

(c)

Fig. 2.3 Savonius VAWTs. (a) traditional configuration; (b) twist type; (c) mix type

2.2.2 Horizontal axis wind turbines (HAWTs)

The application of HAWTs is earlier than VAWTs. In 1930s, a 100 kW HAWT was in service in Yalta, USSR. HAWTs are the most popular and widely used type of wind turbine and are also the main subject of wind turbine research for decades.

Through a long time study and application, it is found that HAWTs have the following advantages: 1) HAWTs have higher efficiency than VAWTs, since the blades always move perpendicularly to the wind, receiving power through the whole rotation. In contrast, blades of all VAWTs move from upwind to downwind side to and fro and blades in the downwind side has less efficiency; 2) HAWTs have the capability of variable blade pitch which can help the turbine to harvest more energy under the rated wind speed, maintain the power above the rated wind speed and stop at the high wind.

In order to harvest more energy through higher efficiencies, the size of HAWTs is growing over the years. Ciang(2008) summarized the increasing of the rotor size with the years. In 1980s, a HAWT generally had the diameter of 15m; in 2007, the diameter is increased to 126m (Ciang et al., 2008). Nowadays, offshore HAWTs have been built up to 8MW and have a blade length up to 80m. The disadvantages of HAWTs are more and more obvious: 1) Large-scale HAWTs suffer from sever fatigue and structural failure problems. The cantilever blades bring about serious fatigue problems. To satisfy the design requirement of fatigue and ultimate strength, the cost of HAWTs increases dramatically with the growing size of the rotor; 2) stronger tower construction is required to support the heavy blades, gearbox, and generator; 3) large-scale HAWTs require a complicate yaw system which largely increase the cost. Therefore, the increasing of the size of HAWT is obviously slow down. It seems that the development of HAWTs comes to a bottleneck.

2.2.3 Vertical axis wind turbines (VAWTs)

The eggbeater-type Darrieus VAWT was invented by a French aeronautical engineer Georges Jean Marie Darrieus who gained the patent in 1931. Actually, his previous patent in 1927 already covered many possible configuration including straight-bladed (H-type) VAWTs. The idea of using the eggbeater shaped is to minimize the blades' bending stress. Darrieus VAWTs, though, had been invented in 1920s, the main development is in 1970s - 1980s. The first known test about the eggbeater-type Darrieus wind turbine was conducted by R.S. Rangi and P. South (South & Rangi, 1975) of the National Research Council of Canada. Then, many research works were carried out by the Sandia National Laboratories (SNL) to develop the eggbeater-type Darrieus rotor including the experimental testing (Reuter & Worstell, 1978) and performance prediction models (J. H. Strickland, 1975) and field testing (Ashwill, 1992). A 34-meter test bed phi-configuration Darrieus with a rotor 34m in diameter was built by Sandia National Laboratories; this VAWT dedicated in May 1988 and also decommissioned in 1998 (Sutherland et al., 2012). The FloWind Corporation had made a great attempt to popularize Darrieus VAWTs in 1980s. In California, hundreds of Eggbeater-type Darrieus VAWTs were built and some of these VAWTs were damaged by their aluminum blades weakening and flying off after operating for only several hundreds of hours (Gipe, 2009). Not one of these turbines is operating today. In Canada, Eole, a phi-configuration Darrieus with a rotor 64 m in diameter and 96m in tall, operated from 1987 to 1993; it was stopped due to the damage of the bearing (Paraschivoiu, 2002). Then the funding for researches on VAWTs is stopped and large size Derrieus VAWTs were gradually out of sight. The main drawback of eggbeater VAWTs is the inability of pitch variation so that many flying off accidences occurred in the high wind.

In the recent years, the interest of researchers refocused on VAWTs due to the potential to be applied in the urban area (small size VAWTs) and the offshore (large size VAWTs). VAWTs have simpler structures than HAWTs and suffer from less fatigue problems. But this time straight-bladed VAWTs are on the hot spot. The reason is that straight-bladed VAWTs have the variable pitch capability if a control system is installed. The early studies of the straight-bladed Darreius were mainly began by Moran (Moran, 1977). From then on, several tests on this type of VAWT were conducted (Bravo et al., 2007; Fiedler & Tullis, 2009; Howell et al., 2010; McLaren et al., 2012). A straight-bladed Darrieus was also applied in the tidal power generation (Khan et al., 2009). From the previous tests, some problems of VAWTs were found. For instance, the aerodynamic forces are not as clear as those of HAWTs; the experimental power coefficient of a small straight-bladed Darrieus is only between 0.25 and 0.35, which is lower than HAWTs; straight-bladed VAWTs are difficult in self-starting. To improve the performance of VAWTs, more effort should be paid.

2.3 Methods for Analyzing VAWTs

2.3.1 Aerodynamic analysis

2.3.1.1 Blade element momentum theory (BEM)

Blade element momentum theory is first used to estimate the aerodynamic forces on blades of HAWTs. The theory is based on the assumption that the rotor can be regarded as an actuator disk. When the airflow across the disk, the pressure would have a sudden drop and the forces acting on the blades are equal to the change in momentum of the airflow. The blade is discretized into many blade elements. Based on the quasi-steady assumption, the aerodynamic forces are calculated by the local relative velocity of each blade element and the aerodynamic coefficients obtained from wind tunnel tests. Since the local velocity at the disk is unknown, the aerodynamic forces should be calculated iteratively. The details of the BEM are introduced below.

BEM is based on the momentum theory. In mathematics, the rotor is modeled as an ideal actuator disk. It is assumed that the flow into and out of this disk is axial. The flow is non-compressible, hence density remains constant, and there is no heat transfer. The trust is uniform in the disk. When the flow gets across the disk, the pressure would drop. The systematic diagram of streamlines flowing through the actuator disk is shown in Fig. 2.4. The distributions of wind speed and pressure are shown in Fig. 2.5(a) and Fig. 2.5(b) respectively. The wind speed and the pressure at the far upstream are V_o and

p_o respectively. p_o is the atmospheric pressure. When the wind gets across the rotor, a portion of wind kinetic energy is converted into the mechanical energy of the rotor, thus the wind speed would be reduced. Hence, the wind speed would decrease from V_o at the far upstream to u_1 at the far downstream. When the flow gets across the disk, the pressure drops suddenly and the drop of pressure is denoted as Δp. Then the pressure would gradually resume the atmospheric pressure p_o at the far downstream.

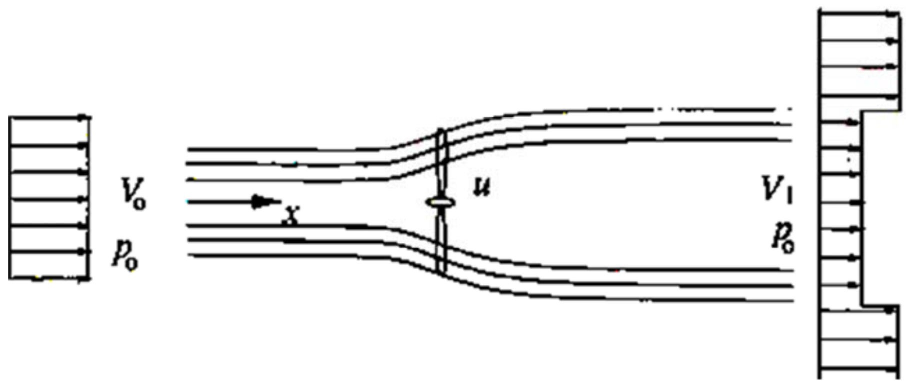

Fig. 2.4 a systematic diagram of streamlines flowing through a rotor of HAWT.

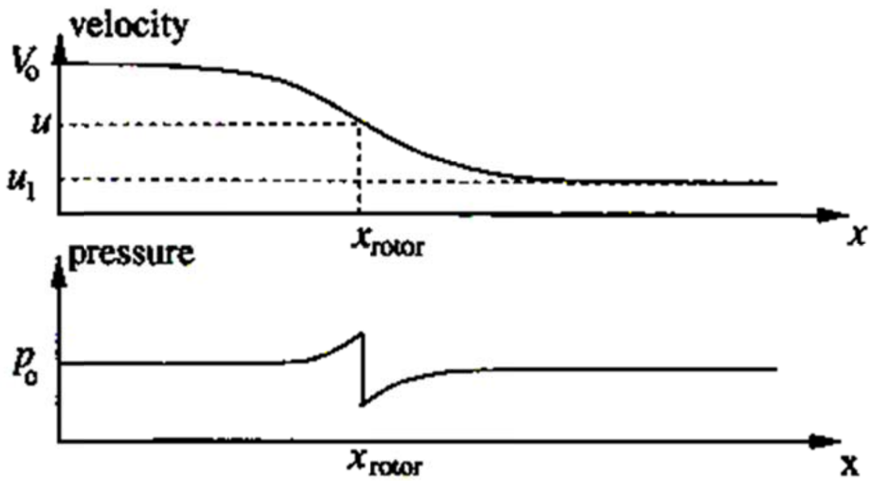

(b)

Fig. 2.5 Distributions of wind speed and pressure. (a) wind speed; (b) pressure.

Based on Bernoulli equations, the streamlines in front and below the disk satisfy

Equation (2.1a) and Equation (2.1b)

$$p_0 + \frac{1}{2}\rho V_0^2 = p + \frac{1}{2}\rho u^2 \quad (2.1a)$$

$$p - \Delta p + \frac{1}{2}\rho u^2 = p_0 + \frac{1}{2}\rho V_1^2 \quad (2.1b)$$

where u is the wind speed at the disk; p is the pressure just in front of the disk. From Equation (2.1a) and Equation (2.1b), there is

$$\Delta p = \frac{1}{2}\rho(V_0^2 - V_1^2) \quad (2.2)$$

Therefore, the trust can be expressed by

$$T = A\Delta p \quad (2.3)$$

where A is the area of the disk. According to the conservation of mass, there is

$$V_0 A_0 = uA = V_1 A_1 \quad (2.4)$$

Because $V_0 > u > u_1$, hence $A_0 < A < A_1$. By applying Equation (2.4) into Equation (2.3), there is

$$T = A\Delta p = \frac{1}{2}\rho A(V_0^2 - V_1^2) \quad (2.5)$$

On the other hand, the whole streamtube shown in Fig. 2.4 is selected as the control volume. According to momentum theorem, it has

$$\rho A_1 V_1^2 - \rho A_0 V_0^2 = -T \quad (2.6)$$

From Equation (2.5) and Equation (2.6), the following relation can be obtained

$$u = \frac{V_0 + V_1}{2} \tag{2.7}$$

Define the induction factor as

$$a = \frac{u}{V_0} \tag{2.8}$$

Hence,

$$V_1 = (2a - 1)V_0 \tag{2.9}$$

The adsorbed power by the rotor can be written as

$$P = \frac{1}{2}\rho V_0^3 A_0 - \frac{1}{2}\rho V_1^3 A_1 = \frac{1}{2}\rho u A(V_0^2 - V_1^2) = 2\rho A a^2 (1-a) V_0^3 \tag{2.10}$$

The power coefficient C_p is defined as

$$C_p = \frac{P}{\frac{1}{2}\rho A V_0^3} = \frac{2\rho A a(1-a)^2 V_0^3}{\frac{1}{2}\rho A V_0^3} = 4a^2(1-\mathrm{a}) \tag{2.11}$$

Therefore, the maximum power coefficient $C_{p,\max}$ can be obtained

$$C_{p,\max} = \frac{16}{27}, \text{ when } a = \frac{2}{3} \tag{2.12}$$

This maximum power coefficient $C_{p,\max}$ is called the Betz limit.

The above derivation can only obtain the maximum power $C_{p,\max}$ of HAWTs but the aerodynamic force of blades is still unknown. To further obtain the aerodynamic force, the BEM theory is used. The essential ideal of the BEM theory is that the whole streamtube shown in Fig. 2.4 is divided into small streamtubes and the momentum theory is applied in these streamtubes. Therefore, the rotor area is divided into annular rings of small thickness, as shown in Fig. 2.6, so that the induction factor are constant throughout the annular ring (disregarding the mean wind profile). An assumption of this approach is that annular rings are independent of one another i.e. there is no interaction between the fluids of neighboring annular rings.

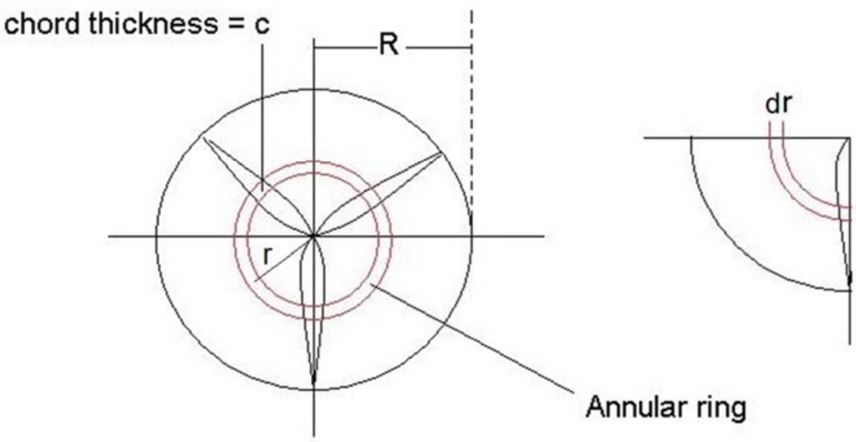

Fig. 2.6 Annular rings as the control volume

In each control volume, the cross area in the rotor section is $2\pi rdr$. Hence, Equation (2.5) can be written as

$$dT = \rho\pi r(V_0^2 - V_1^2)\,\mathrm{d}\,r = 4\pi\rho r V_0^2 a(1-a)\,\mathrm{d}\,r \tag{2.13}$$

where dT is the trust added on the annular ring. The torque can be written as

$$dM = 4\pi r^3 \rho V_0 \omega a a' dr \tag{2.14}$$

where a' is the tangential induction factor which is defined as

$$a' = \frac{u_\theta}{2\omega r} \tag{2.15}$$

where u_θ is the induced tangential velocity.

On the other hand, the trust and the torque can be calculated from the aerodynamic force of the blade. The local wind speed in the rotor plane is shown in Fig. 2.7. $V_o a$ is the axial wind speed at the rotor; $\omega r(1+a')$ is the tangential component of the wind speed in the rotor plane; V_r is the relative wind speed respect to the rotating blade; ϕ is the angle between V_r and the rotor plane; β is the pitch angle of the blade, defined as the angle between the chord line and the rotor plane; $\alpha = \phi - \beta$ is the angle of attack (AOA). L is the lift force; D is the drag force.

$$L = \frac{1}{2}\rho V_r^2 c C_l(\alpha) \tag{2.16a}$$

$$D = \frac{1}{2}\rho V_r^2 c C_d(\alpha) \tag{2.16b}$$

where c is the chord length; C_l and C_d are the lift and drag coefficients which are obtained by wind tunnel tests. These two coefficients are the functions of AOA. Therefore, the axial component and the tangential component of the aerodynamic force can be obtained by

$$p_N = L\cos\phi + D\sin\phi \tag{2.17a}$$

$$p_T = L\sin\phi - D\cos\phi \tag{2.17b}$$

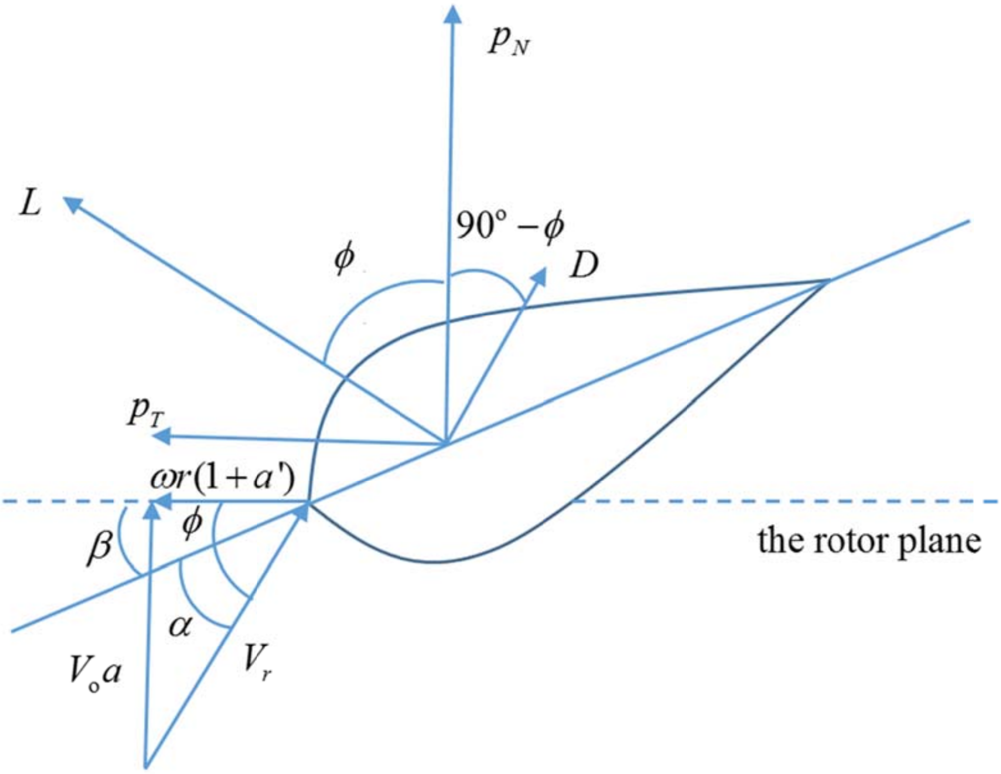

Fig. 2.7 Local wind speed in the rotor plane

Define

$$C_n = C_l \cos\phi + C_d \sin\phi \tag{2.18a}$$

$$C_t = C_l \sin\phi - C_d \cos\phi \tag{2.18b}$$

Hence,

$$C_n = \frac{p_N}{\frac{1}{2}\rho V_r^2 c} \tag{2.19a}$$

$$C_t = \frac{p_T}{\frac{1}{2}\rho V_r^2 c} \tag{2.19b}$$

The relations between V_r and the axial and tangential components can be obtained from Fig. 2.7

$$V_r \sin\phi = V_o a \tag{2.20a}$$

$$V_r \cos\phi = \omega r(1+a') \tag{2.20b}$$

Because the axial component p_N and the tangential component p_T of the aerodynamic force are obtained from only one blade per unit length, the trust and the torque can be obtained by

$$dT = Np_N dr = \frac{1}{2}\rho B \frac{V_o^2 a^2}{\sin^2\phi} cC_n dr \tag{2.21a}$$

$$dM = rNp_T dr = \frac{1}{2}\rho B \frac{V_o^2 a\omega r(1+a')}{\sin^2\phi\cos\phi} cC_t r dr \tag{2.21b}$$

From Equation (2.13), Equation (2.14) and Equation (2.21), the expressions of the two induction factors can be obtained

$$a = 1 - \frac{1}{\dfrac{4\sin^2\phi}{\dfrac{cN}{2\pi r}C_n} + 1} \tag{2.22a}$$

$$a' = \frac{1}{\dfrac{4\sin\phi\cos\phi}{\dfrac{cN}{2\pi r}C_t} - 1} \tag{2.22b}$$

Because ϕ is the function of a and a', Equation (2.22a) and Equation (2.22b) are solved by iteration. If a and a' are solved, the aerodynamic forces of blades can be calculated by Equation (2.16).

The first BEM model for VAWTs was the single streamtube single disk model proposed by Templin (Templin, 1974). Templin regarded the VAWT as a disk and assumed that the entire wind turbine rotor was enclosed by a single streamtube in cross section of which the velocity was uniform. The single disk multiple streamtube model was proposed by Strickland (Strickland, 1975). In the single disk multiple streamtube model, several streamtubes are used and the induced velocity is assumed to be constant in each streamtube. The double disk multiple streamtube theory was further proposed by Paraschivoiu (Paraschivoiu, 2002), Berg (Berg, 1983), and Templin (Templin, 1985). This model suggests two actuator disks to simulate the upwind and downwind side of the rotor so that the induced velocity is different in the upstream and downstream portions of the rotor. The details of this model are introduced in Chapter 8.

There are other momentum models for VAWTs using curvilinear streams rather than rectilinear flow approaching the wind turbine (Gorban et al., 2001), and improving the prediction of local blade Reynolds number when determining the aerodynamic forces acting on the blade (Lian et al., 2008).

BEM is widely used in the aerodynamic forces prediction of HAWTs and VAWTs. However, BEM theory is based on the quasi-steady assumption, which means that the transient processes, such as the inflow fluctuation or turbulence, cannot be considered. Some researchers did improve the BEM to consider the dynamic inflow problem. In fact, it has been shown that the airfoil response takes time to adjust to a changing wake resulting from new inflow or turbine operating conditions (Snel and Schepers 1995). Another limitation is that only blades are considered in BEM theory. In fact, besides blades, the existing of arms and towers would have influence on the flow field and thus aerodynamic forces on blade; while BEM cannot consider the influence of other components of VAWTs.

2.3.1.2 Vortex model

Vortex models are derived from the assumption of incompressible and potential flow, and they are first used to estimate the lift and drag force of airfoil (Chattot & Hafez, 2015). The airfoil is replaced by distributed vortex. The total circulation is conserved and therefore when there is change in relative wind speed or angle of attack, the strength of the distributed vortex would vary and there is vortex shedding into the wake continually. The aerodynamic forces can be calculated by the strength of the distributed vortex according to the Kutta-Joukowski theorem. The shed vortex would induce velocity and change the flow field in turn. The induced velocity can be calculated by the Biot-Savart law. When the freestream velocity and induced velocity are known, the flow field can be updated and the relative velocity can be calculated for the airfoil. Then the aerodynamic forces of the airfoil can be determined using the aerodynamic coefficient obtained from wind tunnel tests. The model can consider the unsteady situation.

The vortex model was first applied by Larsen (Larsen, 1975) and Strickland (J. Strickland et al., 1979) in VAWTs. Scheurich el al. (2013) used the vortex model to study the performance VAWT in unsteady wind conditions. McIntosh & Babinsky (2012) applied this model in calculation of aerodynamic forces for swept bladed VAWTs. Although the accuracy of vortex model is higher than BEM, the computational cost is largely increased but the reliability and accuracy is not as high as computational fluid dynamics (CFD). Therefore, the application of vortex models is limited.

2.3.1.3 Computational fluid dynamics (CFD)

The third major method is the computational fluid dynamics method (CFD). This method can consider the compressible and viscous flow by solving the Navier-Stokes equations directly or indirectly. The Navier-Stokes equations are a set of non-linear, coupled, and partial differential equations. Direct numerical simulation (DNS) is the numerical method that solves the Navier-Stokes equations directly, but this method is extremely computational intensive. In the present stage, this method is only available for the conditions of low Reynolds number and currently prohibitive for practical problems. In this regard, some indirect methods are proposed to solve the Navier-Stokes equations, such as the Reynolds-averaged method and the large eddy simulation (LES). The Reynolds-averaged method averages the Navier-Stokes equations and leads to the Reynolds-averaged Navier-Stokes equations (RANS). This equations introduce new terms and there exists the closure problem. To solve the closure problem, many models have been proposed, such as Spalart–Allmaras, k–ε and k–ω models. On the other hand, LES is another method for solving the Navier-Stokes equations indirectly. Regarding the high computational cost of DNS, the main idea behind LES is to reduce this computational cost by reducing the range of time- and length-scales by a low-pass filter. Such a low-pass filtering, which can be viewed as a time- and spatial-averaging, effectively removes small-scale information from the numerical solution.

CFD becomes more and more popular in the study of wind turbines (Ferreira et al., 2007; Tullis et al., 2008; Vassberg, 2005) and has demonstrated an ability to simulate results that match well with the measured data (Howell et al., 2010; Menet & Bourabaa, 2004; Torresi et al., 2008). Subject to the constraint of computational resources and time, most researchers adopted 2D RANS simulations in the performance study of VAWTs (Amet et al., 2009; Danao et al., 2014; Ferreira et al., 2007; Lanzafame et al., 2014; McLaren, 2011; Scheurich & Brown, 2013; Wekesa et al., 2015). Some researcher claimed that 3D or 2.5D simulation would obtain better prediction in power coefficients (Castelli et al., 2011; Howell et al., 2010; Li et al., 2013; Mukinović et al., 2010).

A review of previous study shows that in most studies, the influence of other components of VAWTs, such as the tower and arms, was considered; on the other hand, although LES can give the most reliable and accurate simulated aerodynamic forces and flow field distribution, the computational cost is much higher than these two methods. Even a sectional model simulated by 2.5D LES requires over 5 million grids (Li et al., 2013), and a 3D LES model is unsolvable for normal computers. A practical simulation method that all components of VAWTs can be considered should be further studied. Moreover, few researchers studied the influence of unsteady inflow by CFD. Some works on this field (Danao et al., 2014; Wekesa et al., 2015) only considered the sinusoidal variation in inflow wind speed. The influence of turbulence on aerodynamic forces is still unclear.

2.3.2 Wind tunnel tests

In order to have a comprehensive understanding of aerodynamics of VAWTs, many wind tunnel tests have been conducted and made some achievements in the recent years. Researchers (Armstrong et al., 2012; Li et al. 2015; Staelens et al. 2003; Fiedler et al. 2009; Hwang et al. 2006; Paraschivoiu et al. 2002) investigated the effect of airfoil type and blade pitch angle on the power performance and flow characteristics in wind tunnel experiments. It was found that the fluctuations of power coefficient appeared to be slightly dependent on blade pitch angles. Li et al. (2016) investigated the pressures acting on the blade surface in the different cross-sections, depending on the pressure measurement system and CFD analyses. They found that the power coefficient reached the maximum value at the blade central height, and gradually decreased when approaching the blade tip, which showed the obvious 3D effect.

The influence of wind speed was also studied by researchers (Song et al., 2008; Li et al., 2014; Islam et al. 2008; Ohlmann et al. 2005). From these studies, it was found that, at the same tip speed ratio, when the wind velocity was higher, the power performance of VAWT was better. The measurements also indicated that wind turbine with higher wind velocity had higher optimum power coefficient and lower optimum tip speed ratio. These works imply the influence of the Reynold's number. Li et al. (2016) and Carpman (2011) further studied the influence of turbulence intensity on the power performance. Their research showed that the output power fluctuated slightly with the increase of turbulence intensity at low tip speed ratios. Output power increased as turbulence intensity was raised at high tip speed ratios.

From the aforementioned wind tunnel tests, it can be found that VAWTs showed obvious 3D effect, while the present researches did not consider the influences of the support structure and arms. Moreover, the study on the effect of wind speed reflected the influence of Reynolds number, but the wind tunnel tests usually cannot reproduce the Reynolds number of large-scale VAWTs. According to the definition of the Reynolds number $\mathrm{Re} = UL/v$ (U is the wind speed; L is the characteristic length; v is the kinematic viscosity), the scaled model requires a high wind velocity produced in the wind tunnel and the required high wind speed is usually not available in wind tunnel. Hence, there are still many limitation in wind tunnel tests, such as limited measurement points, scale effects and experimental costs.

2.3.3 Field measurements

Compared with numerous field tests of HAWTs, the field measurements of VAWTs are limited. The most well-known field tests for VAWTs were conducted by the Sandia National Laboratories (SNL) managed by Sandia Corporation. Sandia built a test bed of a 17m and a 34m eggbeater type VAWTs in 1970s and 1980s respectively (Sutherland et al., 2012). The success of the 17m VAWT encouraged Sandia to build a larger sized 34m VAWT test bed in 1988. A large amount of sensors were installed in this turbine to obtain the responses of the turbine during operation. 72 strain sensors were installed to monitor the responses of the blades and tower, 25 sensors were installed to measure environmental variables which including wind speed and direction, barometric pressure and temperature, 22 sensors were installed to monitor the performance of the turbine, such as blade position, rotor RPM, shaft torque, brake torque, acceleration and cable tension, 29 sensors were installed to monitor the performance of the generator, including power, VAR, current and voltage.

(Sutherland et al., 2012). This 34m VAWT was research oriented and it was decommissioned in 1998. The data from the field measurements were used to validate the analysis method. The most widely used techniques for eggbeater type VAWTs were developed from the work of Sandia (Berg, 1985; Carne et al. 1989; Ferrari, 2012; Jensen et al., 2006; D. Lobitz & Sullivan, 1980; D. W. Lobitz & Ashwill, 1986; Popelka, 1982). Besides this test bed VAWT, researchers also conducted modal tests on several different VAWT at both parking and rotating conditions (Carne et al., 1988, Griffith et al. 2010). However, the field measurement of straight-bladed VAWTs were seldom reported.

2.4 Modelling and Model Updating of VAWTs

2.4.1 Modelling of blades

Nowadays, fiber-reinforced plastics (FRP) laminated shells are widely used in making wind turbine blades (Burton et al., 2001). FRP is a composite material composed of fiber (glass or carbon) and matrix (resin). There are different textile structures that fiber and matrix can be combined together, such as unidirectional FRP (UD FRP) and plain woven FRP (PW FRP). A laminate is composed of multiple layers (plies) of FRP and adjacent layers are usually bonded together by latex. Hence, there exist many interfaces in an FRP laminate. Under different load cases, such as extreme and normal operation loading cases, ultimate strength and fatigue failures may take place in these interfaces (Jones, 1975). According to the first-ply failure criteria (Gohari et al., 2015; Reddy & Pandey, 1987), when one ply of a laminate failure, the laminate is considered out of work. Therefore, the stress or strain analysis at the ply level is important and necessary.

In order to estimate laminar (ply) stresses and strains, a proper modelling method has to be determined. Researchers have proposed several methods to model a wind turbine blade. Some methods focused on the global responses, such as tip displacements and root moments, and accordingly beam elements are used to model the blade (Cesnik & Hodges, 1997; Fleming & Luscher, 2014; Hansen, 2015; Larsen & Nielsen, 2006; Mollineaux et al., 2013; Natarajan et al., 2012).

Other methods focused on the geometrical accuracy and regarded an FRP lamination as an equivalent single layer material based on the classic laminate theory (CLT) (Jureczko et al., 2005; Overgaard et al., 2010) or even isotropic assumption (Mollineaux et al., 2013). However, these two kinds of modelling methods cannot obtain the stresses and strains at ply level. Laminar stresses and strains are so important to the failure analysis of laminates that researchers developed some precise simulation methods using 3D solid or shell laminated elements in the resent years (Castelli et al., 2013; Jensen et al., 2006; Jung et al., 2015; Kubiak & Kaczmarek, 2015; Marin et al., 2009; Song et al., 2011).

2.4.2 Model updating of blades

Only precise modelling is not enough. To obtain accurate laminar stresses and strains, precise elastic constants at each ply are necessary. Usually, the laminar elastic constants of FRP are unknown; even the certified values are given, there exist unavoidable uncertainties due to large manufacturing tolerances unlike the single-constituent material, such as glass fiber and resin which have less uncertainties of the certified values. Therefore, the model updating or calibration techniques are needed (Behmanesh et al., 2015; Brownjohn & Xia, 2000; Friswell & Mottershead, 1995; Jaishi & Ren, 2005).

To identify the elastic constants of composite, researchers proposed either dynamic or static approaches. The dynamic approaches measured mode shapes and natural frequencies (Cugnoni et al., 2007; De Wilde et al., 1984; Deobald & Gibson, 1988; Grédiac & Paris, 1996; Larsson, 1997; Mishra & Chakraborty, 2015; Mishra & Chakraborty, 2015; Moussu & Nivoit, 1993; Schwaar et al., 2012; Van Buren et al.,

2013) and the static approaches measured deformation of a specimen (Avril et al., 2008; Cunha & Piranda, 1999; Genovese et al., 2004; Gras et al., 2013; Lecompte et al., 2007; Molimard et al., 2005; Rahmani et al., 2013). The drawbacks and merits of the dynamic and static approaches have been noticed in the past two decades (Sanayei et al., 1997; Sanayei et al., 2011; Schlune et al., 2009; Xiao et al., 2014). First of all, there are too many mode shapes and natural frequencies to be identified, which needs many sensors and accordingly is difficult to be implemented. Secondly, although an excitation system for dynamic approach may be an easy job for specimen tests, it is a difficult task or even a mission impossible in prototype structures. Thirdly, static measurements can obtain higher accurate data than dynamic ones but they cannot update the mass matrix of the FE model.

On the other hand, most of the methods can only identify the elastic constants of laminated composite rather than laminar properties. Some researchers indeed identified laminar or even constituent properties (A. Mishra & S. Chakraborty, 2015; A. K. Mishra & S. Chakraborty, 2015), but there are too many elastic constants to be identified. A FRP laminar is an orthotropic or transversely isotropic material, which has 9 or 5 independent elastic constants for PW FRP or UD FRP respectively. With the increasing layer number of a laminate, the number of parameters will increase dramatically. It is thus difficult to identify the laminar elastic constants directly.

One solution to this problem is to apply micromechanics in the process of model updating. The objective of micromechanics is to estimate the elastic constants of a composite material by those of its constituents and some geometric parameters. The elastic constants of FRP can vary largely depending on the specific textile structure but the elastic constants of its constituents are usually already known. Thus, if using micromechanics models, the number of updating parameters can be largely reduced.

2.4.3 Modelling of the entire VAWT

For HAWTs, the key issue of establishing a FE model is the rotor-tower coupling problem. Since wind turbines are not structures but mechanisms, the rigid body motions of the rotor bring about challenges in the modeling. In the early years, the rotor (Baumgart, 2002; Hansen, 2015; Kong et al., 2005; Wang et al., 2008; Younsi et al., 2001) and the tower (Bazeos et al., 2002; Negm & Maalawi, 2000; Quilligan et al., 2012) are simply treated separately; however, some researchers studied the rotor-tower coupling and found that the stability problem due to the rotor-tower coupling would not be ignored (Garrad & Quarton, 1986; Larsen & Nielsen, 2007). From then on, more and more researchers focused on the modelling of the whole wind turbine considering the rotor-tower coupling (Kang et al., 2016; Kessentini et al., 2010; Lee et al., 2002; Saravia et al., 2013; Wang et al., 2010). In order to model the rotor-tower coupling, the methods of dynamics of flexible multibody systems are usually used. Based on the assumed mode method, some researchers established analytical models just using a few DOFs. Some researchers even proposed the mixed flexible-rigid body methods that only the flexibility of the blades and tower is considered and the rest components of the wind turbine are regarded as rigid.

For VAWTs, the structural analyses were usually conducted in a rotating reference frame which rotates at the same speed of a VAWT (Thresher et al., 2009). In this reference frame, the rigid motion of the rotor can be eliminated and the VAWT is non-rotating; the centrifugal force and the Coriolis force are added (Berg, 1985; Lobitz & Ashwill, 1986; Popelka, 1982; Carne, 1982; Thresher et al., 2009). This rotating frame method requires the assumption of small motions within the rotating reference frame (Ferrari, 2012; Thresher et al., 2009). In fact, if the tower has a large bending deflection, the base of the rotating frame method that the VAWT is axial symmetric during operation is not valid anymore: the tower is thus assumed to be stiff. Another limitation of this rotating frame method is that the rotational speed must be constant, so the processes of startup and shutdown cannot be considered. Moreover, the previous works did not mention how to deal with the response of the tower. Hence, the response of the tower needs to be further studied when using this method, especially when strains of the tower are required.

2.4.4 Model updating of the entire VAWT

Due to the unavoidable uncertainties in FE modelling, the FE model of wind turbine should be updated by the field measured data. The most common model updating method is using the modal properties. However, conventional modal testing techniques require exciting the structure at several locations which are not easy to be applied to full scale wind turbines. Carne et al. (1982, 1988) extracted modal properties of operational turbine modes by applying the step relaxation method on VAWTs. Although step relaxation was successfully applied on wind turbines at parked condition, it is relatively difficult and time consuming to be applied to rotating turbines. Therefore, Carne et al. (1988) also applied an operational modal analysis (OMA) method where only the responses are required to be measured. The authors compared the results obtained by these two different methods and found that these two results were matched well with each other. Griffith et al. (2010) also conducted in-field tests on a 60 kW, 25 m VAWT at parked condition by using impact hammer, step relaxation and ambient wind excitation and compared the results obtained from various excitation methods.

To validate the FE model of the 34-Meter Test Bed VAWT of Sandia, Carne et al. (1989) compared the measured and simulated results. It was found that the model was not accurate for certain deformations exercised in the substructure tests. The author claimed that these inadequacies did not affect the accuracy of the overall turbine model as these deformations were not important for the low frequency turbine modes.

A review of previous studies shows that although several modal tests for VAWTs were proposed, the model updating of VAWTs were seldom reported. Moreover, the previous studies focused on the eggbeater type VAWTs, and thus the modal tests and model updating of straight-bladed VAWTs are needed to be further studied.

2.5 Structural Analysis

Some reports (Chou et al., 2013) collected 1208 wind turbine incidents and shown that besides 19.4% unknown reason incidents, 19.4% of accidents are attributable to “blade damage”. Other factors of incidents are “fire, 15.3%, structural failure, 10.6%, environmental damage, 8.9%, human injury, 8.4%, fatal accidents, 7.4%, transport, 7.8%, ice throw, 2.8%”. The above statistical data indicates that blade damage was the most common damage type in wind turbine incidents and failure of other structural components was also a main source. Many researchers have devoted themselves to the fatigue and ultimate analyses of wind turbine blades and other structural members.

2.5.1 Fatigue analysis of blades

Most numerical methods for fatigue analyses of HAWT blades are developed by many researchers. Some of them used beam element models (Cárdenas et al., 2012; Hansen et al., 2006; Kubiak & Kaczmarek, 2015) and some used laminated shell elements models (Castelli et al., 2013; Jensen et al., 2006; Jung et al., 2015; Marin et al., 2009; Song et al., 2011). As reviewed in Section 2.4.1, beam elements can only predict global rather than local deformations, while laminar stresses and strains are required in the fatigue and ultimate strength analyses. So, beam elements are improper to predict local stresses and strains in the laminated composite blades. Although some researchers established laminated shell element models, most of these studies adopted simplified concentrated aerodynamic forces instead wind pressures. This simplification may also have some influence on the computation accuracy of local stresses and strains. By considering that a full 3D fluid-structure interaction algorithm is computational intensive (Bazilevs et al., 2011), an alternative method is the synthesis of CFD and FEM, considering the fluid-structure coupling but neglecting the aeroelastic effect. Castelli et al. (2013) used 3D RANS to calculate the aerodynamic force and apply these forces to a 3D blade finite element model to calculate the deformation. However, the structures and aerodynamics of VAWTs are quite different form HAWTs, while the fatigue analyses for VAWT blades are seldom reported. Thus the fatigue damages of VAWTs blades need further study. Moreover, the previous analysis did not consider the influence of the tower, arms and the turbulence on wind loads, which should be included in the further study.

2.5.2 Ultimate strength analysis of blades

The critical locations of failures of HAWT blades were figured out by researchers. Ciang et. al. (2008) summarized six critical-damage locations for HAWTs and four of the six locations are on the blade: (a) 30–35% and 70% in chord length from the blade root; (b) the root of the blade; (c) the maximum chord section; (d) upper spar cap/flange of the spar. Rumsey and Paquette further figured out a multitude of cracks developed near the trailing edge on the tension side of TX-100 blade by fatigue tests (Rumsey & Paquette, 2008). Kirikera et. al. also found two damage locations of a 9m long blade on the compression side, one on the trailing edge and the other on the leading edge (Kirikera et al., 2008).

However, the analyses for VAWTs, especially straight-bladed VAWTs, are rare. After a brief development in 1970s-1980s, VAWTs were out of sight. Due to the lack of cases and tests, the study of the critical damage locations for VAWT blades, is nearly absent and needs further study.

2.5.3 Fatigue analysis of other components

Besides blades, fatigue in other components, such as the tower and gear box, should also be considered. Some researchers devoted themselves into these topics.

Do et al. (2014) presented a complete procedure for analyzing wind turbine towers under normal wind loading in time domain and a relative motion calculation that uses FEM to quantify force nonlinearities and fatigue life estimation for a typical 5-MW wind turbine. Liu & Ishihara (2015) studied fatigue failure accident of wind turbine tower in Taikoyama Wind Power Plant. The evidence of fatigue crack propagation was found at the fracture faces of the turbine tower tube. The service life of the wind turbine was only 12 years and the regular inspection was carried out three months before the accident.

To evaluate the fatigue damage of gearbox, McNiff et al. (1990) developed a "time-at-level" histogram for the loads on the gearbox. In this technique, the torque applied to the gearbox is characterized by the total time the gearbox will be subjected to a given magnitude of torque. The development of these loads is based on a point-by-point binning of the time series data by magnitude. The service lifetime analysis assumes that each torque bin is applied to the gearbox in a quasi-static manner; namely, the torque is a slowly varying function of time. Thomsen and Petersen (Thomsen and Petersen, 1992) conducted a similar study for both stall and pitch controlled wind turbines. American Gear Manufactures Association) and American Wind Energy Association have developed design guidelines for gearboxes used in wind turbine applications (AGMA/AWEA, 1997).

2.5.4 Ultimate strength analysis of other components

Researchers also conducted ultimate strength analyses for other components of wind turbines. For towers, Lavassas et al. (2003) numerically studied responses of a steel 1-MW wind turbine tower under high wind speed; Polyzois et al. (2009) conducted experiment tests and numerical simulations of wind turbine GFRP tower under ultimate loads. For gear boxes, Nejad et al. (2013) used two methods, the multibody simulation and a simplified method, to study the gear transmitted load calculation from the main shaft torque. It was found that good agreement was observed between the simplified model and MBS results for the case study 5 MW gearbox. Then the results of these two methods were used to study the ultimate loads of gear boxes. For shafts, Zhang et al. (2013) analyzed the fracture of a main shaft. The chemical composition and mechanical properties of the material of the shaft and metallographic inspections of the fracture surface were carried by means of electronic microscopes and a theoretical calculation of equivalent stress of the shaft was performed.

2.6 Control of Blade Pitch Angles of VAWTs

2.6.1 Optimal pitch angles

According to wind conditions, wind turbines operate at different states. The 1st state is the start-up state. In this state, wind turbines are parked or idling if the mean wind speed is below the cut-in wind speed. When the mean wind speed rises at the cut-in wind speed, the rotor begins to speed up until the rotational speed arrives at the required value, and then wind turbines are connected to the grid. The required rotational speed of a grid connected wind turbine is determined by the frequency of grid and the number of poles of the generator. In this study, the state of start-up is defined as state 1. The 2nd operation state is the state of power production below the rated wind speed, which is defined as state 2. In this state, wind turbines are connected to the grid, and they generally operate at a specific rotational speed. The 3rd operation state is the state of power production above the rated wind speed, which is defined as state 3. In this state, the rotation speed is also fixed at the same speed as in state 2. The available wind power increases with wind speed in the form of cubic function. While there is a rated power for each generator, generator would be damaged if the power is over the rated value. Hence, the difference between state 2 and state 3 is that there must be some mechanism to reduce the power and prevent the generator from overloading (Spera, 1994). The 4th operation state is the shut-down state which is defined as state 4 in this study. When the wind speed rises above the cutout wind speed, it is important that the rotor should be shut down as soon as possible to prevent the accident of flying off in high wind, which is one of the main failures of wind turbines due to the wear and tear of the braking system (Ciang et al., 2008; Spera, 1994).

Pitch controls have the potentials to benefit wind turbines at the aforementioned four states. In state 1, self-starting would not present much of a problem for HAWTs, and therefore the pitch control is not necessary. However, VAWTs usually need additional power to start up and a pitch control system may increase the aerodynamic torque of VAWTs in this state (Kirke, 1998). In state 2, because the rotation speed is fixed, the power coefficient is varying with the mean wind speed. However, there is only one optimal mean wind speed corresponding to the largest power coefficient C_p for a particular wind turbine, which implies that wind turbines do not operate at the optimal state in a wide range of the operational wind speed region. To improve the efficiency in low wind, some HAWTs are equipped with two generators, one for the high wind speed and one for the low wind speed (Jha, 2010; Spera, 1994), or equipped with a variable speed generator to enable maximum power point tracking (MPPT). HAWTs seldom adopt the pitch control algorithm in this state because pitch regulations in this state would induce unacceptable fluctuation in power (Burton, et al., 2000). However, the aerodynamics of VAWTs is quite different from HAWTs. For VAWTs, the angle of attack (AOA) experiences a cyclic change between positive and negative in one spin in the case of zero pitch, while the variation in AOA of HAWTs is small. Thus zero pitch of VAWTs cannot ensure the optimal torque at all azimuth angle. Indeed, many researchers have devoted themselves to pitch control algorithms of straight-bladed VAWTs in this state (Lazauskas, 1992; Vandenbereghe & Dick, 1986; Hwang et al., 2005; Hwang et al., 2006; Kosaku et al., 2002; Liu et al., 2015; I Paraschivoiu et al., 2009; Zhang et al., 2015). In state 3, the pitch regulation can maintain the power at the rated value for HAWTs. In state 4, the pitch regulation can help HAWTs to shut down efficiently by reducing AOA or inducing the happening of stall. However, for VAWTs, seldom researches are conducted on the pitch control algorithm in state 3 and state 4. Pitch controls have been widely applied in HAWTs, while they were seldom studied for VAWTs until recent years and mainly focused on state 2. Therefore, the study on pitch control is necessary for VAWTs to obtain the optimal pitches to assist the start-up in state 1, to improve the power coefficient in state 2, to maintain the output power at the rated value in state 3 and to assist the shut-down in state 4.

2.6.2 Performance assessment

As introduced above, in different operational states, the control objectives are different. Thus, there are different criteria to assess the performance of VAWTs under pitch control.

For state 1 (starting up), the regulated pitch angle is to assist VAWTs in speeding up. According to the theorem of kinetic energy, the kinetic energy of the rotor comes from the work of aerodynamic torque of all blades. Hence, the torque in one revolution can be used as the index to assess the performance of pitch control in state 1.

For state 2, VAWTs are connected to the grid and operates in the power generation state. The pitch control objective in this state is to increase the generate power. Naturally, the average power in one revolution can be used as the index to assess the effect of pitch control in this state.

For state 3, VAWTs operates at the wind speed above the rated wind speed and the objective of pitch control is to maintain the power at the rated value. Hence, in this state, the difference of generated power and the rated power can be used as an index to assess the performance of pitch control. On the other hand, because pitch regulation in the operation state is not easy, hence, a better pitch control algorithm should use a smaller range of pitch angle so that the power can be kept at the rated value.

For state 4 (parking in the high wind speed), the control objective is to stop VAWTs as quickly as possible. In contrast with state 1, the aerodynamic torque should generate minus work (decreasing the rotational speed). Therefore, the amplitude of the minus work is the larger the better. Hence, as the state 1, the work of the aerodynamic torque of all blades can be used as the index to evaluate the control effect.

2.6.3 Control systems

As introduced in the above discussion, a pitch control system needs to measure the wind speed and wind direction, the rotational speed of rotor, the azimuth angle of blades and the power output if using the feedback algorithm and needs actuators to change the pitch. Therefore, the sensors such as anemometers, tachometers, data acquisition systems and computers are commonly required for all pitch control systems of VAWTs, while researchers proposed different actuating systems.

Some researchers indeed proposed pitch control algorithms for VAWTs (Bhatta et al., 2008; Greenblatt et al., 2012; Paraschivoiu et al, 2009; Pawsey, 2002). However, only conceptual designs and numerical simulations were given; while some researchers conducted wind tunnel or field tests. Ham et al. (1979) proposed a pitch control system which could enable the pitch of each blade to vary in the sinusoidal form. They named this pitch control system as "cycloidal blade system". Fig. 2.8 shows the basic concept of the control mechanism. The magnitude of eccentricity e is defined as the distance from the center of rotation O to the point of the eccentricity point P, as shown in Fig. 2.8. The phase angle of eccentricity ε is defined as the angle between the line OP and the vertical line. The magnitude and the phase angle of the eccentricity are used to adjust the magnitude and direction of the rotor. Fig. 2.9 shows pitch angle variation according to azimuth angle when the maximum pitch angle is 10^{o}. This control system was further developed Vandenbereghe and Dick (1986) to obtain second order harmonic pitch control.

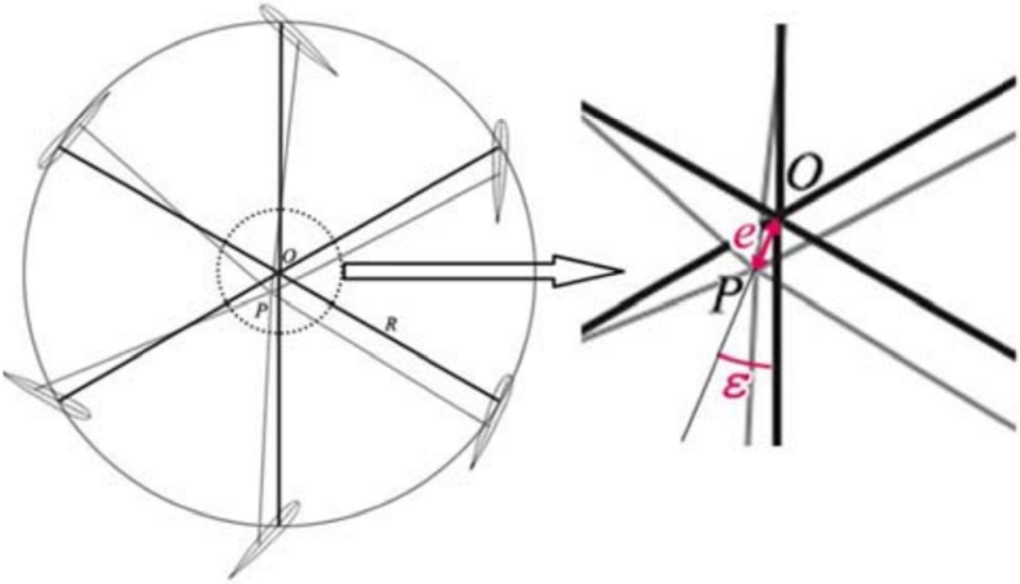

Fig. 2.8 Cycloidal blade system

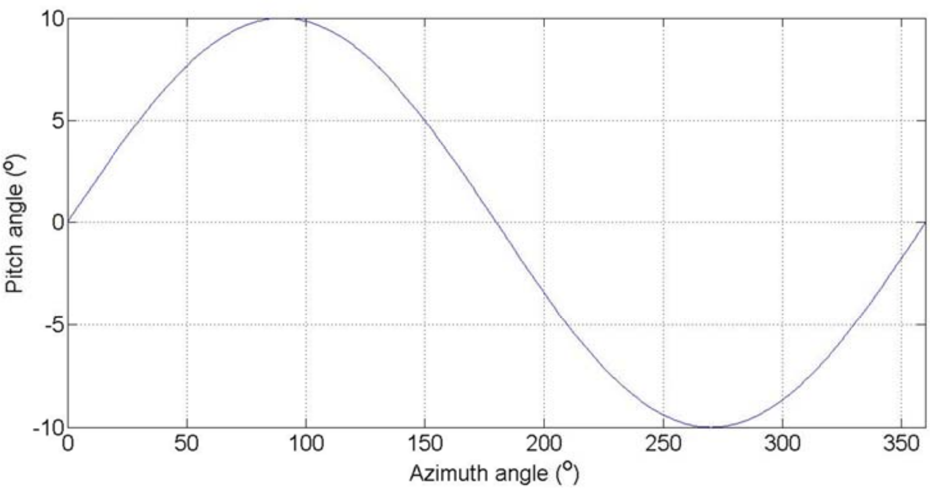

Fig. 2.9 Pitch angle of each blade

Boston (2000) proposed a pitch control system using bevel gears. The configuration of the device is shown in Fig. 2.10. The pitch angles can be changed and the major dimensions of the rotor/blade system were as follows: blade length is 2.4 m; blade chord is 0.56 m; rotor radius R = 1.0 m; number of blades is 3. The blades were suspended between the upper and lower support arms, which, in turn were mounted on a 139mm OD "main shaft" with two concentric inner shafts. The entire rotor system was mounted on a substantial 3m high steel lattice tower which could be tilted by means of hydraulic rams to allow easy access to the rotor assembly and so that the turbine could be lowered when not undergoing field tests.

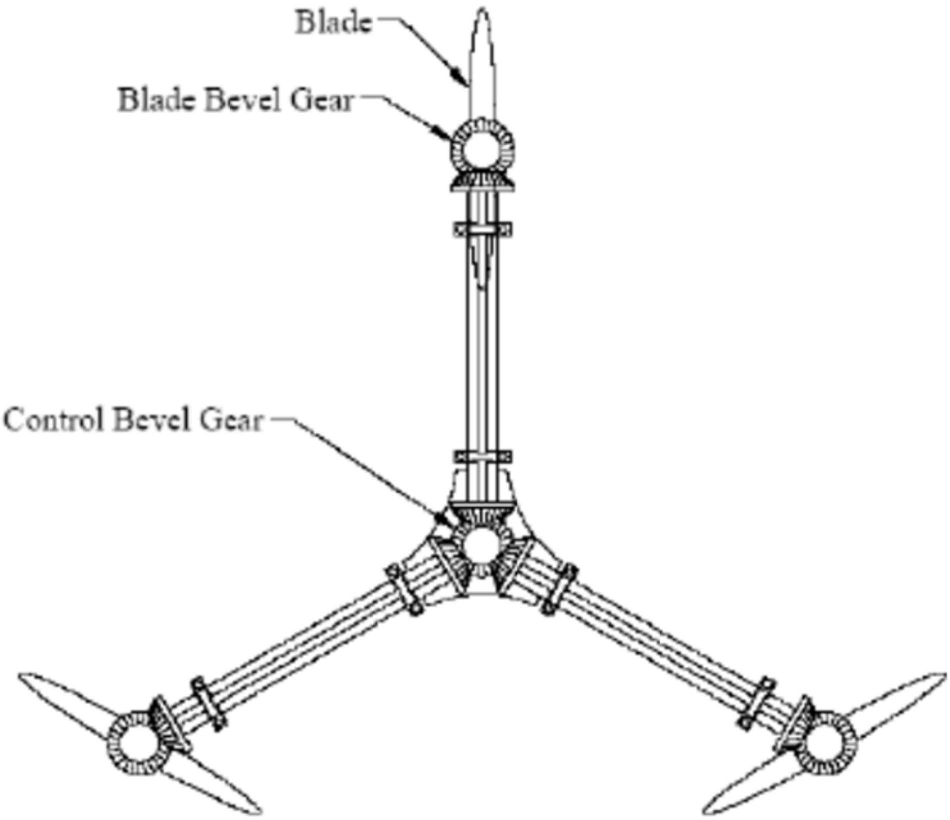

Fig. 2.10 The pitch control mechanism using a generator and bevel gears

A review of previous studies shown that all these studied focused on the improvement of power coefficient (state 2), the pitch control studies on other states can be hardly found in the literatures. Further pitch control studies on other operation states should be conducted.

2.7 Structural Health Monitoring of VAWTs and Smart VAWTs

2.7.1 Structural health monitoring systems

SHM systems are required for large-scale wind turbines. Usually, a wind turbine is established in an uninhabited area and exposed to various environmental effects, such as typhoons, earthquake and collisions. Faults and failures are of frequent occurrence. From 1989 to 2006, 64,000 incident reports form 1,500 onshore wind turbines were collected by the Institute for Solar Energy Technology (Pettersson et al., 2010). Hence, inspection and maintenance must be carried out regularly, and enormous cost and effort are required (Ciang et al., 2008; Fingersh et al., 2006; Walford, 2006). An SHM system can provide the information for companies so that they can monitor the functionality, detect large deformations, ensure the safety and save the cost of inspection and maintenance of wind turbines. Besides these objectives, an SHM system can provide field measurement data for designers that they can validate the present analysis methods which have not been fully verified yet, or just verified by wind tunnel tests.

SHM systems are widely applied in large-scale HAWTs. Many researchers paid their attention to the monitoring of blades. There are several methods for blade monitoring and the most widely used methods are acoustic emission (AE) monitoring and strain monitoring method. Rumsey & Musial (2001) installed an array of AE sensors on the static-test blade. It was found that the AE sensors can indicate damage being generated in the material and figure out the area of eventual structural failure. Joose et al. (2002) applied the AE method on small wind turbine fiber composite blades and found that the AE sensors can both locate and characterize damage processes in blades. Blanch & Dutton (2003) further applied the AE sensors on the operating wind turbine blades and the results shown that the damage can be successfully located. On the other hand, strain sensors are also used in the monitoring of wind turbine blades and has been successfully applied in a 4.5 MW turbine using optical fiber Bragg grating (FBG) sensors (Schroeder et al., 2006). Choi et al. (2008) proposed an integrated solution that monitors structural health condition using strain gauge enabled wireless sensor nodes, and forwards the collected data to the building inspector for risk analysis. The advantages of strain sensors are cost effective and easy installation. However, strain is a local response and thus strain sensors should be placed on the critical locations of failure. Therefore, the fatigue and ultimate strength analyses should be conducted before installation of SHM system.

Researchers also conducted the studies on monitoring of other components of wind turbines. Strain gauges are commonly used to monitor the bending and torsion of shaft and tower; accelerometers are widely used in the monitoring of vibration of the nacelle, drive train and tower (Amirat et al., 2009; Caselitz & Giebhardt, 2005; Hameed et al., 2009).

A review of previous studies shows that although many studies of SHM for HAWTs have been conducted, the reports on SHM for VAWTs are rare. One of the reasons is that VAWTs gain much less development than HAWTs. Therefore, the study on SHM systems for large-scale VAWTs is required.

2.7.2 Concept of smart VAWTs

Generally, wind turbines need both the SHM system and the control system. Both of the systems require sensors, data acquisition systems, and signal transmission systems. Since the primary objectives of these two systems are different, they are currently treated separately. A separate approach is not practical and cost-effective. It is more reasonable to consider these two systems synthetically. Moreover, the power supply is an important factor for the design of both the SHM and control system (Huston, 2010) and usually power from batteries or grid are used. Power from the electric grid is a good choice but it will be cut off in the extreme event, such as hurricane or earthquake. However, the SHM or control systems are valuable and cannot be absent in these cases. Additionally, the power from electric grid sometimes is inconvenient, or unavailable, to sensors and actuators installed in the remote or unapproachable position. Considering the above cases, usually, batteries are the alternative option but recharging or replacing these batteries also brings in troubles which limit the development of SHM or control system. Researchers have proposed many solutions to these problem, such as developing lower-power consumption sensors (Lin et al., 2015) and energy harvesting methods (Chalasani & Conrad, 2008; Shen et al., 2012; Stanton et al., 2010; Zhu et al., 2012). Considering that a VAWT itself is an energy harvesting machine, it is promising that the power of these two systems can be obtained directly from the turbine. Therefore, it is necessary to study a smart VAWT which possesses the abilities of self-sensing, self-diagnosis, self-control and self-power.

CHAPTER 3

WIND LOAD SIMULATION FOR VAWTS BASED ON STRIP ANALYSIS AND CFD

3.1 Introduction

As introduced in Chapter 2, renewable energy, especially wind energy, attracts the growing interest of the world nowadays. In order to better take advantage of wind power, vertical axis wind turbines (VAWTs) have undergone considerable development recently. Therefore, it is important to get a deep understanding of wind loads on a VAWT, not just at the level of aerodynamic forces but also at wind pressure level. This is because in order to assess the power production of a VAWT, the aerodynamic forces, especially the tangential forces on the blades of the VAWT, have to be estimated accurately. On the other hand, a VAWT is subjected to various loadings in different wind conditions. Hence, knowing local stresses/strains of the components, especially the blades, is crucial to the fatigue and ultimate analyses and subsequently the design of a VAWT, and this requires the knowledge of wind pressures. Consequently, only a better understanding of wind loads, including both aerodynamic forces and wind pressures, can lead to a better design of a VAWT.

For VAWTs, a few tools have been proposed to estimate wind loads, which include double multiple streamtube theory (DMST), vortex model, and computational fluid dynamics (CFD) simulation (Paraschivoiu, 2002). DMST is the simplest and most widely-used method. However, DMST cannot consider the influence of the arms and tower on the wind loads acting on the blades. Moreover, this method can only get aerodynamic forces rather than wind pressures on the blades. Although the vortex model can consider the influences of other components and obtain wind pressures, the computational cost is much higher than DMST, and the accuracy of this method is less than CFD. Many researchers now simplify a VAWT as a planar structure and conducted 2D or 2.5D CFD simulation to analyze the aerodynamic forces on VAWTs (Almohammadi et al., 2013; Amet et al., 2009; Castelli et al., 2011; Danao et al., 2014; Ferreira et al., 2007; Hassan et al., 2015; Ismail & Vijayaraghavan, 2015; Lanzafame et al., 2013; Li et al., 2013; Mcintosh et al., 2008; Nini et al., 2014; Scheurich & Brown, 2013; Wang et al., 2010; Wekesa et al., 2015). Nevertheless, wind speed along the height of a VAWT is not uniform, which does not match 2D or 2.5D simulation. Furthermore, the computational cost of CFD turbulence modeling for a 3D VAWT is extremely high (Elkhoury et al., 2015; Nini et al., 2014; Siddiqui et al., 2015). As a result, an efficient simulation method is still needed to estimate the wind loads on the VAWT to take into consideration of the influence of all structural components on wind field of a VAWT and the varying wind speed along the height of the VAWT.

Furthermore, almost all researchers adopt the steady inflow boundary when they use CFD to study wind loads on a VAWT, and the effect of turbulent inflow on wind loads is less investigated. For HAWTs, this problem has been studied for years (Burton et al., 2001). A basic method is to use the blade element momentum theory and the Taylor's frozen hypothesis to calculate the aerodynamic forces. Empirical dynamic inflow models were also proposed in this regard (Snel et al., 1995). However, these methods are for HAWTs only. The aerodynamics of a VAWT is quite different from a HAWT. There are no enough studies to verify the applicability of these methods for VAWTs. As a result, the performance of a VAWT in unsteady wind conditions attract many attentions in recent years (Danao et al., 2013; Danao et al., 2014; Mcintosh et al., 2007, 2008; Scheurich & Brown, 2013; Wekesa et al., 2015). However, only simple sinusoidal variation wind speeds are considered in these studies, which is quite different from real atmospheric turbulent inflow. Therefore, the influence of turbulent inflow on wind loads acting VAWTs deserves further studies.

In this chapter, a framework for determining wind loads, including wind pressures and aerodynamic forces, on the whole VAWT is proposed in Section 3.2. A straight-bladed VAWT built in Guangdong Province, China, in which I was involved, is taken as an example for the sake of easy understanding of the framework in Section 3.2. In order to make sure the validity of the 2D shear stress transition (SST) $k-\omega$ simulation used in this study for computing wind loads on the VAWT, the results from the 2D SST $k-\omega$ simulation and the 2.5 large eddies simulation (LES) are compared in Section 3.3. After a successful comparison, the framework, which is based on the strip analysis method and 2D CFD simulation, is applied to the straight-bladed VAWT to determine its wind loads in Section 3.4. The influences of the existence of arms and tower on the aerodynamic forces and wind pressures on the blades, the variation of mean wind speed along the height of the VAWT, and the effects of the turbulent wind are all considered. After detailed analysis on wind pressures and aerodynamic forces in Section 3.4, Section 3.5 finally evaluates the influences of the existence of the tower, arms and turbulent inflow on aerodynamic forces on the blades.

3.2 Wind Load Simulation Framework for VAWTs

3.2.1 A straight bladed VAWT

The wind load simulation framework to be proposed here is generally applicable for any types of VAWTs. Only for the sake of easy understanding and also because of my personnel involvement, a large-scale lift-type straight-bladed VAWT, as shown in Fig. 3.1, is taken as an example to illustrate the framework.

The lift-type straight-bladed VAWT was constructed at Yang Jiang City of Guangdong Province, China, by the Hopewell Wind Power Limited of Hong Kong. The tower of the VAWT was made of reinforced concrete with a height of 24 m and a diameter of 5 m (see Fig. 3.2). The thickness of reinforced concrete wall of the tower was 250mm. The tower supported a vertical rotor, the rotating parts of the VAWT, of 26m in height and 40m in diameter. Three blades of the rotor were equally arranged at an interval angle of 120^{o}. The blades were of NACA0018 type with the chord length of 2m and the vertical height of 26m. These blades were made of glass fiber reinforced plastic (GFRP) laminate materials and supported by the Y-type steel arms connected to the tower via the main shaft at the top of the tower (the hub height). The ground clearance of the bottom end of the blades was 10.5m. Each Y-type steel arm consisted of a main arm, an upper arm and a lower arm, as shown in Fig. 3.2. The cross section of the main arm was rectangular with the width of 1.6 m and the depth of 1.2 m and the length of the main arm was 10 m. The upper and lower arms supported the blade at one end and were connected to the main arm at another end. The cross section of the upper and lower arm is rectangular, and the cross section has the constant width of 1.2 m and the varying depth from 0.6m at the main arm side to 0.3m at the blade side. Between the lower and upper arms, there is a stiffened link. The diameter of this link is only 0.2m.

The VAWT operated in a designated wind speed range. When the 10-minute mean wind speed at the hub height reached a specific value, called the cut-in wind speed, the wind turbine would begin to operate; when the 10-minute mean wind speed was higher than another specific value, called the cut-out wind speed, the wind turbine should be shut down. The cut-in and cut-out wind speed of this VAWT was set as 5m/s and 21m/s respectively, which means that this VAWT operated in the mean wind speed range from 5m/s to 21 m/s and that the VAWT should be shut down when the mean wind speed was out of this range (below 5m/s or over 21m/s). When connected to the grid, the VAWT was rotating at a specific speed which was determined by the frequency of the grid and the type of generator. For this VAWT, the rotation speed was set as 2.1rad/s. Then, the output power of the VAWT was determined by wind speed. The wind speed corresponding to the rated power of the generator is called the rated wind speed. For this VAWT, the rated wind speed was designated as 14m/s.

Fig. 3.1 A prototype straight-bladed VAWT

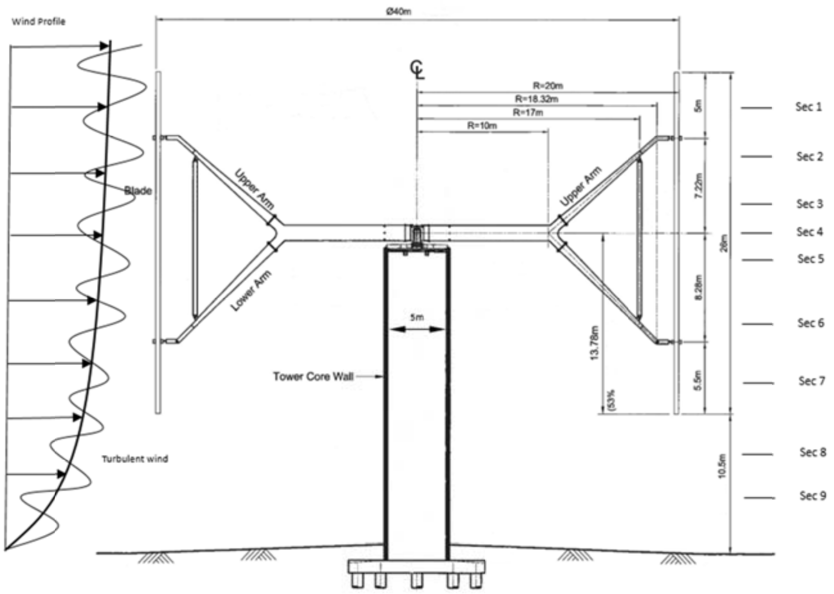

Fig. 3.2 Wind field and structural configuration of VAWT

3.2.2 Wind conditions

In the service life of a wind turbine, it is subjected to different wind conditions, including mainly the operation wind speed condition and the extreme wind speed condition. The design objectives of a wind turbine are different for the two wind conditions. Within the operation wind speed, the wind turbine is generating power and subjected to cyclic loading, so that the fatigue loading is the control factor for the structural safety of the wind turbine. The extreme wind speed and load need to be assessed for the two cases: one is the extreme wind event with a 50 years return period and the other one is the maximum load in operation. Under the extreme wind event, the wind turbine is in still. Furthermore, the extreme wind condition is a small probability event, so that the fatigue in this wind condition is not considered but the ultimate strength of the wind turbine shall be considered.

3.2.2.1 The operation wind speed condition

To determine wind loads on a VAWT during its operation, the mean wind speed and turbulent wind speed shall be considered. In the atmospheric boundary layer, the mean wind speed near the ground approaches to zero and then increases with the increasing of height above the ground. Two types of mean wind speed profiles are often used to describe the mean wind speed in the atmospheric boundary: the semi-empirical logarithmic law and the empirical power law. Due to its simplicity, the power law is used in this study for determining wind loads on a VAWT, as shown in Figure 2. The power law is described by

$$V(z) = V_{\mathrm{hub}} (z / z_{\mathrm{hub}})^{\alpha} \tag{3.1}$$

z is the height above the ground; $V(z)$ is the mean wind speed at z; V_{hub} is the reference mean wind speed at the hub height, z_{hub}; the exponent α is the empirically derived coefficient depending on the stability of the atmosphere and the surface roughness (Simiu & Scanlan, 1986; Xu, 2013). IEC61400-1 gives a suggestion to use the exponent $\alpha = 0.2$ (Commission, 2005).

The turbulent wind speeds at different heights are neither exactly the same nor totally random, but have close relations. Researchers have proposed many power spectra and coherence models to model the turbulent wind at different heights. In this study, only longitudinal turbulent wind is considered because lateral turbulent wind speed is relatively smaller than longitudinal turbulent wind speed and vertical turbulent wind speed will not affect wind loads on the VAWT. It is also assumed that the mean wind speed and longitudinal turbulent wind are uniform across the wind turbine at any given horizontal level. Hence, at each height, the turbulent wind speed can be regarded as a one-dimensional stochastic process.

To simulate longitudinal turbulent wind speed at a given height, the Kaimal spectrum and the corresponding coherence function are selected (Burton et al., 2001).

$$\frac{fS(f,z)}{\sigma_u^2(z)} = \frac{4fL_u(z)/V(z)}{(1+6fL_u(z)/V(z))^{5/3}} \tag{3.2}$$

$$Coh(\Delta z, f) = \exp(-12\sqrt{\left(f\Delta z/\bar{V}\right)^2 + \left(0.12\Delta z/L_c\right)^2}) \tag{3.3}$$

where $S(f,z)$ is the power spectrum of longitudinal turbulent wind at height z; f is the frequency; σ_u is the standard deviation of longitudinal turbulence at height z; L_u is the integral length scale of longitudinal turbulence at height z; Δz is the distance between the two heights ($\Delta z = \left|z_1 - z_2\right|$); $\bar{V}$ is the mean wind speed at the two heights considered, which is equal to $\frac{1}{2}\left(V(z_1)+V(z_2)\right)$; and L_c is the coherence scale parameter.

IEC61400-1 gives the estimations to the values of σ_u, L_u and L_c. The standard deviation of longitudinal turbulence σ_u is determined by

$$\sigma_u = I_{ref}(0.75V + 5.6) \tag{3.4}$$

where I_{ref} is the respected turbulence intensity at a mean wind speed of 15 m/s, which is determined by the wind turbine class defined in IEC61400-1. In this study, $I_{ref} = 0.14$. L_u is determine by

$$L_u = 8.1\Lambda_u$$

where

$$\Lambda_u = \begin{cases} 0.7z, z < 60m \\ 42m, z < 60m \end{cases}$$

Similarly, L_c is also given by $8.1\Lambda_u$ at the mean value of the two different heights $1/2\left(z_1 + z_2\right)$.

Once the cross spectral density function of longitudinal turbulent is established, the algorithm of the spectral representation method proposed by Shinozuka and Jan(Shinozuka & Jan, 1972) can then be used to generate turbulent wind speed time histories along the height of the VAWT.

The turbulent wind speeds at different heights can be regarded as a set of n one-dimensional zero-mean stationary stochastic processes $\{u_j(\mathrm{t})\}(j = 1, 2, \cdots, n)$ at height $z_j, j = 1, 2, \cdots, n$. The cross-spectral density function $\boldsymbol{S}(f)$ of the stochastic processes is given by

$$\boldsymbol{S}(f) = \begin{bmatrix} S_{11}(f) & S_{12}(f) & \cdots & S_{1j}(f) & \cdots & S_{1n}(f) \\ S_{21}(f) & S_{22}(f) & \cdots & S_{2j}(f) & \cdots & S_{2n}(f) \\ \vdots & \vdots & \ddots & \vdots & & \vdots \\ S_{i1}(f) & S_{i2}(f) & \cdots & S_{ij}(f) & \cdots & S_{in}(f) \\ \vdots & \vdots & & \vdots & \ddots & \vdots \\ S_{n1}(f) & S_{n2}(f) & \cdots & S_{nj}(f) & \cdots & S_{nn}(f) \end{bmatrix} \tag{3.5}$$

where $S_{ij}(f) = Coh(\Delta z, f)\sqrt{S(f, z_i)S(f, z_j)}$ in which $\Delta z = \left| z_i - z_j \right|$.

According to Shinozuka and Jan(Shinozuka & Jan, 1972) and Deodatis(Shinozuka & Deodatis, 1991), the stochastic processes $\{u_j(\mathrm{t})\}(j = 1, 2, \cdots, n)$ can be simulated by the following series:

$$u_j(t) = 2\sqrt{2\pi\Delta f}\sum_{m=1}^{j}\sum_{l=1}^{N}\left| H_{jm}(f_{ml})\cos(2\pi f_{ml}t - \theta_{jm}(f_{ml}) + \phi_{ml})\right| \tag{3.6}$$

where N is a sufficiently large number; $\Delta f = f_{up}/N$ is the frequency increment; f_{up} is the upper cutoff frequency, with the condition that when $f > f_{up}$, the value of $\boldsymbol{S}(f)$ is trivial; ϕ_{ml} is the sequence of independent random phase angles, uniformly distributed over the interval $[0, 2\pi]$; f_{ml} is the double-index frequency, determined by $f_{ml} = (l-1)\Delta f + \frac{m}{n}\Delta f \quad l = 1, 2, \cdots, N$; $H_{jm}(f)$ is a typical element of the matrix $\boldsymbol{H}(f)$, which is defined as Cholesky decomposition of cross-spectral density matrix $\boldsymbol{S}(f) = \boldsymbol{H}(f)\boldsymbol{H}^{T*}(f)$; $\theta_{jm}(f)$ is the complex angle of $H_{jm}(f)$ and is given by:

$$\theta_{jm}(f) = \tan^{-1}\left\{\frac{\mathrm{Im}\left[H_{jm}(f)\right]}{\mathrm{Re}\left[H_{jm}(f)\right]}\right\} \tag{3.7}$$

where $\mathrm{Im}\left[H_{jm}(f)\right]$ and $\mathrm{Re}\left[H_{jm}(f)\right]$ are the imaginary and real parts of the complex function $H_{jm}(f)$, respectively.

In order to avoid aliasing, the time step Δt has to be obey the condition:

$$\Delta t \le \frac{1}{2f_{up}} \tag{3.8}$$

3.2.2.2 The extreme wind speed condition

To determine wind loads on a VAWT for the extreme wind speed condition, the extreme wind speed with a 50 years return period should be considered. In this case, the VAWT is locked and stands still.

Similar to the operation wind speed condition, the mean wind profile and the longitudinal turbulent wind speed need to be considered. Since the fatigue analysis is not conducted in the extreme wind condition, only the ultimate strength analysis is required. The extreme wind load is related to the gust wind, and the equivalent static wind loads (ESWL), as reviewed in Chapter 2, can be adopted. In this method, the effect of gust wind is considered by a peak factor g_v

$$V^{'}(z) = V(z)[1 + g_v I(z)] \tag{3.9}$$

where $V^{'}(z)$ is the gust wind speed at height z ; and $I(z)$ is the turbulence intensity. The influence of turbulent wind can be equivalent to the static wind in terms of the peak factor.

By considering the wind profile as shown in Equation (1), the gust wind at any height can be calculated as:

$$V^{'}(z) = V_{hub}\left(\frac{z}{z_{hub}}\right)^{\alpha}[1 + g_v I(z)] \tag{3.10}$$

Researchers proposed different methods to evaluate this peak factor (Chen & Kareem, 2004); and IEC61400-1 suggests the peak factor of approximately 3.5 and gives the steady wind extreme model as

$$V_{e50}(z) = 1.4V_{ref}\left(\frac{z}{z_{hub}}\right)^{0.11} \tag{3.11}$$

V_{e50} is the extreme wind speed with a recurrence period of 50 years; V_{ref} is the reference wind speed depending on the wind turbine class. In this study, the class I is considered, so V_{ref} is equal to 50m/s (Commission, 2005). z_{hub} is the height of the hub. The exponent is taken as 0.11 in the extreme wind condition. Hence, the analysis in the extreme wind condition can be regarded as a steady analysis.

3.2.3 Strip analysis

It is clear from the above discussions that both the mean wind speed and the structural configuration vary along the height of a VAWT and that the turbulent wind speeds at the two different heights are not the same but correlated. Therefore, it is insufficient and improper to determine wind loads by simplifying the VAWT as a planar structure. On the other hand, a truly 3D CFD simulation to determine wind loads on a VAWT is extremely computational intensive as reviewed in Chapter 2.

In order to take the advantage of 2D CFD simulation and at the same time to consider varying wind load on and varying cross section of the VAWT, the strip analysis is proposed in this study. The strip method is widely used in the analysis of propellers (Chattot & Hafez, 2015) and bridges (Davenport et al., 1992). The 3D propeller or the bridge is divided into several sections and the 2D simulation is then conducted on each of the sections. In a similar way, the whole VAWT is divided into several typical cross sections along its height and then the 2D simulation is applied to each of the sections with the simulated mean and turbulent wind speeds.

For the selected VAWT, 9 cross sections are chosen in this study, as shown in Fig. 3.3. The concept of "cell zone" in the figure will be introduced in Section 3.3.1. The heights of sec1-sec9 are listed in Table 3.1. The choice of these sections is based on the structural configuration of each section and the variation of wind speed. In sec1, there are only the cross sections of the three blades, as shown in Fig. 3.3 (a). In sec2 and sec3, the upper arms also appear but the distances from the blades are different, as shown in Fig. 3.3(b - c). In sec4, main arms appear, as shown in Fig. 3.3(d). The difference between sec1 - sec3 and sec5 - sec7 is the tower; sec5 - sec7 are shown in Fig. 3.3(e - g).

In sec8 and sec9, although only the tower appears as shown in Fig. 3.3(h), the wind speed changes dramatically in this region and the two sections are selected. It is worth mentioning that in this study, sec4 is at the hub height z_{hub}.

Table 3.1 The height levels of sec1 – sec9 above the ground

	sec1	sec2	sec3	sec4	sec5	sec6	sec7	sec8	sec9
Height(m)	34.0	29.7	26.1	24.3	22.2	18.1	13.3	7.9	2.6

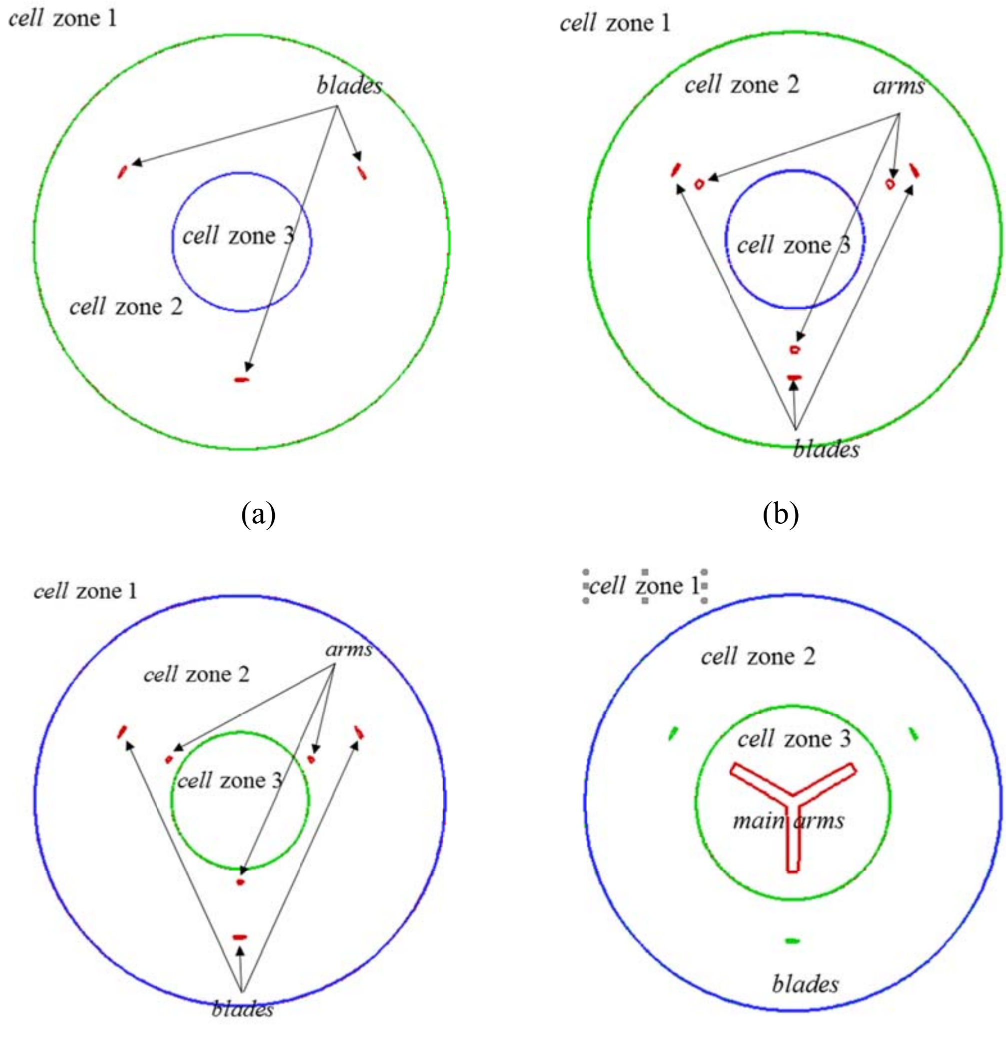

(a) (b) (c) (d)

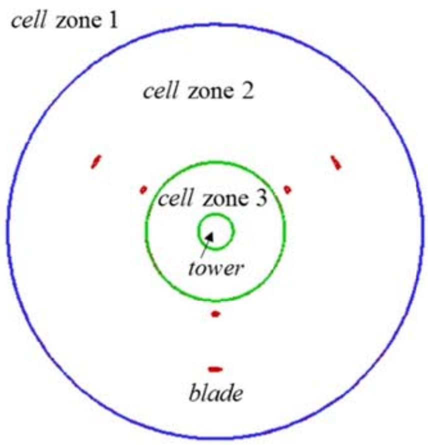

(e)

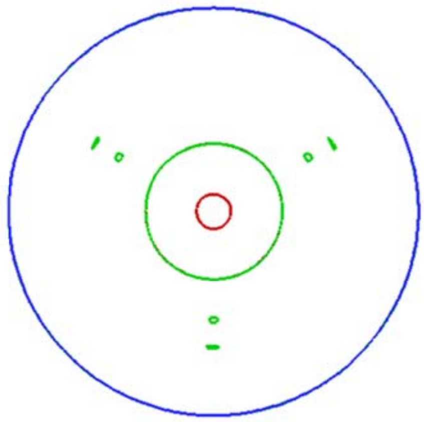

(f)

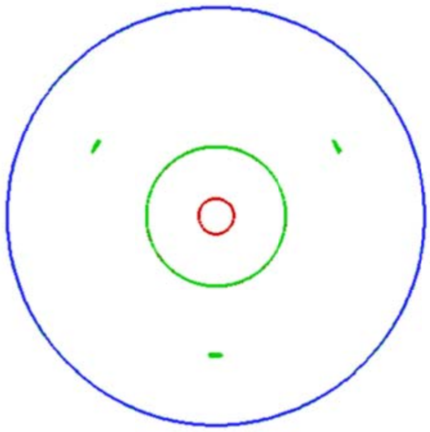

(g)

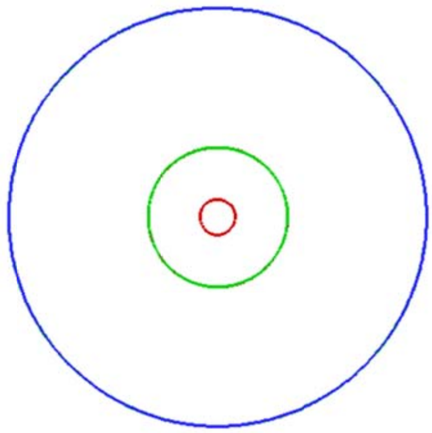

(h)

Fig. 3.3 Selected sections (a) sec1; (b) sec2; (c) sec3; (d) sec4; (e) sec5; (f) sec6; (g) sec7; (h) sec8 and sec9

After wind load simulations are completed for all the 9 sections under the simulated wind field, the simulated wind loads on all the 9 sections will be used collectively and synchronously to yield the 3D wind load field on the VAWT.

3.3 Comparison of 2D SST k-ω and 2.5D LES for Wind Load Simulation

Either 2D or 2.5D CFD simulation can be considered for each cross section and the specific simulation method should be determined first. There are also alternate turbulence models as introduced in Chapter 2. For a VAWT, the most widely used turbulence models are the SST k-ω model and the LES model. Li et al. (Li et al., 2013) suggested using 2.5D LES after having compared different simulation methods with the experimental results and claimed that LES has better prediction in the high angle of attack flow. Nevertheless, the computational cost of LES is high. It is computationally intensive to apply 2.5D LES to so many sections and wind speed cases. On the other hand, SST-RANS, such as SST k-ω, has the advantage over the standard RANS in the ability of predicting flow separation (Menter et al., 2003). 2D SST k-ω simulation is one of the best choices for the VAWT problem concerned in this study due to its efficiency and precision. To make sure that 2D SST k-ω simulation can be applied for wind load simulation of a VAWT, the aerodynamic forces on the blades are simulated by both the 2D SST k-ω model and the 2.5D LES and compared to each other in this section.

3.3.1 CFD simulation strategy

As introduced in Chapter 2, traditional CFD can only simulate the flow field around a stationary stuff. In order to simulate the flow field around a rotating VAWT, the technique of sliding mesh, dynamic mesh and overlapping mesh can be used (Lanzafame et al., 2013; Li et al., 2013; Nini et al., 2014). In consideration of its wide application range and simplicity, the sliding mesh technique is often adopted in the simulation of wind loads on a 2D VAWT (Almohammadi et al., 2013; Castelli et al., 2011; Li et al., 2013; McLaren, 2011). This technique requires the flow field to be discretized into several zones and the data of these zones can be transformed to each other through sliding interfaces. In this study, the sliding mesh technique is adopted in both the 2D SST k-ω simulation and 2.5D LES.

The comparison of the two methods is conducted by taking sec7 as an example, which is a typical section of the VAWT including the tower and blades. The geometry and boundaries of the flow field simulated around the wind turbine are shown in Fig. 3.4.

The radius of the rotor is R=20m. The velocity inlet is located at 400 m (20R) in front of the VAWT and the outlet is placed at 480m (24R) behind the VAWT to ensure the full development of wake. The side boundaries are 400m (20R) away from the center of the rotor to eliminate the blockage effect. A free-slip wall boundary condition is applied, where the normal velocity components and the normal gradients of all velocity components are assumed to be zero.

In order to use the sliding mesh technique, the mesh grids are divided into 3 zones, cell zone 1, cell zone 2 and cell zone 3, as shown in Fig. 3.4. Two non-conformal grid interfaces, specified by sliding mesh boundary condition, separate cell zone 2 from cell zones 1 and 3. The blades or arms are modeled as wall boundaries in cell zone 2, and the tower is modeled in cell zone 3 also as wall boundary. Hence, the meshes in cell zones 1 and 3 are stationary and the cell zone 2 is a rotating ring. The azimuth angle θ is also defined in Fig. 3.4. $\theta \in \left[0, 180^{\circ}\right]$ is the upwind side for the blade and $\theta \in \left[180^{\circ}, 360^{\circ}\right]$ is the downwind side for the blade. In this study, the azimuth angle $\theta = 0$ at the time $t = 0\text{s}$ for the blade.

The grid-independent check is conducted. The y-plus of the results obtained by SST k-ω and LES are smaller than 2. Then more refined mesh grid of the two models have been selected and the results show no obvious influence on the simulated wind load. Therefore, the mesh grid presented in the thesis are chosen. The optimal mesh configurations used in the CFD model are shown in Fig. 3.5. Fig. 3.5(a) is the mesh of the whole flow field; Fig. 3.5(b) shows the grids of cell zone 2; Fig. 3.5(c) shows the detail of the mesh near a blade; Fig. 3.5(d) is the mesh grids of cell zone 3. The numbers of grids in cell zones 1, 2 and 3 are 32,000, 174,600 and 24,432, respectively. The total number of grids in this 2D SST k-ω simulation is 231,032.

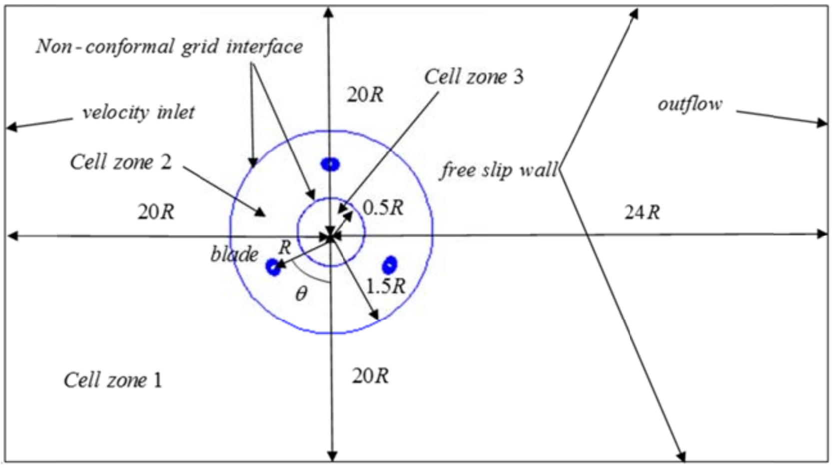

Fig. 3.4 Scheme of geometry and boundaries for wind load simulation

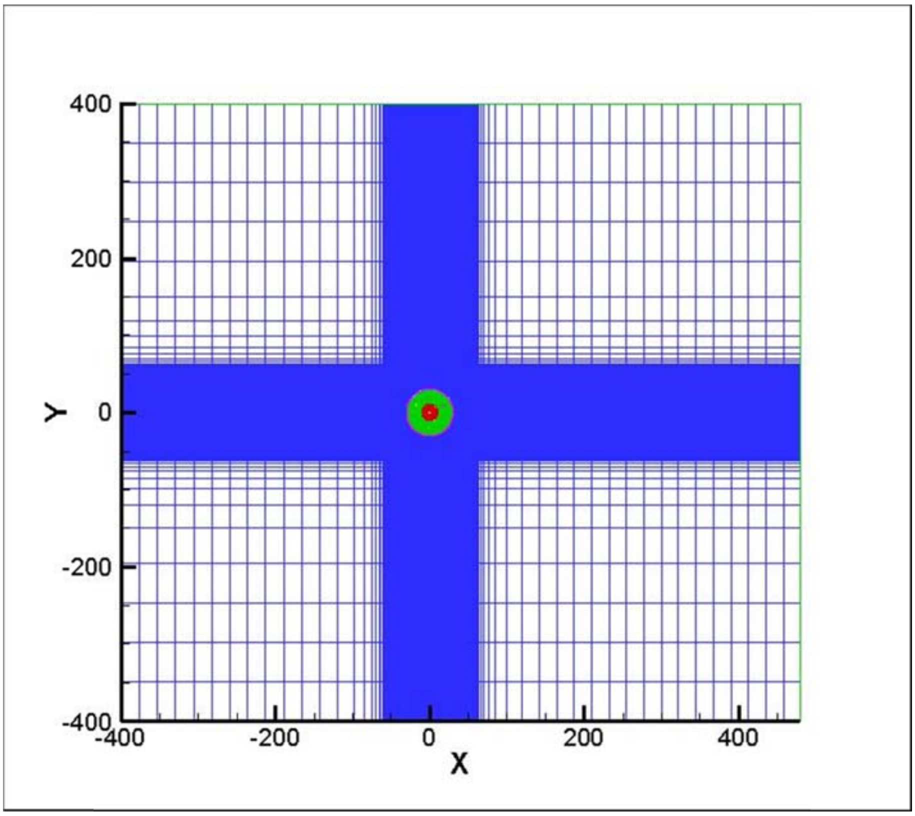

(a)

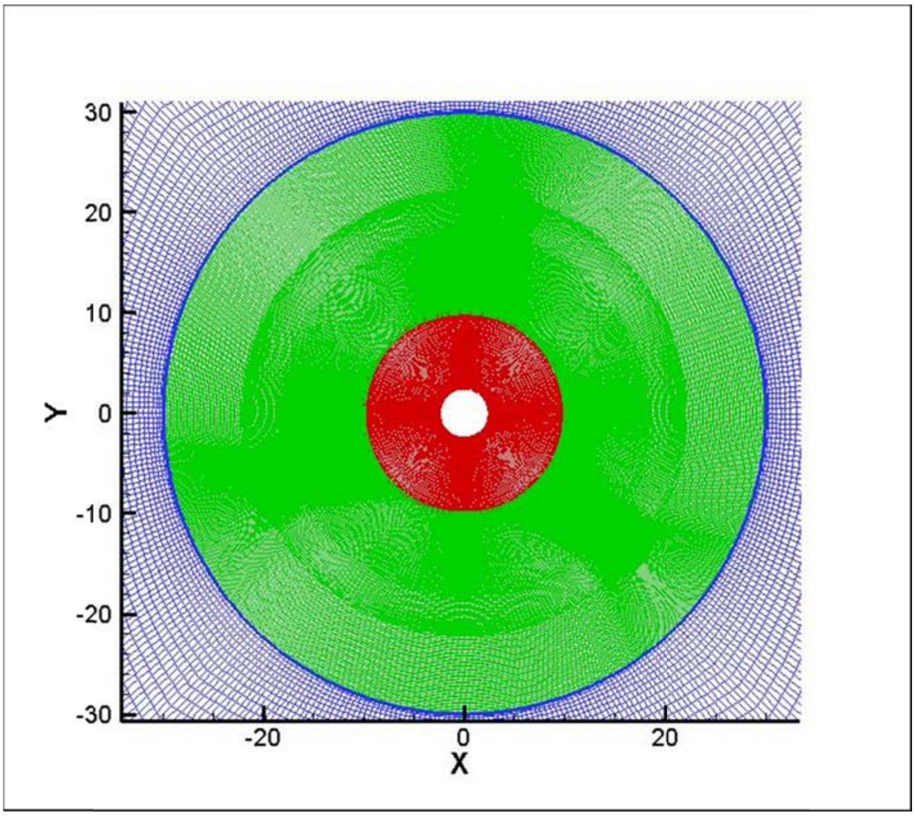

(b)

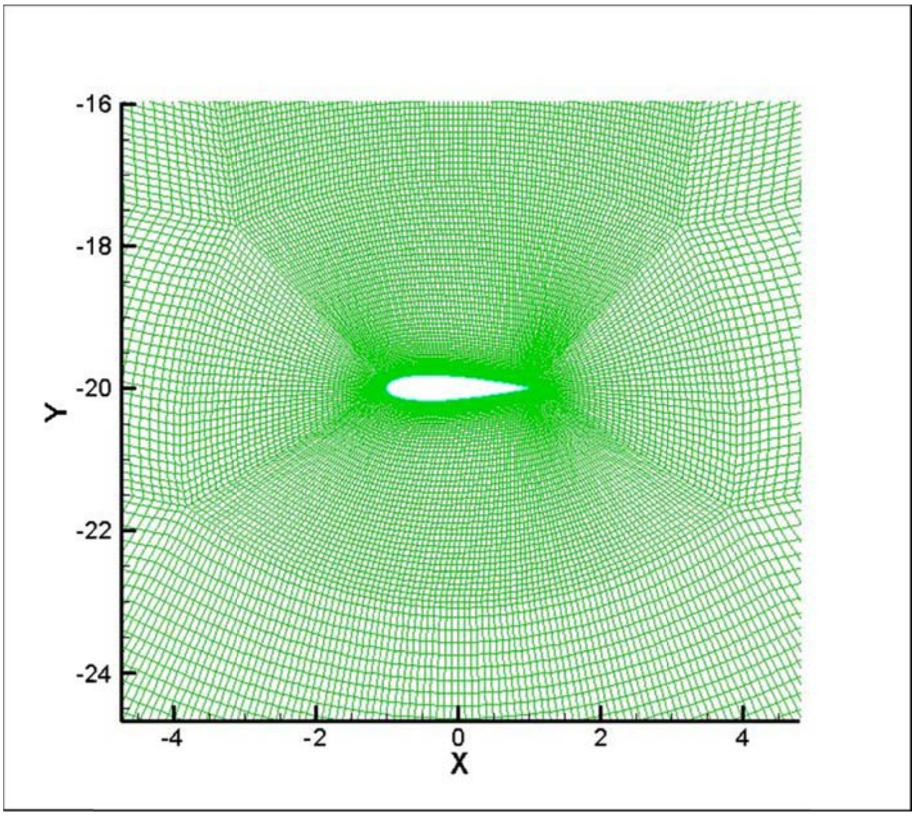

(c)

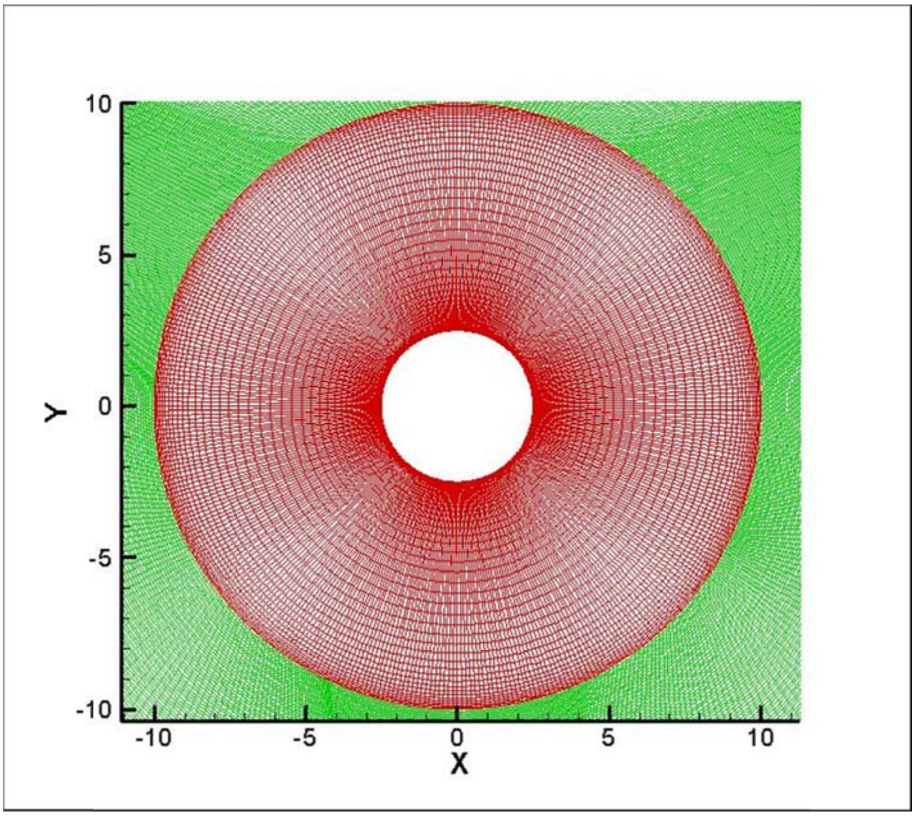

(d)

Fig. 3.5 Mesh grids of the flow field. (a) mesh of the whole flow field; (b) mesh of zone 2 and zone 3; (c) mesh around blade; (d) mesh of zone 3

For the 2.5D LES model, the 2D mesh introduced above is extruded by 0.82m with 40 layers in the vertical (z) direction. Translational periodic conditions are applied on the top and bottom boundaries, which represent that the blades and tower are infinitely long and the influences of finite span are not taken into account. The total number of grids is 9,241,280, which is extremely larger than that of 2D SST k-ω case and computational intensive.

In this CFD simulation, the inflow velocity V_∞ is selected as 10m/s and no turbulence in the inflow is considered. Since the tip speed ratio λ ($= \omega R / V_\infty$) has a determinant influence on the aerodynamic forces (Burton et al., 2001; Paraschivoiu, 2002), λ = 1 and 3 are considered in the simulation as two cases. The rotation speeds are accordingly 0.5rad/s and 1.5rad/s respectively.

3.3.2 Comparison and discussion

The simulated wind loads, including wind pressures and aerodynamic forces, are compared in this subsection. For wind pressures, their time histories at the chosen points and their distribution over the blade cross section at a given azimuth angle are presented. Since 2.5D LES can be regarded as a 3D model, the results are averaged through the thickness to compare with those from the 2D SST k-ω simulation. Conventionally, wind pressures and aerodynamic forces are represented in terms of the pressure coefficient C_p, the normal force coefficient C_n, and the tangential force coefficient C_t and the moment coefficient C_M respectively. The definitions of C_p, C_n, C_t and C_M are expressed by the following equations.

$$C_p = \frac{p}{1/2\,\rho V_\infty^2} \tag{3.12a}$$

$$C_n = \frac{F_n}{1/2\,\rho V_\infty^2 c} \tag{3.12b}$$

$$C_t = \frac{F_t}{1/2\,\rho V_\infty^2 c} \tag{3.12c}$$

$$C_M = \frac{M}{1/2\,\rho V_\infty^2 c^2} \tag{3.12d}$$

where p, F_n, F_t and M are the wind pressure, the normal force, the tangential force and the moment respectively; c is the chord length; ρ is the density of air; and V_∞ is the inflow velocity. To determine the forces and moment by integrating wind pressures over the cross section of the blade, the reference point has to be given and it is usually take the point at $c/4$ away from the leading edge in the chord line. The normal force F_n is then defined as the component of aerodynamic force perpendicular to the chord, from outside to inward; the tangential force F_t is defined as the component of aerodynamic force along the chord line and pointing from the trailing edge to the leading edge; and the moment refers to the reference point with the counter-clock moment as positive in this study.

3.3.2.1 Wind pressures

The simulated wind pressures by the two methods are taken to compare with each other. The comparisons are conducted in two perspectives: one is to compare the time varying wind pressures at the chosen points of the blade section; and the other is to compare the pressure distribution over the cross section of the blade at different azimuth angle θ.

The section of the blade is shown in Fig. 3.6. The abscissa is the chord length of the blade, from the leading edge at 0m to the trailing edge at 2m. The ordinate is the thickness of the blade. Four points on the blade section are chosen: A, B, C and D, as shown in Fig. 3.6. Points A and B have the same abscissa, 0.032m from the leading edge. Points C and D also have the same abscissa, 0.503m from the leading edge. Points A and C are on the lower surface (outside surface of the vertical blade). Points B and D are on the upper surface (inside surface of the vertical blade). The time histories of wind pressures at these four points are shown in Fig. 3.7 for $\lambda = 1$ and Fig. 3.8 for $\lambda = 3$.

It can be seen that the periodicity of wind pressure time history is clear. This cyclic variation is due to the rotation of the VAWT and the mean wind speed. To have a close look, the 1st cycle of the wind pressures at the four points are also plotted in Fig. 3.7 (c) - (d) (for $\lambda = 1$) and Fig. 3.8 (c) - (d) (for $\lambda = 3$). It can be seen that because of the rotation of the VAWT, the wind pressures at points A and B as shown in Fig. 3.6 (c) (or points C and D as shown in Fig. 3.6 (d)) are not equal even at zero azimuth angle. For the case of $\lambda = 1$, the absolute magnitudes of the pressures at A and B increases with the increasing azimuth angle from zero. When the azimuth angle reaches at some value, the magnitudes begin to decrease. For example, the pressure given by LES at point B decreases at about azimuth angle $\theta = 40^{\circ}$. However, the pressure given by SST $k-\omega$ simulation at point B decreases at about azimuth angle $\theta = 60^{\circ}$. The largest pressure differences between A and B given by the two models coincidently appear at these azimuth angle. Then, the pressures at A and B decrease to about zero at the $\theta = 180^{\circ}$ for both the LES and SST $k-\omega$ simulations. In the downwind side, the pressures at A and B remain a small value within a range of azimuth angle. For the results of LES, the pressures at A and B are nearly coincident and keep at a small pressure in the range of $[180^{\circ}, 250^{\circ}]$; the results of SST $k-\omega$ are similar to the LES. After this range of azimuth angle, the pressure at point A becomes negative and the pressure at point B becomes positive for the results from the two models. This is because that in azimuth angle $[180^{\circ}, 360^{\circ}]$, the upwind surface of the blade becomes the downwind surface and vice versa. The variation of the pressures at C and D is similar to the pressures of A and B. Moreover, it can be found that for the pressures given by SST $k-\omega$ simulation at these four points have obvious shifts to the positive pressure, while the pressure difference between A and B and the pressure difference between C and D are close to the corresponding results of LES.

For the case of $\lambda = 3$, the results from the two models are much closer to each other than the case of $\lambda = 1$. For both results, the pressures at A and C are positive in the range of azimuth angle $\theta \in \left[0^{\circ}, 180^{\circ}\right]$ and become negative in the range of $\theta \in \left[180^{\circ}, 360^{\circ}\right]$. Contrarily, the pressures at B and D are negative in the range of $\theta \in \left[0^{\circ}, 180^{\circ}\right]$ and become positive in the range of $\theta \in \left[180^{\circ}, 360^{\circ}\right]$. It is worth mentioning that the maximum pressure difference between A and B (or between C and D) in this case appears at a larger azimuth angle than corresponding azimuth angle of the case $\lambda = 1$.

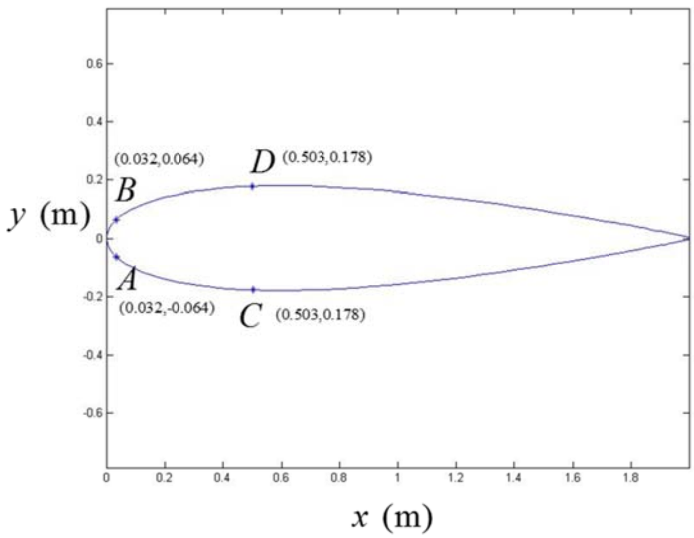

Fig. 3.6 Cross section of a NACA0018 blade

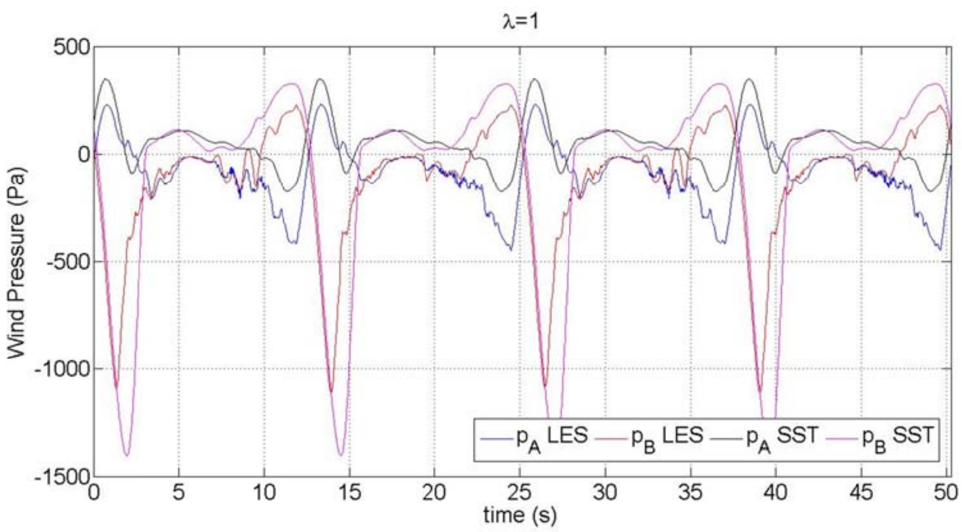

(a)

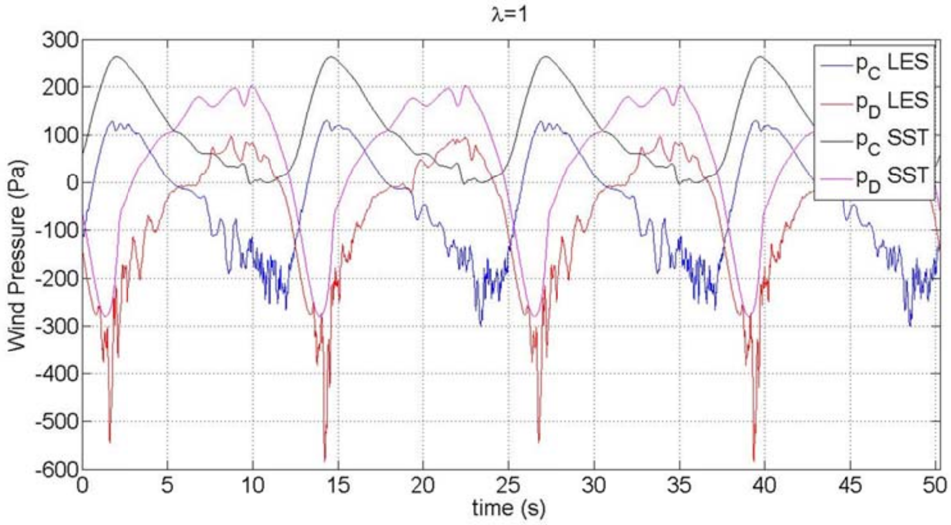
λ=1
p_C LES
p_D LES
p_C SST
p_D SST
Wind Pressure (Pa)
time (s)

(b)

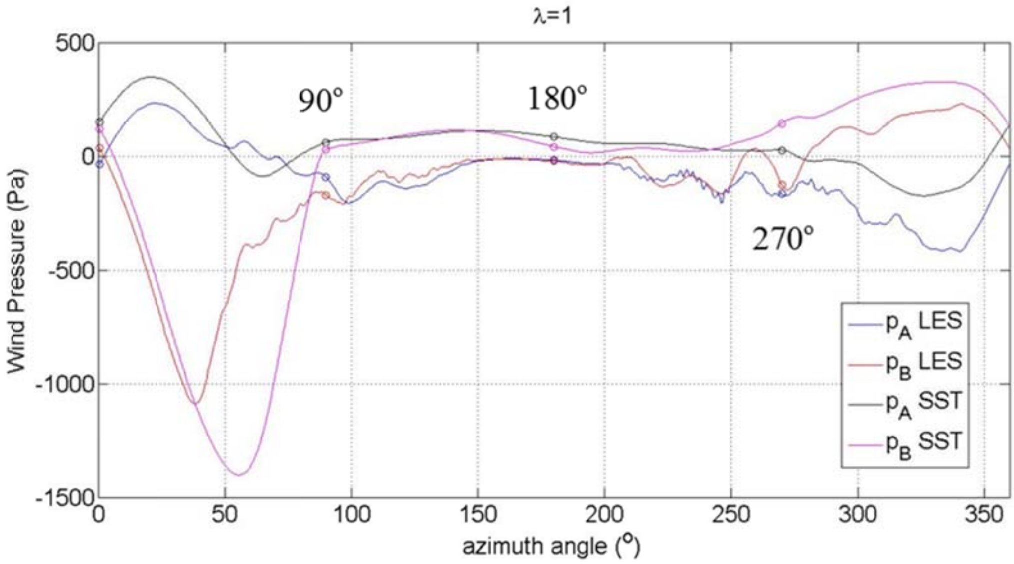
λ=1
90°
180°
270°
p_A LES
p_B LES
p_A SST
p_B SST
Wind Pressure (Pa)
azimuth angle (°)

(c)

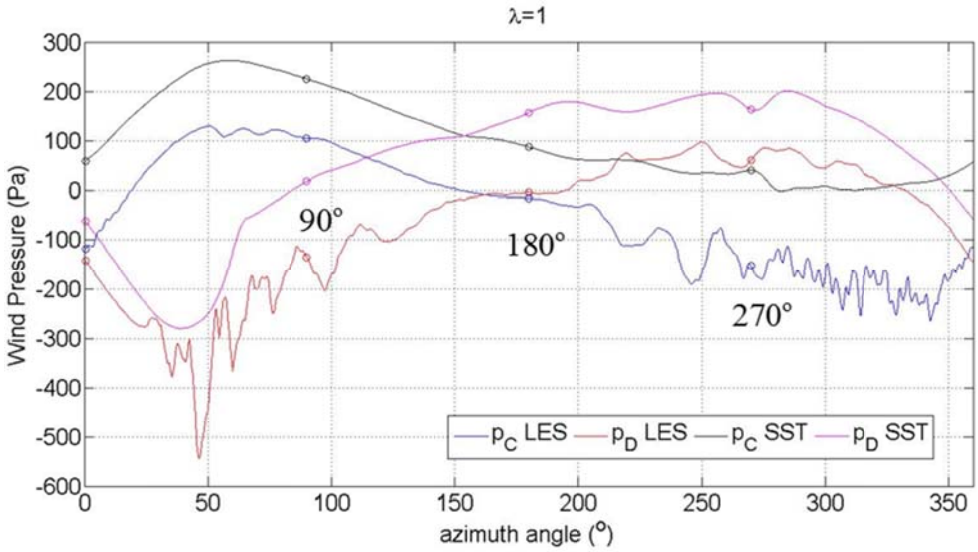

(d)

Fig. 3.7 Wind pressure time histories ($\lambda = 1$) (a) 4 cycles of points A and B; (b) 4 cycles points C and D; (c) the 1st cycle of points A and B; (d) the 1st cycle of points C and D.

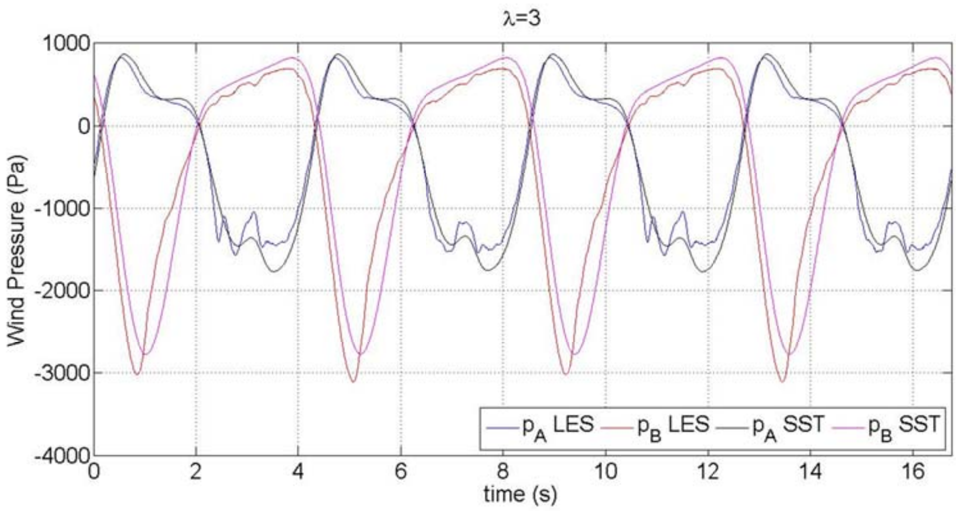

(a)

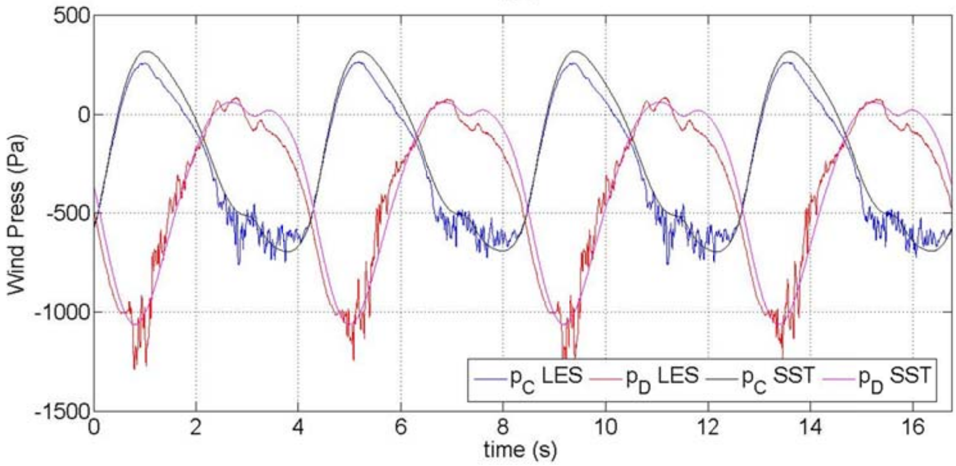
λ=3
Wind Press (Pa)
time (s)
p_C LES
p_D LES
p_C SST
p_D SST

(b)

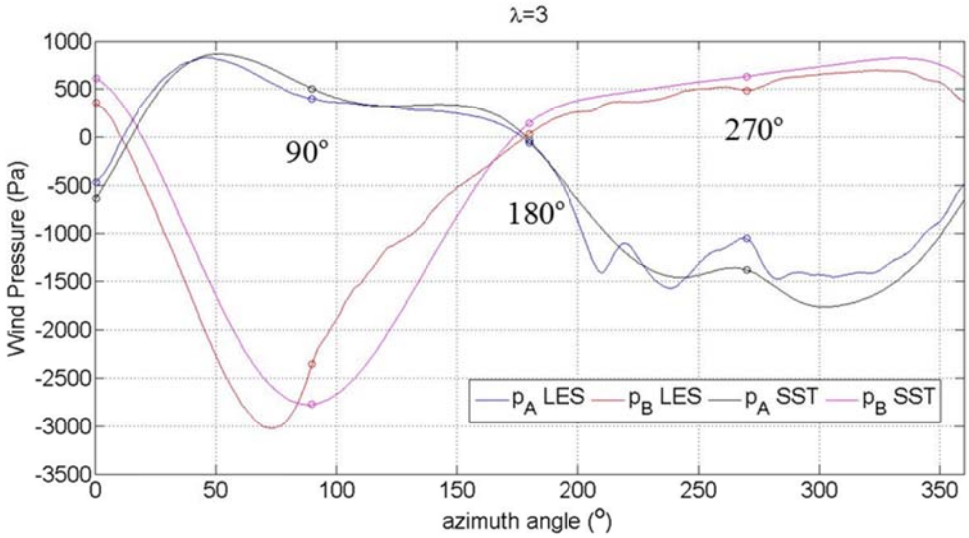
λ=3
Wind Pressure (Pa)
azimuth angle (°)
90°
180°
270°
p_A LES
p_B LES
p_A SST
p_B SST

(c)

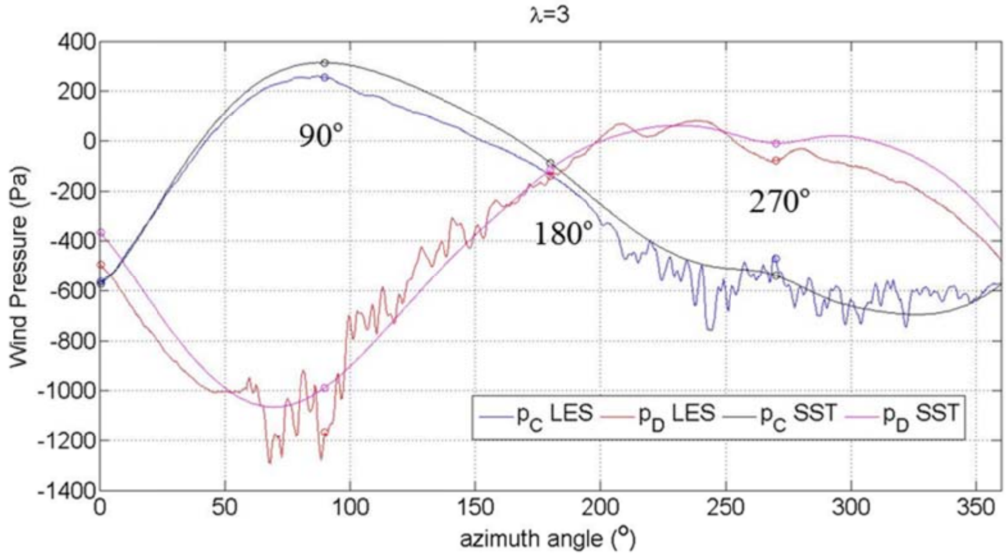

(d)

Fig. 3.8 Wind pressure time histories ($\lambda = 3$). (a) 4 cycles of points A and B; (b) 4 cycles points C and D; (c) the 1st cycle of points A and B; (d) the 1st cycle of points C and D.

The pressure distribution over the cross section of the blade at a given azimuth angle θ is presented in such a graph that the abscissa is the chord length of the blade, from the leading edge at 0m to the trailing edge at 2m, and the ordinate is the wind pressure on the blade. Wind pressure distributions over the cross section of the blade are plotted in Fig. 3.9 and Fig. 3.10 for the case λ =1 and the case λ =3 respectively. The wind direction and the azimuth angle of blade are also shown in these figures; the leading edge is marked by "M" and the trailing edge is marked by "N".

For $\lambda = 1$ and when $\theta = 30^{\circ}$, the pressure distribution patterns obtained by the two methods are similar, as shown in Fig. 3.9(a). The pressures are positive on the outside surface of the blade and they are negative on the inside surface of the blade in general. The pressure difference is mainly concentrated on the leading edge and decays to zero at the trailing edge, which is coincident with the analysis of aerodynamics. (McCormick et al., 1995). The wind pressure given by the SST $k-\omega$ simulation has an obvious shift to the positive pressure side compared with the wind pressures given by LES. When θ=50° (Fig. 3.9(b)), the pressure distribution patterns from the two methods are quite different. The pressure distribution given by SST k-ω remains similar to that at θ=30°, but the negative pressure given by LES decays quickly at the leading edge and becomes relatively flat almost in the whole upper surface (inside surface of the vertical blade). At the azimuth angle $\theta = 70^{\circ}$, both the negative pressures obtained by the two models decay quickly near the leading edge and become flat through the chord line.

It is known that when flow separation occurs, the pressure in the separation area is negative (McCormick et al., 1995). The phenomenon shown in Fig. 3.9 can be explained in the following. When $\theta = 30^{\circ}$, flow separation does not occur for both cases, so the two results are similar. When $\theta = 50^{\circ}$, flow separation already happens in the LES case but not in the SST case, so the pressure distribution of the LES result becomes flat. When $\theta = 70^{\circ}$, the pressure distributions from the two methods imply that flow separations happen in both cases.

In a large tip speed ratio case of $\lambda = 3$, when $\theta = 60^{\circ}$ the pressure distributions obtained by the two methods match well and it seems that no flow separation happens as shown in Fig. 3.10(a). When $\theta = 105^{\circ}$, slight separation computed by the LES can be seen but it does not happen in the SST $k - \omega$ simulation, as shown in Fig. 3.10(b). Anyway, it can be found that in this case, the discrepancy of the results from these two models is small.

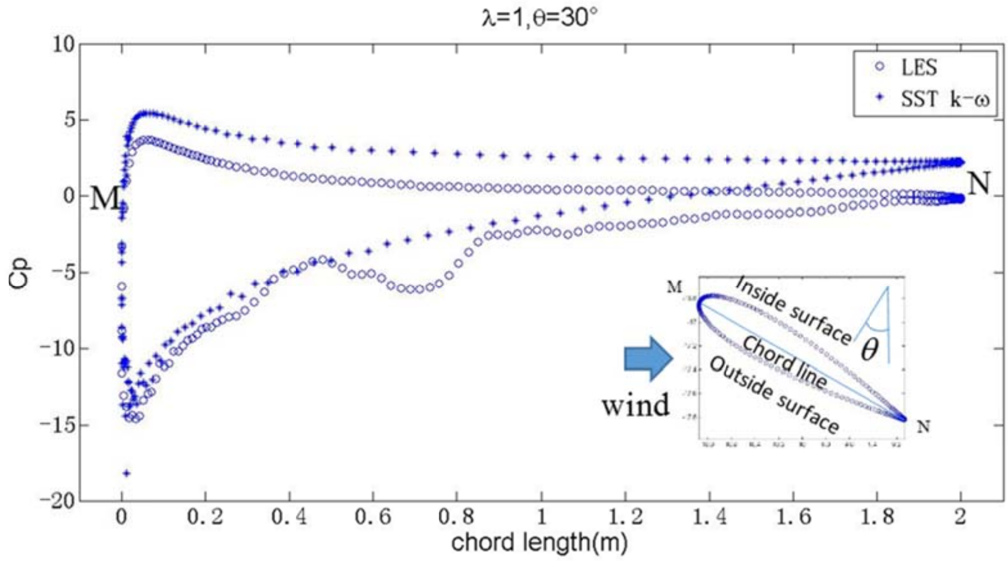

λ=1,θ=30°
LES
SST k-ω
M
N
Cp
chord length(m)
Inside surface
Chord line
Outside surface
θ
wind

(a)

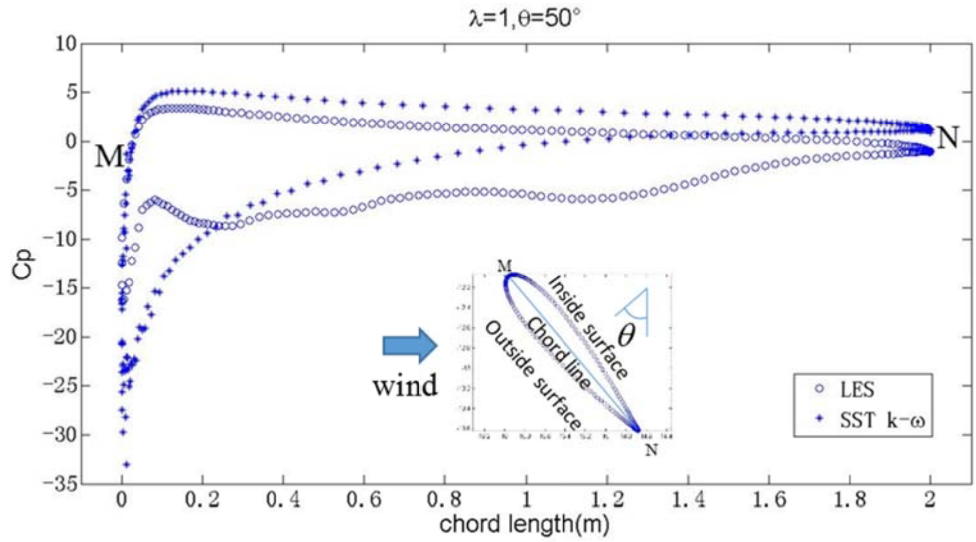

λ=1,θ=50°
LES
SST k-ω
M
N
Cp
chord length(m)
Inside surface
Chord line
Outside surface
θ
wind

(b)

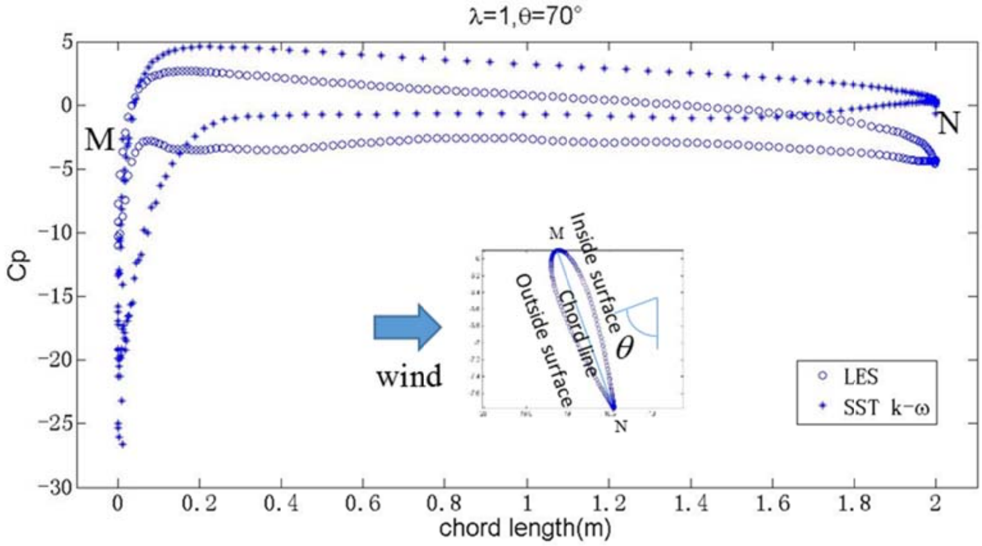

(c)

Fig. 3.9 Wind pressure distributions for the case of $\lambda=1$ (a) $\theta=30^{o}$; (b) $\theta=50^{o}$; (c) $\theta=70^{o}$;

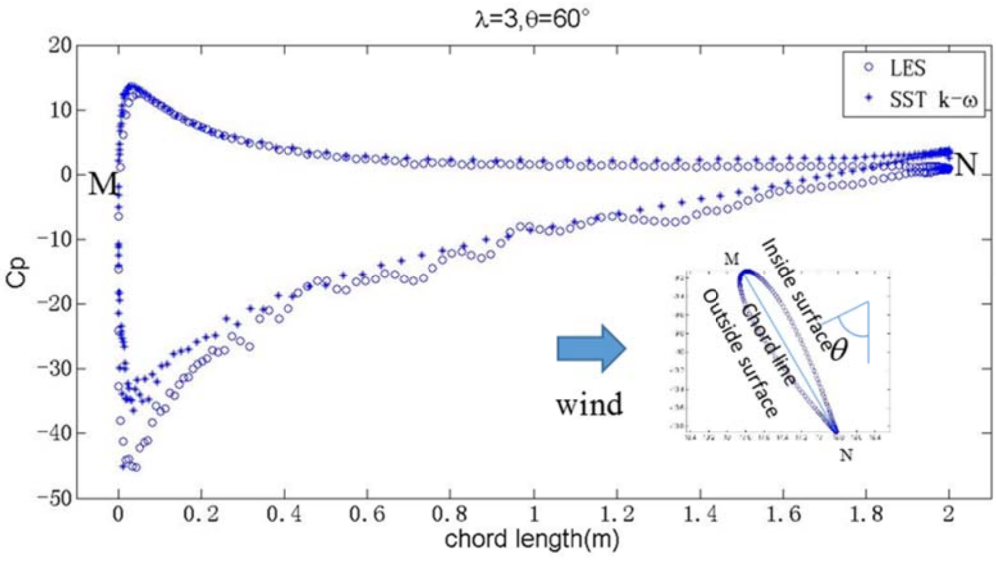

(a)

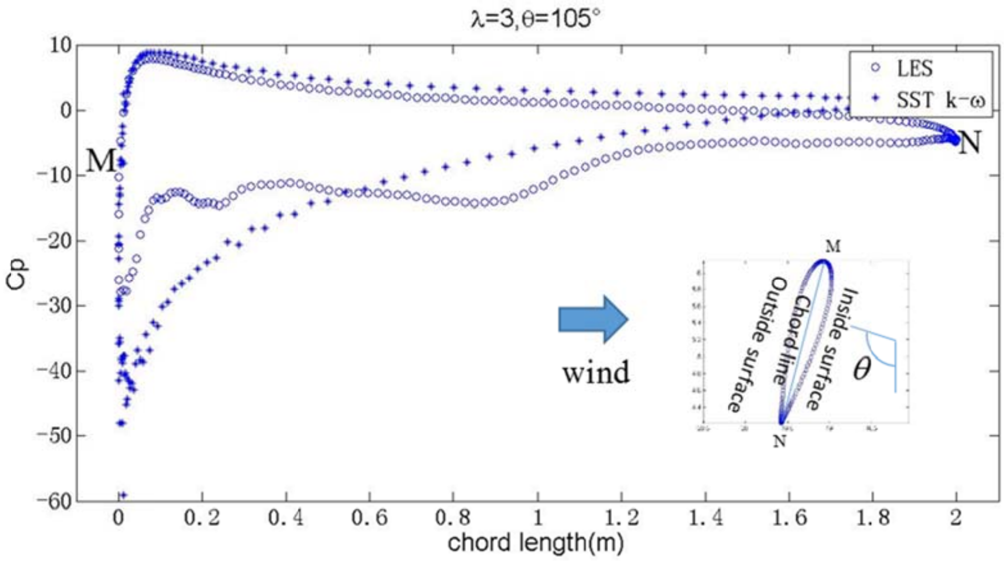

(b)

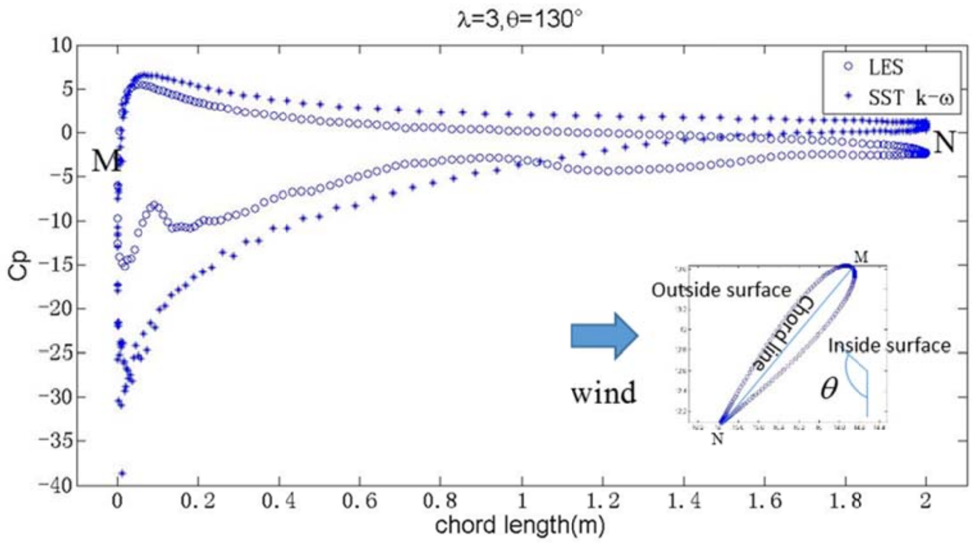

(c)

Fig. 3.10 Wind pressure distributions for the case of $\lambda = 3$ (a) $\theta = 60^{\circ}$; (b) $\theta = 105^{\circ}$; (c) $\theta = 130^{\circ}$

3.3.2.2 Aerodynamic forces

To calculate wind-generated power, the aerodynamic forces, such as tangential forces, acting on the blade are required. These forces can be obtained by integrating the wind pressures over the cross section of the blade. Furthermore, by using Equation (3.12), the normal force coefficient C_n and the tangential force coefficient C_t can be obtained and used in comparison.

The computed C_n and C_t against azimuth angle are shown in Fig. 3.11. It can be found that force coefficients, especially C_n, obtained by the two methods match well for the two tip speed ratio cases. This is because although there exists a pressure shift for the case of $\lambda = 1$, the aerodynamic forces are determined by the pressure difference between the upper and lower surfaces. Because the pressure differences obtained by the SST $k-\omega$ simulation match well with the results of LES, the aerodynamic forces obtained by the two methods are similar. The slight difference is mainly reflected in C_t coefficients. The C_t coefficients from the two methods remain similar when the azimuth angle is small, namely from 0 to some azimuth angle θ_0 : for $\lambda = 1$, $\theta_0 \approx 40^o$ (Fig. 3.11(a)); and for $\lambda = 3$, $\theta_0 \approx 80^o$ (Fig. 3.11(b)). When the azimuth angle is over θ_0, C_t coefficients from the two methods become different. C_t in the 2.5D LES case decreases while C_t in the 2D SST $k-\omega$ case still increases and then decreases at a larger azimuth angle. This discrepancy may be due to the different estimations in flow separation zones by the two methods.

The cases considered in this section show that the normal force coefficients calculated by 2.5D LES and 2D SST k-ω methods are nearly the same and the slight difference is mainly reflected in tangential forces due to the different prediction of the flow separation. Since the normal force is much larger than the tangential force, the normal force is dominant in the structure analysis. In summary, the 2D SST k-ω method is an acceptable alternative to the 2.5D LES method in consideration of both the accuracy of the results and the efficiency of computation.

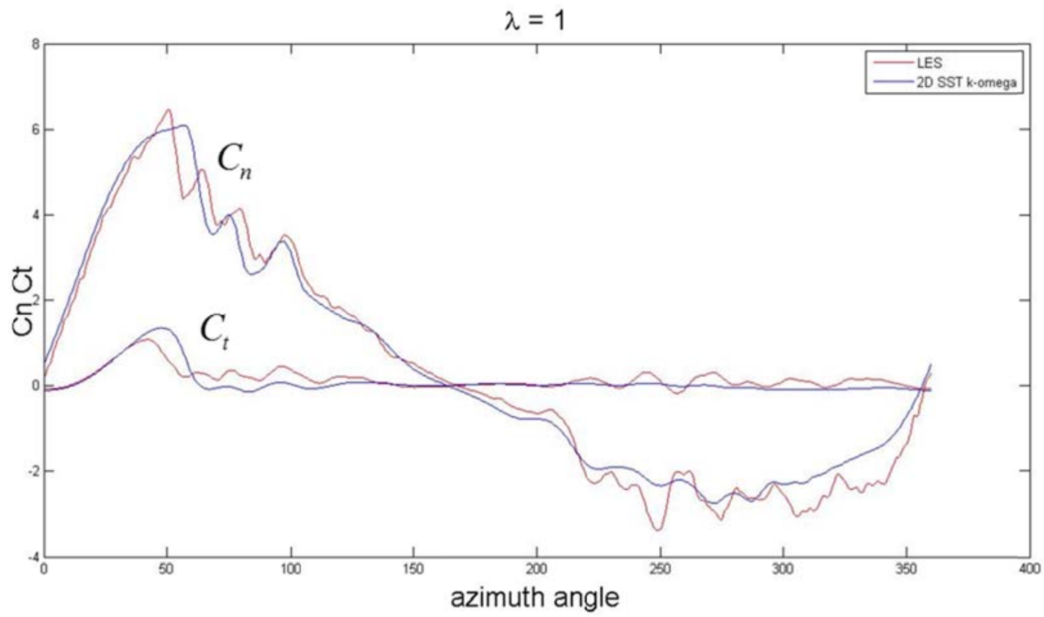

(a)

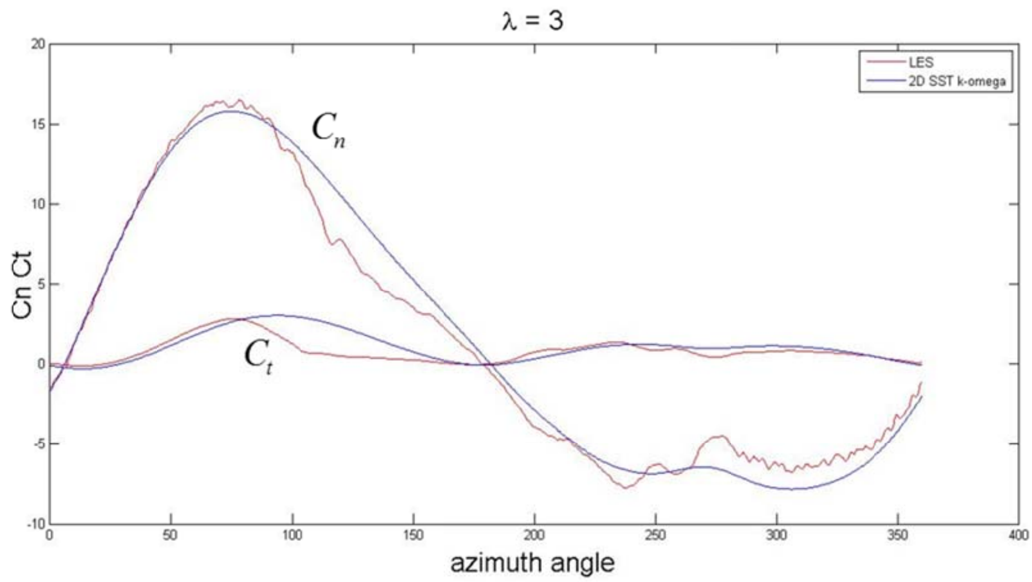

(b)

Fig. 3.11 Comparisons of normal force coefficient C_n and tangential force coefficient C_t. (a) $\lambda = 1$; (b) $\lambda = 3$

3.4 Wind Loads on the Whole VAWT

In order to conduct the fatigue and ultimate strength analyses of the VAWT in Chapters

5 and 6 respectively, the wind pressures on the blade and the aerodynamic forces on the whole VAWT, considering the interference among all the structural components and different wind conditions, are required. The 2D CFD simulation is performed for the chosen 9 cross sections (listed in Table 3.1) and the SST $k-\omega$ turbulence model is adopted. To obtain the spatial wind loads from these discrete sectional results, the interpolation technique is used.

3.4.1 Wind speed simulations

In order to conduct the 2D CFD simulation for the cross sections of the VAWT chosen, the inflow wind speeds and mesh grids in each section must be given from the entire wind field simulated. Firstly, the inflow wind speeds in the 9 cross sections are simulated by the strip method introduced in Section 3.2.2. By taking the rated wind speed (14m/s mean wind speed at the hub height) for example, the wind speed time histories in the 9 cross sections are simulated and the wind speed time history for sec4 is shown in Fig. 3.12. The wind speed time histories for other cross sections are shown in Appendix A. Clearly, the wind speed time history contains both mean wind speed and turbulent wind speed components.

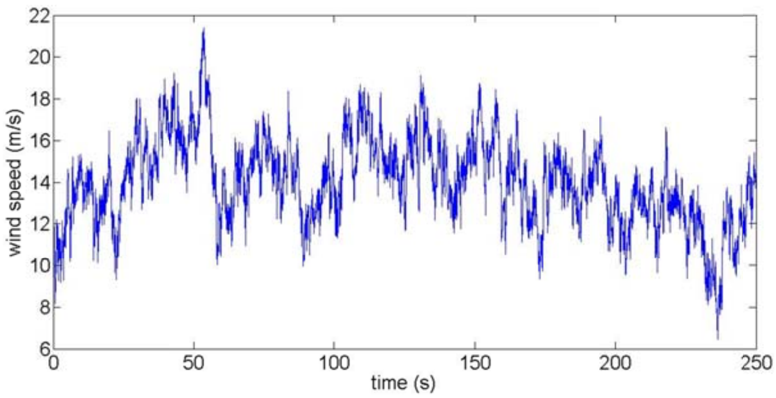

Fig. 3.12 Wind speed time history for sec4

3.4.2 CFD simulation strategy

The CFD simulation strategy and the mesh grids of sec7 are introduced in Section 3.3.1. For the other cross sections, the differences are represented by cell zone 2 and cell zone 3. In these cross sections, the blades and upper/lower arms are modeled in cell zone 2, and the tower is modeled in cell zone 3. Hence, cell zones 1 and 3 are stationary and cell zone 2 is a rotating ring. One exception is sec4, in which the main arms are modeled in cell zone 3, and cell zone 3 is also rotating. The mesh grids of cell zone1 and cell zone2 of sec1 – sec8 are shown in Appendix B. The structural components of the VAWT are all modeled as wall boundaries. Since the diameter of the links, connecting the upper and lower arms, is small (0.2m), they are not considered in the CFD simulation.

The grid numbers of the 9 cross sections are listed in Table 3.2. The validity of these mesh grids is verified by the near wall y-plus values which will be given in Section 3.4.3 and Section 3.4.4.

Table 3.2 the number of grids for 9 sections

Sec1	Sec2	Sec3	Sec4	Sec5	Sec6	Sec7	Sec8	Sec9
217432	299032	279832	238232	277832	277832	231032	88432	88432

In the operating wind speed region (from 5m/s to 21m/s for the specific VAWT in this study), the VAWT is rotating at 2.1rad/s. In this study, the results of the rated wind speed case are taken for example and the wind speed time history of each section is given in Appendix A. The wind loads at other wind speed cases are also simulated and used in Chapters 5 and 6. In the extreme wind speed case, the VAWT is parked. Based on the equivalent static wind theory, the problem is regarded as steady rather than unsteady.

3.4.3 Wind loads in the operating wind speed region

In the operating wind speed region, the VAWT is rotating. In this subsection, the procedure about how to obtain spatial continuous and time varying wind loads from the discrete cross sections is shown and the wind loads on the VAWT are given.

3.4.3.1 Wind Pressures on the Blade

In Chapter 5, the wind pressures on the whole blade are required to conduct fatigue and ultimate strength analyses. The wind pressures in the discrete sections are simulated first and then, the interpolation technique is applied to obtain the wind pressures in an arbitrary cross section.

The wind pressures on the blade in the 7 cross sections are time varying (the blades only presented in sec1-sec7). For example, the time histories of wind pressures at the previously defined points A, B, C and D in sec1 are shown in Fig 13. It can be seen that the time histories are in the same phase as those shown in Fig.7 and Fig.8 and that the periodicity of wind pressure change is obvious due to the rotation of the VAWT. However, the wind pressure time histories shown in Fig. 3.13 are more fluctuating than those shown in Fig. 3.7 and Fig. 3.8. This is because turbulent wind speeds are now considered in the inflow.

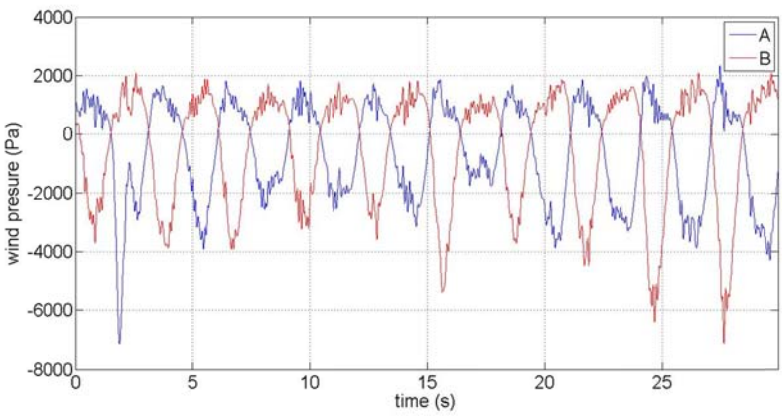

(a)

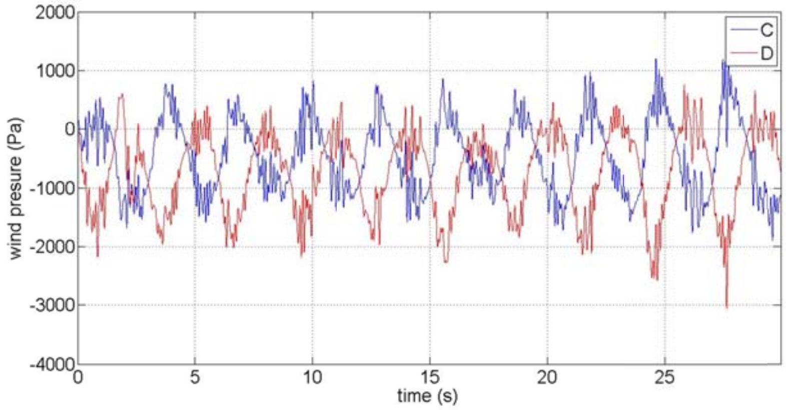

(b)

Fig. 3.13 Time varying wind pressures on sec1. (a) at points A and B;

(b) at points C and D

Moreover, the wind pressures are also varying with height. By taking the time of 18.70s ($\theta = \pi/2$) for example, the wind pressures over the 7 sections at this time are shown in Fig. 3.14. It can be seen obviously that the wind pressures in the higher cross sections are larger than those in the lower sections in terms of the absolute values of negative wind pressures in the leading edge. The wind pressures in sec4 are smaller than others, which reflects the influence of the main arm. Moreover, the wind pressure in the blade tail is nearly equal to zero, which agrees with the Kutta-Joukouski theorem.

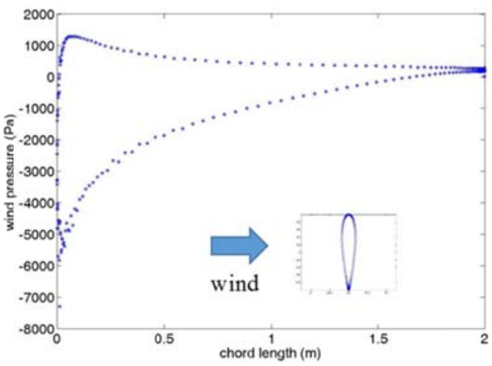

(a)

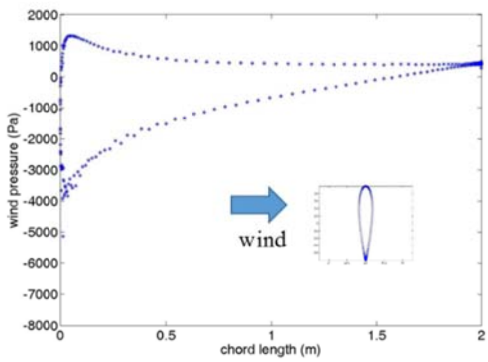

(b)

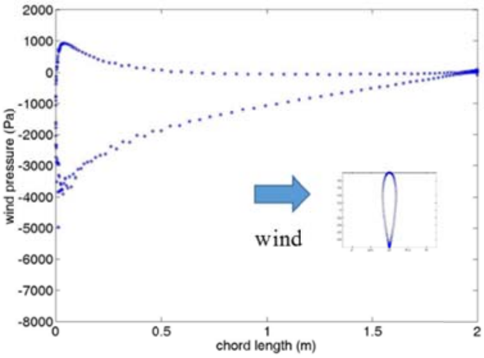

(c)

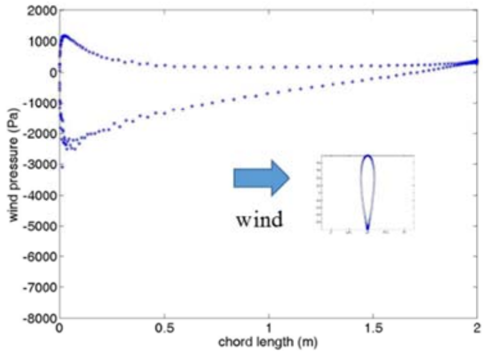

(d)

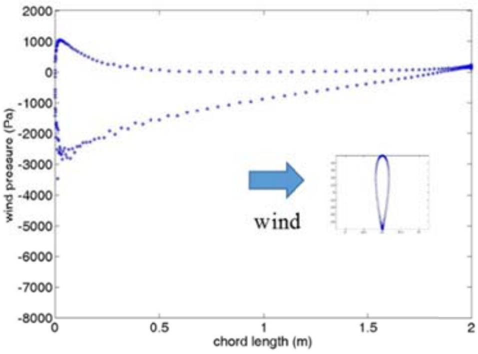

(e)

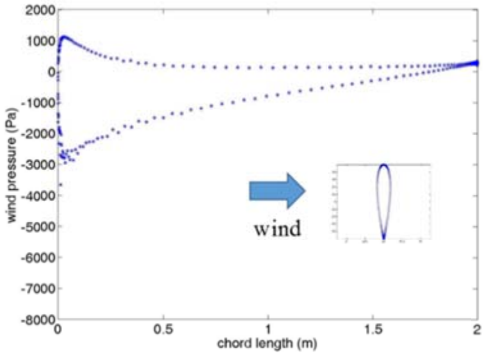

(f)

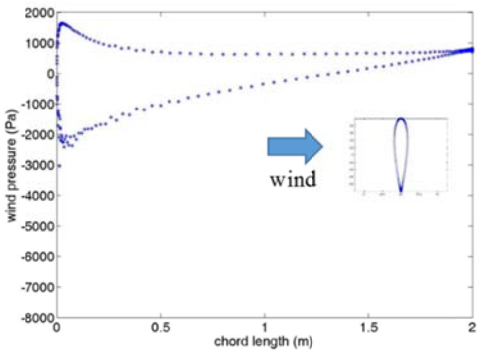

(g)

Fig. 3.14 Wind pressures over the 7 cross sections of a blade. (a) sec1; (b) sec2; (c) sec3; (d) sec4; (e) sec5; (f) sec6; (g) sec 7.

In these simulations, the near-wall y-plus values are calculated and listed in Table 3.3. It can be seen that all y-plus values are less than 2, satisfying the near wall requirement that y-plus should be less than 5 for the SST k-ω model (ANSYS, 2009).

Table 3.3 The near-wall y-plus values

Sec1	Sec2	Sec3	Sec4	Sec5	Sec6	Sec7	Sec8	Sec9
1.4	1.4	1.3	1.1	1.4	1.3	1.3	0.5	0.4

Since the wind pressures will be applied on the FE model of the blade for fatigue and ultimate strength analyses, the spatial distribution and the time history of a specific point in the blade section are required. In order to obtain the spatial continuous distribution of wind pressures and forces along the height of the VAWT, the interpolation technique is needed. There are alternate methods of interpolation, such as nearest, linear or spline methods. Since the variation of the wind pressure through the height is smoothing, the piecewise spline interpolation method is used here.

The 4 points on the blade sections, A, B, C and D, are taken for example again (see Fig. 3.6). The height varying pressures at these points are shown in Fig. 3.15. From Fig. 3.15, it can be seen that due to the influence of the mean wind profile, the negative wind pressure at the higher section is larger than that at the lower section. The positive wind pressure along the height is relatively flat which can be seen from the Fig. 3.15. The distribution of wind pressures is suddenly changed near sec4, which is caused by the existence of the main arm.

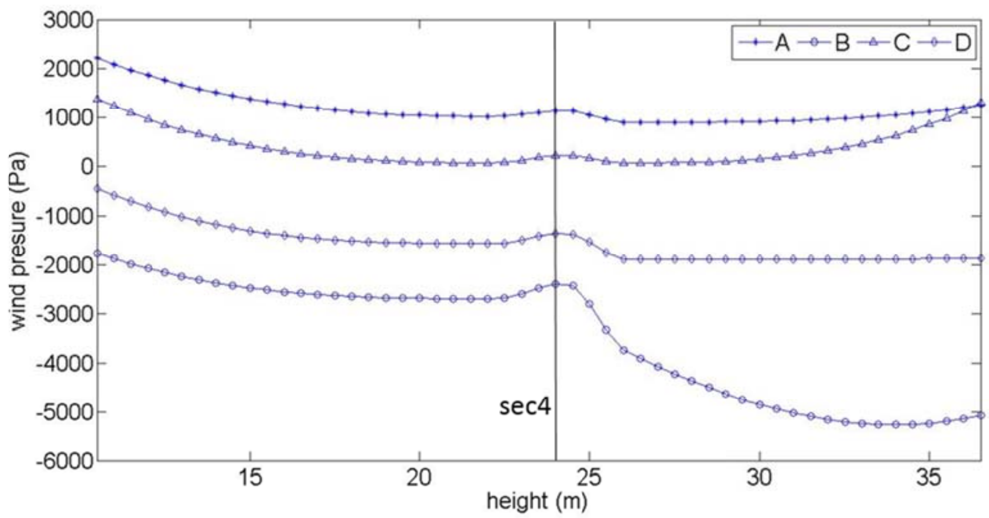

Fig. 3.15 Variation of wind pressures along the height at t=18.70s ($\theta = \pi/2$)

3.4.3.2 Aerodynamic Forces and moment

In Chapter 6, a FE model of the whole VAWT will be established using beam elements and the structural analysis of this model will be carried out, in which the aerodynamic forces other than wind pressures are required. Thus, the aerodynamic forces on the blades, arms and tower are obtained and discussed in this section.

As introduced in Chapter 2, the aerodynamic forces, including normal force, tangential force and moment, can be obtained by integrating the wind pressures over the surfaces of the components. The time varying aerodynamic forces on the blade per unit length along the height of the blade are shown in Fig. 3.16. The two horizontal coordinates are the time and the blade height, respectively, and it is noted that the blade is installed from 10.5m height above the ground to 36.5m height at the top, as shown in Fig. 3.1. The vertical coordinate is the aerodynamic force or moment per unit length. From Fig. 3.16, it can be seen that the aerodynamic forces are varying with height; in general, the closer to the ground, the smaller is the force because of the mean wind speed profile. The tangential force is much smaller than the normal force. Both the normal force and the tangential force are reduced at the mid-span of the blade because of the existence of the main arm. The periodicity is obvious due to the rotation of rotor.

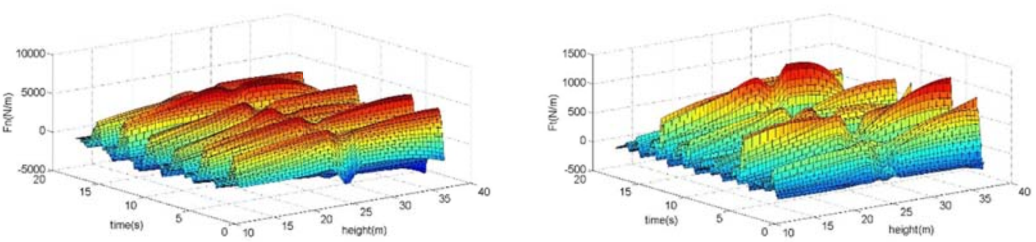

(a) (b)

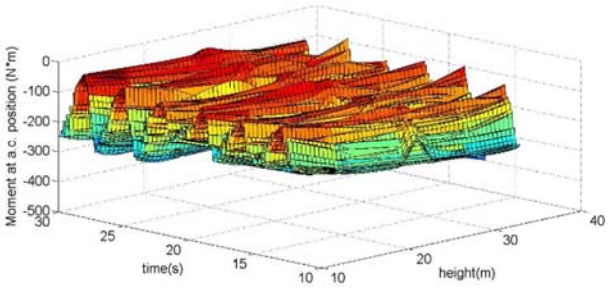

(c)

Fig. 3.16 Aerodynamic forces on a blade: (a) normal force; (b) tangential force; (c) moment

The aerodynamic forces and moment of the upper and lower arms are also simulated. Unlike the blades which are vertical, the upper and lower arms are tilted, one end of which is connected to the blades (the blade end) and the other end of which is connected to the main arm near the tower (the tower end). The lower arm is installed from 16m height above the ground at the blade end to 24.28m height at the tower end; and the upper arm is from 24.28m to 31.50m (shown in Fig. 3.2). Because the CFD simulations are conducted in the horizontal planes, the simulated aerodynamic forces and moment on the upper and lower arms are in the horizontal section with the rotation. These aerodynamic forces at a given horizontal section are represented in the normal force and the tangential forces. The normal force is defined as the component of the aerodynamic force pointing to the center of the rotor; the tangential force is defined as the component of the aerodynamic force orthogonal to the normal force and along the tangential direction (the horizontal section of the upper and lower arm is rotating). The moment is calculated about the geometrical center of the horizontal section of the upper and lower arm. The spatial continuous and time varying aerodynamic forces per unit length of the lower and upper arms are shown in Fig. 3.17. The two horizontal coordinates are the time and the cross section height. It can be found that the aerodynamic force at the end near the tower is always smaller than that at the end near the blade. This is because the wind speed near the tower is much smaller than that near the blade. Moreover, it can also be found that the tangential forces of the upper and lower arms are negative in most of the time, especially at the blade ends. Thus, the upper and lower arms would obstruct the rotation of the VAWT.

The main arms are in the horizontal plane and the wind loads are only simulated in sec4 (see Fig. 3.3(d)). One end of the main arm is connected to the tower and the other end is connected to the lower and upper arms (see Fig. 3.2). Thus, on the main arms only distributed tangential forces are applied. The tangential forces are obtained by integrating wind pressures along the main arm and multiplying the depth of the main arm (1.2m). The tangential force per unit length is shown in Fig. 3.18. The length of the main arm is 10m. The end at 0m is at the tower side and the end at 10m is at the blade side. It can be found that the largest force appears at the middle of the main arm and the force becomes zero at the two ends.

The drag force and lift force of the tower are shown in Fig. 3.19. The height of the tower is from 0m to 24.28m. For the lift force, it becomes very small in the range of 0m~10.5m because the lift force in this height range is only due to the vertex shedding. For the height range above 10.5m, the lift force of tower becomes much larger, which is caused by the rotation of blades and arms, the wake excitation, and the vortex shedding.

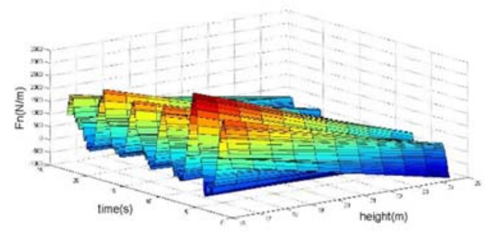

(a)

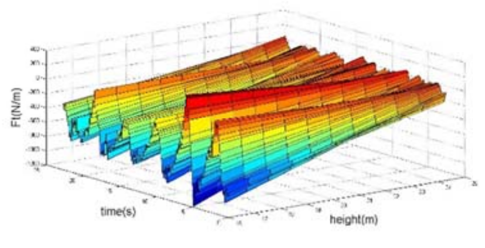

(b)

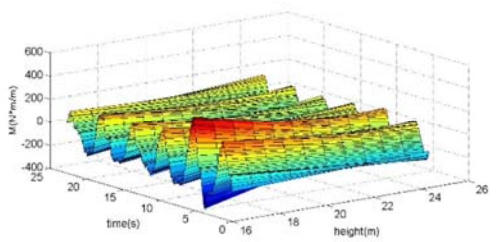

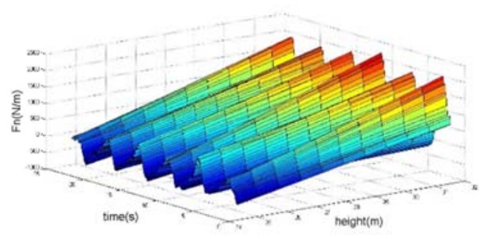

(c) (d)

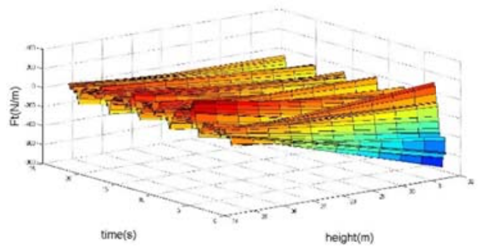

(e)

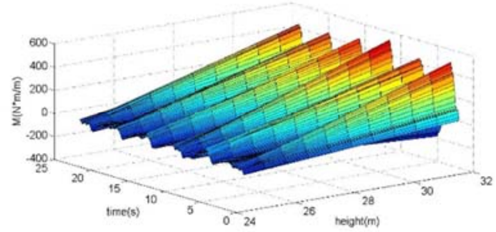

(f)

Fig. 3.17 Aerodynamic forces and moment per unit length. (a) normal force on a lower arm; (b) tangential force on a lower arm; (c) moment on a lower arm; (d) normal force on an upper arm; (e) tangential force on an upper arm; (f) moment on an upper arm.

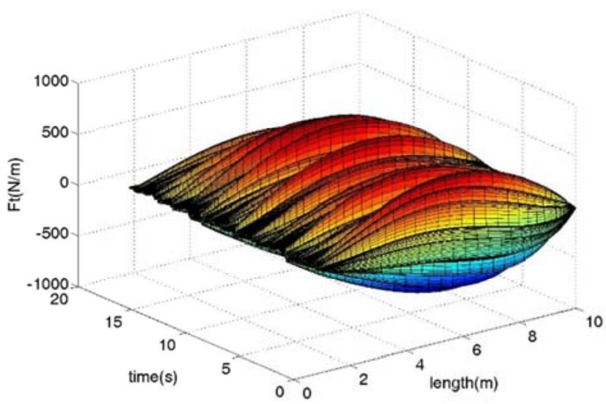

Fig. 3.18 Tangential force on a main arm

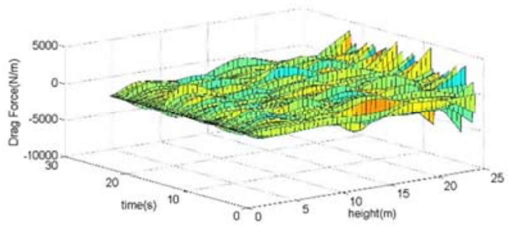

(a)

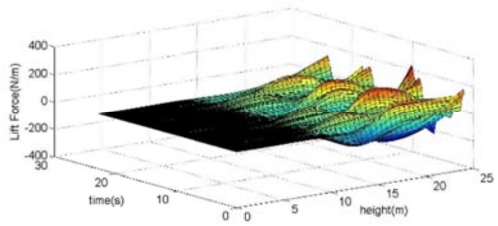

(b)

Fig. 3.19 Aerodynamic forces per unit length on the tower (a) drag force; (b) lift force

3.4.4 Wind loads in the extreme wind speed

In order to conduct the ultimate strength analysis in Chapters 5 and 6, the wind pressures on the blade and the aerodynamic forces on the whole VAWT under the extreme wind speed are also required. The difference is that the VAWT is standing still rather than rotating in this case. Hence, the wind loads vary with the inflow wind direction in the simulation, and the inflow wind direction can be reflected by the azimuth angle (see Fig. 3.4). Similarly to Section 3.4.3, the spatial continuous wind loads in the extreme wind speed shall be obtained.

3.4.4.1 Wind pressures on the blade

The wind pressure on the blade at sec1 is taken as an example and the influence of azimuth angle (wind direction) can be seen from this case.

4 typical azimuth angles, 0^o, 90^o, 180^o and 270^o, are taken as reference; the wind pressures at these wind directions are shown in Fig. 3.20. It can be seen that for the azimuth angle of 0^o, the positive wind pressure is concentrated on the leading edge and the trailing edge only, and the wind pressures are negative over almost all the surfaces of the blade. This is because that the wind speed is reduced at the leading edge but accelerated in over the surface and finally the re-attaches on the tailing edge. For the azimuth angle of 90^o, the pressure distribution is quite different from the operating condition (refer to Fig. 3.14(a)). The wind pressure in the extreme wind case has a large negative value in both the leading and trailing edges plus the leeward surface. This is because that for the steady case, serious flow separations occur at the trailing edge when azimuth angle is large, which result in the large negative wind pressures. For the azimuth angle of 180^o, the wind flow comes to the trailing edge first and then goes through the surface up to the leading edge. In this case, the wind flow is stopped by the trailing edge and the positive pressure is thus induced in this area; the leading edge is the stagnation point in this case, so the pressure at this point is almost zero. For the azimuth angle of 270^o, the wind pressure distribution is similar to that of the azimuth

angle of 90^o. Flow separation happens at the leading edge and the trailing edge, which result in large negative wind pressure at these two positions.

In these simulations, the near-wall y-plus are listed in Table 3.4. It can be seen that the y-plus of this case also satisfies the near wall requirement (y+<5 for SST k-ω).

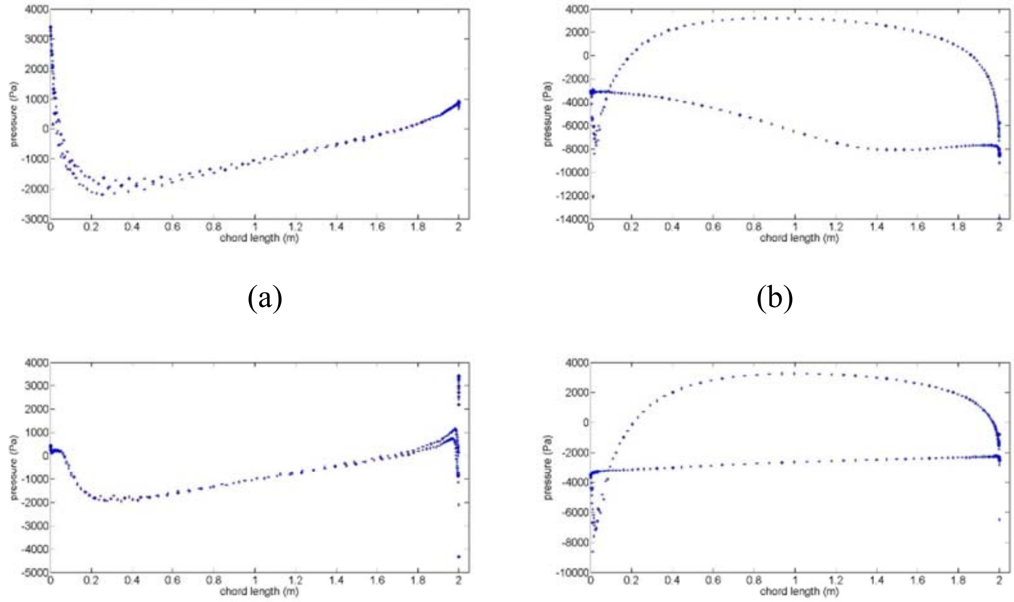

(a) (b) (c) (d)

Fig. 3.20 Wind pressures on the blade. (a) azimuth angle $\theta = 0^o$; (b) azimuth angle $\theta = 90^o$; (c) azimuth angle $\theta = 180^o$; (d) azimuth angle $\theta = 270^o$;

Table 3.4 The near-wall y-plus

Sec1	Sec2	Sec3	Sec4	Sec5	Sec6	Sec7	Sec8	Sec9
1.5	1.1	1.5	1.9	1.6	1.7	1.7	2.5	1.8

3.4.4.2 Aerodynamic Forces and moment

The VAWT with 3 straight blades is 3-fold symmetry, so that only the azimuth angles of the first 120^o are needed to be considered for the extreme wind speed case. In this subsection, the cases of the azimuth angle of 0^o, 30^o, 60^o and 90^o are simulated and the aerodynamic forces and moment on the VAWT at the azimuth angle of 0^o, 30^o, 60^o, 90^o, 120^o, 150^o, 180^o, 210^o, 240^o, 270^o, 300^o and 330^o can then be obtained. The technique of interpolation is used to estimate the aerodynamic forces and moment at other azimuth angles.

Firstly, the normal and tangential forces and the moment on one blade are shown in Fig. 3.21. One of the horizontal axis is the azimuth angle and the other horizontal axis is the height of section. The largest positive normal force on the blade appears at $\theta \in \left[60^{\circ},120^{\circ}\right]$ and the largest negative normal force on the same blade appears at $\theta \in \left[240^{\circ},300^{\circ}\right]$. This is because in the range of these azimuth angle, the drag force is large. In the upwind side $\theta \in \left[60^{\circ},120^{\circ}\right]$, the drag force result in large positive normal force; in the downwind side $\theta \in \left[240^{\circ},300^{\circ}\right]$, the drag force result in large negative normal force. The largest tangential force on the blade appears at $\theta = 90^{\circ}$. The aerodynamic moment on the blade has the largest value at $\theta = 90^{\circ}$ and $\theta = 300^{\circ}$. It can also be found that similar to the operating case, the aerodynamic forces in the higher section are generally larger than those in the lower section, which reflects the influence of the wind profile. Moreover, the forces near sec4 are very different from those in other sections, which implies that the main arm has an obvious influence on the aerodynamic forces on the blade.

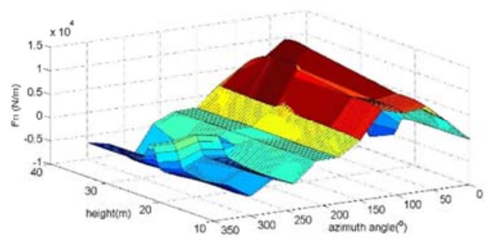

(a)

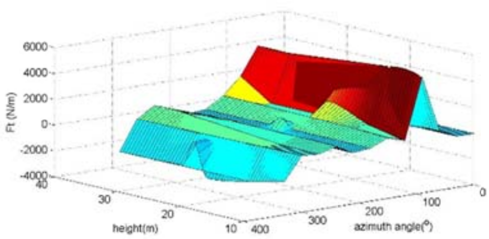

(b)

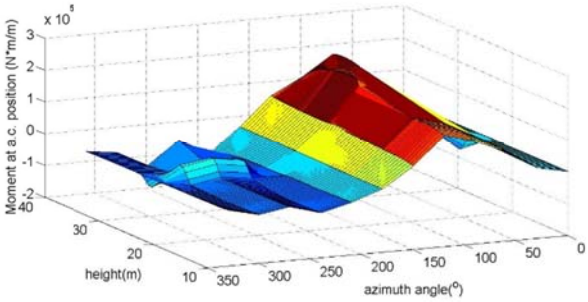

(c)

Fig. 3.21 Aerodynamic forces and moment per unit length on the blade in the extreme wind condition. (a) normal forces F_n; (b) tangential forces F_t; (c) moment M

Secondly, the normal force, tangential force and moment per unit length on the upper and lower arms are shown in Fig. 3.22. For the normal force, it can be found that there are two positive peaks in the upwind side (one at about $\theta = 60^{\circ}$ and the other in the range of $\theta \in \left[120^{\circ}, 150^{\circ}\right]$) and two negative peaks in the downwind side (one at about $\theta = 210^{\circ}$ and the other at about $\theta = 300^{\circ}$). For the tangential force, there are one positive peak and one negative peak in the upwind side. The positive peak appears at about $\theta = 120^{\circ}$ and the negative peaks appears at about $\theta = 30^{\circ}$. The aerodynamic moment reaches the largest positive value near $\theta = 120^{\circ}$ and the largest negative value near $\theta = 330^{\circ}$.

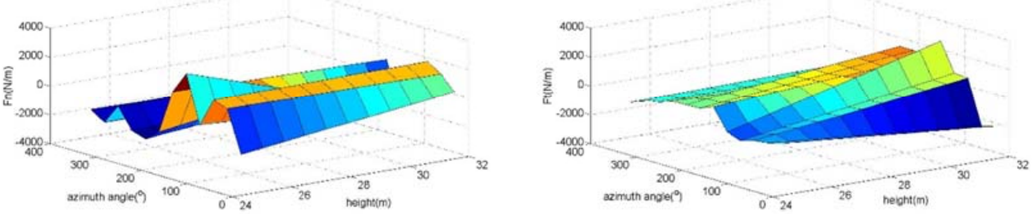

(a) (b)

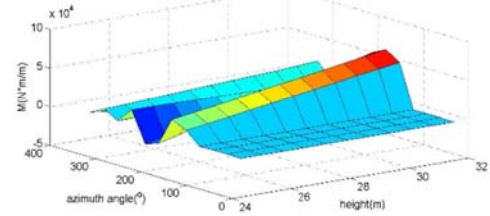

(c)

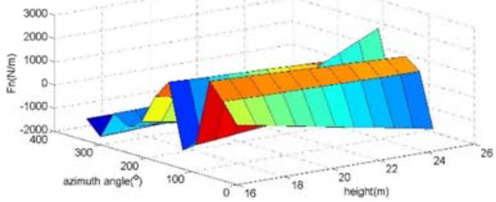

(d)

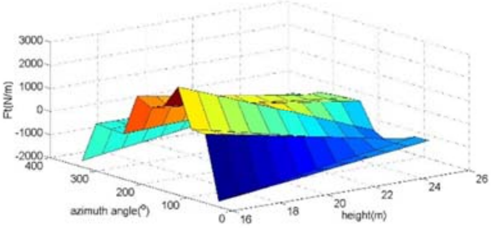

(e)

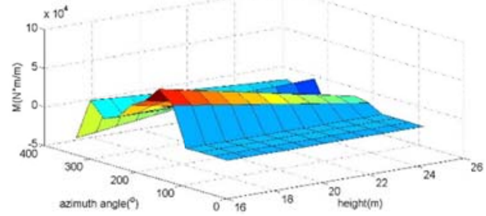

(f)

Fig. 3.22 Aerodynamic forces per unit length on the upper and lower arm. (a) the normal force on the upper arm; (b) the tangential force on the upper arm; (c) the moment on the upper arm; (d) the normal force on the lower arm; (e) the tangential force on the lower arm; (f) the moment of the lower arm;

For the main arm, the tangential force is shown in Fig. 3.23. The tangential force of the main arm reaches the largest positive value at about $\theta = 150^{\circ}$ and reaches the largest negative value at about $\theta = 30^{\circ}$.

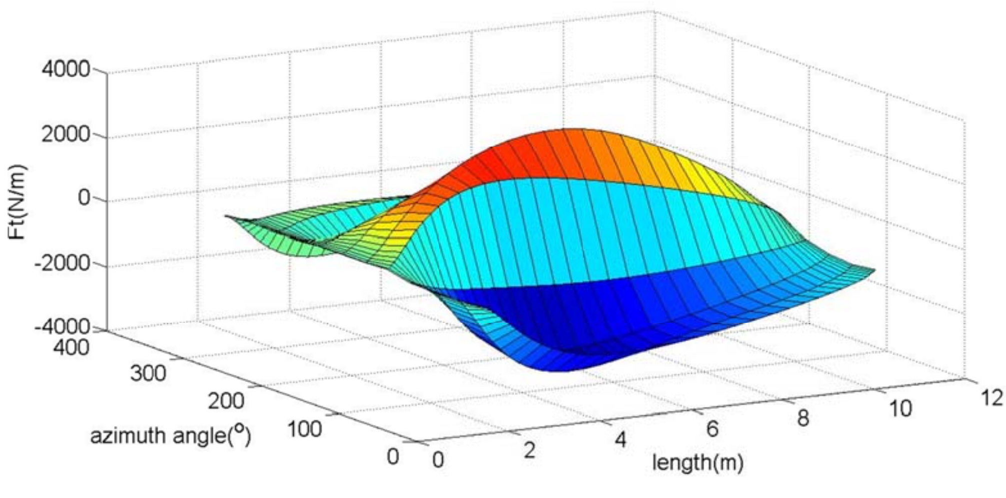

Fig. 3.23 Tangential force per unit length on the main arm

For the tower, the aerodynamic forces are represented in the drag force and the lift force. The lift and drag forces are shown in Fig. 3.24. Because the VAWT is 3-fold symmetric, the aerodynamic forces of the tower at $\theta = 0^{\mathrm{o}}$ are totally the same to those at $\theta = 120^{\mathrm{o}}$. Thus, only the azimuth angle of $\theta \in \left[0^{\mathrm{o}}, 120^{\mathrm{o}}\right]$ are needed to consider. It can be seen that the drag force at the top of tower is larger than the drag force at the bottom; the drag force approaches to zero near the ground. The variation of the drag force with the height of tower is caused by the mean wind profile. The lift force is relatively small in the height range of 0m~10.5m because the lift force in this height range is only due to the vortex shedding, which is similar to the case of operating wind speed region. For the height range above 10.5m, the variation of lift force with the azimuth angle is due to the position of the blades and lower arms.

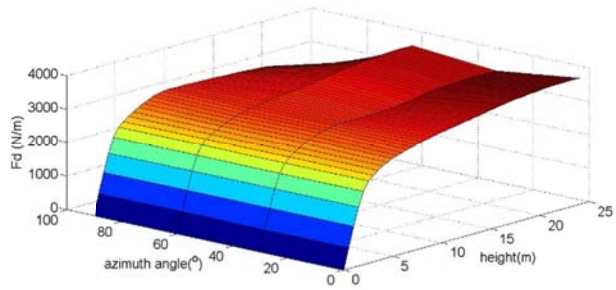

(a)

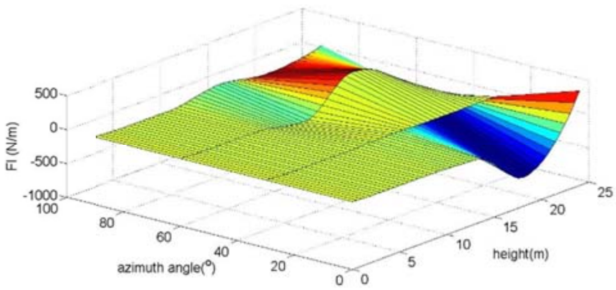

(b)

Fig. 3.24 Drag and lift forces on the tower. (a) drag force; (b) lift force.

3.5 Influences of Tower, Arms, and Turbulence on Blade Aerodynamic Forces

Although the influences of the existence of tower, arms and turbulence on the aerodynamic forces of the blade have been included in the former analysis, the specific influence of each factor is still not clear. Due to the importance of the aerodynamic forces of the blade, a further study and discussion are conducted in this section. The simulation strategies are the same as Section 3.4 for the VAWT under the operation condition.

3.5.1 The influence of the existence of tower and arms

Only three blades appear in sec1 and other components of VAWT are absent from this cross section. To know the influence of the existence of tower and arms, it just needs to compare the aerodynamic forces of the blade in other sections with those in sec1 under the same wind speed and rotation speed. Because the difference between sec1 and sec7 is that the tower appears in sec7 but is absent from sec1, the influence of tower can be assessed by comparing the aerodynamic forces on the blade between sec1 and sec7. On the other hand, because only arms and blades appear in sec2 - sec4 and the tower is absent from these sections, the influences of arms can be known by comparing aerodynamic forces in these sections with those in sec1. The influence of main arm can be known by comparing the results from sec1 and sec4; the influence of the upper arm can be obtained by comparing the results of sec1-sec3. Moreover, the difference of sec2 and sec3 is the distance between the blades and the upper arms, so the influence of distance between the upper arm and the blade can also be revealed. 2D SST k-ω simulation is still used in this section. The simulation strategies are the same as Section 3.4 but without considering turbulent wind.

Sec1, sec2, sec3, sec4 and sec7 are shown in Fig. 3.3. These sections are then divided into 2 groups: one includes sec1 and sec7, the other includes sec1 - sec4. Based on the analysis above, comparing the aerodynamic forces of the first group can reveal the influence of the tower; and by comparing the second group, the influence of the arms can also be known. In these comparisons, for all sections, the steady inflow velocity is 10m/s and rotation speed is 2.1rad/s ($R = 20m$, tip speed ratio $\lambda = 3$).

In sec1 and sec7, the simulated C_n and C_t are shown in Fig. 3.25. It can be seen that comparing with sec1 which is tower free, there is an abrupt reduction in both C_n and C_t in the downwind area of sec7; while in the upwind area, C_n and C_t of both sections match well. From this comparison, it can be concluded that tower shadowing causes a small reduction in both C_n and C_t in the downwind zone and nearly no influence can be seen in the upwind zone.

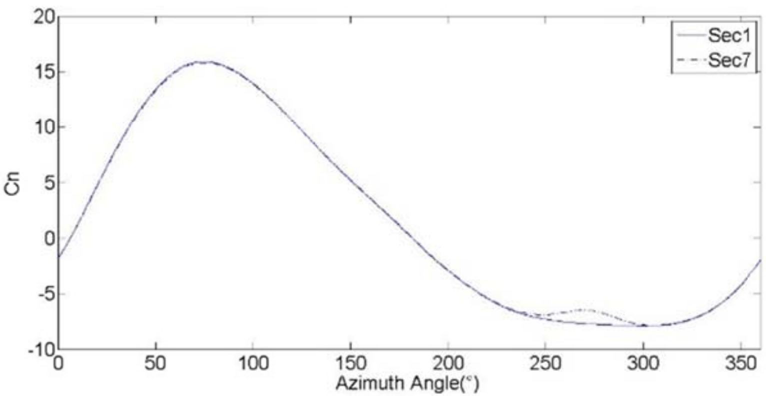

(a)

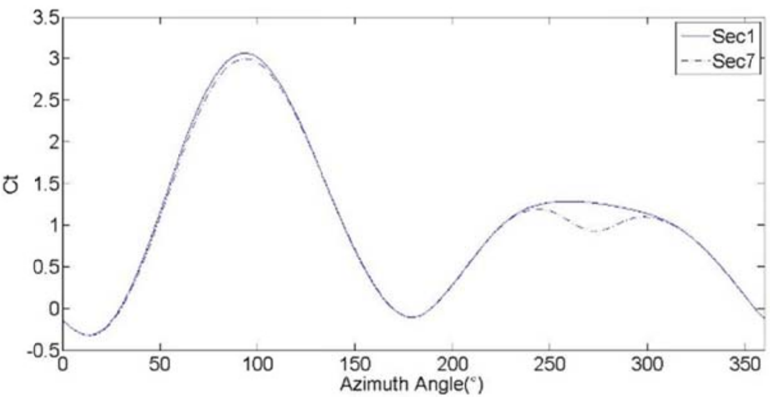

(b)

Fig. 3.25 Comparisons of the aerodynamic coefficients in sec1 and sec7. (a) the normal force coefficient C_n; (b) the tangential force coefficient C_t

For the influence of the arms, C_n and C_t of blades in sec1 - sec4 are shown in Fig. 3.26. Form this figure, it can be found that the main arm has the most prominent influence on the aerodynamic forces of blade. In either upwind or downwind zone, C_n and C_t are strongly influenced by the main arm. For C_n and C_t of the blade in sec2, the aerodynamic coefficients also differ from those in sec1 in both upwind and downwind zones but the influence is less prominent than those of the main arm. For C_n and C_t of sec3, it can be seen that the influence of the upper arm becomes weaker because the arm is away from the blade in this section. From these results, it can be known that the influence of the existence of arms is over that of the tower, in which the influence of the main arm is the most prominence.

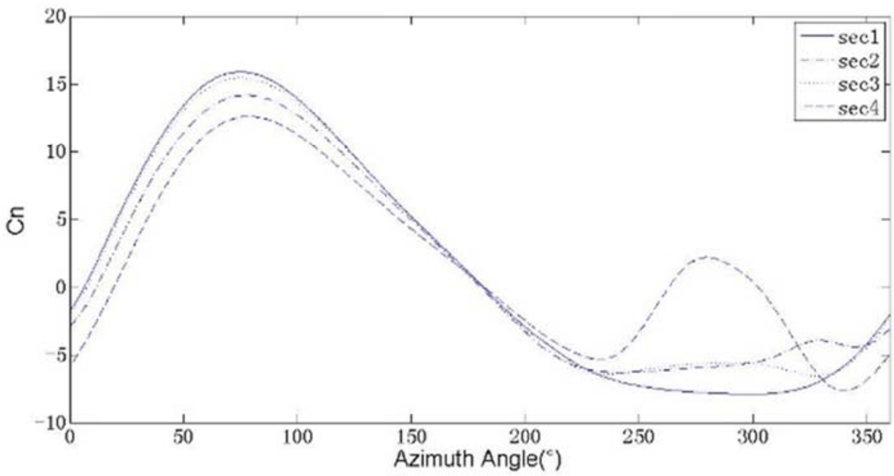

(a)

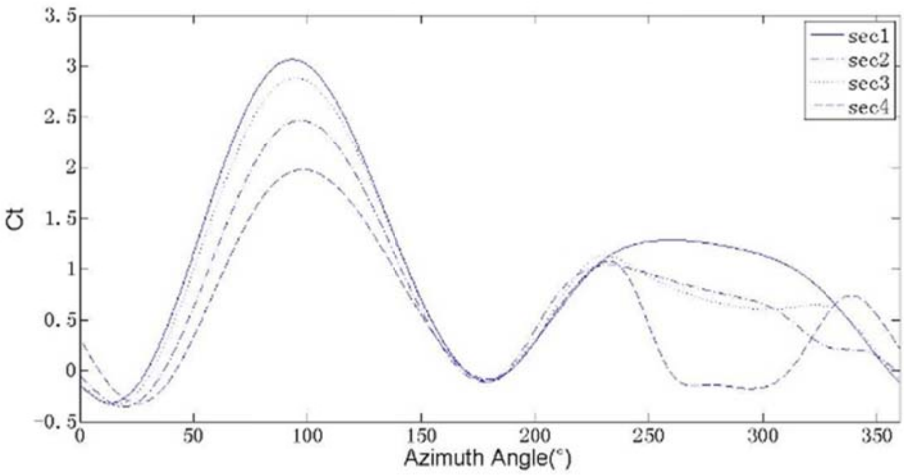

(b)

Fig. 3.26 Comparisons of the aerodynamic coefficients in sec 1 - sec 7. (a) the normal force coefficient C_n; (b) the tangential force coefficient C_t

From the analysis above, it can be concluded that the tower shadow effect of a VAWT is not as important as a HAWT and it just causes a little disturbance of the aerodynamic forces of the blade in the downwind zone, while the influences of the arms on C_n and C_t are large, especially the main arm. Not only fatigue loading (mainly due to the normal force) but also power efficiency (due to the tangential force) are reduced due to the existence of the arms.

3.5.2 The influence of turbulence

The influence of turbulence is discussed in this section. In this section, a simulated time history of longitudinal turbulent wind speed is used as the inflow velocity of CFD in addition to the mean wind speed and the calculated aerodynamic forces of the VAWT blade are compared with those under the steady inflow case. The comparison is conducted for sec1. The rotational speed is 2.1rad/s. The mesh grid and simulation strategies are the same as Section 3.4 for the VAWT under the operation condition. For the turbulent wind, the power spectrum model and the coherence model are the same to those introduced in Section 3.2.2. The simulated time history of wind speed is shown in Fig. 3.27. The mean wind speed is 15.0 m/s and the turbulence intensity is 11.08%. For the steady wind, the mean wind speed is also 15.0 m/s.

10 cycles of C_n and C_t are shown in Fig. 3.28. Here, the mean wind speed of 15 m/s is used in the normalization. The results of the steady inflow case, of which the inlet velocity is 15m/s, are also shown in Fig. 3.28. It can be seen that because of the existence of the turbulence, C_n and C_t are fluctuating around those of the steady inflow case and the turbulence does not induce large change in the total aerodynamic forces.

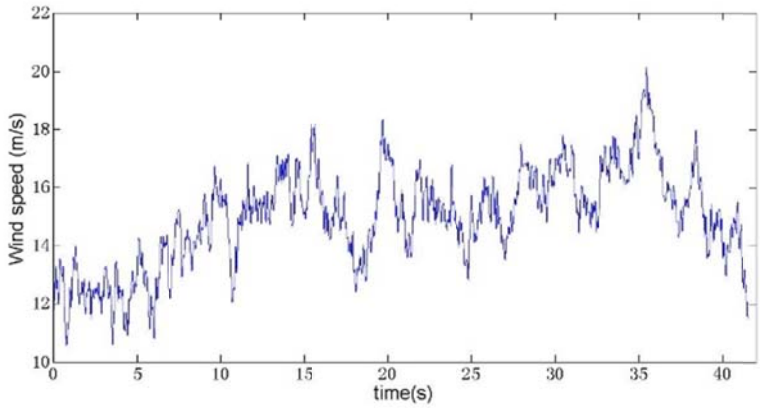

Fig. 3.27 The time history of wind speed

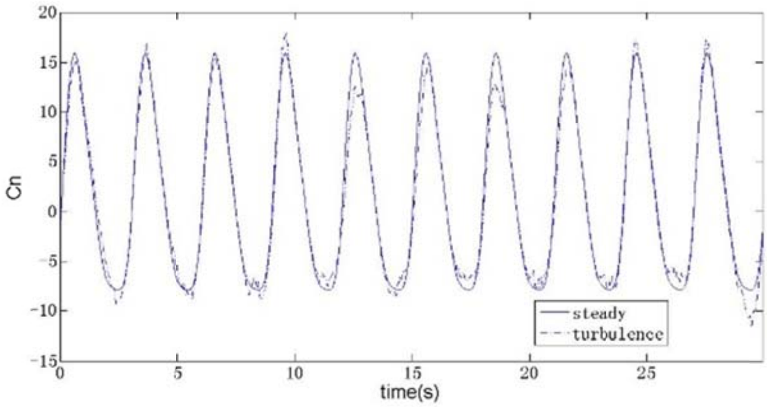

(a)

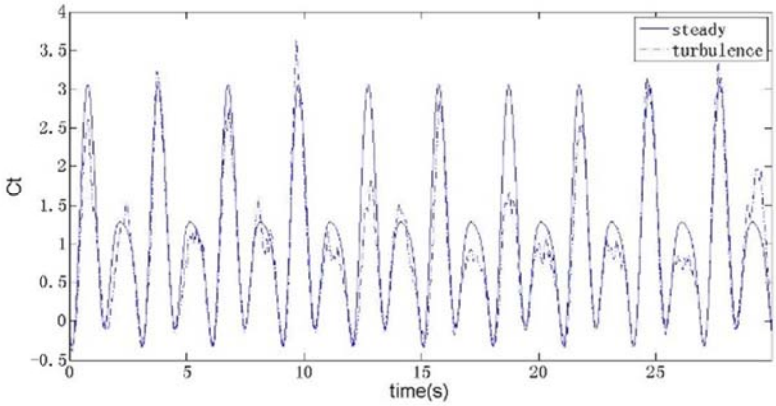

(b)

Fig. 3.28 Comparisons of the aerodynamic coefficients under the steady wind and the turbulent wind. (a) the normal force coefficient C_n; (b) the tangential force coefficient C_t

3.6 Summary

In this chapter, the wind load simulation framework for a VAWT was established. To introduce the framework, the prototype VAWT in Guangdong, China, was taken as an example. From the results of the present study, the following conclusions can be summarized.

(1) Based on the strip analysis method and the 2D SST $k-\omega$ simulation, 9 typical cross sections of a VAWT were chosen and wind load, including wind pressure and aerodynamic forces, in these cross sections were calculated. Continuous wind loads on the whole VAWT were obtained by interpolating the results of the 9 sections. The influences of the mean wind speed profile, turbulence, and all the components of the VAWT were investigated by using the proposed framework. The wind loads in the operating wind speed condition and the extreme wind speed condition were also considered in this chapter.

(2) In order to assess the validity of applying the 2D SST $k-\omega$ simulation to determine wind loads on the VAWT, the results from the 2.5D LES and the 2D SST $k-\omega$ simulation were compared. It was found that these two methods could obtain similar results and the slight difference was only in the tangential force due to the different prediction of flow separation. The 2D SST $k-\omega$ can be used as a proper model for determining wind loads on the VAWT.

(3) Using the 2D SST $k-\omega$ simulation, the influences of the tower and arms on the aerodynamic forces of the blade were further studied. Because the tower was far from the blades of this large VAWT, the influence of the tower is not obvious and only caused small reduction of aerodynamic forces of the blade in the downwind side. The influence of the arms was, however, more obvious. The tangential force, hence the power coefficient, was reduced due to the existence of the arms.

(4) Aerodynamic forces on the VAWT blade under the simulated turbulent wind and steady inflow were compared. It was found that the turbulence caused the fluctuation in wind loads.

To design a VAWT, the fatigue and ultimate strength analyses are required, and the determination of wind loads on the VAWT is the first step. Besides wind loads, an accurate FE model is also required. In the next chapter, an FE model of the blade will be established by considering laminate composite material and the tests will also be conducted to update the FE model.

CHAPTER 4

MODELLING AND MODEL UPDATING OF LAMINATE COMPOSITE BLADES

4.1 Introduction

In Chapter 3, wind pressures on the blade are simulated by the proposed wind load simulation framework. Accordingly, a proper and accurate FE model of a blade is required for the structural analysis of the blade under wind loads. As reviewed in Chapter 2, fiber-reinforced plastics (FRP) laminated shells are widely used in making wind turbine blades (Burton et al., 2001) and a proper FE model of blade should be able to estimate the stress or strain at the ply level.

Nevertheless, only precise modelling is not enough. Usually, the laminar elastic constants of FRP are unknown; even if the certified values are given, there exist unavoidable uncertainties due to large manufacturing tolerances unlike the single-constituent material, such as glass fiber and resin which have less uncertainties of the certified values. Therefore, the model updating or calibration techniques are needed. Most of the methods can only identify the elastic constants of laminated composite rather than laminar properties. Although some researchers indeed identified laminar or even constituent properties, there are too many elastic constants to be identified. A FRP laminar is an orthotropic or transversely isotropic material, which has 9 or 5 independent elastic constants for PW FRP or UD FRP respectively. With the increasing layer number of a laminate, the number of parameters will increase dramatically. It is thus difficult to identify the laminar elastic constants directly.
One solution to this problem is to apply micromechanics in the process of model updating. The objective of micromechanics is to estimate the elastic constants of a composite material by those of its constituents and some geometric parameters. The

elastic constants of FRP can vary largely depending on the specific textile structure but the elastic constants of its constituents are usually already known. Thus, if using micromechanics models, the number of parameters needed to be identified can be largely reduced.

The dynamic approaches, which measure mode shapes and natural frequencies, are usually used in model updating, while, in this study, there are too many mode shapes and natural frequencies to be identified, which needs many sensors and accordingly is difficult to be implemented. Moreover, although an excitation system for dynamic approach may be an easy job for specimen tests, it is a difficult task or even a mission impossible in prototype structures. On the other hand, static measurements can obtain higher accurate data than dynamic ones. Although static approaches cannot update the mass matrix, they are useful in updating the material constants.

In this chapter, a FE model of the composite blade is established using laminate shell elements so that the laminar stresses can be obtained. Micromechanics models are applied in the identification of laminar elastic constants. These models play the role in setting up the connection between the updating parameters and the laminar elastic constants; and the FE model is used to connect the laminar elastic constants and the responses. Sensitivity studies are carried out to determine the parameters of the micromechanics models to be identified. To identify these parameters, static tests are conducted, and displacements and strains are measured. Based on the measured responses and the FE model of the static tests, the chosen parameters of the micromechanics models are updated by the pattern search algorithm. The proposed method is verified by the measured data which are not used in the updating procedure.

4.2 Finite Element Modelling of A Laminated Composite Blade

4.2.1 A laminated composite straight blade of VAWT

The procedures of modelling and model updating of laminated composite blades are presented in the following sections. In order to introduce the procedures, a typical blade should be taken for example. To be consistent with the VAWT discussed in Chapter 3, the straight laminated composite straight blade used in the VAWT is selected. More importantly, such a blade was tested in the laboratory so that the test data can be used for model updating.

The blade section and the composite materials of the VAWT discussed in Chapter 3 are shown in Fig. 4.1. This blade uses NACA0018 foil type as the blade section; the chord length is 2m and the blade length is 26m. The outer shell and shear webs of the blade are composed of three layers, as shown in Fig. 4.1(b). The first and the third layer are made of PW FRP and the middle layer is made of UD FRP. Both PW FRP and UD FRP are made of E-glass and polyester resin. E-glass is used as fiber and polyester resin is used as matrix. The blade is manufactured by the pultrusion technique. These three layers are bonded together by latex.

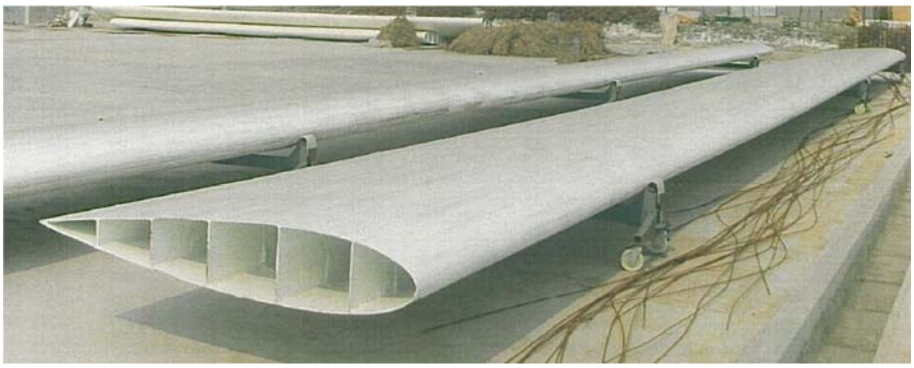

(a)

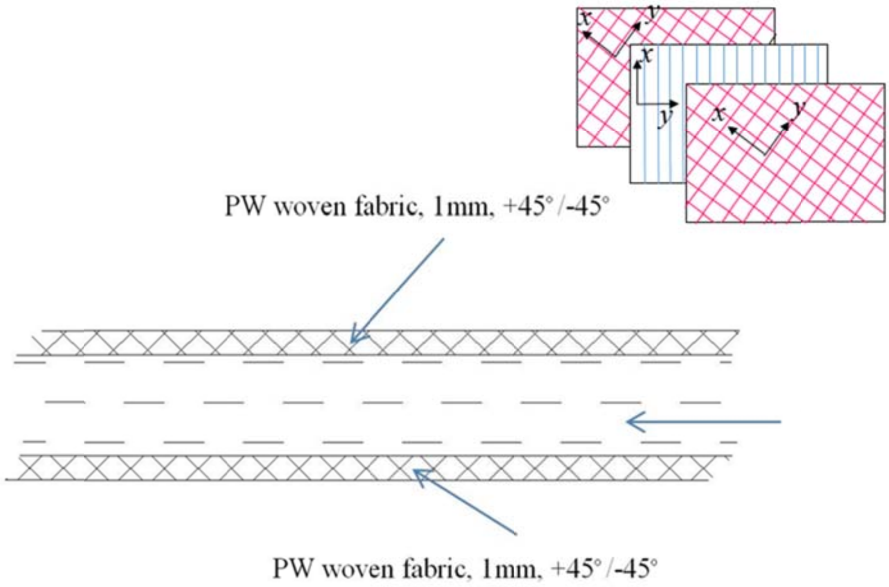

(b)

Fig. 4.1 A laminated composite straight blade (a) the NACA0018 prototype blade; (b) the constituents of the outer shell and shear webs of the blade

In order to define the elastic constants of UD FRP and PW FRP, material coordinates are given in Fig. 4.1(b). From the view of macromechanics, UD FRP is transversely isotropic and PW FRP is orthotropic. The elastic constants of UD FRP can be represented by 5 independent elastic constants E_x, E_y, G_{xy}, G_{yz} and ν_{yx}. Here "*x*" is the direction of the fibers and "*y*" is in the layer perpendicular to it as shown by Fig. 4.1(b). The elastic constants of PW FRP can be represented by 9 independent elastic constants, $E_x, E_y, E_z, G_{xy}, G_{yz}, G_{zx}, \nu_{yx}, \nu_{zy}$ and ν_{zx}. Here, "*x*" and "*y*" are the directions of the warp and weft fibers as shown by Fig. 4.1(b). For the blade in this study, there are a total of 23 (9+5+9) independent elastic constants at ply level. If considering the identity of the first and third layer, there are 14 (9+5) elastic constants.

4.2.2 FE modelling of the blade

There are many different ways to model the laminated composite blade, such as 3D solid elements and equivalent single layer (ESL) shell elements. For 3D solid elements, many elements have to be used in the thickness direction in order to simulate the multi layers of the blade because the scales of solid elements in 3 directions should not be so different that the ill-posedness problem can be avoided. Hence, it is not computational efficient to choose 3D solid elements in the modelling, and using ESL laminated shell elements is a better option.

There are mainly three widely-used laminated composite theories applied in laminated shell elements: classic laminate theory (CLT), first order shear deformation theory (FSDT) and higher-order shear deformation theories (HSDTs) (Khandan et al., 2012). CLT cannot consider shear deformation and is only suitable for thin laminates; FSDT accounts for shear deformation effects based on the assumption of linear variation of in-plane displacements through the thickness; and HSDTs account for shear deformation effects by assuming high order variations of displacements through the thickness. Considering the simulation requirement (obtaining inter-laminar stresses) and computational efficiency, FSDT is adopted in this study.

ANSYS shell91 element is therefore used to model laminated FRP blades. Shell91 can consider up to 100 different layers in an element. The element has 6 degrees of freedom at each node and has total 9 nodes. To introduce FE modelling, the blade used in the tests which will be introduced in Section 4.5, is taken for example. This blade has the same cross section and material to the prototype blade shown in Fig. 4.1(a) but it is only 6 m in length. The FE model of the blade is shown in Fig. 4.2. In each element of this model, there are three layers composed of UD FRP and PW FRP as shown in Fig. 4.1(b). A global coordinate is also given in Fig. 4.2, which can define the fiber directions of the UD FRP and PW FRP. The x axis is along the blade; the z axis is along the chord line; and the y axis is perpendicular to the chord line. The direction of UD FRP fiber of the outer shell is along the x axis; and the direction of shear web UD FRP fiber is along y axis. The directions of fiber in PW FRP are at an angle of 45 degrees to the fiber direction of UD FRP. According to the direction of the fiber and the normal direction of the shell element, the local coordinate for each layer can be determined. In the local coordinate, the z-axis is the normal direction of the shell element; the x-axis is the fiber direction (for PW FRP, since there are two sets of interlaced fibers orthogonal to each other, it can be either one of them); the y-axis is determined by the former defined x and z axis. The elastic constants of each layer are defined in the local coordinate.

In each layer, there are 9 elastic constants ($E_x, E_y, E_z, G_{xy}, G_{yz}, G_{zx}, \nu_{yx}, \nu_{zy}$ and ν_{zx}). For the layer of UD FRP, 5 of 9 elastic constants are independent (E_x, $E_y = E_z$, $G_{yx} = G_{zx}$, G_{zy}, $\nu_{xy} = \nu_{xz}$ and ν_{yz}); for the layer of PW FRP, all 9 elastic constants are independent. Since the two PW FRP layers are the same in this blade, there are 14 independent elastic constants to be determined. However, the elastic constants of different FRP vary largely with the material of the constituents and the specific textile structure. Hence, these elastic constants are needed to be identified.

In this FE model of blade, the connection of the outer shell and the shear web is simulated as rigid. The total element number of this model is 7760 and the total DOFs is 136014. . This FE model is used in the process of model updating in Section 4.6

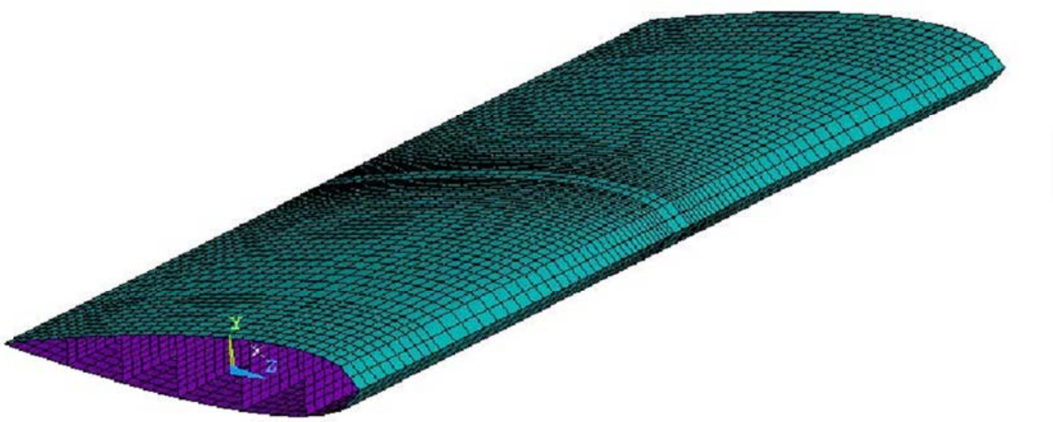

Fig. 4.2 FE model of laminated composite blade

4.3 Model Updating Based on Micromechanics Models

4.3.1 Micromechanics

A composite material is composed of two or more constituents, so there must be some relation between the elastic constants of the composite material and those of the constituents. Micromechanics is the method to analyze composite materials on the level of the individual constituents and predict the material properties of the composite material based on the properties and geometries of the constituents (Hahn & Tsai, 1980).

For a specific composite material, a representative volume element (RVE) is selected first. An RVE is a sub-volume, the elastic constants of which can be regarded as the representative values of the whole material (Hahn & Tsai, 1980; Zvi Hashin & Rosen, 1964; R1 Hill, 1965). A micromechanics model is the relation between the elastic constants of this RVE and those of the constituents.

4.3.2 Model updating based on micromechanics models

As mentioned above, the laminar elastic constants of the laminated FRP material are often not certain even through the certified values are often given because the uncertainties in the manufacture of composites are unavoidable. Hence, the laminar elastic constants of the laminated FRP blade need to be identified in order to obtain accurate laminar stresses and strains. The traditional procedure of model updating is shown in the schematic diagram of Fig. 4.3(a). For the FE model built in Section 4.2.2, to update the aforementioned 14 laminar elastic constants, more than 14 independent responses and modal properties have to be measured and identified. Hence, it is difficult to update the laminar elastic constants directly.

However, from the view of micromechanics, these 14 constants are determined by elastic constants of fiber and matrix, fiber volume fractions V_f and some geometrical parameters. In this blade, for UD FRP and PW FRP, E-glass is used as fiber and polyester resin is used as matrix, both of which are isotropic materials. The elastic constants of E-glass can be represented by Young's modulus E_f, Poisson's ratio ν_f and shear modulus G_f, where the subscript f denotes "fiber". Similarly, elastic constants of polyester resin can be represented by E_m, ν_m and G_m, where the subscript m denotes "matrix".

In the following Section 4.3.3 and Section 4.3.4, the micromechanics models of UD FRP and PW FRP are introduced. Based on these models, the number of parameters to be identified can be reduced in three perspectives. Firstly, to determine the elastic constants of UD FRP and PW FRP, fewer parameters are required. Secondly, most of these parameters have less uncertainty than the 14 laminar elastic constants . For example, the material constants of fiber (E-glass) and matrix (polyester resin) can be measured accurately. Furthermore, not all parameters have equal influence and some parameters have less influence on the laminar elastic constants than the others. Sensitivity studies are needed to choose the most influential ones as the parameters to be identified. Only those parameters of large uncertainties and the most influence are needed to be updated. Based on the micromechanics models, the schematic diagram of the model updating procedure is shown in Fig. 4.3(b).

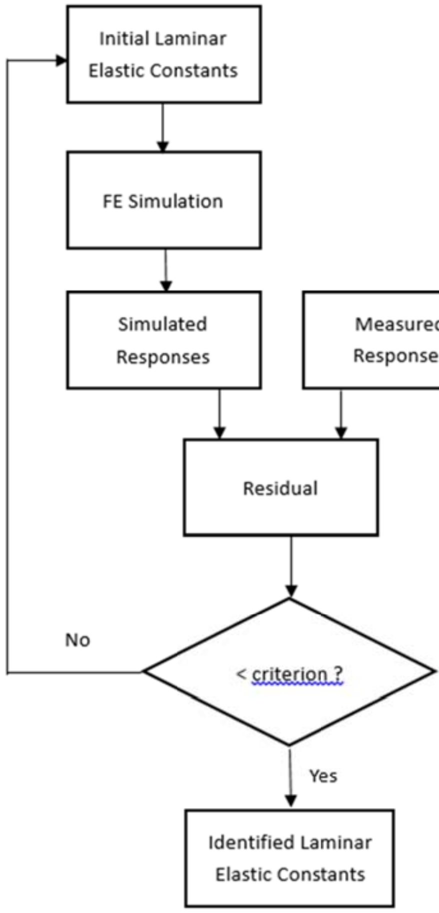
Initial Laminar
Elastic Constants
FE Simulation
Simulated
Responses
Measured
Responses
Residual
No
< criterion ?
Yes
Identified Laminar
Elastic Constants

(a)

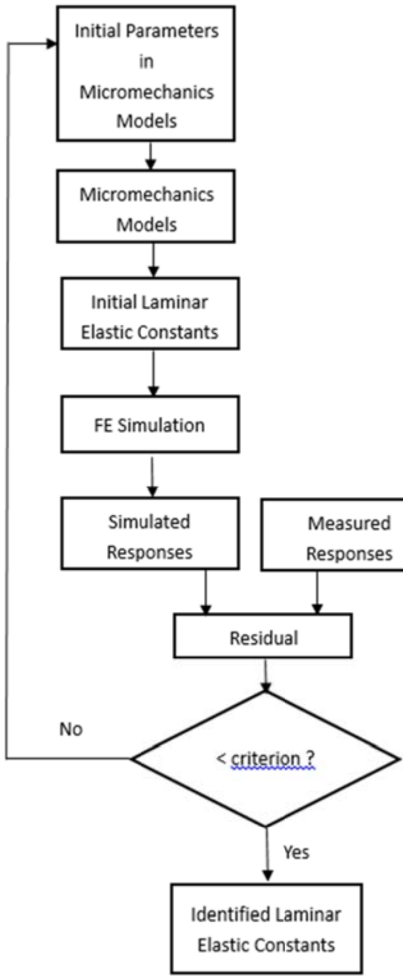

(b)

Fig. 4.3 The schematic diagrams of model updating methods: (a) the direct model updating method; (b) the proposed model updating method based on micromechanics models

4.3.3 Micromechanics models of UD FRP

For UD FRP, many easy-to-use models (formulas) have been proposed and these models are based on different assumptions. First of all, based on the iso-strain (equal strain in the direction of fiber, '*x*' direction) and iso-stress principles (equal stress in '*y*' direction, perpendicular to the fiber), a simple rule of mixtures for the planar problem (Hahn & Tsai, 1980)was first proposed.

$$E_x = V_f E_f + V_m E_m \tag{4.1a}$$

$$\nu_{yx} = V_f \nu_f + V_m \nu_m \tag{4.1b}$$

$$\frac{1}{E_y} = \frac{V_f}{E_f} + \frac{V_m}{E_m} \tag{4.1c}$$

$$\frac{1}{G_{xy}} = \frac{V_f}{G_f} + \frac{V_m}{G_m} \tag{4.1d}$$

where E_x, E_y, G_{xy} and ν_{yx} are the elastic constants of UD FRP and E_f, E_m, G_f, G_m, ν_f and ν_m are the elastic constants of fiber and matrix. V_f and V_m are the fiber volume fraction and the matrix volume fraction, and $V_m = 1 - V_f$.

The research results, however, show that although the Young's modulus E_x and the in-plain Poisson's ratio ν_{yx} can be predicted very well by Eqs (4.1a) and (4.1b), the predicted transverse modulus E_y and shear modulus G_{xy} are not the case of the in-situ state owing to the unreasonable selection of the representative volume element (RVE) (Hahn & Tsai, 1980). Moreover, E_z, G_{xz}, G_{yz}, ν_{zx} and ν_{yz} are not available from Equation (4.1). Hence, researchers proposed other models. Three kinds of commonly used models are introduced here.

Hopkins and Chamis (Chawla, 2012) modified the simple rule of mixtures and they proposed the following formulas:

$$E_x = V_f E_f + V_m E_m \tag{4.2a}$$

$$\nu_{yx} = \nu_{zx} = V_f \nu_f + V_m \nu_m \tag{4.2b}$$

$$E_y = E_z = \frac{E_m}{1 - \sqrt{V_f}(1 - E_m/E_f)} \tag{4.2c}$$

$$G_{xy} = G_{xz} = \frac{G_m}{1 - \sqrt{V_f}(1 - G_m/G_{f12})} \tag{4.2d}$$

$$G_{yz} = \frac{G_m}{1 - \sqrt{V_f}(1 - G_m/G_f)} \tag{4.2e}$$

The Poisson's ratio ν_{yz} can be calculated by $\nu_{yz} = \dfrac{E_y}{2G_{yz}} - 1$.

Another micromechanics model of UD FRP was presented by Hill (R Hill, 1964; R1 Hill, 1965), Hashin (Z Hashin, 1965; Zvi Hashin & Rosen, 1964), Christensen and Lo (Christensen & Lo, 1979)

$$E_x = V_f E_f + (1-V_f)E_m + \frac{4(\nu_f - \nu_m)^2 V_f (1-V_f)}{V_f/k_m + (1-V_f)/k_f + 1/G_{xy}} \tag{4.3a}$$

$$\nu_{yx} = V_f \nu_f + (1-V_f)\nu_m + \frac{4(\nu_f - \nu_m) V_f (1-V_f)}{V_f/k_m + (1-V_f)/k_f + 1/G_{12}} \left(\frac{1}{k_m} - \frac{1}{k_f}\right) \tag{4.3b}$$

$$E_y = E_z = \frac{2}{0.5/K_L + 0.5/G_{yz} + 2\nu_{yx}^2/E_x} \tag{4.3c}$$

$$G_{xy} = G_{xz} = G_m \frac{(G_f + G_m) + V_f (G_f - G_m)}{(G_f + G_m) - V_f (G_f - G_m)} \tag{4.3d}$$

$$G_{yz} = G_m \left(1 + \frac{V_f}{G_m/(G_f - G_m) + (k + 7G_m/3)(1-V_f)/(2k_m + 8G_m/3)} \right) \tag{4.3e}$$

where

$$k_f = \frac{E_f}{3(1-2\nu_f)}, k_m = \frac{E_m}{3(1-2\nu_m)} \tag{4.3f}$$

$$K_L = k_m + \frac{G_m}{3} + \frac{V_f}{\dfrac{1}{k_f - k_m + (G_f - G_m)/3} + \dfrac{1-V_f}{k_m + 4G_m/3}} \tag{4.3g}$$

Equation 4.3(a) – 4.3(g) are called the Hill-Hashin-Chrestensen-Lo (HHCL) model.

Huang also proposed a model for UD FRP, which is based on the assumption that the stresses of matrix are dependent on those of fiber, and this model is also called the bridge model (Huang, 2001). The equations different from the simple rule of mixtures are shown below

$$E_x = V_f E_f + V_m E_m \tag{4.4a}$$

$$\nu_{yx} = \nu_{zx} = V_f \nu_f + V_m \nu_m \tag{4.4b}$$

$$E_y = E_z = \frac{(V_f + V_m a_{11})(V_f + V_m a_{22})}{(V_f + V_m a_{11})(V_f / E_f + V_m / E_m) + V_f V_m (1/E_f - 1/E_m) a_{12}} \tag{4.4c}$$

$$G_{xy} = G_{xz} = \frac{(V_f + V_m a_{66}) G_f G_m}{V_f G_m + V_m a_{66} G_f} \tag{4.4d}$$

$$G_{yz} = \frac{0.5(V_f + V_m a_{44})}{V_f (1/E_f + \nu_f / E_f) + V_m a_{44} (1/E_m + \nu_m / E_m)} \tag{4.4e}$$

where α and β are the two parameters defined in the model. In most cases, $\alpha \in [0.3, 0.5]$ and $\beta \in [0.35, 0.5]$. Huang suggests $\alpha \in [0.3, 0.35]$ and $\beta \in [0.4, 0.45]$ if no other information is available (Huang, 2001).

In this subsection, 3 main micromechanics models of UD FRP are introduced (Equation (4.2) – (4.4)). Although these models are expressed by different formulas, they have similar results and, more importantly, these models have their own ranges of application which has been validated by experiments and it cannot be determined which is the best model for UD FRP.

4.3.4 Micromechanics Models of PW FRP

Woven fabric (WF) composites are different from UD FRP and they consist of two sets of interlaced fibers, known as warp and weft threads using the concepts of textiles. The type of WF composite is determined by the pattern of repeat of the interlaced regions.

PW FRP is the most widely-used woven fabric (WF) composite and extensive studies are carried out on this kind of FRP. Ishikawa and Chou first proposed three models: the mosaic model, the undulation model and the bridging model (Ishikawa & Chou, 1982). Following the work of Ishikawa and Chou, many methods have been proposed to predict the mechanical properties of woven composites (Bednarcyk & Arnold, 2003; Byström et al., 2000; Carvelli & Poggi, 2001; Huang, 2001; Ivanov & Tabiei, 2001; Tanov & Tabiei, 2001; Whitcomb & Tang, 2001). Among these methods, Ivanov and

Tabiei (Ivanov & Tabiei, 2001) caught the geometrical characteristic of PW FRP and chose a simple RVE as shown in Fig. 4.4. This RVE can be divided into 4 sub-cells, ‘f’, ’w’, ‘F’ and ‘W’, representing the undulating interlaced warp yarn and weft yarn. Each sub cell is regarded as UD FRP. In this model, there are two geometric parameters, the braid angle θ_b and the undulation angle β_u as shown in Fig. 4.4. For plain weave, the braid angle θ_b is equal to $\pi/4$ and the undulation angle β_u is determined by manufacture, which is suggested as 0.1651 if no other information available (Ivanov & Tabiei, 2001). The constitutive relation of the RVE can be calculated under the iso-stress and iso-strain assumption. This method has been proved to be simple and valid (Ivanov & Tabiei, 2001).

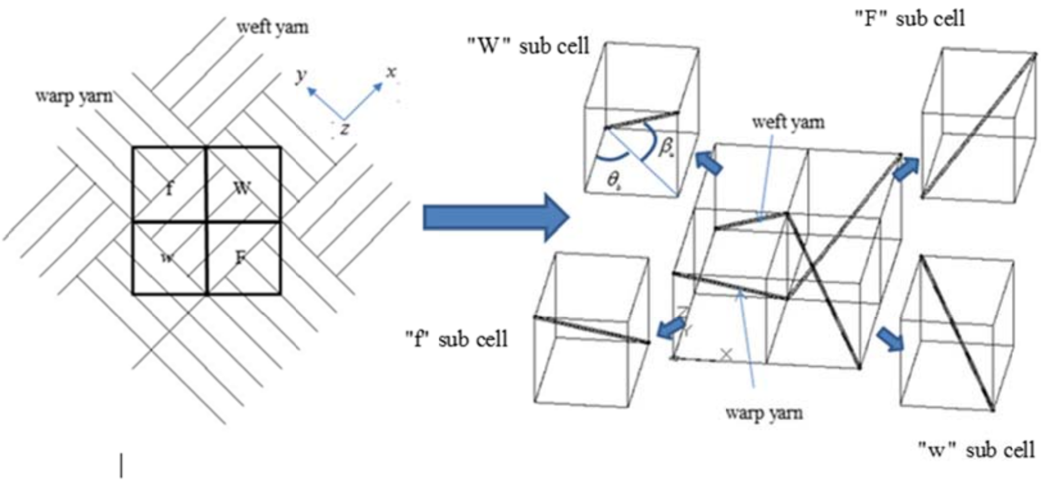

Fig. 4.4 A representative volume element (RVE) of PW FRP

For the PW FRP used in this study, the relations between stresses and strains for the sub cells “f”, “w”, “F” and “W” can be written as

$$\boldsymbol{\sigma}_k^{o} = \boldsymbol{C}\boldsymbol{\varepsilon}_k^{o},\ k = 1,2,3 \text{ or } 4 \tag{4.5}$$

where k=1,2,3 or 4 stands for “f”, “w”, “F” and “W” respectively; $\boldsymbol{\sigma}_k^{o}$ and $\boldsymbol{\varepsilon}_k^{o}$ are the stresses and strains defined in the local coordinate defined in Section 4.2.2. Here, to avoid confusion with the coordinate of the RVE, “1” is used to stand for the direction of the fiber in sub cell instead of “x”; accordingly, “2” and “3” stand for “y” and “z” which are orthogonal to the direction of the fiber. The direction of the fiber in each sub cell is defined and shown in Fig.4.4 as the bold inclined line and the location coordinate is then established accordingly.

The stiffness and flexibility matrix of a sub cell in the local coordinate are shown as follows:

$$\boldsymbol{C} = \boldsymbol{S}^{-1} = \begin{bmatrix} \frac{1}{E_1} & -\frac{\nu_{12}}{E_1} & -\frac{\nu_{12}}{E_1} & 0 & 0 & 0 \\ -\frac{\nu_{12}}{E_1} & \frac{1}{E_2} & -\frac{\nu_{23}}{E_2} & 0 & 0 & 0 \\ -\frac{\nu_{12}}{E_1} & -\frac{\nu_{23}}{E_2} & \frac{1}{E_2} & 0 & 0 & 0 \\ 0 & 0 & 0 & \frac{1}{G_{12}} & 0 & 0 \\ 0 & 0 & 0 & 0 & \frac{1}{G_{23}} & 0 \\ 0 & 0 & 0 & 0 & 0 & \frac{1}{G_{31}} \end{bmatrix}^{-1} \tag{4.6}$$

where $\boldsymbol{C}$ is the stiffness matrix and $\boldsymbol{S}$ is the flexibility matrix for the sub cell. Due to the identity of the four sub cells, the stiffness matrices for these four sub cells are the same; hence the subscript "k" is omitted. The elastic constants in Equation (4.6) can be estimated by the micromechanics models for UD FRP introduced in Section 4.3.3 by using the elastic constants of fiber and matrix as well as its own volume fraction $V_{f,\mathrm{PW}}$.

The stiffness matrix of a sub cell expressed in the local coordinate is needed to be transformed to the form in the coordinate of RVE as shown in Fig. 4.4 by

$$\boldsymbol{C}_k = \boldsymbol{T}_k \boldsymbol{C} \boldsymbol{T}_k^T \tag{4.7}$$

where $\boldsymbol{T}_k$ is the transformation matrix for the sub cell. In the coordinate of RVE, the relations between strains and stresses can be expressed by

$$\boldsymbol{\sigma}_k = \boldsymbol{C}_k \boldsymbol{\varepsilon}_k \tag{4.8}$$

where $\boldsymbol{\sigma}_k$ and $\boldsymbol{\varepsilon}_k$ are the stresses and strains defined in the coordinate of RVE.

To apply the iso-strain and iso-stress principles, the strains and the stresses are divided into the iso-strain components, marked by “n” and iso-stress components, marked by “s”.

$$\boldsymbol{\varepsilon}_k = \begin{bmatrix} \boldsymbol{\varepsilon}_{n,k}^T & \boldsymbol{\varepsilon}_{s,k}^T \end{bmatrix}^T \tag{4.9a}$$

$$\boldsymbol{\sigma}_k = \begin{bmatrix} \boldsymbol{\sigma}_{n,k}^T & \boldsymbol{\sigma}_{s,k}^T \end{bmatrix}^T \tag{4.9b}$$

where

$$\boldsymbol{\varepsilon}_{n,k} = \begin{bmatrix} \varepsilon_{x,k} & \varepsilon_{y,k} & \gamma_{xy,k} \end{bmatrix}^T$$

$$\boldsymbol{\varepsilon}_{s,k} = \begin{bmatrix} \varepsilon_{z,k} & \gamma_{zx,k} & \gamma_{zy,k} \end{bmatrix}^T$$

$$\boldsymbol{\sigma}_{n,k} = \begin{bmatrix} \sigma_{x,k} & \sigma_{y,k} & \tau_{xy,k} \end{bmatrix}^T$$

$$\boldsymbol{\sigma}_{s,k} = \begin{bmatrix} \sigma_{z,k} & \tau_{zx,k} & \tau_{zy,k} \end{bmatrix}^T$$

For the iso-strains and the iso-stresses, there are

$$\boldsymbol{\varepsilon}_{n,1} = \boldsymbol{\varepsilon}_{n,2} = \boldsymbol{\varepsilon}_{n,3} = \boldsymbol{\varepsilon}_{n,4} \tag{4.10a}$$

$$\boldsymbol{\sigma}_{n,1} = \boldsymbol{\sigma}_{n,2} = \boldsymbol{\sigma}_{n,3} = \boldsymbol{\sigma}_{n,4} \tag{4.10b}$$

Accordingly, the stiffness of the sub cell is also divided into 4 sub matrix, as shown below:

$$\begin{bmatrix} \boldsymbol{\sigma}_{n,k} \\ \boldsymbol{\sigma}_{s,k} \end{bmatrix} = \begin{bmatrix} \boldsymbol{C}_{nn,k} & \boldsymbol{C}_{ns,k} \\ \boldsymbol{C}_{sn,k} & \boldsymbol{C}_{ss,k} \end{bmatrix} \begin{bmatrix} \boldsymbol{\varepsilon}_{n,k} \\ \boldsymbol{\varepsilon}_{s,k} \end{bmatrix} \tag{4.11}$$

Volume average strains $\overline{\boldsymbol{\varepsilon}}$ and volume average stresses $\overline{\boldsymbol{\sigma}}$ are defined as

$$\overline{\boldsymbol{\varepsilon}} = \frac{1}{4}\sum_{k=1}^{4} \boldsymbol{\varepsilon}_k \tag{4.12a}$$

$$\overline{\boldsymbol{\sigma}} = \frac{1}{4}\sum_{k=1}^{4} \boldsymbol{\sigma}_k \tag{4.12b}$$

As a result,

$$\boldsymbol{\varepsilon}_{s,k} = \boldsymbol{C}_{ss,k}^{-1}\overline{\boldsymbol{\sigma}}_s - \boldsymbol{C}_{ss,k}^{-1}\boldsymbol{C}_{sn,k}\overline{\boldsymbol{\varepsilon}}_n \tag{4.13a}$$

$$\boldsymbol{\sigma}_{n,k} = \left(\boldsymbol{C}_{nn,k} - \boldsymbol{C}_{ns,k}\boldsymbol{C}_{ss,k}^{-1}\boldsymbol{C}_{sn,k}\right)\overline{\boldsymbol{\varepsilon}}_n + \boldsymbol{C}_{ns,k}\boldsymbol{C}_{ss,k}^{-1}\overline{\boldsymbol{\sigma}}_s \tag{4.13b}$$

By considering the iso-strain and iso-stress principle, the relation between $\begin{bmatrix} \overline{\boldsymbol{\varepsilon}}_n & \overline{\boldsymbol{\sigma}}_s \end{bmatrix}^T$

and $\begin{bmatrix} \bar{\boldsymbol{\sigma}}_n & \bar{\boldsymbol{\varepsilon}}_s \end{bmatrix}^T$ is

$$\begin{bmatrix} \bar{\boldsymbol{\sigma}}_n \\ \bar{\boldsymbol{\varepsilon}}_s \end{bmatrix} = \begin{bmatrix} \boldsymbol{C}_1^* & \boldsymbol{C}_2^* \\ \boldsymbol{C}_3^* & -\boldsymbol{C}_4^* \end{bmatrix} \begin{bmatrix} \bar{\boldsymbol{\varepsilon}}_n \\ \bar{\boldsymbol{\sigma}}_s \end{bmatrix} \tag{4.14a}$$

where

$$\boldsymbol{C}_1^* = \frac{1}{4}\sum_{k=1}^{4}\left(\boldsymbol{C}_{nn,k} - \boldsymbol{C}_{ns,k}\boldsymbol{C}_{ss,k}^{-1}\boldsymbol{C}_{sn,k}\right) \tag{4.14b}$$

$$\boldsymbol{C}_2^* = \frac{1}{4}\sum_{k=1}^{4}\boldsymbol{C}_{ns,k}\boldsymbol{C}_{ss,k}^{-1} \tag{4.14c}$$

$$\boldsymbol{C}_3^* = \frac{1}{4}\sum_{k=1}^{4}\boldsymbol{C}_{ss,k}^{-1} \tag{4.14d}$$

$$\boldsymbol{C}_4^* = \frac{1}{4}\sum_{k=1}^{4}\boldsymbol{C}_{ss,k}^{-1}\boldsymbol{C}_{sn,k} \tag{4.14e}$$

So the stiffness matrix $\bar{\boldsymbol{C}}$ of the RVE can be derived

$$\bar{\boldsymbol{\sigma}} = \bar{\boldsymbol{C}}\bar{\boldsymbol{\varepsilon}} = \begin{bmatrix} \bar{\boldsymbol{C}}_{nn} & \bar{\boldsymbol{C}}_{ns} \\ \bar{\boldsymbol{C}}_{sn} & \bar{\boldsymbol{C}}_{ss} \end{bmatrix} \bar{\boldsymbol{\varepsilon}} \tag{4.15a}$$

where

$$\bar{\boldsymbol{C}}_{nn} = \boldsymbol{C}_1^* + \boldsymbol{C}_2^*\boldsymbol{C}_3^{*-1}\boldsymbol{C}_4^* \tag{4.15b}$$

$$\bar{\boldsymbol{C}}_{ns} = \boldsymbol{C}_2^*\boldsymbol{C}_3^{*-1} \tag{4.15c}$$

$$\bar{\boldsymbol{C}}_{sn} = \boldsymbol{C}_3^{*-1}\boldsymbol{C}_4^* = \bar{\boldsymbol{C}}_{ns}^T \tag{4.15d}$$

$$\bar{\boldsymbol{C}}_{ss} = \boldsymbol{C}_3^{*-1} \tag{4.15e}$$

Then, the laminar elastic constants of PW FRP in the RVE coordinate can be obtained from the flexibility matrix $\bar{\boldsymbol{S}}$ of the RVE as follows:

$$
\bar{\boldsymbol{S}} = \bar{\boldsymbol{C}}^{-1} = \begin{bmatrix} \frac{1}{E_x} & -\frac{\nu_{xy}}{E_x} & -\frac{\nu_{xz}}{E_x} & 0 & 0 & 0 \\ -\frac{\nu_{xy}}{E_x} & \frac{1}{E_y} & -\frac{\nu_{yz}}{E_y} & 0 & 0 & 0 \\ -\frac{\nu_{xz}}{E_x} & -\frac{\nu_{yz}}{E_y} & \frac{1}{E_z} & 0 & 0 & 0 \\ 0 & 0 & 0 & \frac{1}{G_{xy}} & 0 & 0 \\ 0 & 0 & 0 & 0 & \frac{1}{G_{yz}} & 0 \\ 0 & 0 & 0 & 0 & 0 & \frac{1}{G_{zx}} \end{bmatrix} \tag{4.16}
$$

More details can be seen in Ivanov and Tabiei's work (Ivanov & Tabiei, 2001).

4.4 Sensitivity Study and the Determination of Updating Parameters

As introduced in Section 4.2.3, the parameters in micromechanics models, such as fiber volume fraction V_f ($V_{f,\mathrm{UD}}$ and $V_{f,\mathrm{PW}}$) and the elastic constants of fiber (E_f, ν_f and G_f) and matrix (E_m, ν_m and G_m), are now selected as the candidate parameters to be updated. Theoretically, all of these parameters have to be identified. However, some parameters have less uncertainty, such as E_f, ν_f, G_f, E_m, ν_m and G_m; and some parameters are acknowledged that have less influence to the elastic constants of the UD FRP, such as the poison ratios ν_f and ν_m. Hence, it is not practical to update all of the candidate parameters. Therefore, sensitivity studies of the elastic constants of UD FRP and PW FRP with respect to the candidate parameters are conducted to figure out the influential parameters. Among these influential parameters, only those have large uncertainty and high sensitivity needed to be identified.

4.4.1 The sensitivity study of UD FRP

Three different micromechanics models of UD FRP are introduced in Section 4.3.1.

Because these models have different assumptions, they have their own range of application. Therefore, it is necessary that all these three models are included in the sensitivity study.

Based on these models, the elastic constants of UD FRP (E_x, $E_y = E_z$, $G_{yx} = G_{zx}$, G_{zy}, $\nu_{xy} = \nu_{xz}$ and ν_{yz}) can be estimated by E_f, ν_f, G_f, E_m, ν_m, G_m and $V_{f,\mathrm{UD}}$. The definition of the material coordinate is given in Section 4.2.1. The sensitivities of the elastic constants of UD FRP with respect to the candidate parameters (E_f, ν_f, G_f, E_m, ν_m, G_m and $V_{f,\mathrm{UD}}$) are studied in this subsection.

Since the sensitivity study is carried out at the given initial values, the initial value of $V_{f,\mathrm{UD}}$ is selected as 0.5 and the initial elastic constants of Glass and resin are shown in Table 4.1. The mechanical properties of UD FRP predicted by these initial values are shown in Table 4.2. It can be seen that though the equations of these three models are different, the results are basically the same, especially E_x and ν_{yx}.

Table 4.3 shows the change ratios of the elastic constants of UD FRP when the candidate parameters are changed by 30%. The subscripts - 'Chamis', 'HHCL' and 'Huang', stand for the model used. For example, E_{x_Chamis} is the modulus estimated by the Chamis model.

From Table 4.3, it can be seen that for E_x, the three models give the same results and $V_{f,\mathrm{UD}}$ and E_f are the most two influential factors. For the other Young's modulus E_y and shear modulus G_{xy} and G_{yz}, obviously, the most dominant factor is the fiber volume fraction $V_{f,\mathrm{UD}}$. The elastic constants of matrix are the secondly influential parameters. However, $V_{f,\mathrm{UD}}$ has nearly no effect to Poisson's ratio ν_{yx} and ν_{zy}.

Table 4.1 Properties of E-Glass and Resin

	E (GPa)	G (GPa)	ν
E-Glass	70	29.17	0.20
Resin	3.5	1.3	0.35

Table 4.2 Predicted elastic constants by different models when $V_{f,\mathrm{UD}} = 0.5$

	E_x(GPa)	E_y(GPa)	G_{xy}(GPa)	G_{yz}(GPa)	ν_{yx}	ν_{zy}
Chamis	36.7500	10.66	3.9751	3.9751	0.3250	0.3412
HHCL	36.7528	9.0452	3.4614	3.1129	0.3180	0.4529
Huang	36.7500	10.2337	3.4614	3.4491	0.3250	0.4835

Table 4.3 Sensitivity study of elastic constants of UD FRP with respect to the candidate updating parameters

	$V_{f,\mathrm{UD}}$ (%)	E_f (%)	ν_f (%)	G_f (%)	E_m (%)	ν_m (%)	G_m (%)
E_{x_Chamis}	27.14	28.57	0.00	0.00	1.43	0.00	0.00
E_{x_HHCL}	27.14	28.57	0.00	0.00	1.43	0.07	0.00
E_{x_Huang}	27.14	28.57	0.00	0.00	1.43	0.00	0.00
E_{y_Chamis}	40.23	2.55	0.00	0.00	25.93	0.00	0.00
E_{y_HHCL}	42.27	1.00	-0.11	1.56	5.95	22.70	18.59
E_{y_Huang}	44.65	3.39	-0.27	0.00	24.74	8.03	0.00
G_{xy_Chamis}	40.54	0.00	0.00	2.47	0.00	0.00	26.05
G_{xy_HHCL}	45.70	0.00	0.00	2.63	0.00	0.00	25.84
G_{xy_Huang}	45.70	0.00	0.00	2.63	0.00	0.00	25.84
G_{yz_Chamis}	40.54	0.00	0.00	2.47	0.00	0.00	26.05
G_{yz_HHCL}	43.73	0.00	0.00	2.04	1.66	6.44	24.66
G_{yz_Huang}	45.71	2.64	-0.58	0.00	25.82	-6.65	0.00
ν_{yx_Chamis}	-2.31	0.00	13.85	0.00	0.00	16.15	0.00
ν_{yx_HHCL}	-2.46	-0.05	18.21	-0.04	0.42	16.55	-0.36
ν_{yx_Huang}	-2.31	0.00	13.85	0.00	0.00	16.15	0.00

ν_{zy_Chamis}	-0.87	10.02	0.00	-9.47	101.93	0.00	-81.24
ν_{zy_HHCL}	-3.27	3.21	-0.35	-1.51	13.54	49.02	-15.61
ν_{zy_Huang}	-2.23	2.24	0.94	0.00	-2.63	48.24	0.00

4.4.2 The sensitivity study of PW FRP

In this study, the model proposed by Ivanov and Tabiei is chosen to estimate the elastic constants of PW FRP (E_x , E_y , E_z , G_{xy} , G_{yz} , G_{zx} , ν_{yx} , ν_{zy} and ν_{zx}). In this model, the candidate updating parameters are fiber volume fraction $V_{f,\mathrm{PW}}$, braid angle θ_b , undulation angle β_u and the properties of fiber and matrix, E_f, G_f, ν_f, E_m, G_m and ν_m. The sensitivity study of these elastic constants with respect to the candidate updating parameters is conducted below.

The initial values of elastic constants of the constituents are listed in Table 4.1; the other initial values are chosen as $V_{f,\mathrm{PW}}=0.5$, $\theta_b=\pi/4$ and $\beta_u=\arctan(1/6)$. The elastic constants of PW FRP predicted by the initial values are listed in Table 4.4.

Table 4.5 lists the change ratios of the elastic constants when the candidate parameter is changed by 30%. From Table 4.5, it can be found that the same to UD FRP, for Young's modulus (E_x , E_y and E_z) and shear modulus (G_{xy} , G_{yz} and G_{zx}), the most influential factor is still the fiber volume fraction $V_{f,\mathrm{PW}}$, but $V_{f,\mathrm{PW}}$ has nearly no influence on Poisson's ratio (ν_{yx} , ν_{zy} and ν_{zx}) as in the case of UD FRP.

Table 4.4 Predicted properties of PW woven using the initial values

E_x(GPa)	E_y(GPa)	E_z(GPa)	G_{xy}(GPa)	G_{yz}(GPa)	G_{zx}(GPa)
20.9718	20.9718	10.9071	3.4610	3.3848	2.0873

ν_{yx}	ν_{zy}	ν_{zx}
0.1475	0.4565	0.4565

Table 4.5 The sensitivity study of PW FRP

	$V_{f,\mathrm{PW}}$ (%)	θ_b (%)	β_u(%)	E_f(%)	ν_f (%)	G_f(%)	E_m(%)	ν_m(%)	G_m(%)
E_x	43.03	-22.54	-1.89	4.56	0.79	3.60	7.63	6.27	20.43
E_y	43.03	37.00	-1.89	4.56	0.79	3.60	7.63	6.27	20.43
E_z	42.97	-2.35	0.26	5.30	-0.71	0.39	27.08	36.09	6.97
G_{xy}	31.92	-7.79	-4.79	20.93	-1.22	0.56	25.88	19.91	24.16
G_{yz}	45.26	15.60	2.24	3.14	-0.53	1.62	19.44	-1.07	9.36
G_{zx}	45.26	-11.89	2.24	3.14	-0.53	1.62	19.44	-1.07	9.36
ν_{yx}	-10.31	-32.55	-1.96	16.29	3.01	-4.95	23.75	23.83	-1.76
ν_{zy}	3.80	116.38	0.37	-8.99	6.58	2.53	-12.18	26.11	0.04
ν_{zx}	3.80	22.34	0.37	-8.99	6.58	2.53	-12.18	26.11	0.04

4.4.3 Determine the updating parameters

Through sensitivity studies conducted in Section 4.4.1 and Section 4.4.2, the influential parameters to the mechanical properties of UD FRP and PW FRP are figured out. For example, $V_{f,\mathrm{UD}}$ and $V_{f,\mathrm{PW}}$ are the most influential factors which dominates all elastic constants of UD FRP and PW FRP except Poisson's ratios; some properties of constituents, such as E_f and E_m, are also influential to some properties of FRP. However, not all these parameters are needed to be updated.

The uncertainties of the candidate updating parameters are also needed to be discussed. If the certified values of the parameters are known and the uncertainties of these parameters are low, these parameters do not need to be updated even though they are influential. For the elastic constants of fiber and matrix, such as E-Glass and resin, the certified values are known. Due to the mature manufacturing technique, the uncertainty is relatively low. For the fiber volume fractions $V_{f,\mathrm{UD}}$ and $V_{f,\mathrm{PW}}$, the uncertainties are relatively large. $V_{f,\mathrm{UD}}$ and $V_{f,\mathrm{PW}}$ can vary largely in different products and the variations are always unknown. Through simple geometric analysis, the maximum fiber volume fraction is 0.785 for square packing and 0.907 for hexagonal packing (Chawla, 2012). Therefore, the range of $V_{f,\mathrm{UD}}$ and $V_{f,\mathrm{PW}}$ is from 0 to 0.907. For the geometric parameters of PW FRP, the undulation angle β_u is controlled by manufacturers and differs in different products, theoretically $\beta_u \in (0, \pi/2)$; the braid angle θ_b is equal to $\pi/4$ except very special cases. It can be found that the parameters with the largest uncertainty are $V_{f,\mathrm{UD}}$, $V_{f,\mathrm{PW}}$ and β_u.

Reminding the discussion of the sensitivity study in Section 4.4.1 and 4.4.2, the influences of $V_{f,\mathrm{UD}}$ and $V_{f,\mathrm{PW}}$ are much larger than β_u while the influence of β_u is quite small. Hence, the fiber volume fractions of UD FRP, $V_{f,\mathrm{UD}}$, and the PW FRP, $V_{f,\mathrm{PW}}$, are chosen as the updating parameters for the VAWT blade in this study.

4.5 Blade Tests

As shown in the schematic diagram Fig. 4.3(b), in order to update the fiber volume fractions $V_{f,\mathrm{UD}}$ and $V_{f,\mathrm{PW}}$, the FE model of the blade shall be established and the experimental tests of the blade shall be conducted. The measured data are then used to compare with the computed data of the FE model, from which $V_{f,\mathrm{UD}}$ and $V_{f,\mathrm{PW}}$ are updated by reducing the difference between the measured and computed results. In this section, static tests of the blade mentioned in Section 4.2.1 are conducted. These tests were conducted by the Hopewell Wind Power Limited of Hong Kong.

4.5.1 Test setups

In order to offer measured data for model updating, bending tests of the NACA0018 laminated composite blade were conducted. The composite which makes up the blade has shown in Fig. 4.1(b). For the bending test, the overview of the test is shown in Fig. 4.5(a) and the configuration is shown in Fig. 4.6. As introduced in Section 4.2.1, the chord length of the blade is 2m and the length of the blade is 6m. This blade is the same as the blade shown in Fig. 4.1 except the blade length. Three steel brackets were used to fasten the blade at its middle position and its two ends. The bracket was made of steel plate, and the thickness of the steel plate was about 10 mm. The width of the bracket is 300mm.The steel brackets are very stiff compared with that of the blade. Each steel bracket was supported by two actuators at the leading and trailing edges of the blade. The two brackets at the end of the blade were taken as the two fixed supports and the actuators were locked without action, which can be regarded as columns. The actuators (jacks) supporting the middle bracket were simultaneously controlled to give the vertical forces upward to the blade. The middle bracket was 2.32m apart from the adjacent two brackets as shown in Fig. 4.6(b).

Fig. 4.5 Blade test over view

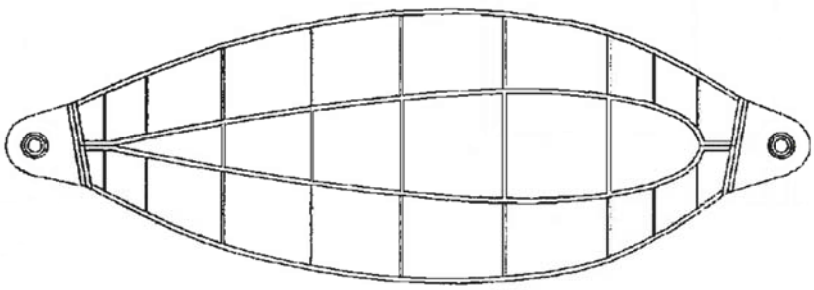

(a)

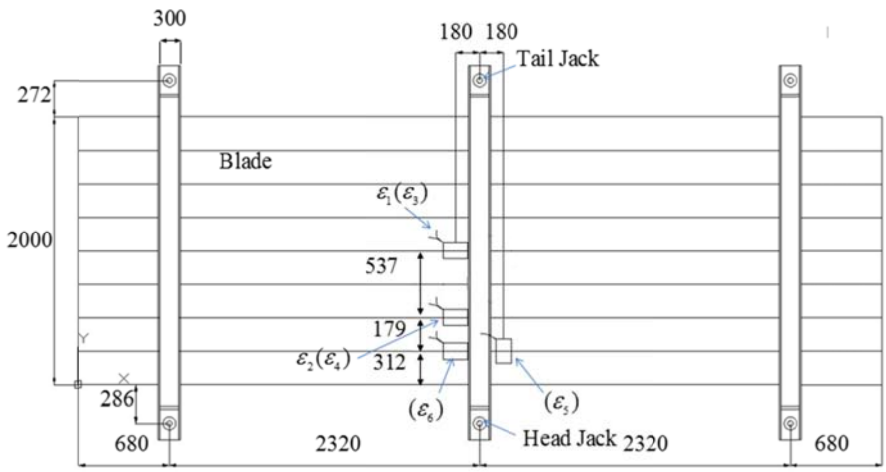

(b)

Fig. 4.6 Configuration of test setup and measurement positions (a) side view; (b) plain view

In these tests, two actuators, two load cells, two LVDTs and 6 resistance strain gauges were used. The actuators at the ends of the blade were used as the columns. The locations of these sensors are shown in Fig. 4.6. The external forces were applied at the mid-span of the blade through the two hydraulic jacks (actuators). Load cells were installed between the jacks and the blade, as shown in Fig. 4.7. Displacements were measured at the head and tail jack by the two LVDTs. In order to measure the stresses of the blade at its critical locations, strain gauges ε_1 and ε_2 were stuck on the top of the blade and $\varepsilon_3 \sim \varepsilon_6$ were stuck on the bottom; all strain gauges measured longitudinal strains except for ε_5 that measured the transverse strain. The dynamic resistance strain gauge data acquisition system is shown in Fig. 4.8.

Fig. 4.7 Load cell

Fig. 4.8 Dynamic resistance strain gauge data acquisition system

4.5.2 Measurement Results

A series of bending tests were conducted, in which the total external force at the mid-span increased from 41229.6N to 66796.8N. In this study, only the measured responses from the case of 66796.8N (39361.7N at head and 27435.1N at tail) are considered. The applied forces and the results of the bending test used in this study are shown in Table 4.6.

Table 4.6 Measured data

Force at head (N)	39361.70
Force at tail (N)	27435.10
Disp. at head jack (mm)	7.9
Disp. at tail jack (mm)	8.5
Bending Disp. d_{bend} (mm)	8.2
ε_1 (10^{-6})	651
ε_2 (10^{-6})	739

ε_3 (10^{-6})	-662
ε_4 (10^{-6})	-785
ε_5 (10^{-6})	220
ε_6 (10^{-6})	-796

The bending displacement d_{bend} is the mean value of those measured at head jack and tail jack at the mid-span, which measures the deflection. Among the measured data, d_{bend}, ε_1, ε_2 and ε_3 are used in the model updating in this section and the other data are used to verify the proposed method.

4.6 Model Updating and Discussion

4.6.1 Finite element model of tested blade

A FE model of the blade is established according to the bending tests of the blade, which is shown in Fig. 4.10(a). As introduced in Section 4.2.2, element shell91 is used to model the blade. The brackets are also simulated by shell91 but the four columns are simulated by element beam4. At each end of the bracket, there are two steel fins, which are used to connect the bracket to the two columns through the shafts. The steel fins are simulated by shell91 but the shaft and column are simulated by element beam4. The connection between the bracket and the column is regarded as a pin support, as shown in Fig. 4.10(b). The measurement data recorded during the tests are used to identify the laminar elastic constants of the blade through the FE model updating.

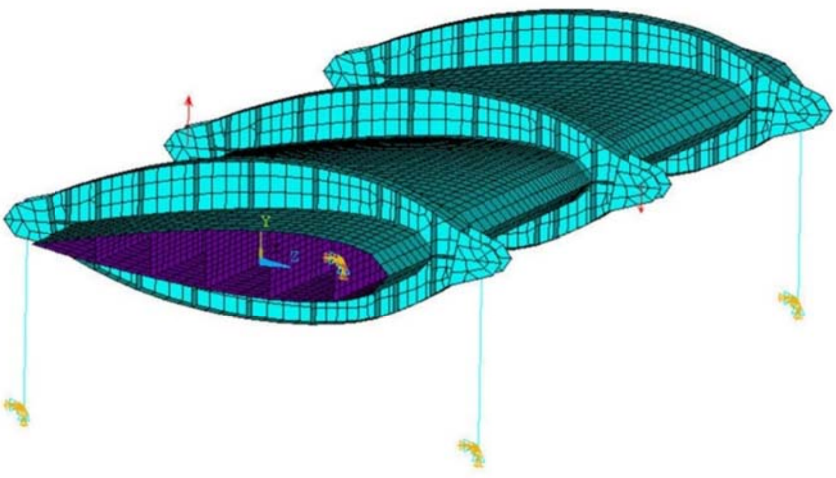

(a)

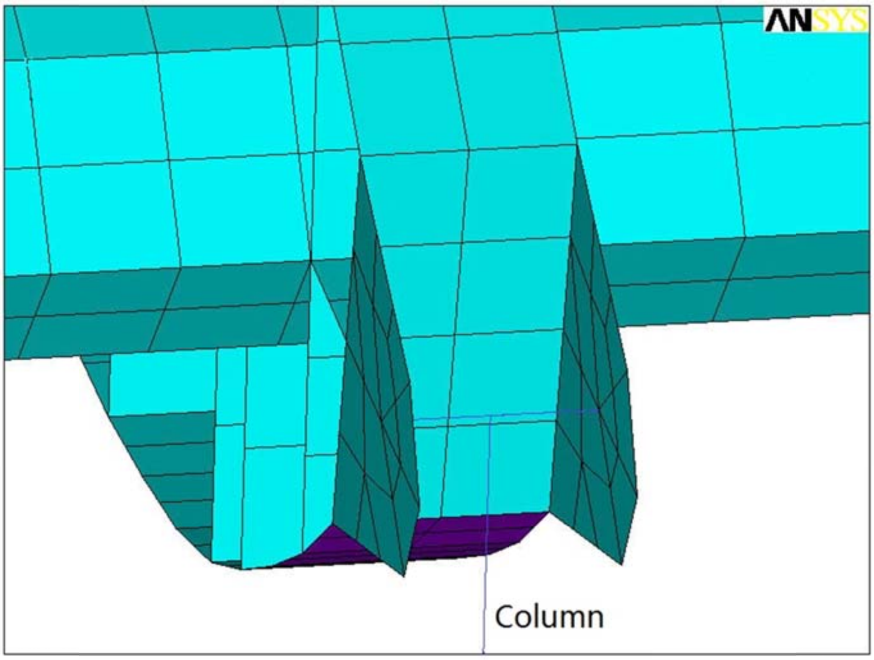

(b)

Fig. 4.10 Finite element model of tested blade (a) overview; (b) the connection between bracket and column

Since the volume fractions of the blade materials are unknown, $V_{f,\mathrm{UD}} = 0.5$ and $V_{f,\mathrm{PW}} = 0.5$ are used as the initial values. By using the micromechanics models introduced in Section 4.3 and the elastic constants of fiber and matrix listed in Table 4.1, the initial laminar elastic constants of the UD FRP and PW FRP are predicted and listed in Table 4.2 and Table 4.4 respectively. Furthermore, by applying the vertical forces used in the bending test of the blade to the FE model, the initial blade responses, corresponding to the bending test of the blade, are predicted and listed in Table 4.7.

Table 4.7 Initial bending responses predicted by initial constants

Response	Chamis	HHCL	Huang
d_{bend} (mm)	5.2	5.5	4.8
ε_1 (10^{-6})	380	387	355
ε_2 (10^{-6})	432	437	419
ε_3 (10^{-6})	-379	-387	-354
ε_4 (10^{-6})	-434	-438	-421
ε_5 (10^{-6})	154	161	147
ε_6 (10^{-6})	-430	-439	-415

It can be seen that the predicted responses are considerably different from the measured values listed in Table 4.6, which implies that the initial laminar elastic constants estimated by $V_{f,\mathrm{UD}} = 0.5$ and $V_{f,\mathrm{PW}} = 0.5$ are not coincident with the real values of the blade. Therefore, the FE model updating shall be performed.

4.6.2 Model Updating

4.6.2.1 The objective function

In this study, only parts of the measured responses (d_{bend}, ε_1, ε_2 and ε_3) from the bending test are used to update the fiber volume fractions ($V_{f,\mathrm{UD}}$ and $V_{f,\mathrm{PW}}$) using the proposed model updating algorithm. The other measured data are used to validate the accuracy of the proposed model updating algorithm.

The objective function of the model updating is to minimize the following index.

$$\text{Minimize: } f_{obj} = \omega_{bend} err_{bend} + \omega_{\varepsilon 1} err_{\varepsilon 1} + \omega_{\varepsilon 2} err_{\varepsilon 2} + \omega_{\varepsilon 3} err_{\varepsilon 3} \quad (4.17)$$

where

$$err_{bend} = \left| \left(d_{bend,\mathrm{FEM}} - d_{bend,measured} \right) / d_{bend,measured} \right|$$

$$err_{\varepsilon 1} = \left| \left(\varepsilon_{1,\mathrm{FEM}} - \varepsilon_{1,measured} \right) / \varepsilon_{1,measured} \right|$$

$$err_{\varepsilon 2} = \left| \left(\varepsilon_{2,\mathrm{FEM}} - \varepsilon_{2,measured} \right) / \varepsilon_{2,measured} \right|$$

$$err_{\varepsilon 3} = \left| \left(\varepsilon_{3,\mathrm{FEM}} - \varepsilon_{3,measured} \right) / \varepsilon_{3,measured} \right|$$

The above four errors are the relative errors between the measured and computed responses. The positions of the responses d_{bend}, ε_1, ε_2 and ε_3 can be seen in Fig. 4.6. The subscripts 'FEM' and 'measured' stand for the computed and measured results respectively. ω_{bend}, $\omega_{\varepsilon 1}$, $\omega_{\varepsilon 2}$ and $\omega_{\varepsilon 3}$ are the weight coefficients.

4.6.2.2 The pattern search algorithm

The optimization method adopted in this study is the pattern search algorithm, which is used to find the best values of $V_{f,\mathrm{UD}}$ and $V_{f,\mathrm{PW}}$ so that the objective function, Equation (4.17), reaches its minimum value (Torczon, 1997). Pattern search is a direct optimization method that does not need the gradient of the objective function. This method changes one updating parameter ($V_{f,\mathrm{UD}}$ or $V_{f,\mathrm{PW}}$) at a time by steps of the same magnitude, and when no such increase or decrease in any one parameter can further decreases the objective function, the step magnitude is then halved and the process is repeated until the steps are deemed sufficiently small (smaller than the predefined termination tolerance). It is proved that the pattern search method can converge to a global optimal solution (Torczon, 1997). The detail of the pattern search can be found in Lewis and Torczon's paper (Lewis & Torczon, 2000).

In this study, the termination tolerance for iteration on f_{obj} is 0.0001 and the iteration will also be terminated when the step magnitude is less than 0.001. Through minimizing the objective function, the two fiber volume fractions can be obtained.

4.6.3 Sensitivity study and discussion

To determine the weight coefficients in the objective function, the sensitivity study of d_{bend}, ε_1, ε_2 and ε_3 with respect to $V_{f,\mathrm{UD}}$ and $V_{f,\mathrm{PW}}$ is first conducted. The sensitivities at the point $V_{f,\mathrm{UD}}=0.5$ and $V_{f,\mathrm{PW}}=0.5$ are calculated. The results are shown in Table 4.8.

Table 4.8 Sensitivities of responses with respect to fiber volume fractions

	d_{bend}	ε_1	ε_2	ε_3
$\Delta V_{f,\mathrm{UD}}:25\%$	25.70%	26.76%	25.6%	26.74%
$\Delta V_{f,\mathrm{PW}}:25\%$	6.12%	5.37%	5.85%	5.33%

The second row of Table 4.8 is the change ratios of responses when $V_{f,\mathrm{UD}}$ increases 25% ($V_{f,\mathrm{UD}}=0.625$) while $V_{f,\mathrm{PW}}$ holds as 0.5. It can be found that the change ratios of the four responses are also nearly 25%. The third row is the change ratios of responses when $V_{f,\mathrm{PW}}$ increases 25% ($V_{f,\mathrm{PW}}=0.625$) while $V_{f,\mathrm{UD}}$ holds as 0.5. In this case, the change ratios of the four responses are about 5%. Therefore, either $V_{f,\mathrm{UD}}$ or $V_{f,\mathrm{PW}}$ has nearly equal influence on the four responses, and accordingly the weight coefficients $\omega_{bend}=\omega_{\varepsilon1}=\omega_{\varepsilon2}=\omega_{\varepsilon3}=1$.

On the other hand, it can be seen that the sensitivity of the responses with respect to $V_{f,\mathrm{PW}}$ are much lower than to $V_{f,\mathrm{UD}}$. One of the reasons is because that the thickness of PW FRP layers is just 2mm (1mm+1mm) while the thickness of UD FRP layer is 6mm. In another word, the accuracy of the updated $V_{f,\mathrm{PW}}$ is less than that of $V_{f,\mathrm{UD}}$.

4.6.4 Results and discussion

The measured data are shown in Table 4.6. The identified fiber volume fractions by the three micromechanics models are listed in Table 4.9. It can be seen that these three models obtain similar results of $V_{f,\mathrm{UD}}$ and $V_{f,\mathrm{PW}}$. However, compared with the initial values of 50%, the updated fiber volume fraction of UD FRP is now in the range of 15% - 20% while the updated fiber volume fraction of PW FRP is in the range of 50%-75%. This is because of the less sensitivity of the responses with respect to $V_{f,\mathrm{PW}}$ than to $V_{f,\mathrm{UD}}$, as discussed in Section 4.6.3. The identified results of $V_{f,\mathrm{UD}}$ are more reliable than $V_{f,\mathrm{PW}}$.

Using the identified results, the bending displacement d_{bend} and bending strain (ε_1 - ε_6) can be estimated. The measured data and the corresponding predicted results are shown in Table 4.10. Compared with the initial responses listed in Table 4.7, the relative errors of the predicted results are listed in Table 4.11. It can be found that the errors of d_{bend}, ε_1, ε_2 and ε_3 are very small after updating because they are used in the objective function, which indicates the validity of the pattern search algorithm. The other measured data, including ε_4, ε_5 and ε_6, are used to verify the updating results. It can be seen that the numerical results match well with the measured data after updating by the proposed method. For ε_4, ε_5 and ε_6, the relative errors are reduced to about 5% after updating. The reduction in errors of ε_4, ε_5 and ε_6 indicates that the micromechanics models can give good predictions of the laminar elastic constants of the laminated blade, and the FE model can simulate the tests well. Hence the comparisons in this section verify the effectiveness of the proposed method.

It can also be seen that the results obtained by the three micromechanics models for UD

FRP are similar except for ε_5. The only difference is in the result of ε_5 which is the strain in the lateral direction. The relative error in the result obtained by the Huang's model is only 2.47% while the relative errors in the results obtained by the Chamis model and the HHCL model are 8.03% and 15.2%. From this point of view, the Huang's model obtains better results.

Table 4.9 Identified fiber volume fractions

	Chamis	HHCL	Huang
$V_{f,UD}$	0.1680	0.1543	0.1855
$V_{f,PW}$	0.6387	0.7481	0.5352

Table 4.10 Numerical simulation results of the bending test

	Measured	Chamis	HHCL	Huang
Used for updating				
d_{bend} (mm)	8.2	8.2	8.2	8.2
ε_1 (10^{-6})	651	654	658	648
ε_2 (10^{-6})	739	747	734	742
ε_3 (10^{-6})	-662	-654	-659	-648
Used for validation				
ε_4 (10^{-6})	-785	-750	-738	-745
ε_5 (10^{-6})	220	203	178	215
ε_6 (10^{-6})	-796	-762	-746	-758

Table 4.11 Estimation errors before and after updating

	Chamis		HHCL		Huang	
Used for updating						
	Before	After	Before	After	Before	After
err_{bend}	36.1%	0.03%	33.5%	0.02%	41.1%	0.08%
$err_{\varepsilon 1}$	41.7%	0.43%	40.5%	0.44%	45.5%	0.44%
$err_{\varepsilon 2}$	41.5%	1.08%	40.9%	0.17%	43.3%	0.39%
$err_{\varepsilon 3}$	42.7%	1.23%	41.5%	1.20%	46.5%	2.11%

	Used for validation					
	Before	After	Before	After	Before	After
$err_{\varepsilon 4}$	44.7%	4.48%	44.2%	5.34%	46.4%	5.13%
$err_{\varepsilon 5}$	29.8%	8.03%	27.0%	15.2%	33.4%	2.47%
$err_{\varepsilon 6}$	46.0%	4.26%	44.9%	4.68%	47.9%	4.84%

Now, using the updated FE model, the laminar strains and stresses of the blade due to the bending can be estimated more accurately. The contours of σ_x in three layers of the blade are shown in Fig. 4.11.

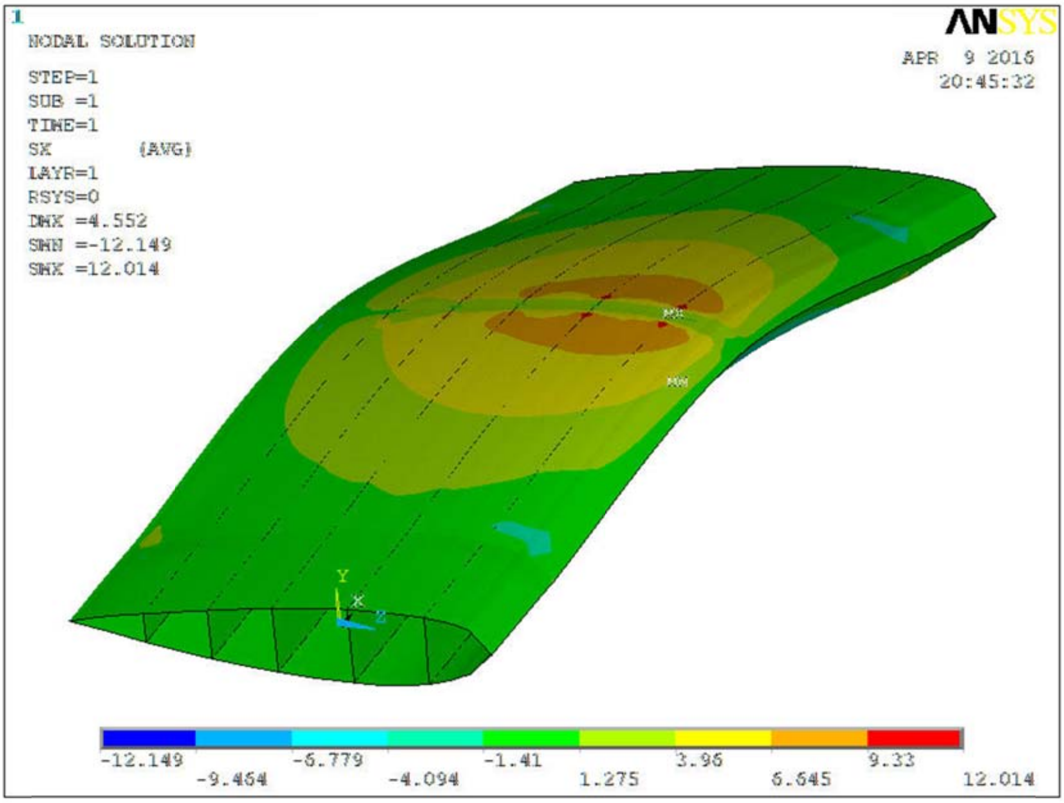

(a)

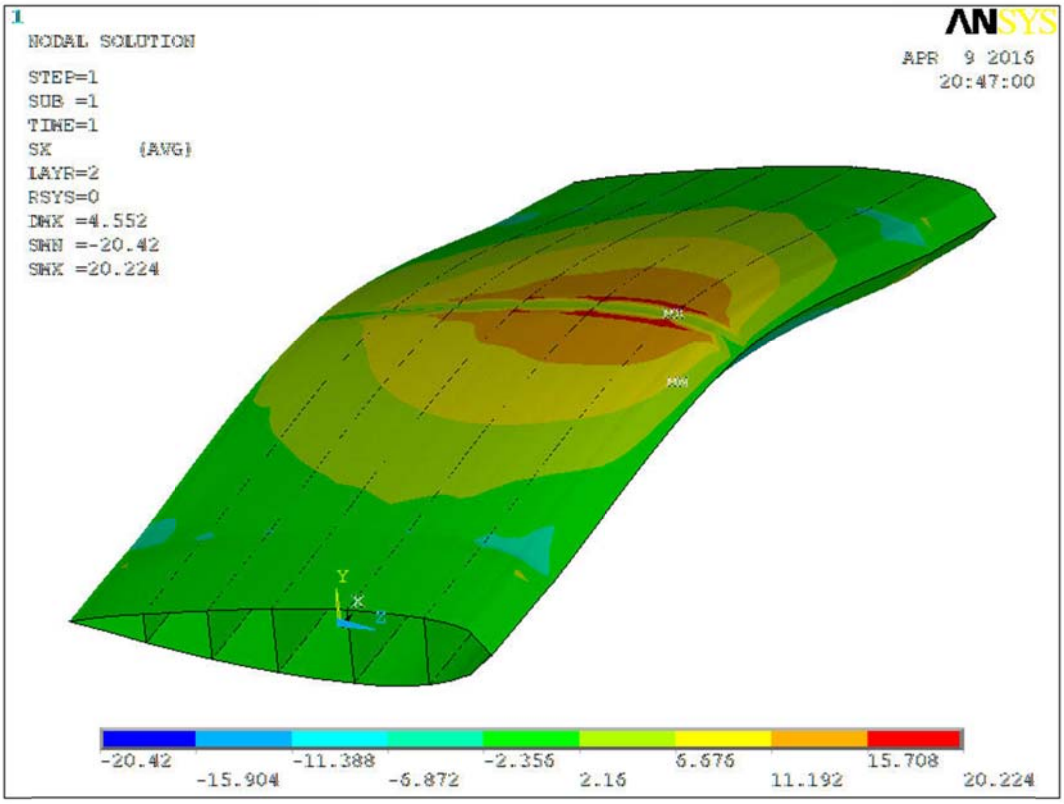
1
NODAL SOLUTION
STEP=1
SUB =1
TIME=1
SX (AVG)
LAYR=2
RSYS=0
DMX =4.552
SMN =-20.42
SMX =20.224
ANSYS
APR 9 2016
20:47:00
Y
X
Z
MX
MN
-20.42
-15.904
-11.388
-6.872
-2.356
2.16
6.676
11.192
15.708
20.224

(b)

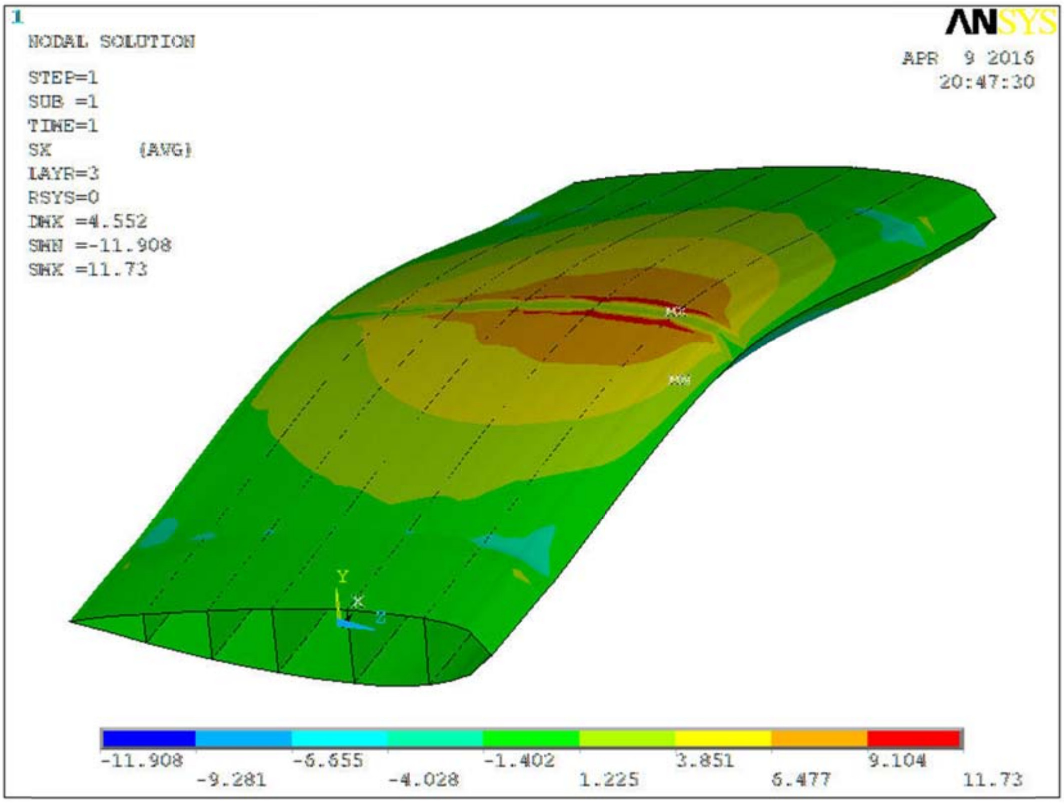
1
NODAL SOLUTION
STEP=1
SUB =1
TIME=1
SX (AVG)
LAYR=3
RSYS=0
DMX =4.552
SMN =-11.908
SMX =11.73
ANSYS
APR 9 2016
20:47:30
Y
X
Z
MX
MN
-11.908
-9.281
-6.655
-4.028
-1.402
1.225
3.851
6.477
9.104
11.73

(c)

Fig. 4.11 Contour of laminar stress σ_x (a) inner layer; (b) middle layer; (c) outer layer.

4.7 Summary

To obtain the laminar stresses and strains, a FE model of blade was established using laminated composite shell elements (ANSYS shell91). In this study, a typical laminated composite straight blade was taken for example, which was made of UD FRP and PW FRP.

To update the laminar elastic constants of the FE model, a model updating method was proposed based on the micromechanics approach in this chapter. Micromechanics models were applied in the process of updating the laminar elastic constants of the blade, so that the direct identification of these constants can be avoided and the number of updating parameters can be reduced. Sensitivity and uncertainty analysis were also conducted to determine the parameters to be updated. It is found that the fiber volume fraction is the most influential parameter with the largest uncertainty for both UD FRP and PW FRP. With the aid of micromechanics models, the number of updating parameters can be significantly reduced to 2 in this case (fiber volume fractions of UP-FRP and PW FRP).

Bending tests were conducted and displacements and strains were measured. A FE model of the laminated composite blade according to the blade tests was established using ANSYS shell91 element. The sensitivity of the responses with respect to the fiber volume fractions of UD FRP and PW FRP is studied. It is found that the measured responses are insensitive to the change of $V_{f,PW}$ and the identified results of $V_{f,UD}$ are more reliable. One of the reasons is because that the thickness of UD FRP is 6mm and that of PW FRP composite is only 1 mm and hence the elastic constants of UD FRP are dominant.

Based on the proposed model updating method and the pattern search algorithm, the updating parameters (fiber volume fractions for UP FRP and PW FRP) were identified. It was found that after updating, both the local strain responses and the global displacement matched well with the measurements and the fiber volume fractions were updated successfully. From the comparison between the numerical and measurement results, it seems that the Huang's model can obtain more accurate results.

Up to this chapter, the wind pressures of the blade can be simulated by the framework proposed in Chapter 3 and the FE model can be established to obtain the laminar stresses and strains. In the next chapter, the fatigue and ultimate analysis of the blade will be conducted. The fatigue critical locations and the ultimate damage locations will also be figured out.

CHAPTER 5

FATIGUE AND ULTIMATE STRENGTH ANALYSES OF LAMINATED COMPOSITE BLADES

5.1 Introduction

Wind turbines are often built in areas of harsh environment. During operation, large cyclic stresses in wind turbine blades will be produced by time-varying wind loads, and the number of cycles will be in the order of 10^8 to 10^9 over a 20 to 30 years life time. Besides fatigue loads, a wind turbine is also subjected to ultimate loads in the extreme wind condition. The collapses of wind turbines due to failures of blades are reported in many references (Gipe, 2005). Moreover, because a wind farm is usually uninhabited, the regular inspection and maintenance are costly. Hence, structural health monitoring (SHM) systems are sometime installed in large wind turbines to monitor their functionality and safety while reducing human inspection cost. The sensor placement for a SHM system then becomes a challenging tasks because sensors like strain gauges are only sensitive to damage when sensors are close to damage. Therefore, to improve the design of the wind turbine blade and guide the sensor installation for a SHM system, the fatigue and ultimate strength analyses are required and the critical locations of fatigue and ultimate strength failure need to be figured out.

For horizontal axis wind turbines (HAWTs), the field measurement and experimental tests play an important role in the fatigue and ultimate strength analyses. Data bases of fatigue load spectra, such as WISPER/WISPERX, were established based on the abundant field measurements in Europe wind farms (Kelley, 1995; Sutherland, 1999). Aided by the measured data, some numerical and analytical analyses have been proposed to estimate the fatigue life of HAWT blades (Burton et al., 2001; Kong et al., 2005; Nijssen, 2006; Shokrieh & Rafiee, 2006; Sutherland, 1999). For the ultimate strength analysis, tests of full scale models were carried out in the laboratory and the corresponding FE simulations have been then conducted to enable further detailed analyses of HAWT blades (Jørgensen et al., 2004; Jensen et al., 2006). Based on the fatigue and ultimate strength analyses, the critical locations of fatigue and strength failures of HAWT blades were figured out by researchers. However, the analyses for VAWTs, especially straight-bladed VAWTs, are rare.

In this chapter, accurate numerical simulations are conducted to compensate for the lack of field measurement and experimental tests. Since a wind load simulation method is proposed in Chapter 3 and the updated laminar elastic constants for the FE model of laminated FRP straight blade is given in Chapter 4, a fatigue and ultimate strength analysis framework is proposed in this chapter based on the works of Chapter 3 and Chapter 4. A laminated composite straight blade of VAWT is taken for example to introduce this framework. A refined 3D finite element model of the blade is established, and the numerical simulations under different load conditions are conducted. Stress and strain time-histories in each ply of the blade are calculated. In the fatigue analysis, fatigue-critical locations are figured out. The influences of turbulence and mean wind on fatigue life are specified. Parametric analyses are also conducted to study the influences of material strengths, damping ratio, modal frequencies and wind speed distribution (Weibull model parameters) on fatigue life. For the ultimate strength analysis, the influence of the wind direction on the stress of the blade is considered and the failure-critical locations and the locations with large inter-laminar stresses are also figured out.

5.2 The Framework of Fatigue and Ultimate Strength Analyses

In Chapter 3, a wind load simulation method based on strip analysis and CFD is proposed. This method takes account of the influences of the mean wind profile, the turbulence and the wind-structure interaction among all structural components. Wind loads under different wind conditions are also considered. Since the blades and other components, such as arms and tower, are simulated as the wall boundary conditions, the aeroelastic effect is ignored. In Chapter 4, a refined blade model is established and updated based on the micromechanics modes and static tests in order to obtain accurate laminar strains and stresses which are necessary for the fatigue and ultimate strength analyses. Based on these works, a framework of the fatigue and ultimate strength analyses for a laminated composite blade can be proposed.

The procedure of the framework is shown in Fig. 5.1. There are three parts in this framework. The first part is to determine the design loads, including wind loads and inertial forces, in which wind loads can be obtained by the method proposed in Chapter 3. The second part is to establish a properly FE model and conduct the model updating of the blade aimed to obtain accurate laminar elastic constants. Finally, the fatigue and ultimate strength analyses can be conducted in the third part. As introduced in Chapter 2, for HAWTs, the experiences of fatigue and strength failures have been accumulated for over a century and the study on this topic are still undergoing, while VAWTs, especially straight-bladed VAWTs, are lack of field measurements and structure-oriented experimental tests. The proposed framework can offer the information on fatigue and strength failures for the design of VAWTs, which is an effective solution to the present situation of the development of VAWTs.

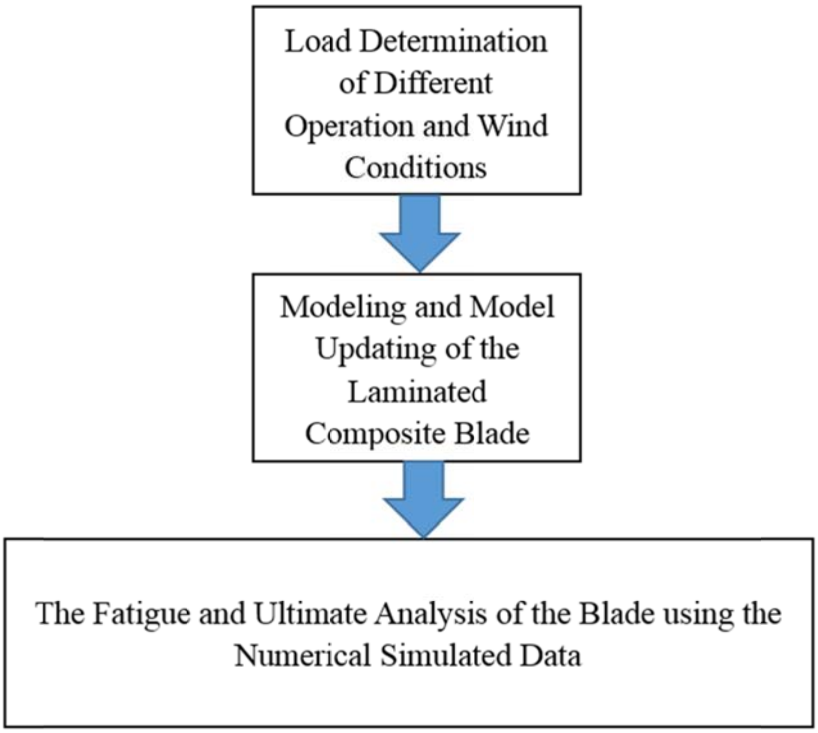

Fig. 5.1 A framework of the fatigue and ultimate strength analysis for a laminated composite blade

5.3 The Finite Element Model of the Composite Straight Blade

The laminated composite straight blade of the VAWT established by the Hopewell Wind Power Limited of Hong Kong is considered, as shown in Fig. 4.1 of Chapter 4. The length of the blade is identical to the blade used in CFD simulation in Chapter 3 but different from the blade used in Chapter 4. The blade in Chapter 4 is just for model updating and is only 6 m in length; the length of the blade in Chapter 3 and this chapter is 26 m. Nevertheless, the material of the blade is identical to the blade updated in Chapter 4.

Fig. 5.2 the blade and the bracket

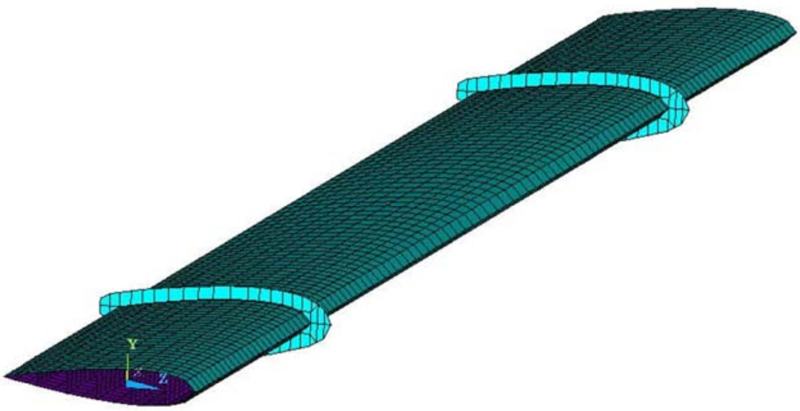

(a)

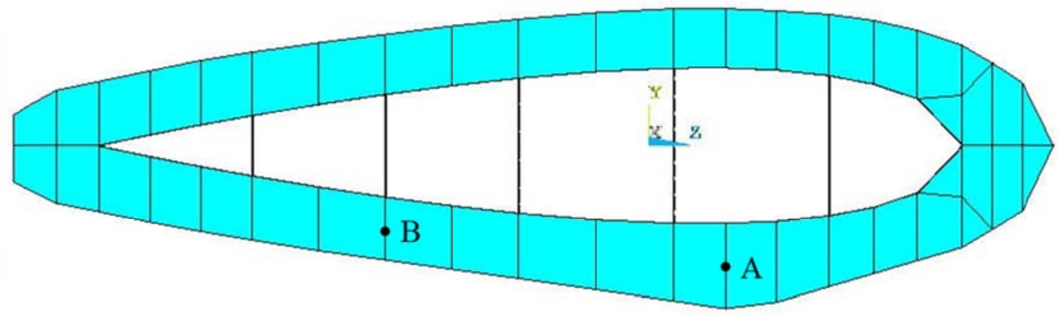

(b)

Fig. 5.3 Finite element model of the blade. (a) Overview; (b) side view.

The finite element model of the blade used in this chapter is established by ANSYS Shell91 and shown in Fig. 5.3(a), and the side view of the blade model is shown in Fig. 5.3(b). Shell91 has 8 nodes and each node has 6 DOFs, u_X, u_Y, u_Z, θ_X, θ_Y and θ_Z, where u_X is the displacement in the direction of X; u_Y is the displacement in the direction of Y; u_Z is the displacement in the direction of Z; θ_X is the rotation on X-axis; θ_Y is the rotation on Y-axis; and θ_Z is the rotation on Z-axis. As introduced in Chapter 3, the blade has a NACA0018 cross section with 2m chord length. The length of the blade is 26m. There are two identical steel brackets are used to fasten the blades near its two ends. The bracket is made of a steel stiffener and a steel flange. The stiffener is welded to the middle of the flange by butt weld as T shape. The stiffener is 15 mm in thickness and about 150mm in width. The flange is 30 mm in thickness 200 mm in width. Assumed that the flange of the bracket has a good contact with the blade, the flange and the blade are simulated in one element with four layers (3 layers of the blade and 1 layer of the flange). The connection between the element of stiffener and the element of flange is rigid. The laminar elastic constants of the blade are identical to those identified in Chapter 4. Rayleigh damping is used in this study and the damping ratio is chosen as 0.5%. In this FE model, there are 7927 elements and 22752 nodes and the number of DOFs is 136512.

As introduced in Chapter 3, the blade actually is supported by the upper and lower arms. The upper or lower arm are connected to the bracket at the positions of A and B. In actuality, a shear load pin is installed at A and an actuator is connected at B; the pitch angle can be changed by actuators. The blade is rotating on the tower, which is difficult in the simulation. The widely used method is to ignore the influence of the vibration of arms and tower on the blade. In the simulation of this chapter, the calculation is conducted in the reference frame XYZ as shown in Fig. 5.3, which is attached to the blade. The X-axis coincide with the shear center of the blade. The top of the blade is at X=0 m and the bottom of the blade is at X=26 m. The elements belong to the area Y<0 are close to the tower of the VAWT, which are denoted as tower side (inner side) of the blade and the elements belong to the area Y>0 are denoted as the outer side of the blade. In this reference frame, nodes at A and B of the two brackets are regarded as the fixed pin joints and the blade can be regarded as a structure without any rigid motion. Therefore, the analysis of the blade is decoupled from the analysis of other components and only the inertial forces (the centrifugal force and the Coriolis' force) are needed to be considered in this reference frame, which brings about a great convenience in the simulation. Such a simplification is widely accepted in the analysis of HAWTs blade (Castelli et al., 2013; Jørgensen et al., 2004; Jensen et al., 2006; Kong et al., 2005; Kubiak & Kaczmarek, 2015; Marin et al., 2009; Mollineaux et al., 2013; Nijssen, 2006; Rumsey & Paquette, 2008).

The stresses and strains of the blade are expressed in the element reference frames, of which the x-axis is the same to the X-axis and the z-axis is normal to the element plane and y-axis is determined by the other two axes. So in each ply, σ_z, τ_{zx} and τ_{zy} are the inter-laminar stresses and σ_x, σ_y and τ_{xy} are the in-plane stresses; ε_z, γ_{zx}, γ_{zy}, ε_x, ε_y and γ_{xy} are the corresponding strain. Through the thickness of the shell element, the strains are continuous but the stresses are discontinuous. Take σ_x and ε_x for example, the distribution of σ_x and ε_x through the thickness of the outer shell of the blade are shown in Fig. 5.4. The thickness of the outer shell is 8mm. The 1st and 3rd layer are 1mm in thickness (the 1st layer is the inner surface of the outer shell and the 3rd layer is the outer surface of the outer shell), which are made of PW FRP; the 2nd layer is 6mm in thickness, which is made of UD FRP. It is obvious that σ_x is continuous inside each layer but is discontinuous between two adjacent layers; while ε_x is continuous through the thickness of the outer shell.

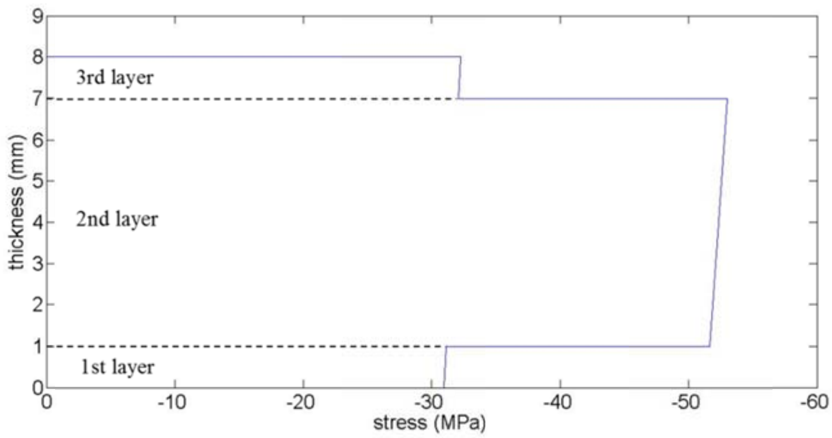

(a)

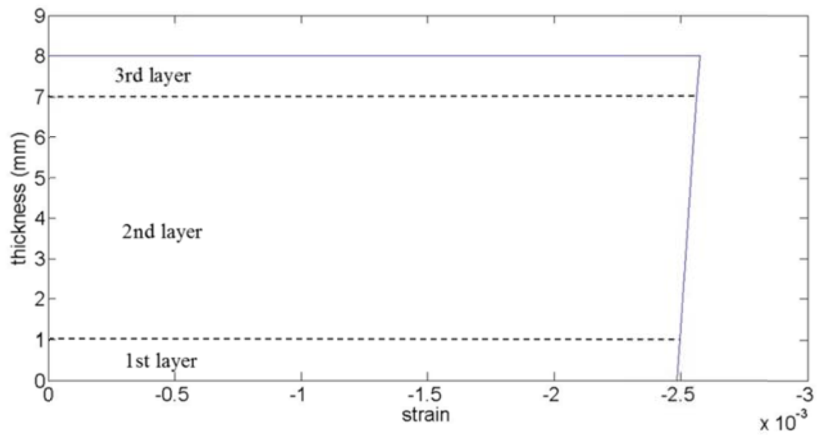

(b)

Fig. 5.4 The distribution of σ_x and ε_x through the thickness of the outer shell of the blade. (a) σ_x; (b) ε_x.

The first 5 natural frequencies are listed in Table 5.1 and the corresponding mode shapes are shown in Fig. 5.5. The 1st , 2nd , 3rd and 5th modes are the 1st to 4th flatwise bending modes, respectively; the 4th mode is the 1st chordwise bending mode. As introduced in Chapter 3, the rotational speed of the considered VAWT is only 0.33Hz (2.1rad/s) while the fundamental modal frequency is 2.30Hz. It can be estimated that the first mode shape is dominated in the responses of the blade.

Table 5.1 Natural frequencies of the first 5 modes

	1st	2nd	3rd	4th	5th
f (Hz)	2.30	3.29	5.10	7.70	9.69

(a)

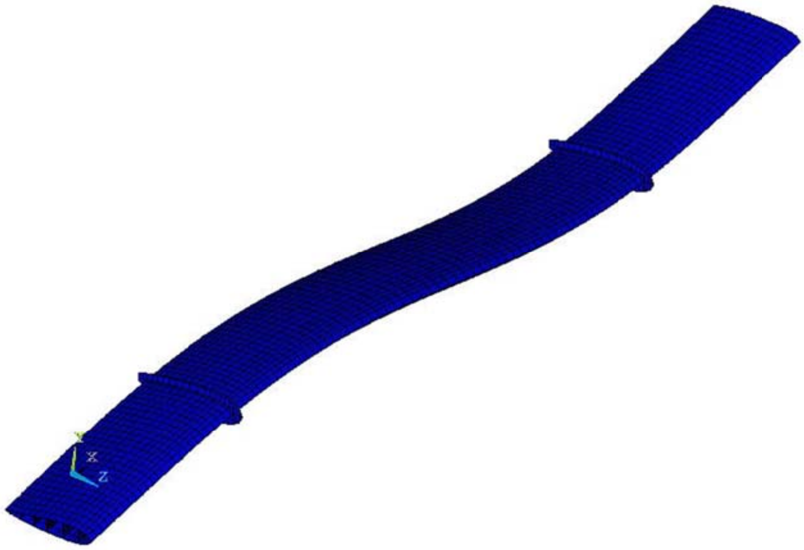

(b)

(c)

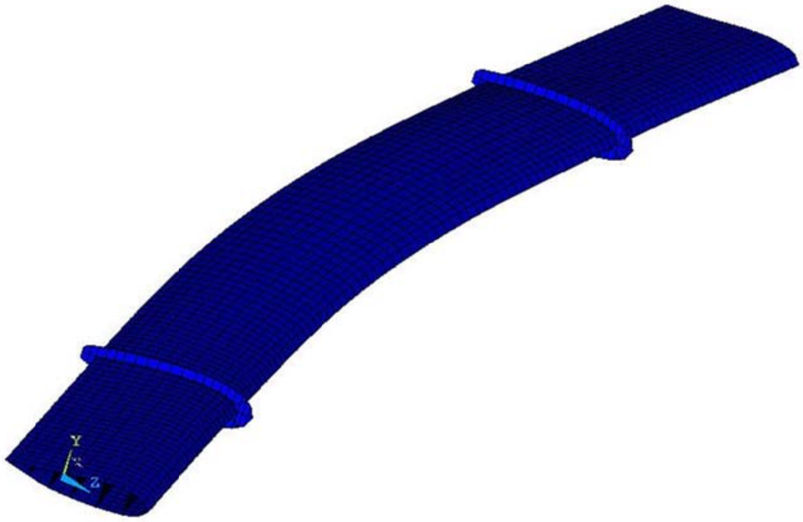

(d)

(e)

Fig. 5.5 Mode shapes of the blade. (a) 1^{st} mode; (b) 2^{nd} mode; (c) 3^{rd} mode; (d) 4^{th} mode; (e) 5^{th} mode.

5.4 Load Cases

5.4.1 The operation and external conditions

In the service life, a wind turbine will be exposed to different operation and external conditions. The load cases and the analysis type, the fatigue or ultimate strength analysis, are determined by the combination of operation and external condition. The operation conditions of a modern grid-connected wind turbine are divided into 8 types by IEC61400-1:

(1) power production (normal operation);

(2) power production plus occurrence fault;

(3) start up;

(4) normal shut down;

(5) emergency shut down;

(6) parked (standing still or idling);

(7) parked and fault condition;

(8) transport, assembly, maintenance and repair.

The external conditions are divided into 8 types in IEC61400-1:

(1) normal turbulence model (NTM);

(2) normal wind profile model (NWP);

(3) extreme wind speed model (EWM);

(4) extreme turbulence model (ETM);

(5) extreme wind shear (EWS);

(6) extreme direction change (EDC);

(7) extreme operation gust (EOG);

(8) extreme coherent gust with direction change (ECD).

Nevertheless, the above classifications are for HAWTs and some of the requirements of IEC61400-1 may be not suitable to VAWTs. For example, the wind load is not sensitive to wind direction for VAWTs; hence the ECD is unlikely to cause extreme wind loads on the blade. Moreover, it is difficult to consider all operation and external conditions, and only the most importance factors are included in this study. For the operation conditions, to simplify the analysis, only the conditions of power production and standing still, which occupy the largest proportion of the service life, are considered in this study. Actually, the conditions of startup, normal shut down and idling should also be considered. However, because the proportion of these conditions in the service life is small and they will bring about large difficulties in the wind load simulation, the influences of these conditions are ignored in this study. For external conditions, only normal wind conditions (NTM and NWP) and extreme wind speed (EWS) are considered in this study for simplicity.

Considering that a wind turbine is parked in the extreme wind speed and that the fatigue in the extreme wind speed can be ignored, two combinations of operation and external conditions are considered in this study: 1) normal wind conditions in the power production; and 2) extreme wind speed when the VAWT is parked. The fatigue analysis is only conducted in the first combination and the ultimate strength analysis needs to consider the maximum load in both situations.

5.4.2 Loads on the blade

As introduced in Chapter 3, a wind turbine generates power in the mean wind speed region between the cut-in wind speed and the cutout wind speed, which is defined as the operation wind speed region. When the mean wind speed is out of this region, the wind turbine is parked or idling. For the VAWT considered in this study, the cut-in wind speed V_{in} is 5 m/s and the cutout wind speed V_{out} is 21 m/s. In the operation wind speed region, the VAWT operates at the rotational speed of 2.1 rad/s. The loads on the blade in these conditions are introduced below.

5.4.2.1 Loads on the blade in operation wind speed region

In this situation, the VAWT is rotating and the mean wind profile and turbulence are considered. For HAWTs, if not considering the mean wind profile, the wind load on the blade caused by mean wind speed can be regarded as static because the relative angle of attack is invariant when rotational speed and the mean wind speed are unchanged. Different from HAWTs, under the unchanged rotational speed and mean wind speed, the relative angle of attack is cyclically changing, so the mean wind speed still causes the cyclic wind load on the blade of a VAWT. Due to the mean wind profile, the wind load caused by the mean wind speed varies with the height of the blade, larger at the top and smaller at the bottom. Due to the existing of the turbulence, the wind load would represent fluctuation around the wind load caused by the mean wind speed. More details can be found in Chapter 3.

Due to the rotation of the blade, inertial forces are acted on the blade. There are two components of inertial forces: the centrifugal force and the Coriolis' force. The first component is caused by the rotation of the blade and the second component is caused by the vibration of the blade when rotating. These inertial forces are volume forces. The centrifugal force at an arbitrary point on the blade can be calculated by

$$F_{cen} = \rho\omega^2 r \tag{5.1}$$

where ρ is the density of the material of the blade; ω is the rotational speed of the blade; and r is the distance between the point to the rotational axis. The direction of the centrifugal force is from the rotational axis towards to the point. The Coriolis's force at an arbitrary point on the blade can be calculated by

$$F_{Cor} = 2\rho\omega v \tag{5.2}$$

where v is the radial velocity of the point. The direction of the force is perpendicular to the rotation axis and to the velocity of the body in the rotating frame. The Coriolis's force is important in the high speed rotational machine but can be ignored in the wind turbine, because the rotational speed and the vibration speed of the blade are low; most studies ignored this effect (Marin et al., 2009; Shokrieh & Rafiee, 2006; Song et al., 2011).

Of course, sole weight is also considered but the sole weight for VAWTs is not as important as for HAWTs. For HAWTs, sole weight of the blade causes large bending moment at the root, which is the main source of the fatigue loading; while for VAWTs, sole weight will not cause any fatigue. Especially for straight-bladed VAWTs, sole weight of a blade acts as an axial force; thus, the strain caused by sole weight can be ignored compared with the strain caused by the bending of the blade.

In the numerical simulation, wind pressures are acted on the surface of the blade shell; the inertial forces and sole weight are acted as volume forces.

5.4.2.2 Loads on the blade in the extreme wind speed

In the extreme wind speed, the VAWT is parked. In this situation, the blade is only subjected to the sole weight and the wind load caused by the extreme wind speed. However, the wind load varies with the wind direction. Hence, it is necessary to take the wind direction into account in the ultimate strength analysis. The details of wind load in the extreme wind speed can be found in Chapter 3.

5.5 The Fatigue Analysis

5.5.1 The overview of the fatigue analysis for a laminated FRP blade

The fatigue analysis for a laminated FRP blade is not much different from the fatigue analysis of steel material. For the steel material, the rainflow counting method is applied to the stress time history, and the number of stress cycles in different stress range levels can be obtained. The number of cycle to failure of each stress range level can be estimated by S-N curve. Then, a cumulative damage model, such as the Palmgren-Miner's rule, is used to evaluate the fatigue damage of the blade. As reviewed in Chapter 2, the fatigue damage is defined as:

$$D = \sum_i \frac{n_i}{N_i} \tag{5.3}$$

where n_i is the cycle number of the equivalent zero-mean stress range $\sigma_{r,i}$ in a given time period; N_i is the number of cycle to failure at the stress range $\sigma_{r,i}$; and D is defined as the fatigue damage. Fatigue failure occurs when $D \geq 1$.

For traditional materials, such as steel, S-N curves are used to determine the fatigue damage of the given stress cycles. However, composite material fatigue databases, such as DOE/MSU, FACT and others, cannot cover all FRP, the fatigue life of which will be different with changes in stacking, material and fiber volume fractions. On the other hand, it is found that “data from constant stress amplitude fatigue test become intelligible if stress ranges are converted into initial strain ranges” (Burton et al., 2001). It means that if using the $\varepsilon - N$ curve instead of the S-N curve, fatigue test results of laminates with different layups are conformed to the same curve (Burton et al., 2001). Strain used in the $\varepsilon - N$ curve is the initial value which is measured at the start of the test. The reason why emphasizing ‘initial’ is because the Young’s modulus reduces over time during a fatigue test and the test is carried out under the same stress range. This result has been adopted by the GL rules (Germanischer, 2010).

If the strain time history of a designated time period is available, the fatigue damage in a designated time period can be calculated directly. However, the service life of a wind turbine is more than 20 years, and it is unrealistic to conduct the numerical simulation in such a long time. The considered operation and external conditions are determined in Section 5.4.1 and the loads on the blade for the considered conditions are also introduced in Section 5.4.2. These conditions are essentially determined by the mean wind speed. Hence, an alternative method is as follows: firstly, the operation mean wind speed range is discretized into several wind speed bins; secondly, the fatigue damages in a short term, 10 minutes for example, at the center of the bins are obtained by numerical simulations; finally, the proportion of these short term damage in the total fatigue damage for the designated time period is evaluated by the mean wind speed distribution, so the final fatigue damage can be calculated. For such a method, the mean wind speed distribution of the designated time period must be given first.

The wind speed at a site is a stochastic process but the mean wind speed is also influenced by some deterministic factors, such as the local climate and the local land terrain; therefore, the wind speed distributions in two different years would represent the similarity to some extent. Of course, the annual wind speed distribution would still vary year by year and usually, a representative annual mean speed at a site needs to be averaged over 10 or more years. However, the service life of a wind turbine is more than 20 years and the history records are not always available for the site under consideration. It is unrealistic to measure the wind speed for such a long time. Hence, a time period of one year is an acceptable choice for the fatigue analysis.

Furthermore, the fatigue critical locations should be figured out. It is important to find out these locations, not only because the fatigue life of a wind turbine blade is determined by the fatigue life at these locations but also because it can improve the blade design and guide the sensor installation for a SHM system. It is not practical to calculate the fatigue damages of all nodes in the blade and then choose the nodes with the largest fatigue damage. The analysis should be conducted from other perspectives.

5.5.2 $\varepsilon - N$ curve and the Goodman diagram for fatigue damage evaluation

In GL rules, strain cycles, other than stress cycles, are used to evaluate the fatigue damage of FRP. The cycle number to failure N of a laminated FRP plate is estimated by an $\varepsilon - N$ curve which can be expressed in the form of Equation (5.4).

$$N = K(\varepsilon_r)^{-m} \tag{5.4}$$

where N is the number of cycle to failure; K is an empirical constant related to the material; m is the slop parameter ($m = 9$ for laminates with polyester matrixes and

$m=10$ for laminates with epoxy matrixes); and ε_r is the strain range. However, this $\varepsilon - N$ is given in the condition of strain ratio $R = \frac{\varepsilon_{\max}}{\varepsilon_{\min}} = -1$. $\varepsilon_{\max}$ and $\varepsilon_{\min}$ are the maximum and minimum strain in one strain cycle. $R=-1$ means that the mean strain $\bar{\varepsilon} = \frac{1}{2}(\varepsilon_{\max} + \varepsilon_{\min})$ is zero. In reality, the mean value of strain cycles is not likely to be equal to zero; in this case, Goodman diagram is required to convert the strain range ε_r with non-zero mean strain ε_r to the strain range ε_A with zero mean strain equivalently. The GL rule suggests the Goodman diagram as shown in Fig. 5.6. The diagram can be expressed by Equation (5.5).

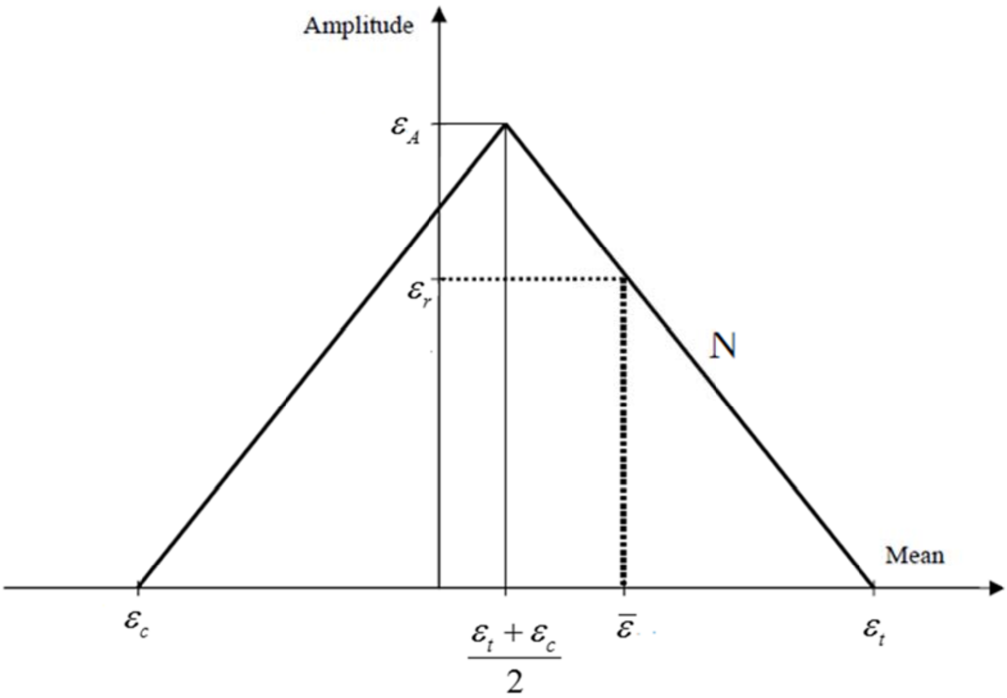

Fig. 5.6 Goodman diagram

$$N = \left[\frac{\varepsilon_t + |\varepsilon_c| - |2\gamma_1 \bar{\varepsilon} - \varepsilon_t + |\varepsilon_c||}{2\gamma_2 \varepsilon_r} \right]^m \tag{5.5}$$

where ε_t is the tensile ultimate strain; ε_c is the compressive ultimate strain; $\overline{\varepsilon}$ is the mean strain; ε_r is the strain range; γ_1 and γ_2 are partial safety factors for the material. In this study, $\gamma_1 = 2.64$ and $\gamma_2 = 1.96$ according to the requirements of GL rules; $\varepsilon_t = 2.4\%$ and $\varepsilon_c = -2.0\%$; m is equal to 9 in this study ; $\overline{\varepsilon}$ and ε_r use the values given by numerical simulations. It is worth mentioning that the $\varepsilon - N$ curve and the Goodman diagram are obtained by the data from experimental tests while these fatigue tests are carried out by uniaxial cyclic in-plane loading. For metals like steel and aluminum which are isotropic, usually the 1st principle stress is used in the fatigue damage estimation. However, a laminated FRP plate is orthotropic thus the 1st principle strain cannot be used in Equation (5.5). Therefore, the strain applied in Equation (5.5) is the concerned laminar normal strain, ε_x or ε_y for example, and the influence of the other strains which are not concerned is ignored. This simplified method is used in the fatigue design of wind turbine blade at the present stage (Kong et al., 2005; Marin et al., 2009; Sutherland, 1999). Although some researches have been performed on the influence of multi-axial loading, the results are still limited (M Quaresimin, 2015; Marino Quaresimin et al., 2010).

5.5.3 Wind speed distribution and wind speed bins

In this study, the fatigue analysis was conducted in the condition that the wind turbine is operating in the normal wind. The variation of the normal wind speed is mainly caused by the monsoon. And Weibull distribution is widely used to describe the wind speed distribution due to the monsoon. So the candidate used the Weibull function to describe the wind speed distribution in one year in the fatigue analysis and did not consider other distribution functions. The annual mean wind speed distribution can be described by Weibull model, as shown in Equation (5.6)

$$f(u) = \frac{k}{\lambda}\left(\frac{u}{\lambda}\right)^{k-1} \exp\left[-\left(\frac{u}{\lambda}\right)^{k}\right] \tag{5.6}$$

where k is the shape parameter and λ is the scale parameter. For the site considered in this study, $k=2.0$ and $\lambda=8.1$.

For the VAWT under consideration, the cut-in and cut-out wind speed of the VAWT in this study are 5m/s and 21m/s respectively. This mean wind speed region is discretized into 8 wind speed bins and the size of each bin is 2m/s. The centers of these bins are 6m/s, 8m/s, 10m/s, 12m/s, 14m/s, 16m/s, 18m/s and 20m/s. The probability of the mean wind speed in one of the wind speed bin can be calculated by Equation (5.6). For example, the probability of the mean wind speed in the range between 5m/s and 7m/s is

$$P_6 = \int_5^7 \frac{k}{\lambda}\left(\frac{u}{\lambda}\right)^{k-1} \exp\left[-\left(\frac{u}{\lambda}\right)^k\right] du \tag{5.7}$$

where P_6 is the probability of the mean wind speed in this range; the subscript "6" represents the center of the wind speed bin. Accordingly, P_8, P_{10}, P_{12}, P_{14}, P_{16}, P_{18} and P_{20} can also be calculated. So, the time length (in second) of the mean wind speed within one of the wind speed bin in *n* years can be calculated as

$$T_i = 365 \times 24 \times 3600 n P_i,\ i = 6, 8, 10, \cdots, 20 \tag{5.8}$$

where *i* represents the center of the wind speed bin; and T_i is the total time length of the mean wind speed within the wind speed bin in *n* years in second.

The wind load on the blade at these mean wind speeds can be simulated by the method proposed Chapter 3. The rotational speed of the blade is 2.1rad/s (20rpm), and the inertial forces on the blade can then be calculated.

5.5.4 Fatigue critical locations

To assess the fatigue critical locations, the strain time history of any node of the blade must be calculated. In reality, the blade is rotating around the tower, which is difficult to simulate. A simplified method that the calculation is conducted in the reference frame XYZ attached to the blade (shown in Fig. 5.3(a)) is introduced in Section 5.3. The schematic diagram of the reference frame XYZ is shown in Fig. 5.7, in which $X_oY_oZ_o$ are the global static reference frame. The reference frame XYZ together with the blade is rotating around the tower. In this reference frame, the blade can be regarded as a structure without any rigid motion and only inertial forces are needed.

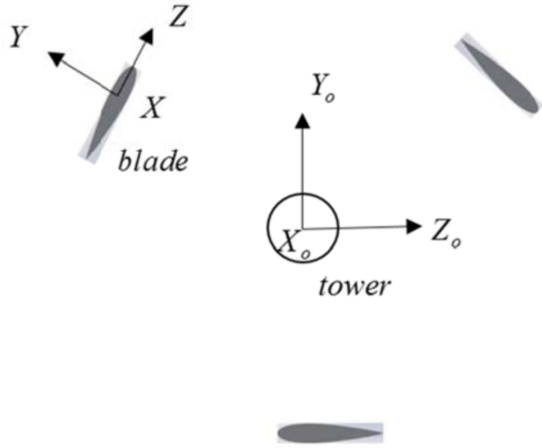

Fig. 5.7 A schematic diagram of the reference frame used in the simulation

In this subsection, the wind pressures simulated in the wind speed bins are applied on the FE model and the responses of the blade can be obtained by solving the dynamic equation

$$\boldsymbol{M}\ddot{\boldsymbol{u}}+\boldsymbol{C}\dot{\boldsymbol{u}}+\boldsymbol{K}\boldsymbol{u}=\boldsymbol{F}_W+\boldsymbol{F}_G+\boldsymbol{F}_I \tag{5.9}$$

where $\boldsymbol{M}$ is the mass matrix; $\boldsymbol{C}$ is the Rayleigh damping matrix; $\boldsymbol{K}$ is the stiffness matrix; $\boldsymbol{u}$ is the displacement vector composed of all displacements and rotations of all nodes in the reference frame XYZ; $\dot{\boldsymbol{u}}$ is the velocity vector composed of all velocities and rotational velocities of all nodes; $\ddot{\boldsymbol{u}}$ is the acceleration vector composed of all accelerations and rotational accelerations of all nodes; $\boldsymbol{F}_W$ is the force vector of wind load; $\boldsymbol{F}_G$ is the force vector of gravity; $\boldsymbol{F}_I$ is the force vector of initial force, including the centrifugal force and the Coriolis's force. The damping matrix $\boldsymbol{C}$ is determined by

$$\boldsymbol{C} = a_0\boldsymbol{M} + a_1\boldsymbol{K} \tag{5.10}$$

where a_0 and a_1 are the mass proportional damping and the stiffness proportional damping. a_0 and a_1 are determined by the first 2 natural frequencies

$$a_0 = \frac{4\pi\xi f_1 f_2}{f_1 - f_2} \tag{5.11a}$$

$$a_1 = \frac{4\pi\xi}{f_1 - f_2} \tag{5.11b}$$

where f_1 and f_2 are the first 2 natural frequencies as listed in Table 5.1; and ξ is the damping ratio of 0.005. Equation (5.9) is solved by the constant average acceleration method offered by ANSYS, so all mode shapes of the FE model is naturally considered in the solution. The strain can be extracted from the calculated displacement vector $\boldsymbol{u}$.

By taking the mean wind speed of 14 m/s at the hub height for example, the numerical simulation is conducted by applying the inertial forces, the sole weight and the wind pressures obtained in Chapter 3 on the FE model. Since the blade is made of the laminated FRP with three layers as introduced in Chapter 4, the strains in these three layers are different. However, according to the higher order shear deformation theory for laminated composite materials, the strains in the cross section linearly varies with the thickness. Therefore, only the strain at the top of the outer layer of the outer shell is needed in the fatigue analysis (refer to the strain at 8mm in Fig. 5.4.). For the shear web, the strain at the top of the layer of the outer side is selected.

3 arbitrary nodes of the blade element are selected and the locations of these nodes are

shown in Fig. 5.8. The time histories and power spectrum of the strains at these 3 arbitrary nodes are shown in Fig. 5.9.

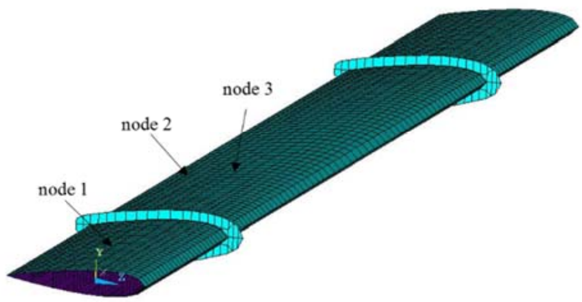

Fig. 5.8 The locations of 3 arbitrary nodes

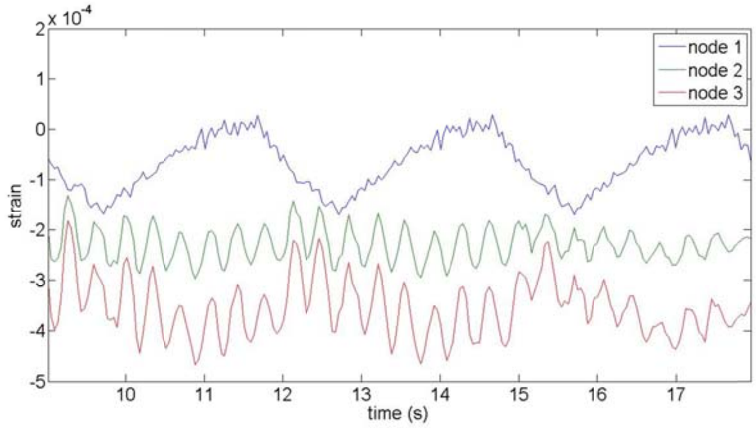

(a)

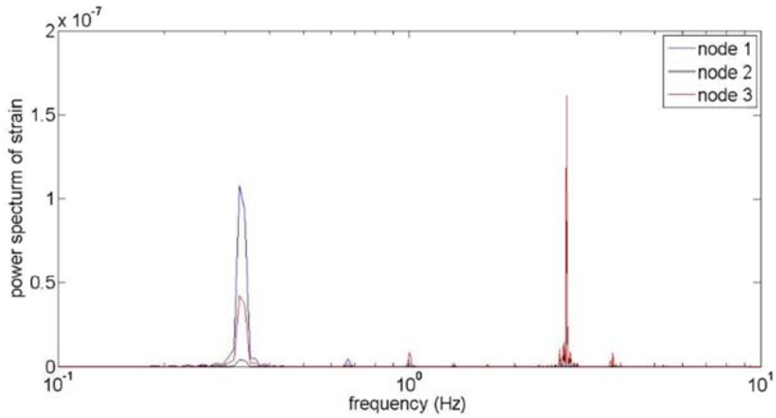

(b)

Fig. 5.9 time histories and power spectrum of strains at 3 arbitrary nodes. (a) time history; (b) power spectrum

It can be found that two periodicities of these time histories are obvious. The lower frequency component is due to the rotation of the blade and the higher frequency component is due to the turbulence-induced vibration of the blade in the first mode. The strains at these nodes are either in phase or in opposite phase. Actually, the strains of the whole blade are in phase or in opposite phase, which implies that the cycle number of the strain at any point of the blade is almost the same and the differences are only $\bar{\varepsilon}$ and ε_r. In another word, n_i in $D = \sum_i \frac{n_i}{N_i}$ is the same and the difference is in N_i which is determined by $\bar{\varepsilon}$ and ε_r. Referring to Equation (5.3) and Equation (5.5), the strain with larger $\bar{\varepsilon}$ and ε_r will result in larger fatigue damage. So, the fatigue-critical locations can be found in the nodes with the largest $\bar{\varepsilon}$ and ε_r.

To figure out the positions of the nodes with large $\bar{\varepsilon}$ and ε_r, a line C at the largest thickness of the blade section on the outer shell is selected as shown in Fig. 5.10. By taking ε_x for example, the $\bar{\varepsilon}$ and ε_r on the line can be calculated and shown in Fig. 5.11. It can be found that the nodes of large $\bar{\varepsilon}$ are coincident with the nodes of large ε_r. These nodes are near the supports and the mid-span of the blade.

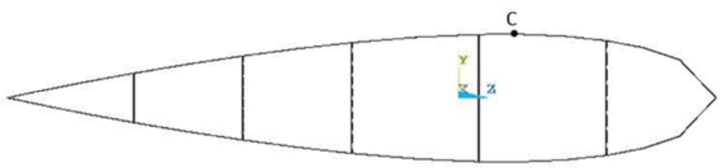

Fig. 5.10 Line C at the largest thickness of the blade section on the outer shell

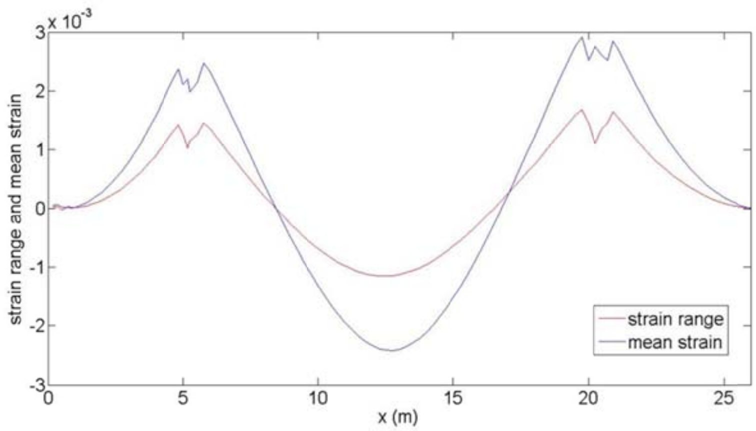

Fig. 5.11 Mean strain and strain range along line C

It can be explained by the boundary conditions of the blade and the characteristics of the loads. For the blade considered in this study, $\overline{\varepsilon}$ and ε_r are mainly due to the cyclic wind load and the constant centrifugal force. Because the rotational speed is constant, the centrifugal force is static and nearly uniform along the blade, and the nodes with large strain appear at the supports and the mid-span of the blade. The wind load is cyclic as shown in Chapter 3. The wind load is distributed along the blade and the non-uniform is due to the mean wind profile. Under the cyclic wind load, the nodes with large ε_r appear at the supports and the mid-span of the blade. Hence, the strain will fluctuate around the value caused by the centrifugal force under all external forces, and the nodes with large $\overline{\varepsilon}$ also appear at the supports and the mid-span of the blade. Therefore, according to the above discussion, the fatigue-critical locations can be preliminarily located at the supports and the mid-span of the blade.

Now the fatigue critical locations can be found in the section of the blade at the supports and the mid-span. According to the above discussion, the mean strain is mainly determined by the centrifugal force. Under this force, the strain linearly varies with the thickness of the section. Hence, the largest mean strains of ε_x and ε_y occur near the outer shell of the blade. It means that the critical locations are the nodes with the largest strain range near the outer shell of the blade. For ε_x, the node of the largest ε_x range with positive mean value is found at the lower support. This node is at the most thickness of the blade section in the tower side, which is defined as node 1. The node of the largest ε_x range with negative mean value is also found at the lower support; this node is at the most thickness of the blade section in outer side, which is defined as node 2. Node 1 and node 2 are on the outer shell of the blade; the nodes of the largest ε_x range in the shear webs are also considered. The node of the largest strain range with positive mean value in the shear web is at the lower support, which is denoted as node 3; the node of the largest strain range with negative mean value in the shear web is also at the shear web, which is denoted as node 4. Node 3 is adjacent to node 1; node 4 is adjacent to node 2. For ε_y, both the largest strain ranges with positive and negative mean value occur at the bond joint connecting the shear web to the outer shell of the blade at the lower support, shown in Fig. 5.12. Node 5 is defined as the node of the largest ε_y range with positive strain and Node 6 is the node of the largest negative strain range. Both node 5 and node 6 are close to node 2 in the outer side of the blade.

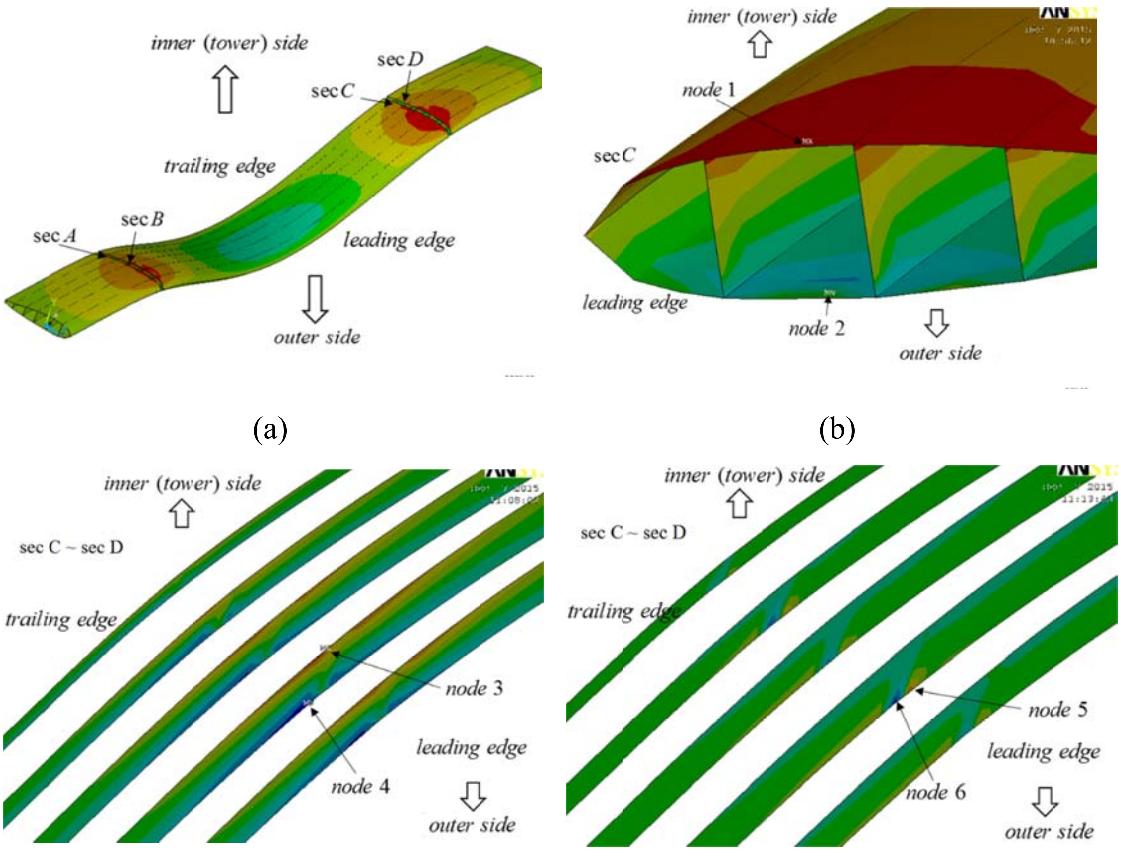

(a) (b)

(c) (d)

Fig. 5.12 Fatigue critical sections. (a) over view; (b) node 1 and node 2; (c) node 3 and node 4; (d) node 5 and node 6

5.5.5 Fatigue analysis for the fatigue critical locations

In this section, fatigue lives of the figured out FCLs will be estimated using the $\varepsilon - N$ curves defined in Section 5.5.2. First of all, the strain time histories of node 1 - 6 at the center of each wind speed bin introduced in Section 5.5.3 are predicted. By taking 14m/s for example, the time histories of strain at node 1 - 6 are shown in Fig. 5.13. The strain time histories of node 1 - node 4 are about ε_x and the strain time histories of node 5 and node 6 are about ε_y . It can be seen that node 1, 3 and 5 have positive mean strain and node 2, 4 and 6 have negative mean strain.

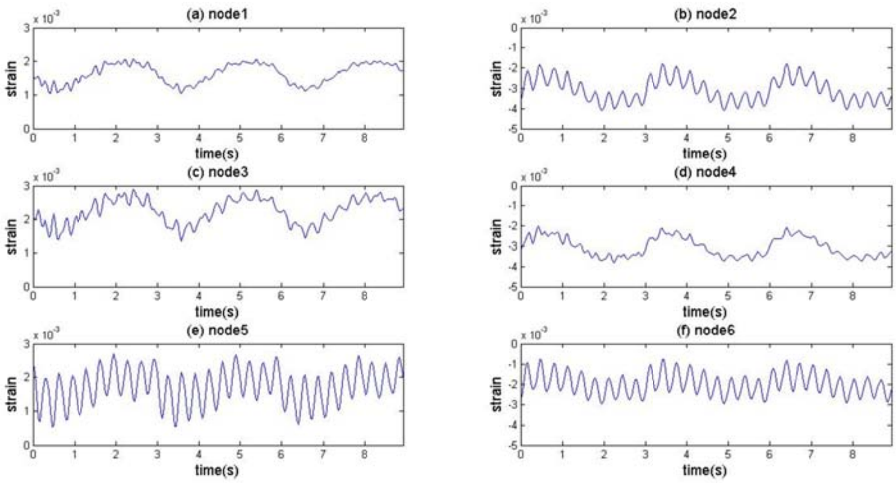

Fig. 5.13 Strain time histories of node 1 - node 4. (a) ε_x of node 1; (b) ε_x of node 2; (c) ε_x of node 3; (d) ε_x of node 4; (e) ε_y of node 5; (f) ε_y of node 6.

The rain-flow counting method is used to classify the strain time history into a set of simple strain reversals with different mean values and strain range, so allowing the application of Miner's rule in order to assess the fatigue life of a structure subject to complex loading. The first step of the method is to reduce the time history to a series of peaks and troughs, which are then termed extremes. Then, each group of four successive extremes is examined in turn to determine whether the values of the two intermediate extremes lie between the values of the initial and final extremes. If so, the two intermediate extremes are counted as defining a stress cycle, which is then included in the cycle count, and the two intermediate extremes are deleted from the time history. The process is continued until the complete series of extremes forming the time history has been processed in this way. Then the sequence remaining will consist simply of a diverging and a converging part from which the final group of stress ranges can be extracted.

The strain time histories in 10 minutes are simulated under the mean wind speeds at the center of the wind speed bins introduced in Section 5.5.3. The cycle numbers of different strain range and mean value of node 1 - node 6 are obtained by the rain-flow method. These numbers of cycle are in 10 minutes. Divided by 600s (10 min) and multiplying the time length of the mean wind speed within the corresponding wind speed bin, these numbers can be extended to the numbers within 20 years. The time length of the mean wind speed within a wind speed bin can be calculated by the method introduced in Section 5.5.3. The numbers of cycle in 20 years are shown in Fig. 5.14. From Fig. 5.14, it can be seen that the statistics pattern of cycle number is quite clear for these 6 nodes. Strain cycles can be departed into two groups: the one with scattering mean strains and small strain ranges and the one with centralized mean strains and large strain ranges. In addition, the strain ranges of node 2, node 5 and node 6 are obviously larger than the other three nodes.

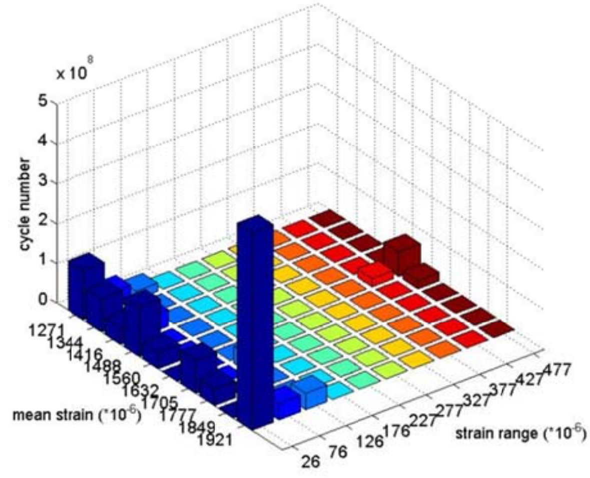
x 10^8
cycle number
mean strain (*10^-6)
strain range (*10^-6)

(a)

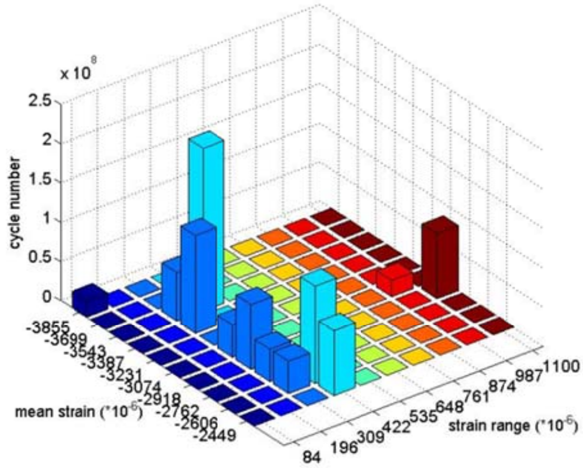
x 10^8
cycle number
mean strain (*10^-6)
strain range (*10^-6)

(b)

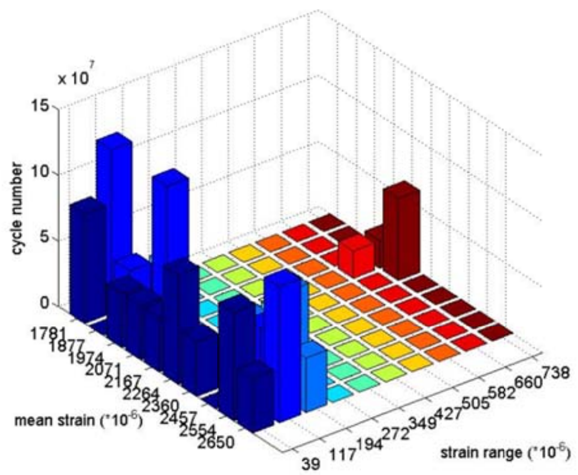
x 10^7
cycle number
mean strain (*10^-6)
strain range (*10^-6)

(c)

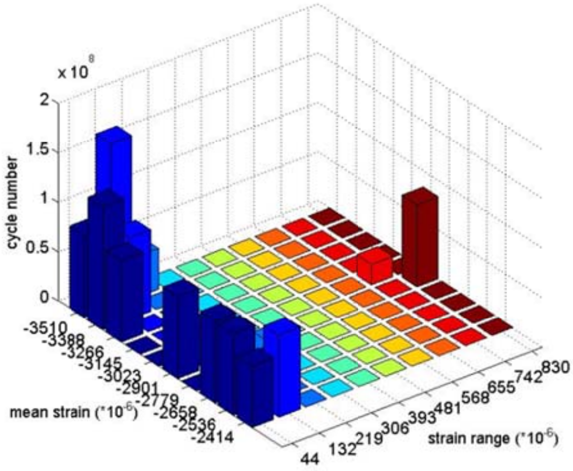
x 10^8
2
1.5
1
0.5
0
cycle number
-3510
-3388
-3266
-3145
-3023
-2901
-2779
-2658
-2536
-2414
mean strain (*10^-6)
44
132
219
306
393
481
568
655
742
830
strain range (*10^-6)

(d)

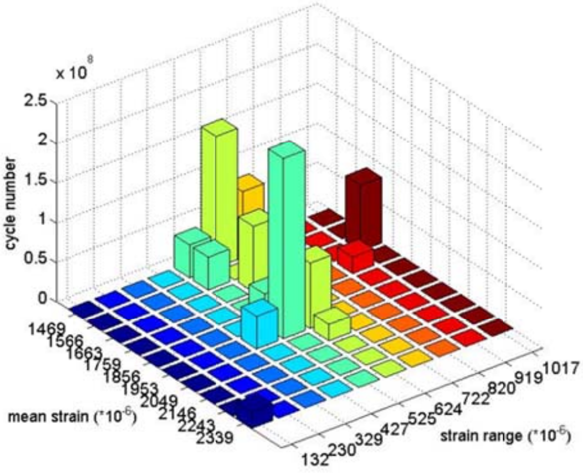
x 10^8
2.5
2
1.5
1
0.5
0
cycle number
1469
1566
1663
1759
1856
1953
2049
2146
2243
2339
mean strain (*10^-6)
132
230
329
427
525
624
722
820
919
1017
strain range (*10^-6)

(e)

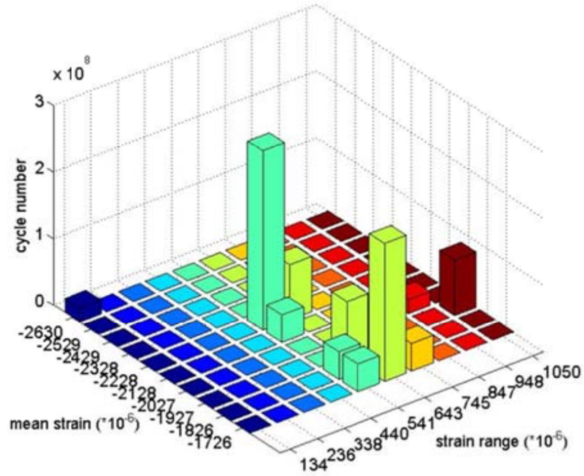
x 10^8
3
2
1
0
cycle number
-2630
-2529
-2429
-2328
-2228
-2128
-2027
-1927
-1826
-1726
mean strain (*10^-6)
134
236
338
440
541
643
745
847
948
1050
strain range (*10^-6)

(f)

Fig. 5.14 Rain-flow counting matrix plot. (a) node 1; (b) node 2; (c) node 3; (d) node 4; (e) node 5; (f) node 6.

The fatigue damages and the fatigue lives of these nodes are calculated based on the $\varepsilon - N$ curves introduced in Section 5.5.2. The fatigue damages of different strain ranges and mean strains are shown in Fig. 5.15 and the fatigue damage are listed in Table 5.2. Comparing Fig. 5.14 with Fig. 5.15, it can be found that although the cycle number of small strain ranges is much larger than that of the large strain ranges, the fatigue damages of the large strain ranges are dominant. And from Table 5.2, it can be found that the fatigue life of this blade is determined by compressive fatigue damage of node 2. Although the fatigue damage of node 2 is only 0.1020, the fatigue mechanism of composite material is complex and the uncertainty of the fatigue design of composite material is very large. The fatigue damage of 0.1020 cannot lead to the conclusion of safety. It can be explained by the Goodman diagram (Fig. 5.6) recommended by the GL rule. This phenomenon is different from metals of which the fatigue problem in the compressive stress state is not obvious. Researches on this topic have found that the reduction in the resistance to the fatigue of FRP at the compressive strain state is due to micro-buckling, fiber crushing, splitting of the matrix, buckling delamination of a surface layer, shear band formation, etc. (Brøndsted et al., 2005; Budiansky & Fleck, 1993). Therefore, the fatigue life of the blade is determined by the fatigue damage in the area of node 2.

Moreover, it is worth noting that although the cycles with small strain ranges themselves can be neglected when considering fatigue damage, these small strain cycles have an influence on determining the largest strain range, which still play an important role in fatigue life, which will be proved in Section 5.5.6.

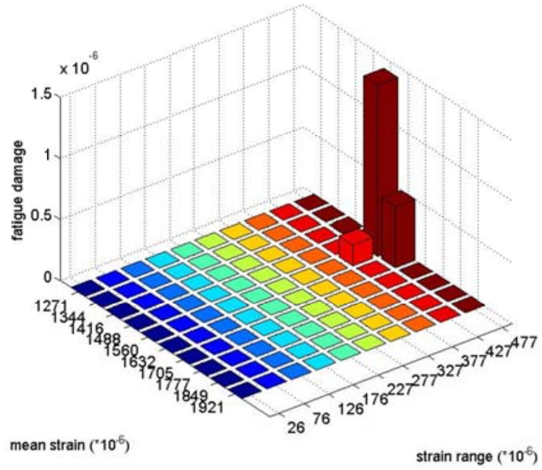

x 10^-6
1.5
1
0.5
0
fatigue damage
1271 1344 1416 1488 1560 1632 1705 1777 1849 1921
mean strain (*10^-6)
26 76 126 176 227 277 327 377 427 477
strain range (*10^-6)

(a)

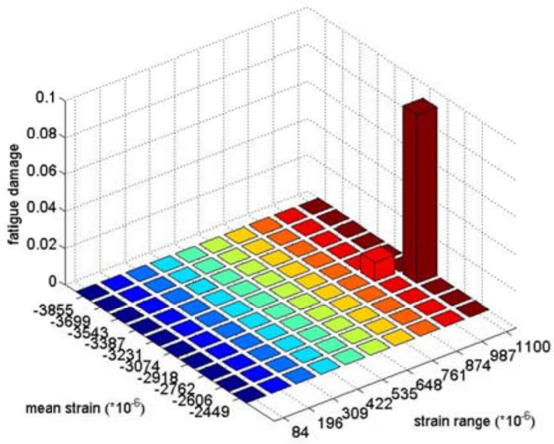

0.1
0.08
0.06
0.04
0.02
0
fatigue damage
-3855 -3699 -3543 -3387 -3231 -3074 -2918 -2762 -2606 -2449
mean strain (*10^-6)
84 196 309 422 535 648 761 874 987 1100
strain range (*10^-6)

(b)

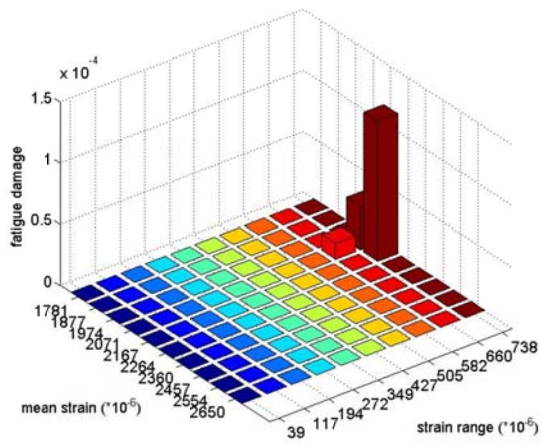

x 10^-4
1.5
1
0.5
0
fatigue damage
1781 1877 1974 2071 2167 2264 2360 2457 2554 2650
mean strain (*10^-6)
39 117 194 272 349 427 505 582 660 738
strain range (*10^-6)

(c)

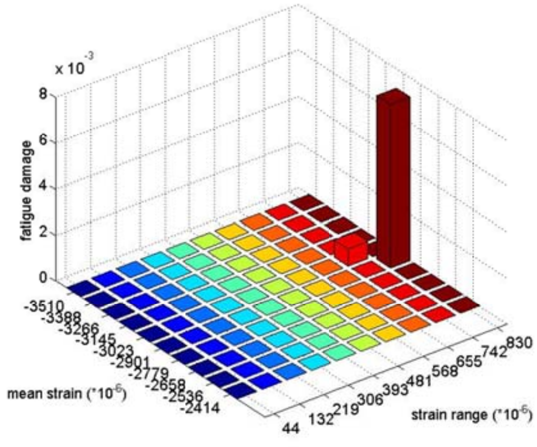

(d)

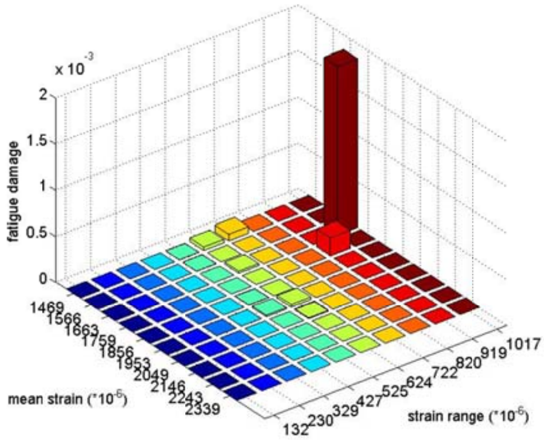

(e)

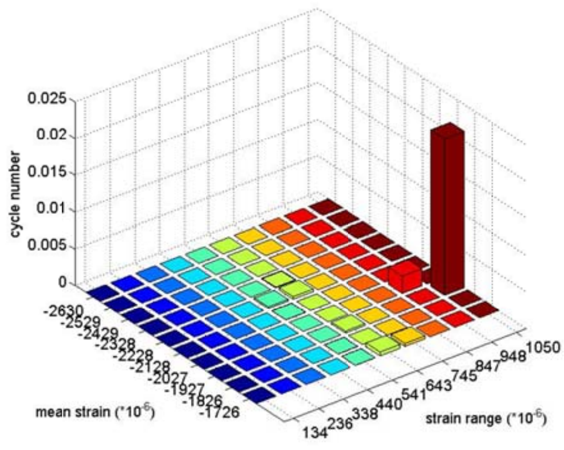

(f)

Fig. 5.15 The matrix plot of fatigue damages of different mean strain and strain range. (a) node 1; (b) node 2; (c) node 3; (d) node 4; (e) node 5; (f) node 6.

Table 5.2 Fatigue damage of node 1 - node 6 in 20 years

	Node 1	Node 2	Node 3	Node 4	Node 5	Node 6
Fatigue Damage	0.4581e-6	0.1020	0.1626e-3	0.0186	0.0186e-3	0.0122

5.5.6 Parameter Studies

The fatigue life of a blade is influenced by many factors, such as the ultimate strains of the material (included in the Goodman diagram), the damping ratio and natural frequencies. In this section, parametric studies are conducted to evaluate these influences.

5.5.6.1 The influence of the ultimate tensile and compressive strain

First of all, the influence of material ultimate strains is considered. An $\varepsilon - N$ curve gives the fatigue life at strain ratio $R = -1$ and fatigue lives at other strain ratios can be determined by a Goodman diagram, the equation of which is given by Equation (5.5). The ultimate tensile and compressive strains play an important role in the Goodman diagram and hence will have an influence on the fatigue life estimation. Strains of Node 2 (compression) and node 5 (tension) are taken for example. Fig. 5.16 shows the influence of ultimate strains on the fatigue damage D. Fig. 5.16 (a) shows the influence of the ultimate tensile strain on the fatigue damage of node 5; Fig. 5.16 (b) shows the influence of the ultimate compressive strain on the fatigue damage of node 5; Fig. 5.16 (c) shows the influence of the ultimate tensile strain on the fatigue damage of node 2.; Fig. 5.16 (d) shows the influence of the ultimate compressive strain on the fatigue damage of node 2. It can be seen that the influences of the ultimate compressive strain on node 5 and the ultimate tensile strain on node 2 can be ignored. Because node 5 is in tensile, the ultimate compressive strain has nearly no influence on the fatigue damage; the ultimate tensile strain of node 2 which is in compressive has neither influence on the fatigue damage. From the other two figures, it can be found that increasing ultimate tensile (compressive) strains of a node in tension (compression) cyclic strain range will dramatically decrease the fatigue damage. Indeed, this correlation can be explained by Equation (5.5): $1/N$ and the ultimate strain are approximatively conformed to an inverse correlation in a log-log diagram.

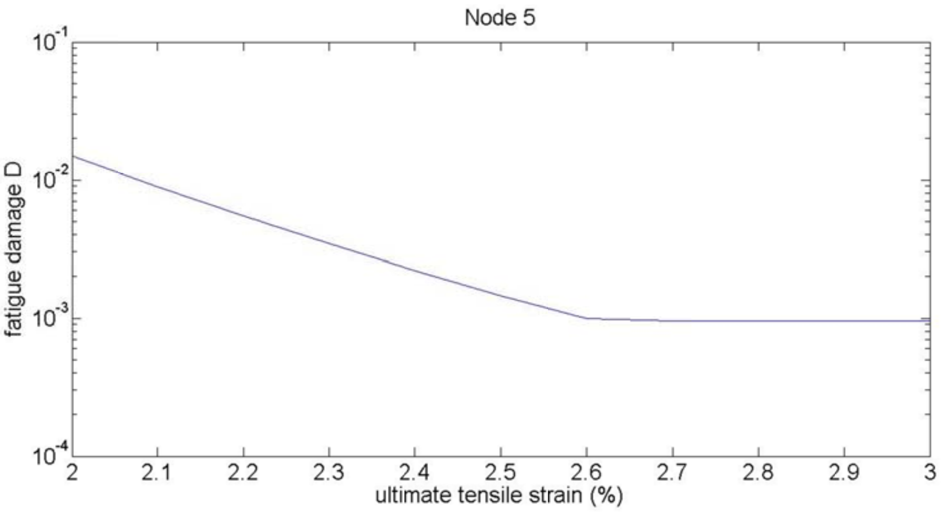

(a)

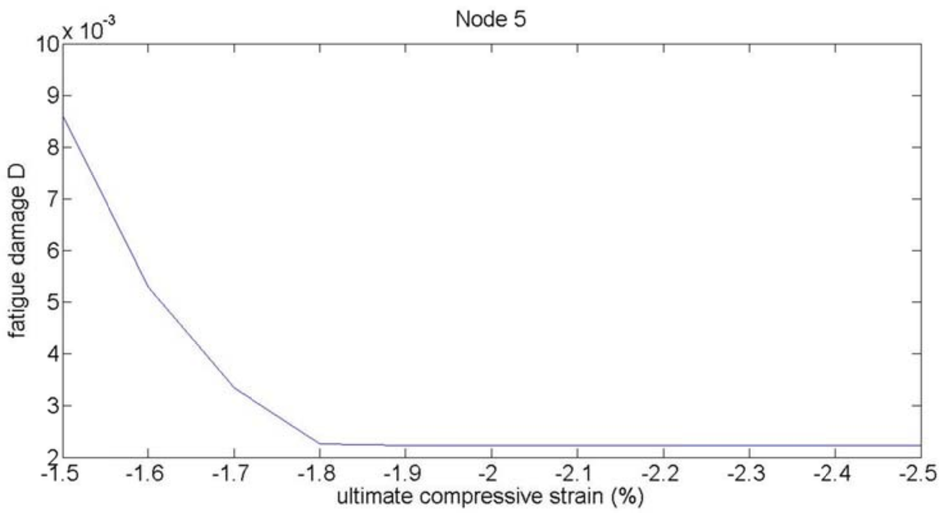

(b)

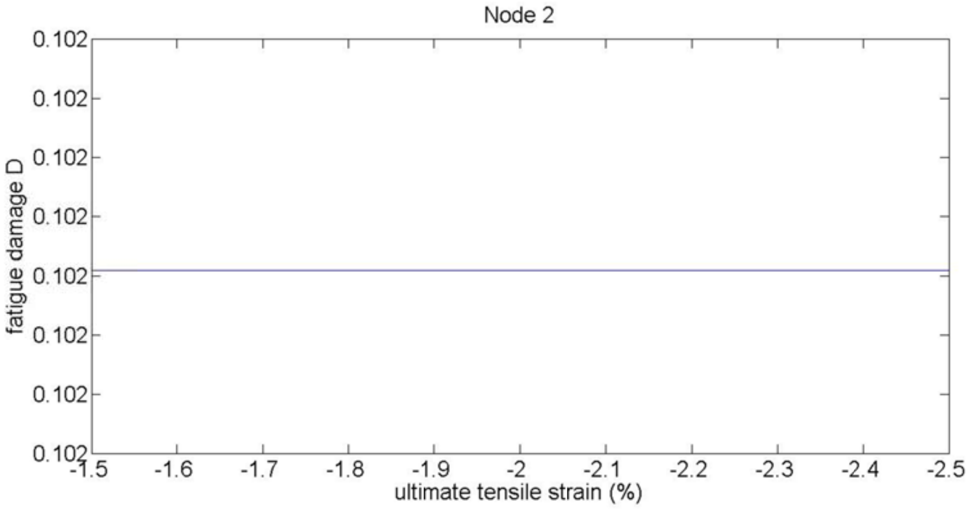

(c)

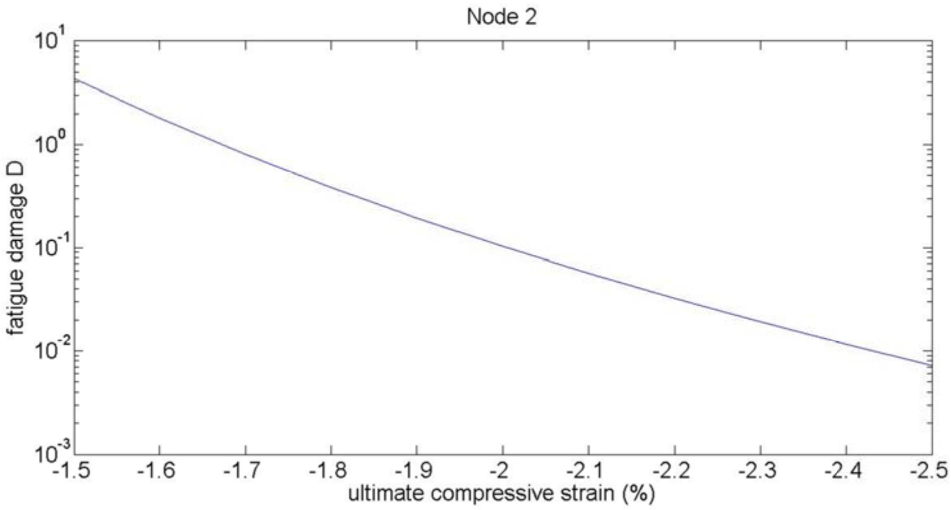

(d)

Fig. 5.16 The influence of the ultimate strain to fatigue damage: (a) the ultimate tensile strain on node 5; (b) the ultimate compression strain on node 5; (b) the ultimate tensile strain on node 2; (b) the ultimate compression strain on node 2

5.5.6.2 The influence of the damping ratio

Secondly, the influence of the damping ratio on the fatigue damage is also considered. In this study, damping ratios of 0.001, 0.005, 0.01 and 0.05 are adopted. By taking the mean wind speed of 14m/s for example, for each damping ratio, the ε_x time history of node 2 at 14m/s is shown in Fig. 5.17 (a). It has been known that the strain cycles due to rotation are dominant, other than those of the cycles caused by turbulence, which can be proved by the power spectrum of these time histories shown in Fig. 5.17

(b). In Fig. 5.17 (b), there are two components in these strain time histories as analyzed above: one is at 0.33Hz, representing the responses induced by rotation which have the same strain range for all damping ratio cases and the other is at 2.30Hz, which exactly is the 1st modal frequency of the blade. The magnitude at 2.30Hz is reduced obviously when damping ratio increases but the magnitude at 0.33Hz does not change. These results demonstrate that the strain time history is composed of two components, one is the forced vibration under the aerodynamic force due to rotation, which has a large strain range and the other is 1st mode vibration with a small strain range.

In order to evaluate the damping ratio effect on fatigue life, fatigue damages of these cases in 20 years are shown in Fig. 5.18. It is found that the fatigue damage and the damping ratio are nearly conformed to an inverse correlation in a log-log diagram. In these cases, the strain range caused by rotation is unchanged and the reduction of strain range of 1st mode vibration causes decreasing of the largest strain range, which results in the fatigue damage reduction.

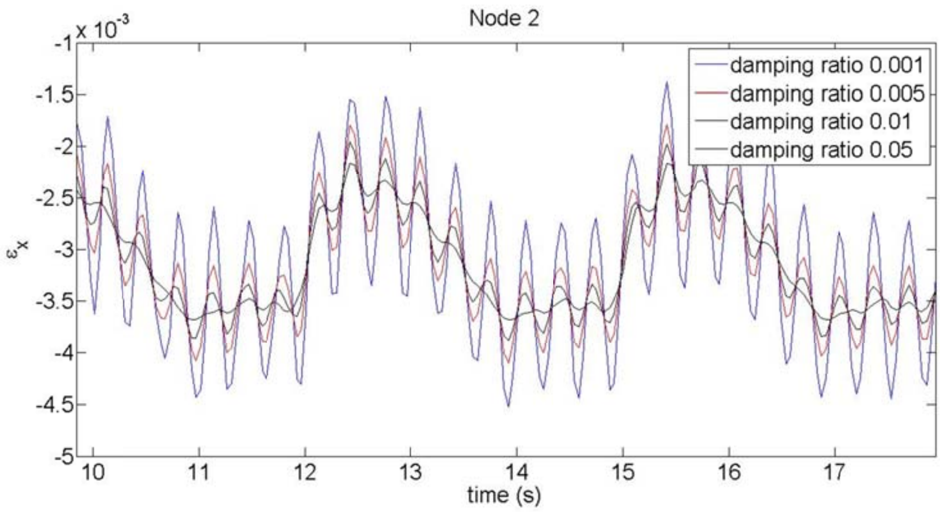

(a)

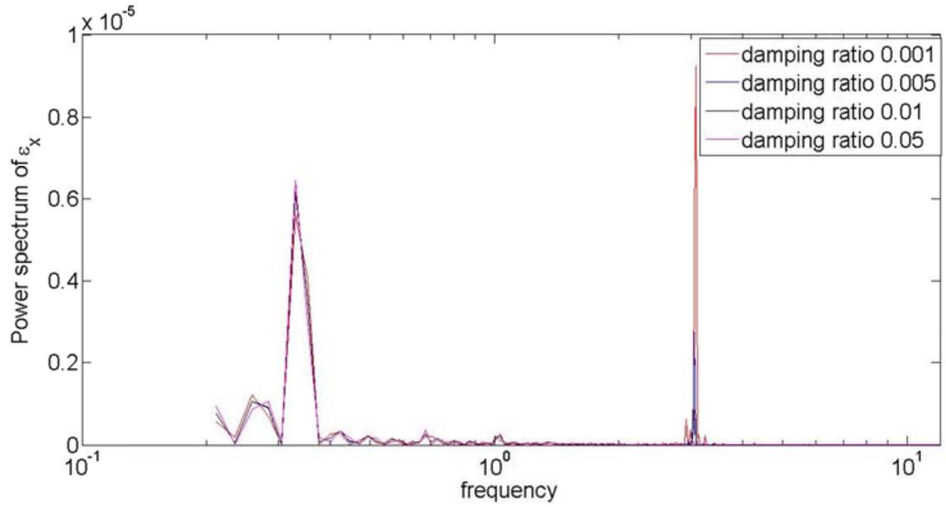

(b)

Fig. 5.17 Strain response of node 2. (a) time history; (b) power spectrum

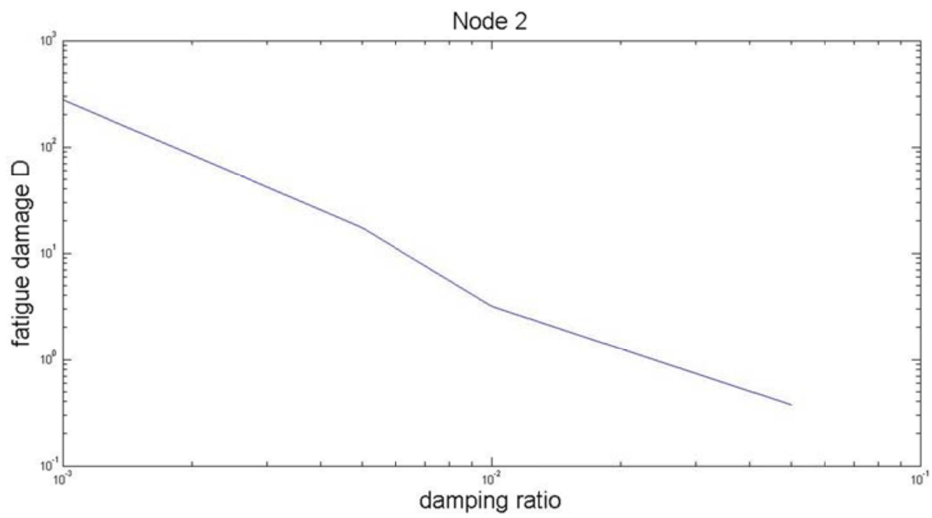

Fig. 5.18 The influence of damping ratio on fatigue damage D

5.5.6.3 The influence of natural frequencies

Thirdly, besides the damping ratio, the influence of natural frequencies is also evaluated. For the blade adopted in this study, only the fundamental frequency is included in the responses of the blade because the frequency of excitation (0.33Hz) is much lower than the fundamental frequency (2.30Hz); hence, the study is focused on the influence of the fundamental frequency in this particular case. Three blades with different fundamental frequency are adopted. The fundamental frequencies of this case are listed in Table 5.3 and the damping ratio of these three blades is 0.005. The change of fundamental frequency is realized by the change of elastic constants of the blade. Case 2 adopts the laminar elastic constants identified in Chapter 4; the Young's modulus and shear modulus are multiplied by 0.8 as the laminar elastic constants of Case 1; the Young's modulus and shear modulus are multiplied by 1.2 as the laminar elastic constants of Case 3.

Table 5.3 Fundamental frequency of the blade

	Case 1	Case 2	Case 3
Freq (Hz)	2.10	2.30	2.49

For each blade, the ε_x time history of node 2 at 14m/s is shown in Fig. 5.19 (a). The power spectrum of these time histories are shown in Fig. 5.19 (b). It can be seen that the natural frequency has influences not only on the strain ranges induced by rotation but also on the 1st modal responses, unlike the case of damping ratio which just has an influence on the fundamental mode. This is because that the blade becomes stiffer when the fundamental frequency raising from 2.1Hz to 2.49Hz, and hence the responses will be reduced. On the other hand, the frequencies of the excitation, including both the aerodynamic forces due to rotation (0.33Hz) and the forces caused by turbulence (wind power), are mainly in the low frequency range (<1Hz); when the fundamental frequency raising from 2.10Hz to 2.49Hz, moving away from the excitation frequency region, both two kinds of responses will be reduced.

The fatigue damages in 20 years of these three blades are listed in Table 5.4. It can be seen that the fundamental frequency on the fatigue damage is very sensitive.

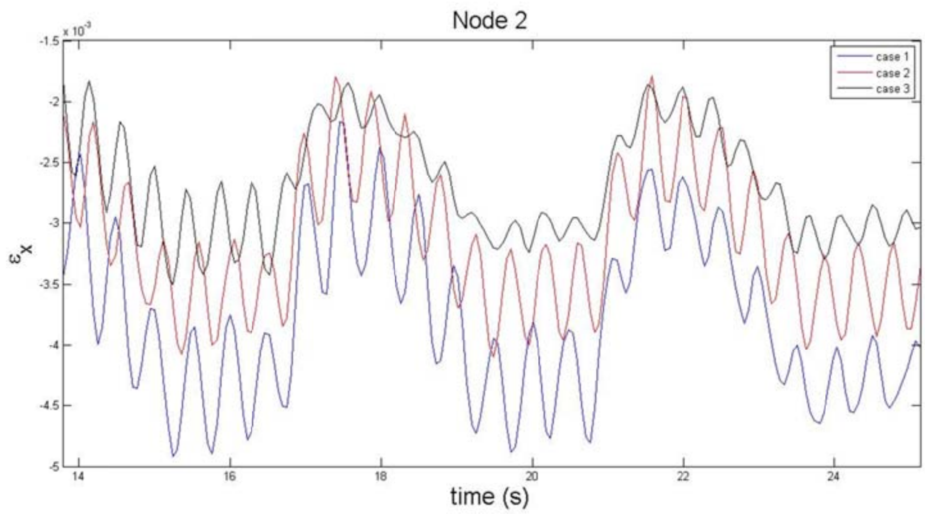

(a)

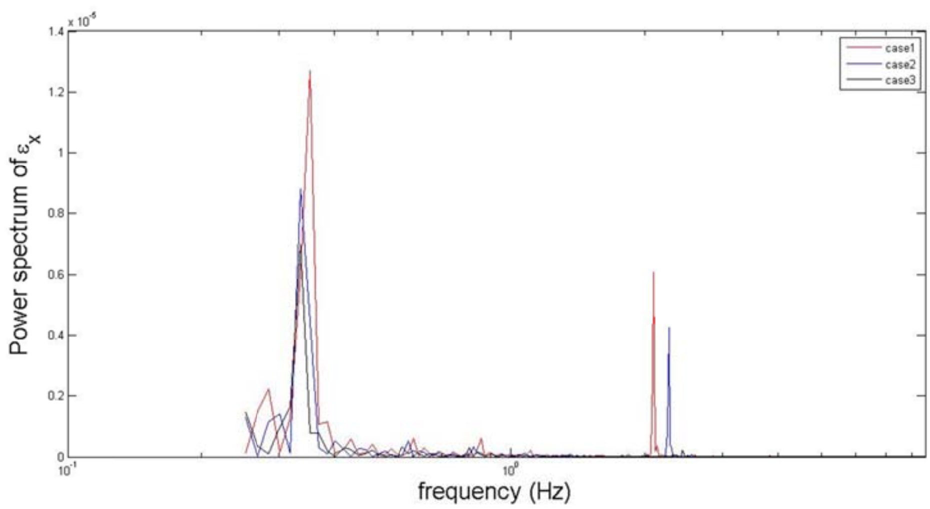

(b)

Fig. 5.19 Strain response of node 2. (a) time history; (b) power spectrum

Table 5.4 the fatigue damage of the blades with different fundamental natural frequency

	Case 1	Case 2	Case 3
Fundamental frequency (Hz)	2.10	2.30	2.49
Fatigue damage D	0.7659	0.1020	0.003

5.6 The Ultimate Strength Analysis

5.6.1 The overview of the ultimate strength analysis for a laminated FRP blade

To evaluate the failure-critical locations of the blade, a failure criteria is required. Researchers have proposed many failure criteria for the laminated FRP material, among which the Tsai-Wu criteria is most widely used. The early age failure criteria are the non-interactive criteria which do not consider the interaction between stresses, such as the maximum stress or strain criteria. Unlike the non-interactive failure criteria, the Tsai-Wu criteria include all stresses. This is particularly important for evaluating the failure of matrix, because the combined effect of transverse tension and shear stress can lead to failure before either of the stresses reaches their corresponding ultimate value. The Tsai-Wu criteria is applied in the failure analysis of each ply of the laminated blade.

In the extreme wind speed condition, the VAWT is parked and hence only wind pressures are applied on the blade. The design wind speed is defined in Chapter 3 following the suggestion of IEC61400-1. In this case, the influence of the turbulence is included in the equivalent static wind load. Due to the standing still of the VAWT, the wind direction has an influence on the responses of the blade. In the numerical study, the direction of wind can be represented by the azimuth angle. The extreme wind loads at different azimuth angles have been obtained in Chapter 3. In this study, the most dangerous azimuth angle and the failure-critical locations of the blade are figured out.

5.6.2 The Tsai-Wu failure criteria

The Tsai–Wu failure criterion is based on a phenomenological method. This failure criterion is a specialization of the general quadratic failure criterion proposed by Gol'denblat and Kopnov (Gol'denblat & Kopnov, 1965) and has the form:

$$
\begin{aligned}
&F_1\sigma_1 + F_2\sigma_2 + F_3\sigma_3 + F_4\tau_{12} + F_5\tau_{23} + F_6\tau_{31} \\
&\quad + F_{11}\sigma_1^2 + F_{22}\sigma_2^2 + F_{33}\sigma_3^2 + F_{44}\tau_{12}^2 + F_{55}\tau_{23}^2 + F_{66}\tau_{31}^2 \\
&\quad\quad + 2F_{12}\sigma_1\sigma_2 + 2F_{23}\sigma_2\sigma_3 + 2F_{13}\sigma_1\sigma_3 \le 1
\end{aligned}
\tag{5.12}
$$

where

$$F_1 = \frac{1}{T_1} - \frac{1}{C_1};\, F_2 = \frac{1}{T_2} - \frac{1}{C_2};\, F_3 = \frac{1}{T_3} - \frac{1}{C_3};\, F_{11} = \frac{1}{T_1C_1};\, F_{22} = \frac{1}{T_2C_2};\, F_{33} = \frac{1}{T_3C_3};\, F_{44} = \frac{1}{S_{12}^2};$$

$$F_{55} = \frac{1}{S_{23}^2};\, F_{66} = \frac{1}{S_{31}^2}$$

In Equation (5.12), $\sigma_i, i = 1,2,3$ are the normal stress in the three directions of anisotropy; τ_{12}, τ_{23} and τ_{31} are the corresponding shear stress; "*T*", "*C*" and "*S*" represent the ultimate tensile stress, the ultimate compressive stress and the ultimate shear stress respectively; the coefficients F_{12}, F_{23} and F_{13} are obtained from experiment tests. If no enough experimental data, the values of these coefficients can be chosen as $F_{12} = \frac{-1}{\sqrt{T_1C_1T_2C_2}}$, $F_{23} = \frac{-1}{\sqrt{T_2C_2T_3C_3}}$ and $F_{13} = \frac{-1}{\sqrt{T_1C_1T_3C_3}}$.The Tsai-Wu criterion predicts failure when the failure index in a laminar reaches 1.

For a ply of a laminated FRP, the criteria can be simplified as

$$F_1\sigma_1 + F_2\sigma_2 + F_{11}\sigma_1^2 + 2F_{12}\sigma_1\sigma_2 + F_{22}\sigma_2^2 + F_{44}\tau_{12}^2 \le 1 \tag{5.13}$$

As introduced in Chapter 4, the blade is made of a laminated FRP with 3 layers: the 1st and 3rd layer of PW FRP and the 2nd layer of UD FRP. Because the ultimate strength data of the composite materials of the blade is unavailable, the data from DOE / MSU composite material fatigue database are used (Mandell & Samborsky, 2009). In the analysis of this section, according to the tests of 90D155, D155B2 and 45D155 in DOE / MSU database, T_1, C_1, T_2, C_2 and S_{12} of UD FRP, are selected as 773MPa, -653MPa, 26MPa, -123MPa and 106MPa respectively. Here, the direction of “1” is the fiber direction of UD FRP. According to the test of ROV1 and 45D155P2 in DOE / MSU database, T_1, C_1, T_2, C_2 and S_{12} of PW FRP are set as 380 MPa, -240 MPa, 380 MPa, 240 MPa and 97MPa. Here, “1” and “2” are the directions of warp and weft.

In the following subsection, the Tsai-Wu strength index

$$P = F_1\sigma_1 + F_2\sigma_2 + F_{11}\sigma_1^2 + 2F_{12}\sigma_1\sigma_2 + F_{22}\sigma_2^2 + F_{44}\tau_{12}^2 \quad (5.14)$$

is used to evaluate the failure-critical locations. The larger is the Tsai-Wu strength index, the more likely a failure occurs.

5.6.3 The wind load

The wind pressures considered in this section are given in Chapter 3 according to the requirement of IEC61400-1.

5.6.4 The ultimate strength analysis

In this subsection, the responses of the blade at different azimuth angles are given. The azimuth angles considered in this study are 0^o, 30^o, 60^o, 90^o, 120^o, 150^o, 180^o, 210^o, 240^o, 270^o, 300^o and 330^o. At each azimuth angle, the stresses in each laminar of the blade can be obtained and the value of P defined in Section 5.6.4 can be calculated. Comparing the results of all azimuth angles, the failure critical locations (with large P value) are the same for each azimuth angle, which are the supports and the mid-span of the blades for each azimuth angle. The largest Tsai-Wu strength index appears at the upper support of the blade. By taking 90^o for example, the Tsai-Wu strength indices P in the three laminas are shown in Fig. 5.20. The largest Tsai-Wu strength index in each lamina (P_{max}) is also given in the figure.

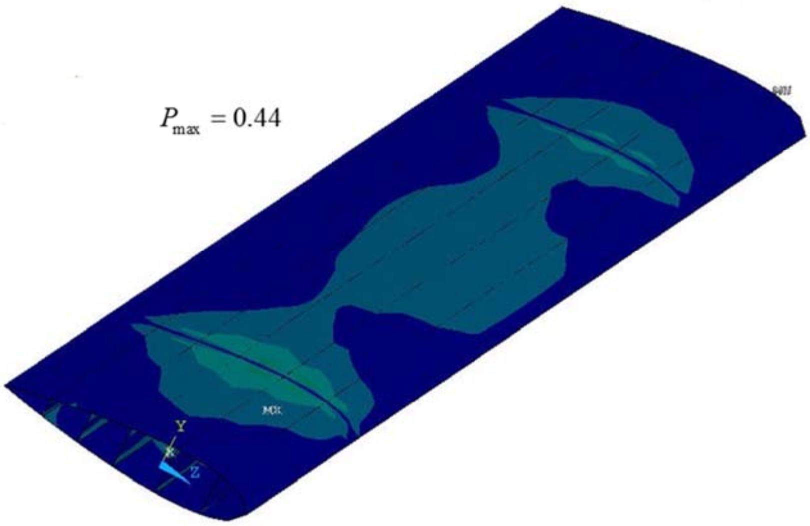

(a)

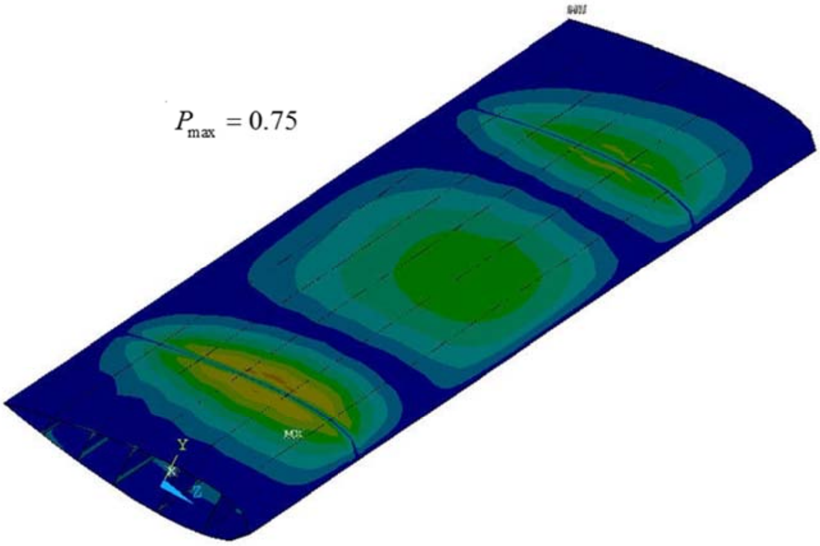

(b)

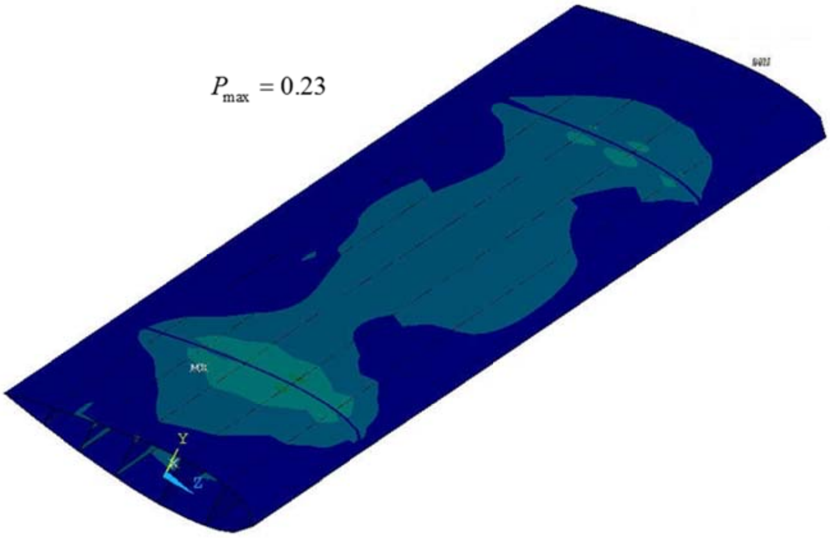

(c)

Fig. 5.20 the Tsai-Wu strength index *P.* (a) lst lamina; (b) 2^{nd} lamina; (c) 3^{rd} lamina.

The least favorable azimuth angle can also be figured out. The graph of P_{max}-versus-azimuth angle are shown in Fig. 5.21. It can be seen that P_{max} in the 2^{nd} lamina is generally larger than the index in the 1^{st} and 3^{rd} lamina. It can be also found that there are two peaks of P_{max}: one is in the upwind side (in the range between 60° and 90°) and the other is in the backwind side (near 240°). Hence, the least favorable azimuth angle is between 60° and 90°.

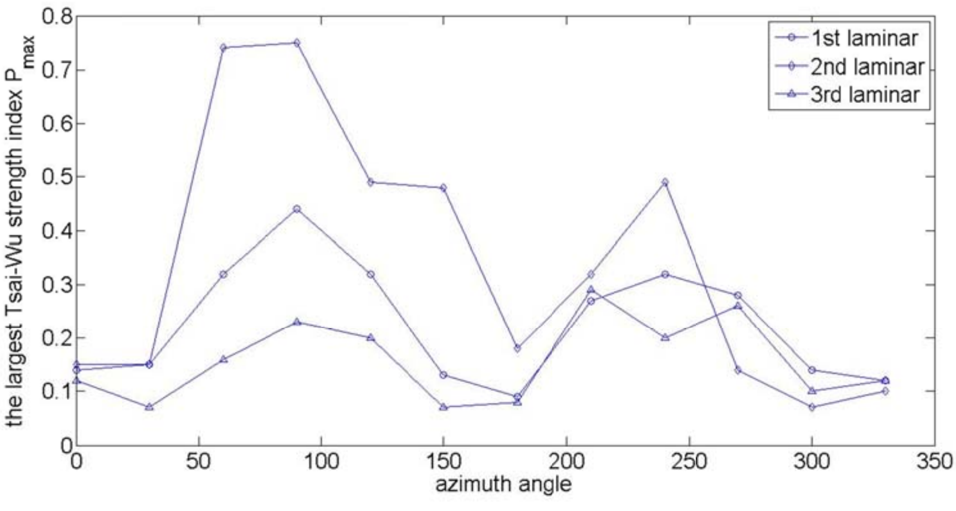

Fig. 5.21 P_{max}-versus- azimuth angle

5.6.5 The interlaminar stresses distribution

The interlaminar stresses are much smaller than the in-plane stresses according to the theory of plate and shell, but they are the main reasons of delamination of laminated FRP plates (Allix & Ladevèze, 1992; O'Brien, 1982; Panigrahi & Pradhan, 2009). Although many researchers have worked on this topic (Chin et al., 2015; Hwu et al., 1995; Marat-Mendes & Freitas, 2010; Reeder, 1992), there is still no a common accepted criteria in engineering applications. In this subsection, the distribution of interlaminar stresses, including τ_{zx}, τ_{zy} and σ_z, at the azimuth angle of 0^o, 30^o, 60^o, 90^o, 120^o, 150^o, 180^o, 210^o, 240^o, 270^o, 300^o and 330^o are obtained. Then, the variation of the interlaminar stresses with the azimuth angle is studied and the locations with large interlaminar stresses are figured out.

From Fig. 5.4, it is known that the stresses through the thickness of a laminated FRP plate are discontinuous. The maximum (the largest magnitude positive) and minimum (the largest negative) stress of τ_{zx}, τ_{zy} and σ_z in the 3 layers are shown in Table 5.5. These τ_{zx}, τ_{zy} and σ_z are selected from the middle of each layer. It can be found that for τ_{zx}, the 2nd layer has larger stress than the other two layers. The large positive and negative τ_{zx} appear in two azimuth angle range: one is between 60^o and 90^o and the other is near 330^o. For τ_{zy}, generally the 3rd layer has larger stress than the other two layers. Similar to τ_{zx}, there are two peaks of the positive and negative τ_{zy}: one is between 60^o and 90^o and the other is near 330^o. σ_z is much smaller than τ_{zx} and τ_{zy}. The same as τ_{zy}, the 3rd layer has larger σ_z than the other two layers. There is no obvious peak of compressive σ_z in the considered azimuth angles, and there are also two peaks in σ_z : one is between 60° and 90° and the other is near 330°.

Table 5.5 Interlaminar stresses at different azimuth angles

	τ_{zx} (KPa)		τ_{zy} (KPa)		σ_z (KPa)	
	Min	Max	Min	Max	Min	Max
0°						
1st lamina	-82	72	-120	128	-0.42	0.39
2nd lamina	-268	274	-175	166	-2.95	2.73
3rd lamina	-226	219	-369	357	-5.48	5.07
30°						
1st lamina	-42	48	-78	67	-0.53	0.69
2nd lamina	-173	174	-146	132	-3.74	4.82
3rd lamina	-72	91	-118	147	-6.95	8.95
60°						
1st lamina	-162	174	-291	256	-0.56	0.57
2nd lamina	-502	504	-309	315	-3.93	4.01
3rd lamina	-375	367	-613	591	-7.30	7.44
90°						
1st lamina	-138	153	-248	227	-0.40	0.91
2nd lamina	-497	435	-325	257	-2.86	6.38
3rd lamina	-284	308	-537	481	-5.32	11.86
120°						
1st lamina	-91	89	-161	148	-0.56	0.81
2nd lamina	-349	347	-344	171	-3.94	5.68
3rd lamina	-213	175	-301	309	-7.33	10.54
150°						
1st lamina	-100	100	-161	163	-0.28	0.34
2nd lamina	-338	388	-234	210	-2.00	2.43
3rd lamina	-289	252	-447	451	-3.72	4.53
180°						
1st lamina	-56	51	-84	90	-0.41	0.34
2nd lamina	-192	193	-119	115	-2.91	2.43
3rd lamina	-159	159	-254	260	-5.40	4.51
210°						
1st lamina	-124	116	-187	199	-0.40	0.50
2nd lamina	-354	361	-234	230	-2.83	3.5192
3rd lamina	-295	316	-498	490	-5.26	6.53
240°						
1st lamina	-64	56	-94	99	-0.54	0.43
2nd lamina	-200	178	-104	108	-3.78	3.01

3rd lamina	-126	114	-175	199	-7.02	5.59
270^o						
1st lamina	-111	70	-153	107	-0.43	0.53
2nd lamina	-316	313	-193	163	-3.07	3.71
3rd lamina	-233	204	-379	380	-5.70	6.89
300^o						
1st lamina	-42	38	-59	73	-0.56	0.32
2nd lamina	-149	153	-71	82	-3.96	2.30
3rd lamina	-54	49	-77	105	-7.36	4.27
330^o						
1st lamina	-188	172	-276	307	-0.38	0.50
2nd lamina	-577	574	-381	366	-2.68	3.51
3rd lamina	-474	435	-760	698	-4.97	6.53

The distributions of τ_{zx} (at the middle of 2nd layer) at the azimuth angle of 60^o and 330^o are shown in Fig. 5.22(a) and Fig. 5.22(b) and the distributions of τ_{zy} (at the middle of 3nd layer) at the azimuth angle of 60^o and 330^o are shown in Fig. 5.22(c) and Fig. 5.22(d). It can be seen that the minimum τ_{zx} and τ_{zy} occur at the upper support and the maximum τ_{zx} and τ_{zy} occur at the lower support at azimuth angle of 60^o; the minimum τ_{zx} and τ_{zy} occur at the lower support and the maximum τ_{zx} and τ_{zy} occur at the upper support at azimuth angle of 330^o. The distributions of σ_z (at the middle of 3nd layer) at the azimuth angle of 60^o and 330^o are shown in Fig. 5.22(e) and Fig. 5.22(f). It can be seen that the maximum σ_z occurs at the leading edge near the mid-span of the blade.

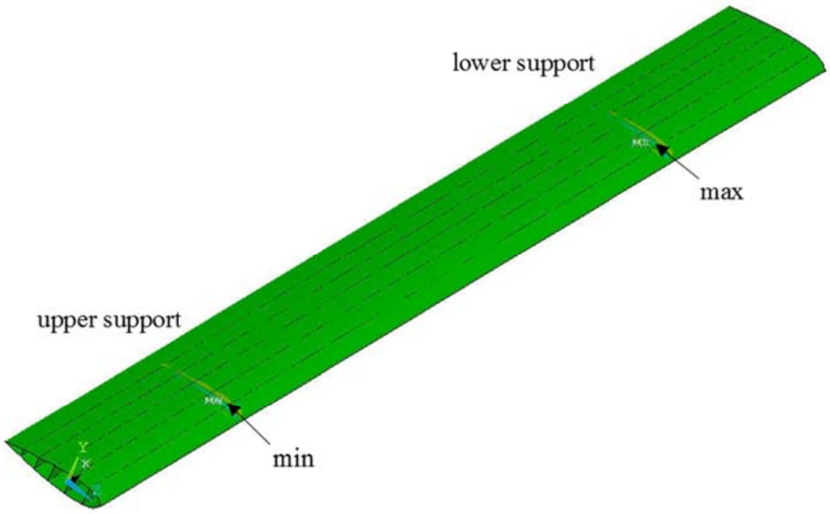
lower support
max
upper support
min

(a)

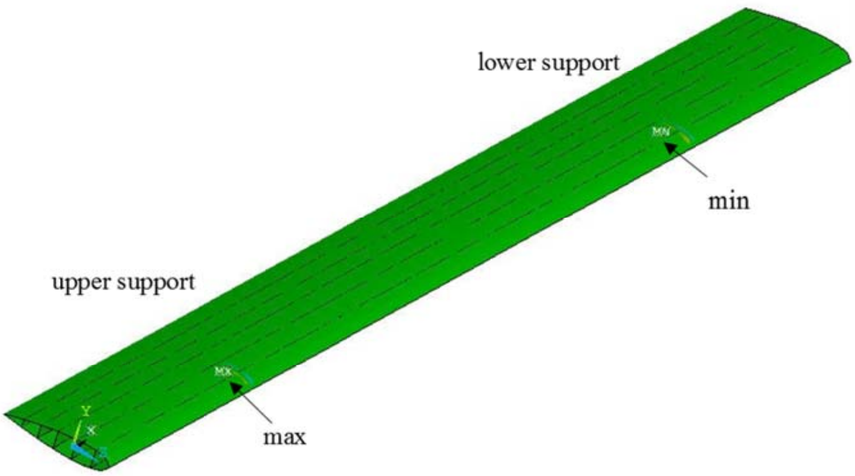
lower support
min
upper support
max

(b)

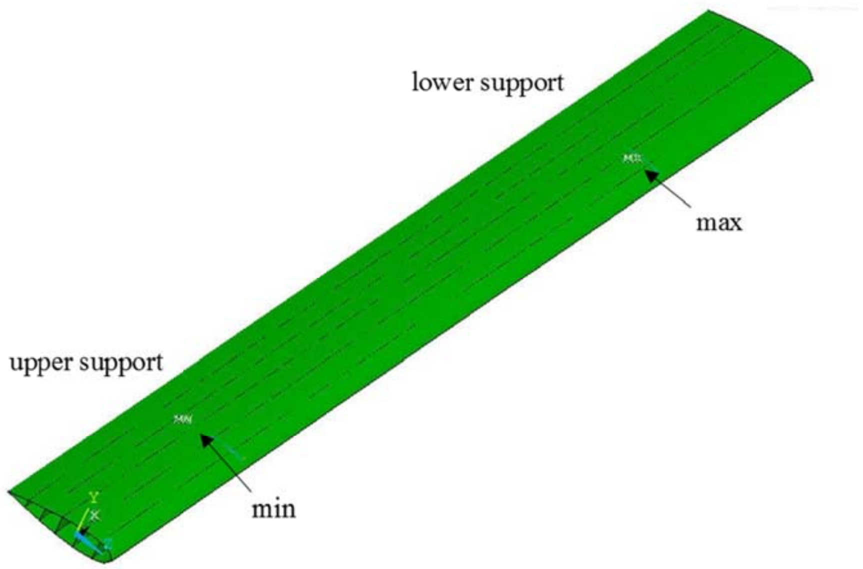
lower support
max
upper support
min

(c)

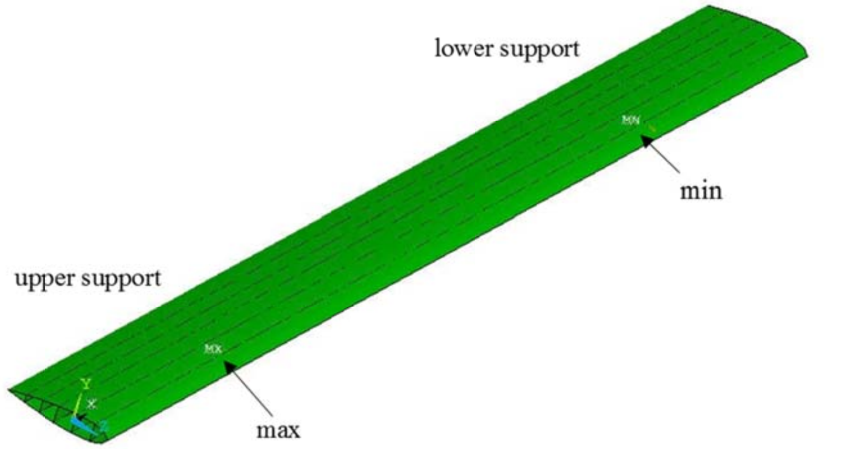
lower support
min
upper support
max

(d)

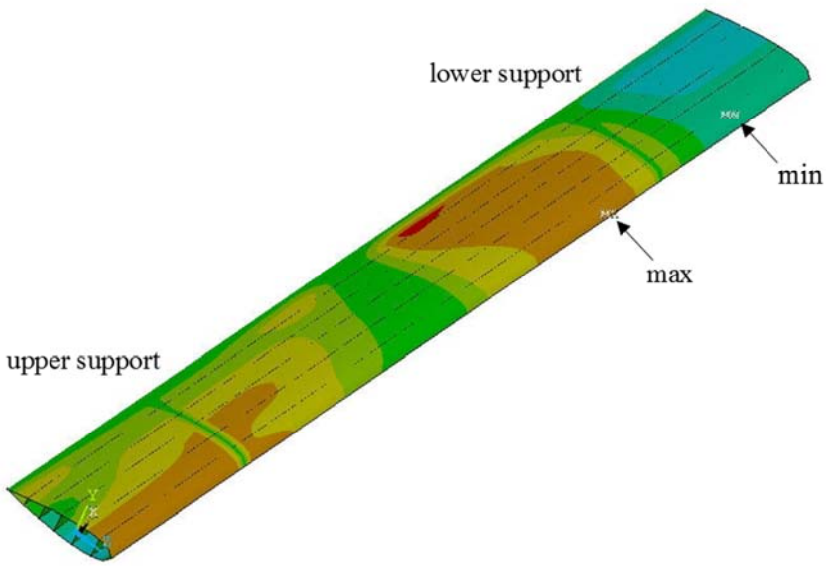

(e)

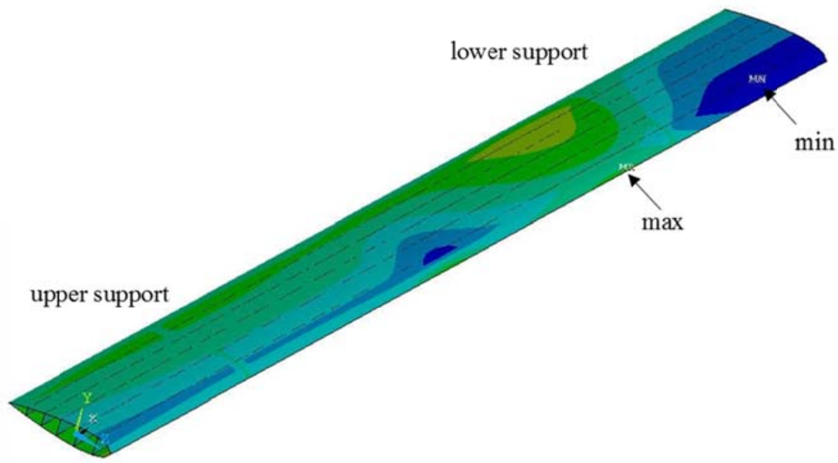

(f)

Fig. 5.22The distributions of interlaminar stresses at the azimuth angles of 60^o and 330^o . (a) τ_{zx} at 60^o; (b) τ_{zx} at 330^o; (c) τ_{zy} at 60^o; (d) τ_{zy} at 330^o; (e) σ_z at 60^o; (f) σ_z at 60^o.

5.7 Summary

Based on the works of Chapter 3, Chapter 4, and the above analysis in this chapter, a framework for the fatigue and ultimate strength analyses of VAWTs was proposed to give a solution to the problem due to lacking in field measurements and experimental tests in the present situation of the development of VAWTs.

Firstly, a refined FE model of a laminated composite straight blade was established and the responses of the blade under different operation and wind conditions were predicted. Based on these responses, the fatigue and ultimate strength analyses were conducted in this chapter.

Under the condition of power production and normal turbulent wind, the fatigue critical locations were figured out. The locations at the supports and the mid-span of the blade have larger fatigue damage than other position of the blade. Among these locations, the position of the largest fatigue damage is in the cross section at the lower support. In this cross section, the positions subjected to compressive cyclic loads have the larger fatigue damage than those subjected to tensile cyclic loads.

Parameter studies were also conducted and the influences of the ultimate tensile and compressive strains, damping ratio and fundamental frequency were studied. For the point subjected to tensile cyclic loads, a larger ultimate tensile strain can lead to smaller fatigue damage while the influence of an ultimate compressive strain can be neglected; for the point subjected to compressive cyclic loads, a larger ultimate compressive strain can reduce the fatigue damage while the influence of an ultimate tensile strain can be ignored. Moreover, it was found that the fatigue damage is sensitive to the damping ratio and fundamental frequency; increasing the damping ratio and fundamental frequency can dramatically decreases the fatigue damage. It was also found that for the particular blade in this study, the responses of the blade are composed of two frequency components, one is the forced vibration under the aerodynamic force due to rotation, which has a large strain range and the other is the excited 1st mode vibration with small strain ranges.

The ultimate strength analysis in the extreme wind speed was also considered. In this case, the wind turbine was parked. The influence of the wind direction on the response of the blade was studied. It was found that the least favorable azimuth angle is in the upwind side, in the range of azimuth angle between 60^o and 90^o. The failure-critical location was in the cross section at the upper support. Besides the critical-failure locations predicted by the Tsai-Wu criteria, the locations with large interlaminar stresses were also figured out.

In this chapter, only the blade of the VAWT was studied; the fatigue and ultimate strength analyses of the whole straight-bladed VAWT except for the blades are conducted in the next chapter.

CHAPTER 6

FATIGUE AND ULTIMATE STRENGTH ANALYSIS OF VAWTS

6.1 Introduction

In Chapter 3, a simulation method of wind loads on a VAWT is proposed. This method can simulate wind loads on all components of a VAWT and take the interaction between different components into account but the aeroelastic effect is ignored in this method. Chapter 5 focuses on the fatigue and ultimate strength analysis of straight blades of the VAWT introduced in Chapter 3. The blade is made of laminated composite. To obtain the stresses in each layer, laminated shell elements are used in the FE modeling. In reality, the blade is supported by upper and lower arms. Under the assumption that the deflection of upper and lower arms can be ignored, blades can be studied solely in the rotating reference frame. By using the simulated wind pressures in Chapter 3 and the FE model of blade, the critical locations of fatigue and strength failure of the blade are figured out to aid in the design and guide the sensor placement for monitoring. On the other hand, the fatigue and ultimate strength analysis of other components of the VAWT is also needed to be conducted. A FE model of the whole VAWT is thus required. It is ideal that all components of the VAWT are modeled by shell or solid elements as done for blades in Chapter 5 but it will be computationally prohibited. Because other components of the VAWT are made of steel or reinforced concrete other than laminated composite materials, the analyses of which are routine, therefore, these components can be modeled by beam elements. Moreover, the structural analysis of blades and the whole wind turbine for HAWT are generally conducted separately. In considering that blades have been studied in Chapter 5 in detail, blades can also be modeled by beam elements so that the influence of blades on other components is taken into account. In summary, beam elements are used to model all components of the VAWT in the fatigue and ultimate strength analysis of the whole VAWT. Actually, there are many researchers aimed to solve this problem based on different techniques, such as multi-scale modelling, dynamic condensational and sub modelling. But this topic is not addressed in this thesis.

As reviewed in Chapter 2, the key issue of establishing a FE model of HAWT is the rotor-tower coupling problem. Since wind turbines are not structures but mechanisms, the rigid body motions of the rotor bring about challenges in the modeling. In the early years, the rotor and the tower are simply treated separately; later, more and more researchers used the multibody system (MBS) method to consider the rotor-tower coupling. For VAWTs, the structural analyses were usually conducted in a rotating reference frame which rotates at the same speed of a VAWT (Thresher et al., 2009). In this reference frame, the rigid motion of the rotor can be eliminated and the VAWT is non-rotating; the centrifugal force and the Coriolis force are added. However, these works did not mention how to deal with the response of the tower. Hence, the response of the tower needs to be further studied when using this method, especially when strains of the tower are required.

In this chapter, to compensate for the lack of experiences and researches on VAWTs as highlighted in Chapter 5, a framework for fatigue and ultimate strength analysis of a VAWT except its blades is proposed. To introduce this framework, a straight bladed VAWT is taken as an example. A FE model of a straight-bladed VAWT is established by beam elements. The rotating frame method is used for analyzing fatigue damage and ultimate strength of all components of the VAWT except for blades and tower. The response of the tower is then obtained by a two-step calculation method. Based on this two-step calculation method, the fatigue analysis of the whole turbine in the normal wind conditions and the ultimate strength analysis in the extreme wind conditions are conducted. The fatigue critical locations of the VAWT in operation conditions and the failure-critical locations in the extreme wind conditions are figured out.

6.2 The Framework of the Fatigue and Ultimate Strength Analysis for A VAWT

In Chapter 3, a wind load simulation method based on strip analysis and CFD is proposed. This method can simulate wind loads on all components of a VAWT and considers the influences of the mean wind profile, the turbulence and the wind-structure interaction among components. Wind loads under different wind conditions are also given. The restriction of this method is that the aeroelastic effect is ignored because the blades and other components, such as arms and tower, are simulated as the wall boundary conditions in CFD simulation. Based on this work, a framework of the fatigue and ultimate strength analysis for the components of the VAWT except blades is proposed here.

The procedure of the framework is shown in Fig. 6.1. There are three parts in this framework. The first part is to determine the design loads on all components of the VAWT, including aerodynamic forces, the inertial force, the gravity force, and the Coriolis's force. Wind loads can be obtained by the method proposed in Chapter 3. The second part is to build the FE model of the VAWT. The third part is to conduct model updating based on the field measured data which will be introduced in Chapter 7. Finally, the fatigue and ultimate strength analysis of the VAWT except blades can be conducted. As introduced in Chapter 2, for HAWTs a large number of failure reports on fatigue and strength failures have been accumulated and the study on this topic are still ongoing, while VAWTs, especially straight-bladed VAWTs, are lack of field measurements and structure-oriented experimental tests. The proposed framework can offer the information on the fatigue and ultimate failure to facilitate the structural design of VAWTs, especially straight-bladed VAWTs.

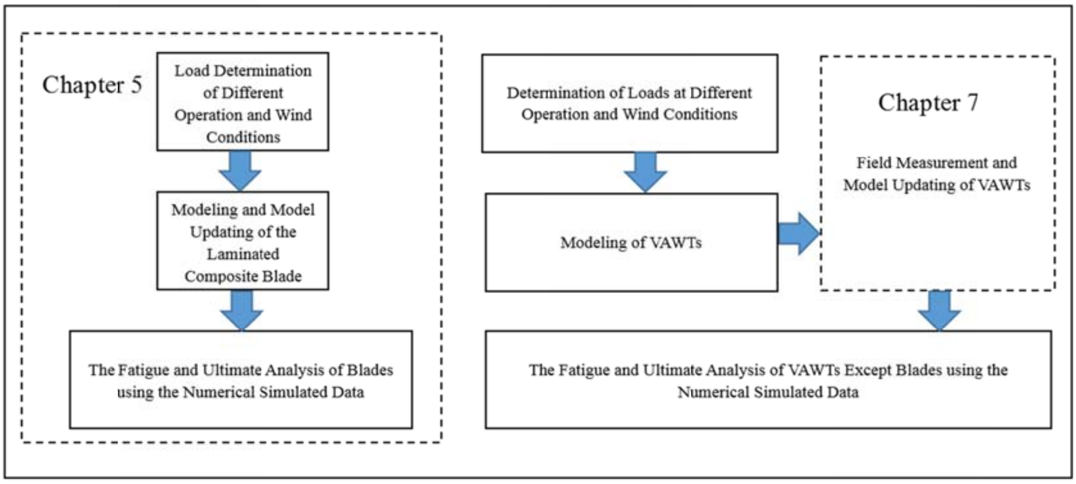

Fig. 6.1 A framework of the fatigue and ultimate strength analysis for the whole VAWT

6.3 FE Modeling of A VAWT

6.3.1 The FE model of the straight-bladed VAWT

To conduct the fatigue and ultimate strength analysis of VAWTs, the straight-bladed VAWT introduced in Chapter 3 is taken for example. The finite element model is shown in Fig. 6.2. ANSYS beam188, a geometry exact beam element, is used to model all components of the VAWT, including the tower, the shaft, the hub, the main arms, the upper and lower arms, the links and the blades. The tower of the VAWT is made of reinforced concrete with a height of 24 m and a diameter of 5m. The thickness of reinforced concrete wall of the tower is 250mm. The tower supports a vertical rotor, the rotating parts of the VAWT, of 26m in height and 40m in diameter. Three blades of the rotor are equally arranged at an interval angle of 120^{o}. The length of blades is 26m. These blades are supported by the Y-type steel arms connected to the tower via the main shaft at the top of the tower (the hub height). The ground clearance of the bottom end of the blades is 10.5m. Each Y-type steel arm consisted of a main arm, an upper arm and a lower arm. The cross section of the main arm is rectangular with the width of 1.6 m and the depth of 1.2 m and the length of the main arm is 10 m. The upper and lower arms support the blade at one end and are connected to the main arm at another end. The cross section of the upper and lower arm is rectangular, and the cross section has the constant width of 1.2 m and the varying depth from 0.6m at the main arm side to 0.3m at the blade side. Between the lower and upper arms, there is a stiffened link. The diameter of the link is 0.2m. More details of the VAWT can refer to Chapter 3.

In this FE model, the tower is modelled by 26 beam elements; the hub by 8 beam elements; the shaft by 20 elements; each main arm by 20 elements; each upper arm by 28 elements; each lower arm by 28 elements; each link by 27 elements; and each blade by 50 elements. There are total 519 elements, 673 nodes and 4020 DOFs in the FE model of the VAWT. The connections between the components are shown in Fig. 6.3. The hub is connected to the top of tower by rigid joint; the shaft is connected to the hub by two hinge joints, one at the top of the hub and the other at the bottom of the hub; the main arms are connected to the top of the shaft by rigid joints; the upper and lower arms are connected to the main arms by rigid joints; the links are connected to the upper and lower arms by hinge joints; the blades are connected to the upper and lower arms by hinge joints.

There are many uncertainties in a finite element model, such as the deviation in material properties and geometry. Before using the finite element model, it is better to update it by field measurement data. This model-updating work will be explained in Chapter 7. The model used in this chapter is already updated. The material properties of the components of the VAWT are listed in Table 6.1.

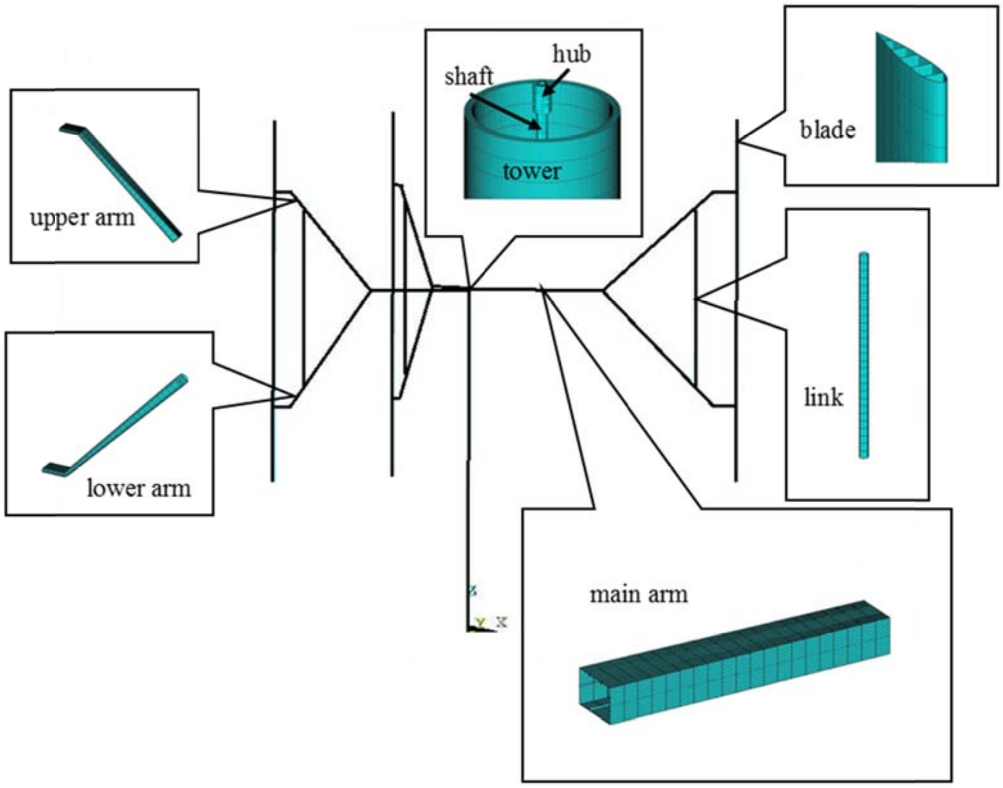

Fig. 6.2 The finite element model of a straight-bladed VAWT

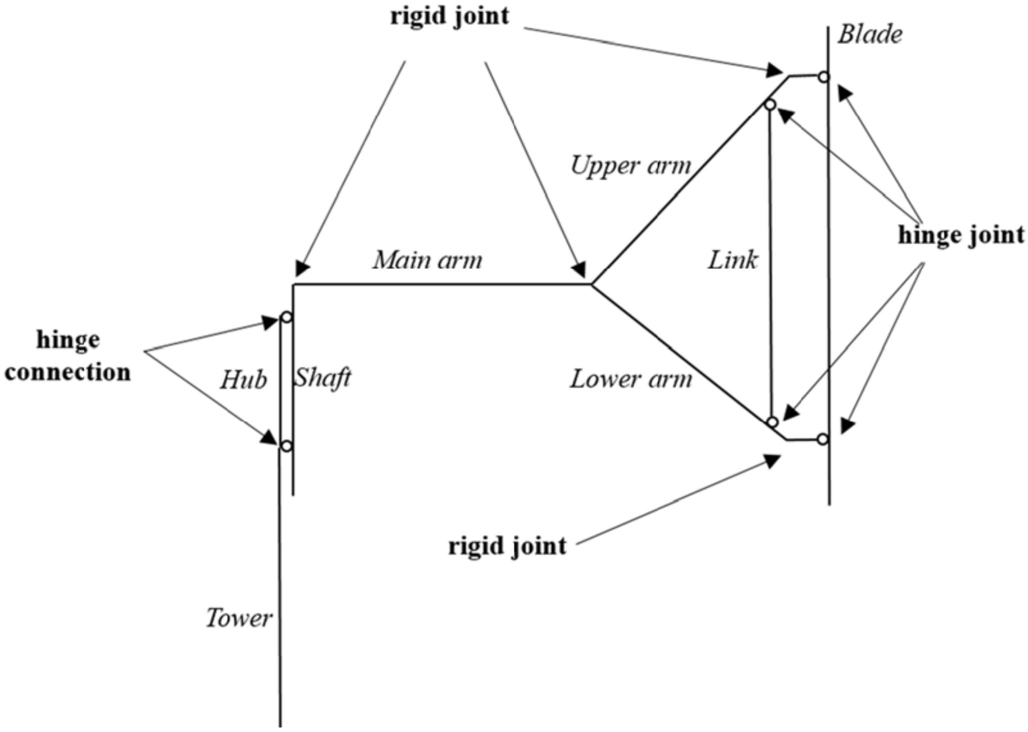

Fig. 6.3 Connections between componnets of the straight-bladed VAWT

Table. 6.1 The material properties of the components of the finite element model

	$E (\times 10^9 \text{ N/m}^2)$	ν	$\rho (\text{kg/m}^3)$
Tower	25.74	0.20	2500
Shaft	206.00	0.30	7850
Hub	25.74	0.30	2500
Main Arms	164.80	0.30	7850
Upper and Lower Arms	206.00	0.30	7850
Links	206.00	0.30	7850
Blades	29.20	0.30	1800

The first 10 mode shapes of the VAWT are shown in Appendix B. The corresponding natural frequencies are shown in Table 6.2. The modal analysis is conducted for the case that the rotor is locked. The 1st mode shape is the torsion of shaft; the 2nd and the 3rd mode shape are the bending of shaft; the 4th mode shape is the vertical bending of main arm; the 5th and the 6th mode are the horizontal bending of the upper and lower arms; the 7th, the eighth and the ninth mode shape are the combination of torsion and bending of the lower and upper arms; and the 10th mode shape is the bending of the blade.

It can be found that the frequency of the tower is not within the range of first 10 modes. Actually, the frequency of the 1st bending mode of the tower is up to 3.77Hz which indicates that the tower is stiff. Special attentions are paid on the resonance of the tower by most codes and literatures (Burton et al., 2001; Germanischer, 2010). As introduced in Chapter 3, the design rotational speed of the rotor of the straight-bladed VAWT is 2.1rad/s, that is 0.334Hz defined as 1P. The frequencies of the blade passing are 2P and 3P for 2-blade and 3-blade wind turbines respectively. For the wind turbine considered in this study, the blade passing frequency 3P is 1.00Hz. To avoid the resonance of the tower, the 1st natural frequency of the tower should be away from 1P and 3P at least 5% (Germanischer, 2010) or even 15% (Burton et al., 2001). In this case, the frequency of the 1st bending mode of the tower, 3.77 Hz, is far away from 1P (0.334 Hz) and 3P (1.00 Hz). Such a high natural frequency of the tower is difficult to be obtained by the steel tubular tower which is most-commonly used nowadays. Indeed, the resonances of other components are also needed to be avoided. 1P and 3P should avoid the natural frequencies of the shaft modes and 1P should avoid the natural frequencies of the modes of blades and arms. The 1^{st} mode of this VAWT is the torsion of shaft; the frequency of 1^{st} mode is 0.27Hz which is 19% away from 1P and 73% away from 3P. The 2^{nd} and 3^{rd} mode of the VAWT are the bending modes of shaft; the common frequency is 0.82Hz which is 59% away from 1P and 22% away from 3P. The 4^{th} mode of the VAWT is the vertical bending of arms; the frequency of the 4^{th} mode is 1.15Hz which is 71% away from 1P. Therefore, at the design rotational speed 2.1rad/s (1P, 0.334Hz), all components of the VAWT can avoid resonance.

Table. 2 The first 10 natural frequencies of the VAWT FE model

Mode	1	2	3	4	5	6	7	8	9	10
Freq.(Hz)	0.27	0.82	0.82	1.15	1.51	1.52	1.90	1.91	2.03	2.49

6.3.2 The dynamic analysis method

Modern large wind turbines are all grid connected and generally operate at a specific rotational speed. Depending on the type of generator, the rotation mode of the rotor will have a slight difference: a synchronous generator operates exactly at a given rotational speed and an asynchronous generator, although, can operate at various speeds, the largest allowable variation is only 5%. If the rotational speed of the rotor is assumed to be constant, the rotating frame method can be used to analyze the structural responses of a VAWT (Thresher et al., 2009). In the rotating reference frame which rotates at the same speed of the rotor, the rigid motion of the VAWT can be eliminated and just the inertial forces need to be considered. The aerodynamic forces on the whole VAWT can be obtained by the method proposed in Chapter 3. Therefore, the dynamic analysis of the VAWT becomes a traditional analysis of a structure.

Firstly, the rotating reference frame *XYZ* can be established, as shown in Fig. 6.4. The origin of the reference frame *XYZ* is set at the bottom of the tower; *Z*-axis of the reference frame is along the VAWT tower and the other two axes (*X*-axis and *Y*-axis) are normal to the tower. The reference frame is rotating with the rotor of the VAWT at the same rotational speed on Z-axis. The reference frame $X_oY_oZ_o$ is on the earth and the origin is also set at the bottom of the tower. At the azimuth angle of 0^o, these two reference frames coincide with each other as shown in Fig. 6.4(a); when the rotor rotates to the azimuth angle of θ, the reference frame XYZ also rotates around the tower by an angle of θ, as shown in Fig. 6.4(b). In this non-inertial reference frame, the VAWT is not rotating. Indeed, in this reference, the tower is rotating around the rotor on its own axis of symmetry, which is not the reality. But if the bending stiffness of the tower in any direction is unchanged, it will not cause any error if neglecting the rotation of the tower in the reference frame XYZ. Because the tower usually has the shape of cylinder which is axially symmetric, this condition is satisfied. Nevertheless, the forces acting on the tower and described in the stationary frame $X_oY_oZ_o$ are needed to be transformed to the rotating frame XYZ. Take the force $\boldsymbol{F}$ for example. $\boldsymbol{F}$ is described in the form of force components F_{X_o}, F_{Y_o} and F_{Z_o} in $X_oY_oZ_o$, as shown in Fig. 6.4(a). $\boldsymbol{F}$ is described in the form of force components F_X, F_Y and F_Z in XYZ, as shown in Fig. 6.4(b). When the rotating frame rotates to the azimuth angle of θ, the relation between the force components in the frame $X_oY_oZ_o$ and the force components in the frame XYZ can be written as

$$F_X = F_{X_o} \cos\theta - F_{Y_o} \sin\theta \tag{6.1a}$$

$$F_Y = F_{X_o} \sin\theta + F_{Y_o} \cos\theta \tag{6.1b}$$

$$F_Z = F_{Z_o} \tag{6.1c}$$

and

$$F_{X_o} = F_X \cos\theta + F_Y \sin\theta \tag{6.2a}$$

$$F_{Y_o} = F_X \sin\theta - F_Y \cos\theta \tag{6.2b}$$

$$F_{Z_o} = F_Z \tag{6.2c}$$

Take the wind load on a node of the tower for example. The time histories of two components of wind load in the frame $X_oY_oZ_o$ are shown in Fig.6.5. Assumed that the rotational speed of the VAWT is 2.1rad/s, the azimuth angle of the rotating frame $\theta = 2.1t$. Using Equation (6.1), the components of wind load in the frame *XYZ* are shown in Fig.6.6.

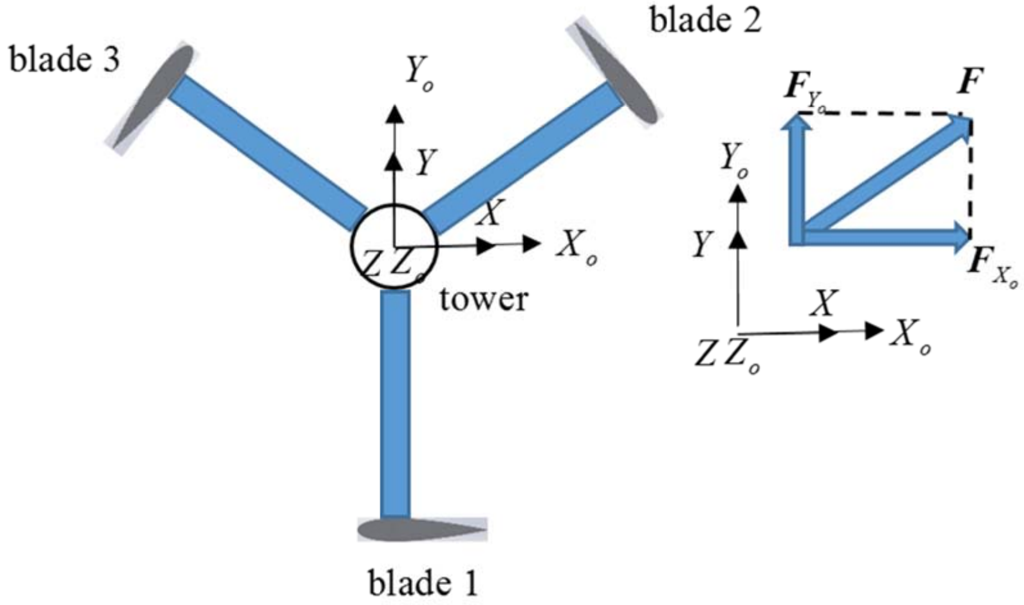

(a)

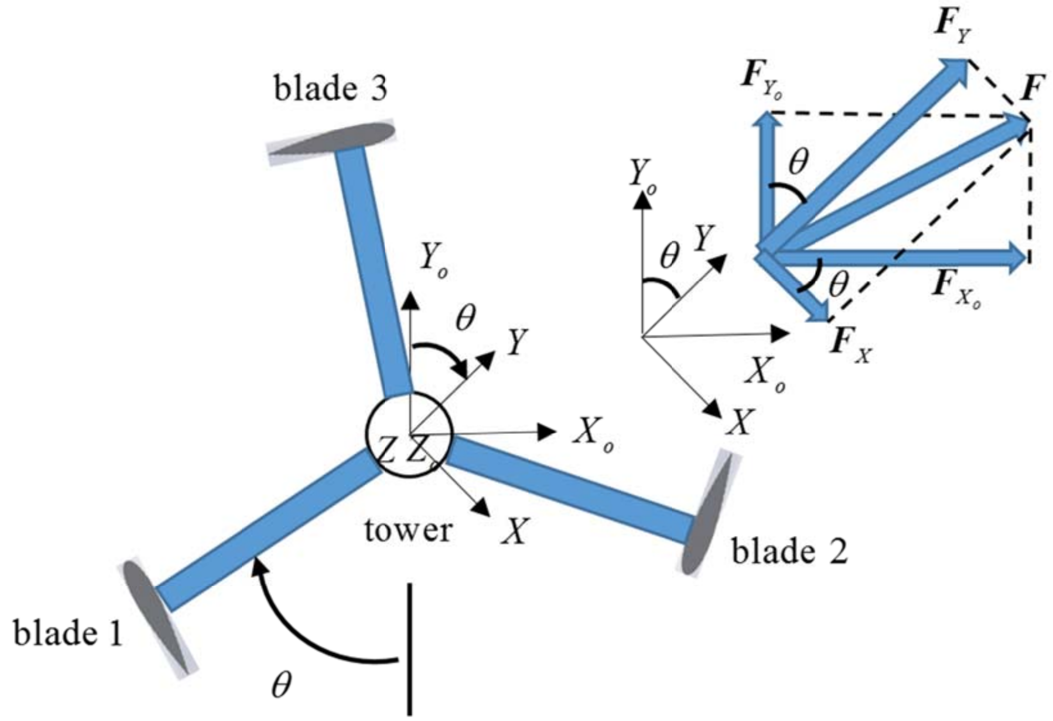

(b)

Fig. 6.4 The calculation reference frameworks. (a) at the azimuth 0°; (a) at the azimuth θ.

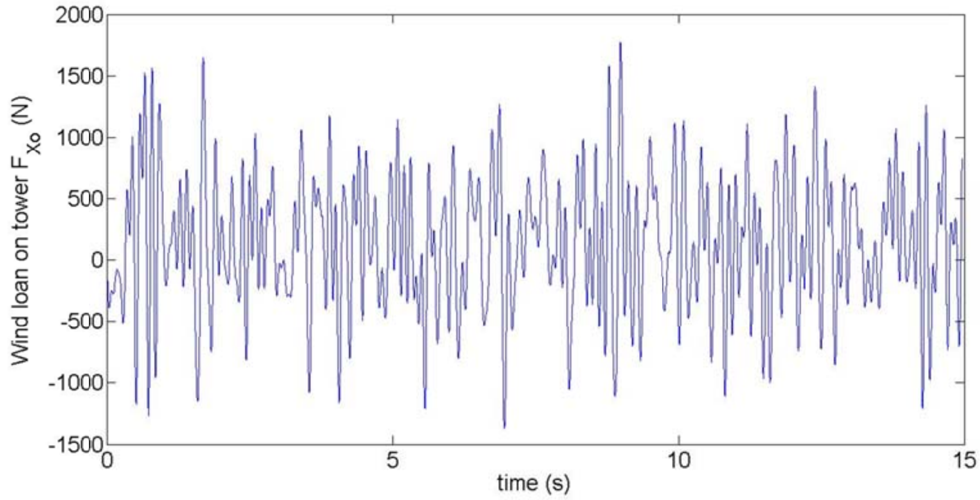

(a)

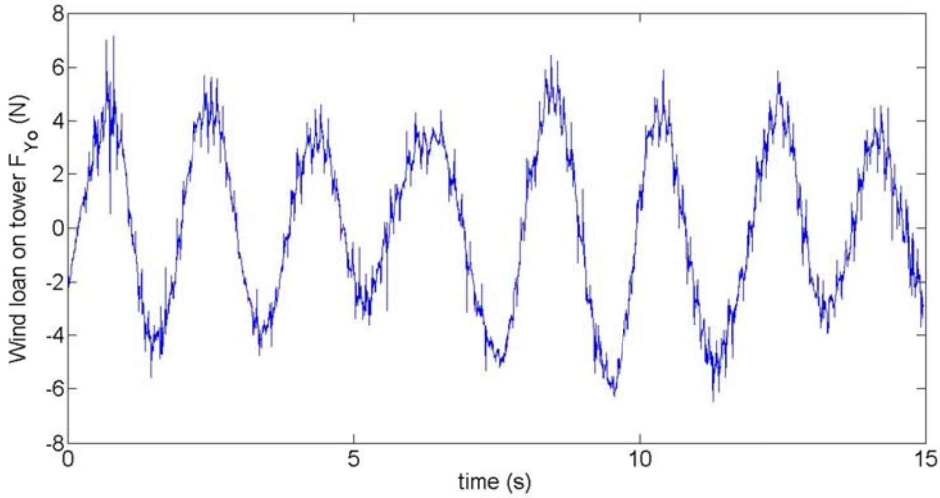

(b)

Fig. 6.5 Wind load on the tower described in the stationary frame $X_oY_oZ_o$. (a) the component in X_o-axis; (b) the component in Y_o-axis.

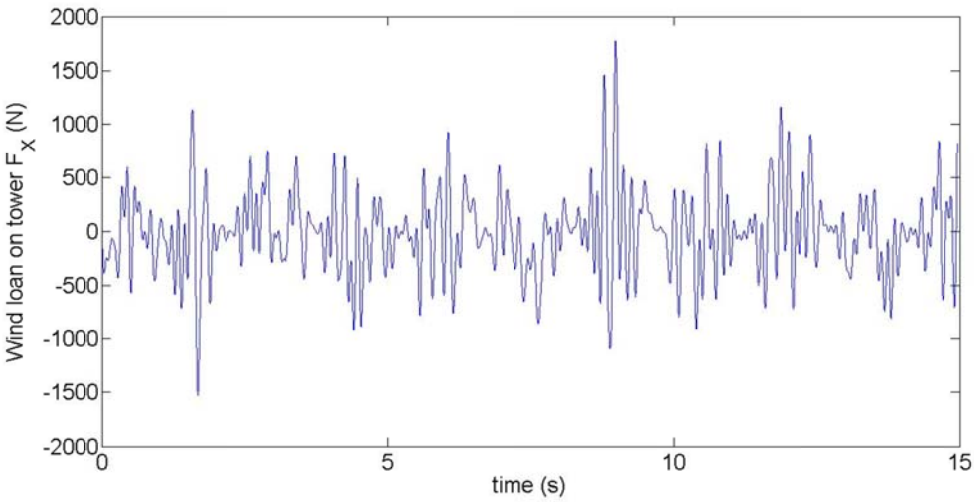

(a)

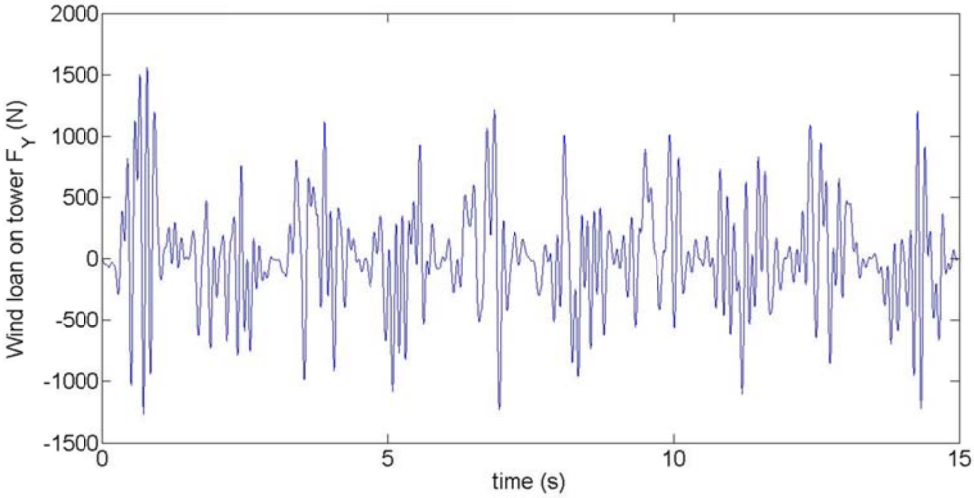

(b)

Fig. 6.6 Wind load on the tower described in the rotating frame *XYZ*. a) the component in X-axis; (b) the component in Y-axis.

So, in the reference frame *XYZ*, the VAWT can be regarded as a structure without any rigid body displacement and only non-inertial forces have to be acted on the rotor. The shaft and the hub can be connected by hinge joints. The dynamic equation of the rotor and the tower in the rotating reference frame *XYZ* can be written as

$$\boldsymbol{M}\ddot{\boldsymbol{u}} + \boldsymbol{C}\dot{\boldsymbol{u}} + \boldsymbol{K}\boldsymbol{u} = \boldsymbol{F}_W + \boldsymbol{F}_G + \boldsymbol{F}_E + \boldsymbol{F}_C \tag{6.3}$$

where $\boldsymbol{M}$ is the mass matrix of the whole VAWT; $\boldsymbol{C}$ is the damping matrix of the whole VAWT; $\boldsymbol{K}$ is the stiffness matrix the whole VAWT; $\boldsymbol{u}$ is the displacement vector of the whole VAWT measured in the rotating reference frame *XYZ*; $\dot{\boldsymbol{u}}$ and $\ddot{\boldsymbol{u}}$ are the corresponding velocity vector and acceleration vector in the rotating reference frame *XYZ*;; $\boldsymbol{F}_W$ is the wind load on the whole VAWT which are obtained in Chapter 3 and described in the rotating frame *XYZ* by Equation (6.1); $\boldsymbol{F}_G$ is the gravity force on the whole VAWT which is constant; $\boldsymbol{F}_E$ is the carrier inertial force (centrifugal force) on the rotor; and $\boldsymbol{F}_C$ is the Coriolis's force on the rotor. The positive direction of $\boldsymbol{F}_E$ is outward from the rotational axis to the point the force acted on. The positive direction of $\boldsymbol{F}_C$ is oppose to the direction determined by the cross product of the angular vector and the velocity $\dot{\boldsymbol{u}}$. The expressions of $\boldsymbol{F}_E$ and $\boldsymbol{F}_C$ are

$$\boldsymbol{F}_E = -\boldsymbol{M\Omega\Omega}(\boldsymbol{r}+\boldsymbol{u}) \tag{6.4}$$

$$\boldsymbol{F}_C = -2\boldsymbol{M\Omega}\dot{\boldsymbol{u}} \tag{6.5}$$

where $\boldsymbol{\Omega}$ is the spin matrix determined by the rotational speed of the reference frame *XYZ*; $\boldsymbol{r}$ is the original position vector of the VAWT in the rotating reference XYZ. The "original" means the position when the displacement $\boldsymbol{u}$=0. Hence, Equation (6.3) can be rewritten as

$$\boldsymbol{M}\ddot{\boldsymbol{u}} + (\boldsymbol{C}+\boldsymbol{C}_C)\dot{\boldsymbol{u}} + (\boldsymbol{K}-\boldsymbol{S})\boldsymbol{u} = \boldsymbol{F}_W + \boldsymbol{F}_G + \boldsymbol{F}_E^{'} \tag{6.6}$$

where $\boldsymbol{C}_C = 2\boldsymbol{M\Omega}$ is the additional damping matrix due to the Coriolis force; $\boldsymbol{S} = -\boldsymbol{M\Omega\Omega}$ is the soften matrix due to rotation; and $\boldsymbol{F}_E^{'} = -\boldsymbol{M\Omega\Omega r}$ is the constant component of the centrifugal force.

The strain of the VAWT can be obtained by

$$\boldsymbol{\varepsilon} = \boldsymbol{Bu} \tag{6.7}$$

where $\boldsymbol{\varepsilon}$ is the strain vector; and $\boldsymbol{B}$ is the geometric matrix (Bathe, 2006). Compared with the flexible multibody dynamic method, this modeling scheme is much more convenient.

The problem is the calculation of the response of the tower. In reality (in the reference frame $X_oY_oZ_o$), the rotor is rotating and the tower is stationary. Thus, in the reference frame *XYZ*, the rotor is static and the tower should be rotating around the *Z*-axis. Nevertheless, as discussed above, due to the axial symmetry of the tower, the bending stiffness of it would not be changed during rotating around the reference frame *XYZ*. Thus the interaction between the rotor and the tower would not be influenced by disregarding the rotation of the tower in the reference frame *XYZ*. But the response of the tower cannot be obtained from Equation (6.3) directly, because a static point of the tower in the rotating reference frame *XYZ* is actually rotating in the static reference frame $X_oY_oZ_o$. So the responses of tower cannot be directly obtained from Equation (6.3).

To obtain the responses of the tower, a two-step method is proposed here. The first step is calculating Equation (6.3). When the response of the tower is obtained, the tower should be calculated independently in the reference frame $X_oY_oZ_o$ in the second step. The interacted forces by the rotor can be calculated from Equation (6.3). The dynamic equation of the tower in the static reference frame $X_oY_oZ_o$ can be written as

$$\boldsymbol{M}_T\ddot{\boldsymbol{u}}_T + \boldsymbol{C}_T\dot{\boldsymbol{u}}_T + \boldsymbol{K}_T\boldsymbol{u}_T = \boldsymbol{F}_{R_o} + \boldsymbol{F}_{W_o} + \boldsymbol{F}_G \tag{6.8}$$

where $\boldsymbol{M}_T$ is the mass matrix of the tower and hub; $\boldsymbol{C}_T$ is the damping matrix of the tower and hub; $\boldsymbol{K}_T$ is the stiffness matrix of the tower and hub; $\boldsymbol{u}_T$ is the displacement vector of the tower and hub; $\dot{\boldsymbol{u}}_T$ is the velocity vector of the tower and hub; $\ddot{\boldsymbol{u}}_T$ is the acceleration vector of the tower and hub; $\boldsymbol{F}_{R_o}$ is the reaction force from the shaft described in the stationary frame $X_oY_oZ_o$; $\boldsymbol{F}_{W_o}$ is the wind load on the tower described in the stationary frame $X_oY_oZ_o$; and $\boldsymbol{F}_G$ is the gravity force of the tower. Here, $\boldsymbol{F}_{R_o}$ can be obtained from the results of Equation (6.3) and the detail is introduced as follows.

After calculating Equation (6.3), the displacement vector $\boldsymbol{u}$ measured in the rotating reference frame *XYZ* is known, and thus the reaction forces from the shaft can be calculated. The shaft is connected to the top and bottom of the hub as introduced in Section 6.3.1. Here, the connection at the bottom of hub is taken for example to introduce the method of obtaining the reaction force from the shaft. The elements and nodes at this connection are shown in Fig. 6.7. Element *m* and element *n* are the elements of the shaft. There are two nodes in each element. Node *i* and node *j* are the nodes of element *m*; node *i* and node *k* are nodes of element *n*. Node *l* is the node at the bottom of hub and node *j* is the node of shaft. Node *j* and node *l* are hinge connected. The element stiffness matrix of element *m* is $\boldsymbol{k}_m$ and the element stiffness matrix of element *n* is $\boldsymbol{k}_n$. The displacement vector of node *i* is $\boldsymbol{u}_i$; the displacement vector of node *j* is $\boldsymbol{u}_j$; the displacement vector of node *k* is $\boldsymbol{u}_k$. The element stiffness and the displacement vectors are presented in the rotating reference frame *XYZ*.

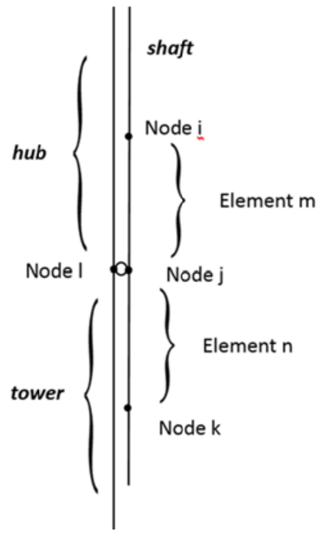

Fig. 6.7 The elements and nodes at the connection of the hub and shaft (at the bottom of hub)

Therefore, the nodal forces in element *m* and element *n* can be calculated by

$$\begin{bmatrix} \boldsymbol{f}_{mi} \\ \boldsymbol{f}_{mj} \end{bmatrix} = \boldsymbol{k}_m \begin{bmatrix} \boldsymbol{u}_i \\ \boldsymbol{u}_j \end{bmatrix} \tag{6.9a}$$

$$\begin{bmatrix} \boldsymbol{f}_{nj} \\ \boldsymbol{f}_{nk} \end{bmatrix} = \boldsymbol{k}_n \begin{bmatrix} \boldsymbol{u}_j \\ \boldsymbol{u}_k \end{bmatrix} \tag{6.9b}$$

where $\boldsymbol{f}_{mi}$ and $\boldsymbol{f}_{mj}$ are the nodal forces of node *i* and node *k* in element *n* respectively;

$\boldsymbol{f}_{nj}$ and $\boldsymbol{f}_{nk}$ are the nodal forces of node *i* and node *k* in element *n* respectively. According to the law of action-reaction, the reaction force $\boldsymbol{f}_{Rj}$ from the shaft is

$$\boldsymbol{f}_{Rj} = -(\boldsymbol{f}_{mj} + \boldsymbol{f}_{nj}) \tag{6.10}$$

The same method can be conducted on the connection at the top of hub. Therefore, the total reaction force from the shaft is known. It is worth noting that the force obtained from Equation (6.9) is presented in the rotating reference frame *XYZ*; Equation (6.2) can be used to obtain the reaction force $\boldsymbol{F}_{R_o}$ in the stationary frame $X_oY_oZ_o$. Now the responses of the tower can be calculated from Equation (6.8).

Because the tower is made of reinforced concrete, the equivalent Young's modulus is used in the FE simulation. Hence, the calculation of stresses of concrete and steel cannot use the equivalent Young's modulus directly. The strain must be calculated first by

$$\boldsymbol{\varepsilon}_T = \boldsymbol{B}_T \boldsymbol{u}_T \tag{6.11}$$

where $\boldsymbol{\varepsilon}_T$ is the strain vector of tower; and $\boldsymbol{B}_T$ is the geometric matrix of the tower (Bathe, 2006). The stress of concrete and steel can be obtained by

$$\boldsymbol{\sigma}_C = \boldsymbol{D}_C \boldsymbol{\varepsilon}_C \tag{6.12a}$$

$$\boldsymbol{\sigma}_S = \boldsymbol{D}_S \boldsymbol{\varepsilon}_T \tag{6.12b}$$

where D_C and D_S are the material matrix of concrete and steel respectively.

6.4 The Load Cases

As introduced in Chapter 5, the load cases of the VAWT are determined by the operation and external conditions as summarized in IEC61400-1(Commission, 2005). In Chapter 5, only the blade is studied and in this chapter, not only a single blade but also the whole VAWT are included. In accordance with Chapter 5, two situations are considered in this chapter: 1) the power production and normal turbulence wind condition (the operation wind speed condition) and 2) the extreme wind speed condition when the VAWT is parked. More details and the reasons of selecting these two situations can refer to Chapter 5. The fatigue analysis is conducted in the first situation and the ultimate strength analysis is conducted in the second situation.

In the operation wind speed condition, the VAWT is subjected to wind loads and inertial forces. The wind loads on the components of the VAWT (including the tower, the main arms, the upper and lower arms and the blades) can be simulated by the method proposed in Chapter 3. In this method, the influences of the wind profile, the turbulence and the interaction of different components are included. The inertial forces (including the centrifugal force and the Coriolis' force) are only applied on the rotor (including the blades, the upper and lower arms and the main arms).

In the extreme wind speed condition, because the VAWT is parked, only wind loads are applied on the VAWT. As the wind loads in the operation wind speed condition, the wind loads in the extreme wind speed condition can also be simulated by the method proposed in Chapter 3. Moreover, because the wind loads depend on the wind direction, the influence of the wind direction needs to be included. In the simulation, the wind direction is reflected by the azimuth angle as treated in Chapter 3 and Chapter 5.

6.5 The Fatigue Analysis

6.5.1 The overview of the fatigue analysis of the VAWT

The fatigue analysis should include the response of the VAWT in the operation wind speed range for a designated time (20 years in this study). Firstly, the rainflow counting method is applied to the stress time history, and the number of stress cycles in different stress range levels can be obtained. Then the number of cycle to failure of each stress range level can be estimated by S-N curve and the Goodman diagram is used to transfer the stress range with non-zero mean to the zero-mean stress range. Finally, the Palmgren-Miner's rule is used to evaluate the fatigue damage of the blade:

$$D = \sum_i \frac{n_i}{N_i} \tag{6.13}$$

where n_i is the cycle number of the equivalent zero-mean stress range $\sigma_{r,i}$ in a given time period; N_i is the number of cycle to failure at the stress range $\sigma_{r,i}$; and D is defined as the fatigue damage. Fatigue failure occurs when $D \geq 1$.

Obviously, it is impossible to simulate the stress time history in 20 years directly. As introduced in Chapter 5, the alternative method is to discretize the mean wind speed range into different wind speed bins and simulate the stress time history in a short term, 10 minutes for example, at the center of these bins. The fatigue damage in these bins for the short term is calculated and then extended to the fatigue damage in 20 years by the wind speed distribution.

6.5.2 S-N Curve and the Goodman diagram

The S-N curve for steel is determined by the GL rule, as shown in Equation (6.14a).

$$N = N_D \left(\frac{\Delta\sigma_D}{\Delta\sigma}\right)^3,\ N < 5\times10^6 \tag{6.14a}$$

$$N = N_D \left(\frac{\Delta\sigma_D}{\Delta\sigma}\right)^5,\ N \geq 5\times10^6 \tag{6.14b}$$

In which, $N_D = 5\times10^6$ and $\Delta\sigma_D$ is the stress range corresponding to N_D in the case of $R = -1$ where $R = \sigma_{\max}/\sigma_{\min}$; $\sigma_{\max}$ and $\sigma_{\min}$ are the maximum and minimum stress in a stress cycle; and $\Delta\sigma$ is the stress range corresponding to the case of zero-mean. The equivalent $\Delta\sigma$ of the stress range $\sigma_r = \sigma_{\max} - \sigma_{\min}$ with the mean stress $\bar{\sigma} = \frac{\sigma_{\max} + \sigma_{\min}}{2}$ can be obtained by the Goodman diagram introduced in Chapter 5. For steel, the ultimate tensile strength and the ultimate compressive strength is the same, thus the equation of the Goodman diagram can be written as

$$\Delta\sigma = \sigma_r (1 - \frac{|\bar{\sigma}|}{\sigma_s}) \tag{6.15}$$

where σ_s is the ultimate tensile strength (the absolute value of the ultimate compressive strength).

For the concrete tower, the S–N curve for concrete compression loading is given by DIN 1045-1 and EN 1992- 1-1 (de Normalisation, 1991; Normung, 2003). The S-N curve is written as Equation (6.16).

$$\lg n = 14 \frac{1 - S_{\max}}{\sqrt{1 - S_{\min} / S_{\max}}} \tag{6.16}$$

with

$$S_{\max} = \sigma_{ck,\max} / f_{ck,\mathrm{fat}}$$

$$S_{\min} = \sigma_{ck,\min} / f_{ck,\mathrm{fat}}$$

where

$\sigma_{ck,\max}$ is the magnitude of the maximum concrete compression stress;

$\sigma_{ck,\min}$ is the magnitude of the minimum concrete compression stress;

$f_{ck,\mathrm{fat}} = 0.85 f_{ck} (1 - f_{ck} / 250)$

where

f_{ck} is the characteristic compressive strength. In this study, C40 concrete is used then f_{ck} = 26.8MPa.

6.5.3 Wind speed distribution and wind speed bins

The annual mean wind speed distribution can be described by Weibull model, as shown in Equation (6.17)

$$f(u) = \frac{k}{\lambda}\left(\frac{u}{\lambda}\right)^{k-1} \exp\left[-\left(\frac{u}{\lambda}\right)^{k}\right] \tag{6.17}$$

where k is the shape parameter and λ is the scale parameter. For the site considered in this study, $k = 2.0$ and $\lambda = 8.1$.

In this study, the VAWT operates in the mean wind range from the cut-in wind speed to the cutout wind speed at a constant rotational speed of 2.1rad/s. For the VAWT taken into consideration in this study, the cut-in wind speed is 5m/s and the cutout wind speed is 21 m/s; when the mean wind speed is below 5m/s or over 21m/s, the VAWT is parked. In this study, the mean wind speed range is discretized into 8 wind speed bins and the centers of these bins are 6m/s, 8m/s, 10m/s, 12m/s, 14m/s, 16m/s, 18m/s and 20m/s.

6.5.4 The fatigue critical locations and fatigue analysis for steel components

In this section, the responses of the VAWT in the operation wind speed range are simulated and the fatigue analysis is conducted. Since the blade has been analyzed in Chapter 5, the shaft, the main arms, the upper and lower arms and the tower are focused in this chapter. In this subsection, the shaft, the main arms and the upper and lower arms which are made of steel are considered firstly.

The fatigue-critical locations are the positions suffering the largest fatigue damage during the service life. However, it is impossible to calculate the fatigue damage of all the positions of the VAWT. In Chapter 5, the fatigue-critical locations are figured out due to the simplicity of the blade structure. But the structure of the VAWT is complex and there are many different mode shapes with close natural frequencies, and stresses distribution in the components of VAWTs are complex during operation. It is difficult to figure out the fatigue critical locations by a simple way as Chapter 5.

In this case, a method to figure out the fatigue-critical locations is to consider the dominant mode shapes. As introduced in Section 6.4, the VAWT is subjected to wind loads and inertial force. Based on the following facts that 1) the main frequency of the load acting on the rotor is 1P (0.334Hz) and the main frequencies of the load acting on the tower are 1P (0.334Hz) and 3P (1.00Hz); 2) the energy of turbulent wind mainly concentrates in the low frequencies, say 0Hz – 1Hz; 3) the centrifugal force is time-invariant due to the constant rotational speed; 4) the Coriolis force which is determined by the rotation speed and vibration speed is small, an assumption can be drawn that the dominant mode shapes of the VAWT are the first four mode shapes (0.27Hz, 0.82Hz, 0.82Hz and 1.15Hz). The 1st mode is the torsion of shaft. In this mode, the shaft is in torsion; the main arms and the upper and lower arms are in horizontal bending. The shear stress (in-plane shear stress of the cross section) distribution of the shaft and the normal stress (normal to the cross section) of the main arm and the upper and lower arms are shown in Fig. 6.8. In the 1st mode, it can be seen that the largest shear stress occurs near the top of shaft; the largest normal stress occurs at the root of the main arm. The normal stresses of the upper and lower arm are generally smaller than that of the main arm. The 2nd and 3rd modes are the bending of shaft. In these two modes, the shaft and the main arm are in bending. The normal stresses of these components are shown in Fig. 6.9. It can be seen that the largest normal stress of shaft occurs at the top of shaft and the largest normal stress occurs at the root of main arm. The normal stresses of the upper and lower arm are still smaller than that of the main arm. The 4th mode of the VAWT is the vertical bending of arms and the deformation of shaft is small. Thus the normal stress distribution in the arms is shown in Fig. 6.10. It can be seen that the largest stress occurs at the root of main arm. The stresses of the upper and lower arm are still in a lower level than that of the main arm.

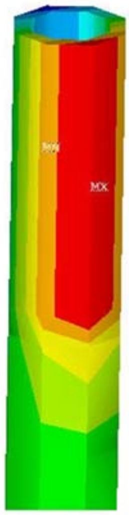

(a)

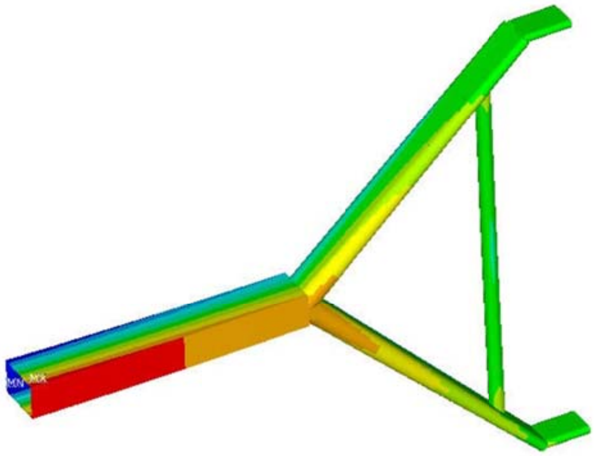

(b)

Fig. 6.8 The stresses distribution of the 1st mode. (a) shear stress of the shaft; (b) normal stress of the arms

(a)

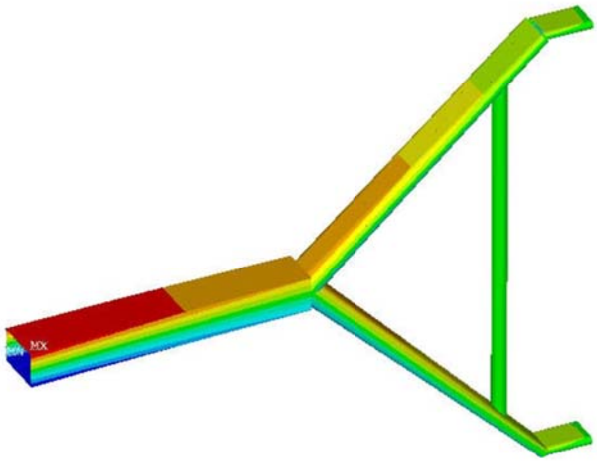

(b)

Fig. 6.9 The stresses distribution of the 2^{nd} and 3^{rd} modes. (a) normal stress of the shaft; (b) normal stress of the arms

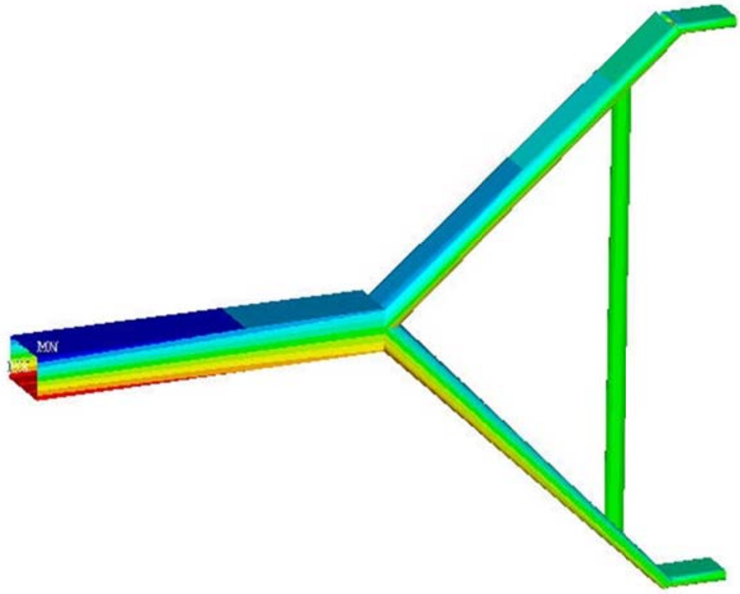

Fig. 6.10 The normal stress distribution in the arms of the 4th mode

Therefore, three critical section A, B and C of the main arm and the shaft are selected, which are shown in Fig. 6.11. The section A and the section B are two cross sections of main arm at two ends; the section A is at the root of the main arm and the section B is at the connection between the main arm and the upper and lower arms. The selection of the section B is to give a comparison to the fatigue damage in the section A. The section C is on the shaft at the height of the main arms. In the sections A and B, the normal stress due to vertical bending ($\sigma_{x,\mathrm{vA}}$ and $\sigma_{x,\mathrm{vB}}$) and the normal stress due to horizontal bending ($\sigma_{x,\mathrm{hA}}$ and $\sigma_{x,\mathrm{hB}}$) are extracted at the point A1, B1, A2 and B2 respectively as shown in Fig. 6.11 (a); two normal stresses due to bending of the shaft $\sigma_{x,\mathrm{C1}}$ and $\sigma_{x,\mathrm{C2}}$ in the section C are also obtained at the point C1 and C2 as shown in Fig. 6.11(b). Here, the subscript "x" means that direction of the stress is normal to the cross section.

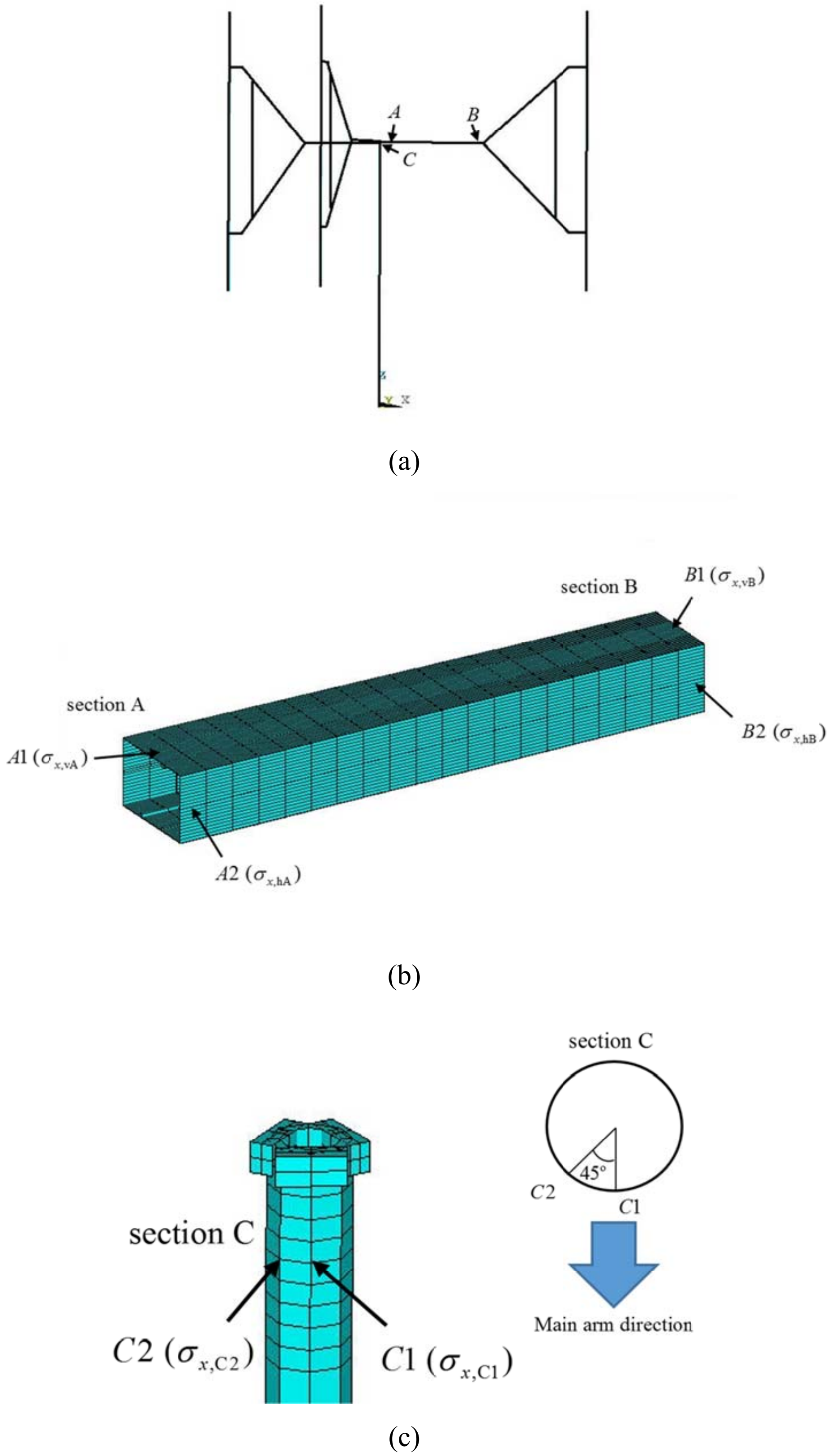

Fig. 6.11 The positions of the output stresses. (a) the positions of section A, B and C; (b) the output positions in the section A and B; (c) the output positions in the section C.

Under the mean wind speeds of the center of each bin (6m/s, 8m/s, 10m/s, 12m/s, 14m/s, 16m/s, 18m/s and 20m/s), the stress time histories at the fatigue-critical locations are shown in Fig. 6.12. Firstly, it can be seen that with the increasing of the wind speed, the amplitudes of $\sigma_{x,\mathrm{vA}}$, $\sigma_{x,\mathrm{vB}}$, $\sigma_{x,\mathrm{hA}}$, $\sigma_{x,\mathrm{hB}}$, $\sigma_{x,\mathrm{C1}}$ and $\sigma_{x,\mathrm{C2}}$ are all enlarged. Secondly, the amplitude of $\sigma_{x,\mathrm{vA}}$ is larger than other stresses.

When the 10 min stress time histories at A1, A2, B1, B2, C1 and C2 under different mean wind speeds are obtained, the cycle numbers of different stress range and mean value are obtained by the rain-flow method as introduced in Chapter 5. These numbers of cycle are in 10 minutes. Divided by 600s (10 min) and multiplying the time length of the mean wind speed, these numbers can be extended to the numbers in 20 years. The time length of each mean wind speed in 20 years can be calculated by the wind speed distribution function as introduced in Chapter 5.

Using the S-N curve, the fatigue damage in 20 years at these 6 typical points in the section A, B and C are listed in Table. 3. From the fatigue damages of these 6 typical points, it can be seen that the largest fatigue damage 0.3476 occurs at the root of main arm, caused by the vertical bending normal stress $\sigma_{x,\mathrm{vA}}$ of main arm. The second largest fatigue damage 0.2687 occurs at the root of main arm, which is caused by the horizontal bending normal stress of main arm. The shaft has least fatigue damage than other components of the VAWT. Therefore, the fatigue life of the typical VAWT considered in this study is dominated by the fatigue damage at the root of main arms. It is worth noting that although the fatigue damage of shaft is small, the fatigue in this location should not be ignored because the influences of misalignment of the rotor and eccentric mass are not considered in this study.

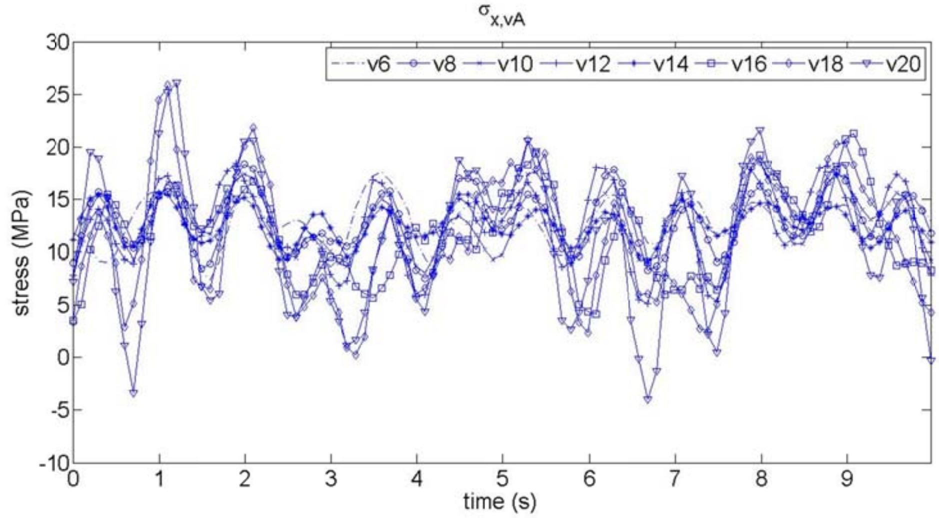

σx,vA
v6 v8 v10 v12 v14 v16 v18 v20
stress (MPa)
time (s)

(a)

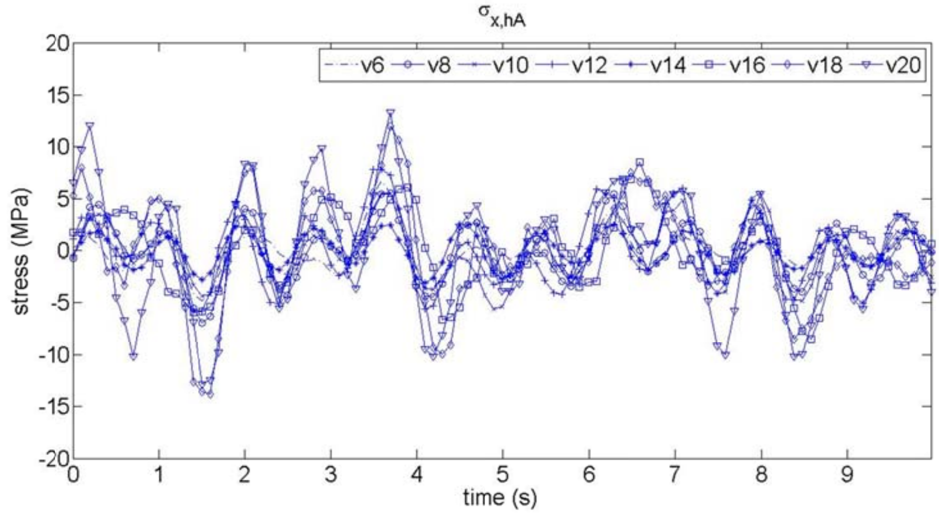

σx,hA
v6 v8 v10 v12 v14 v16 v18 v20
stress (MPa)
time (s)

(b)

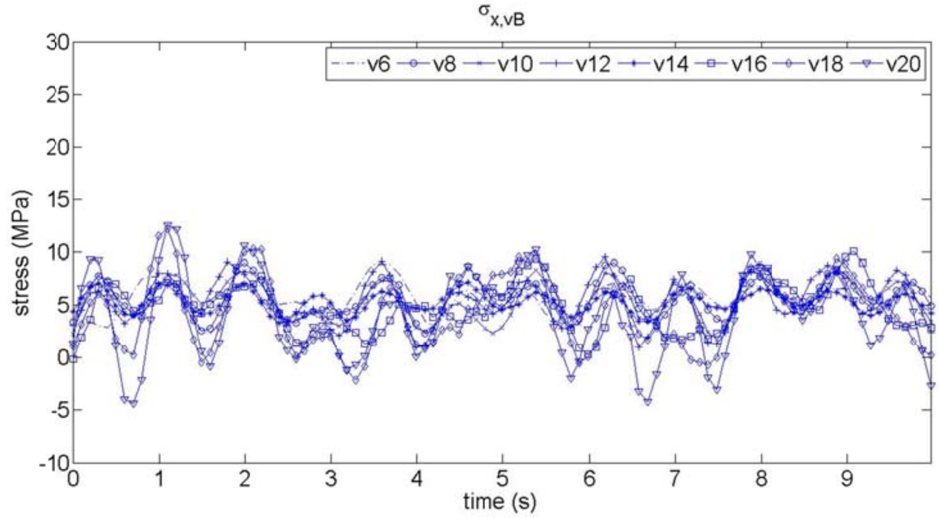

σx,vB
v6 v8 v10 v12 v14 v16 v18 v20
stress (MPa)
time (s)

(c)

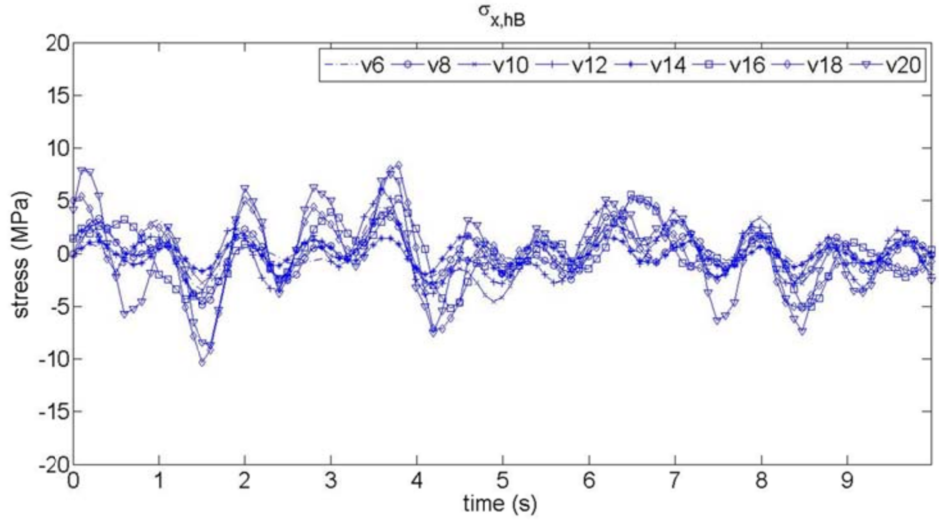

$\sigma_{x,hB}$
v6
v8
v10
v12
v14
v16
v18
v20
stress (MPa)
time (s)

(d)

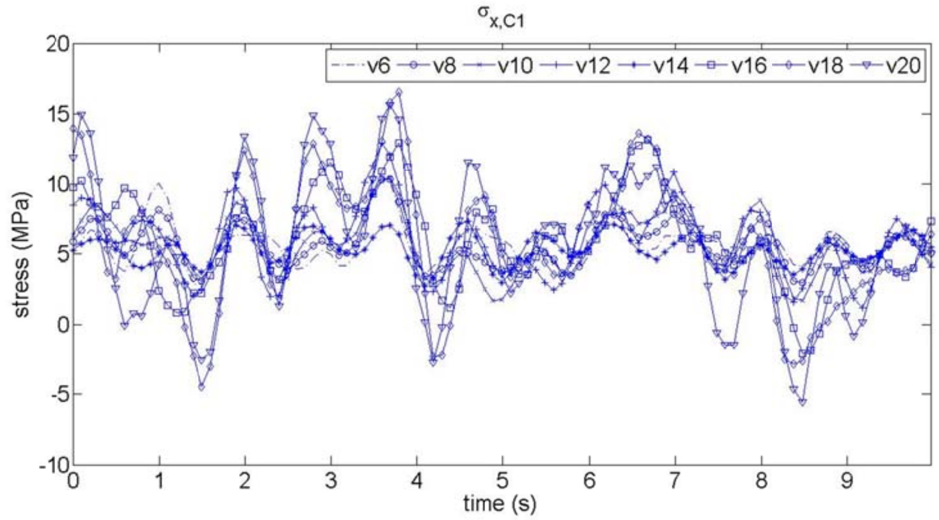

$\sigma_{x,C1}$
v6
v8
v10
v12
v14
v16
v18
v20
stress (MPa)
time (s)

(e)

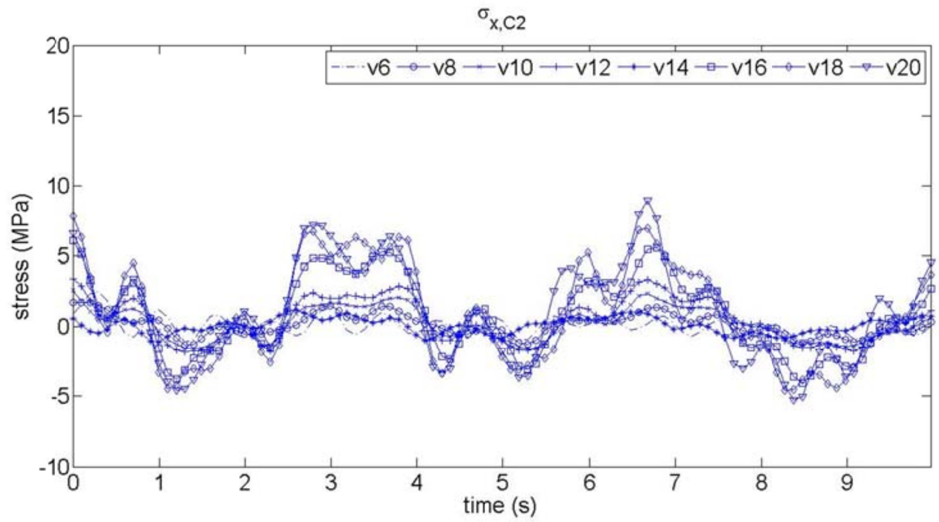

$\sigma_{x,C2}$
v6
v8
v10
v12
v14
v16
v18
v20
stress (MPa)
time (s)

(f)

Fig. 6.12 the simulated time histories of the stresses. (a) $\sigma_{x,\mathrm{vA}}$; (b) $\sigma_{x,\mathrm{hA}}$; (c) $\sigma_{x,\mathrm{vB}}$; (d) $\sigma_{x,\mathrm{hB}}$; (e) $\sigma_{x,\mathrm{C1}}$; (f) $\sigma_{x,\mathrm{C2}}$.

Table 6.3 Fatigue damage D of the fatigue-critical locations in 20 years

	$\sigma_{x,\mathrm{vA}}$	$\sigma_{x,\mathrm{hA}}$	$\sigma_{x,\mathrm{vB}}$	$\sigma_{x,\mathrm{hB}}$	$\sigma_{x,\mathrm{C1}}$	$\sigma_{x,\mathrm{C2}}$
Fatigue Damage D	0.3476	0.2687	0.0099	0.0088	0.0179	0.6567e-4

6.5.5 The fatigue critical locations and fatigue analysis for the concrete tower

The forces on the tower are the gravity force, the wind load and the reaction forces from the shaft. The gravity force is the uniform volume force; the wind load is distributed along the tower and the direction of the wind load is horizontal; the forces from the shaft provided by the rotor are acted at the top of the tower. Under these forces, the largest stress and stress range appear at the bottom of the tower which is the fatigue-critical location. Therefore, the cyclic stresses at the bottom of the tower are considered. It is ideal that the fatigue analysis is conducted on both concrete and steel bar. But the problem is the details of the reinforced steel bars are not available, so in this study, the fatigue analysis is focus on the concrete tower.

The section D at the bottom of tower is selected, which is shown in Fig. 6.13(a). In the section D, the stresses ($\sigma_{Z_o,\mathrm{D1}}$ and $\sigma_{Z_o,\mathrm{D2}}$) are extracted at the point D1 and D2 as shown in Fig. 6.13(b). As introduced in Section 6.3.1, the response of tower is calculated in the static reference frame $X_oY_oZ_o$. The stresses $\sigma_{Z_o,\mathrm{D1}}$ and $\sigma_{Z_o,\mathrm{D2}}$ are obtained in this reference. The subscribe "Z_o" means that the stresses $\sigma_{Z_o,\mathrm{D1}}$ and $\sigma_{Z_o,\mathrm{D2}}$ are along the tower (Z_o-axis). The simulated time histories of $\sigma_{Z_o,\mathrm{D1}}$ and $\sigma_{Z_o,\mathrm{D2}}$ at the mean wind speed of 14 m/s are shown in Fig. 6.14; the time histories of $\sigma_{Z_o,\mathrm{D1}}$ and $\sigma_{Z_o,\mathrm{D2}}$ at other mean wind speeds are given in Appendix C. In Fig. 6.14, the blue line is the time history of $\sigma_{Z_o,\mathrm{D1}}$ and the red line is the time history of $\sigma_{Z_o,\mathrm{D2}}$. It can be seen that the mean values of these stresses are different; the mean of $\sigma_{Z_o,\mathrm{D1}}$ is larger than that of $\sigma_{Z_o,\mathrm{D2}}$. One component of the mean stress is due to the sole weight of the wind turbine. The difference in the mean values of $\sigma_{Z_o,\mathrm{D1}}$ and $\sigma_{Z_o,\mathrm{D2}}$ is caused by the wind direction. D1 is at the leeward side of the tower, and thus the bending moment caused by the mean wind effect will induce an extra stress component to the mean value of $\sigma_{Z_o,\mathrm{D1}}$; because the bending moment caused by the mean wind speed will not influence $\sigma_{Z_o,\mathrm{D2}}$, the mean value of $\sigma_{Z_o,\mathrm{D2}}$ is smaller than $\sigma_{Z_o,\mathrm{D1}}$.

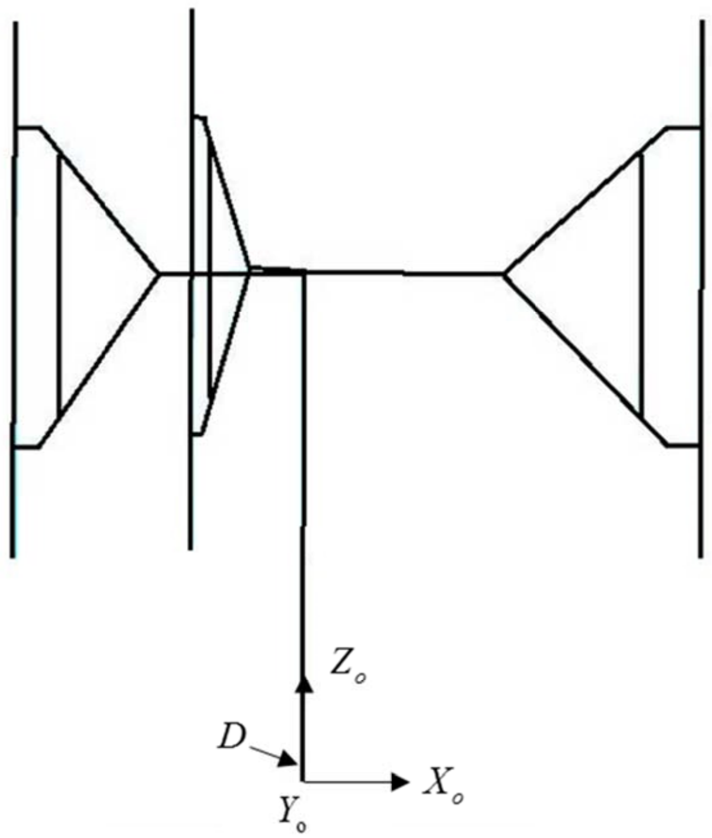

(a)

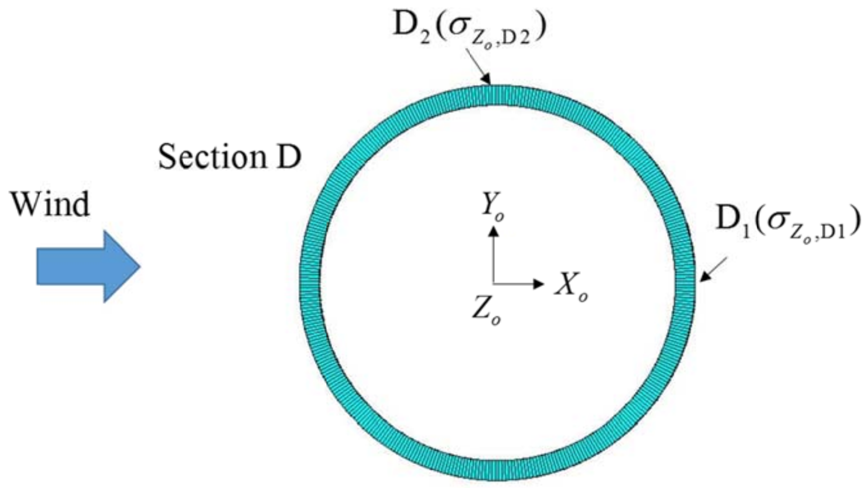

(b)

Fig. 6.13 The position of the output stresses. (a) the positions of cross section D; (b) the output positions in the cross section D;

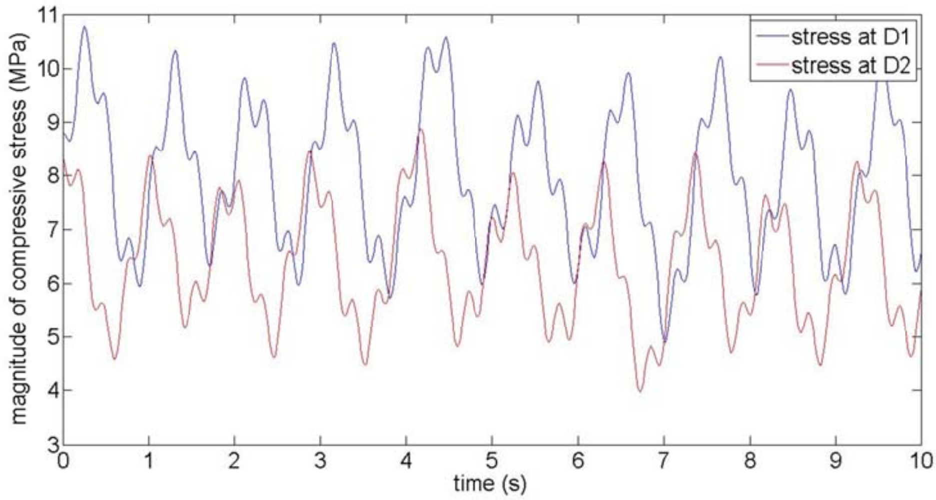

Fig. 6.14 $\sigma_{Z_o,\mathrm{D1}}$ and $\sigma_{Z_o,\mathrm{D2}}$

Using the Miner's rule and the S-N curve of concrete given by Equation (6.16) in Section 6.5.2, the fatigue damages in 20 years of D1 and D2 are listed in Table 6.4. It can be found that the fatigue damage at D1 is larger than that at D2, which is caused by the mean value of compressive stress. As mentioned above, the mean stress at D1 is larger than that at D2. Although the stress ranges of $\sigma_{Z_o,\mathrm{D1}}$ and $\sigma_{Z_o,\mathrm{D2}}$ are the same, a larger mean stress would reduce the cycle number to failure thus increases the fatigue damage.

Table 6.4 Fatigue damage of D_1 and D_2 in 20 years

	D_1	D_2
Fatigue damage	0.1017	0.0029

6.6 The Ultimate Strength Analysis

6.6.1 The overview of the ultimate strength analysis

In the extreme wind speed condition, wind turbines must be parked, because in such a high wind speed, the rotor is prone to the danger of flight off. Although wind turbines would also vibrate in this condition, the probability of this case is small and hence the fatigue damage caused in this condition is small compared with those in the operation wind speed condition; the fatigue analysis can be neglected. Therefore, only the ultimate strength analysis is needed to be conducted in the extreme wind speed.

In this study, the von Mises stress is used to evaluate the failure-critical locations. The von Mises stress is corresponding to the von Mises yield criterion which suggests that the yielding of materials occurs when the second deviatoric stress invariant J_2 reaches a critical value. The definition of J_2 is

$$J_2 = \frac{1}{6}[(\sigma_1 - \sigma_2)^2 + (\sigma_2 - \sigma_3)^2 + (\sigma_1 - \sigma_3)^2] \tag{6.18}$$

where σ_1, σ_2 and σ_3 are the 1st, 2nd and 3rd principle stress respectively. The von Mises yield criterion is applied best to ductile materials, such as steel. The von Mises stress is defined to predict the yielding, the expression of which is

$$\sigma_v = \sqrt{\frac{(\sigma_1 - \sigma_2)^2 + (\sigma_2 - \sigma_3)^2 + (\sigma_1 - \sigma_3)^2}{2}} \tag{6.19}$$

As mentioned in Section 6.3, because the VAWT is parked, the wind direction has the influence on the magnitude of the Von Mises stress at the failure-critical location. Hence the factor of wind direction should be included in the analysis.

6.6.2 The wind load

In the extreme wind condition, the VAWT is parked and the wind direction has an influence on the wind load. As introduced in Chapter 3, when the wind direction is fixed in the simulation, the azimuth angle of the rotor can represent the wind direction. In accordance to Chapter 3, 4 azimuth angles are considered in this study: 0^o, 30^o, 60^o, 90^o. (Different from Chapter 5, because only a blade is considered in Chapter 5 and the whole VAWT is included. The azimuth angle 120^o coincides with 0^o).

The aerodynamic forces used in this section are given in Chapter 3 according to the requirement of IEC61400-1.

6.6.3 The failure critical locations and the ultimate strength analysis

Because the blade has been analyzed in Chapter 5, only the arms and the shaft are focused in this section. Through comparison of the von Mises stress at each azimuth angle, the locations of large von Mises stress in each component coincide with the fatigue-critical locations. Thus, the von Mises stresses at A1, A2, B1, B2, C1, C2, D1 and D2 are considered. The detail locations of these points are shown in Fig. 6.11 and Fig. 6.13.

The von Mises stresses at these locations are shown in Fig. 6.15. The von Mises stresses vary with the azimuth angle. For the main arm, it can be seen that the largest stress appear at the 60^o in the front wind side and 240^o in the back wind side. And $\sigma_{\mathrm{v,vA}}$ at A1 and $\sigma_{\mathrm{v},vB}$ at B1 caused by the vertical bending are larger than the stresses $\sigma_{\mathrm{v,hA}}$ at A2 and $\sigma_{\mathrm{v,hB}}$ at B2 caused by the horizontal bending. For the von Mises stresses $\sigma_{\mathrm{v,C1}}$ and

$\sigma_{v,C2}$ of the shaft, there are three peak stresses in a cycle due to the three-blade structure and the peaks occur at the azimuth angle 30°, 150° and 270°. For von Mises stresses $\sigma_{v,D1}$ and $\sigma_{v,D2}$ of the tower, there are also three peeks in a cycle. It can be seen that the peaks of $\sigma_{v,D1}$ appear at the azimuth angles of 60°, 180° and 300°; the peaks of $\sigma_{v,D2}$ appear at the azimuth angles of 30°, 150° and 270°. However, $\sigma_{v,D2}$ is much smaller than $\sigma_{v,D1}$ due to the influence of the mean wind direction, hence, the critical failure location of the tower is dominated by $\sigma_{v,D1}$. Therefore, in the extreme wind speed condition, the dangerous azimuth angles are 60° and 240° for main arms; the dangerous azimuth angles of the shaft are 30°, 150° and 270°; the dangerous azimuth angles of the tower are 60°, 180° and 300°.

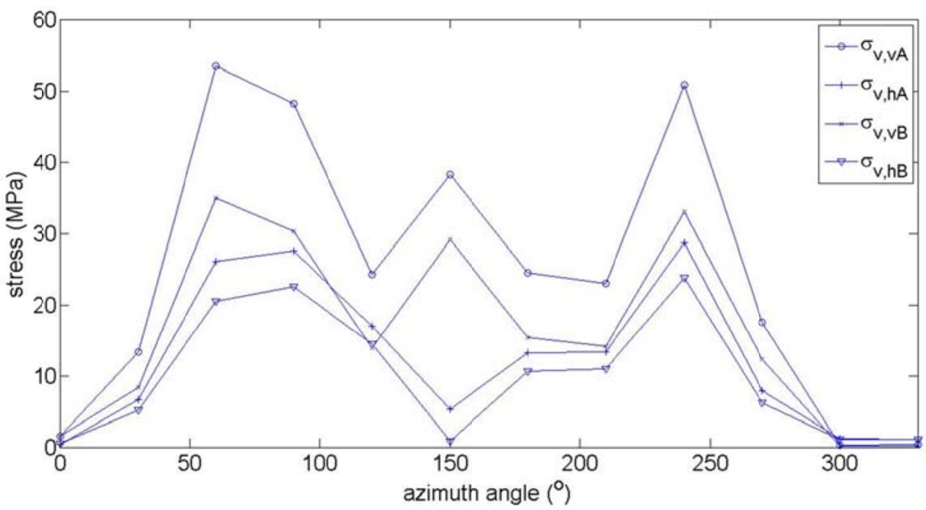

(a)

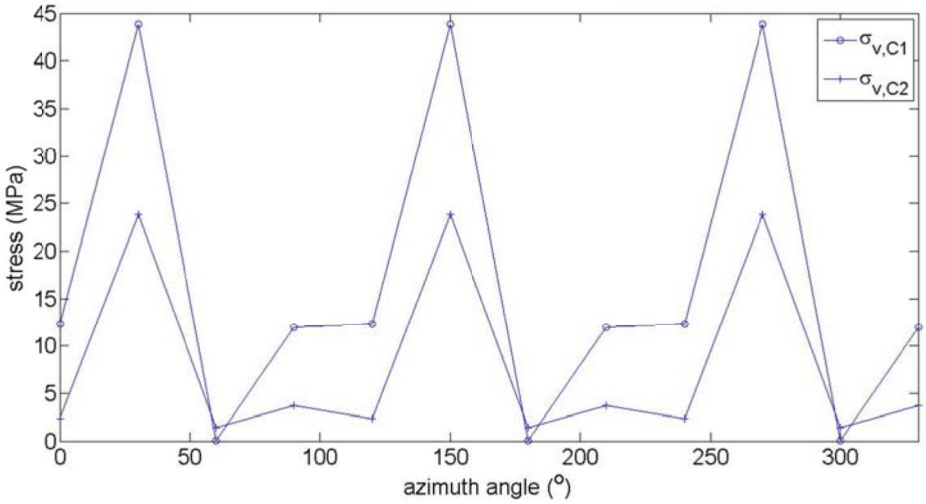

(b)

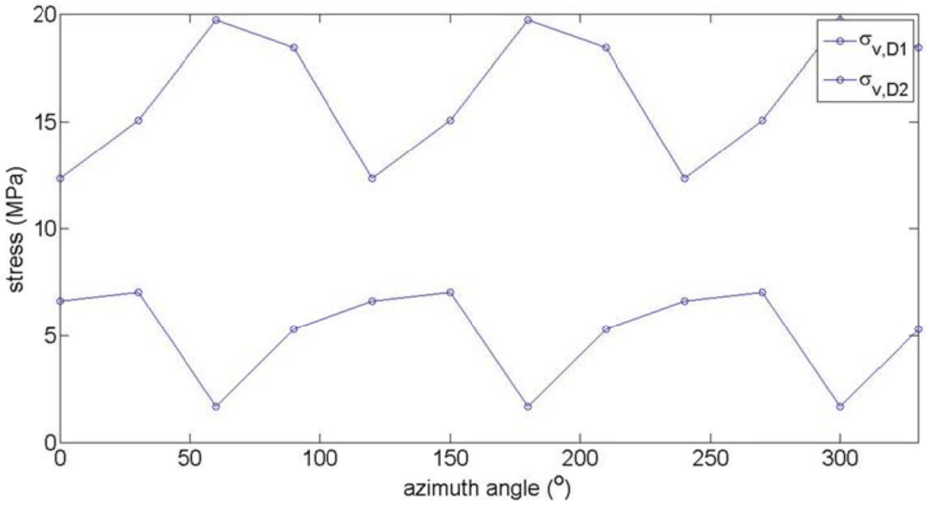

(c)

Fig. 6.15 The von Mises stresses. (a) at A1, A2, B1 ande B2; (b) at C1 and C2; (c) at D1 and D2

6.7 Summary

A framework for fatigue and ultimate strength analysis of VAWTs was proposed in this chapter. A straight-bladed VAWT was taken for example. Since blades had been analyzed in Chapter 5, a FE model of the VAWT was established by ANSYS element beam188 and the modal analysis was conducted. To eliminate the rigid motion of the VAWT and conduct the analysis conveniently, the rotating frame method was used and the VAWT could be regarded as a structure in the rotating frame which rotates at the same speed of the rotor. However, the response of the tower cannot be obtained directly. A two-step calculation scheme was thus proposed to calculate the response of the tower. The first step was to solve the dynamic equation of the VAWT in the rotating frame. In the second step, the reaction forces from the rotor were acted on the tower so that the analysis of tower could be decoupled from the rotor. Then the dynamic equation of the tower was calculated in the stationary reference frame.

Based on the FE model and the rotating frame method, the fatigue analysis was then conducted. The fatigue critical locations of the rotor were figured out. The largest fatigue damage occurs at the root of main arms. Although the fatigue damage of shaft was small for this typical VAWT, the fatigue of shaft could not be ignored because the misalignment of the rotor and eccentric mass were not considered. The fatigue critical location of the tower was at the bottom and the fatigue damages of the tower were calculated. It was found that a larger fatigue damage occurs in the leeward side of the tower.

The ultimate strength analysis of the rotor and tower were conducted. In the extreme wind speed, the VAWT was locked. The influence of wind direction was also considered and the wind direction can be replaced by the azimuth angle in the analysis. For the rotor, the strength failure critical locations were the roots of main arm and the shaft. The dangerous azimuth angles of the main arm were 60^o and 240^o; the dangerous azimuth angles of the shaft were 30^o, 150^o and 270^o. For the tower, the fatigue critical location was at the bottom and in the leeward side. The dangerous azimuth angles were 30^o, 150^o and 270^o.

Because the frameworks proposed in Chapter 5 and this chapter have not been verified yet, the field measurement and validation are conducted in Chapter 7. The model updating of the FE model used in this chapter is also introduced in Chapter 7.

CHAPTER 7

MODEL UPDATING AND VALIDATION BY FIELD MEASUREMENT

7.1 Introduction

A wind load simulation method is presented in Chapter 3 and based on the simulated wind load, the frameworks of fatigue and ultimate strength analysis of blades and VAWTs are conducted in Chapter 5 and Chapter 6 respectively. However, these frameworks have not been validated yet. In this regard, the field measurement shall be conducted and the measurement data have to be analyzed so that the dynamic characteristics of VAWT can be obtained to update the FE model and the comparisons between the measured responses and the simulated ones can be carried out to verify the proposed frameworks. Therefore, it is important to conduct field measurements for VAWTs.

The Hopewell Wind Power Limited of Hong Kong established a 288kW straight-bladed VAWT in Guangdong Province, China. The details of the VAWT can refer to the introduction of Chapter 3. To evaluate the performance of the turbine, the Hopewell Wind Power Limited sought for the help from our research group to conduct field measurements which I was involved in. A measured system was designed for this VAWT and field tests were conducted intermittently from February, 2012 to May, 2012.

In this chapter, the introduction to the field measurements of a straight-bladed VAWT is given. The field measurements are aimed at validating the frameworks proposed in Chapter 5 and Chapter 6. The field test was in the help of the Hopewell Wind Power Limited of Hong Kong. The field measurement system is introduced first. Based on this system, the wind speed and direction and the responses of different components, such as shaft, main arm, upper arm and blade, were recorded. Using these data, the natural frequencies of the VAWT are identified. Based on the measured data, model updating is also conducted for the FE model used in Chapter 6. Finally, the measured results are used to compare with the results of simulation in the frequency domain.

7.2 Field Measurements

7.2.1 The measurement set-up

The measurement set-up is introduced first. The objectives of the field measurements were to offer the data for model updating and more importantly, to validate the proposed frameworks for fatigue and ultimate strength analyses. Hence, the sensors should record the wind condition, the rotational speed and the responses of the VAWT to identify the first several natural frequencies and to monitor the local responses (such as strains) at the concerned locations according to the analyses of Chapter 5 and Chapter 6. Considering these objectives, in this field measurement, one anemometer, one laser displacement sensor, two accelerometers and three resistance strain gauge were installed. The placement of these sensors should fulfil the aforementioned requirements.

The anemometer was installed at the height of 10m above the ground. The location of the anemometer and the wind rose map are shown in Fig. 7.1. It can be seen that the prevailing wind direction was the northeast and the second prevailing wind direction was the southeast. Because there were ponds in the north east of the VAWT and woods near the coastal, the anemometer was finally located in the southeast of the VAWT, 70 meters away from the wind turbine. In this regard, 2 channels were required.

The rotational speed measurement system is shown in Fig. 7.2. A special gear wheel with 12 teeth was installed on the shaft and rotated together with the rotor. Three teeth of the gear wheel, corresponding to the three blades, had different length with the others. A laser displacement sensor was installed on the tower to record the azimuth angle of the gear wheel. So, the rotation speed of the rotor could be measured and 1 channel was required for this purpose.

Fig. 7.1 Locations of the VAWT and the wind mast

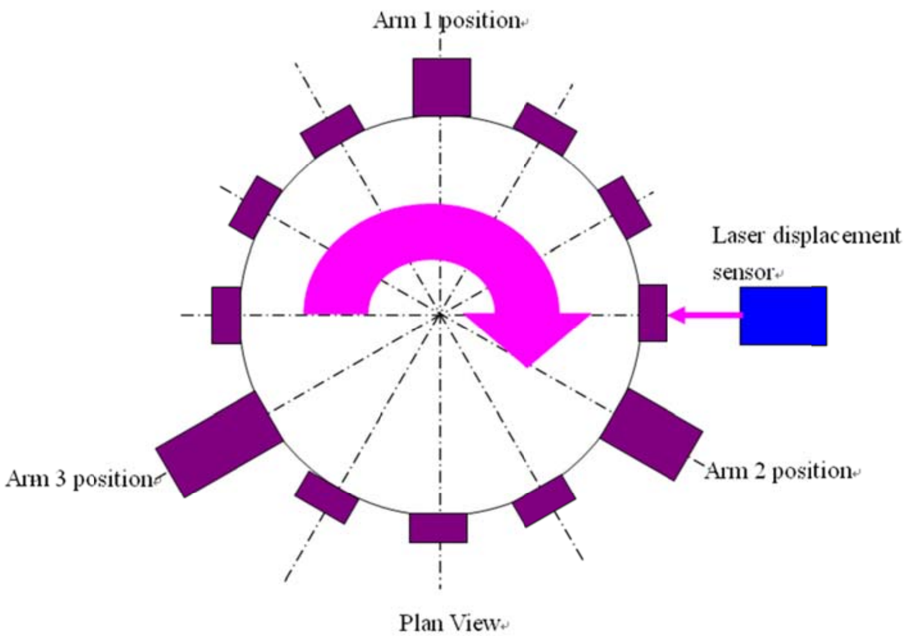

Fig. 7.2 Rotational speed measurement

The placement of sensors in the VAWT must be able to identify the first several natural frequencies. Based on the preliminary numerical analysis, the first few mode shapes are the torsion and bending of the shaft, the vertical and horizontal bending of the main arms, the torsion of the main arms and the bending of the blades. The sensors must be installed in these components and be able to capture all these deformations. The details are introduced below.

According to the analysis of Chapter 5, the critical damage locations of the blade are near the supports, hence a resistance strain gauge was installed at 500mm below the upper support of a blade. The detail is shown in Fig. 7.3 (a). In this measurement, 1 channel was required. Similarly, based on the analysis of Chapter 6, the locations of potential damages are the shaft and the roots of main arms. Resistance strain gauges were installed at these positions; and the bending strain of the shaft and the vertical bending strain of the main arm were measured. The details are shown in Fig. 7.3 (b). 2 channels were required for the measurement of strain of the shaft and 1 channel for the strain of main arm. Besides the responses of the components with potential damages, the deformations of the arms are also needed to monitor in order to evaluate the performance of the VAWT. So, two uniaxial accelerometers are installed, one at the end of a main arm measuring the vertical acceleration A_v and the other at end of the upper arm measuring the horizontal acceleration A_t. The details are shown in Fig. 7.3 (c). 2 channels are required.

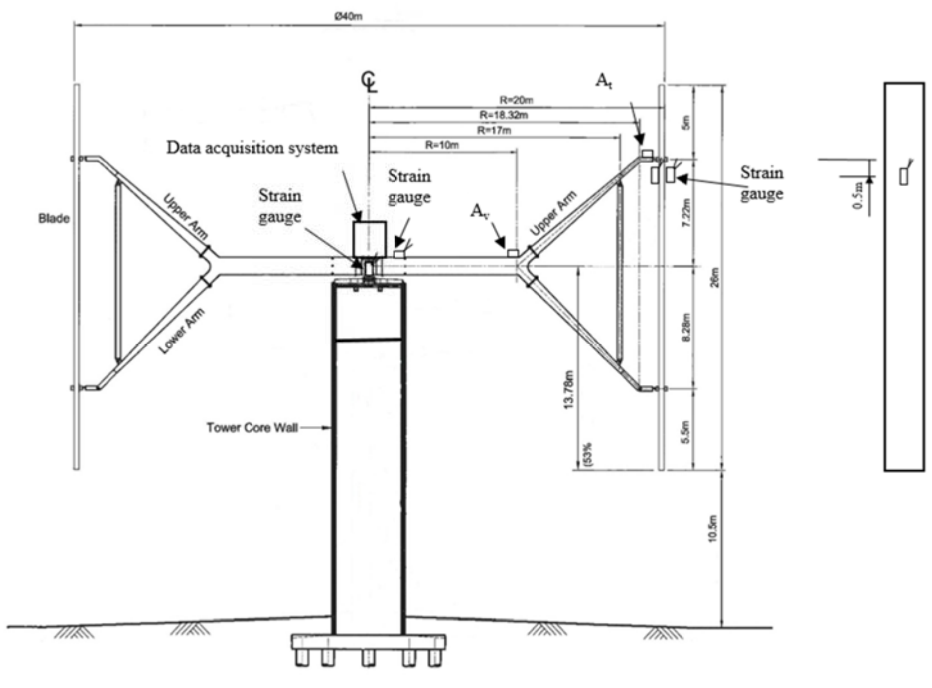

(a)

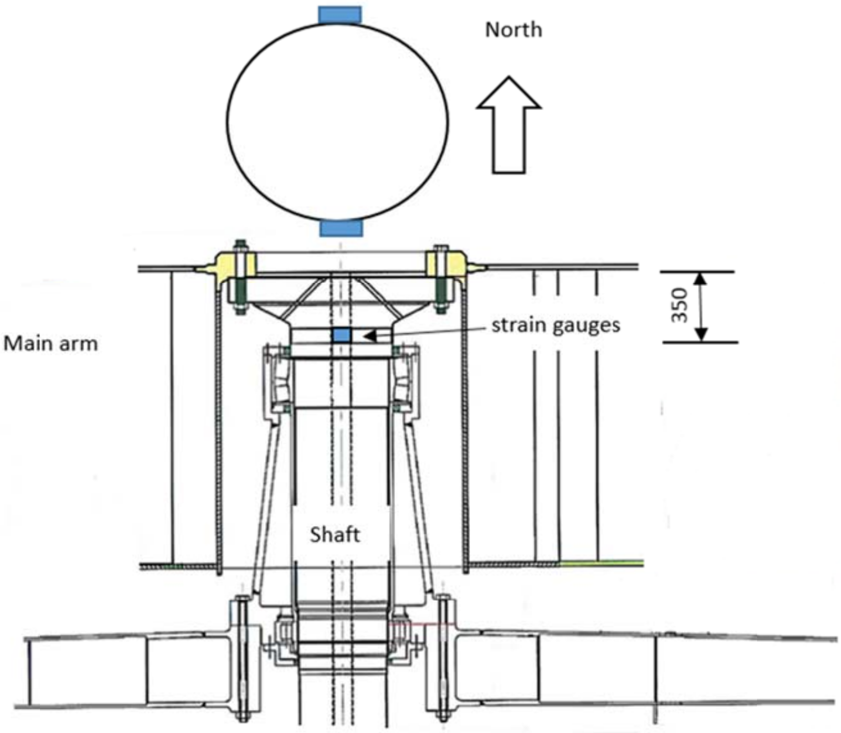

(b)

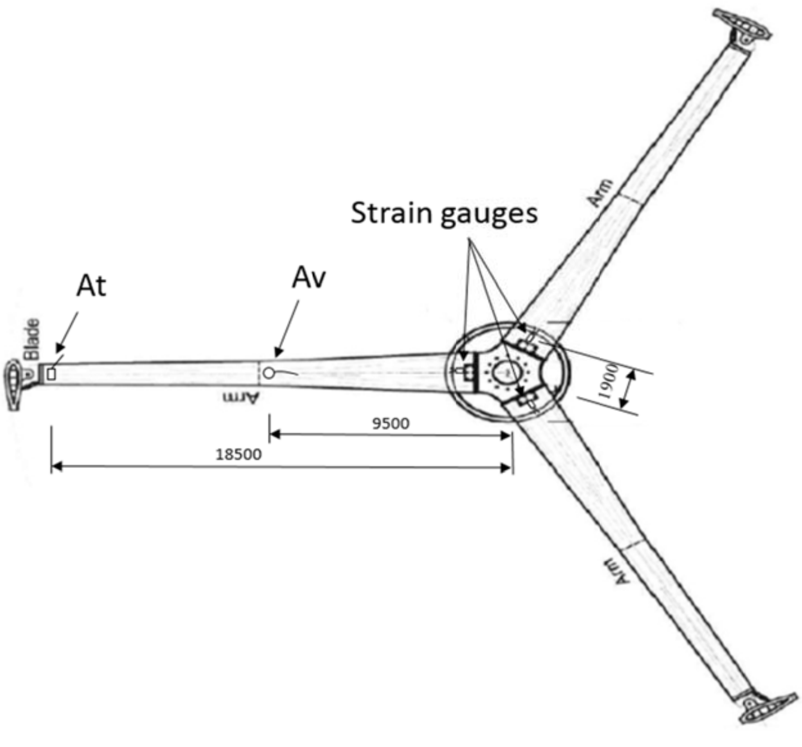

(c)

Fig. 7.3 Sensor placement. (a) overview of the VAWT; (b) strain gauges on the shaft;

(c) accelerometers on the arm.

(a)

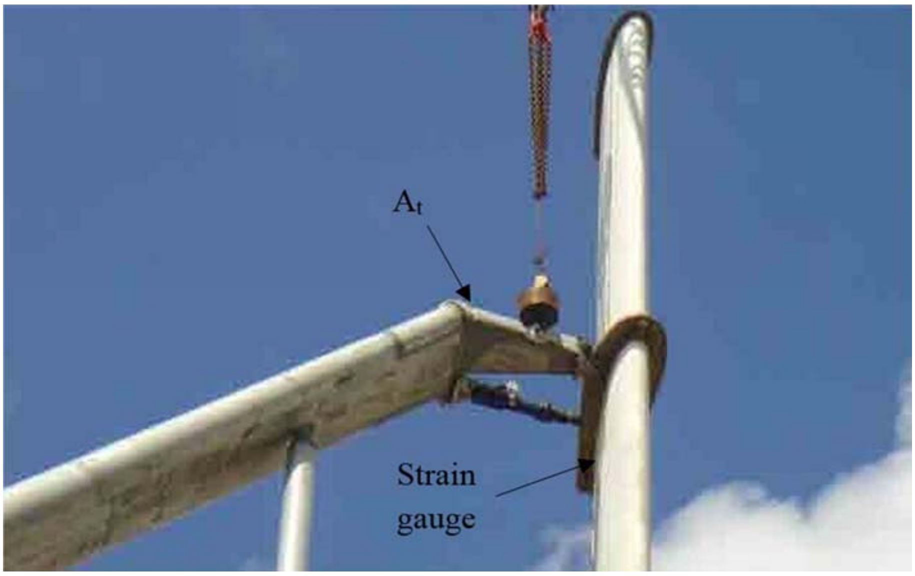

(b)

Fig. 7.4 Pictures of the VAWT and the locations of the sensors. (a) tower and the main arm; (b) upper arm

The pictures of the VAWT during the construction are shown in Fig. 7.4. Two data acquisition systems were used, one for the sensors rotating with the rotor and the other for the stationary sensors. The schematic diagrams of data acquisition systems are shown in Fig. 7.5. The sampling frequency of the acquisition system for the rotational part is 25Hz and the sampling frequency of the acquisition system for the stationary part is 100Hz.

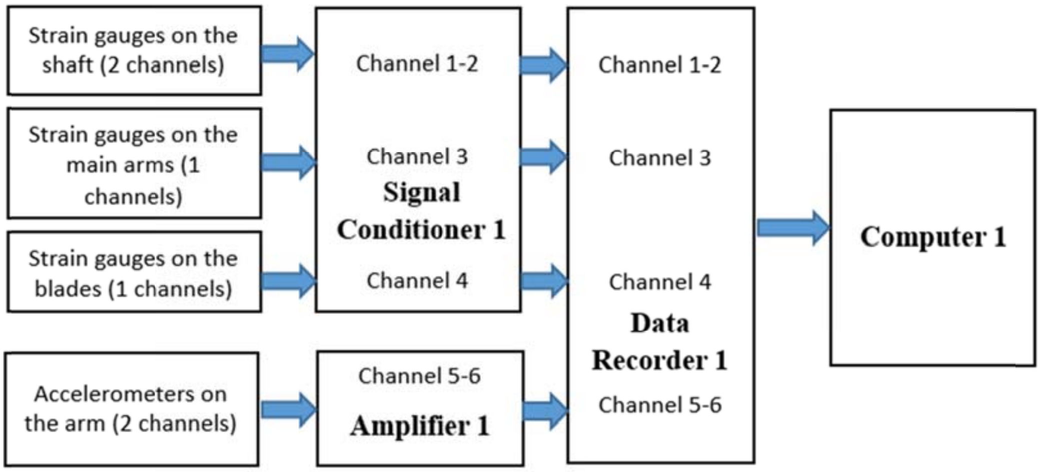

(a)

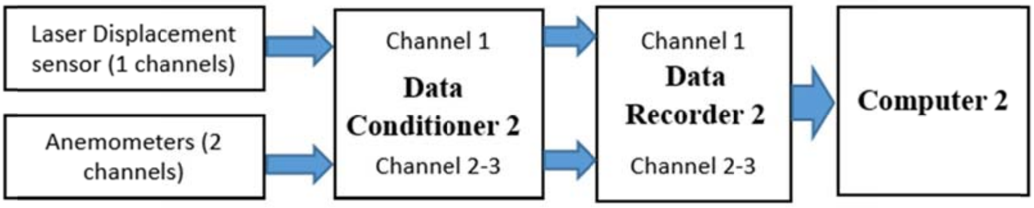

(b)

Fig. 7.5 Data acquisition system. (a) for the rotational part; (b) for the stationary part.

7.2.2 Measurement data

Based on the measurement system introduced above, the field tests were conducted. Three typical cases are presented in this subsection to show the influences of wind speed and rotational speed on the measured results. The data of Case **1** were recorded at March 15, 2012; the data of Case 2 were recorded at April 1, 2012; the data of Case 3 were recorded at March 1, 2012. The time histories in 60 minutes of each case are selected and analyzed in this study.

The rotational speeds of the three cases are listed in Table 7.1. In Case 1, the VAWT is locked; the VAWT was rotated at the rotational speed of 0.57rad/s in Case 2 and at the rotational speed of 0.67rad/s in Case 3. The measured wind speeds are shown in Fig. 7.6. The mean speeds of the three cases are listed in Table 7.2. It can be seen that Case 2 has the largest wind speed and Case 1 has the smallest wind speed.

Table 7.1 Rotational speeds of the three cases

	Case 1	Case 2	Case 3
Rotational Speed (rad/s)	0	0.57	0.67

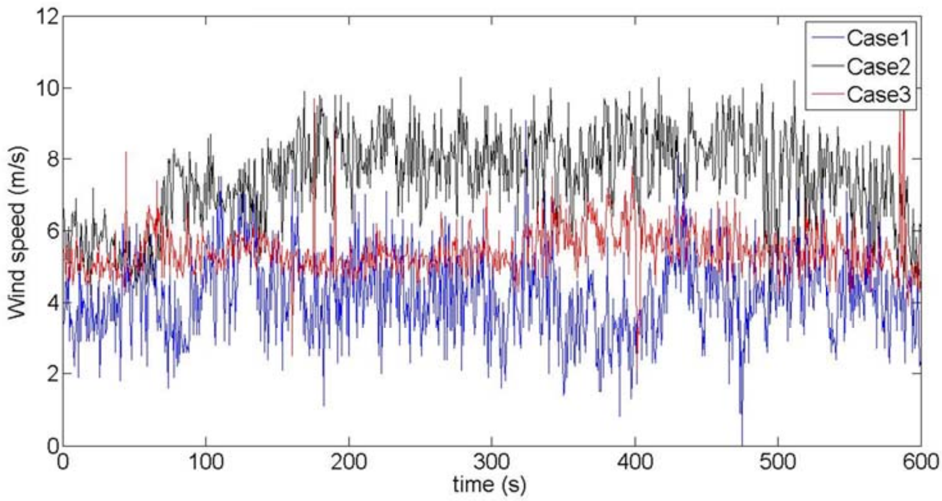

Fig. 7.6 Wind speeds of the cases

Table 7.2 Mean wind speed

	Case 1	Case 2	Case 3
Mean Wind Speed (m/s)	3.19	8.42	4.68

Under the operation and wind conditions of Case 1, Case 2 and Case 3, the strain of the blade, the tangential acceleration of the upper arm, the vertical acceleration of the main arm, the bending strain of the main arm and the bending strain of the shaft were measured. The time histories of these responses are shown in Fig. 7.7. Fig. 7.7 (a) shows the time histories of strain of the blade. In this figure, it can be seen that the cycles due to the rotation of the rotor are clear. The strain in Case 2 has the largest amplitude because of the higher wind speed. There are no obvious cycles which can be observed from the strain in Case 1, for the rotational speed of the turbine in Case 1 is zero. Compared with the strain in Case 2, the strain in Case 3 has smaller amplitude due to the lower wind speed. The cycle of strain in Case 2 is longer than that in Case 3 because the rotational speed (0.57rad/s) in Case 2 is smaller than 0.64rad/s in Case 3. Fig. 7.7 (b) shows the time histories of tangential acceleration of the upper arm, which are more fluctuating than the strain of the blade. The cycles due to rotation are not as clear as the strain of blade but the cycles of higher frequency can be observed in this figure. Case 2 also has the largest amplitude because of the higher wind speed. Similar phenomena can also be found in other responses as shown in Fig. 7.7 (c) - Fig. 7.7 (e). Fig. 7.7 (c) shows the time histories of vertical acceleration of the main arm; Fig. 7.7 (d) shows the time histories of bending strain of the main arm; Fig. 7.7 (e) shows the time histories of bending strain of the shaft. The amplitudes of responses of Case 2 are larger than those of Case 1 and Case 3 because of the larger wind speed; high frequency cycles can be observed in these figures.

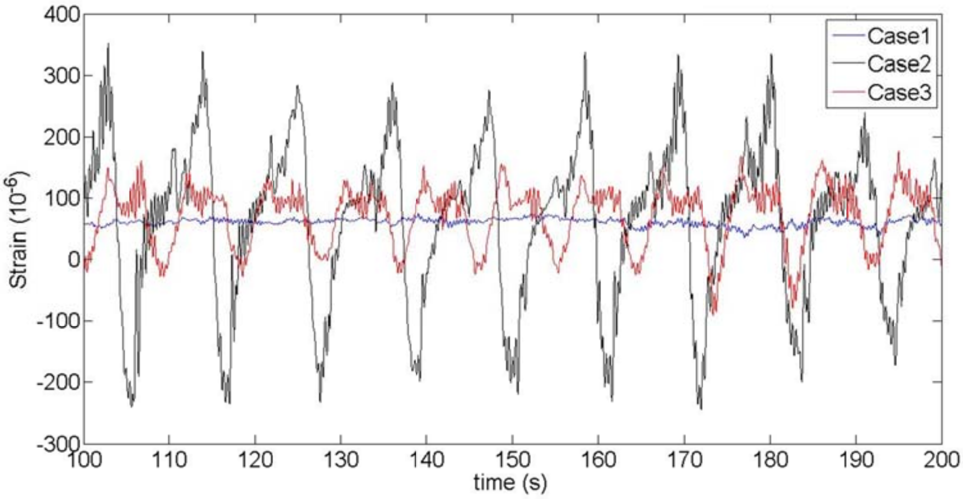

(a)

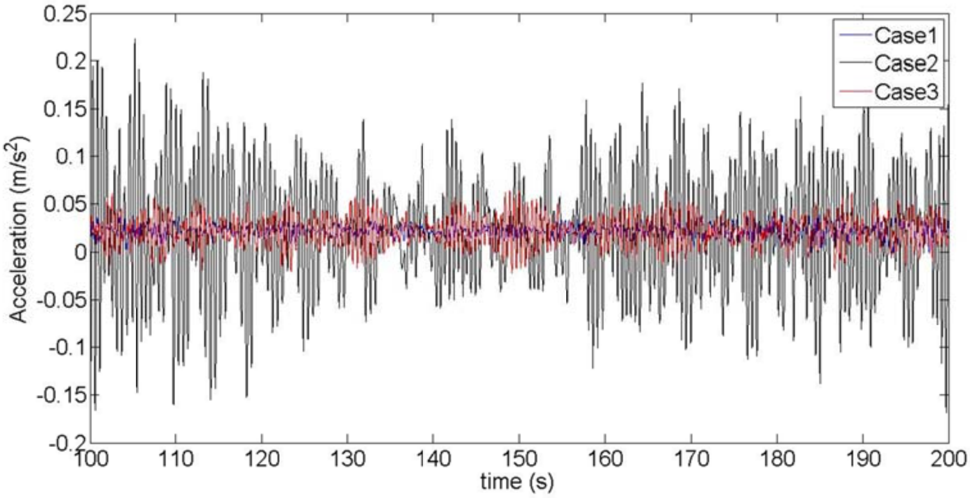

Case1
Case2
Case3
Acceleration (m/s^2)
time (s)

(b)

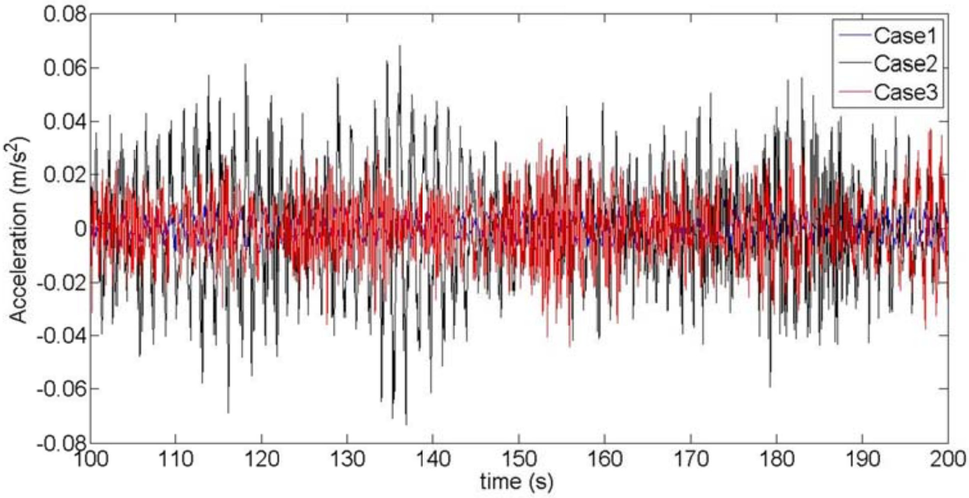

Case1
Case2
Case3
Acceleration (m/s^2)
time (s)

(c)

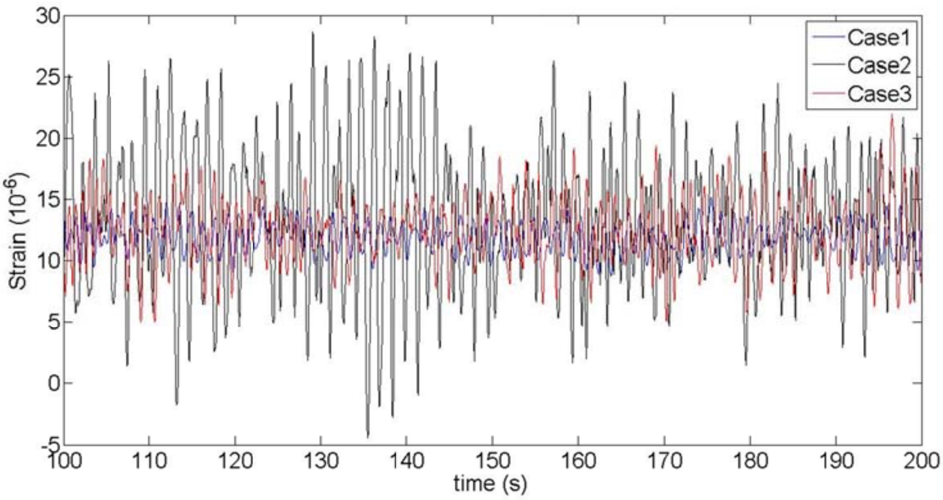

Case1
Case2
Case3
Strain (10^{-6})
time (s)

(d)

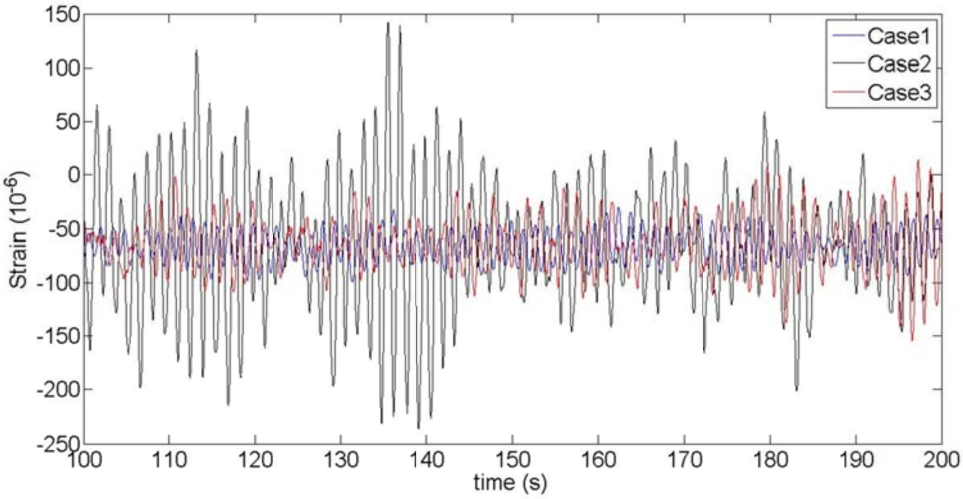

(e)

Fig. 7.7 The time histories of the measured responses. (a) strain of blade; (b) tangential acceleration of upper arm; (c) vertical acceleration of main arm; (d) bending strain of main arm; (e) bending strain of shaft.

The power spectrum densities (PSD) of the measured responses are calculated and normalized by the maximum value of PSD of the corresponding response as shown Fig.7.8. Firstly, it is found that the frequency of rotation of the rotor and its multiples can be detected from the normalized PSD. Take the normalized PSD of bending strain of the shaft for example. There is no peak in the PSD of Case 1 because the rotational speed is 0rad/s. While, there are many peaks in PSD of Case 2 and these peaks occur at the frequencies of 0.09Hz, 0.18Hz, 0.27Hz, etc. These frequencies coincide with the rotational speed (0.57rad) and its multiples. Similarly, there are peaks of PSD of Case 3 and these peaks occur at the frequencies of 0.11Hz, 0.22Hz, 0.32Hz, 0.43Hz, etc., which are exactly the frequency of rotational speed (0.67rad) and its multiples. These peaks related to the rotational speed occur in PSD of all responses in Cases 2 and Case 3, but do not occur in PSD of responses in Case 1.

Secondly, the natural frequencies of the VAWT can be identified by the peaks in the PSD of responses. Excluding the peaks related to rotational speed, the common peaks in the PSD of the three cases are due to mode shapes of the VAWT and the corresponding frequencies are the natural frequencies. From the PSD of strain of the blade shown in Fig. 7.8(a), it can be seen that the common peaks appears at 2.5Hz, 3.8Hz, 4.6Hz, 5.2Hz and 6.1Hz. From the PSD of the measured tangential acceleration shown in Fig. 7.8(b), 11 common peaks of the three cases occur at 0.27Hz, 0.72Hz, 1.7Hz, 1.9Hz, 2.0Hz, 3.0Hz, 3.8Hz, 5.7Hz, 6.1Hz, 8.0Hz and 9.1Hz. From the PSD of the measured vertical acceleration shown in Fig. 7.8(c), 9 obvious common peak of the three cases show up at 0.72Hz, 1.2Hz, 1.9Hz, 3.0Hz, 3.8Hz, 4.6Hz, 5.7Hz, 6.1Hz and 8.0Hz. From the PSD of the measured strain at the main arm shown in Fig. 7.8(d), 6 obvious common peaks of the three cases are found at 0.72Hz, 1.2Hz, 1.7Hz, 1.9Hz, 3.8Hz and 4.6Hz. The normalized PSD of bending strain of the shaft is shown in Fig. 7.8(e). From the PSD of measured bending strain of the shaft, it can be seen that 7 obvious common peaks of the three cases occur at 0.72Hz, 1.7Hz, 1.9Hz, 3.0Hz, 3.8Hz, 5.2Hz and 5.7Hz. The natural frequencies depicted by the normalized PSD of responses are listed in Table 7.3.

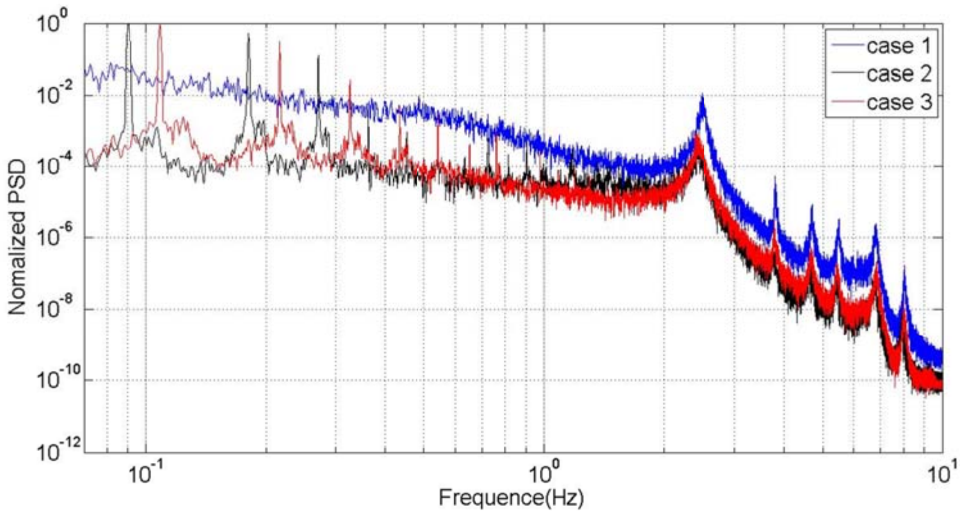

(a)

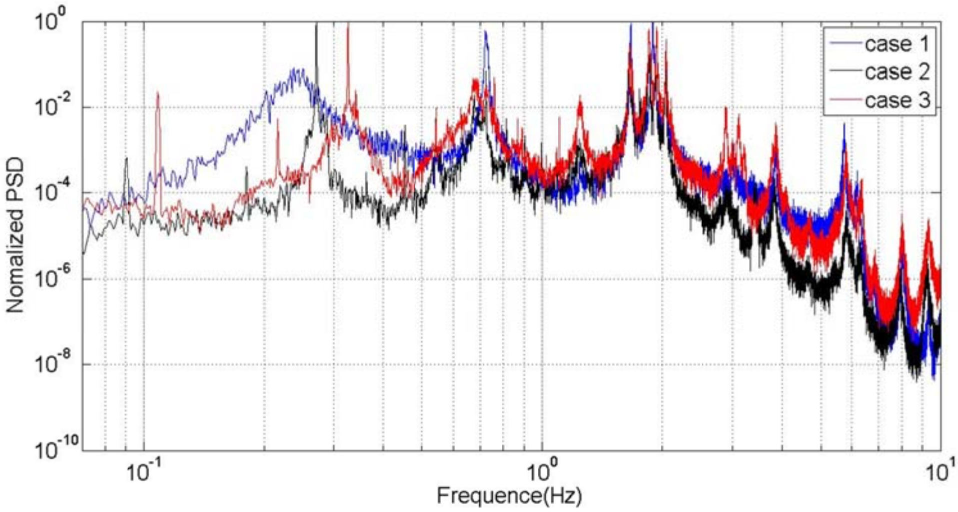
Nomalized PSD
Frequence(Hz)
case 1
case 2
case 3

(b)

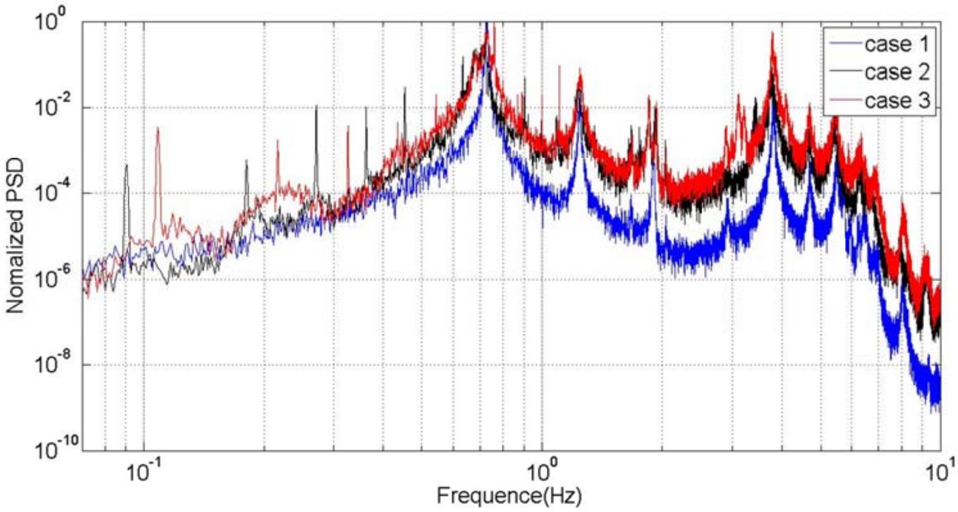
Nomalized PSD
Frequence(Hz)
case 1
case 2
case 3

(c)

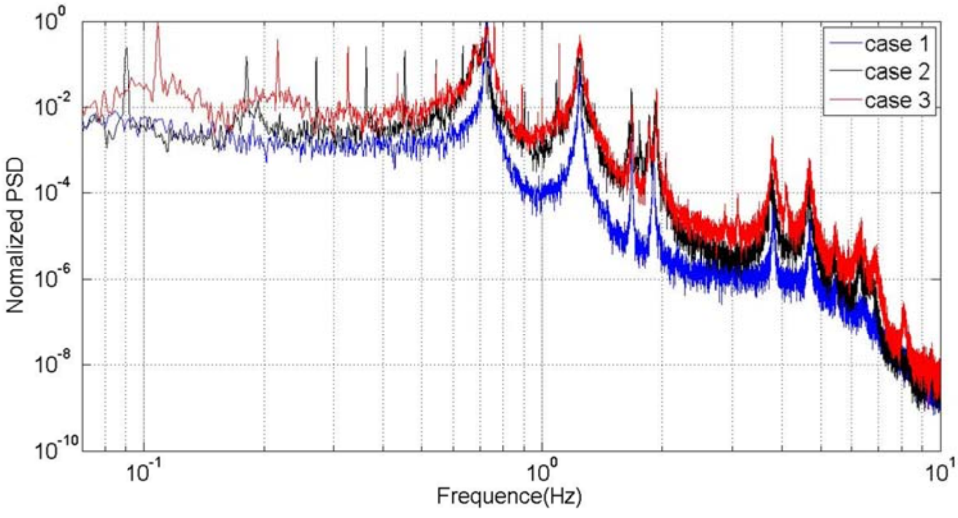
Nomalized PSD
Frequence(Hz)
case 1
case 2
case 3

(d)

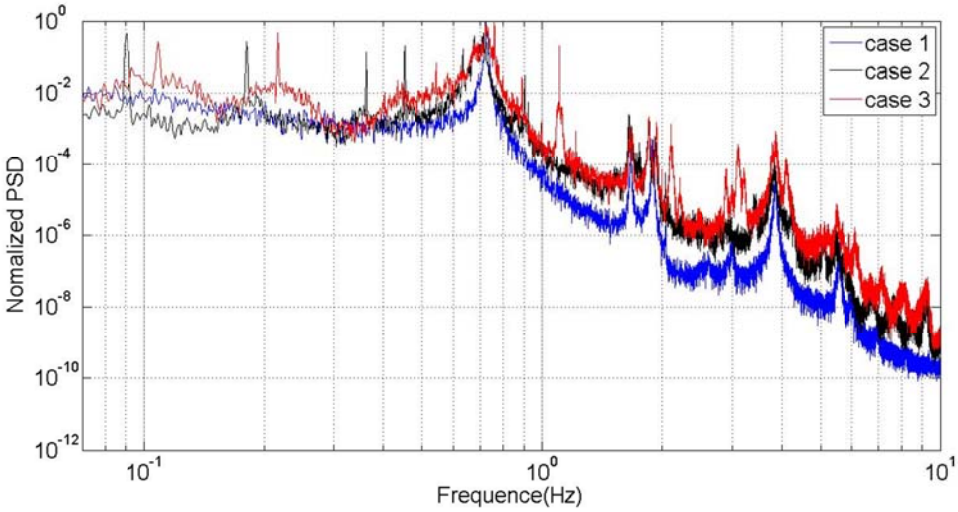

(e)

Fig. 7.8 Normalized PSD of responses. (a) strain of blade; (b) tangential acceleration of upper arm; (c) vertical acceleration of main arm; (d) bending strain of main arm; (e) bending strain of shaft.

Table 7.3 Possible natural frequencies and associated responses

f (Hz)	0.27	0.72	1.2	1.7	1.9	2.0	2.5	3.0	3.8	4.6	5.2	5.7	6.1	8.0	9.1
ε_{blade}	-	-	-	-	-	-	√	-	√	√	√	-	√	-	-
A_t	√	√	-	√	√	√	-	√	√	-	-	√	√	√	√
A_v	-	√	√	-	√	-	-	√	√	√	-	√	√	√	-
ε_{arm}	-	√	√	√	√	-	-	-	√	√	-	-	-	-	-
ε_{hub}	-	√	-	√	√	-	-	√	√	-	√	√	-	-	-

However, the mode shapes of the VAWT could not be measured due to the very limited number of sensors. In order to find the mode shapes corresponding to the depicted natural frequencies, the modal analysis results of the FE model are used. The mode shapes of the FE model are shown in Appendix C. The mode shape corresponding to 0.27Hz is the torsion of the shaft; the mode shape corresponding to 0.72Hz is the bending of the shaft; the mode shape corresponding to 1.2Hz is the vertical bending of the arms; the mode shape corresponding to 1.7Hz is the horizontal bending of the arms; the mode shapes corresponding to 1.9Hz and 2.0Hz are the combination of torsion of main arms and bending of lower and upper arms; the mode shape corresponding to 2.5Hz is the bending of the blade. The mode shapes of higher natural frequency are not included in the first 10 mode shapes in Appendix C.

7.3 Model Updating Based on the Measurement Data

The FE model in Chapter 6 is established according the design drawings of the VAWT. However, the uncertainties are unavoidable due to the simplification of the beam model, boundary conditions, the large tolerance of manufacture and variation in material properties. Usually, these uncertainties are considered by updating the stiffness and mass of the components through changing the material properties and geometry sizes of elements in the model updating process.

To ensure the accuracy of the dynamic analyses, the FE model was updated with reference to the first 6 natural frequencies depicted in Section 7.2.2. The updating was carried out by the pattern search optimization method which has been introduced in Chapter 4 to minimize the following objective function:

$$\text{Minimize}: J = \sum_i \omega_{\lambda,i}[\lambda_i^N(r_1, r_2, \cdots, r_n) - \lambda_i^M]^2 \tag{7.1}$$

where λ_i denotes the i^{th} modal frequency; the superscript "N" denotes the FE result; ω_i denotes the weighting factor for the i^{th} modal frequency; $r_1, r_2, \cdots, r_n$ denote the parameters for updating. In this study, identical weighting factors are used.

After removing low sensitivity parameters, a total of 4 parameters are selected to be updated by the natural frequencies: the thickness of the shaft, the Young's modulus of the main arms, the Young's modulus of the upper and lower arms and links and the

Young's modulus of the blades. These parameters do not really reflect the uncertainties of the FE model in geometry size and material properties but reflect the synthesized uncertainties in simplification, connection, geometry size, material properties and other unknown factors. All the selected updating parameters and their initial and updated values are listed in Table 7.4. The results shown that the Young's modulus of the upper and lower arms and links are the same as the initial value after updating. The reason is that the sensitivity of the natural frequencies to other parameters are higher than this parameter, therefore, the updating of other parameters are dominant in the optimization process.

Table. 7.4 Initial and updated values of parameters

Parameter No.	Description	Initial	Updated
1	Thickness of shaft	0.10m	0.05m
2	Young's modulus of main arms	206.00e10N/m^2	164.80 e10N/m^2
3	Young's modulus of upper and lower arms and links	206.00 e10N/m^2	206.00 e10N/m^2
4	Young's modulus of blades	30.00 e10N/m^2	29.20 e10N/m^2

The comparison of measured and computed modal frequencies is presented in Table 7.5. It shows that the differences between measured and computed natural frequencies are reduced after updating. The 1st and 2nd modes are the torsion and bending of the shaft. By reducing the thickness of shaft, the 1st natural frequency is decreased from 0.51Hz to 0.25Hz and the 2nd natural frequency is decreased from 0.89Hz to 0.79Hz. The 3rd, 4th and 5th modes are corresponding to the arms. By reducing the Young's modulus of main arms, the 3rd natural frequency is decreased from 1.72Hz to 1.23Hz, the 4th natural frequency is decreased from 2.23Hz to 1.61Hz and the 5th natural frequency is decreased from 2.90Hz to 2.09Hz. The 6th mode is the bending of the blade. By reducing the Young's modulus of blade, the 6^{th} natural frequency is decreased from 3.15Hz to 2.23. Obviously, after updating the computed natural frequencies are much closer to the measured ones.

Table 7.5 Comparison of modal frequencies

Mode	Measured (Hz)	Initial (Hz)	Updated (Hz)	Description
1st	0.27	0.51	0.25	Torsion of shaft
2nd	0.72	0.89	0.79	Bending of shaft
3rd	1.20	1.72	1.23	Vertical bending of arms
4th	1.70	2.23	1.61	Horizontal bending of arms
5th	1.90	2.90	2.09	Combination of torsion of main arm and bending of lower and upper arms
6th	2.50	3.15	2.23	Bending of blades

7.4 Validation of the Numerical Simulation

The simulation method of wind loads on VAWTs is presented in Chapter 3. Based on this work, the frameworks of fatigue and ultimate strength analysis for blades and VAWTs are proposed in Chapter 5 and Chapter 6 but they need to be validated by using field measurement data.

A common method is to compare the computed and measured responses directly in the time domain. However, it is difficult to conduct in this way in this study. This is because the response measured on-site is indeed a stochastics process. "Stochastics" indicate uncertainties which mainly come from two aspects in this case: the wind load and the FE model. It is very difficult, if not impossible, to measure the wind load directly. To measure the distributed wind pressures and aerodynamic forces on the blades, the arms, and the tower, a tremendous number of pressure sensors and load cells are required. Moreover, there is also uncertainty to reproduce the wind load according to the measured wind speed. The on-site wind speed is measured at specific location and at a specific height; however, the wind speed in the whole flow field must be known if the wind load shall be reproduced accurately. The other source of "stochastic" is the uncertainty of the FE model. Even if a FE model has been updated by tests and field measured data, it is impossible to eliminate all uncertainties in geometrics, materials and connections. Hence, it is difficult to reproduce the field measured responses. So, in this study, the comparison is conducted in the frequency domain in terms of PSD functions.

7.4.1 The operational and external conditions

To compare the measured and simulated responses, the operational and external conditions of the measurement and simulation must be as the same as possible. Here, the operational condition is mainly the rotational speed and the external condition is mainly the wind field.

In reality, the wind speed is spatial and temporal varying. Due to the atmospheric boundary layer, the mean wind speed near the ground approaches to zero and then increases with the increase of height above the ground. For the turbulence, there exists the spatial correlation between the turbulent wind speeds at two spatial points. However, in the filed measurement the measured wind speed is only at the specific location and at the specific height (10m); the lateral correlation of turbulence is not considered as introduced in Chapter 3. To match with the wind field on-site as far as possible, the simulated mean wind speed and turbulence intensity must be the same as the measured one at the measured height. However, the wind speed profile has to be selected according to the terrain condition of the site.

In this study, the data recorded at April 1, 2012 are used to compare with the simulated results. To simulate the wind speed, a measured 10 min wind speed time history is adopted. The 1 minute average wind direction is shown in Fig. 7.9. The wind speed time history is shown in Fig. 7.10(a). The mean value and the turbulent intensity of the simulated wind speed at 10m height are listed in Table 7.6. The measured mean speed is 6.20m/s and the turbulence intensity is 11.44%. The turbulence integral scale parameter can also be calculated from the measured wind speed based on the Taylor's hypothesis and gains 15.6m. These values are applied in Kaimal spectrum and exponential coherence model introduced in Chapter 3 and the Shinozuka method (Shinozuka & Jan, 1972) is used to simulate the time history of wind speed. The time history of wind speed is also shown in Fig. 7.10(a) and the power spectrums of the measured and simulated wind speed are shown in Fig. 7.10(b). It can be seen that the simulated wind speed matches well with the measured one. The simulated time histories of wind speeds at the 9 cross sections defined in Chapter 3 are shown in Appendix E.

The rotational speeds used in the simulation and the real case must be the same as well. The time histories of measured rotational speed are shown in Fig. 7.11. By using the simulation method introduced in Chapter 6, the rotational speed of the VAWT is fixed at 0.5655rad/s. Though there is a fluctuation in the measured rotational speed, the amplitude of change is only 1%. Hence, it is reasonable to assume that such a small variation in rotational speed has no influence on the wind loads.

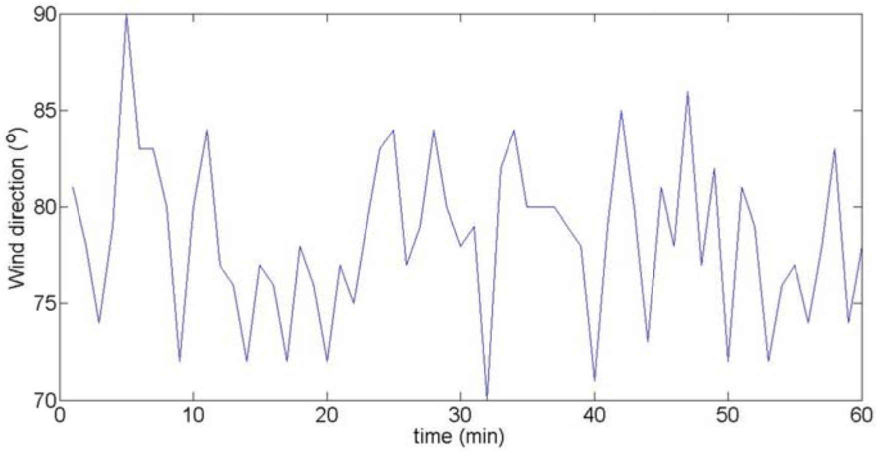

Fig. 7.9 1 min average wind direction

Table 7.6 Mean wind speed and turbulence intensity

	Measured	Simulated
Mean Wind Speed (m/s)	6.20	6.20
Turbulence Intensity	11.44%	11.29%

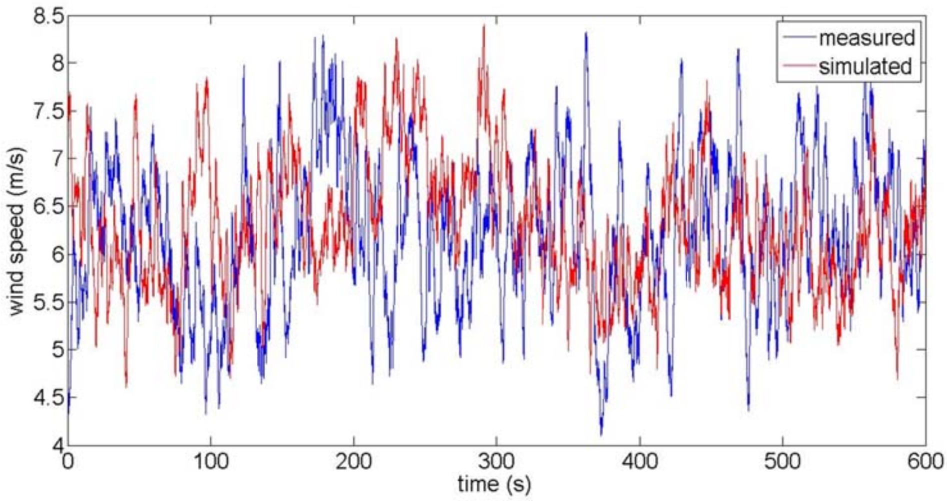

(a)

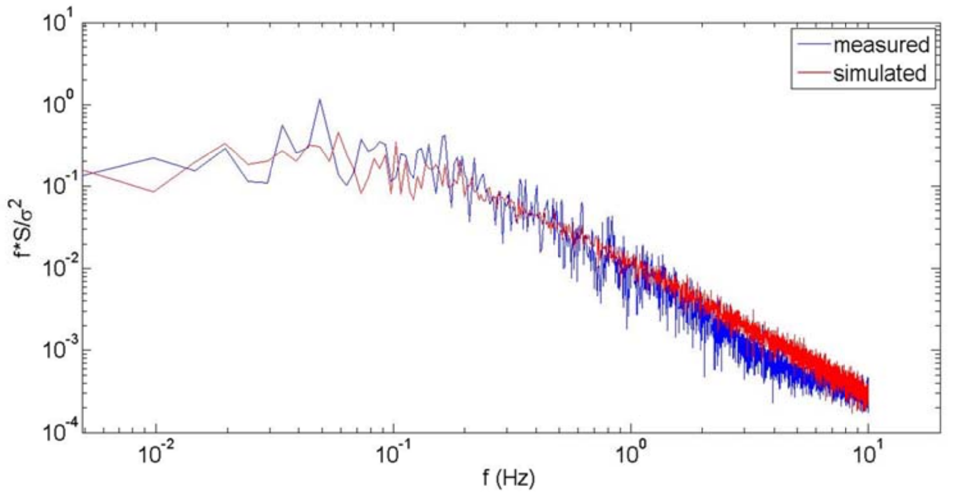

(b)

Fig. 7.10 Turbulent wind speed (a) time history; (b) PSD

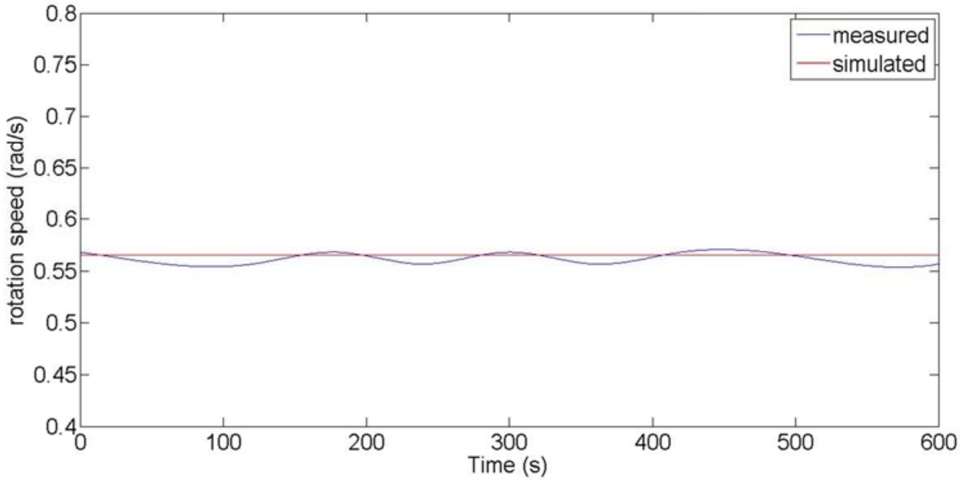

Fig. 7.11 measured and simulated rotational speeds

7.4.2 Comparisons of the measured and simulated responses

Based on the external and operational conditions, the wind load can be simulated by the method proposed in Chapter 3 and the responses of the VAWT can be simulated by the frameworks introduced in Chapters 5 and 6. The comparisons of responses at the locations of sensors can be given and the results are shown below.

The measured and simulated bending strains of the blade are shown in Fig. 7.12(a). From Fig. 7.12(a), it can be seen that the magnitude and mean value of the simulated and measured strains of the blade match with each other in general. The main strain cycle is due to the rotation of the VAWT. The PSDs of the measured and simulated strain of blade are shown in Fig. 7.12(b). There exist several peaks in PSD, generally, which can be divided into two groups: one is due to the operation wind loads and the other is due to natural frequencies. Compared with Fig. 7.8(a), it can be found that the peaks in the low frequency zone of Fig. 7.12(b) are caused by rotation. The frequencies of these peaks are 0.09Hz, 0.18Hz, 0.27Hz and others which exactly are the multiples of the rotational frequency of the VAWT. The simulated and measured PSDs match well at these frequencies. The second dominant frequency component at

2.5Hz is due to the first vibration mode of the blade. Although the magnitude of the component at 2.5Hz of the measured strain is larger than that of the simulated results, the shape of the measured and simulated PSDs are similar.

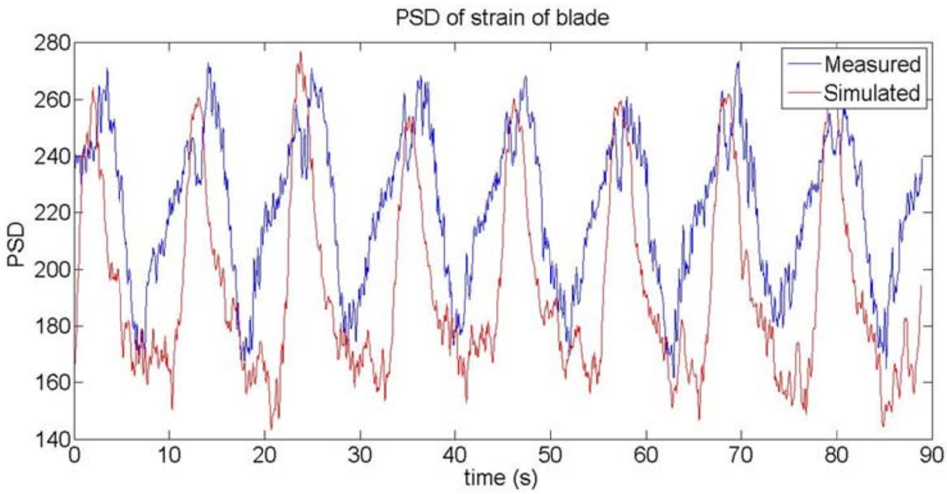

(a)

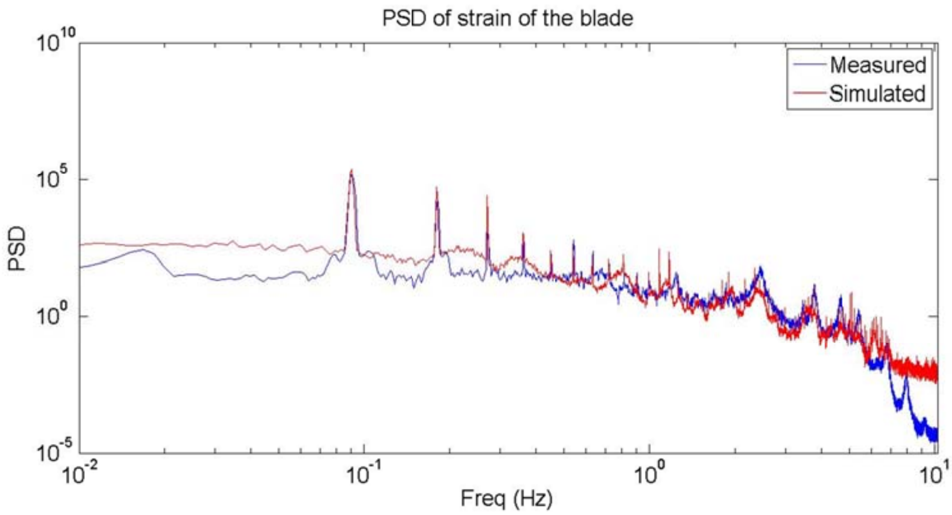

(b)

Fig. 7.12 Measured and simulated strains of the blade (a) time history; (b) PSD

The simulated and measured tangential accelerations of the upper arm are shown in Fig. 7.13(a). It can be seen that the cycles of the two results are the same but the fluctuating of the measured acceleration is larger than that of simulated one. The simulated and measured PSDs are shown in Fig. 7.13(b). The locations of peaks due to rotation of the two PSD are coincided. However, the magnitude of the measured PSD is larger than the simulated one. For the peaks due to mode shapes, the two PSDs have similar shape but the magnitude of measured result is still larger than that of simulated one.

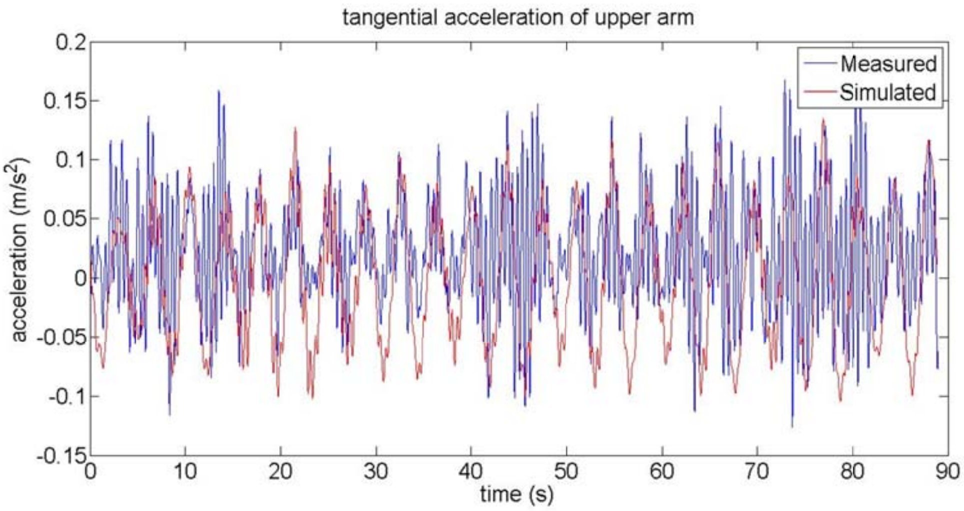

(a)

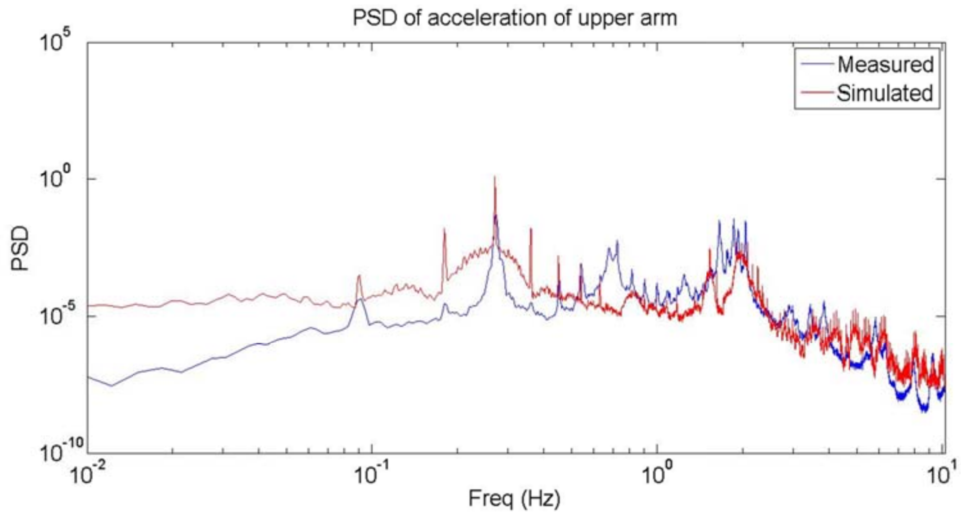

(b)

Fig. 7.13 Measured and simulated tangential accelerations of upper arm (a) time history; (b) PSD

The simulated and measured vertical accelerations of the main arm are shown in Fig. 7.14(a) and the corresponding PSDs are shown in Fig. 7.14(b). From the time histories of accelerations shown in Fig. 7.14(a), it can be seen that the cycles of these two results are clear and match with each other. Nevertheless, the fluctuating of the simulated result is larger than that of the measured one. In Fig. 7.14(b), the 4 major peaks of the PSD obtained from the measured data at 0.72Hz, 1.2Hz, 1.9Hz and 3.8Hz are also reproduced by the simulated results. The magnitudes of these 4 peaks of the measured and simulated responses are similar. Hence, the PSDs obtained from the measured and simulated data match with each other.

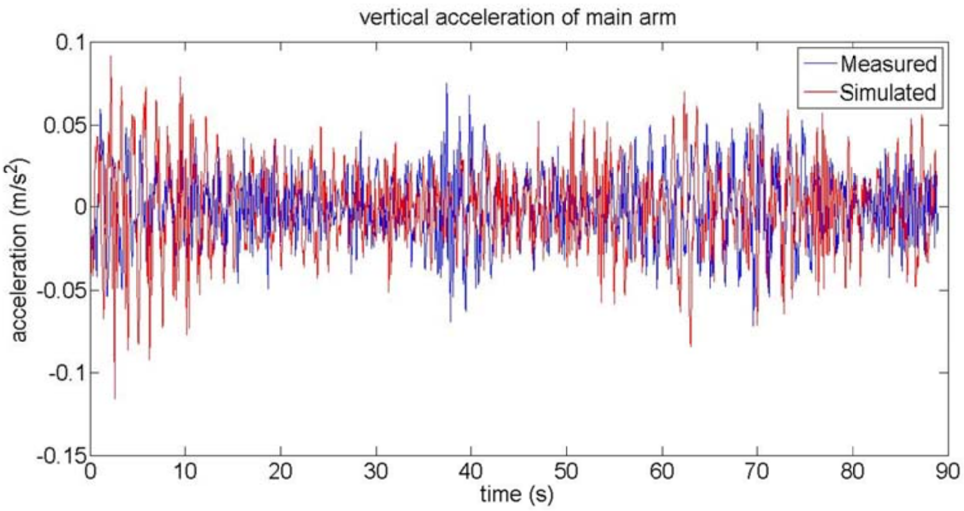

(a)

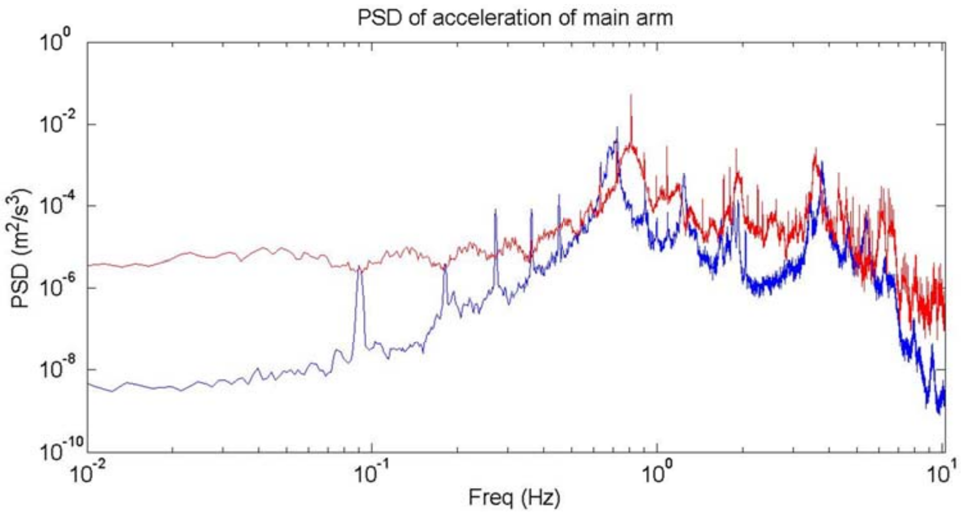

(b)

Fig. 7.14 Measured and simulated vertical accelerations of main arm (a) time history; (b) PSD

The simulated and measured strain time histories of the main arm are shown in Fig. 7.15(a) and the corresponding PSDs are shown in Fig. 7.15(b). From the time histories of strain shown in Fig. 7.15(a), it can be seen that these two results are quite different. For the measured result, it can be clearly counted that there are 24 cycles in 89s (0.27Hz). However, these cycles are not clear in the simulated time history. Nevertheless, the cycles of higher frequencies in the simulated time history are larger than those in the measured one. The phenomena can be explained by the PSD of these two results. Although the peaks of these two results due to rotation can match with each other, the magnitudes of the peaks due to the excited mode shapes are quite different. The peak at 0.27Hz is appeared in the PSD of measured data but absent in that of simulated result, while the magnitude of the peak at 1.23Hz of the simulated PSD is larger than the peak of PSD obtained from measured data. The reason causing such difference is not clear.

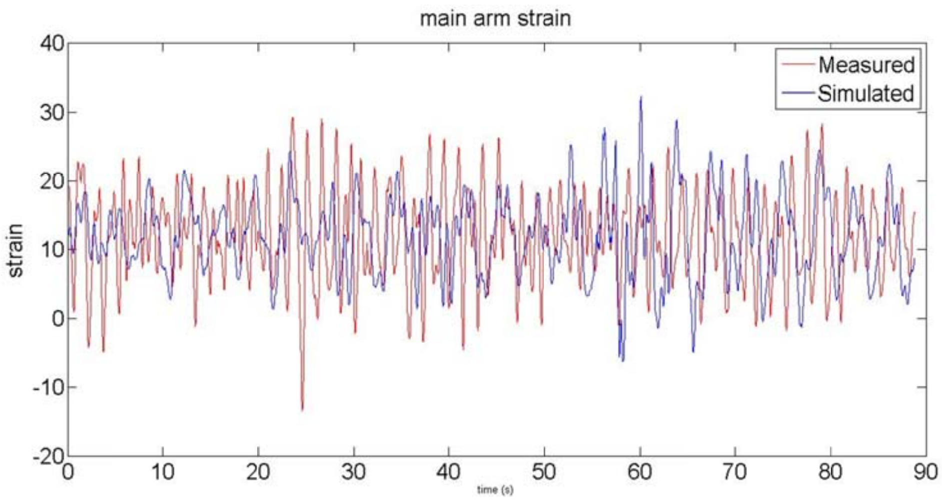

(a)

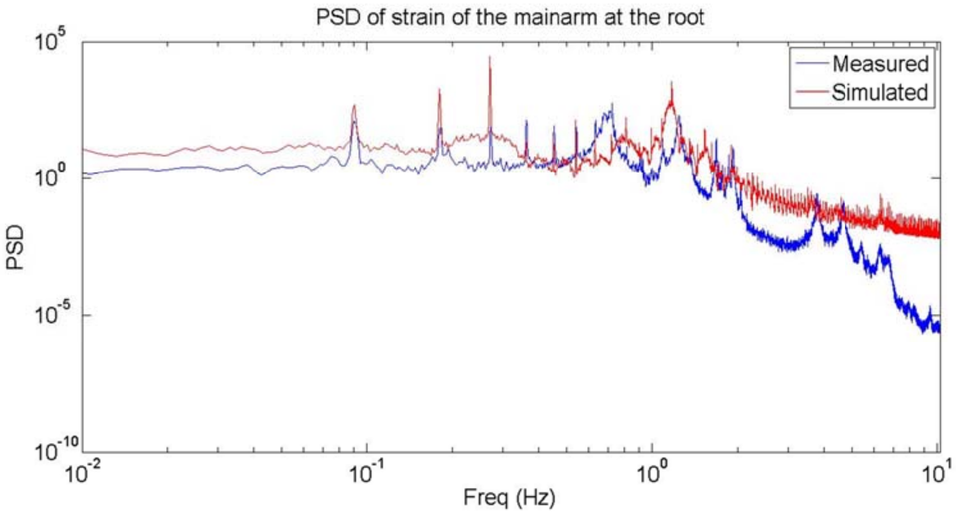

(b)

Fig. 7.15 Measured and simulated strains of the main arm (a) time history; (b) PSD

The simulated bending strains of the shaft are also shown in Fig. 7.16 (a). It can be seen that although the simulated strain has larger magnitude of fluctuating strain, the simulated and measured strains have similar shape. The PSDs of the measured and simulated bending strains of the shaft are shown in Fig. 7.16. It can be found that these two curves have similar shape. The peaks due to the rotation in the two PSDs are coincided with each other; the peaks due to natural frequencies in the two PSDs have similar magitudes.

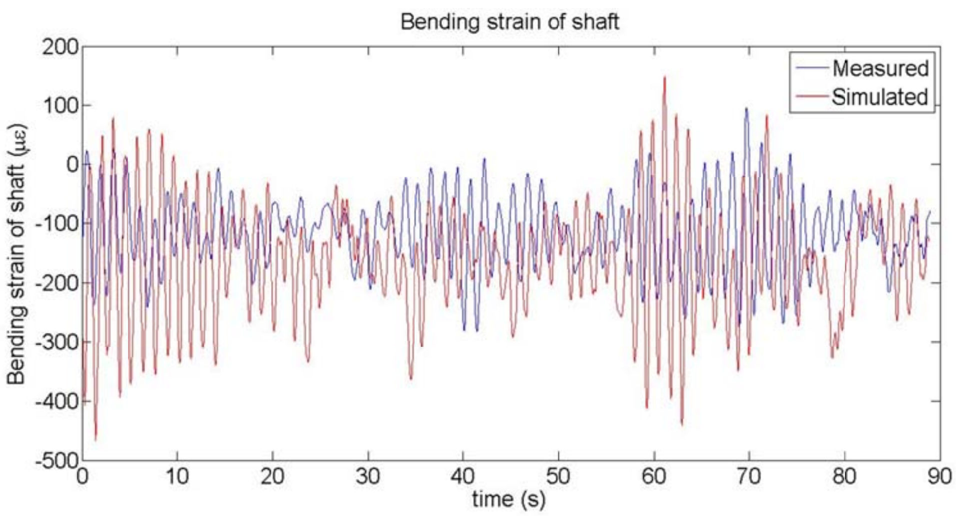

(a)

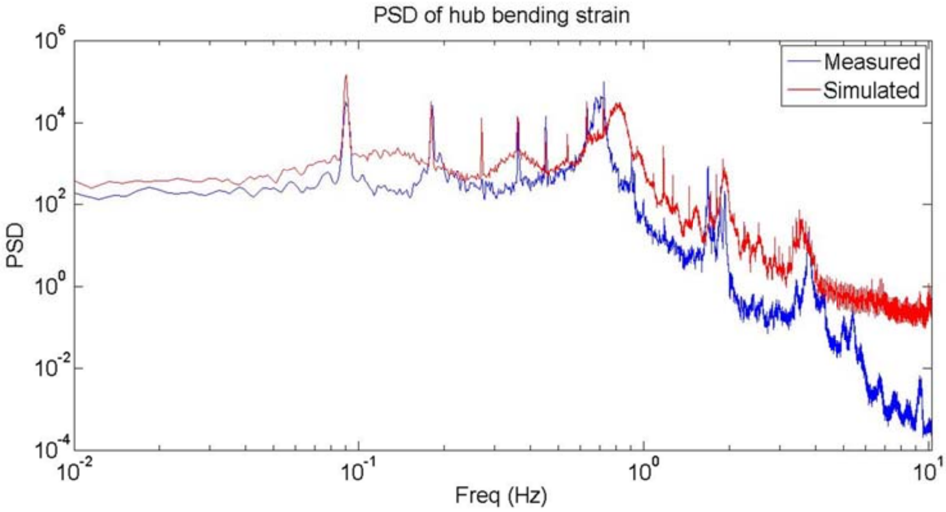

(b)

Fig. 7.16 Measured and simulated shaft bending strains (a) time history; (b) PSD

On the whole, the simulated responses can reproduce the measured results in the frequency domain in general although there are still some discrepancies between the measured and simulated results. The proposed analysis framework is thus validated to some extent of satisfaction by the field measurement data, and the analyses and results obtained from Chapter 5 and Chapter 6 are acceptable in general.

7.5 Summary

In this chapter, field tests were conducted on a VAWT. A field measurement system was established for the VAWT. According to the analyses of Chapter 5 and Chapter 6, strain gauges were attached on the shaft, main arm and blade. To monitor the global deformation of the VAWT, an accelerometer was installed on the main arm monitoring the vertical acceleration and another accelerometer was installed on the top of upper arm to monitor the tangential acceleration. Comparing the measured data of different conditions, the influences of wind speed and rotational speed were clarified. Natural frequencies were also depicted from the peaks of the normalized PSDs of measured responses. The FE model used in Chapter 6 was then updated by the identified natural frequencies. Under the same operational and external conditions as the measurement, the responses of the VAWT were calculated and the responses at the locations of sensors were compared with the measured data. The PSDs of the measured and simulated responses were calculated and the comparison was mainly conducted in the frequency domain. It was found that the shape of PSDs obtained by these two results were similar and matched with each other in general. Therefore, the frameworks proposed in Chapters 5 and 6 were validated to some extent of satisfaction.

Since the results from Chapter 5 and Chapter 6 are validated to some extent, an SHM system can be established accordingly. Because the measurement system introduced in this chapter was temporal and uncomplete. A complete SHM for the VAWT will be introduced in the next chapter. Since a control system is generally used in modern wind turbines. A control system of VAWT will also be given in next chapter. Consider the following facts that 1) both of the SHM system and control system need sensors; 2) sensors need power supply; 3) a VAWT itself generates power. A concept of smart VAWT is proposed in next chapter.

CHAPTER 8

STRUCTURE HEALTH MONITORING AND CONTROL

8.1 Introduction

As introduced in Chapter 2, wind turbines operate at four different states. The 1st state is the start-up state. Wind turbines are parked or idling if the mean wind speed is below the cut-in wind speed. When the mean wind speed rises at the cut-in wind speed, the rotor begins to speed up until the rotational speed arrives at the required value, and then wind turbines are connected to the grid. The required rotational speed of a grid connected wind turbine is determined by the frequency of grid and the number of poles of the generator. In this study, the state of start-up is defined as state 1. The 2nd operation state is the state of power production below the rated wind speed, which is defined as state 2. In this state, wind turbines are connected to the grid, and they generally operate at a specific rotational speed. The 3rd operation state is the state of power production above the rated wind speed, which is defined as state 3. In this state, the rotation speed is also fixed at the same speed as in state 2. The difference between state 2 and state 3 is that there must be some mechanism to reduce the power and prevent the generator from overloading (Spera, 1994). The 4th operation state is the shut-down state which is defined as state 4 in this study. When the wind speed rises above the cutout wind speed, it is important that the rotor should be shut down as soon as possible to prevent the accident of flying off in high wind, which is one of the main failures of wind turbines due to the wear and tear of the braking system (Ciang et al., 2008; Spera, 1994).

Pitch controls have the potentials to benefit wind turbines at the aforementioned four states. In state 1, VAWTs usually need additional power to start up and a pitch control system may increase the aerodynamic starting torque of VAWTs. In state 2, because the rotation speed is fixed, the power coefficient is varying with the mean wind speed. For VAWTs, the angle of attack (AOA) experiences a cyclic change between positive and negative in one spin in the case of zero pitch. Thus zero pitch of VAWTs cannot ensure the optimal torque at all azimuth angle. Pitch control can improve the power efficiency of VAWTs. In state 3, the pitch regulation can maintain the power at the rated value. In state 4, the pitch regulation can help VAWTs to shut down efficiently by reducing AOA or inducing the happening of stall. However, for VAWTs, seldom researches are conducted on the pitch control algorithm in state1, state 3 and state 4. Pitch controls have been widely applied in HAWTs, while they were seldom studied for VAWTs until recent years and mainly focused on state 2. Therefore, the study on pitch control is necessary for VAWTs to achieve the following four objectives: assisting the start-up in state 1, improving the power coefficient in state 2, maintaining the output power at the rated value in state 3 and assisting the shut-down in state 4.

On the other hand, SHM systems are required for large-scale wind turbines. Usually, a wind turbine is established in an uninhabited area and exposed to various environmental effects, such as typhoons, earthquake and collisions. An SHM system can provide the information for companies so that they can monitor the functionality, detect large deformations, ensure the safety and save the cost of inspection and maintenance of wind turbines. Besides these objectives, for VAWTs, an SHM system can provide field measurement data for designers that they can validate the present analysis methods which have not been fully verified yet, or just verified by wind tunnel tests. SHM systems are widely applied in large-scale HAWTs. However, the reports on SHM systems for VAWTs are rare. One of the reasons is that VAWTs gain much less development than HAWTs. Therefore, the study on SHM systems for large-scale VAWTs is required.

Generally, wind turbines need both the SHM system and the control system. Both of the systems require sensors, data acquisition systems, and signal transmission systems. Since the primary objectives of these two systems are different, they are currently treated separately. A separate approach is not practical and cost-effective. It is more reasonable to consider these two systems synthetically. Moreover, the power supply is an important factor for the design of both the SHM and control system (Huston, 2010) and usually power from batteries or grid are used. Considering that a VAWT itself is an energy harvesting machine, it is promising that the power of these two systems can be obtained directly from the turbine. Therefore, it is necessary to study a smart VAWT which possesses the abilities of self-sensing, self-diagnosis, self-control and self-power.

In this chapter, the straight-bladed VAWT introduced in Chapter 3 is taken for as a case study. In fact, the number and the chord length of blades have an influence on the optimal tip speed ratio of a wind turbine. At the optimal tip speed ratio, a wind turbine has the largest power coefficient. The 3-blade VAWT is most studied at present, the thesis did not consider other VAWTs. Two pitch control algorithms for the four operation states are studied firstly. Considering that a large number of pitch variation cases are involved, the computational cost is very high if using CFD. To conduct this study in an effective way, the double-multiple streamtube theory (DMST) is adopted in the analyses. Based on this study, a four-state pitch control algorithm for straight-bladed VAWTs is proposed and a pitch control system is also given. Secondly, an SHM system for VAWTs is proposed based on the works of Chapter 5 and Chapter 6. Finally, by synthesizing the SHM, control system and power supply system for VAWTs, the concept of smart VAWT is given.

8.2 The Control System for VAWTs

8.2.1 Double-Multiple Streamtube Theory (DMST)

DMST is used in this chapter on pitch control algorithms. This theory is developed from the blade element momentum theory (BEM) for HAWTs. BEM regards the rotor of HAWTs as an actuator disk as reviewed in Chapter 2. When the airflow across the disk, the pressure would have a sudden drop and the forces acting on the blades are equal to the change in momentum of the airflow. In DMST, the wind field is discretized into several stream tubes. DMST is developed from the BEM for VAWTs in the way that in each streamtube, the upwind and downwind sides are regarded as two actuator disks and the BEM theory is applied two times in these two actuator disks separately. Moreover, two assumptions are adopted by DMST: one is that the airflow has fully developed in the middle of upwind and downwind side, so that the pressure at this point has resumed the atmospheric pressure; and the other is that the streamtube expansion can be ignored, so that the area of the streamtube is uniform.

In DMST, the radius of the rotor is R and the wind field is discretized into several stream tubes as shown in Fig. 8.1 for a VAWT. V_∞ is the inflow wind speed of the far upstream; V_u is the wind speed in the upwind rotor; V_d is the wind speed in the downwind rotor; V_e is the wind speed inside the rotor; V_w is the wind speed in the far wake; p_0 is the pressure of the far upstream; p_u is the pressure in front of the upstream actuator; Δp_u is the pressure drop due to the upwind actuator; p_d is the pressure in front of the downstream actuator; Δp_d is the pressure drop due to the downwind actuator; A is the area of the streamtube; θ is the azimuth angle at which the streamtube comes across the upwind side of the rotor; and $\Delta\theta$ is the angular width of the streamtube.

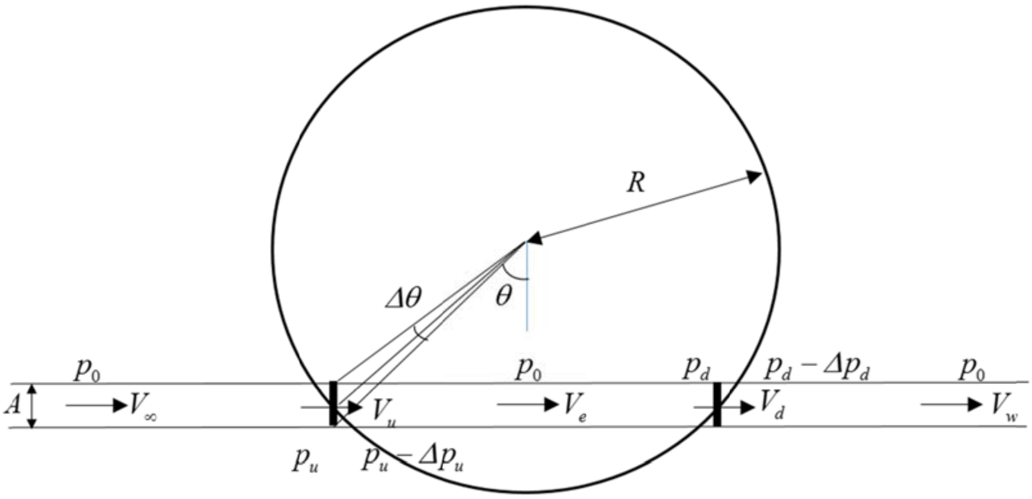

Fig. 8.1 wind speeds and pressures in a streamtube

By applying the Bernoulli equation on the streamline from the far upstream to the upwind actuator of a VAWT and the streamline from the upwind actuator to the middle point between upwind and downwind actuators, we get

$$\frac{1}{2}\rho V_\infty^2 + p_0 = \frac{1}{2}\rho V_u^2 + p_u \tag{8.1}$$

$$\frac{1}{2}\rho V_u^2 + p_u - \Delta p_u = \frac{1}{2}\rho V_e^2 + p_0 \tag{8.2}$$

Hence,

$$\Delta p_u = \frac{1}{2}\rho(V_\infty^2 - V_e^2) \tag{8.3}$$

The streamwise force exerted by the upwind actuator disk $\overline{F}_u$ is

$$\overline{F}_u = \Delta p_u A = \frac{1}{2}\rho A(V_\infty^2 - V_e^2) \tag{8.4}$$

On the other hand, by the Newton's law, $\overline{F}_u$ is equal to the mass flux through the upwind actuator disk times the net velocity change

$$\overline{F}_u = \rho V_u A(V_\infty - V_e) \tag{8.5}$$

Equation (8.4) and Equation (8.5) give

$$V_u = \frac{V_\infty + V_e}{2} \tag{8.6}$$

So Equation (8.5) can be rewritten as

$$\bar{F}_u = 2\rho V_u A(V_\infty - V_u) = 2\rho A a_u (1 - a_u) V_\infty^2 \tag{8.7}$$

where $a_u = V_u / V_\infty$ is defined as the upwind induction factor. Considering the cross section area of the streamtube $A = R\Delta\theta \sin\theta$, where R is the radius of the rotor and $\Delta\theta$ is the angular width of the streamtube. Equation (8.7) can be written as

$$\bar{F}_u = 2\rho R\Delta\theta a_u (1 - a_u) V_\infty^2 \sin\theta \tag{8.8}$$

Similarly, the streamwise force exerted by the downwind actuator disk $\bar{F}_d$ is

$$\bar{F}_d = 2\rho R\Delta\theta a_d (1 - a_d) V_e^2 \sin\theta \tag{8.9}$$

where $a_d = V_d / V_e$ is defined as the downwind induction factor.

From the aerodynamics point of view, $\bar{F}_u$ and $\bar{F}_d$ are actually the average of aerodynamic drag force F_u and F_d respectively. Based on the quasi-steady assumption, the aerodynamic drag force can be calculated by the local relative velocity of the blade and the aerodynamic coefficients obtained from wind tunnel tests. The AOA of the blade at the azimuth angle of θ is shown in Fig. 8.2(a). The aerodynamic drag force F ($= F_u$ or F_d) and the normal F_n and tangential force F_t are shown in Fig. 8.2(b)

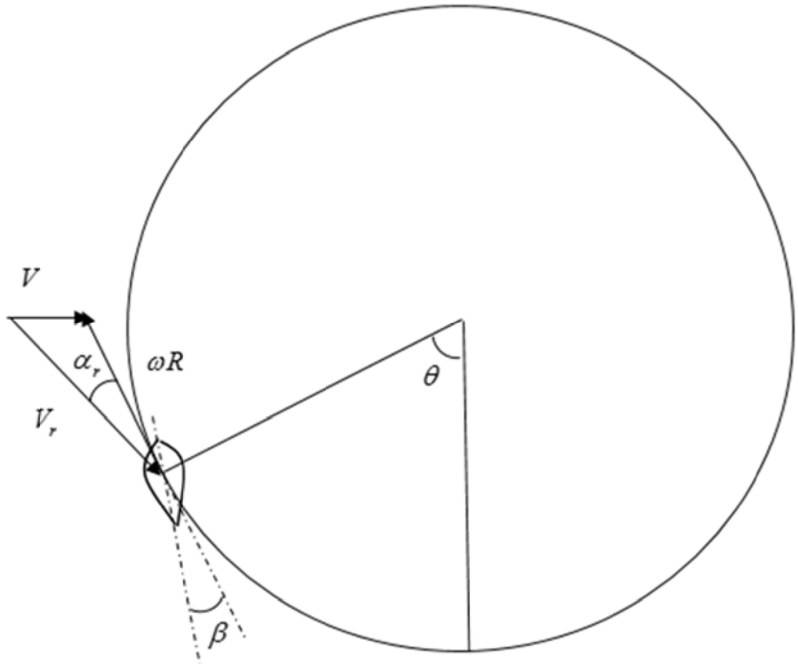

(a)

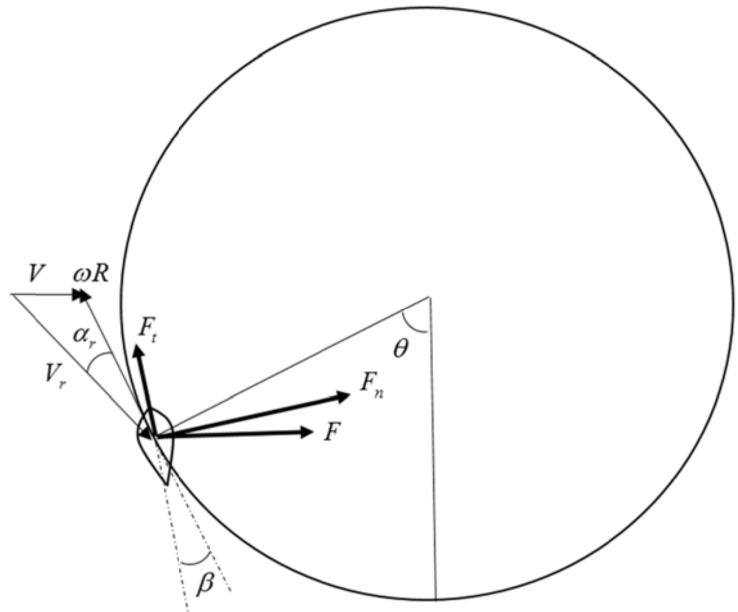

(b)

Fig. 8.2 The relative wind speed, AOA and the corresponding aerodynamic forces. (a) the relative wind speed and AOA; (b) aerodynamic forces

The relative wind speed V_r can be calculated by

$$V_r = \sqrt{(V\cos\theta)^2 + (V\sin\theta + \omega R)^2},\ V = V_u\ or\ V_d \tag{8.10}$$

The AOA for a zero pitch case can be calculated by Equation (8.11).

$$\alpha_r = \arctan(\frac{V\sin\theta}{\omega R + V\cos\theta}) = \arctan(\frac{\sin\theta}{\lambda + \cos\theta}),\ V = V_u \text{ or } V_d \tag{8.11}$$

The tip speed ratio is defined as $\lambda = \omega R/V$. From Equation (8.11), at a given azimuth angle θ, it can be seen that if λ is small, the AOA range is large and vice versa. When the pitch angle $\beta \neq 0$, the AOA can be estimated by Equation (8.12)

$$\alpha = \alpha_r + \beta = \arctan(\frac{\sin\theta}{\lambda + \cos\theta}) + \beta,\ V = V_u \text{ or } V_d \tag{8.12}$$

For the pitch control $\beta = \beta(\theta)$, it just needs to use different pitch angle in the corresponding stream tube.

Then, the normal force and tangential force can be obtained by

$$F_n = \frac{1}{2}\rho V_r^2 c\Delta h C_n(\alpha) \tag{8.13a}$$

$$F_t = \frac{1}{2}\rho V_r^2 c\Delta h C_t(\alpha) \tag{8.13b}$$

where F_n is the normal force; C_n is the normal force coefficient obtained by wind tunnel tests; F_t is the tangential force; C_t is the tangential force coefficient obtained by wind tunnel tests; V_r is the relative wind speed as shown in Fig. 8.2; c is the chord length of the blade and as introduced in Chapter 3, c is equal to 2m in this study; Δh is the height of the blade. In this study, the VAWT is regarded as 2D, Δh is equal to 1m so that the aerodynamic per unit length is obtained. C_n and C_t are the function of AOA, which can be calculated by the lift coefficient c_l and the drag coefficient c_d as shown in Equation (8.3); c_l and c_d are obtained by wind tunnel tests or numerical simulations. c_l and c_d of NACA0018 in the AOA region from 0^o to 180^o are shown in Fig. 8.3. C_l and C_d in the AOA region from 0^o to -180^o can be obtained by the relations: $C_l(\alpha) = -C_l(-\alpha)$ and $C_d(\alpha) = C_d(-\alpha)$. These C_l and C_d will be used in the subsequent sections. It can be seen that the stall happens at $\alpha = 21^o$, where C_l has a sudden drop, and the largest C_l before the stall is reached at the AOA α equal to 16^o. C_d remains at a small value when $\alpha < 14^o$ and suddenly jumps at $\alpha = 21^o$. These features will be further used and discussed in the subsequent sections.

$$C_t(\alpha) = C_l(\alpha)\sin\alpha - C_d(\alpha)\cos\alpha \tag{8.14a}$$

$$C_n(\alpha) = C_l(\alpha)\cos\alpha + C_d(\alpha)\sin\alpha \tag{8.14b}$$

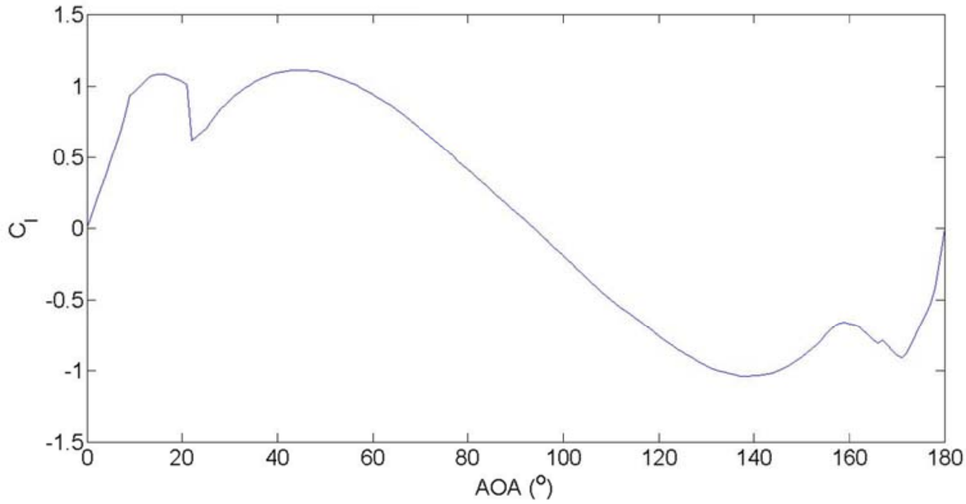

(a)

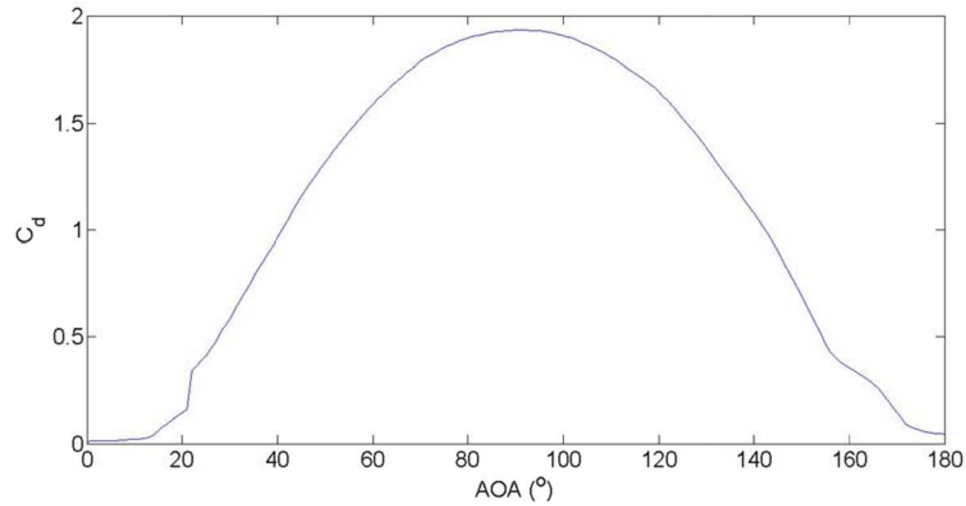

(b)

Fig. 8.3 Lift coefficient C_l and drag coefficient C_d of NACA0018. (a) C_l; (b) C_d.

From Fig. 8.2(b), it can be obtained that the relation between the drag force F_u or F_d and the tangential and normal force is

$$F = F_n \sin(\theta+\beta) - F_t \cos(\theta+\beta), \ \ F = F_u \ or \ F_d \tag{8.15}$$

Substituting Equation (8.13a) and Equation (8.13b) into Equation (8.15), one can derive

$$F = \frac{1}{2}\rho V_r^2 c\Delta h\left[C_n \sin(\theta+\beta) - C_t \cos(\theta+\beta)\right], \ \ F = F_u \text{ or } F_d \tag{8.16}$$

This equation is for the instantaneous force experienced while a blade element is between $\theta \pm \Delta\theta$. When no blade is present, the force is zero. For a rotor with N identical blades, a given streamtube at the upwind or downwind side is swept N times by blades during one revolution; in each time, the amplitude of force added by blades is given in Equation (8.16) and the duration is $\Delta\theta/\omega$. The time-averaged drag force can be obtained by multiplying an additional factor of $N\Delta\theta/(2\pi)$ in Equation (8.17)

$$\bar{F} = \frac{N\Delta\theta\rho V_r^2 c\Delta h}{4\pi}\left[C_n \sin(\theta+\beta) - C_t \cos(\theta+\beta)\right], \ \ \bar{F} = \bar{F}_u \text{ or } \bar{F}_d \tag{8.17}$$

Considering that Equation (8.8) (or Equation (8.9)) and Equation (8.17) describe the same force from two aspects, one can derive

$$a_u = \frac{1}{1+G_u(a_u)} \tag{8.18a}$$

$$a_d = \frac{1}{1+G_d(a_d)} \tag{8.18b}$$

where

$$G_u(a_u) = \frac{Nc\Delta h}{8\pi R \sin\theta}\left[C_n \sin(\theta+\beta) - C_t \cos(\theta+\beta)\right]\left(\frac{V_r}{V_u}\right)^2 \tag{8.19a}$$

$$G_d(a_d) = \frac{Nc\Delta h}{8\pi R \sin\theta}\left[C_n \sin(\theta+\beta) - C_t \cos(\theta+\beta)\right]\left(\frac{V_r}{V_d}\right)^2 \tag{8.19b}$$

where V_r in Equation (8.19a) is the relative wind speed at the upwind side while V_r in Equation (8.19b) is the relative wind speed at the downwind side. Equation (8.18) and Equation (8.19) give the iterative algorithm to calculate the induction factors a_u and a_d.

After calculating a_u and a_d, the aerodynamic forces can be obtained by Equation (8.13). The aerodynamic torque can be obtained by

$$T = \left(F_t \cos\beta - F_n \sin\beta\right) R \tag{8.20}$$

and the power can be calculated by

$$P = \left(F_t \cos\beta - F_n \sin\beta\right) \omega R \tag{8.21}$$

Substituting Equation (8.13) and Equation (8.14) into Equation (8.20), it obtains

$$\begin{aligned} T &= \frac{1}{2}\rho V_r^2 c\Delta h\left[\mathrm{C}_l(\alpha)\sin(\alpha-\beta) - C_d(\alpha)\cos(\alpha-\beta)\right] R \\ &= \frac{1}{2}\rho V_r^2 c\Delta h R\left[\mathrm{C}_l(\alpha)\sin\alpha_r - C_d(\alpha)\cos\alpha_r\right] \end{aligned} \tag{8.22}$$

where α_r is defined in Equation (8.11), representing the AOA of zero-pitch. The AOA region $|\alpha| < 21^{\circ}$ is defined as the stall free region for the blade of NACA0018 where stall does not happen; the AOA region $|\alpha| \geq 21^{\circ}$ is defined as the post stall region where the stall happened. From Equation (8.22), it can be seen that in the stall free region, C_d remains at a small value as shown in Fig. 8.3(b) and hence the torque

T is mainly offered by the lift force ($\frac{1}{2}\rho V_r^2 c\Delta h\, C_l$). That is why this type of VAWT is called lift-type. In this region, the torque T remains positive. From Fig. 8.3(a) and Fig. 8.3(b), it can be seen that in the AOA region $14^\circ < \alpha < 16^\circ$, C_l has little increase and it gradually decreases when $\alpha > 16^\circ$; C_d gradually increases when $\alpha > 14^\circ$. Hence, when $|\alpha| < 14^\circ$ the larger is the AOA $|\alpha|$, the larger is the torque *T*; when $14^\circ < |\alpha| < 30^\circ$, the torque *T* is decreased gradually. When AOA enter the post stall region, C_l will drop and C_d will jump and hence the torque T is largely reduced. In the post stall region, the larger is the AOA $|\alpha|$, the smaller is the torque T. When $|\alpha|$ is increased to a certain extent, the torque *T* will turn negative.

8.2.2 The startup algorithm

The difficulty in the startup is one of the main drawbacks of VAWTs and a pitch control system can benefit the turbine in this process. In the startup process, the rotational speed of a VAWT would increase from 0 to a specific value. As shown in Equation (8.12), Equation (8.13) and Equation (8.20), the aerodynamic torque is determined by the rotational speed, the wind speed and the pitch angle. The rotational speed and the wind speed cannot be controlled, and therefore the influence of pitch angle on the torque is studied in this subsection. Two control schemes are considered: one is the fixed pitch control algorithm in one revolution and the other is the sinusoidal pitch control algorithm in one revolution.

A VAWT with a 40m diameter rotor and 2m chord length NACA0018 blades is taken for example. The VAWT has 3 blades. The cut in wind speed is 5m/s and the considered rotational speed range is from 0.1rad/s to 1.0rad/s.

8.2.2.1 Control scheme 1: Fixed Pitch

The aerodynamic torque is calculated by Equation (8.20) and the influence of the pitch β on the aerodynamic torque is studied through the numerical simulation by DMST. The fixed pitch angles from -10° to 6° are considered here, as shown in Table 8.1. The aerodynamic torques per length and the corresponding AOAs at the rotational speeds of 0.1rad/s, 0.5rad/s and 1.0rad/s are shown in Fig. 8.4. A positive torque means that the torque is in the same direction of the rotation of the rotor, i.e. clockwise in this study; a negative torque means counter-clockwise and will obstruct the rotation of the rotor. The cases of other rotational speeds are given in Appendix F.

Table 8.1 the considered fixed pitch angles

Case	1	2	3	4	5	6	7	8	9
β (^{o})	-10	-8	-6	-4	-2	0	2	4	6

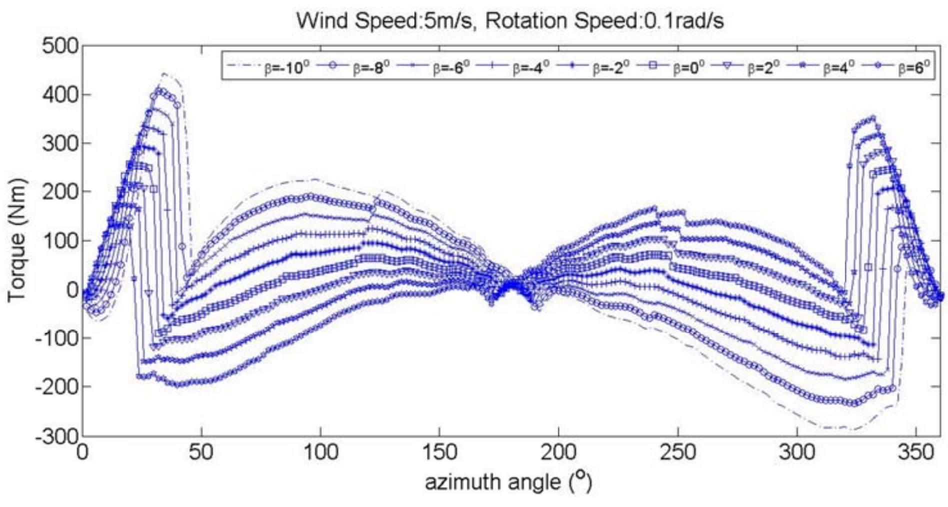

(a)

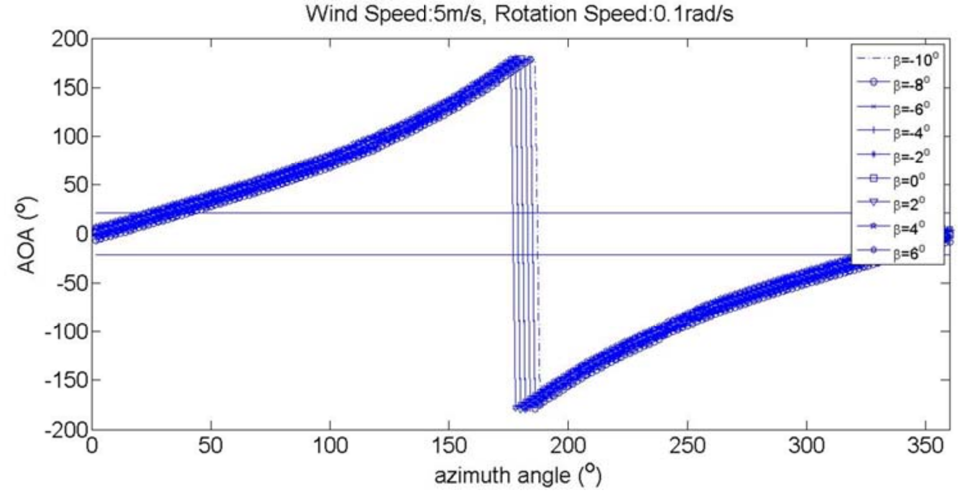
Wind Speed:5m/s, Rotation Speed:0.1rad/s
AOA (°)
azimuth angle (°)
β=-10°
β=-8°
β=-6°
β=-4°
β=-2°
β=0°
β=2°
β=4°
β=6°

(b)

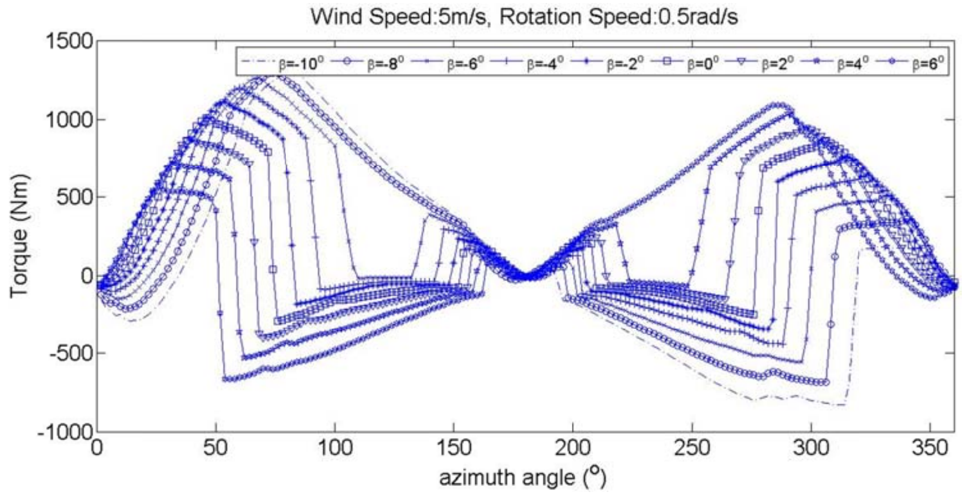
Wind Speed:5m/s, Rotation Speed:0.5rad/s
Torque (Nm)
azimuth angle (°)
β=-10° β=-8° β=-6° β=-4° β=-2° β=0° β=2° β=4° β=6°

(c)

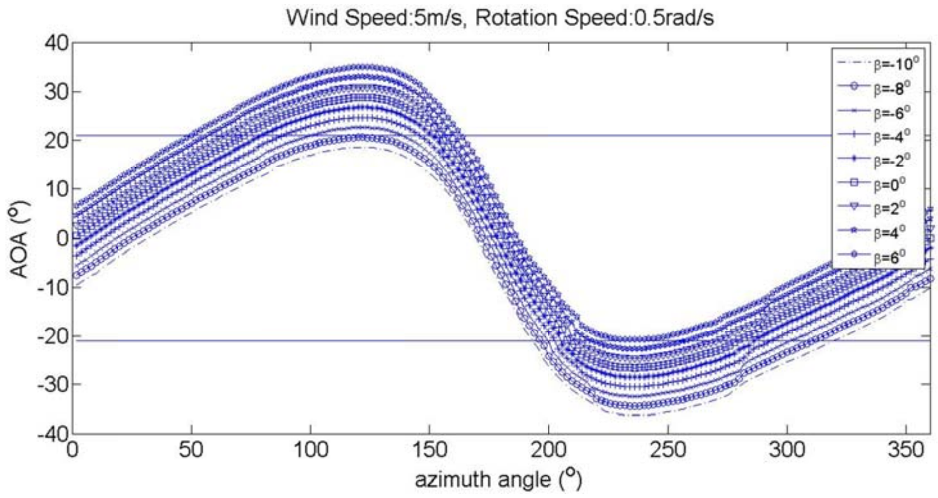
Wind Speed:5m/s, Rotation Speed:0.5rad/s
AOA (°)
azimuth angle (°)
β=-10°
β=-8°
β=-6°
β=-4°
β=-2°
β=0°
β=2°
β=4°
β=6°

(d)

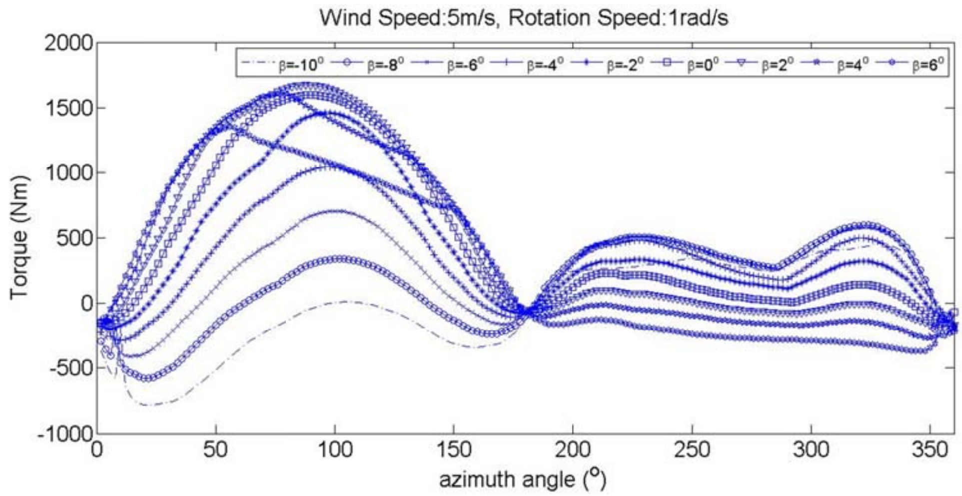

(e)

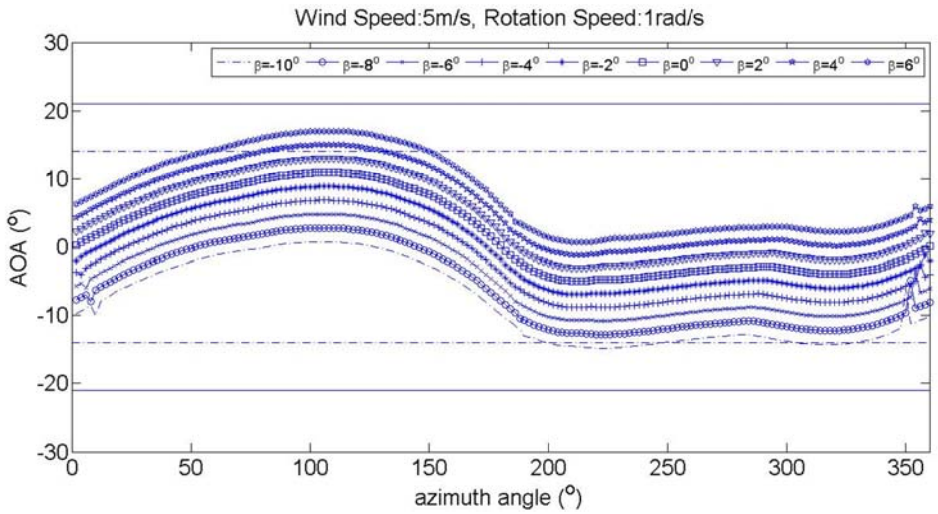

(f)

Fig. 8.4 the aerodynamic torques T per length and the corresponding AOAs for the fixed pitch cases. (a) T at $\omega = 0.1\, rad/s$; (b) AOA at $\omega = 0.1\, rad/s$; (c) T at $\omega = 0.5\, rad/s$; (d) AOA at $\omega = 0.5\, rad/s$; (e) T at $\omega = 1.0\, rad/s$; (f) AOA at $\omega = 1.0\, rad/s$.

For $\omega = 0.1\, \mathrm{rad/s}$, the AOA α ranges of different fixed pitches are shown in Fig. 8.4(b). The solid lines correspond to $|\alpha| = 21^{\mathrm{o}}$. As introduced in Section 8.2.1, when $|\alpha| > 21^{\mathrm{o}}$, stall will happen. At this rotational speed, all AOA ranges are from -180$^{\mathrm{o}}$ to 180$^{\mathrm{o}}$ and hence stall is unavoidable. Taking the zero pitch case ($\beta = 0^{\mathrm{o}}$, case 6) for example, it can be seen from Fig. 8.4(a) that when $\theta < 30^{\mathrm{o}}$, the AOA $\alpha < 21^{\mathrm{o}}$ and thus stall does not happen. When $\theta \geq 30^{\circ}$, $\alpha \geq 21^{\circ}$ and thus stall will happen and the torque will drop from about 250Nm to about -90Nm (dynamic stall is not considered in this study). With the increasing of the azimuth angle θ, the torque will first increase to about 60Nm and then decrease to about 10Nm at $\theta = 180^{\circ}$. When $180^{\circ} < \theta < 330^{\circ}$, there is still $|\alpha| > 21^{\circ}$. The torque will first increase to 70Nm and then decrease to -80Nm at $\theta = 330^{\circ}$. When $\theta > 330^{\circ}$, the AOA enters the stall free region and the aerodynamic torque has a sudden jump to 230Nm. With the further increasing of the azimuth angle θ, the torque will decrease to -10Nm with the decreasing of AOA. At this rotational speed, a revolution can be divided into 4 regions: 1) the azimuth region where stall does not happen in the upwind side ($0^{\circ} < \theta < 30^{\circ}$ for zero-pitch), denoted as region 1; 2) the azimuth region where stall happens in the upwind side ($30^{\circ} \leq \theta \leq 180^{\circ}$ for zero-pitch) , denoted as region 2; 3) the azimuth region where stall happens in the downwind side ($180^{\circ} < \theta \leq 330^{\circ}$ for zero-pitch) , denoted as region 3; 4) the azimuth region where stall does not happen in the downwind side ($330^{\circ} < \theta \leq 360^{\circ}$ for zero-pitch) , denoted as region 4. The influences of fixed pitch on the torque and the AOA in these four regions are shown in Fig. 8.4(a) and Fig. 8.4(b) respectively. The influence of fixed pitch in the whole revolution is uniform: a positive fixed pitch will increase the AOA and a negative fixed pitch will decrease it. Hence, the azimuth region 1 of a positive fixed pitch case is smaller than that of a negative fixed pitch, because the AOA of a positive fixed pitch will make the blade leave the stall free region earlier while leaving the stall free region of the AOA of a negative fixed pitch will make the blade leave the stall free region later. So, the torque of a negative fixed pitch case can further increase to a higher level than that of a positive one. In azimuth region 2, $\alpha > 21^{\circ}$ and the AOA α is decreased by a negative fixed pitch and is increased by a positive one. As discussed in Section 8.2.1, a larger AOA $|\alpha|$ in the post stall region will obtain smaller torque. Hence, in azimuth region 2, the torque of a negative fixed pitch case is larger than that of a positive fixed pitch. While, in azimuth region 3, the AOA turns negative; a negative fixed pitch will increase the AOA $|\alpha|$ and a positive one will decrease it. Hence, the torque of a positive fixed pitch case is larger than that of a negative fixed pitch in this azimuth region. In azimuth region 4, the AOA of a positive fixed pitch case will enter the stall free region in advance and thus obtain a large torque in a larger azimuth region.

With the increasing of rotational speed, the range of AOA is narrowed down. In the case of $\omega = 0.5\,\text{rad}/s$, there is no stall for the cases of $\beta = -10^{\circ}$ and -8° in the upwind side and $\beta = 6^{\circ}$ in the downwind side as shown in Fig. 8.4(c). With the further increasing of rotational speed, there are more and more cases that no stalls happen. When $\omega = 1.0\,\text{rad}/s$, no stall happens for all cases as shown in Fig. 8.4(f). The solid lines correspond to $|\alpha| = 21^{\circ}$ and the dash dot lines correspond to $|\alpha| = 14^{\circ}$. At this rotational speed, all AOA regions of fixed pitch cases are inside the stall free region. Taking the zero pitch case for example (case 6), in the upwind side, the AOA is increased from 0° to the maximum value of 11° at the azimuth $\theta = 107^{\circ}$, then with the increasing of the azimuth, AOA is decreased to 0° at the azimuth $\theta = 180^{\circ}$. In the whole downwind side, the AOA is negative. $|\alpha|$ increases from 0° to about 4° at the azimuth $\theta = 200^{\circ}$, then with the increasing of the azimuth, $|\alpha|$ maintains at 4° in the azimuth region $200^{\circ} < \theta < 330^{\circ}$, then $|\alpha|$ decreases to 0° at the azimuth $\theta = 360^{\circ}$. The influences of fixed pitch on the torque and the AOA are shown in Fig. 8.4(e) and Fig. 8.4(f) respectively. As introduced in the above analysis, a positive fixed pitch would increases the AOA in the whole upwind side and a negative pitch would decrease it. Therefore, in the upwind side, a negative fixed pitch would produce less torque than the zero pitch. Although the positive fixed pitches of 4° and 6° increases the AOA, the AOAs of these two cases are larger than 14° and thus the torques are reduced. The largest torque is obtained by the positive fixed pitch of 2°, which increases the AOA and maintains $\alpha < 14^{\circ}$ at the same time. In the downwind side, a negative fixed pitch would increase $|\alpha|$ and thus the torque, while a positive fixed pitch would decrease $|\alpha|$ and thus the torque. The largest torque is obtained by the fixed pitch of -8° because in some azimuth regions, $|\alpha|$ of the fixed pitch case of -10° is larger than 14° and thus the torque is reduced.

From the above analyses, it can be found that a fixed pitch has reversed influences on the torque in the upwind and downwind sides no matter whether stall happens or not. Therefore, a fixed pitch cannot increase the torque in both upwind and downwind side.

8.2.2.2 Control scheme 2: Variable Pitch

In this section, the pitch angle in sinusoidal variation is studied. The relation between the pitch angle β' and the azimuth angle θ is shown in Equation (8.23).

$$\beta' = \beta \sin\theta \tag{8.23}$$

Different amplitudes β are considered, which are selected as the same as the fixed pitches in Section 8.2.2.1, see Table 8.1. The simulated aerodynamic torques and the corresponding AOA at the rotational speeds of 0.1rad/s, 0.5rad/s and 1.0rad/s are shown in Fig. 8.5.

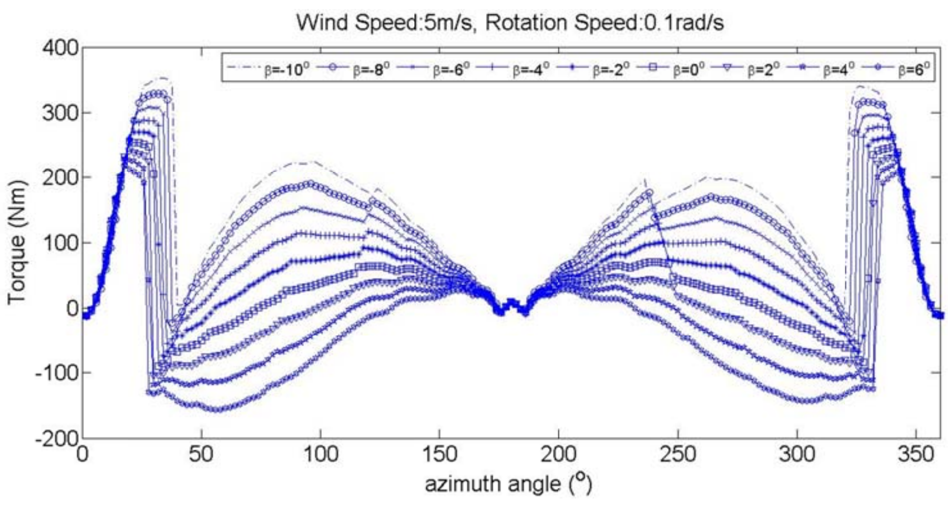

(a)

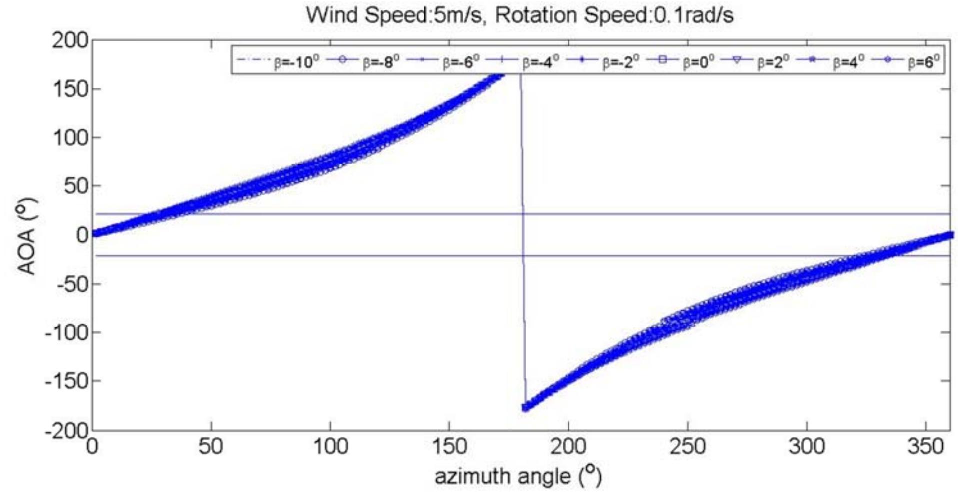
Wind Speed:5m/s, Rotation Speed:0.1rad/s
β=-10° β=-8° β=-6° β=-4° β=-2° β=0° β=2° β=4° β=6°
AOA (°)
azimuth angle (°)

(b)

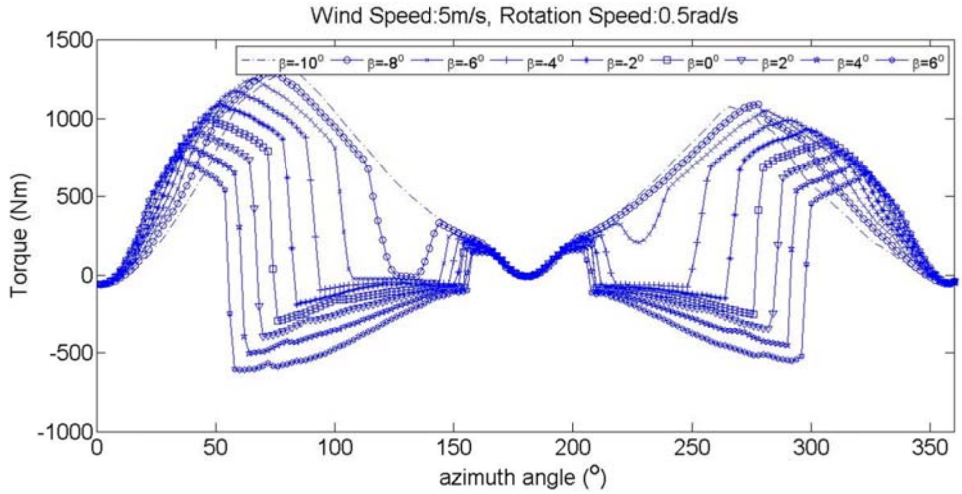
Wind Speed:5m/s, Rotation Speed:0.5rad/s
β=-10° β=-8° β=-6° β=-4° β=-2° β=0° β=2° β=4° β=6°
Torque (Nm)
azimuth angle (°)

(c)

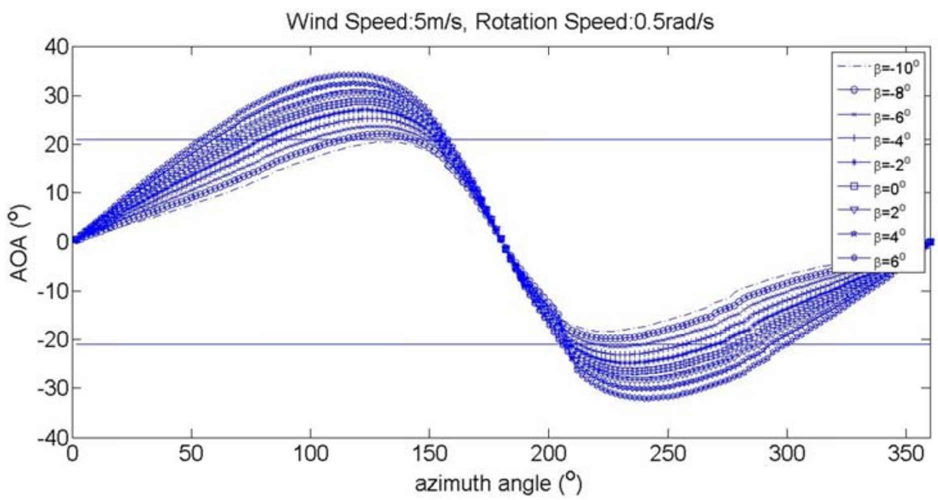
Wind Speed:5m/s, Rotation Speed:0.5rad/s
β=-10°
β=-8°
β=-6°
β=-4°
β=-2°
β=0°
β=2°
β=4°
β=6°
AOA (°)
azimuth angle (°)

(d)

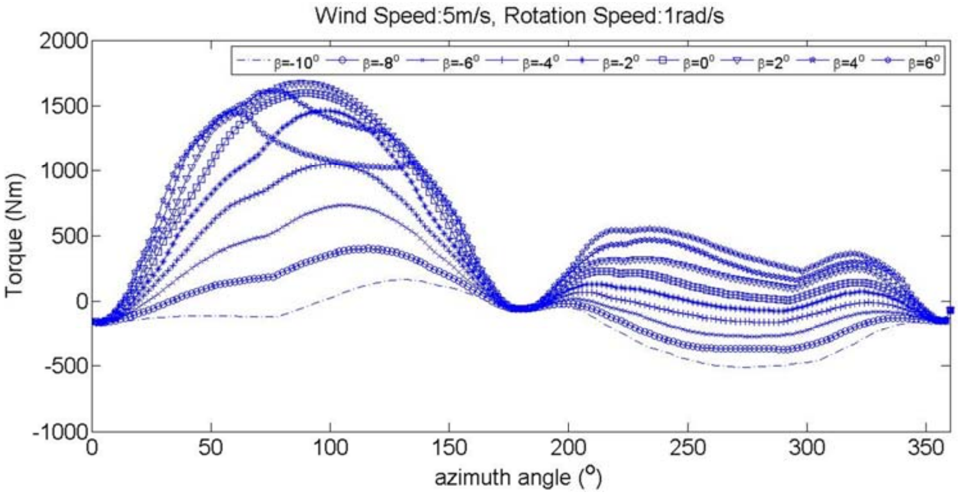

(e)

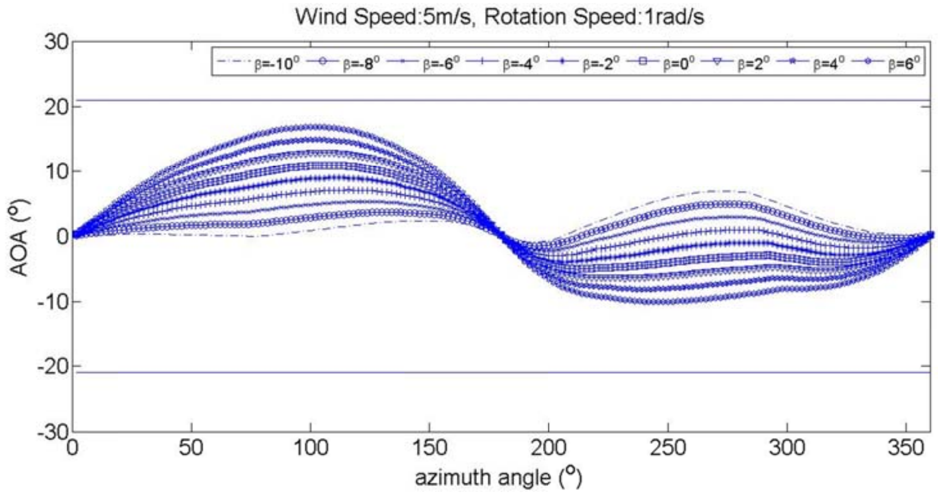

(f)

Fig. 8.5 the aerodynamic torques T per length and the corresponding AOA for the variable pitch cases. (a) T at $\omega = 0.1 rad/s$; (b) AOA at $\omega = 0.1 rad/s$; (c) T at $\omega = 0.5 rad/s$; (d) AOA at $\omega = 0.5 rad/s$; (e) T at $\omega = 1.0 rad/s$; (f) AOA at $\omega = 1.0 rad/s$.

The torques and the AOAs of the case ω =0.1rad/s are shown in Fig. 8.5(a) and Fig. 8.5(b) respectively. It can be seen that stall is still unavoidable, which is the same as the fixed pitch cases, and a revolution can also be divided into 4 regions as the fixed pitch cases, but the influences of a sinusoidal pitch on the torque and the AOA stalls are quite different. A sinusoidal pitch with positive amplitude can increase $|\alpha|$ in both upwind and downwind sides and a sinusoidal pitch with negative amplitude can decrease $|\alpha|$ in the whole revolution. Therefore, a negative amplitude can prolong azimuth region 1 and 4 and decreases $|\alpha|$ in azimuth region 2 and 3. The result is that the negative amplitude of -10° produce the largest torque in most of a revolution.

In the case of $\omega = 0.5\,\mathrm{rad}/s$, stall does not appear in case 1 ($\beta = -10^{\circ}$) in both upwind and downwind side as shown in Fig. 8.5(d). In the case of $\omega = 1.0\,\mathrm{rad}/s$, no stall occurs and it is found that a positive amplitude can increase the torque while a negative one would just decrease it. The reason is that a positive amplitude can enlarge $|\alpha|$ in both the upwind and downwind sides and thus the torque is increased.

From the above analyses, it can be found that a sinusoidal pitch variation has the same influences on the torque: either increasing or reduction in the whole revolution, which is different from the fixed pitch cases. When stall does not happen, a positive amplitude can produce larger torque; when stall happens, a negative amplitude can produce larger torque.

8.2.2.3 Discussions

From Section 8.2.2.1 and Section 8.2.2.2, it can be found that a positive fixed pitch can enlarge $|\alpha|$ in the upwind side and can decrease it in the downwind side; a negative fixed pitch can decrease $|\alpha|$ in the upwind side and increase it in the downwind side. While a sinusoidal pitch variation with a positive amplitude can increase $|\alpha|$ in both the upwind and downwind sides; a sinusoidal pitch variation with a negative amplitude can decrease $|\alpha|$ in the whole revolution. Therefore, a fixed pitch has reversed influences on the torque in the upwind side and the downwind side, no matter whether stall happens or not. However, the previous analyses focus on one blade, three blades should be considered in the startup process.

Moreover, it still needs further studies to determine which algorithm can provide better performs in the startup state and how to control the pitch at a specific wind speed and rotational speed. Furthermore, in the previous analyses, only the cut-in wind speed 5m/s is considered. Actually, a VAWT can start up at a higher wind speed, and hence more wind speeds shall be considered.

Because the kinetic energy of the rotor comes from the work of wind load, the work of wind load can be used as an index to evaluate the effect of pitch control in the startup process at a specific wind speed and rotational speed. By comparing the works done by the aerodynamic torques of the three blades in one revolution, the optimal pitch angle corresponding to the largest work at different wind speeds and rotational speeds can be selected. For example, in the wind speed of 5m/s and the rotational speed of 0.1rad/s, the works (calculated by the torque per length) of different cases are shown in Fig. 8.6(a). In Fig. 8.6(a), a positive work means that the work generated by the positive torque which is in the same direction of the rotation of the rotor, i.e. clockwise in this study. It can be seen that the sinusoidal pitch variation with the amplitude of -10^o produces the largest positive work. In the wind speed of 5m/s and the rotational speed of 0.5rad/s, the works (calculated by the torque per length) of different cases are shown in Fig. 8.6(b). It can be seen that the sinusoidal pitch variation with the amplitude of -10^o also produces the largest positive work. However, in the wind speed of 5m/s and the rotational speed of 1.0 rad/s, the sinusoidal pitch variation with the amplitude of 4^o produces the largest positive work (see Fig. 8.6 (c)). From the above three cases, it can be found that sinusoidal pitch control can produce larger works than those produced by the fixed pitch control.

Considering the wind speed range from 5m/s to 10m/s and the rotational speed range from 0.1rad/s to 1.0rad/s, the available maximum powers of the two control algorithms at each wind speed and rotational speed are shown in Fig. 8.7(a) and Fig. 8.7(b). It can be found that the sinusoidal pitch control can obtain larger work than the fixed pitch scheme at any wind speed and rotational speed. Moreover, the rotational speed is increasing in the startup process, the fixed pitch control actually would change the pitch frequently while producing less work than the sinusoidal one, which is not practical. Therefore, the sinusoidal pitch control should be used in the startup process. To provide the reference pitch for the sinusoidal control, the optimal pitch angle amplitudes corresponding to the maximum power at each wind speed and rotational speed are given in Fig. 8.8. It can be found that at a low rotational speed, the sinusoidal pitch variation with the amplitude of -10^{o} gets the largest work of the torque. With the increasing of rotational speed, the optimal pitch angle amplitude is transformed from negative to positive. This is because the range of AOA is diminishing. When stall does not happen, the optimal pitch angle amplitude would become positive.

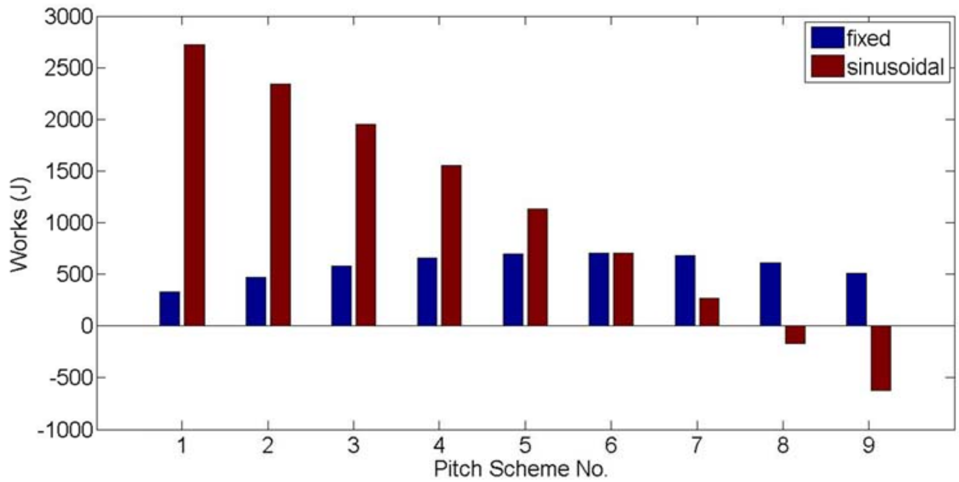

(a)

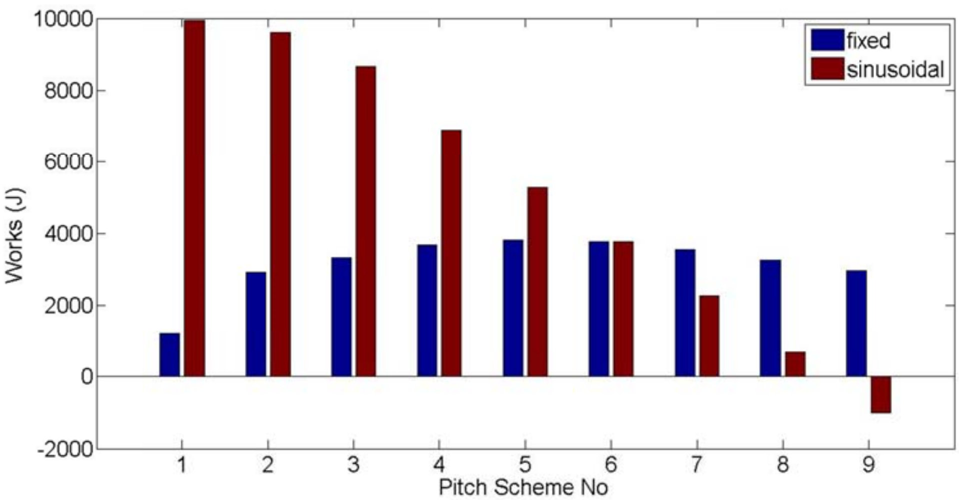

(b)

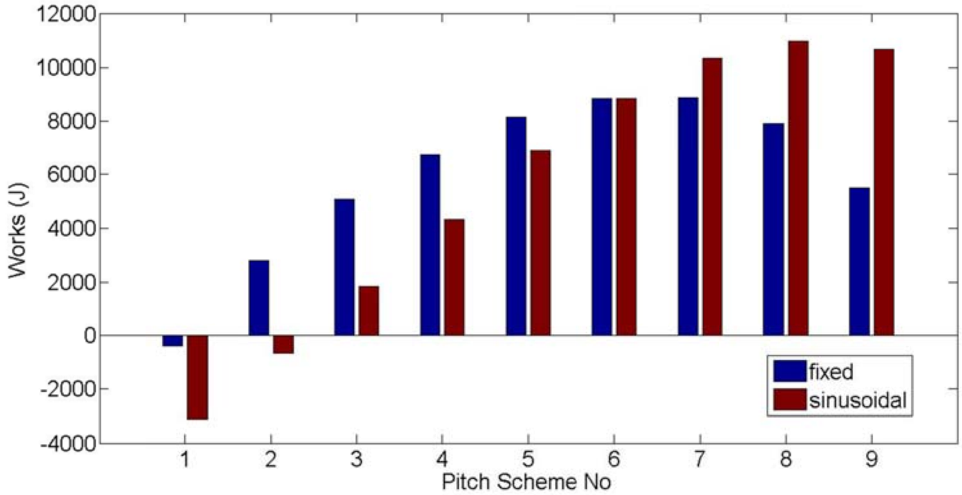

(c)

Fig. 8.6 The works of different cases. (a) 0.1rad/s; (b) 0.5rad/s; (c) 1.0rad/s

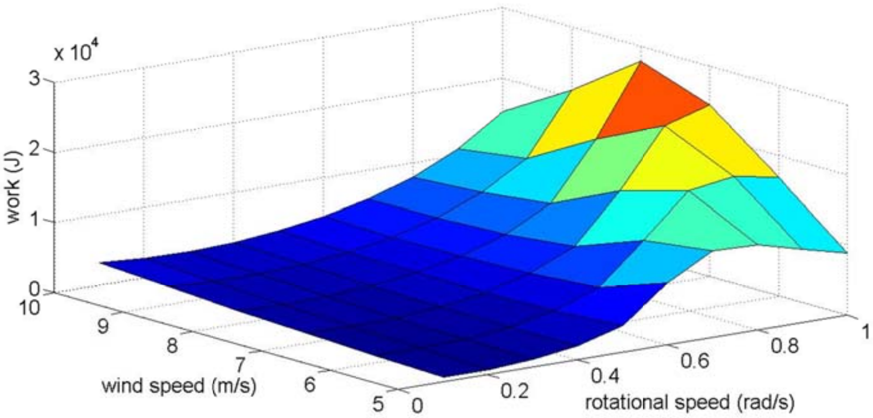

(a)

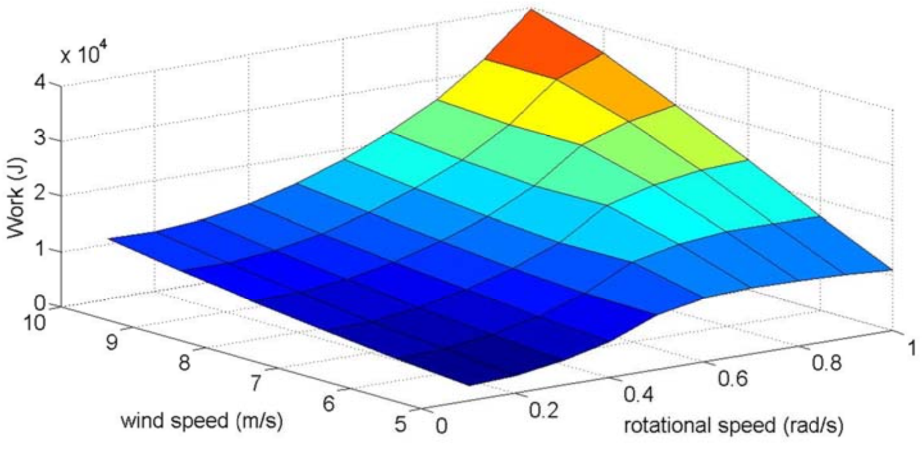

(b)

Fig. 8.7 The maximum works. (a) fixed pitch; (b) sinusoidal pitch

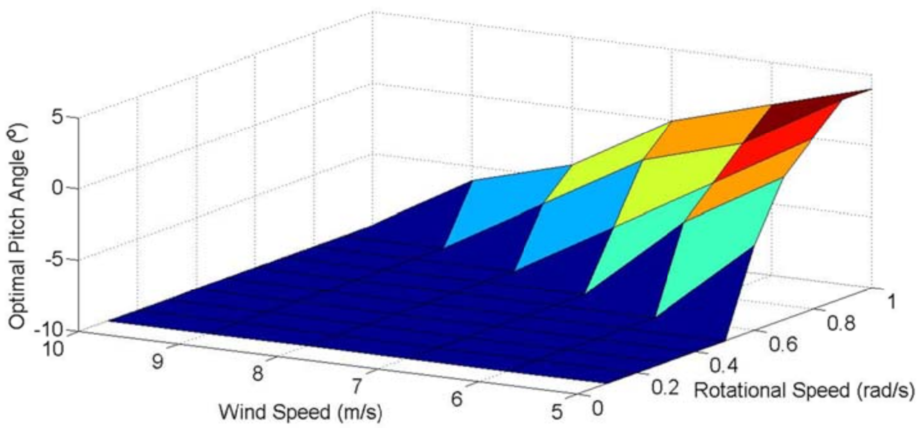

Fig. 8.8 The optimal pitch angle amplitude for variable pitch control in the start-up state

8.2.3 The power maximization algorithm

When a wind turbine is grid-connected, the rotational speed is basically locked. As shown in Equation (8.12), Equation (8.13) and Equation (8.20), the dominative factors of aerodynamic torque are the wind speed and the pitch angle. In this section, the rotational speed is fixed at 2.1rad/s, and the influence of pitch angle on the power maximization is studied. Similar to the startup control, two control schemes, the fixed pitch and the sinusoidal variation pitch, are considered. In this state, the fixed pitch control means that the pitch is fixed at the same mean wind speed; when the wind speed changes, the pitch can be changed accordingly. The considered wind speed region is from the cut-in wind speed (6m/s) to the rated wind speed (14m/s).

Firstly, the fixed pitch control is considered. The selected pitches are the same as those in Section 8.2.2.1 and listed in Table 8.1. The output power generated by the aerodynamic torques of the three blades in one revolution at different wind speeds is shown in Fig. 8.9. The power P is calculated by $P=T\omega$. The sign of power P is determined according to the definition. Because the direction of rotation is unchanged, the sign of ω remains positive all the time. So the positive power is the work produced by the positive torque in the unit time; the negative power is the work produced by the negative torque in the unit time. It can be found that at the low wind speed, 5m/s for example, the positive fixed pitch can produce more power than the zero-pitch case and $\beta = 6°$ produces the largest power. With the increasing of the wind speed, the optimal fixed pitch is decreased from $\beta = 6°$ to $\beta = -2°$ at the wind speed of 14m/s.

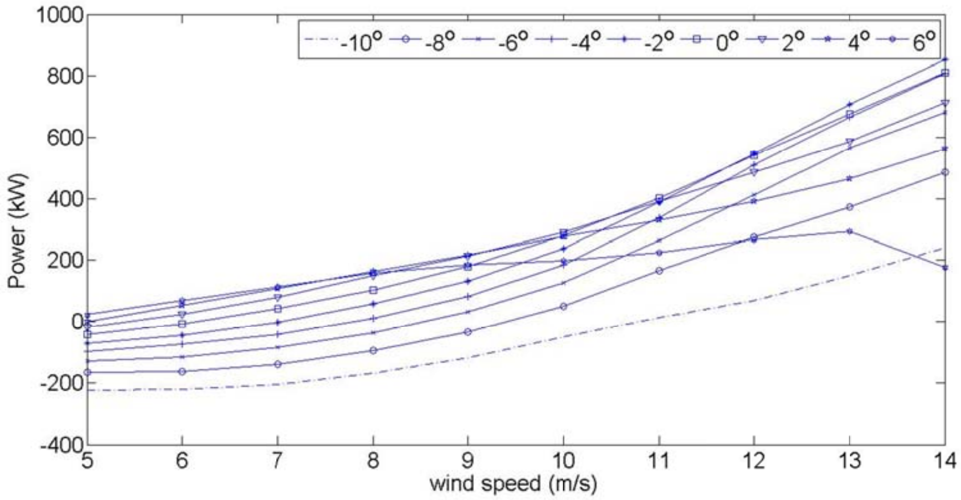

Fig. 8.9 the output power versus the wind speed for the fixed pitch cases.

These phenomena can be explained by the region of AOA in one revolution. The AOA curves at different wind speeds can refer to Appendix G. As discussed in Section 8.2.2.1, when the wind speed is low, the region of AOA is small. Hence the positive pitch can increase the AOA and thus the torque. With the increasing of wind speed, the range of AOA is enlarged. When the wind speed increases to a certain extent, stall happens. According to the analyses in Section 8.2.2.1, the fixed pitch should be negative to decrease the AOA.

Secondly, the sinusoidal variation pitches which are the same as those in Section 8.2.2.2 are considered in this study. The output power at different wind speeds is shown in Fig. 8.10. Similar to the fixed pitch control, it can be found that at the low wind speed, the maximum power corresponds to a positive amplitude of sinusoidal pitch, which is produced by the amplitude of $\beta = 6^\circ$. With the increasing of wind speed, the optimal pitch amplitude is decreased from $\beta = 6^\circ$ to $\beta = 0^\circ$ at the wind speed of 14m/s. It is found that the zero pitch produces the largest power while all cases of sinusoidal pitch cannot produce more power. These phenomena can also be explained by the distribution of AOA as the fixed pitch case, which will not be repeated here. The AOA curves at different wind speeds can refer to Appendix G.

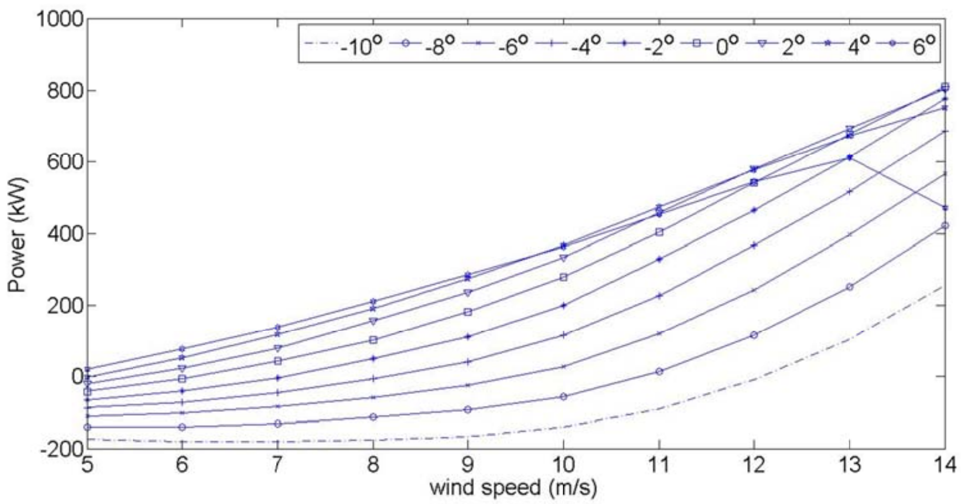

Fig. 8.10 the output power versus the wind speed for the variable pitch cases.

To evaluate the effects of these control algorithms and figure out the optimal pitch angle, the largest positive powers at different wind speeds presented in Fig. 8.9 and Fig. 8.10 are compared. The optimal fixed pitch angles at different wind speeds are shown in Fig. 8.11(a) and the optimal amplitudes of sinusoidal pitch are shown in Fig. 8.11(b). The optimal powers obtained by using these two control algorithms are shown in Fig. 8.12. It can be found that the more power can be produced by the sinusoidal pitch control algorithm than the fixed pitch scheme at most wind speeds. Therefore, the sinusoidal pitch should still be used and the pitch control at different wind speeds should refer to Fig. 8.11(b).

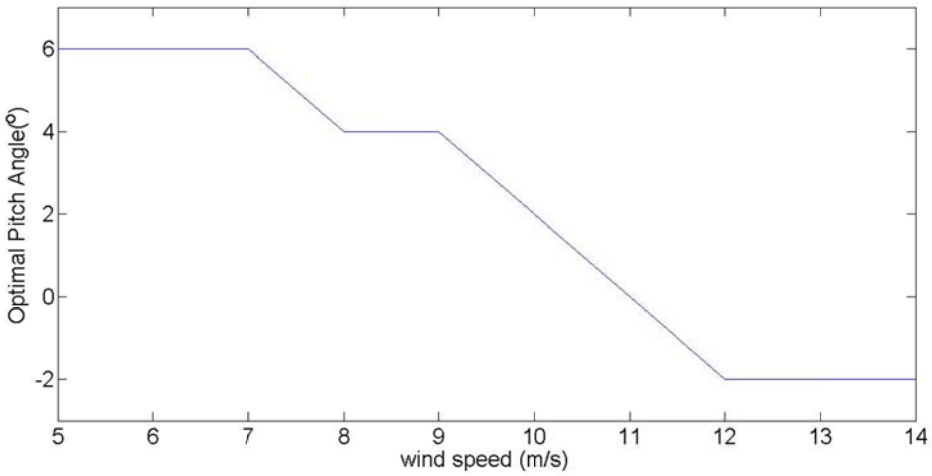

(a)

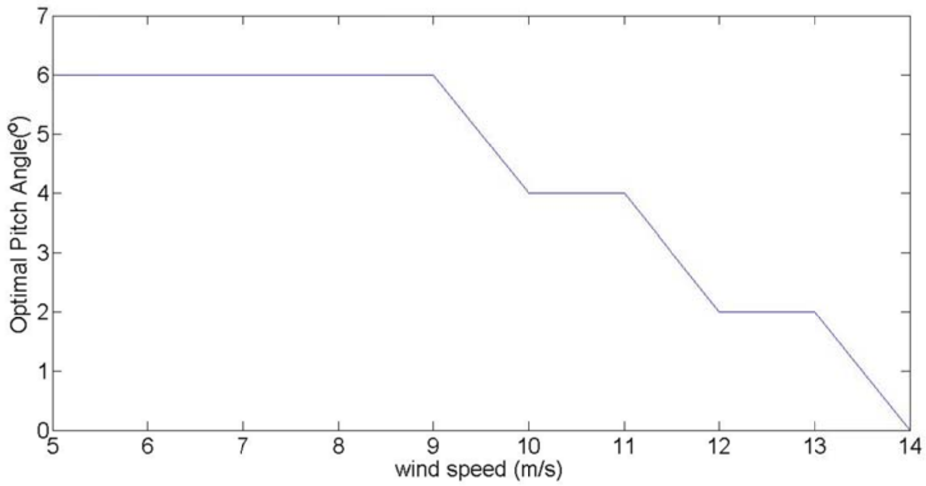

(b)

Fig. 8.11 The reference pitch in state 2. (a) the optimal pitch angle for the fixed pitch control ; (b) the optimal amplitude for sinusoidal pitch angle control.

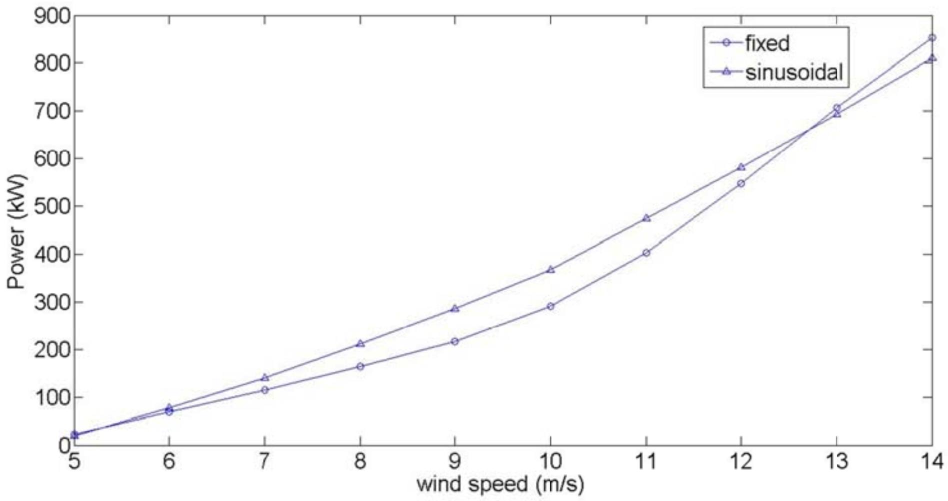

Fig. 8.12 Optimal powers obtained by the two control algorithms

It is also found that the fixed control algorithm can obtain more power than the sinusoidal one at the wind speed of 14m/s. The reason can also be explained by the distribution of AOA at this wind speed. At the wind speed of 14m/s, the AOAs versus azimuth θ of the fixed pitch control are shown in Fig. 8.13. The solid lines indicate the azimuth of 21^{o} where the stall will happen; the dash dot lines indicate the azimuth of 14^{o} which corresponds to the largest torque as introduced in Section 8.2.2.1. The AOA of zero pitch just gets across the dash dot line in the upwind side while the AOA in the downwind side is inside the region of dash dot lines. The dash dot line indicates the AOA which corresponds to the largest torque. Hence, a minus pitch angle of 2^{o} can enlarge the torques in both the upwind and downwind sides. On the other hand, the AOAs versus the azimuth $\theta$of the sinusoidal control are shown in Fig. 8.14. The AOA of zero pitch just gets across the dash dot line in the upwind side. The dash dot line indicates the AOA which corresponds to the largest c_l. It means that further increasing of AOA will just decrease the torque. A minus amplitude will increase the torque in the upwind side but will decrease the torque in the downwind side. Hence, the sinusoidal pitch control cannot produce more power than the zero pitch at this wind speed. Therefore, the fixed pitch control can produce more power than the sinusoidal control at this wind speed.

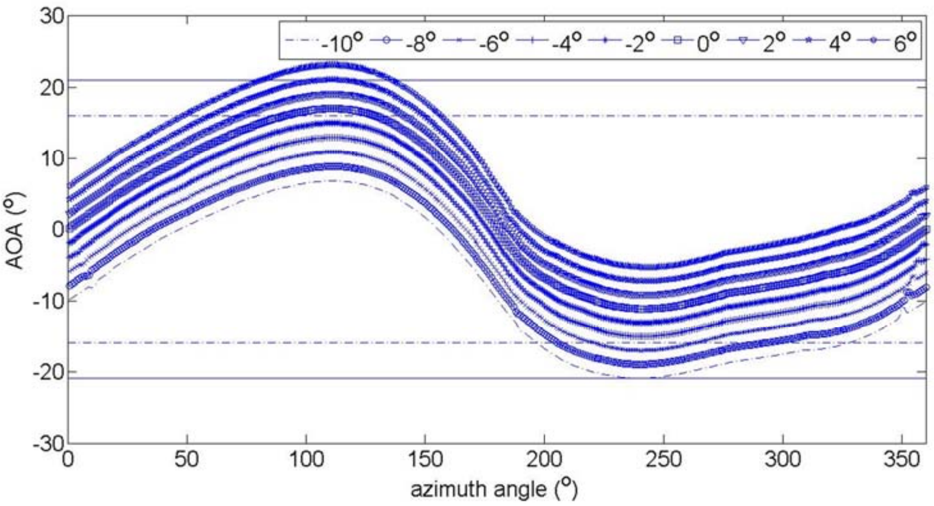

Fig. 8.13 AOA of the fixed pitch cases at the wind speed of 14m/s

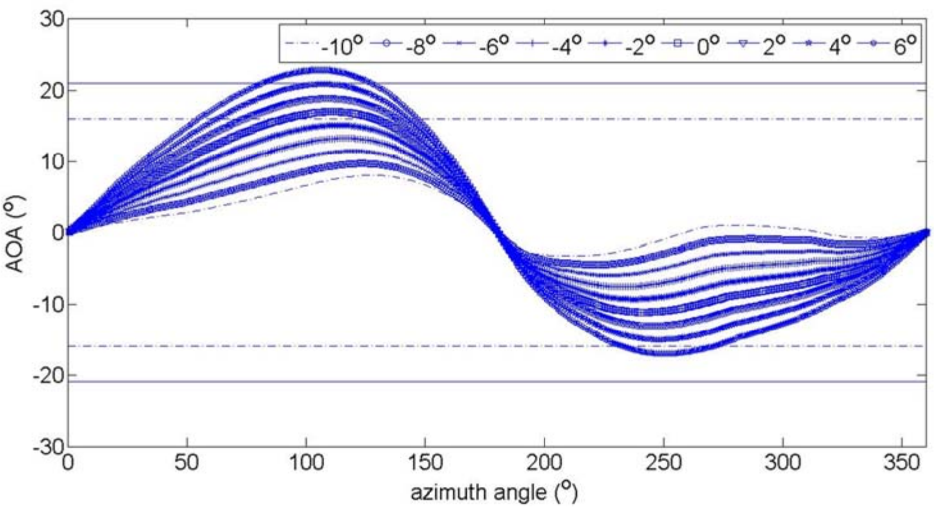

Fig. 8.14 AOA of the sinusoidal pitch cases at the wind speed of 14m/s

8.2.4 The power control algorithm

The produced power is not the higher the better. There is a rated power for every wind turbine and the wind speed corresponding to the rated power is called the rated wind speed. When the wind speed is above the rated wind speed, it is required to maintain the power in the rated value. In this study, the rated wind speed is selected as 14m/s in this study and the rotational speed is still 2.1rad/s. The rated power is about 800kW. The power versus wind speed of the zero pitch case is shown in Fig. 8.15. It can be found that when the wind speed increases, the power still increases and reaches the maximum value of about 1000kW at the wind speed of 16m/s and then the power would decrease to about 600kW. Hence, the zero pitch case cannot satisfy this requirement.

It hopes to adjust the pitch and maintain the power as the rated value in the high wind. Two pitch control schemes are considered in this subsection as the previous analyses: the fixed pitch in one revolution and the variable pitch in one revolution. The fixed pitch angles are listed in Table 8.1. The produced powers are shown in Fig. 8.15. The straight line is the target rated power. It is obvious that through adjusting the pitch angle, the rated power cannot be obtained by the fixed pitch control in the wind speed range from 19m/s to 20m/s. The sinusoidal variation pitches which are the same as those in Section 8.2.2.2 are also considered. The powers of the sinusoidal pitch control are shown in Fig. 8.16. It can be seen that the power is possible to be maintained at the rated value from the rated wind speed (14m/s) to the cutout wind speed (20m/s) by adjusting the amplitude of sinusoidal pitch according to the mean wind speed. It means that the optimal pitch angle amplitudes in different wind speeds can be selected by comparing the corresponding produced power with the rated power, which is shown in Fig. 8.17. The powers of the cases with and without pitch controls are shown in Fig. 8.18. The sinusoidal pitch control can maintain the power at the rated value in the whole wind speed region but the fixed pitch control cannot produce the rated power in the wind speed region from 19m/s to 20m/s.

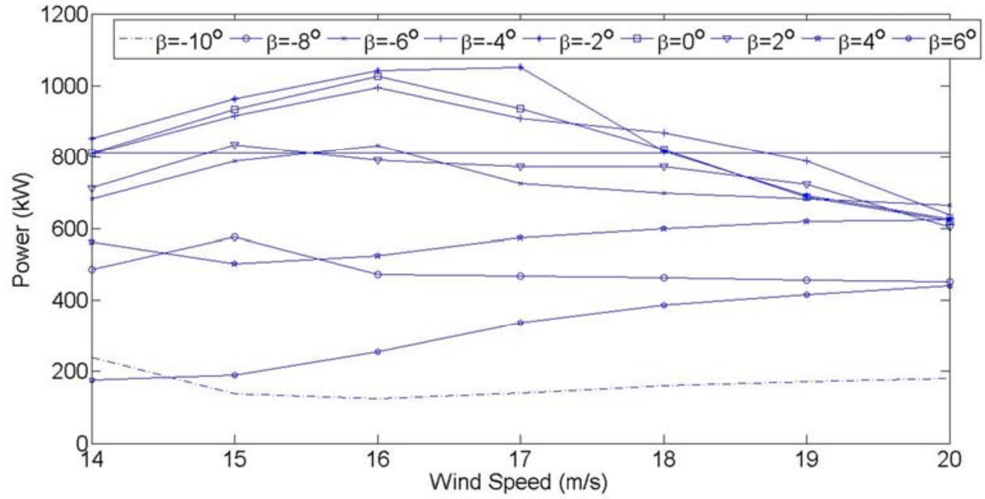

Fig. 8.15 The output power versus the wind speed for different fixed pitch cases

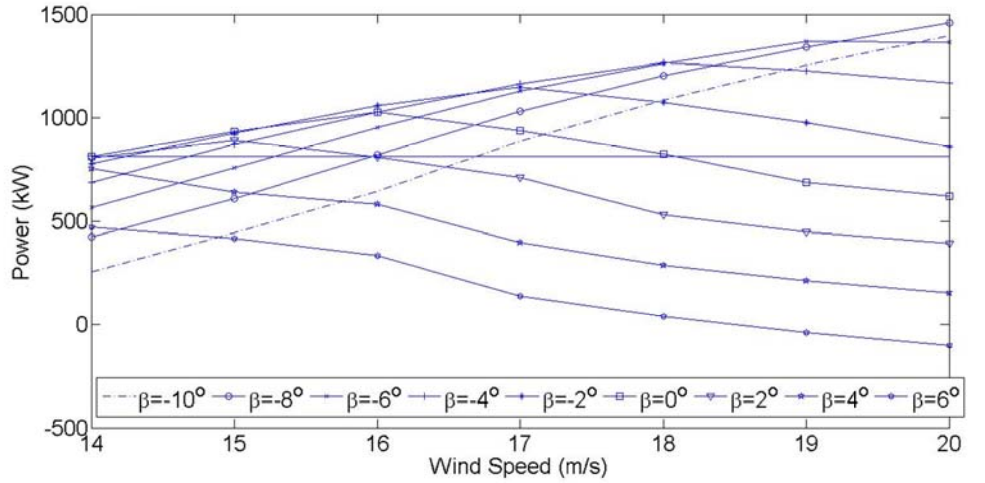

Fig. 8.16 The output power versus the wind speed for different variable pitch cases

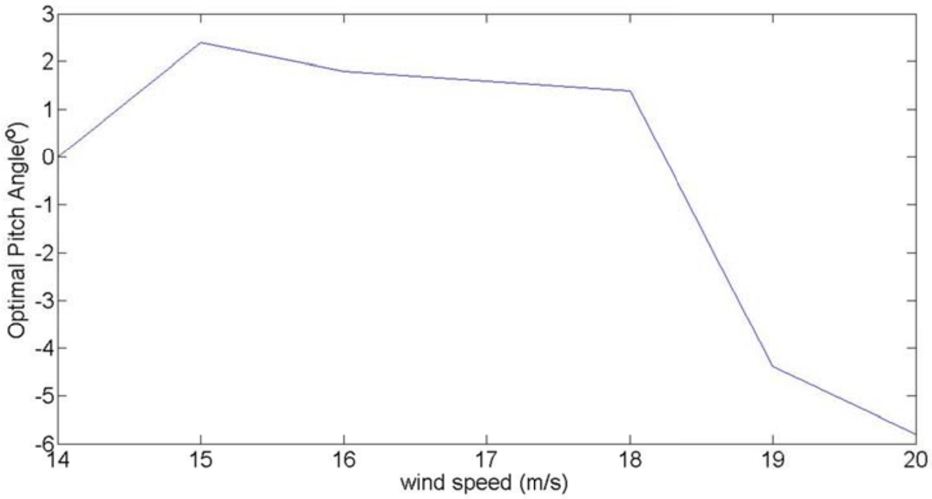

(a)

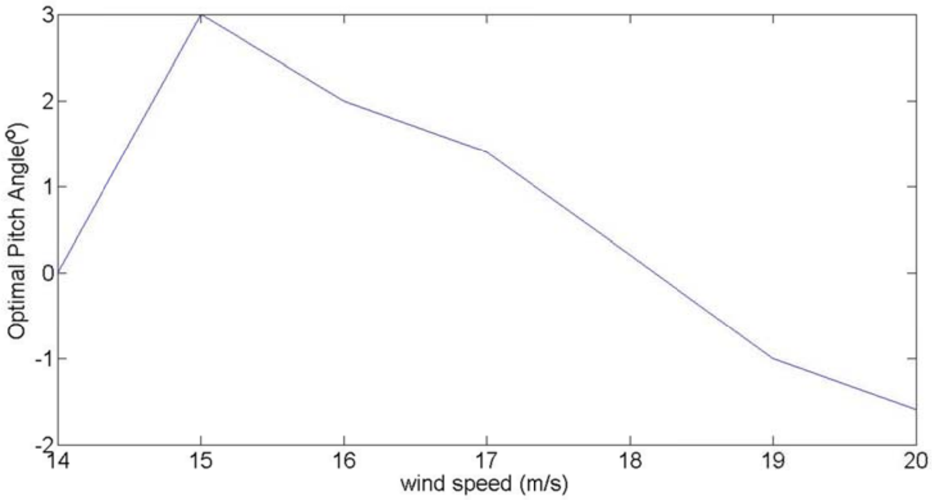

(b)

Fig. 8.17 The optimal fixed pitch and the optimal pitch amplitude. (**a**) the optimal fixed pitch angle; (b) the optimal amplitude for sinusoidal pitch angle control.

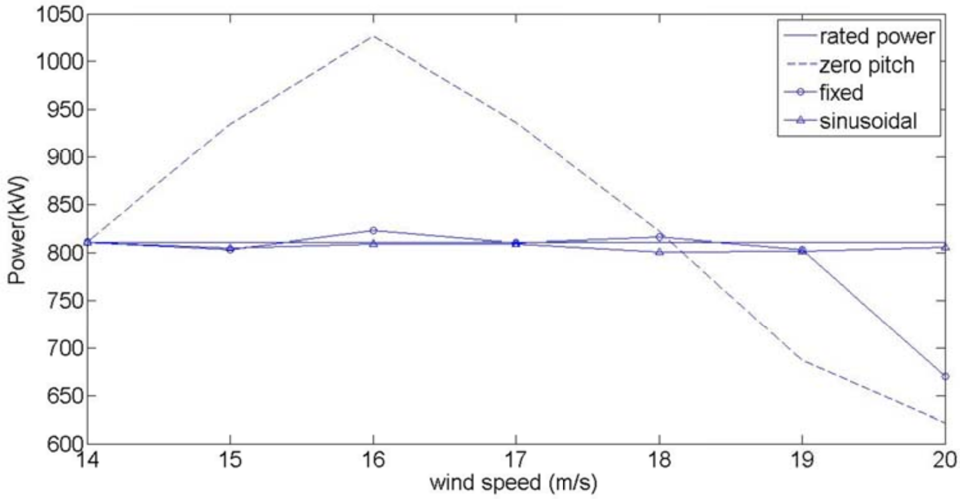

Fig. 8.18 The power production of the cases with and without pitch control

8.2.5 The parking algorithm

When the wind speed reaches a specific value, a wind turbine should be delinked from the grid and parked. This wind speed is called the cutout wind speed. In 1980s, there are many reasons why the concept of VAWT is given up and one of these is the difficulty in parking a VAWT in the high wind speed. In those years, the research interest is focused on the Φ-type VAWT which cannot change its pitch.

In this section, the possibility of the aid of the pitch control in parking is studied. For the VAWT considered in this study, the cutout wind speed is selected as 20m/s. The rotational speeds from 2.1rad/s down to 0.1rad/s are included. And the fixed pitch control and the sinusoidal variation pitch control are considered.

8.2.5.1 Control scheme 1: Fixed Pitch

There are two ways to shut down a wind turbine by pitch regulation: one is to decrease the AOA so that the torque can be reduced; and the other is to increase the AOA so that the stall can happen. Because the first method needs more precise sensing and control systems than the second one, the method of stall has a wider application in HAWTs. In this section, the stall shut-down method is adopted. To study the influence of fixed pitches on the torque, three fixed pitch angles are selected: $\beta = -10^{\circ}$, 0° and 10°. For the rotational speeds of 2.1rad/s, 1.0rad/s and 0.1rad/s and the wind speed of 20m/s, the torques and the corresponding AOA of the three cases in a cycle are shown in Fig. 8.19. The torques and AOA of other rotational speeds can refer to Appendix H.

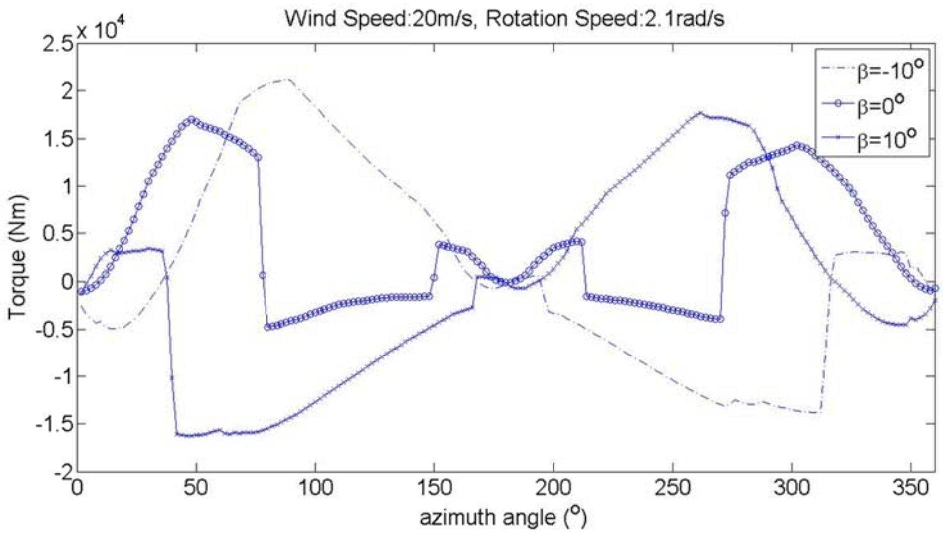

(a)

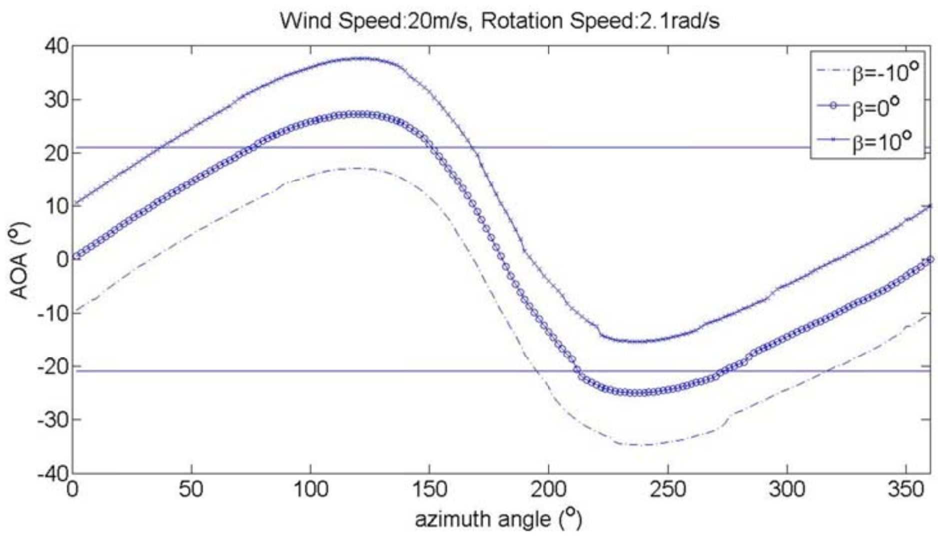

(b)

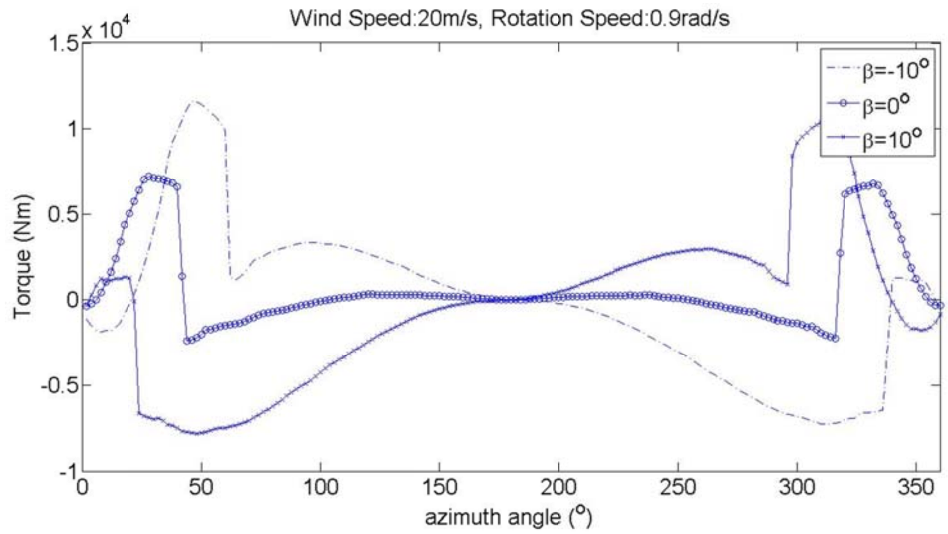

Wind Speed:20m/s, Rotation Speed:0.9rad/s
x 10^4
1.5
1
0.5
0
-0.5
-1
Torque (Nm)
0
50
100
150
200
250
300
350
azimuth angle (°)
β=-10°
β=0°
β=10°

(c)

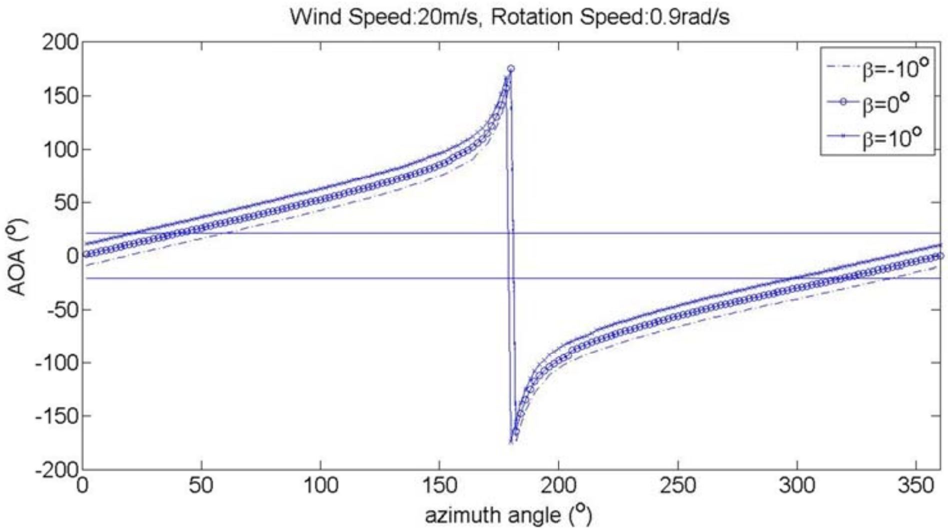

Wind Speed:20m/s, Rotation Speed:0.9rad/s
200
150
100
50
0
-50
-100
-150
-200
AOA (°)
0
50
100
150
200
250
300
350
azimuth angle (°)
β=-10°
β=0°
β=10°

(d)

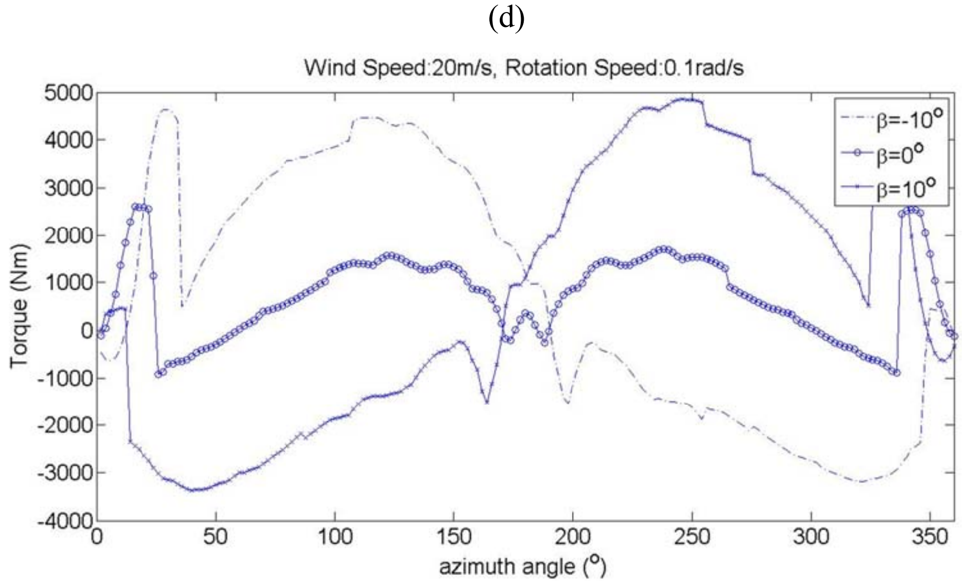

Wind Speed:20m/s, Rotation Speed:0.1rad/s
5000
4000
3000
2000
1000
0
-1000
-2000
-3000
-4000
Torque (Nm)
0
50
100
150
200
250
300
350
azimuth angle (°)
β=-10°
β=0°
β=10°

(e)

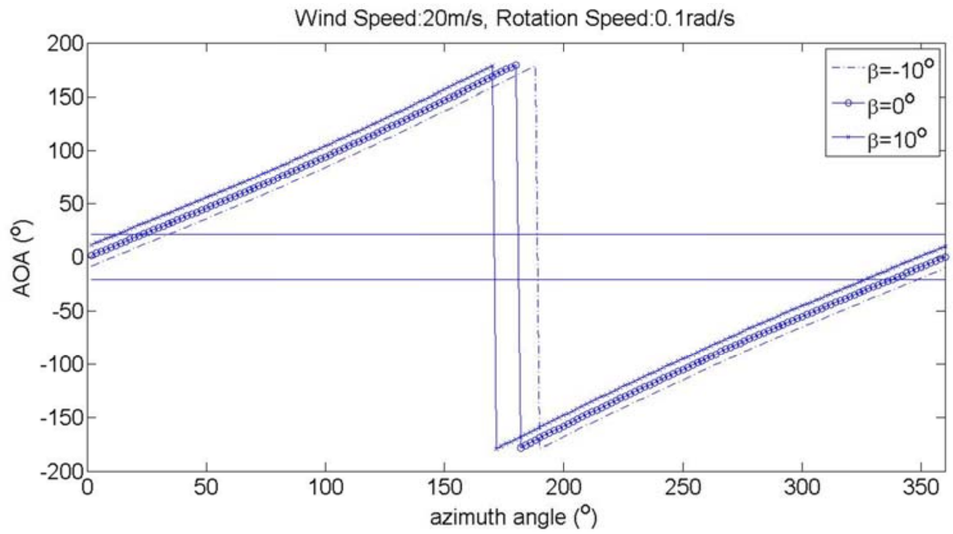

(f)

Fig. 8.19 the aerodynamic torques T per length and the corresponding AOAs for the fixed pitch cases. (a) T at $\omega = 2.1\,rad/s$; (b) AOA at $\omega = 2.1\,rad/s$; (c) T at $\omega = 0.9\,rad/s$; (d) AOA at $\omega = 0.9\,rad/s$; (e) T at $\omega = 0.1\,rad/s$; (f) AOA at $\omega = 0.1\,rad/s$.

It can be found that in these rotational speed cases, the sign of the torque is different in the upwind side and the downwind side for the nonzero fixed pitch cases ($\beta = -10^{\circ}$ and 10°). That is because a fixed pitch could only increase the minus torque either in the upwind side or in the downwind side; in the other side, a fixed pitch has an opposite effect. From Fig. 8.19, it can also be found that the stall region is larger in a lower rotational speed. Because λ is usually small in the high wind speed, so the stall is usually unavoidable; with the decreasing of the rotational speed, λ will become smaller and the stall region is enlarged. Comparing these three cases in all rotational speeds, it is found that the fixed pitch algorithm cannot offer the negative torque in a whole revolution.

8.2.5.2 Control scheme 2: Variable Pitch

The sinusoidal variation pitch control is considered here. Correspondingly, three amplitudes are considered, $\beta = -10^{\circ}$, 0° and 10°. The relation between the pitch angle and the azimuth is the same as that in Section 8.2.2.2 and the expression is shown in Equation (8.11). Like the discussion of Section 8.2.2.3 and Section 8.2.3, this variation pitch control has the same influence on AOA (enlarging or reducing AOA) in both the upwind and downwind sides.

For the rotational speeds of 2.1rad/s, 0.9rad/s and 0.1rad/s and the wind speed of 20m/s, the torque and the corresponding AOA of the three cases are shown in Fig. 8.20. It can be seen that the case of $\beta = 10^{\circ}$ can produce minus torques in both the upwind side and the downwind side. This is because that the positive amplitude $\beta = 10^{\circ}$ can enlarge the AOA in both sides and remain the AOA in the stall region as far as possible. The minus amplitude ($\beta = -10^{\circ}$) just narrows down the stall region; so the positive torques are enlarged contrarily, which goes against parking.

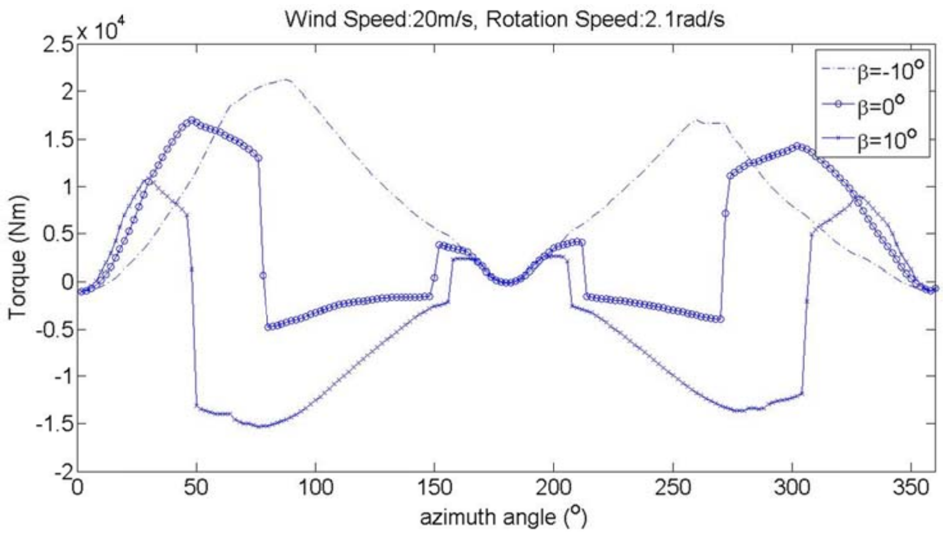

(a)

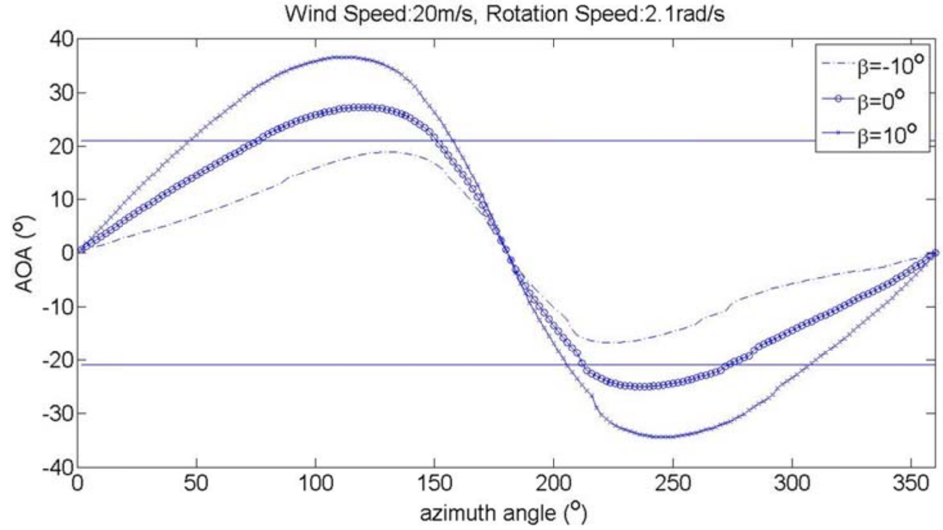

Wind Speed:20m/s, Rotation Speed:2.1rad/s
AOA (°)
azimuth angle (°)
β=-10°
β=0°
β=10°

(b)

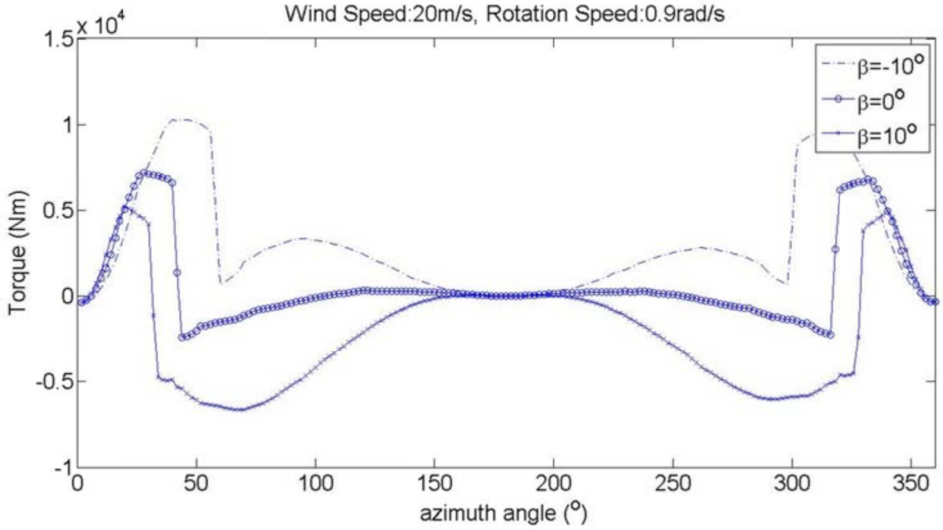

Wind Speed:20m/s, Rotation Speed:0.9rad/s
x 10^4
Torque (Nm)
azimuth angle (°)
β=-10°
β=0°
β=10°

(c)

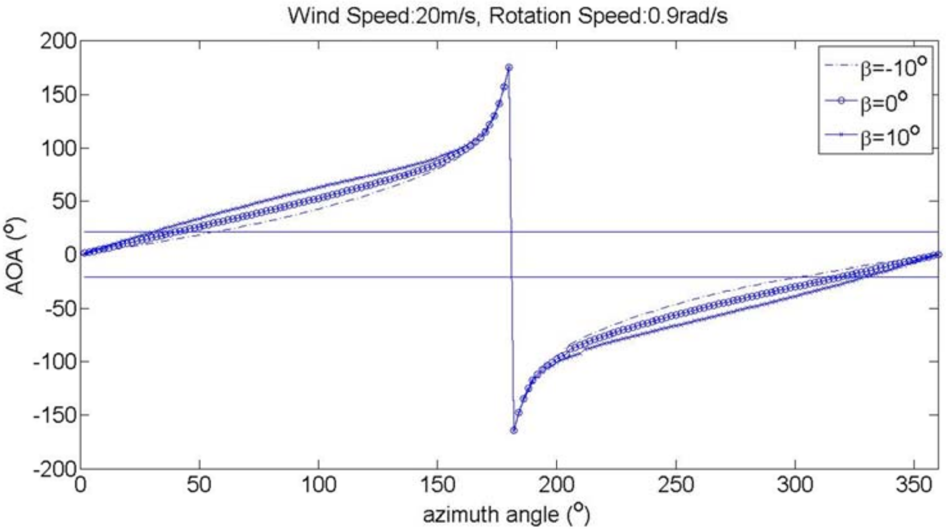

Wind Speed:20m/s, Rotation Speed:0.9rad/s
AOA (°)
azimuth angle (°)
β=-10°
β=0°
β=10°

(d)

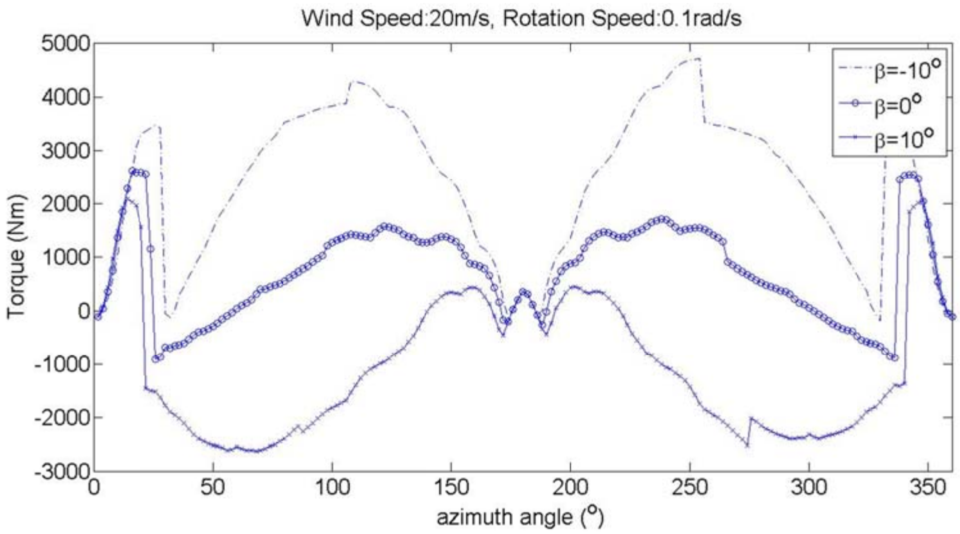

(e)

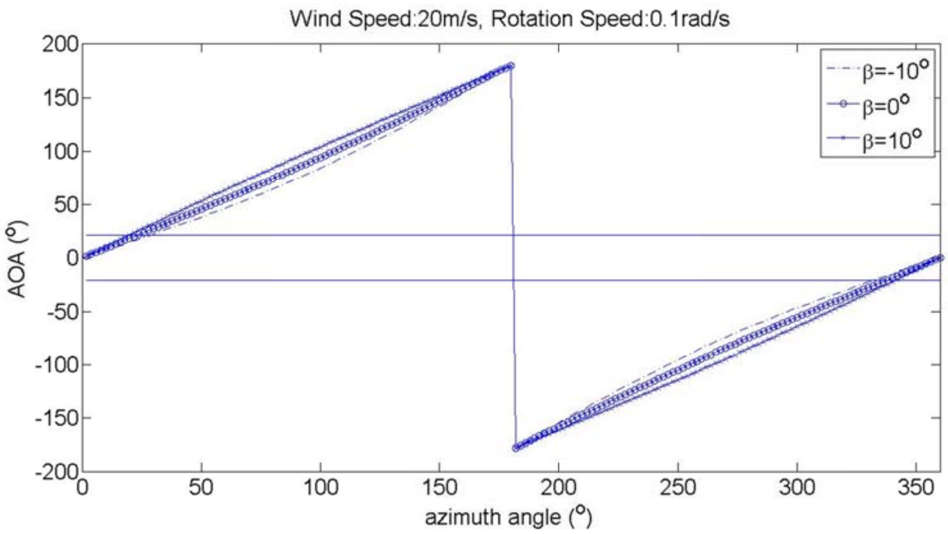

(f)

Fig. 8.20 The torque T and AOA versus azimuth angle for the sinusoidal variation pitch cases. (a) T at $\omega = 2.1\,rad/s$; (b) AOA at $\omega = 2.1\,rad/s$; (c) T at $\omega = 0.9\,rad/s$; (d) AOA at $\omega = 0.9\,rad/s$; (e) T at $\omega = 0.1\,rad/s$; (f) AOA at $\omega = 0.1\,rad/s$;

8.2.5.3 Discussions

Different from Section 8.2.2 and Section 8.2.3, the object of pitch control in this state is not to prevent stall but keep the AOA in the stall region as far as possible. The analyses of Section 8.2.5.1 and Section 8.2.5.2 show the shut-down capability of pitch control. In the previous analysis, two control schemes are studied, one is the fixed pitch control algorithm and the other is the sinusoidal pitch control algorithm. It is found that a fixed pitch cannot offer the negative torque in a whole revolution to shut down the rotor while a sinusoidal pitch can offer the negative torque in both upwind and downwind sides.

The previous analyses are conducted in the wind speed of 20m/s. However, the turbine may be shut down in a wider range of wind speed. The two control algorithms should be further studied in the wind speed region from 20m/s to 25m/s and in the rotational speed region from 0.1rad/s to 2.1rad/s. The selected fixed pitches and pitch amplitudes are the same as those in Section 8.2.2.1 and Section 8.2.2.2. The same as the startup process, the work in one revolution is used as the index to evaluate the effect of shut-down. By comparing the work of the aerodynamic torque in one revolution, the optimal pitch angle corresponding to the largest negative work at different wind speeds and rotational speeds can be selected. Take the wind speed of 20m/s for example, the works of the fixed pitch and sinusoidal pitch control at the rotational speeds of 2.1rad/s, 1.0rad/s and 0.1rad/s are shown in Fig. 8.21. It can be seen that in these three rotational speeds, the work is decreased with the increasing of amplitude of sinusoidal pitch; when the amplitude $\beta = 6^{\circ}$ ($\beta = 10^{\circ}$ is just for reference which is not an available pitch in this study), the largest minus work is obtained. While the fixed pitch control can hardly produce the negative torque and thus cannot satisfy the requirement of shut-down. Therefore, the sinusoidal pitch control should be used in the process of shut-down. Through considering the whole wind speed region and the rotational speed region, the optimal amplitudes of sinusoidal pitch control are shown in Fig. 8.22. It can be seen that the largest positive amplitude of 6° can obtain the largest minus torque at different wind speed and rotational speed.

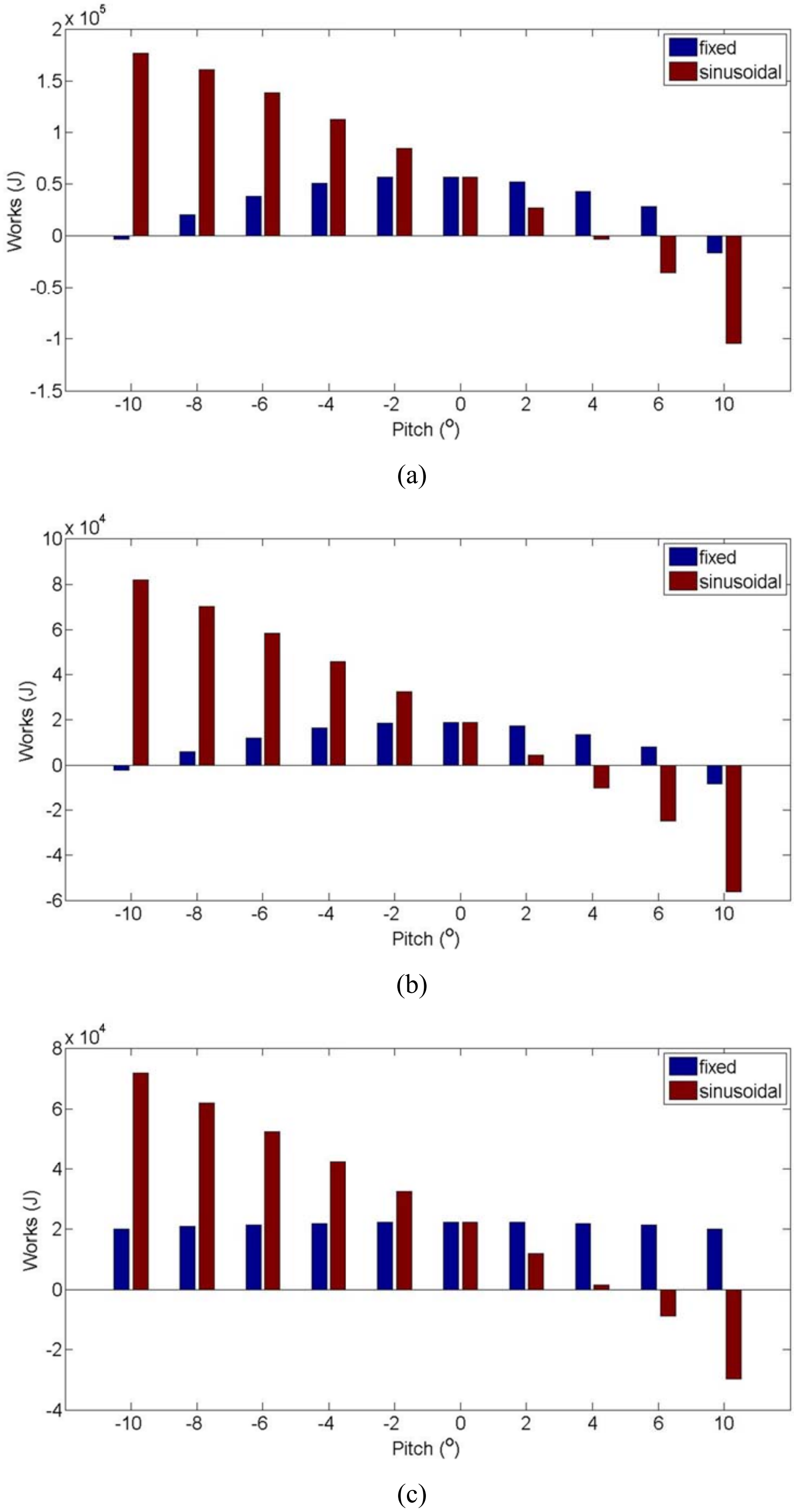

Fig. 8.21 The works of different cases. (a) 2.1rad/s; (b) 1.0rad/s; (c) 0.1rad/s.

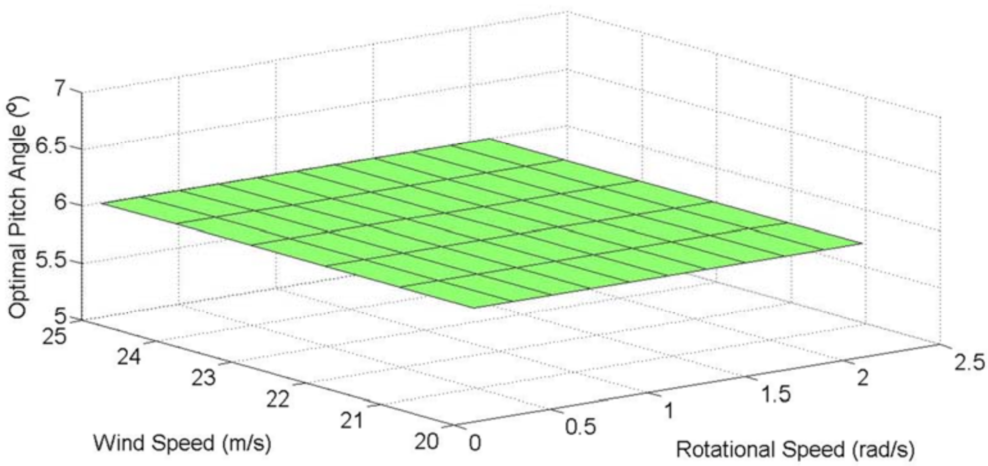

Fig. 8.22 The optimal pitch angle amplitude for variable pitch control in the shut-down state

8.2.6 The pitch control system

8.2.6.1 Control algorithm

Based on the studies in this subsection, the flowchart of the pitch control is shown in Fig. 8.23. The signals of the wind speed (V) and the rotational speed (ω) are continuingly transferred to the operational state indicator to determine the present state of the VAWT. When the operational state is determined (state 1, state 2, state 3 or state 4), the target pitch angle (β) is selected from the references values given in Section 8.2.2.3, Section 8.2.3, Section 8.2.4 and Section 8.2.5.3. The target value is transferred to the controller and the controller would give an order to the actuator to regulate the pitch. The pitch angles are also needed to be measured and transferred to the controller. By comparing the measured pitch and the target one, the difference between these two values can be evaluated. If the difference is not acceptable, the controller should continue to send an order to actuators to further regulate the pitch. If the difference is under the tolerance, the motion is finished and the control procedure should go back to the operational state indicator. This flowchart assumes that the actuators can act quickly and the time delay is not considered.

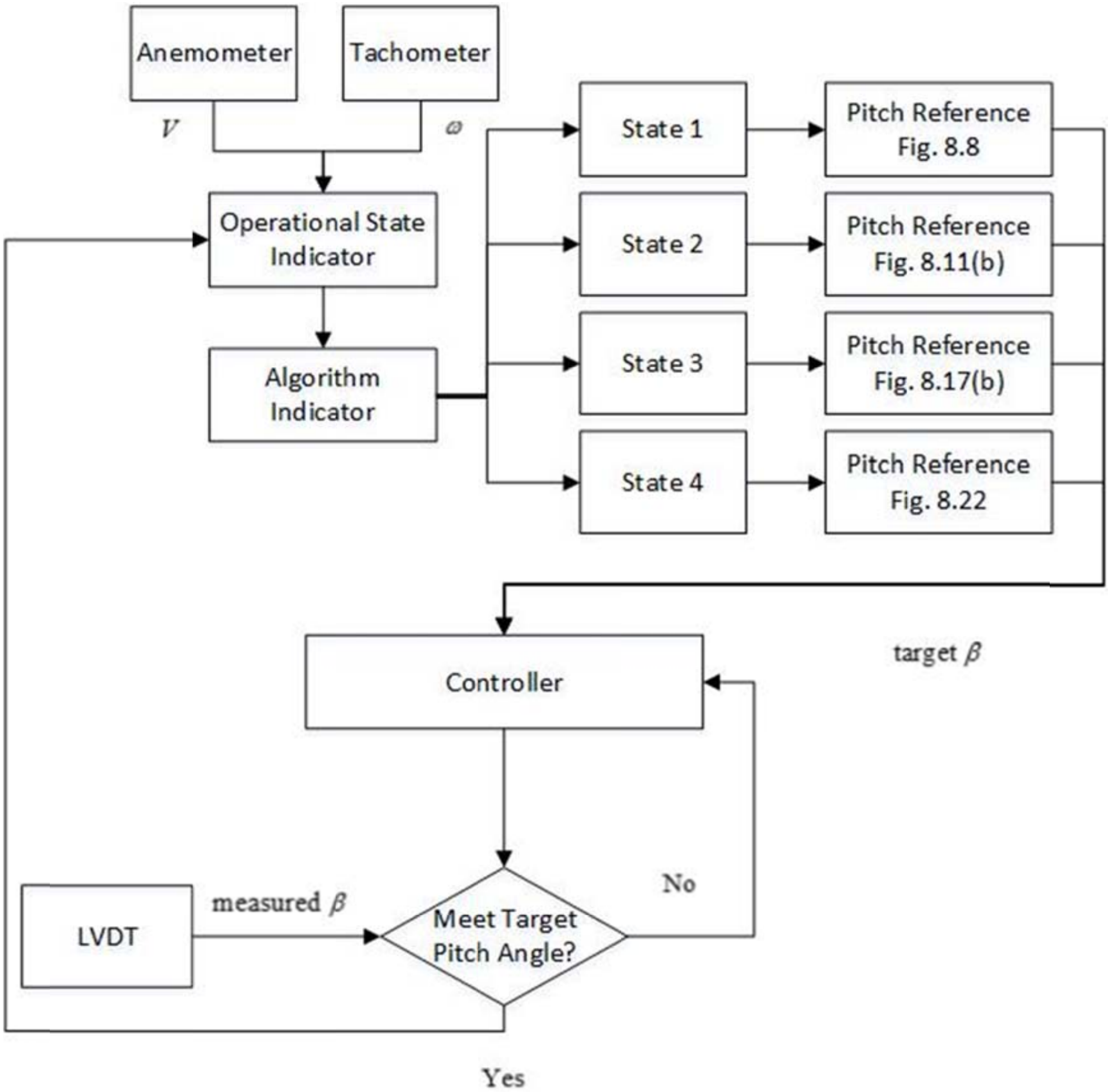

Fig. 8.23 The flowchart of pitch control

8.2.6.2 Sensors, actuators and control system

The pitch control system is established for the straight-bladed VAWT introduced in Chapter 3. Firstly, the number and types of sensors and actuators should be decided. In the previous analyses, the wind speed and the rotational speed are required to determine the operational state; the pitch angle of each blade is needed to be changed to the target value at different azimuth angles. Therefore, an anemometer is needed to monitor the wind speed. The location of the anemometer is the same as that introduced in Chapter 7. The pitch angle is uniform along the blade while the mean wind speed is varying with height. Because the power of a wind turbine is usually estimated using the mean wind speed at the hub height, the anemometer is installed at the hub height. A tachometer is needed to monitor the rotational speed and the azimuth angle. The tachometer is composed by a laser displacement sensor and a special gear wheel. A laser displacement sensor is fixed at the tower and a gear wheel is fixed at the shaft which is rotating with the rotor. The heights of the gear teeth in the direction of the three arms are different. The laser displacement sensor can record the distance variation and identify the azimuth angle of the arms and blades. 6 actuators are needed to be installed on all the upper and lower arms to regulate the pitch of blade. 6 LVDTs are needed to be installed on all the upper and lower arms to monitor the pitch of blade. The actuators and LVDTs are installed at the connection between the blade and the upper and lower arms, as shown in Fig. 8.24. In this way, the pitch angle can be measured by the LVDT. The systematic diagram of the tachometer is shown in Fig. 8.25. The summary of the sensors and actuators is listed in Table 8.2.

Table 8.2 Summary of the sensors and actuators

	Anemometer	Tachometer	Actuator	LVDT
Wind mast	1	-	-	-
Shaft	-	1	-	-
Upper arm	-	-	3	3
Lower arm	-	-	3	3
Total	1	1	6	6

Finally, the control system is shown in Fig. 8.26. The system is divided into two groups: one is the rotating parts and the other is the stationary parts. The power of the control system is obtained from the electrical grid. For the rotating parts, the transmission cables are connected to carbon brushes and supply the power to the rotating sensors, data recorder, computer and actuators. For the stationary parts, the power is directly obtained from the electrical grid. Data recorders are needed to record the measured data. 2 channels are needed for the anemometer, one for wind speed and the other for wind direction; 1 channel is needed for the tachometer; 6 channels are needed for the LVDTs. The signals of LVDTs are recorded by the data recorder of the rotating parts and transferred to the computer 1; the sampling frequency is 25Hz. These signals of LVDTs would be processed and the corresponding pitch angles are obtained. The signals of anemometer and tachometer are recorded by the data recorder of the stationary parts and transferred to the computer 2; the sampling frequency is 25Hz. After processed by the computer 2, the wind speed, rotational speed and azimuth angle are then transferred to the computer 1 through carbon brushes. Then, the operational indicator in the computer 1 can identify the present operational state and determine the appropriate algorithm. Based on the referenced pitch angle proposed in Section 8.2.2.3, Section 8.2.3, Section 8.2.4 and Section 8.2.5.3, control commands are sent to the actuators. If the target pitch angle is not attained, further control commands would be sent to the actuators until the accomplishment of the control objective. The control commands would be continuingly sent to the actuators depending on the operational and wind condition.

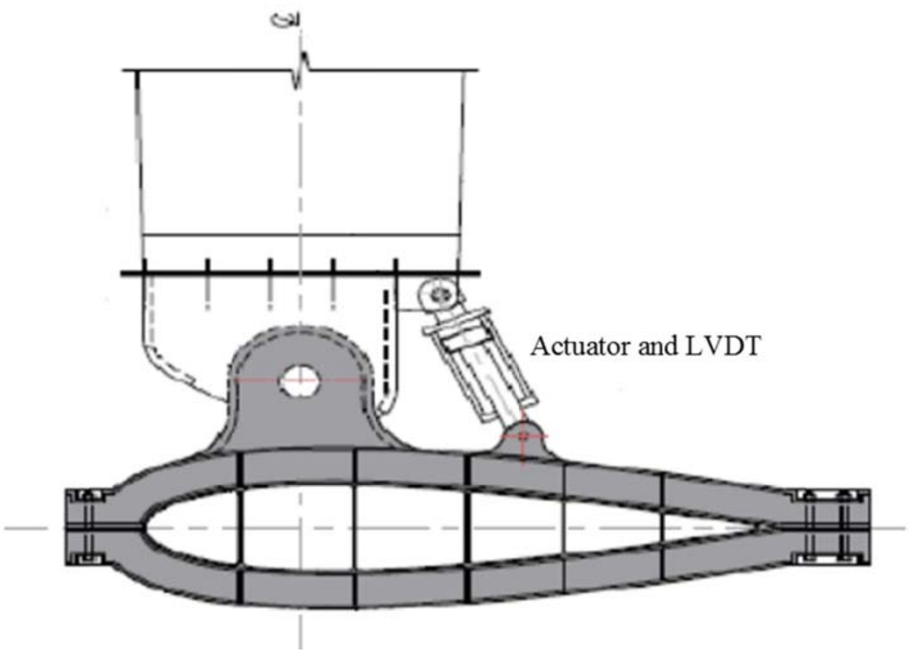

Fig. 8.24 Actuator and LVDT

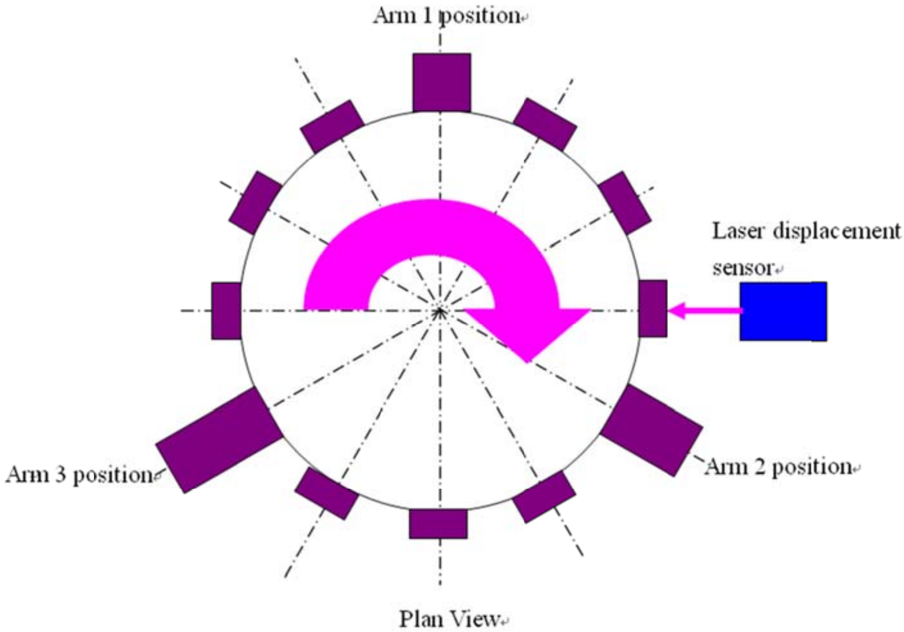

Fig. 8.25 Schematic diagram of rotational speed measurement scheme

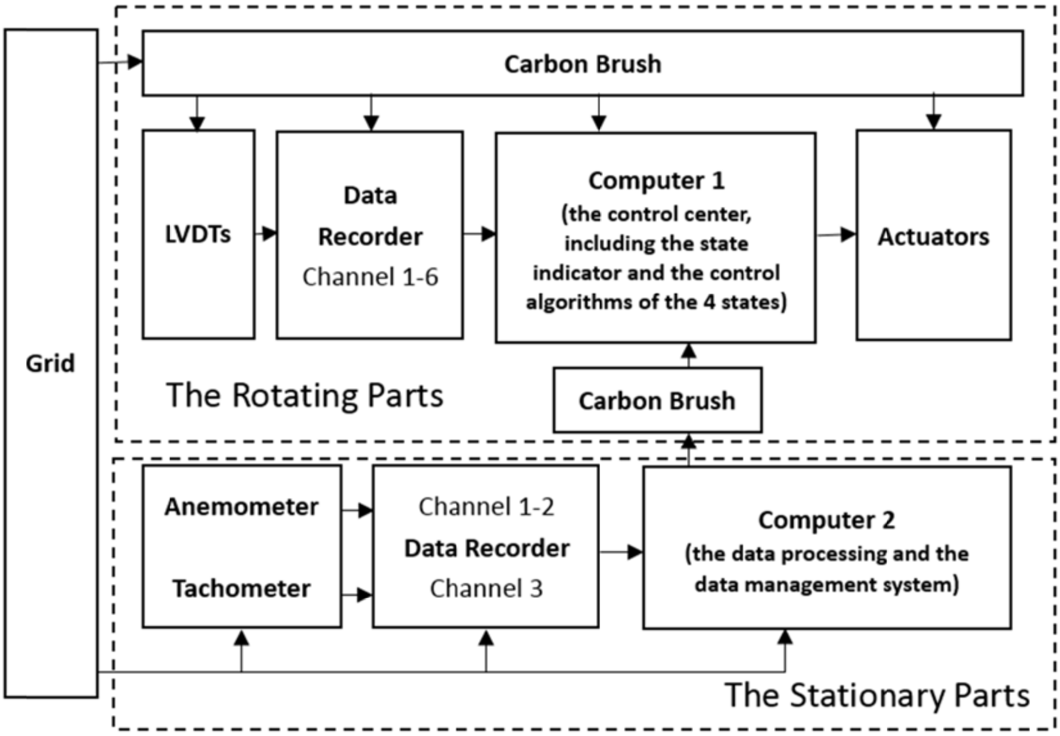

Fig. 8.26 Control system

8.3 Smart Vawts: A Synthesized SHM, Control and Power Supply System

Besides the control system, the SHM system for a large VAWT is also needed. In this subsection, the SHM system for a large VAWT is proposed. To introduce this system, the straight-bladed VAWT is taken for example. Generally, a complete SHM system is composed of 5 subsystems: a sensing system, a data acquisition and transmission system, a data processing system, a data management system and a structure evaluation system (Xu & Xia, 2011). The data processing system and the data management system are common; the structure evaluation system is based on the works of Chapter 5, Chapter 6 and Chapter 7. Hence, this section is focused on the first two subsystems. Then, a synthesized SHM, control and power supply system is given.

8.3.1 SHM System

8.3.1.1 Sensor types

Generally, SHM has five main objectives: to monitor loading and responses of a structure, to assess its performance under various service loads, to verify or update the rules used in its design stage, to detect its damage or deterioration, and to guide its inspection and maintenance (Xu & Xia, 2011). However, for a particular structure, these objectives are not equally important. At the present stage, large-scale VAWTs only get the interest of researchers and have not fully accepted by the industry. The large-scale VAWTs established in the last century have all broken down or been abandoned; and the number of large-scale VAWTs at the present time is limited. Hence, there is not enough data and engineering experience to verify the present theories of loading, wind power production and design guides. So, particularly for VAWTs at the present stage, a SHM should be installed in a large-scale VAWT to monitor the wind condition, to ensure the functionality and safety, and to guide the inspection and maintenance.

Based on these objectives, the following sensor types are used. In order to monitor the wind speed and wind profile, anemometers are required at different heights. Because the rotational speed is an important parameter for a wind turbine, it has to be monitored. There are many methods to measure the rotational speed and one of the most widely used methods is to use a laser displacement sensor which is adopted in this plan. To monitor the deformation of a VAWT, displacement sensors, accelerometers and strain gauges are required. To monitor global deformations, accelerometers are needed to be installed at the components, such as tower, main arms, upper and lower arms. To monitor the swing of the shaft, two laser displacement sensors are used. To monitor local deformations, strain gauges are installed at the potential damage locations of tower, shaft, main arm and blades. To assess the wind power and monitor the service loads, load cells are installed at the supports of the blade and the links connecting upper and lower arms. A summary of the number, types and locations of sensors is first given in Table 8.3.

Table. 8.3 Summary of the sensors

	Anemometer	Laser Meter	Accelerometer	Strain Gauges	Load cell	LVDT
Wind mast	2	-	-	-	-	-
Tower	-	-	2	4	-	-
Shaft	-	1	-	12	-	2
Main arm	-	-	6	3	-	-
Upper arm	-	-	6	-	3	3
Lower arm	-	-	6	-	3	3
Link	-	-	-	-	3	-
Blade	-	-	-	30	-	-
Total	2	1	20	49	9	8

8.3.1.2 Sensor installation

The details of the placements of sensors are shown in Fig. 8.27.

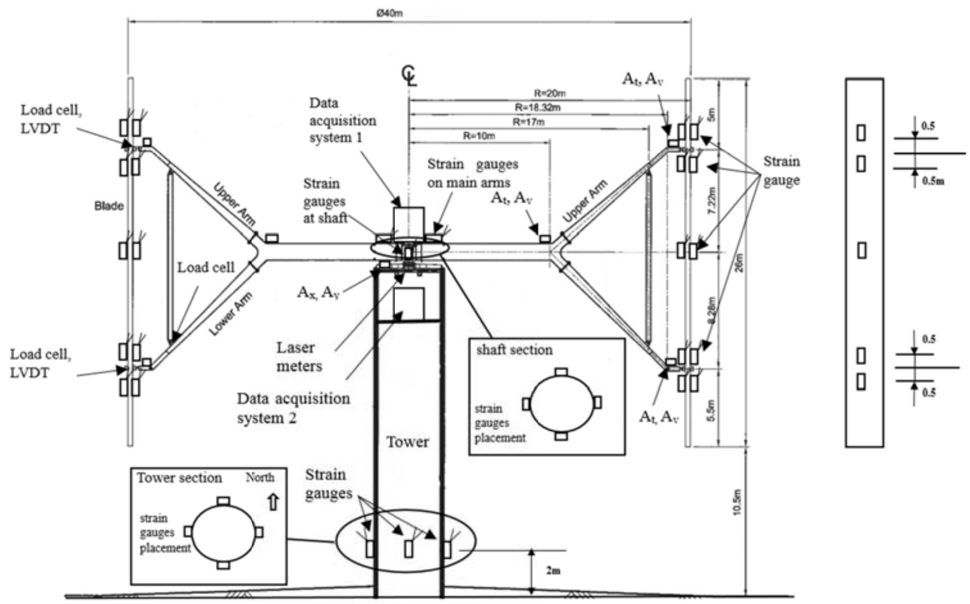

(a)

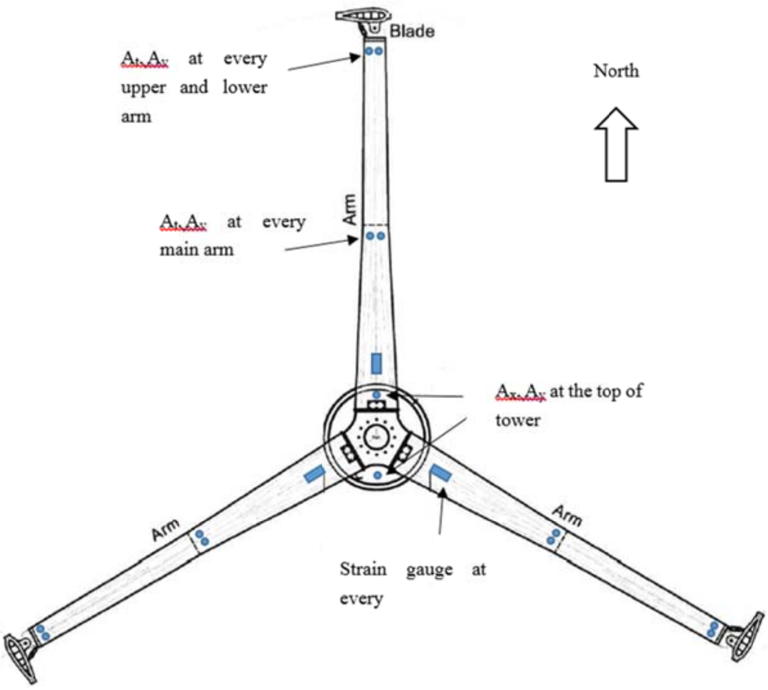

(b)

Fig. 8.27 Sensor placement. (a) front view; (b) top view.

The location of the wind mast has been introduced in Chapter 7. Two anemometers are installed at 10m and 26m of the wind mast. One anemometer is set at 10m because the present statistic data of mean wind speed are given at this height. In order to compare with these data, the anemometer is also installed at 10m. Since the wind speed at the hub height is usually used in the design of wind turbines, the other anemometer is set at 26m which is the hub height of the VAWT. Using these two anemometers, the wind profile can also be estimated. Each anemometer records the wind speed and the wind direction, requiring 2 channels; so a total of 4 channels are needed.

The rotational speed of the rotor is an important parameter for monitoring a wind turbine. Not merely because a wind turbine must be connected to the grid at a specific rotational speed, but also the blade loads is mainly determined by the rotational speed. The blade loads are composed of the aerodynamic forces and the centrifugal forces. As introduced in Chapter 3, the aerodynamic forces are determined by the wind speed and rotational speed. From Chapter 5, it can be known that the centrifugal forces are the dominant component of the blade loads for the VAWT. Therefore, monitoring the blade loads requires the measurements of the rotational speed and the wind speed. The systematic diagram of the tachometer has been introduced in Section 8.2.6 and shown in Fig. 8.25. A laser displacement sensor and a gear wheel are used to monitor the rotational speed and the azimuth angle and only 1 channel is needed.

In order to monitor the global deformation of the VAWT, accelerometers are used. According to the modal analysis in Chapter 4, the first few modes include the torsion and bending of the shaft, the bending and torsion of the arms, the bending of the blade and the bending of the tower. Since the deformation of the shaft can be identified by the motion of arms, hence, to monitor the deformation of the shaft, the main arms and the upper and lower arms, accelerometers are installed at the end of main arms, as well as upper and lower arms, as shown in Fig. 8.27. In each location, two uniaxial accelerometers are used; one records the vertical acceleration and the other records the tangential one. So, 6 accelerometers in the main arms, 6 in the upper arms and 6 in the lower arms are applied; as a result, a total of 18 channels are needed. To monitor the bending of the tower, two uniaxial accelerometers are installed at the top of the tower. One records the acceleration in the north-south direction and the other records the acceleration in the east-west direction; two channels are needed. So a total of 20 accelerometers are used and 20 channels are required.

Besides monitoring the deformation of the components mentioned above, the compression of the links are needed to be monitored in case of buckling. 3 single axis load cells are installed at the pins connecting between the links and the lower arms. 3 channels are required.

On the other hand, in addition to the global deformations, the local deformations, such as strains at the locations of potential damages, are also needed to be monitored and strain gauges are generally used. According to the study of Chapters 5 and 6, these locations are the top of the shaft, the roots of the main arms, the supports of the blades and the root of the tower. Moreover, the deformations of the blades also need to be monitored. Considering the influence of accelerometers in the aerodynamic forces of the blades, strain gauges, due to their flat shape, are applied in the blade monitoring. Hence, 4 resistance strain gauges are installed at the 2m height of the tower as shown in Fig. 8.27(a). Because the VAWT is established in the coastal, 2 meters is a safe height to prevent flooding. The half-bridge configuration is applied and only 2 channels are needed. 4 rosette strain gauges are installed at the shaft to measure the bending and torsion strain; the half-bridge configuration is also used resulting in 4 channels requirement. 3 resistance strain gauges are installed at the roots of the main arms and 3 channels are needed. To monitor the deformation of the blades, 10 resistance strain gauges are installed at 5 sections of each blade, as shown in Fig. 8.27(a). In each section, two strain gauges in the half bridge configuration are installed. The bending strains of the blade at the sections near two supports are monitored; the strains at the mid span of the blades are also measured. So, 5 channels are required for each blade and total 15 channels are needed.

Another local deformation is the swing of the shaft. For a rotation machine, many abnormalities can be identified by the axis orbit (Jardine et al., 2006). Particularly for a VAWT, the axis orbit is reflected by the swing of the shaft. Hence, it is important to monitor the swing of the shaft and identify the axis orbit. In order to record the relative displacement to the tower, two LVDTs are installed on the top floor of the tower. The details are shown in Fig. 8.28. 2 channels are required in this case.

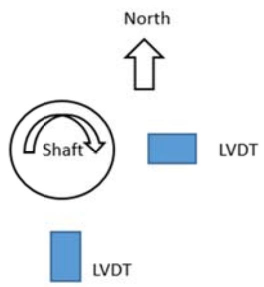

Fig. 8.28 Shaft swing measurement scheme

Furthermore, the assessments of wind power production and the present theories of wind loads for the VAWT require the measurement of blade loads and the generated power. Hence, load cells need to be installed at the connection between blades and arms and the generated power needs to be monitored. The details of load cell installation are shown in Fig. 8.29. Two load cells are shown in this figure. One is two axes and the other is single axis. So, 4 load cells and 6 channels are required for each blade and there are a total of 12 load cells and 18 channels for the three blades. The LVDTs here are used to monitor the pitch angle and calculate the normal and tangential forces. A total of 6 channels are needed. 1 channel is required to record the generated power. So, a total of 25 channels are needed in these measurements.

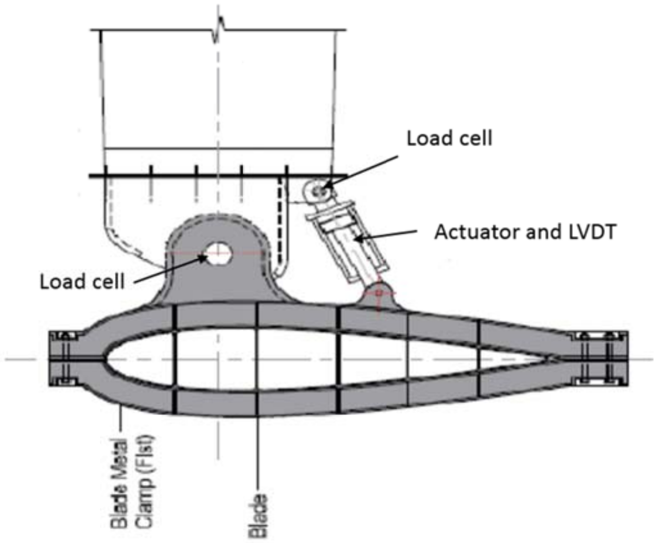

Fig. 8.29 the placement of load cells and LVDT

8.3.1.3 SHM system

Based on the introduction to the sensor types and installation, the SHM system is summarized in Fig. 8.30 (a) - (c). The sensing system and the data acquisition and process system used in this SHM system can be divided into two groups: one is the rotating parts (on the blades, arms and shaft) and the other is the stationary parts (on the tower and the wind mast).

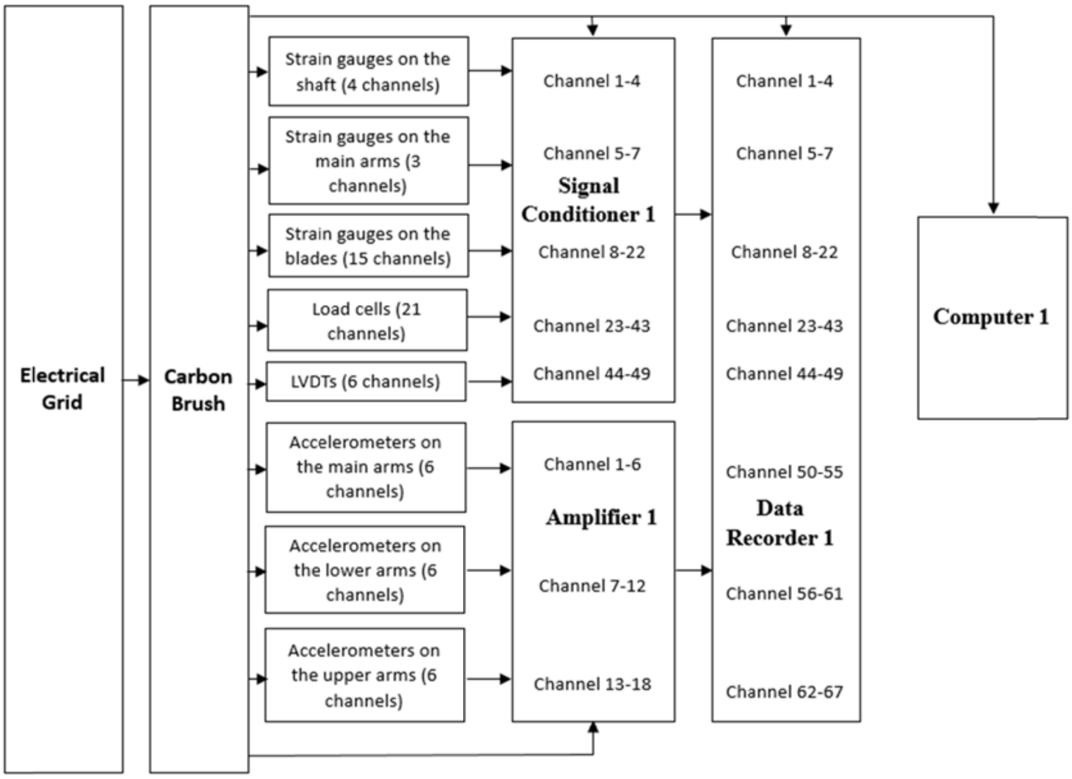
Electrical Grid
Carbon Brush
Strain gauges on the shaft (4 channels)
Strain gauges on the main arms (3 channels)
Strain gauges on the blades (15 channels)
Load cells (21 channels)
LVDTs (6 channels)
Accelerometers on the main arms (6 channels)
Accelerometers on the lower arms (6 channels)
Accelerometers on the upper arms (6 channels)
Channel 1-4
Channel 5-7
Signal Conditioner 1
Channel 8-22
Channel 23-43
Channel 44-49
Channel 1-6
Amplifier 1
Channel 7-12
Channel 13-18
Channel 1-4
Channel 5-7
Channel 8-22
Channel 23-43
Channel 44-49
Channel 50-55
Data Recorder 1
Channel 56-61
Channel 62-67
Computer 1

(a)

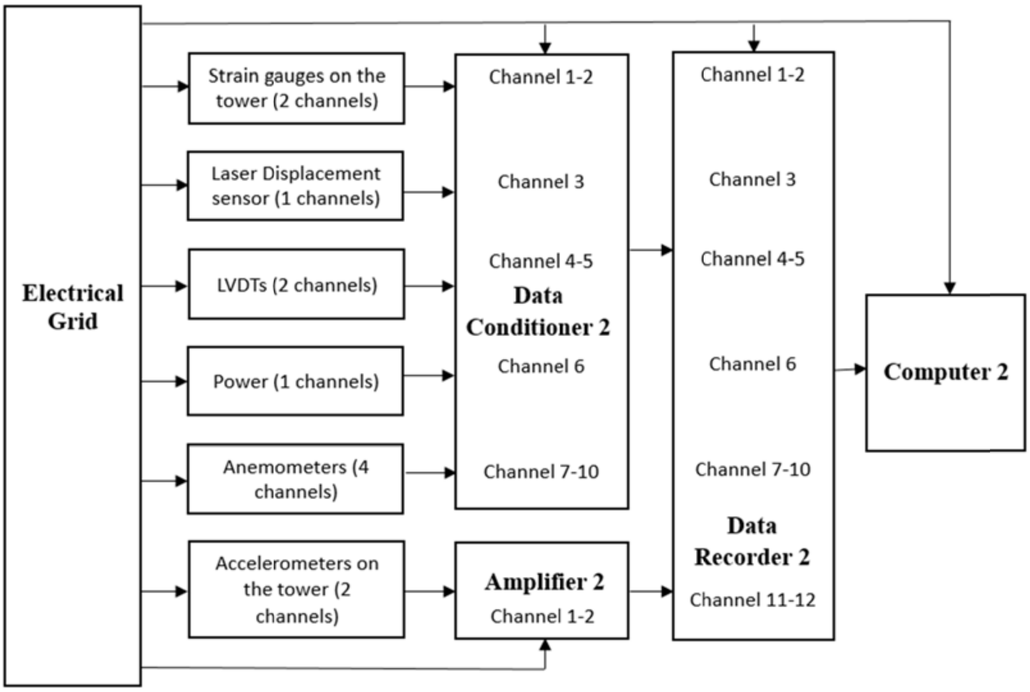
Electrical Grid
Strain gauges on the tower (2 channels)
Laser Displacement sensor (1 channels)
LVDTs (2 channels)
Power (1 channels)
Anemometers (4 channels)
Accelerometers on the tower (2 channels)
Channel 1-2
Channel 3
Channel 4-5
Data Conditioner 2
Channel 6
Channel 7-10
Amplifier 2
Channel 1-2
Channel 1-2
Channel 3
Channel 4-5
Channel 6
Channel 7-10
Data Recorder 2
Channel 11-12
Computer 2

(b)

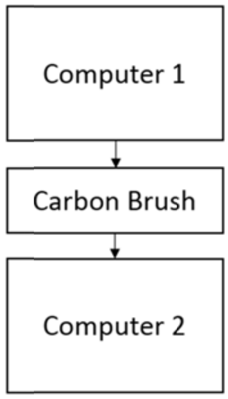

(c)

Fig. 8.30 the SHM system. (a) the rotating parts; (b) the stationary parts; (c) data transmission.

The power for the sensors and equipment is obtained normally from the power grid. For the rotating parts, carbon brushes are used to transmit the current from the stationary transmission cables to the rotating ones, so that the equipment of the rotating parts can obtain the power supply, as shown in Fig 8.30(a). For the stationary parts, the power is normally obtained from the electrical grid, as shown in Fig. 8.30(b).

2 sets of signal conditioners are used to receive signals from load cells and strain gauges as shown in Fig 8.30(a) and Fig 8.30(b). One set is for the rotating parts and there are a total of 49 channels: 4 for strain gauges on the shaft, 3 for the strain gauges on the main arms, 15 for strain gauges on the blades, 21 for load cells and 6 for LVDTs. The other set is for the stationary parts and there are a total of 8 channels: 4 for the anemometers, 2 for the strain gauges on the tower, 1 for the laser displacement sensor and 1 for the generated power.

2 sets of charge amplifiers were used to receive signals from accelerometers as shown in Fig 8.5(a) and Fig 8.5(b). One set is for the rotating parts and there are a total of 18 channels: 6 for accelerometers on the main arms, 6 for accelerometers on the upper

arms and 6 for accelerometers on the lower arms. The other set is for the stationary parts and there are 2 channels for the accelerometers on the top of the tower. 2 sets of data recorders are required. One set is to record the data from the rotating parts and there are 67 channels (49 for conditioners and 18 for amplifiers). The other set is to record the data from the stationary parts and there are a total of 10 channels. The sampling frequency of these two data recorders is 25Hz.

2 sets of computers are used to process and store the data. One is installed on top of the center of rotor, rotating with the VAWT; the other is installed in the tower. These two computers act as the data processor systems, the data management systems and the structure evaluation systems. When there is a fault, an alarm would be given. Considering the convenience in getting the stored data, carbon brushes are used to transfer the data from the rotating computer to the stationary one, as shown in Fig. 8.30(c).

8.3.2 A Concept of Smart VAWTs

A pitch control system is proposed in Section 8.2.6. The objectives of this control system are to benefit the VAWT in the states of start-up when the wind speed reaches the cut-in wind speed, to maximize the power production when the wind speed is higher than the cut-in wind speed and lower than the rated wind speed, to maintain the power at the rated value when the wind speed is higher than the rated wind speed and lower than the cut-off wind speed and to benefit the VAWT in the state of shut-down when wind speed is larger than the cut-off wind speed. On the other hand, a SHM system is given in Section 8.3.1.3. This SHM system can monitor the wind condition, ensure the functionality and safety of the VAWT, and guide the inspection and maintenance.

By comparing these two systems, it can be found that there are common sensors (such as the anemometer, LVDTs and the tachometer) and data acquisition and processor systems. It is not efficient that these two systems are designed separately. Moreover, when a fault happens, it is promising that a command can be sent from the SHM system to the control system so that the VAWT can be shut down in time. Furthermore, since a VAWT itself is an energy harvesting machine, it is amazing if the generated power can be offered to the equipment of the SHM and control systems.

Hence, it is natural to integrate the SHM and the control systems so that a VAWT can be a self-sensing, self-diagnosis, self-control and self-power system. A schematic diagram of the synthesized system is given in Fig. 8.31. In this system, two sets of power supplies are used. When the VAWT is in the operation condition, one part of power is offered to the sensors and equipment and the other part is transmitted to the electrical grid. When the VAWT is shut down, the power is produced by the generator while the SHM system still need power supply. In this case, the power can be obtained from the grid. To deal with the transition of the power supply mode and the electrical grid outage, batteries are used, such as uninterruptible power systems (UPS). The power from the generator or the grid is first connected to the batteries and the power is supplied by batteries. The same as Section 8.2.6 and Section 8.3.3, the sensors, actuators and equipment are divided into two groups: one is the rotating parts and the other is the stationary parts. Data from the anemometers installed on the wind mast and the sensors installed on the tower are sampled and stored by the data acquisition systems of the stationary parts; data from the sensors on the shaft, arms and blades are sampled and stored by the data acquisition system of the rotating parts. Among the data of the stationary parts, the wind speed, the rotational speed and the azimuth angles are transferred to computer 1 of the rotating parts for the control objective. Computer 1 is the control center, which includes the operational state indicator and the control algorithms of the 4 states. The detail of the control procedure can refer to Section 8.2.6. Computer 2 is the SHM center, which includes the data processing system, the data management system and the structure evaluation system. Moreover, when a fault is found by the SHM system, the shut-down command would be sent to the control system to stop the rotating of the rotor. By considering the convenience in getting the stored data, the data in computer 1 are transferred to computer 2 for storage. In such a VAWT, the SHM system, the control system and the power supply system are synthesized. Hence in a sense, it can be called the smart VAWT.

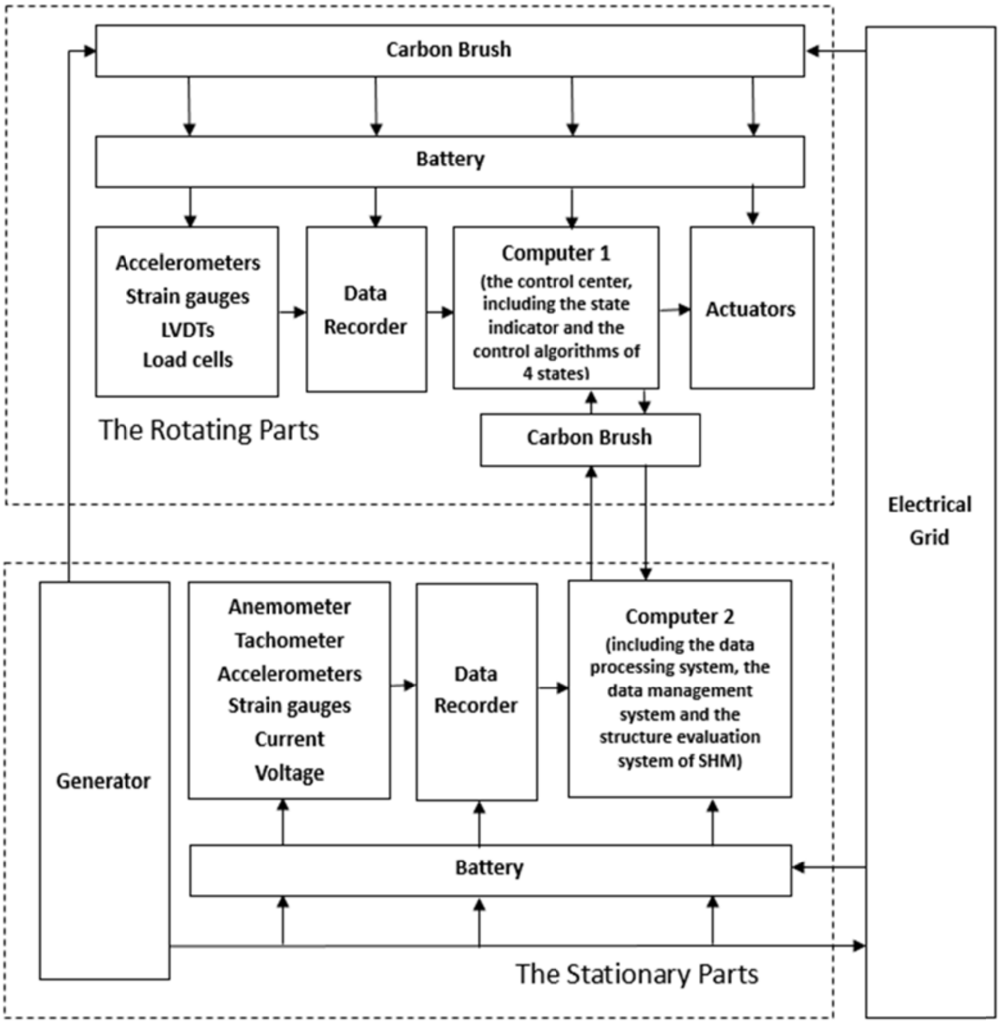

Fig. 8.31 The concept of smart VAWT

8.5 Summary

Two pitch control algorithms, the fixed pitch (in one revolution) and the variable pitch (in one revolution), are studied. For the fixed pitch scheme, the influence on the AOA is different in the upwind side and in the downwind side. And the sinusoidal variation pitch can either enlarge or reduce the AOA in both sides depending on the sign of the amplitude. Through comparing these two algorithms in the four operational states, the sinusoidal pitch control is adopted. For the startup and operation under the rated power, the pitch is adjusted to maximize the aerodynamic torque. For the cases that the stall happens, the sinusoidal variation pitch with a minus amplitude ($\beta < 0$) can prevent stall in both the upwind side and the downwind side; but the constant pitch can only accomplish this requirement in one side and has an opposite effect in the other side. For the cases that the stall does not happen, the sinusoidal variation pitch with an appropriate positive amplitude ($\beta > 0$) can enlarge the AOA in both sides and prevent stall at the same time. In the state of operation above the rated wind speed, the sinusoidal pitch control can maintain the power at the rated value with a smaller range of pitch regulation than the fixed pitch control. It is the same as the parking problem, the objective of which is not preventing but remaining the pitch in the stall region. Again, the sinusoidal variation with a large positive amplitude ($\beta > 0$) can accomplish the requirement and the fixed pitch control is useless. The reference pitch angles at different wind speeds and rotation speeds are given and a control system is proposed.

On the other hand, based on the works of Chapter 5 and Chapter 6, a SHM system for VAWTs is proposed. To monitor wind speed and wind profile, 2 anemometers are installed at different heights. To measure the rotational speed, 1 laser displacement sensor is used. To monitor global deformations of components, 2 accelerometers are installed at the top of tower to monitor the bending vibration in two direction; 2 accelerometers are installed on each main arm, upper arm and lower arm to monitor the vibration in normal and tangential direction. To monitor the local deformation at the critical locations of fatigue and strength failure, 4 strain rosettes are attached on the shaft to monitor torsion and bending; 4 strain gauges are attached at the bottom of tower to monitor bending in two direction; 3 strain gauges are attached at the root of main arms to monitor vertical bending. 2 LVDT are installed to monitor the swing of shaft. Furthermore, 1 load cell is installed on each upper arm, lower arm and link to monitor the service loads. 1 LVDT is installed on each upper arm and lower arm to monitor pitch angle. 2 sets of data acquisition systems are used, one for the sensors installed on the rotor which are rotating and the other for the sensors installed on the tower and the wind mast which are stationary.

Finally, a concept of smart VAWTs is given. The smart VAWT should synthesize the systems of SHM, control and power generation so that the VAWT can be self-sensing, self-diagnosis, self-control and self-powered. In this VAWT, two sets of power supply, from the generator and the grid, should be used in case that one set is out of service. The VAWT should choose the control algorithm in different operational states based on the sensing system and the sensing system should also identify faults associated with the control.

Notably, the smart VAWT is still in the conceptual level, and none of this VAWT prototype can be found in the world. A great amount of research and effort is required to establish such a smart VAWT step by step in the future.

CHAPTER 9

CONCLUSIONS AND RECOMMENDATIONS

9.1 Conclusions

This thesis focused on the fatigue and ultimate strength analyses of large-scale vertical axis wind turbines (VAWTs) and the establishment of structural health monitoring (SHM) and control systems. In particular, this research was devoted to: (1) proposing a method of wind load simulation for VAWTs which considers the influences of interaction of all components, mean wind profile and turbulence; (2) establishing a FE model of blade and updating the laminar elastic constants by static tests; (3) proposing a framework of the fatigue and ultimate strength analyses of blade and figuring out the critical locations of fatigue and ultimate strength failure; (4) proposing a framework of the fatigue and ultimate strength analyses of VAWTs except blades and figuring out the critical locations of fatigue and ultimate strength failure; (5) conducting the field measurement and validate the frameworks by comparing the measured and simulated responses; (6) studying the pitch control algorithms in different operation states and proposing a pitch control system, proposing a SHM system based on the works of the structural analyses and proposing a conceptual smart VAWT which synthesizes the functions of SHM, control and power supply. The main contributions and conclusions of this dissertation were summarized as follows:

1. A method of wind load simulation for VAWTs was proposed and the influences of interaction of components, mean wind profile and turbulence were considered. In this study, a straight-bladed VAWT was taken for example and the sliding mesh method was used to simulate the rotation of the rotor. The proposed method was based on the strip analysis and the 2D CFD simulation using SST $k-\omega$ model. The validity of 2D SST

$k-\omega$ for VAWTs was accessed by comparing the simulation results of 2.5D large eddy simulation (LES). It was found that the two results were similar. Then 2D CFD simulations were conducted at 9 different heights of the VAWT. In these simulations, all components were modelled and the inflow velocities took the mean wind profile and turbulence into account. After having obtained the results in these 9 sections, the wind pressures and aerodynamic forces on the VAWT were interpolated in spatial domain. The influences of the tower and arms on the aerodynamic forces of the blade were further studied. The results showed that the influence of the tower was not obvious while the influence of the arms was, however, more obvious so that the tangential force, hence the power coefficient, was reduced due to the existence of the arms. The influence of turbulent inflow wind speed was also studied and the results showed that the turbulence caused the fluctuation in wind loads .

2. A micromechanics-based updating method was proposed to update the laminar elastic constants of laminated composite blades. A straight laminated fiber reinforced plastic (FRP) blade was taken for example, which is composed of unidirectional FRP (UD FRP) and plain weave FRP (PW FRP). A refined FE model of blade was established using laminated composite shell elements (ANSYS shell91) to obtain the laminar stresses and strains. To update the laminar elastic constants of the model, the micromechanics approach was adopted. Micromechanics models were applied in the process of updating, so that the direct identification of these laminar elastic constants can be avoided and the number of updating parameters can be reduced. A straight composite blade which was composed of unidirectional fiber reinforced plastic (UD FRP) and plain weave fiber reinforced plastic (PW FRP) was taken for example. Sensitivity and uncertainty analyses were also conducted to determine the parameters to be updated. It was found that the fiber volume fraction is the most influential parameter with the largest uncertainty for both UD FRP and PW FRP. Bending tests were conducted and displacements and strains were measured. Using the pattern search algorithm, the updating parameters (fiber volume fractions for UP FRP and PW FRP) were identified and the laminar elastic constants were reconstructed by the

micromechanics models. It was found that after updating, both the local strain responses and the global displacement matched well with the measured data and the fiber volume fractions were updated successfully.

3. A framework for the fatigue and ultimate strength analyses of blades was proposed to give a solution to the problem of lacking in field measurements and experimental tests of large-scale VAWTs in the present stage. A refined FE model of a laminated composite straight blade was established and the responses of the blade under different operation and wind conditions were predicted. Based on these responses, the fatigue analyses were conducted and the fatigue-critical locations were figured out. For the typical straight blade, the locations at the supports and the mid-span of the blade had larger fatigue damage than other positions of the blade. Among these locations, the position of the largest fatigue damage was in the cross section at the lower support. In this cross section, the positions subjected to compressive cyclic loads had the larger fatigue damage than those subjected to tensile cyclic loads. Parameter studies were also conducted and the influences of the ultimate tensile and compressive strains, damping ratio and fundamental frequency were studied. For the point subjected to tensile cyclic loads, a larger ultimate tensile strain can lead to smaller fatigue damage while the influence of an ultimate compressive strain can be neglected; for the point subjected to compressive cyclic loads, a larger ultimate compressive strain can reduce the fatigue damage while the influence of an ultimate tensile strain can be ignored. Moreover, it was found that the fatigue damage is sensitive to the damping ratio and fundamental frequency; increasing the damping ratio and fundamental frequency can dramatically decrease the fatigue damage. It was also found that for the typical blade in this study, the responses of the blade were composed of two frequency components, one is the forced vibration under the aerodynamic force due to rotation, which has a large strain range and the other is the excited 1st mode vibration with small strain ranges. The ultimate strength analysis in the extreme wind speed was also conducted and the influence of the wind direction on the response of blade was studied. The least favorable azimuth angle was in the

upwind side, in the range of azimuth angle between 60^o and 90^o. The critical location of strength failure was in the cross section at the upper support. The locations with large interlaminar stresses were also figured out.

4. A framework for fatigue and ultimate strength analysis of other components of VAWTs besides blades was proposed. A straight-bladed VAWT was taken for example. A FE model of the whole VAWT was established by ANSYS element beam188 and the modal analysis was conducted. To eliminate the rigid motion of the VAWT and conduct the analysis conveniently, the rotating frame method was used and the VAWT could be regarded as a structure in the rotating reference frame which rotates at the same speed of the rotor. A two-step calculation scheme was proposed to calculate the responses of the rotor and tower. The first step was to solve the dynamic equation of the VAWT in the rotating frame. In the second step, the reaction forces from the rotor were acted on the tower so that the analysis of tower could be decoupled from the rotor. Then the dynamic equation of the tower was calculated in the stationary reference frame. Based on the FE model and the rotating frame method, the fatigue analysis was then conducted. The fatigue critical locations of the rotor and tower were figured out. The largest fatigue damage occurs at the root of main arms. Although the fatigue damage of shaft was small for this typical VAWT, the fatigue of shaft could not be ignored because the misalignment of the rotor and eccentric mass were not considered in this study. The fatigue critical location of the tower was at the bottom. It was found that larger fatigue damage occurred in the leeward side of the tower. The ultimate strength analyses of the rotor and tower were also conducted and the influence of wind direction was also taken into account. For the rotor, the strength failure critical locations were the roots of main arm and the shaft. The dangerous azimuth angles of the main arm were 60^o and 240^o; the dangerous azimuth angles of the shaft were 30^o, 150^o and 270^o. For the tower, the fatigue critical location was at the bottom and in the leeward side. The dangerous azimuth angles were 30^o, 150^o and 270^o.

5. Field tests of a straight-bladed VAWT were conducted to validate the proposed frameworks for the fatigue and ultimate strength of VAWTs. A field measurement system was established. Strain gauges were attached on the shaft, main arm and blade; an accelerometer was installed on the main arm monitoring the vertical acceleration; an accelerometer was installed on the top of upper arm to monitor the tangential acceleration. Comparing the measured data of different conditions, the influences of wind speed and rotational speed were clarified. Natural frequencies were also depicted from the peaks of the normalized PSDs of measured responses. The FE model of the VAWT was updated by the identified natural frequencies. Then under the same operational and external conditions as the measurement, the responses of the VAWT were calculated. Comparing the simulated and measured responses in frequency domain, it was found that these two results matched well. Therefore, the proposed frameworks were validated.

6. Control and SHM systems were proposed and a conceptual smart VAWT was given. Firstly, two pitch control algorithms, fixed pitch (in one revolution) and variable pitch, were studied. For the fixed pitch scheme, the influence on the AOA is different in the upwind side and in the downwind side; the sinusoidal variable pitch can either enlarge or reduce the AOA in both sides depending on the sign of the amplitude. In the states of startup and operating under the rated wind speed, the pitch can be adjusted to maximize the aerodynamic torque. In these states, there are two different cases, one is that stall happens and the other is that stall does not happen. For the cases that stall happens, the sinusoidal pitch control algorithm with a minus amplitude ($\beta < 0$) can prevent or hinder stall in both the upwind side and the downwind side; but the fixed pitch can only accomplish this requirement in one side and has an opposite effect in the other side. For the cases that stall does not happen, the sinusoidal pitch control algorithm with an appropriate positive amplitude ($\beta > 0$) can enlarge the AOA in both sides and prevent or hinder stall at the same time. There is hardly any effect of the fixed pitch scheme. In the state of operating above the rated wind speed, the

sinusoidal pitch control algorithm can maintain the power at the rate value within a smaller pitch angle range than the fixed pitch control algorithm. In the state of shut-down, the objective of pitch control is not preventing but remaining the pitch angle in the stall region. Again, the sinusoidal variation with a large positive amplitude ($\beta > 0$) can accomplish the requirement and the fixed pitch control algorithm is useless. According the above studies, a pitch control system was proposed for a typical straight-bladed VAWT. Besides the control system, a SHM system was also proposed based on the results of the fatigue and ultimate strength analyses. For the typical straight bladed VAWT, 2 anemometers were installed at different heights to monitor the wind speed and wind profile; 1 laser displacement sensor was used to measure the rotational speed; 2 accelerometers were installed at the top of tower to monitor the bending vibration in two direction; 2 accelerometers were installed on each main arm, upper arm and lower arm to monitor the vibration in normal and tangential direction; 4 strain rosettes were attached on the shaft to monitor torsion and bending; 4 strain gauges were attached at the bottom of tower to monitor bending in two direction; 3 strain gauges were attached at the root of main arms to monitor vertical bending. 2 LVDTs were installed to monitor the swing of shaft; 1 load cell is installed on each upper arm, lower arm and link to monitor the service loads; 1 LVDT is installed on each upper arm and lower arm to monitor pitch angle. 2 sets of data acquisition systems are used, one for the sensors installed on the rotor which are rotating and the other for the sensors installed on the tower and the wind mast which are stationary. A concept of smart VAWTs was also given. The smart VAWT should synthesize the systems of SHM, control and power supply so that the VAWT can accomplish the objectives of self-sensing, self-inspecting, self-control and self-power.

9.2 Recommendations for Future Studies

Although some progress has been made in this thesis on the topic of the fatigue and ultimate strength analyses of VAWTs with SHM and control, several important issues require further studies.

1. The proposed method to obtain wind load is based on the strip analysis and 2D CFD simulation, therefore, the 3D effect is not considered. In further studies, full scale 3D CFD simulations or wind tunnel tests should be conducted to evaluate the influence of 3D flow field. One key issue of the straight-bladed VAWTs is the influence of existing of arms on aerodynamic forces. Although this influence has been preliminarily studied in the thesis, more accurate results should be obtained by full scale 3D simulation.

2. In the thesis, VAWTs are assumed to operate at the constant rotational speed in the CFD simulation. Therefore, the wind loads in the startup and shutdown cases are unknown. In fact, the simulation of the startup and shutdown processes is coupled with the dynamics of the rotor. In this regard, most of literatures on CFD simulations of wind turbines, either VAWTs or HAWTs, only consider the constant speed operating process; only BEM are used in the simulation of the varying speed operating process, which is based on the quasi-steady assumption and the dynamic stall is usually not considered. Due to the importance of startup and shutdown for VAWTs, further studies should be focused on the CFD simulation of the varying speed operating process.

3. A micromechanics-based updating method is proposed to identify the laminar elastic constants of laminated composite blades. Due to the limited data of experimental tests, the uncertainties in material properties of fiber and matrix are not considered. Moreover, only analytical micromechanics models, which need simplifications, are used in the proposed method. However, many complex composite materials do not have analytical models. A more general and accurate method of establishing the micromechanics model for a specific composite material is using finite element method. In further studies, a better designed test should be conducted to

offer more data so that the uncertainties in constituents can be considered and more accurate micromechanics models should be used in the process of updating.

4. In the analysis of VAWTs, the rotating reference frame method is usually used. However, this method is only limited to the case that the turbine is rotating at the constant speed and the tower is axial-symmetric. Although a wind turbine which using a synchronous generator or induction generator indeed operates at a constant rotational speed, the one equipped with a direct-driven generator does not. A more general approach is to use the flexible multi-body dynamics method, which has been widely used in the analysis of HAWTs. Further studies should be focused on modelling VAWTs by the flexible multi-body dynamics method.

5 In the model updating of the whole VAWT, the shaft's thickness and Young's moduli of the material are taken as the updating parameters. Although the shaft's thickness and Young's moduli of the material can be measured accurately, the connection between different components and the boundary condition are difficult to be simulated accurately by the FE model. Therefore, these uncertainties are included in the chosen parameters. A better way to dealt with this problem is to modify the FE model — using constraint element, i.e. MPC184 of ANSYS, to simulate the connection between main arms and the shaft — and to update the stiffness of the corresponding elements. This modification should be conducted in further studies.

6. In this study, the pitch control algorithm is based on DMST which is a kind of BEM method and thus requires the quasi-steady assumption. However, the process of pitch varying is inherent unsteady and the algorithm is only valid in the condition that the rotational speed is low, which is usually right for large-scale wind turbine. Nevertheless, the influence of dynamic stall due to pitch varying is still unclear. In the further study, CFD simulation of pitch varying should be conducted to validate or modify the proposed pitch control algorithm.

7 The pitch control system proposed in Chapter 8 is just a schematic design. Wind tunnel tests or field tests should be further conducted to evaluate the effectiveness of the control system.

8 Pitch control is usually used to improve the power coefficient in the low wind situation and limit the output power in the high wind situation. It is possible that pitch control could be used to reduce the fatigue damage during operation. In further studies, the research on this topic could also be conducted.

9 The SHM system given in Chapter 8 involves many sensors and devices. Considering the cost, the system was not been installed in the test bed VAWT in Yang Jiang City. In further study, the SHM system should be installed and more field measurement should be conducted.

10 The smart VAWT in Chapter 8 is just a conceptual design. To date, there is still no such a VAWT. More efforts should be paid on this area to realize the smart VAWT.

11 In this thesis, only a single VAWT is considered. Actually, there are many wind turbines in a wind farm and the wake of a wind turbine will have an influence on the performance of the turbine behind it. So far, researchers already have a deep understanding of the wake of HAWTs and developed some placement schemes of multiple HAWTs. While the research of VAWTs on this topic is still in the preliminary stage. Therefore, the wake of VAWT and the placement of multiple VAWTs should be further studied.

APPENDIX A

SIMULATED WIND SPEED TIME HISTORIES

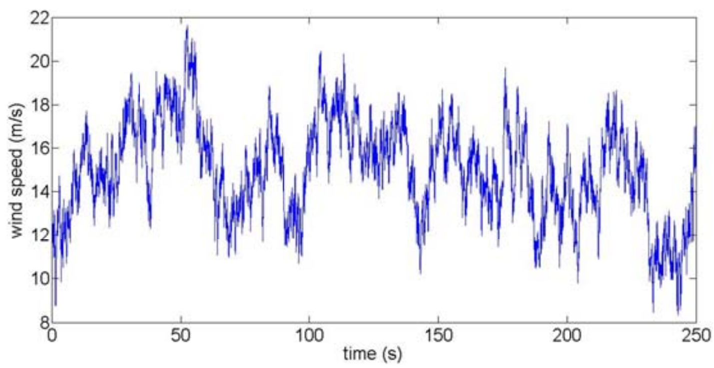

(a)

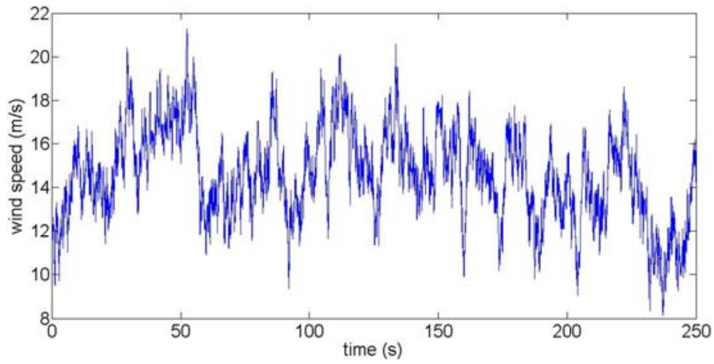

(b)

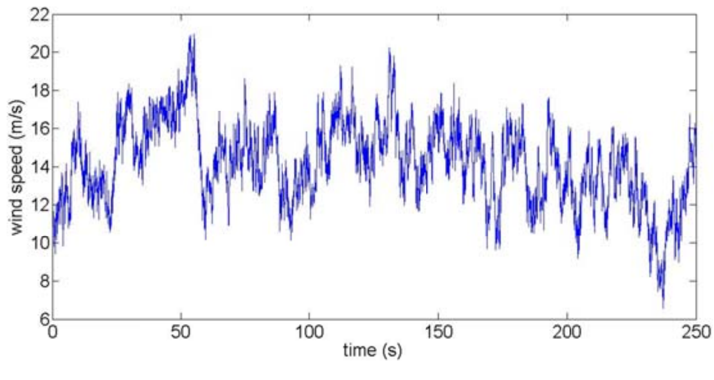

(c)

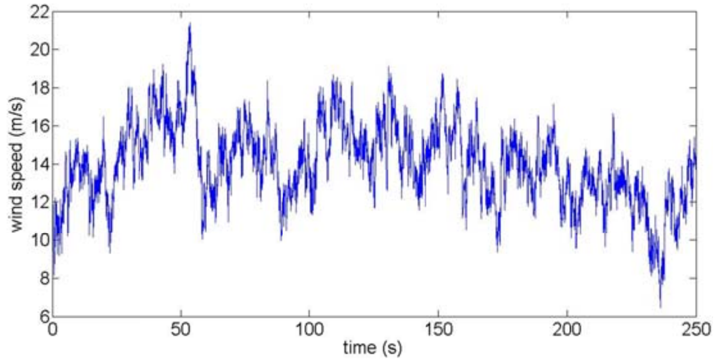

22
20
18
16
14
12
10
8
6
wind speed (m/s)
0
50
100
150
200
250
time (s)

(d)

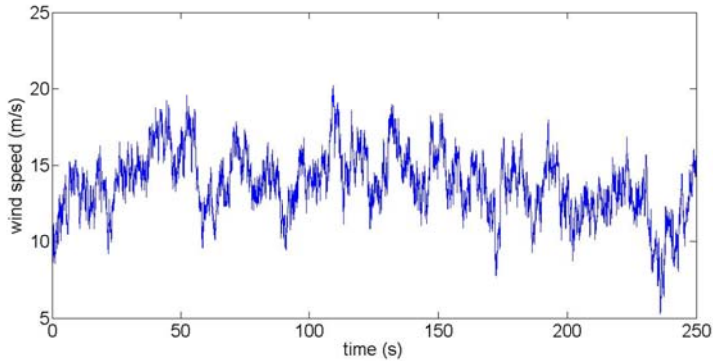

25
20
15
10
5
wind speed (m/s)
0
50
100
150
200
250
time (s)

(e)

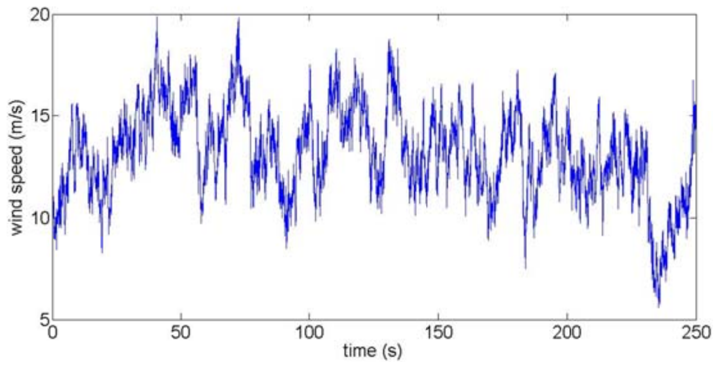

20
15
10
5
wind speed (m/s)
0
50
100
150
200
250
time (s)

(f)

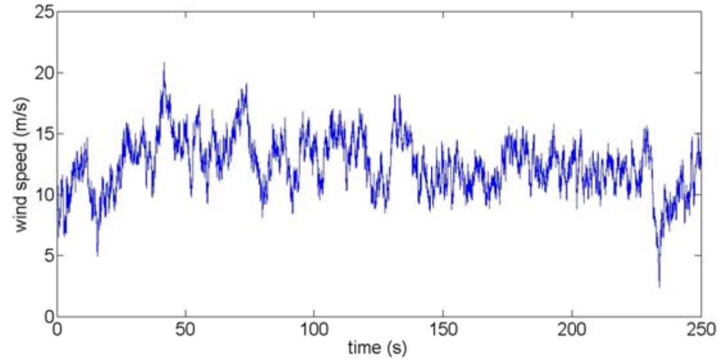

(g)

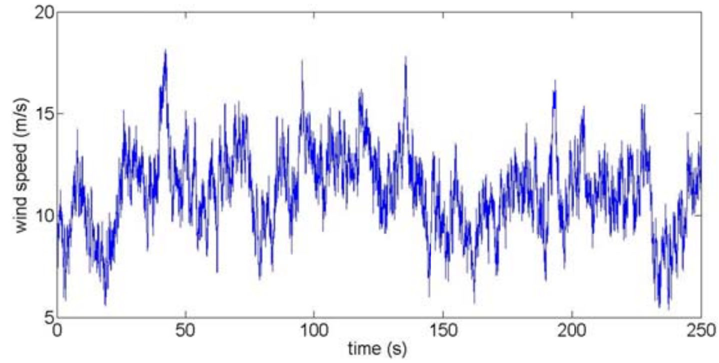

(h)

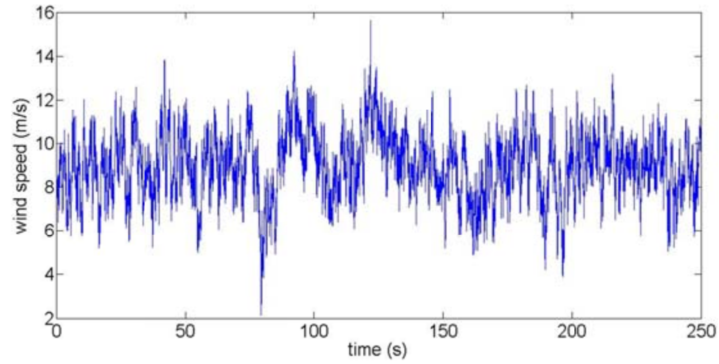

(i)

Fig. A the simulated wind speed time histories. (a) sec1; (b) sec2; (c) sec3; (d) sec4; (e) sec5; (f) sec6; (g) sec7; (h) sec8; (i) sec9;

APPENDIX B

MESH GRIDS OF CFD SIMULATION

The mesh grids of sec7 have been introduced in Section 3.1. The grids of other cross sections are shown here. Because the mesh grids of cell zone1 in all sections are the same and sec8 and sec9 are identical, the mesh of sec1-sec6 and sec8 are listed.

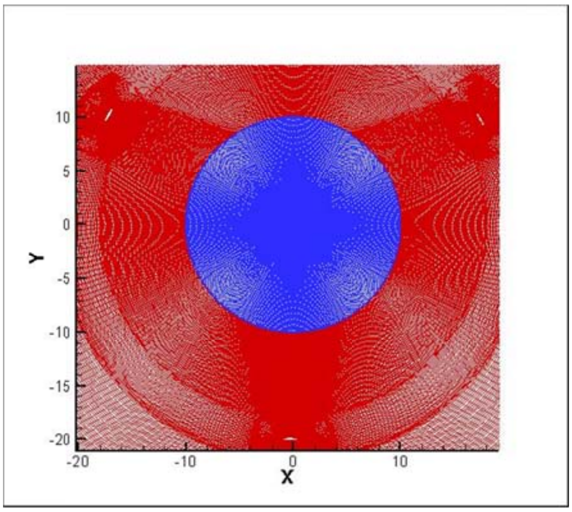

(a)

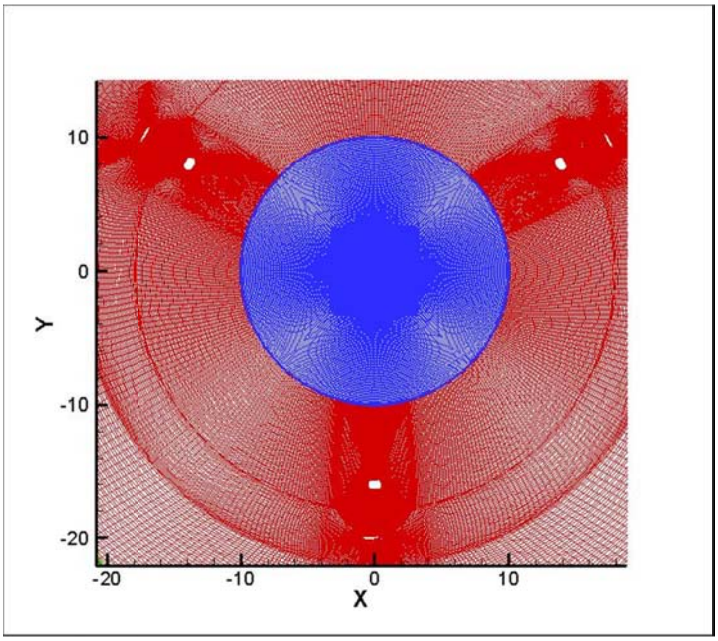

(b)

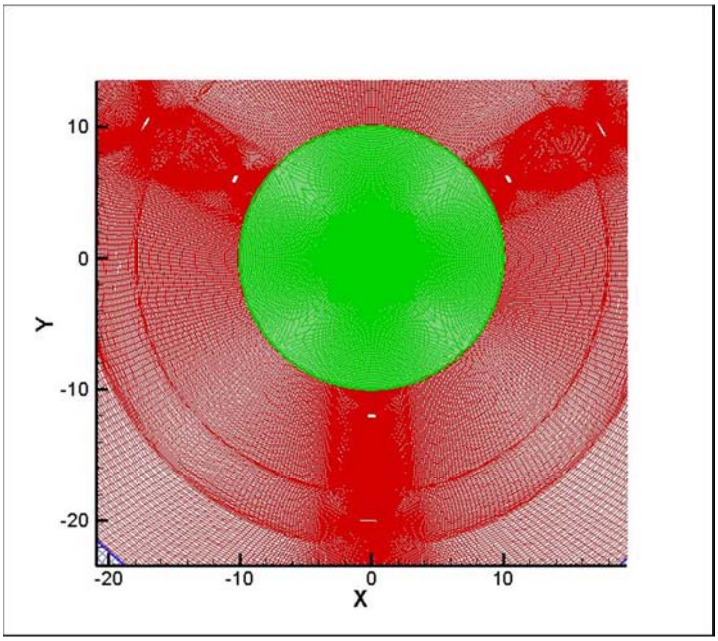

(c)

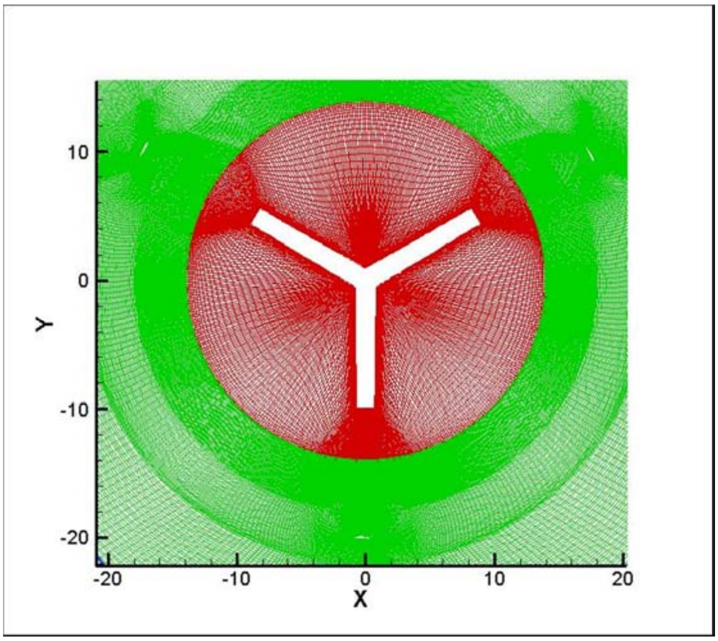

(d)

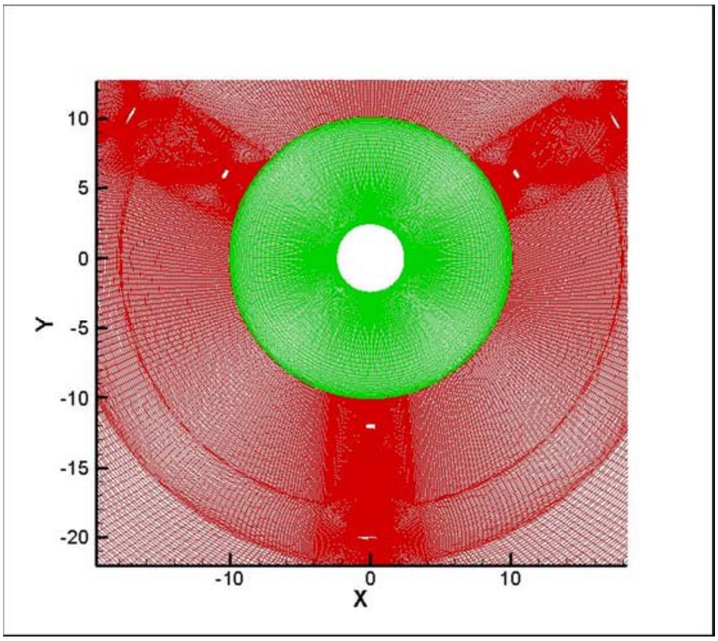

(e)

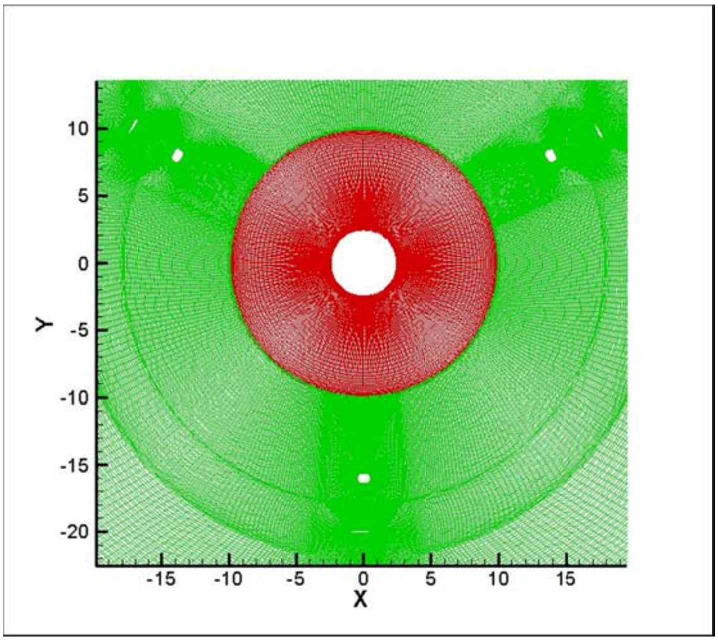

(f)

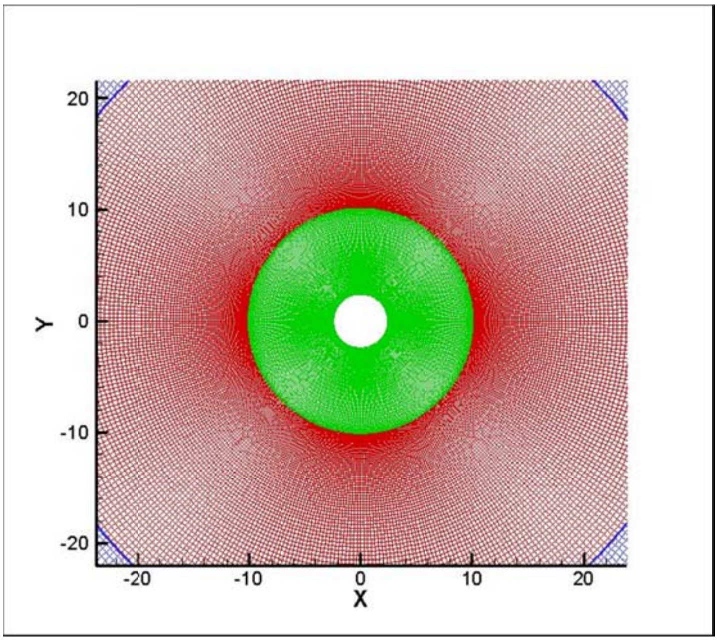

(g)

Fig. B Mesh grids of cell zone 2 and cell zone 3. (a) sec1; (b) sec2; (c) sec3; (d) sec4; (e) sec5; (f) sec6; (g) sec8

APPENDIX C

MODE SHAPES OF THE STRAIGHTBLADED VAWT

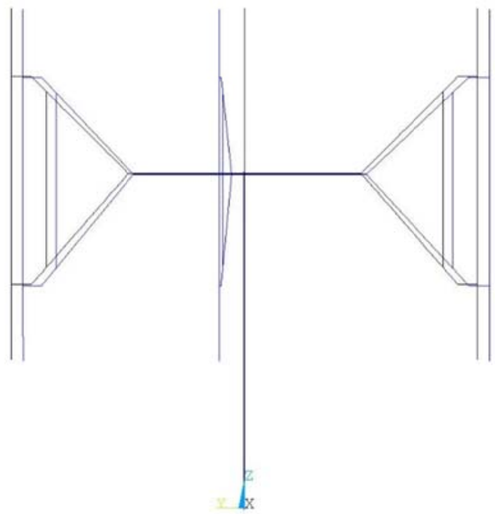

(a)

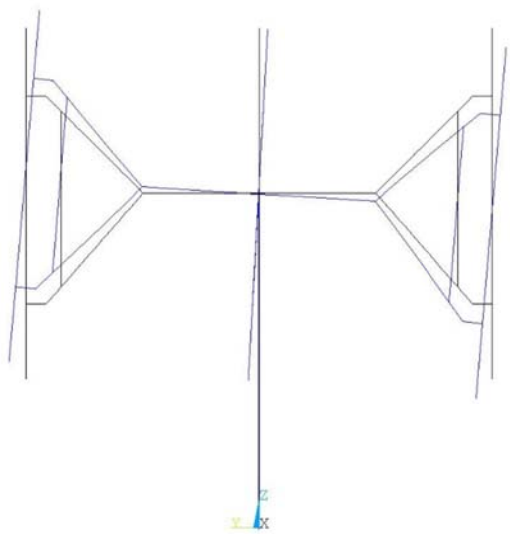

(b)

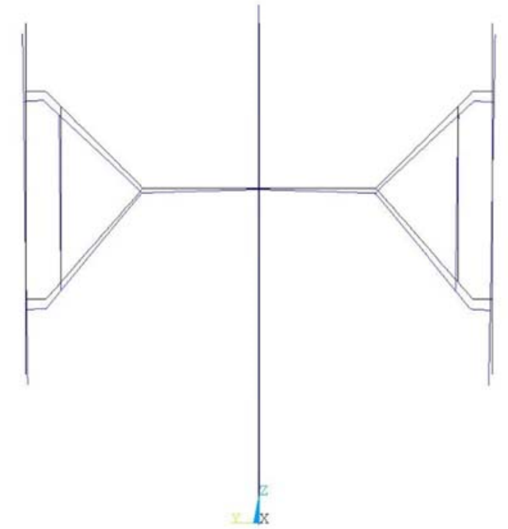

(c)

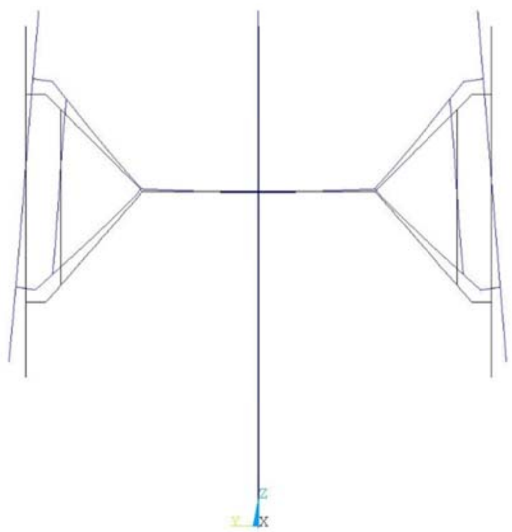

(d)

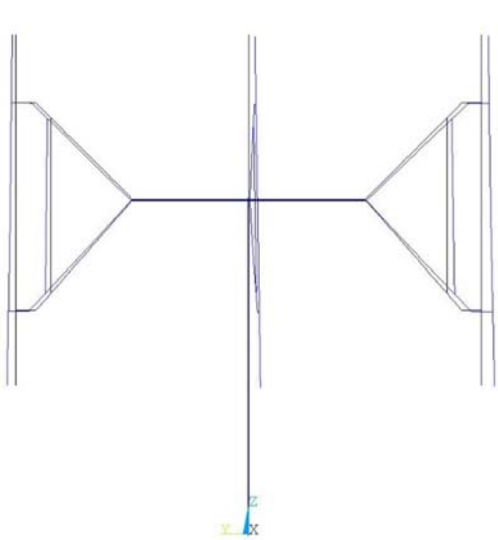

(e)

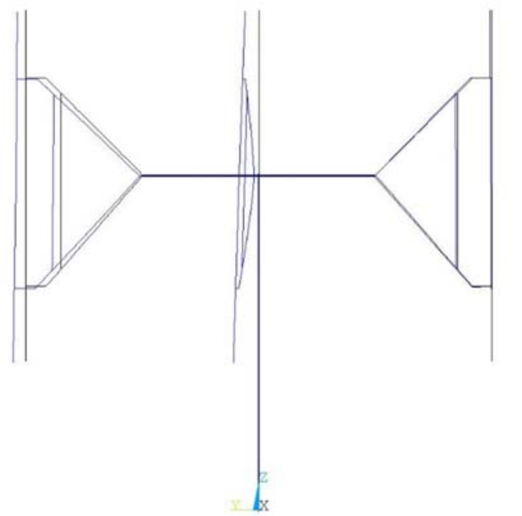

(f)

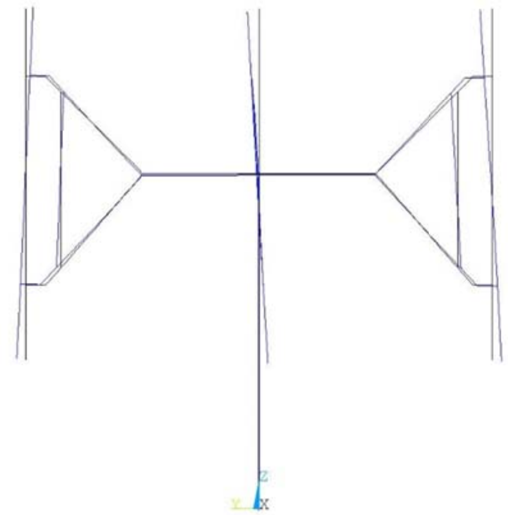

(g)

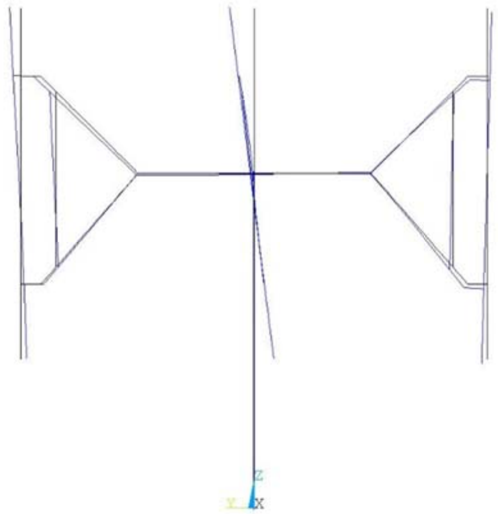

(h)

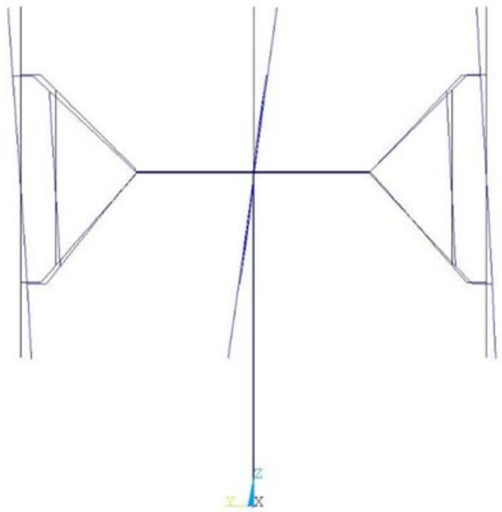

(i)

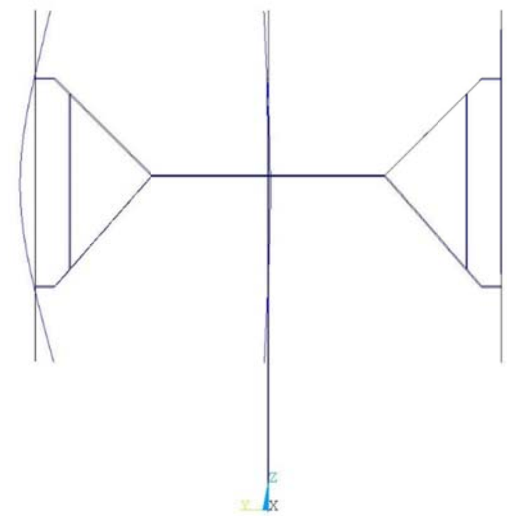

(j)

Fig. C the first 10 mode shape of the VAWT FE model. (a) 1^{st} mode; (b) 2^{nd} mode; (c) 3^{rd} mode; (d) 4^{th} mode; (e) 5^{th} mode ; (f) 6^{th} mode; (g) 7^{th} mode; (h) 8^{th} mode; (i) 9^{th} mode; (j) 10^{th} mode.

APPENDIX D

STRAIN TIME HISTORIES OF TOWER

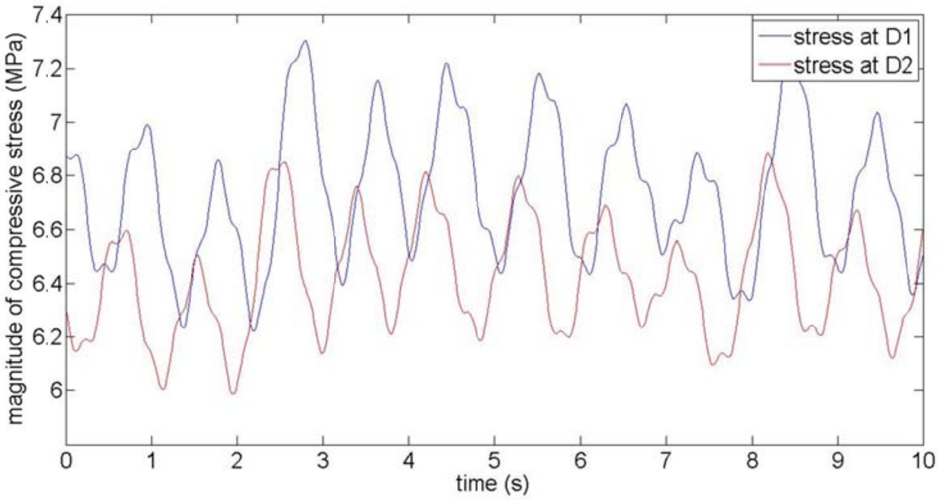

(a)

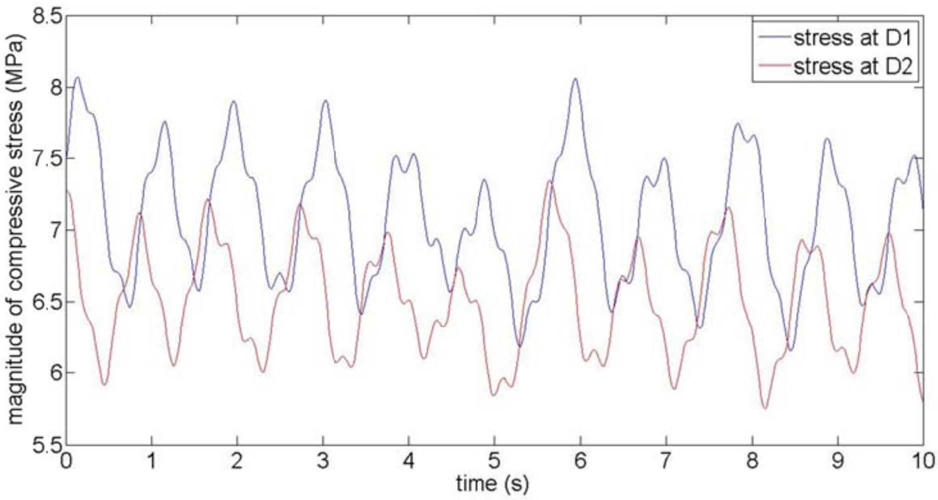

(b)

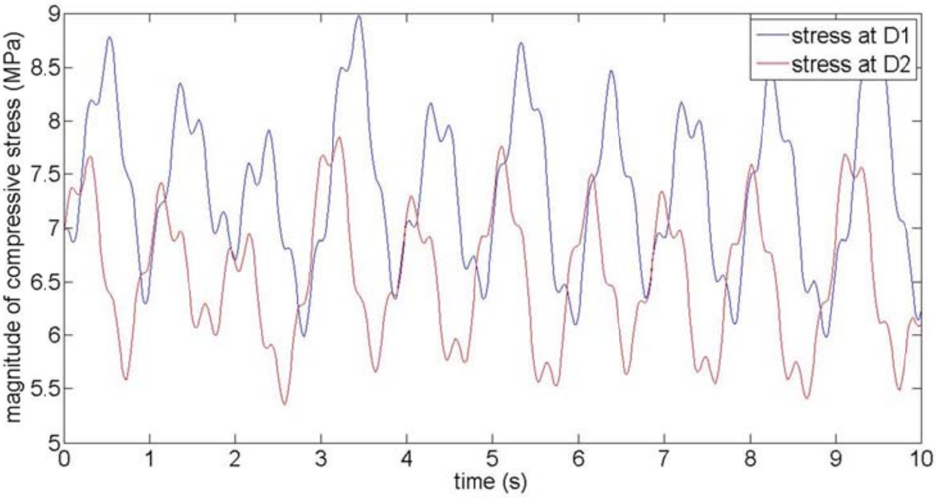

stress at D1
stress at D2
magnitude of compressive stress (MPa)
time (s)

(c)

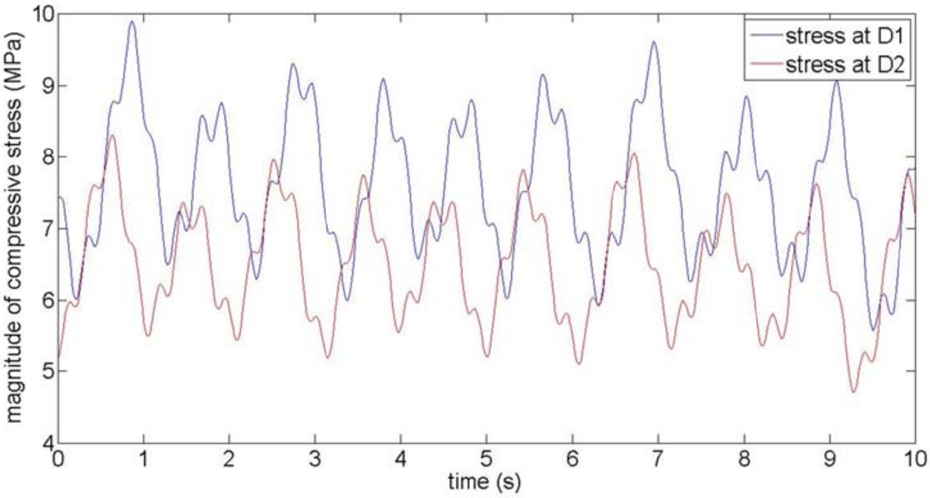

stress at D1
stress at D2
magnitude of compressive stress (MPa)
time (s)

(d)

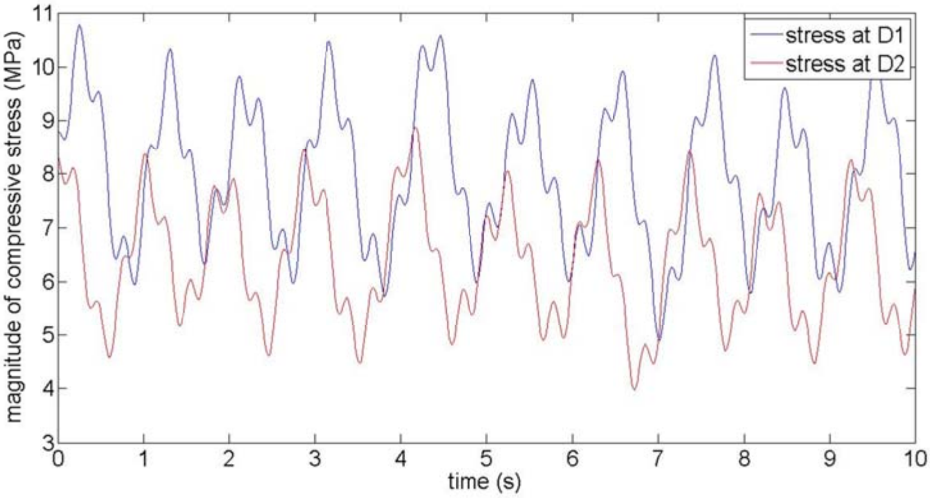

stress at D1
stress at D2
magnitude of compressive stress (MPa)
time (s)

(e)

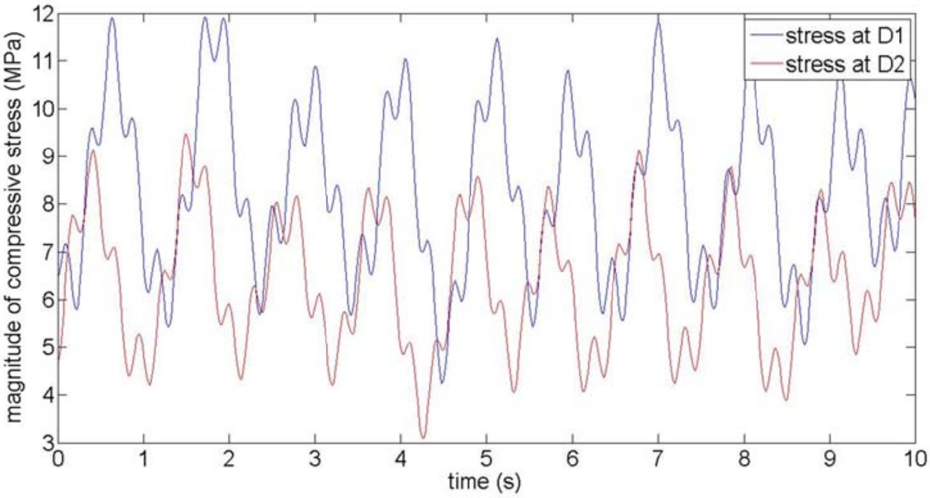

(f)

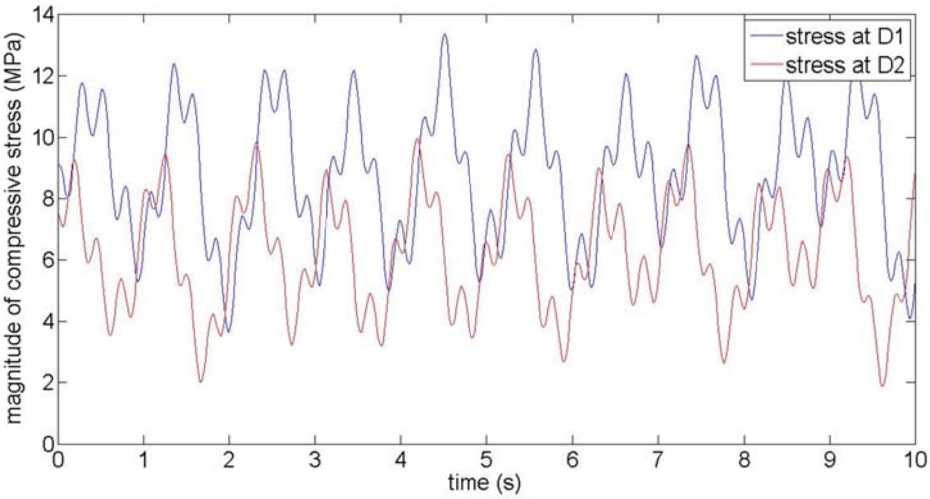

(g)

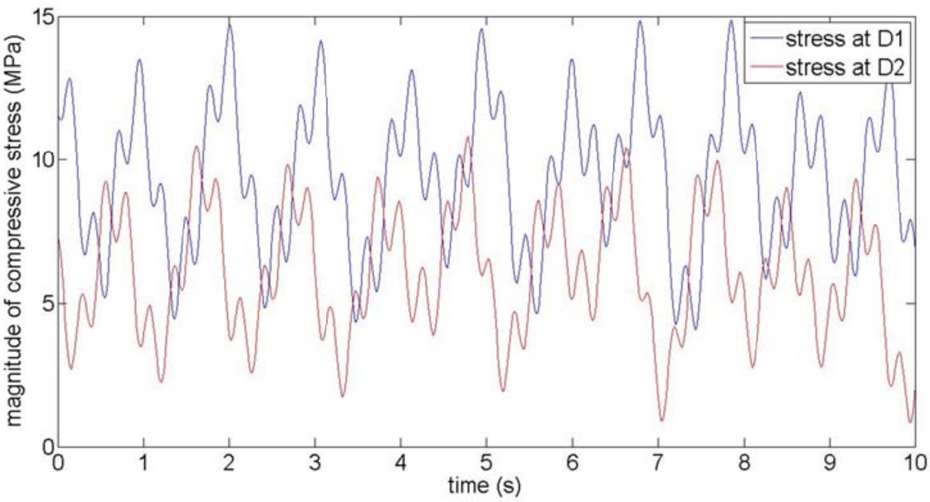

(h)

Fig. D time histories of $\sigma_{Z_o,\mathrm{D1}}$ and $\sigma_{Z_o,\mathrm{D2}}$ at different mean wind speed. (a) 6 m/s;

(b) 8 m/s; (c) 10 m/s; (d) 12 m/s; (e) 14 m/s; (f) 16 m/s; (g) 18 m/s; (h) 20 m/s;

APPENDIX E

SIMULATED WIND SPEEDS BASED ON THE FIELD MEASURED DATA

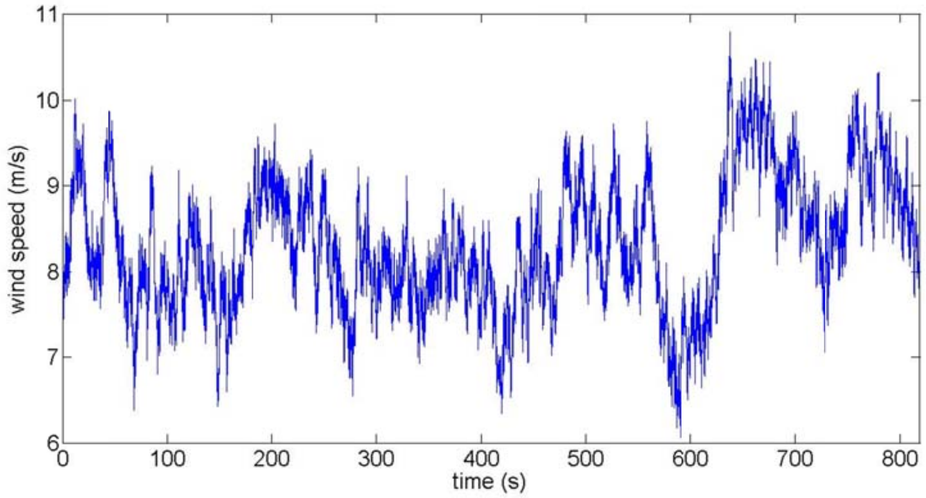

(a)

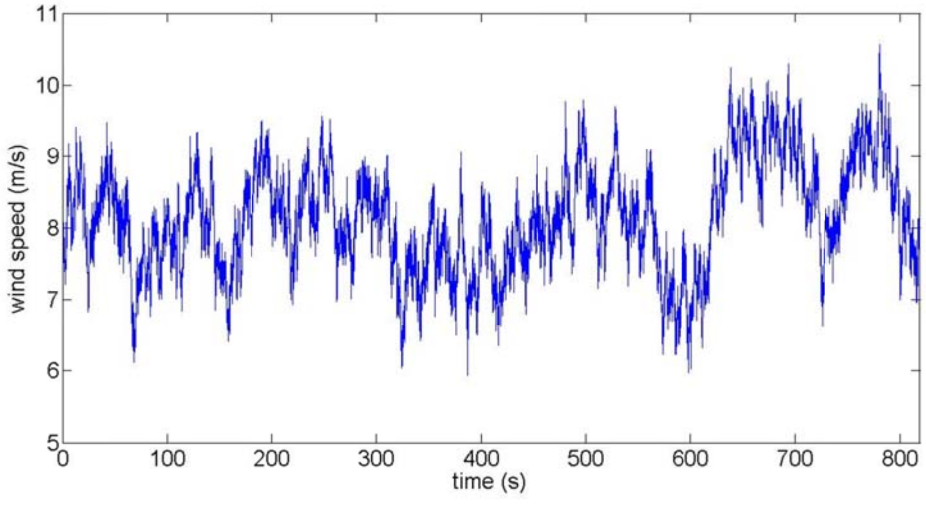

(b)

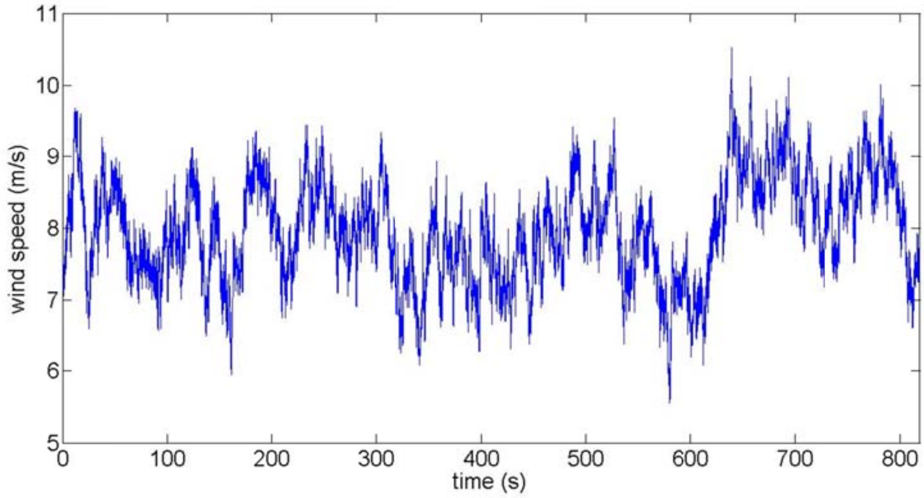

(c)

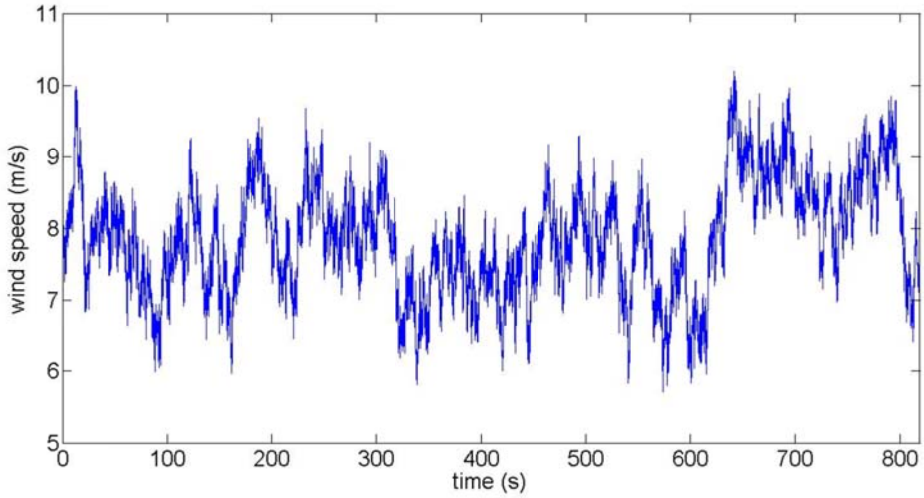

(d)

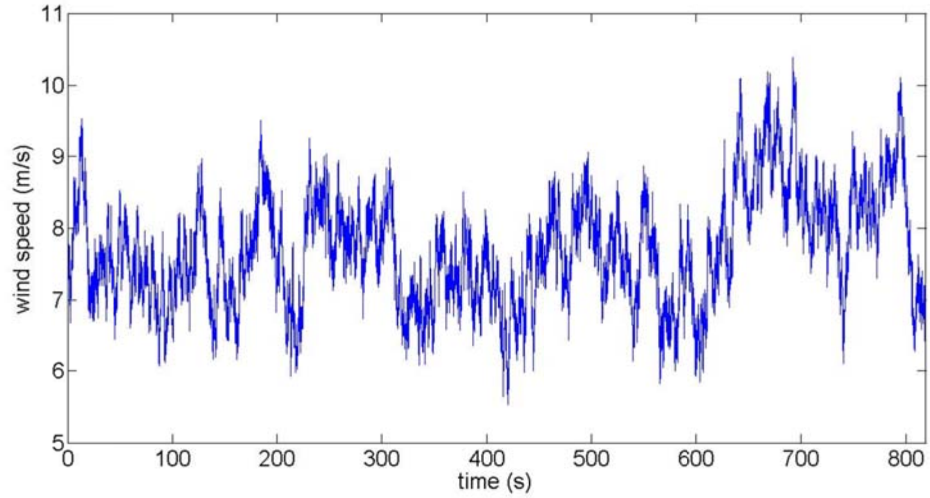

(e)

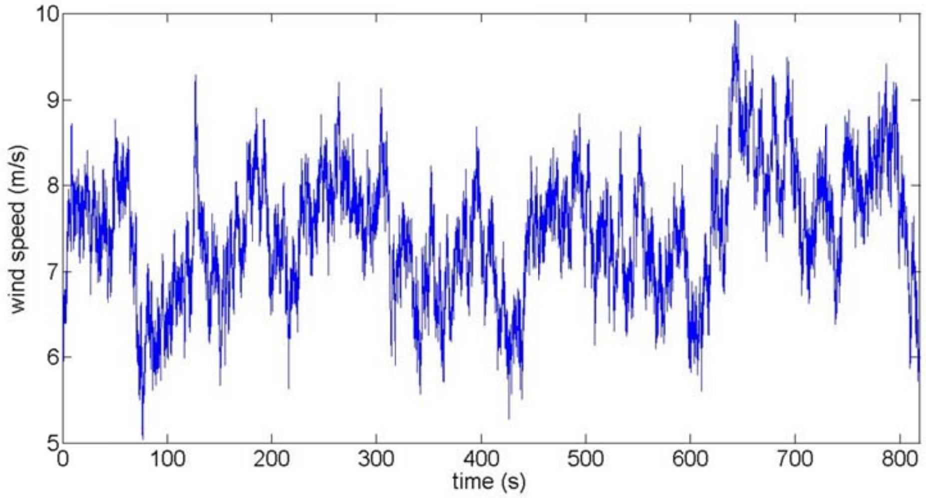

(f)

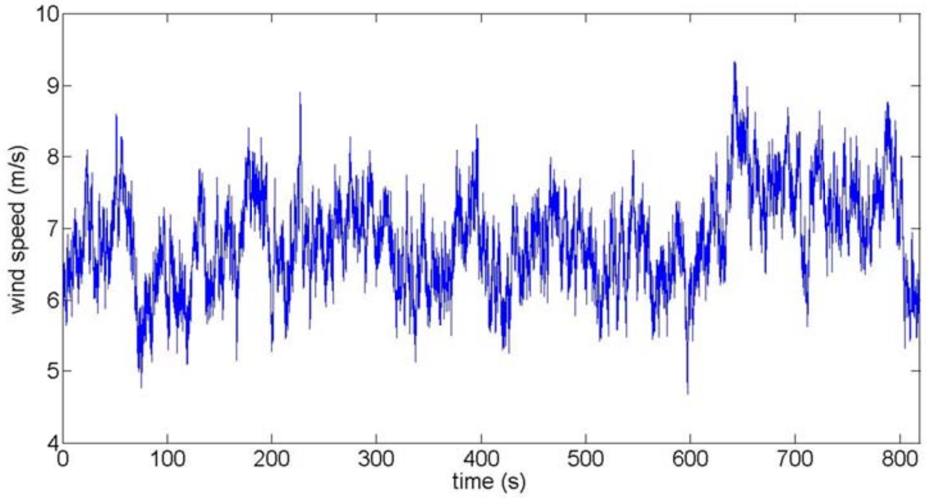

(g)

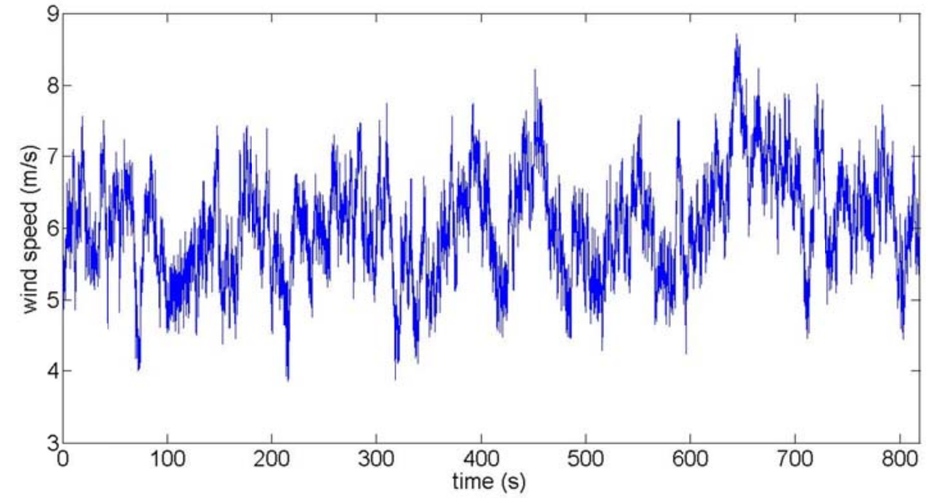

(h)

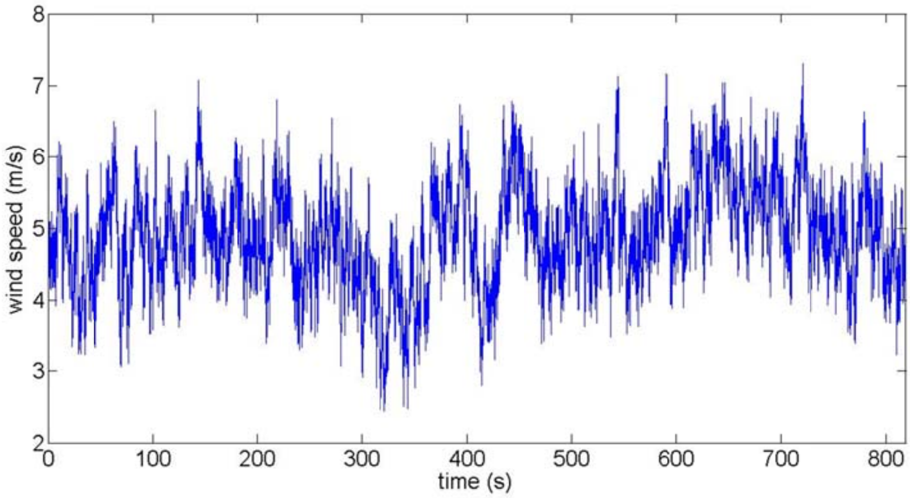

(i)

Fig. E Simulated wind speeds for simulation and validation of Chapter 7. (a) sec1; (b) sec2; (c) sec3; (d) sec4; (e) sec5; (f) sec6; (g) sec7; (h) sec8; (**i**) sec9;

APPENDIX F

TORQUE AND AOA IN THE STARTUP STATE

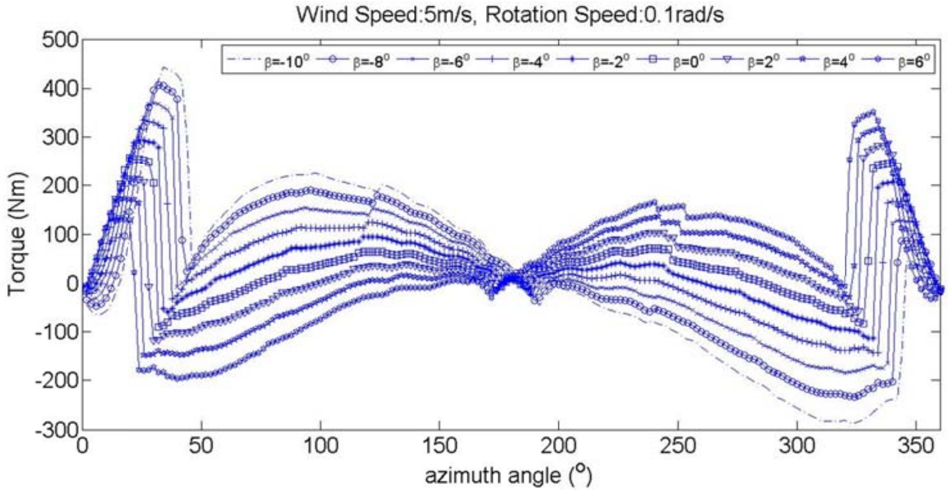

(a)

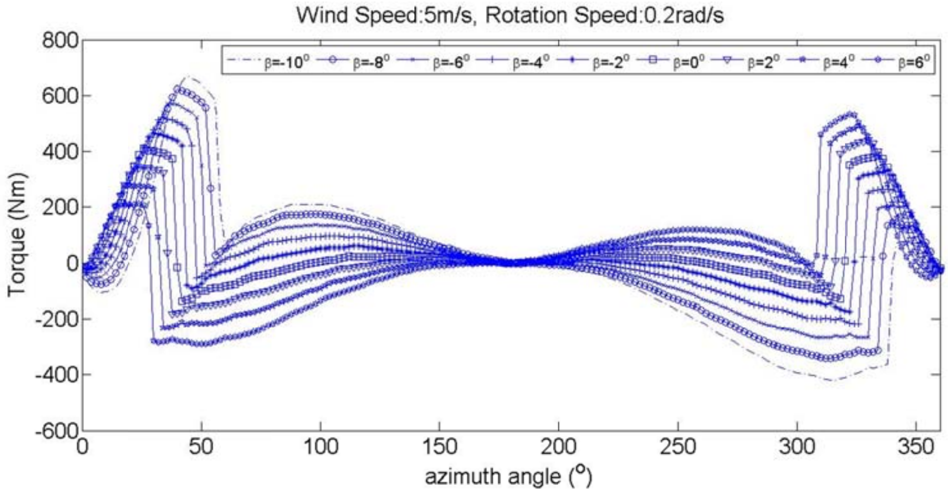

(b)

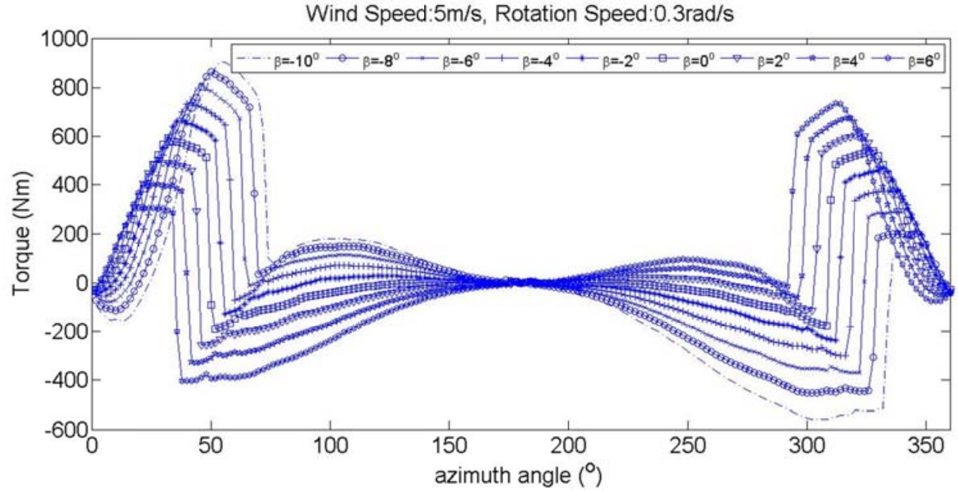
Wind Speed:5m/s, Rotation Speed:0.3rad/s
β=-10° β=-8° β=-6° β=-4° β=-2° β=0° β=2° β=4° β=6°
Torque (Nm)
azimuth angle (°)

(c)

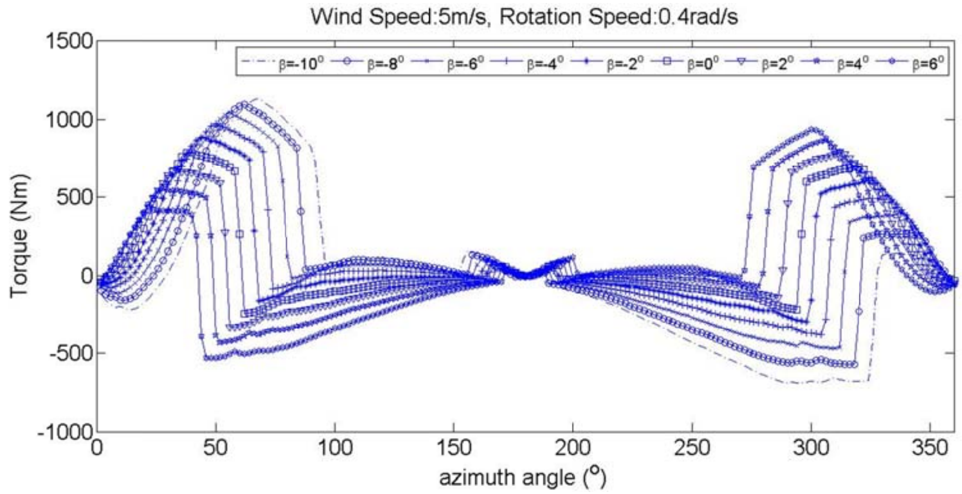
Wind Speed:5m/s, Rotation Speed:0.4rad/s
β=-10° β=-8° β=-6° β=-4° β=-2° β=0° β=2° β=4° β=6°
Torque (Nm)
azimuth angle (°)

(d)

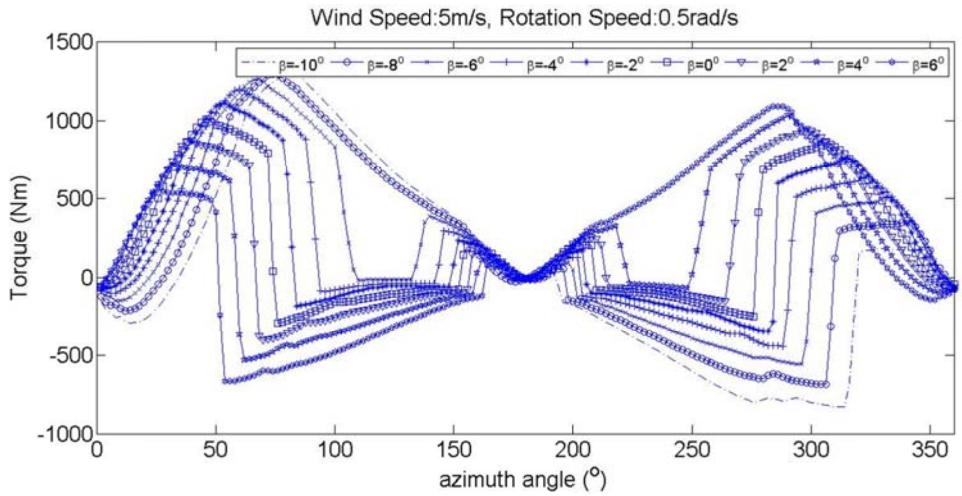
Wind Speed:5m/s, Rotation Speed:0.5rad/s
β=-10° β=-8° β=-6° β=-4° β=-2° β=0° β=2° β=4° β=6°
Torque (Nm)
azimuth angle (°)

(e)

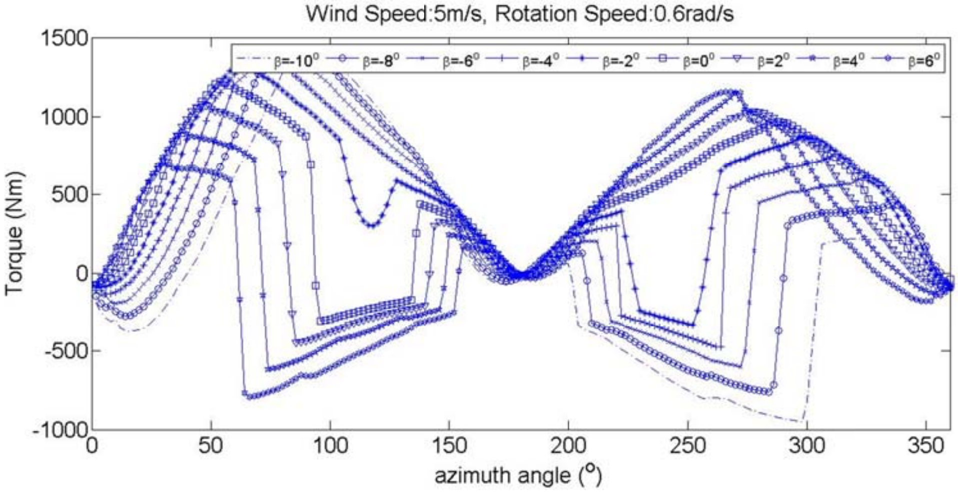

Wind Speed:5m/s, Rotation Speed:0.6rad/s
β=-10° β=-8° β=-6° β=-4° β=-2° β=0° β=2° β=4° β=6°
Torque (Nm)
azimuth angle (°)

(f)

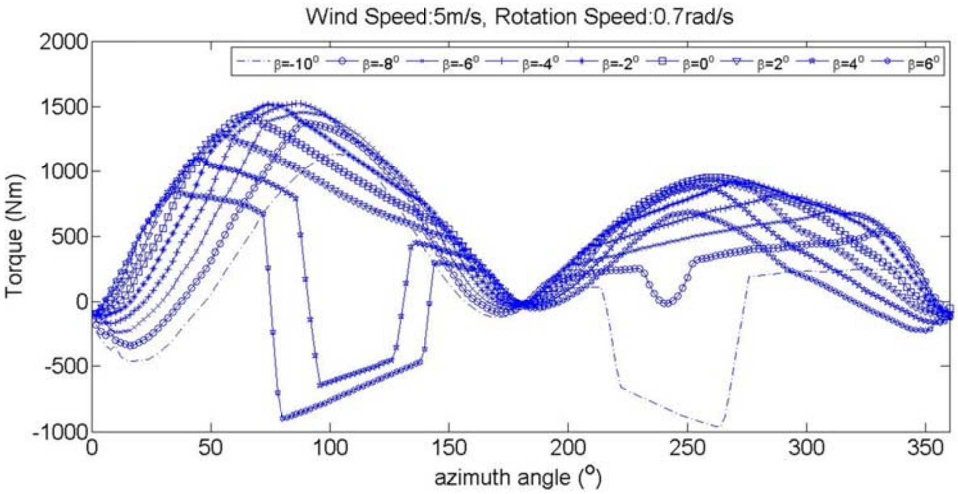

Wind Speed:5m/s, Rotation Speed:0.7rad/s
β=-10° β=-8° β=-6° β=-4° β=-2° β=0° β=2° β=4° β=6°
Torque (Nm)
azimuth angle (°)

(g)

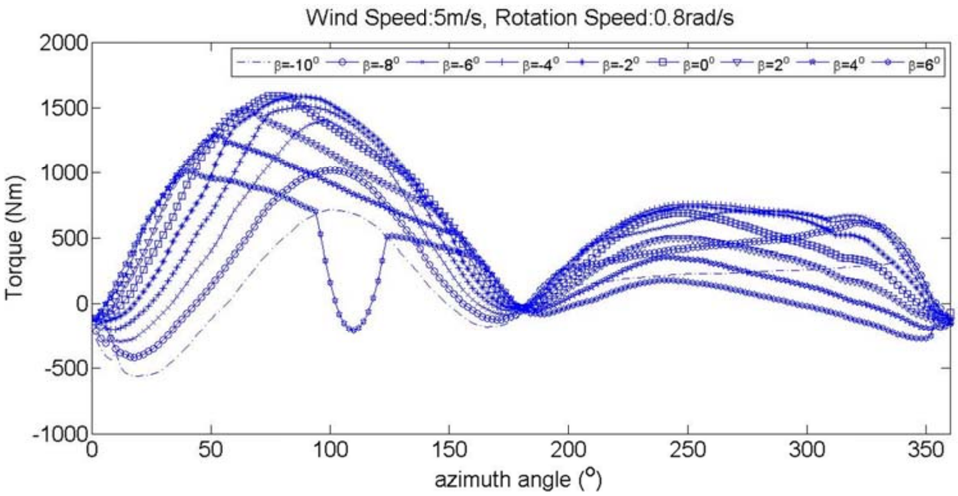

Wind Speed:5m/s, Rotation Speed:0.8rad/s
β=-10° β=-8° β=-6° β=-4° β=-2° β=0° β=2° β=4° β=6°
Torque (Nm)
azimuth angle (°)

(h)

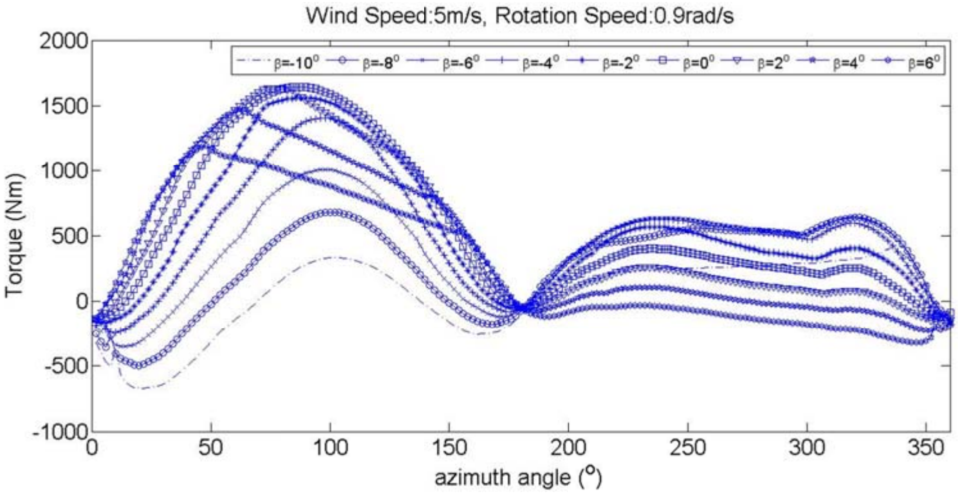

(i)

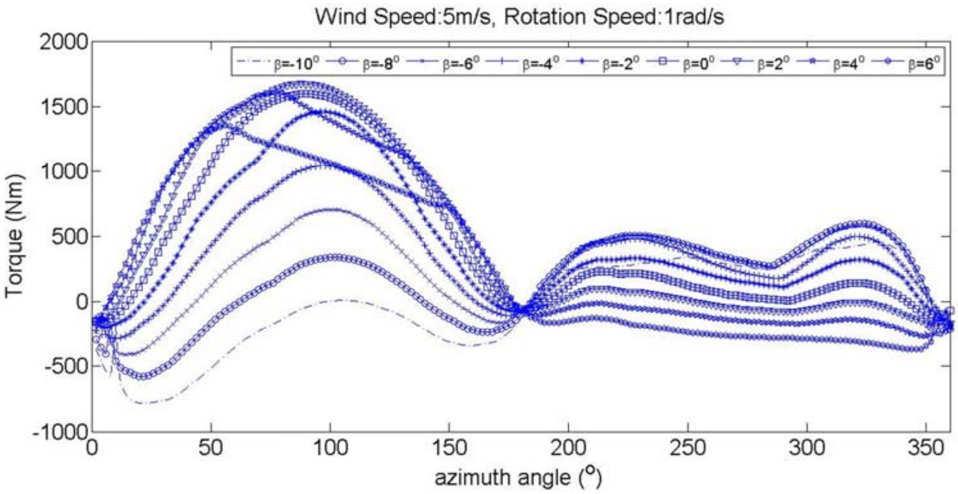

(j)

Fig. F.1 the aerodynamic torques T per length for the fixed pitch cases. (a) $\omega = 0.1\, rad/s$; (b) $\omega = 0.2\, rad/s$; (c) $\omega = 0.3\, rad/s$; (d) $\omega = 0.4\, rad/s$; (e) $\omega = 0.5\, rad/s$; (f) $\omega = 0.6\, rad/s$; (g) $\omega = 0.7\, rad/s$; (h) $\omega = 0.8\, rad/s$; (i) $\omega = 0.9\, rad/s$; (j) $\omega = 1.0\, rad/s$;

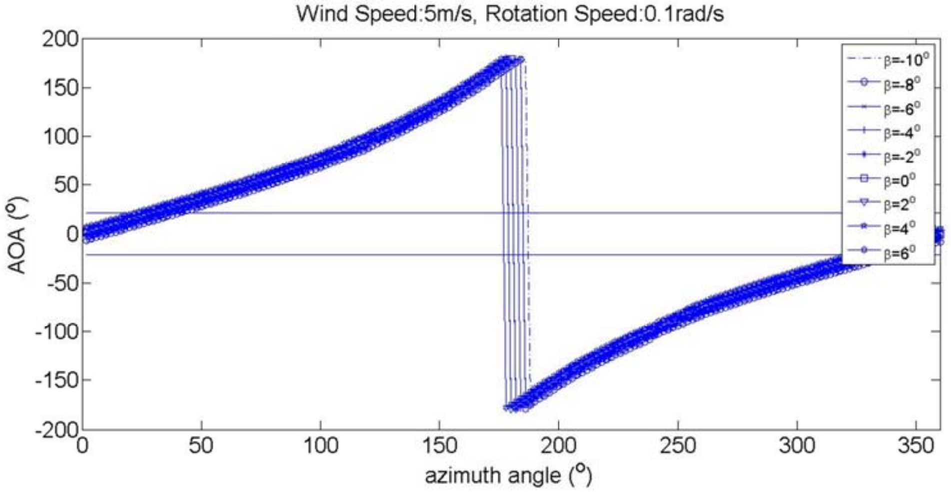
Wind Speed:5m/s, Rotation Speed:0.1rad/s
AOA (°)
azimuth angle (°)
β=-10°
β=-8°
β=-6°
β=-4°
β=-2°
β=0°
β=2°
β=4°
β=6°

(a)

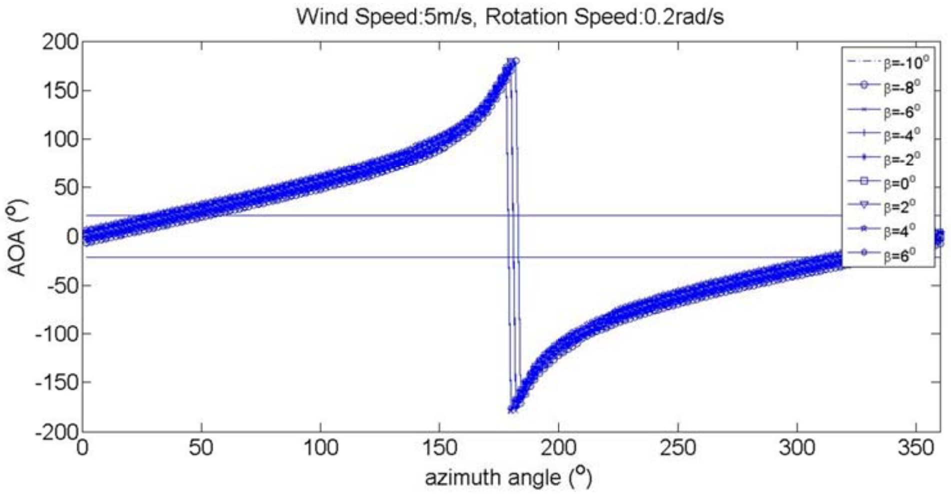
Wind Speed:5m/s, Rotation Speed:0.2rad/s
AOA (°)
azimuth angle (°)
β=-10°
β=-8°
β=-6°
β=-4°
β=-2°
β=0°
β=2°
β=4°
β=6°

(b)

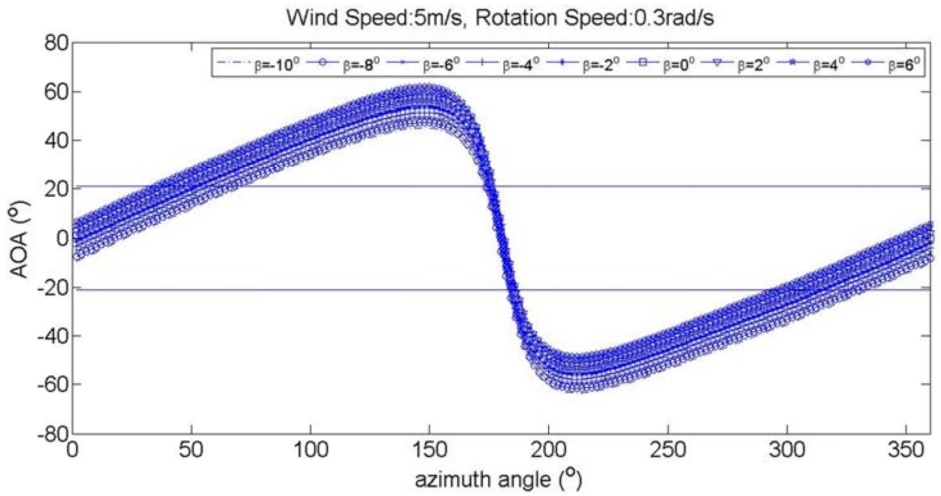
Wind Speed:5m/s, Rotation Speed:0.3rad/s
AOA (°)
azimuth angle (°)
β=-10° β=-8° β=-6° β=-4° β=-2° β=0° β=2° β=4° β=6°

(c)

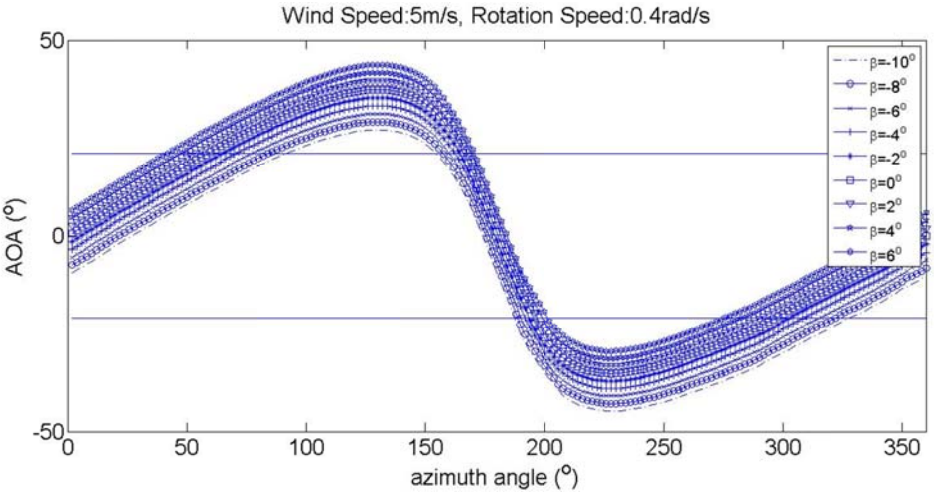
Wind Speed:5m/s, Rotation Speed:0.4rad/s
AOA (°)
azimuth angle (°)
β=-10°
β=-8°
β=-6°
β=-4°
β=-2°
β=0°
β=2°
β=4°
β=6°

(d)

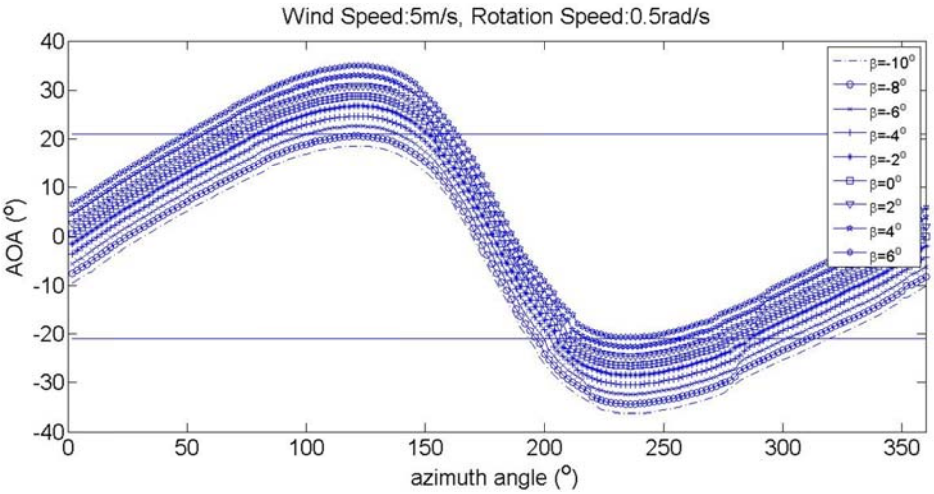
Wind Speed:5m/s, Rotation Speed:0.5rad/s
AOA (°)
azimuth angle (°)
β=-10°
β=-8°
β=-6°
β=-4°
β=-2°
β=0°
β=2°
β=4°
β=6°

(e)

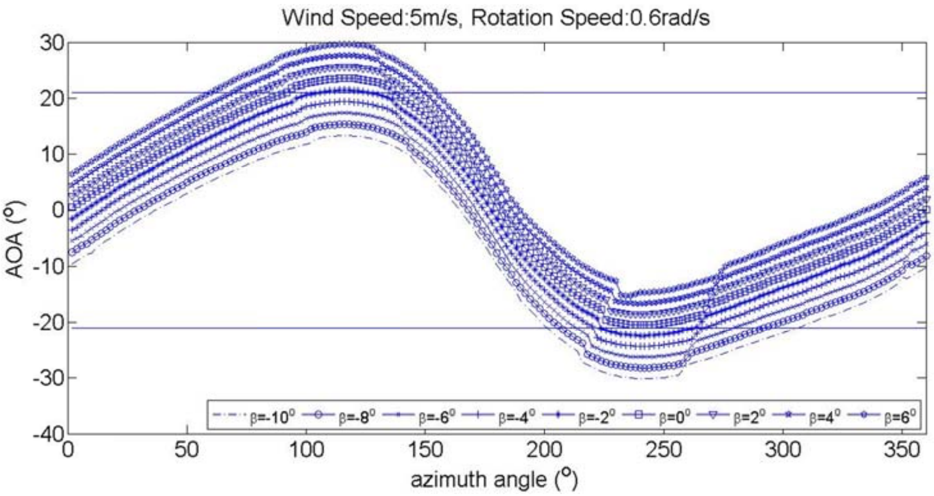
Wind Speed:5m/s, Rotation Speed:0.6rad/s
AOA (°)
azimuth angle (°)
β=-10° β=-8° β=-6° β=-4° β=-2° β=0° β=2° β=4° β=6°

(f)

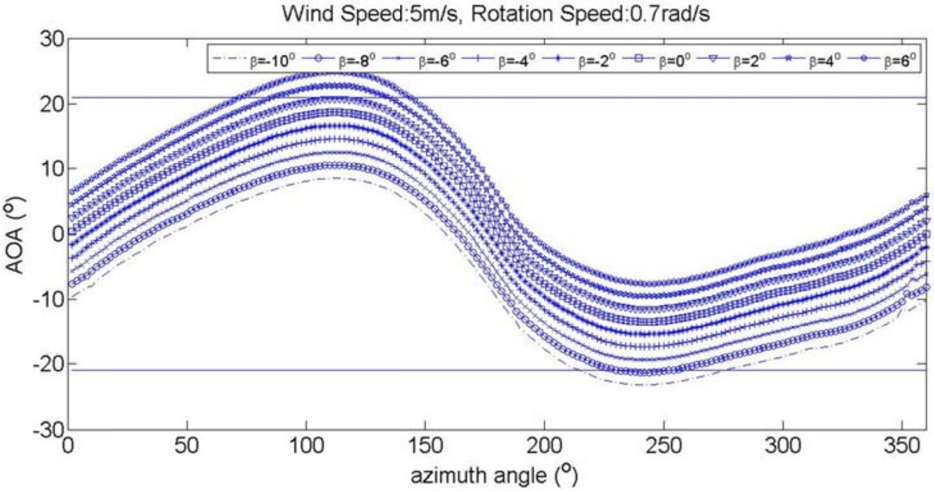
Wind Speed:5m/s, Rotation Speed:0.7rad/s
β=-10° β=-8° β=-6° β=-4° β=-2° β=0° β=2° β=4° β=6°
AOA (°)
azimuth angle (°)

(g)

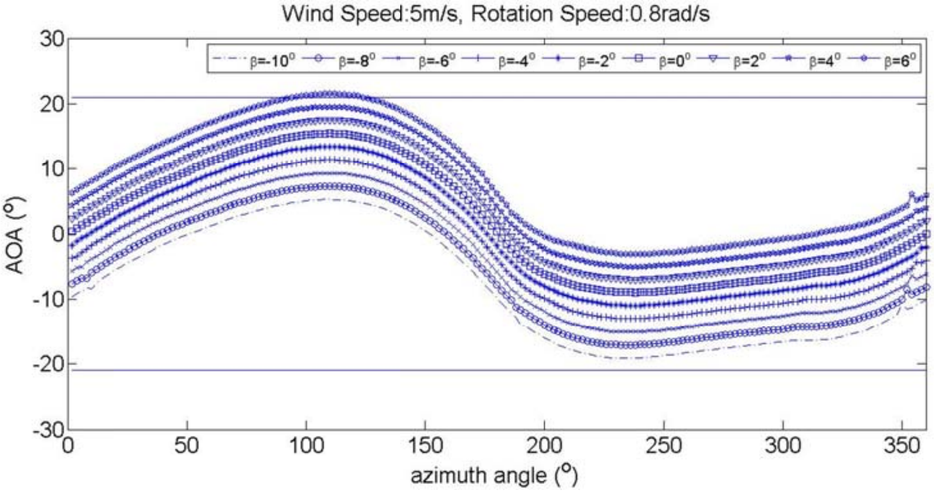
Wind Speed:5m/s, Rotation Speed:0.8rad/s
β=-10° β=-8° β=-6° β=-4° β=-2° β=0° β=2° β=4° β=6°
AOA (°)
azimuth angle (°)

(h)

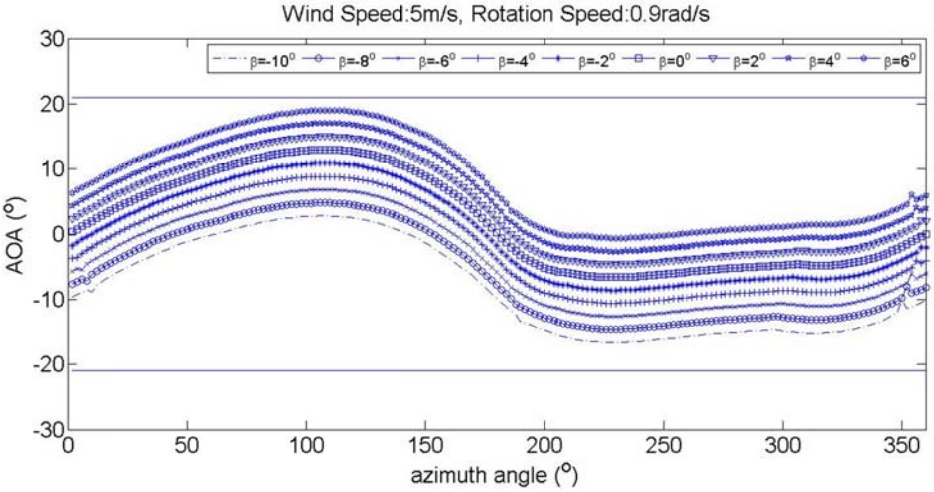
Wind Speed:5m/s, Rotation Speed:0.9rad/s
β=-10° β=-8° β=-6° β=-4° β=-2° β=0° β=2° β=4° β=6°
AOA (°)
azimuth angle (°)

(i)

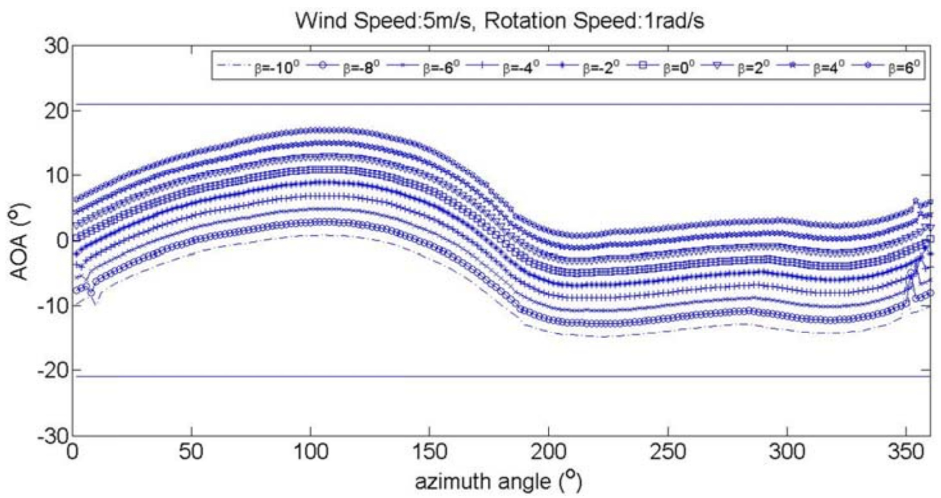

(j)

Fig. F.2 The AOA versus azimuth angle for the fixed pitch cases. (a) $\omega = 0.1\, rad/s$; (b) $\omega = 0.2\, rad/s$; (c) $\omega = 0.3\, rad/s$; (d) $\omega = 0.4\, rad/s$; (e) $\omega = 0.5\, rad/s$; (f) $\omega = 0.6\, rad/s$; (g) $\omega = 0.7\, rad/s$; (h) $\omega = 0.8\, rad/s$; (i) $\omega = 0.9\, rad/s$; (j) $\omega = 1.0\, rad/s$;

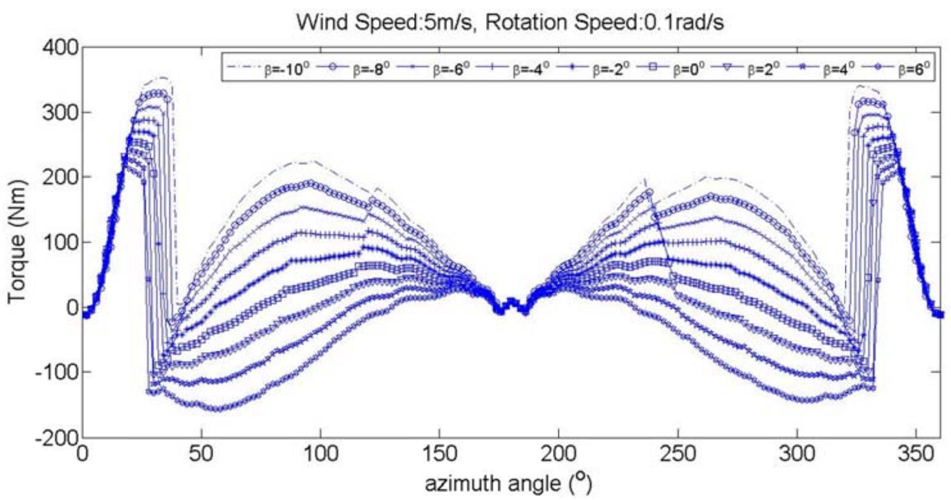

(a)

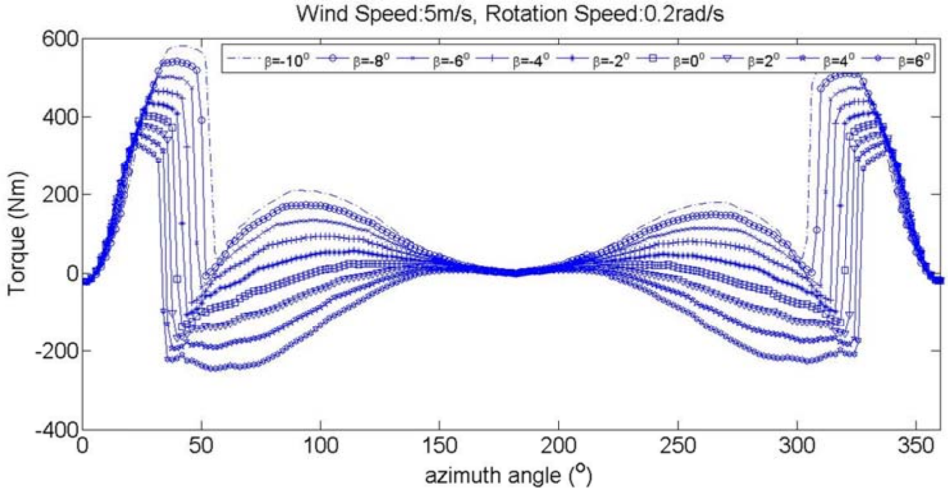
Wind Speed:5m/s, Rotation Speed:0.2rad/s
β=-10°
β=-8°
β=-6°
β=-4°
β=-2°
β=0°
β=2°
β=4°
β=6°
Torque (Nm)
azimuth angle (°)

(b)

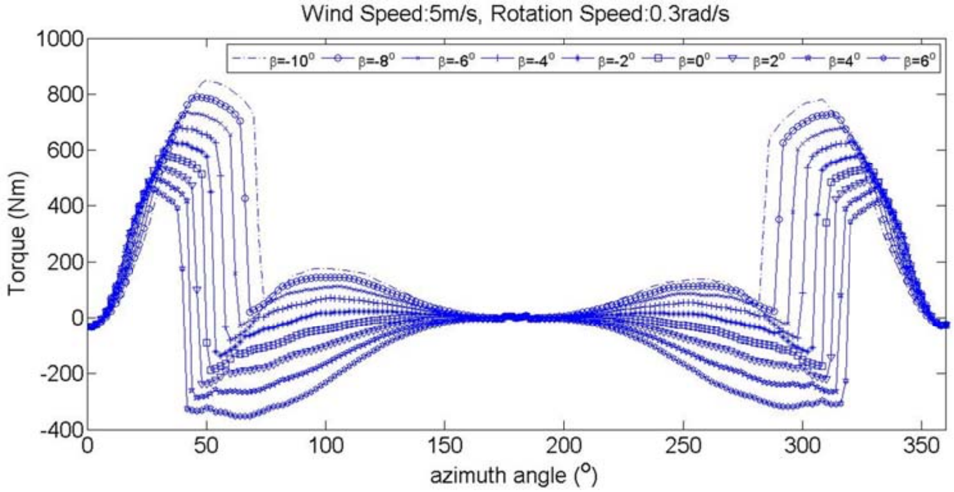
Wind Speed:5m/s, Rotation Speed:0.3rad/s
β=-10°
β=-8°
β=-6°
β=-4°
β=-2°
β=0°
β=2°
β=4°
β=6°
Torque (Nm)
azimuth angle (°)

(c)

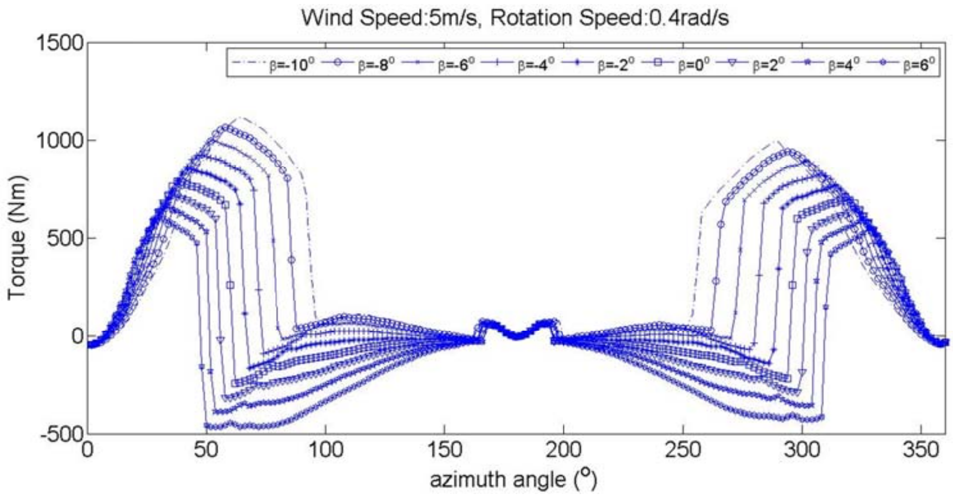
Wind Speed:5m/s, Rotation Speed:0.4rad/s
β=-10°
β=-8°
β=-6°
β=-4°
β=-2°
β=0°
β=2°
β=4°
β=6°
Torque (Nm)
azimuth angle (°)

(d)

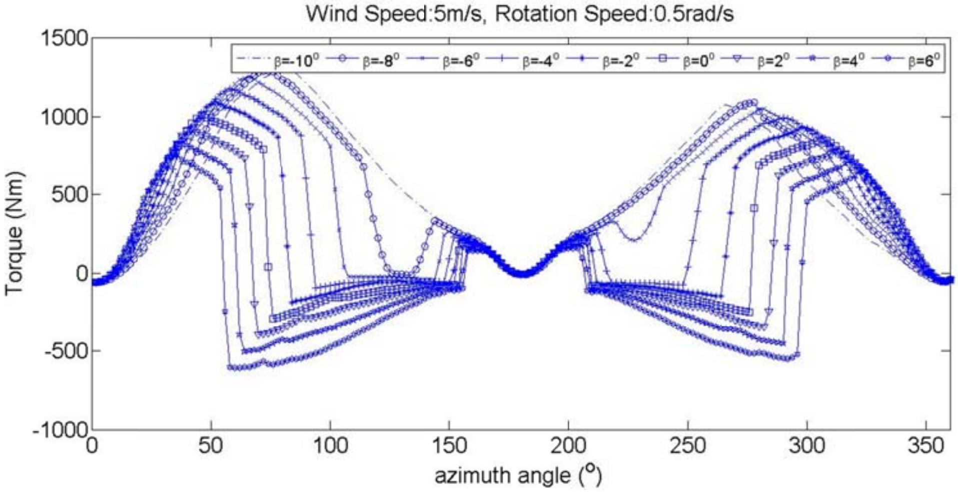
Wind Speed:5m/s, Rotation Speed:0.5rad/s
β=-10° β=-8° β=-6° β=-4° β=-2° β=0° β=2° β=4° β=6°
Torque (Nm)
azimuth angle (°)

(e)

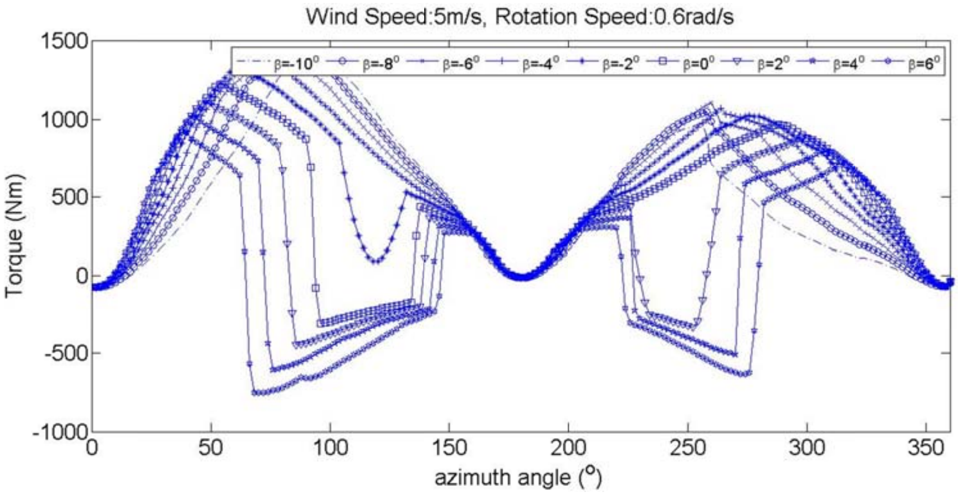
Wind Speed:5m/s, Rotation Speed:0.6rad/s
β=-10° β=-8° β=-6° β=-4° β=-2° β=0° β=2° β=4° β=6°
Torque (Nm)
azimuth angle (°)

(f)

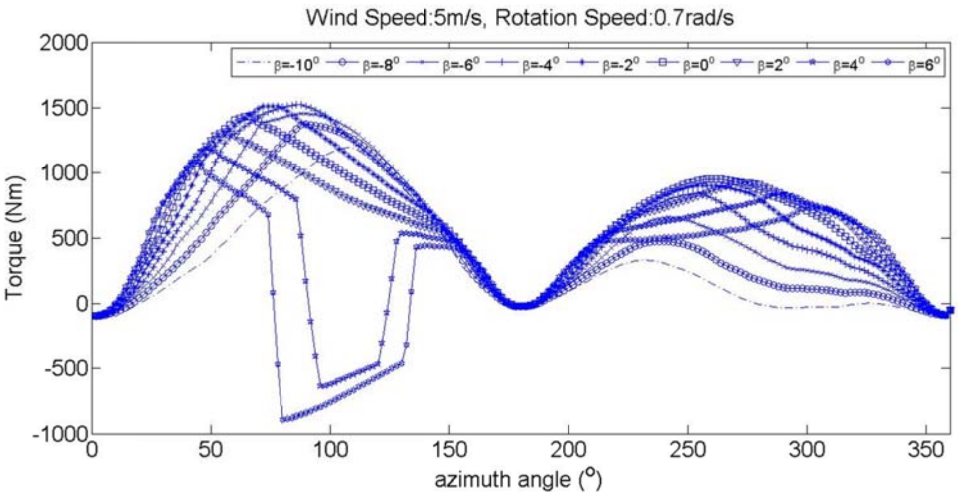
Wind Speed:5m/s, Rotation Speed:0.7rad/s
β=-10° β=-8° β=-6° β=-4° β=-2° β=0° β=2° β=4° β=6°
Torque (Nm)
azimuth angle (°)

(g)

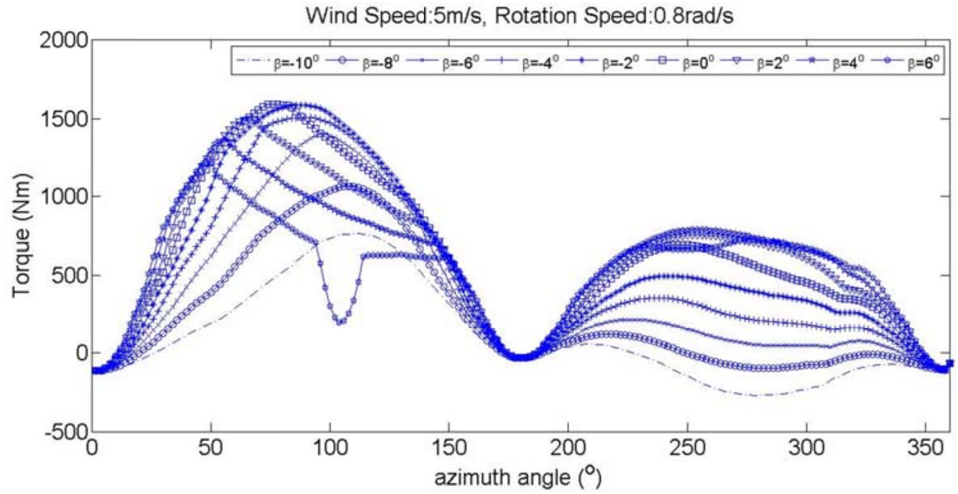

(h)

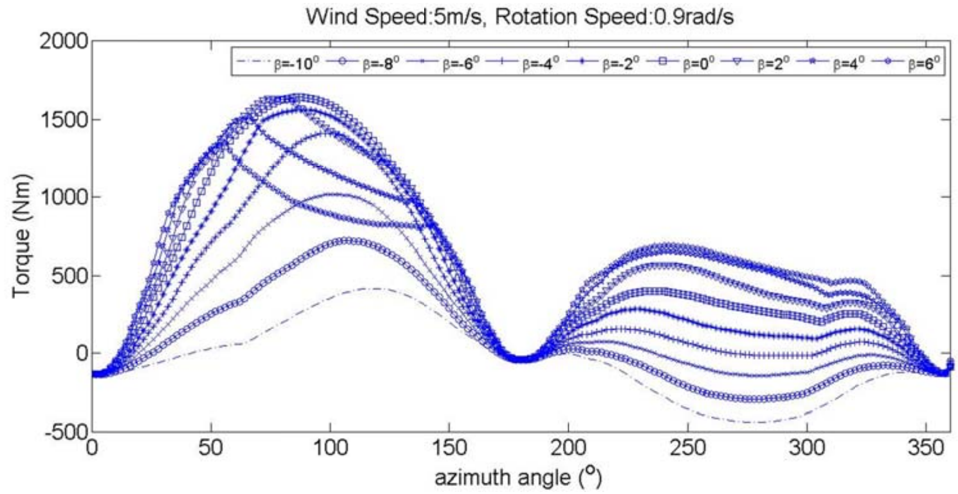

(i)

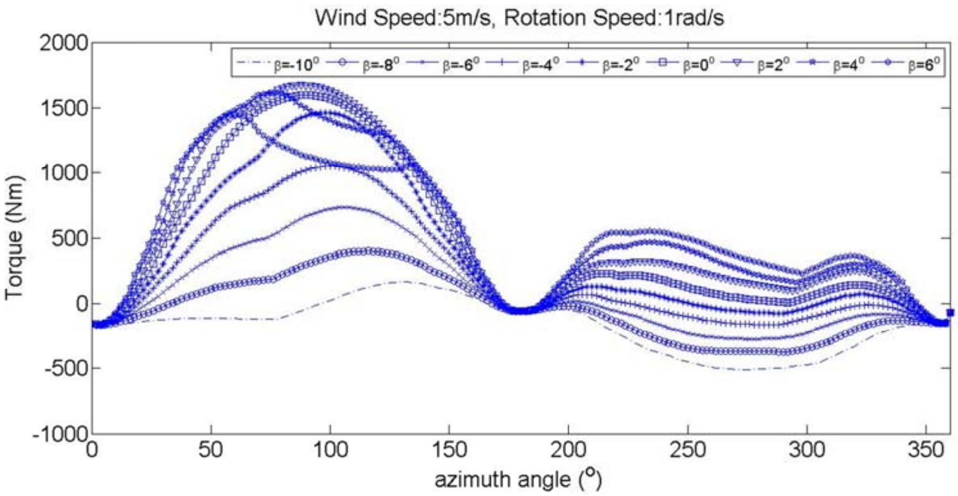

(j)

Fig. F.3 the aerodynamic torques T per length for the variable pitch cases. (a) $\omega = 0.1\,rad/s$; (b) $\omega = 0.2\,rad/s$; (c) $\omega = 0.3\,rad/s$; (d) $\omega = 0.4\,rad/s$; (e)

$\omega = 0.5\,rad/s$; (f) $\omega = 0.6\,rad/s$; (g) $\omega = 0.7\,rad/s$; (h) $\omega = 0.8\,rad/s$; (i) $\omega = 0.9\,rad/s$; (j) $\omega = 1.0\,rad/s$;

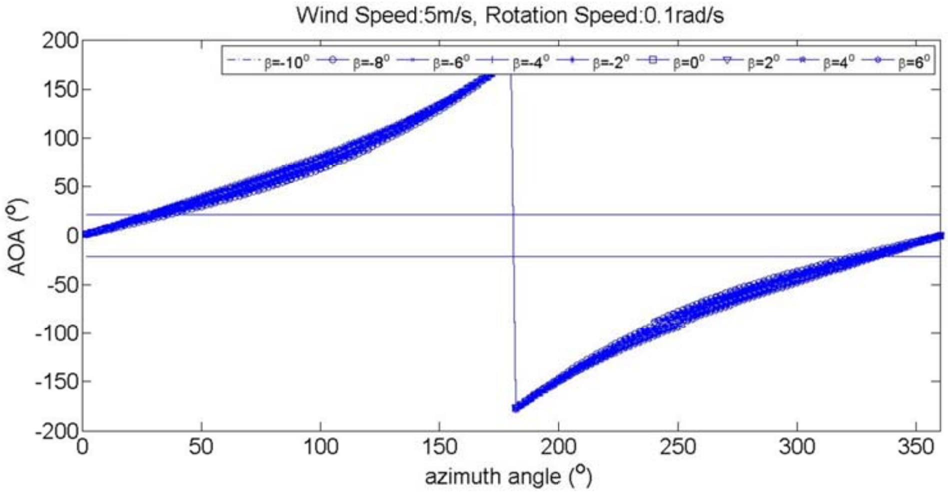

(a)

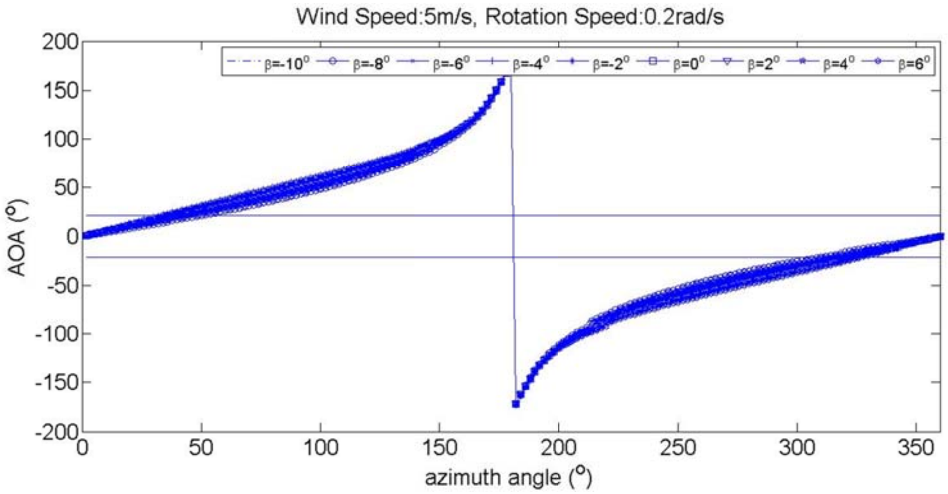

(b)

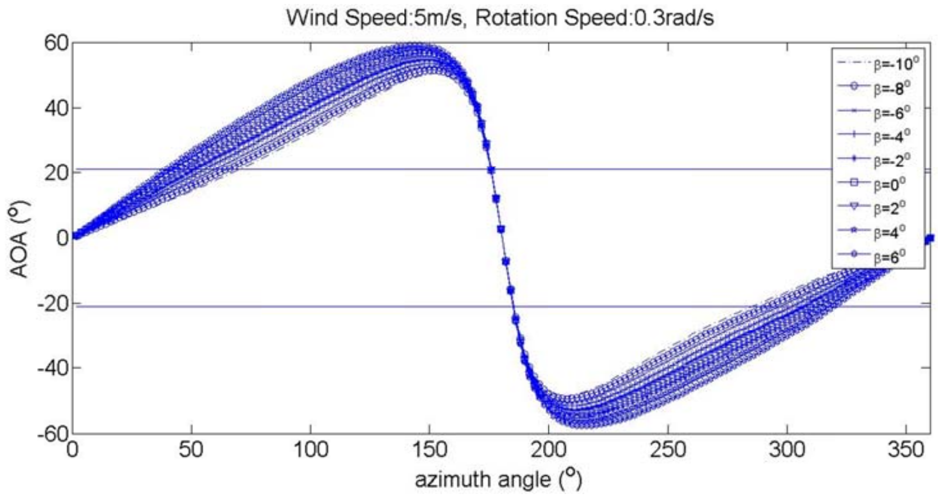

(c)

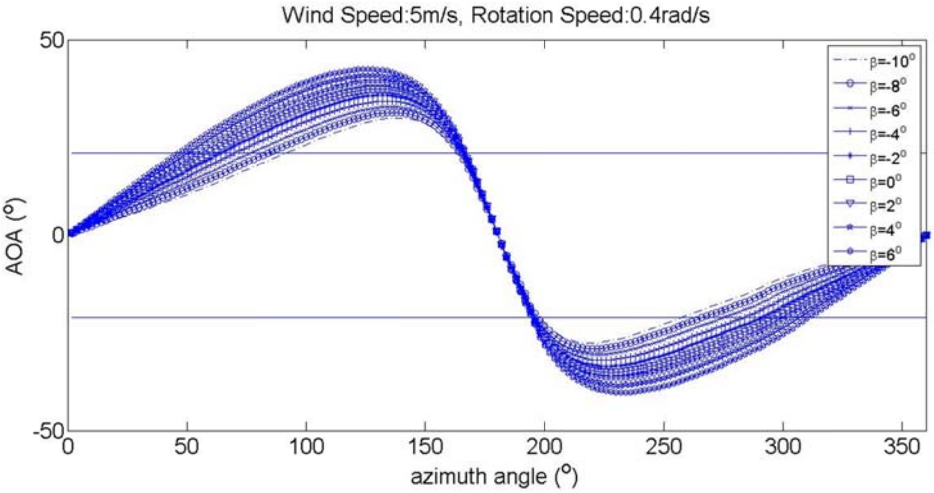
Wind Speed:5m/s, Rotation Speed:0.4rad/s
AOA (°)
azimuth angle (°)
β=-10°
β=-8°
β=-6°
β=-4°
β=-2°
β=0°
β=2°
β=4°
β=6°

(d)

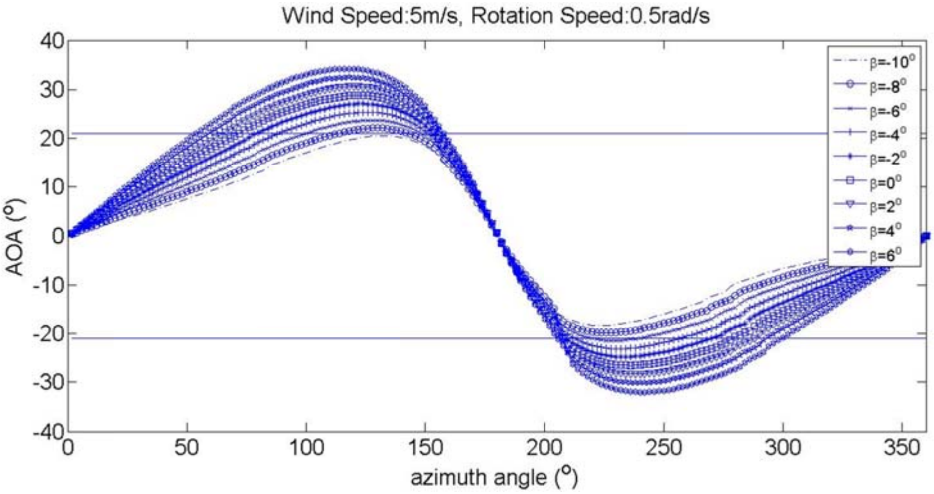
Wind Speed:5m/s, Rotation Speed:0.5rad/s
AOA (°)
azimuth angle (°)
β=-10°
β=-8°
β=-6°
β=-4°
β=-2°
β=0°
β=2°
β=4°
β=6°

(e)

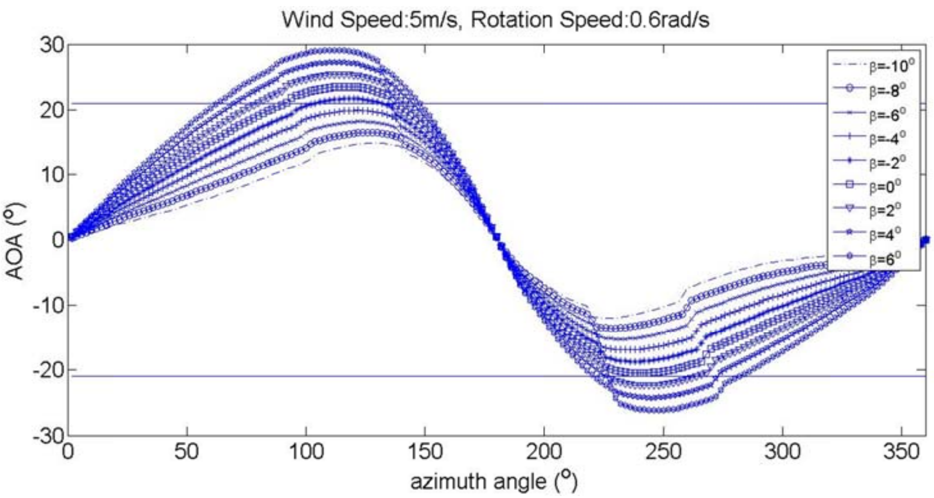
Wind Speed:5m/s, Rotation Speed:0.6rad/s
AOA (°)
azimuth angle (°)
β=-10°
β=-8°
β=-6°
β=-4°
β=-2°
β=0°
β=2°
β=4°
β=6°

(f)

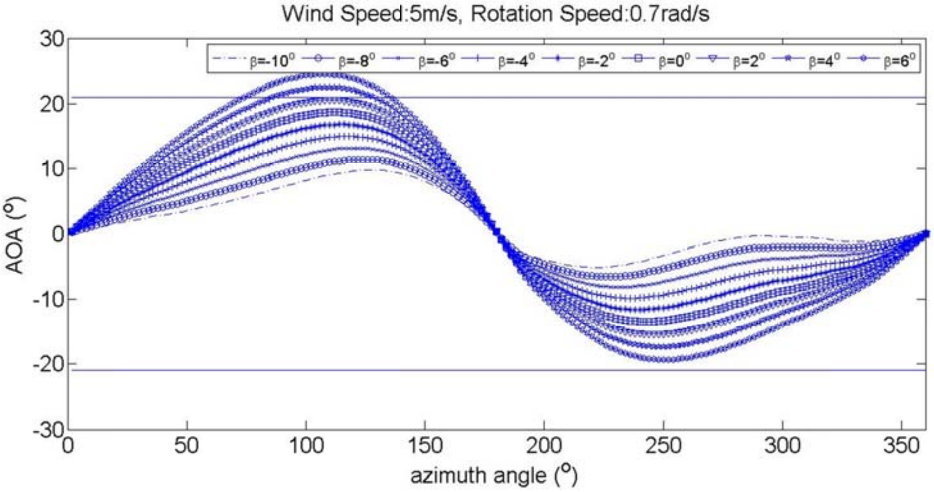
Wind Speed:5m/s, Rotation Speed:0.7rad/s
β=-10° β=-8° β=-6° β=-4° β=-2° β=0° β=2° β=4° β=6°
AOA (°)
azimuth angle (°)

(g)

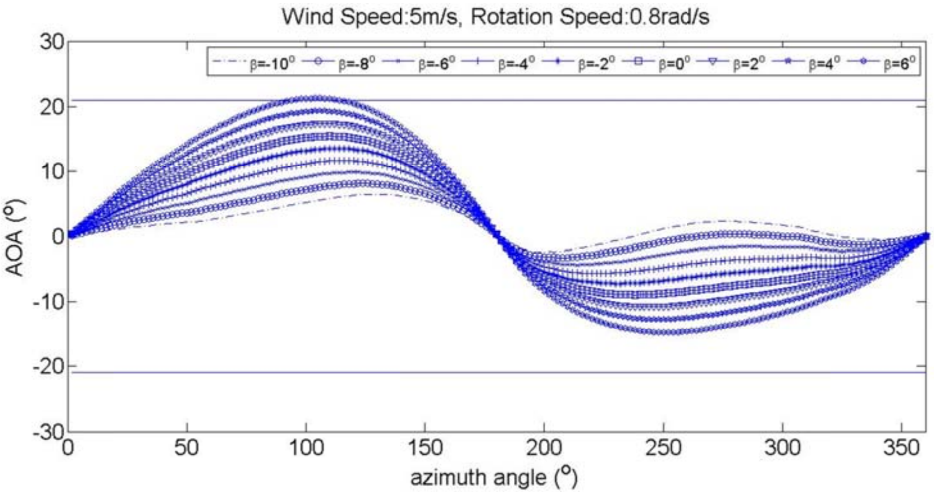
Wind Speed:5m/s, Rotation Speed:0.8rad/s
β=-10° β=-8° β=-6° β=-4° β=-2° β=0° β=2° β=4° β=6°
AOA (°)
azimuth angle (°)

(h)

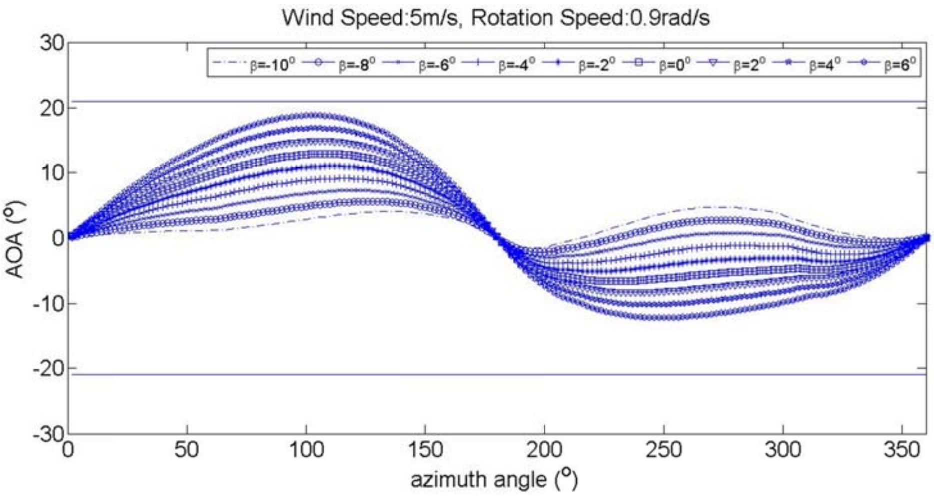
Wind Speed:5m/s, Rotation Speed:0.9rad/s
β=-10° β=-8° β=-6° β=-4° β=-2° β=0° β=2° β=4° β=6°
AOA (°)
azimuth angle (°)

(i)

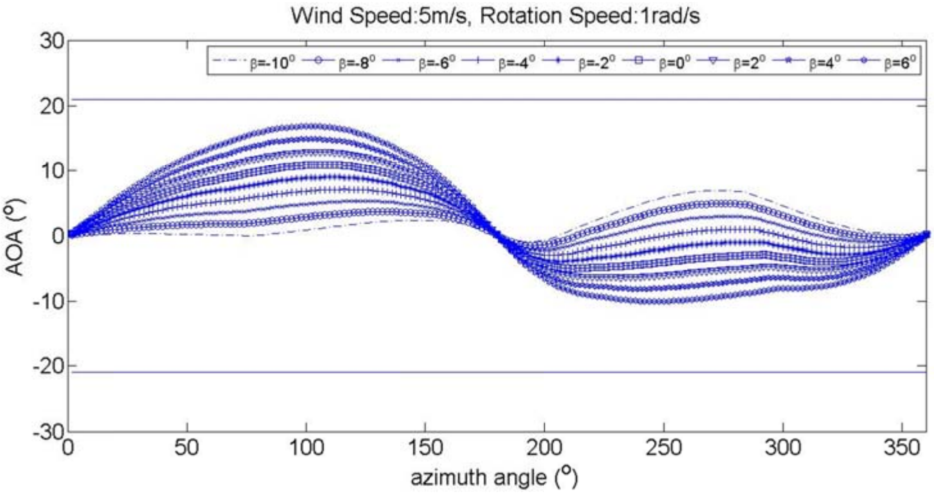

(j)

Fig. F.4 The AOA versus azimuth angle for the variable pitch cases. (a) $\omega = 0.1\,rad/s$; (b) $\omega = 0.2\,rad/s$; (c) $\omega = 0.3\,rad/s$; (d) $\omega = 0.4\,rad/s$; (e) $\omega = 0.5\,rad/s$; (f) $\omega = 0.6\,rad/s$; (g) $\omega = 0.7\,rad/s$; (h) $\omega = 0.8\,rad/s$; (i) $\omega = 0.9\,rad/s$; (j) $\omega = 1.0\,rad/s$;

APPENDIX G

AOA IN THE OPERATION STATE UNDER RATED WIND SPEED

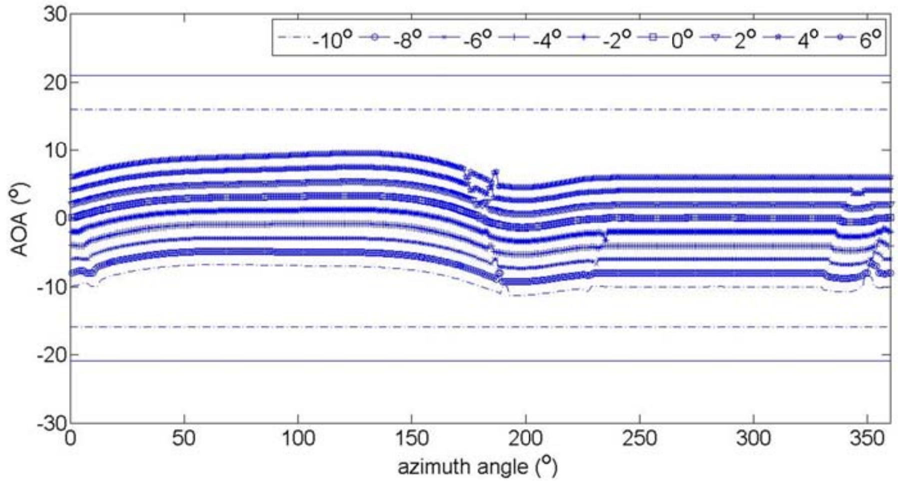

(a)

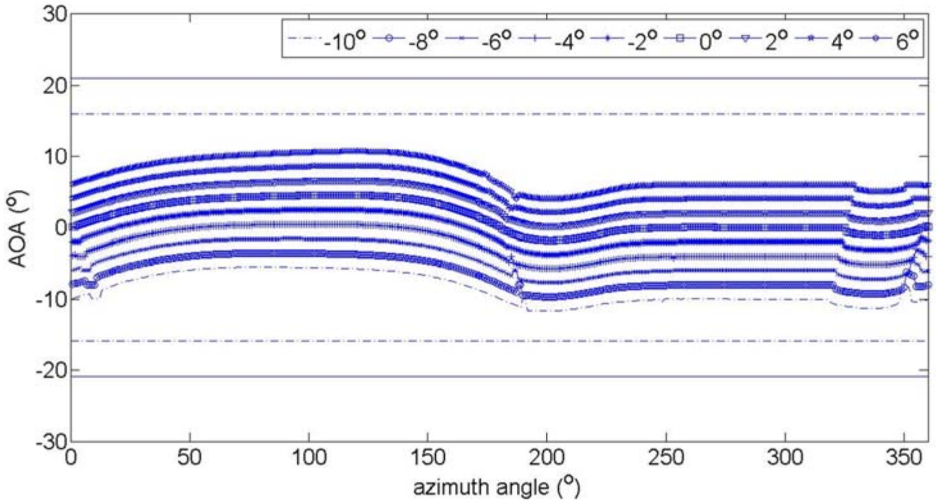

(b)

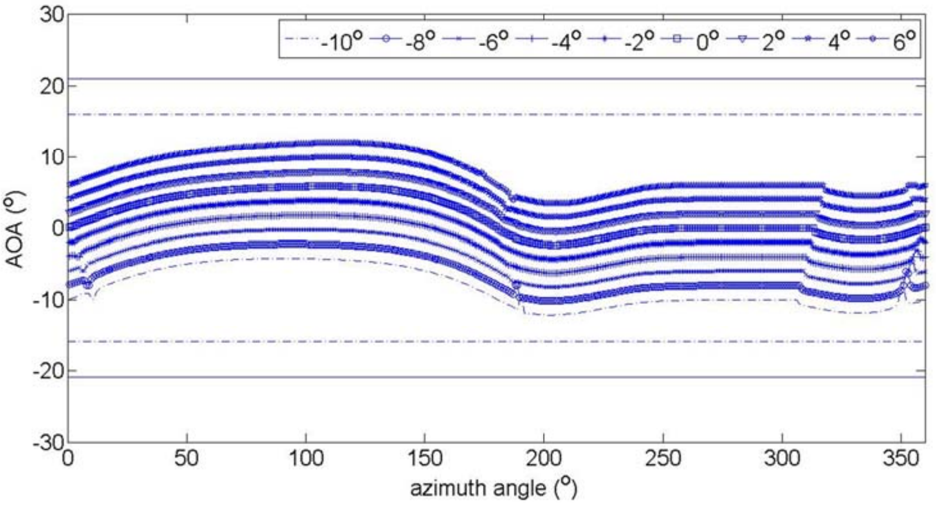
-10° -8° -6° -4° -2° 0° 2° 4° 6°
AOA (°)
azimuth angle (°)

(c)

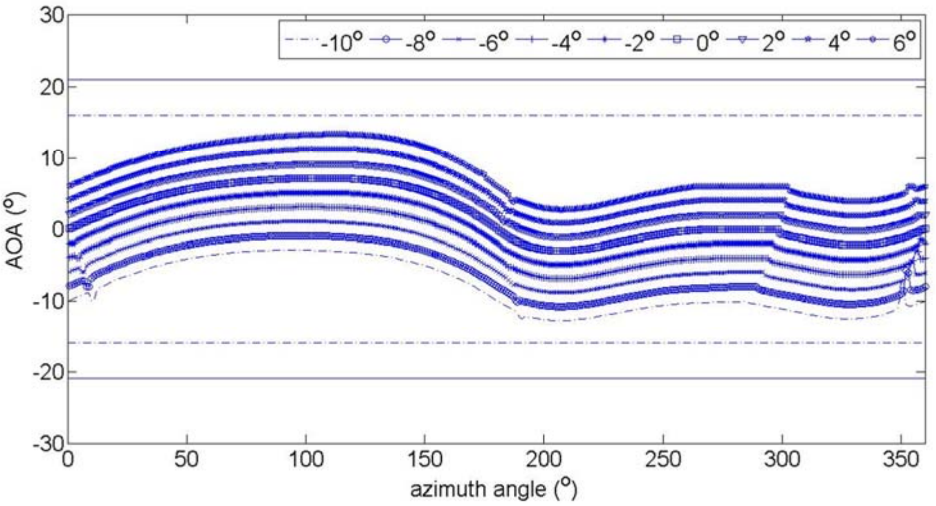
-10° -8° -6° -4° -2° 0° 2° 4° 6°
AOA (°)
azimuth angle (°)

(d)

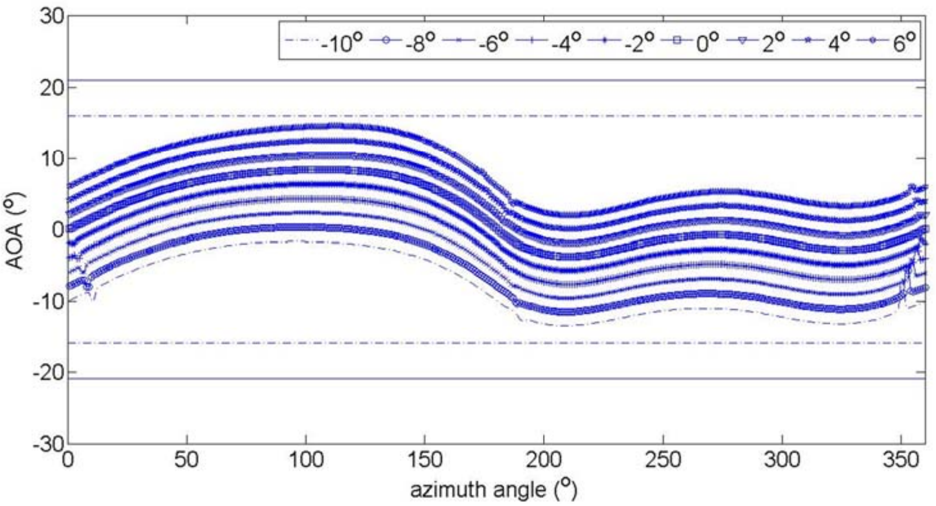
-10° -8° -6° -4° -2° 0° 2° 4° 6°
AOA (°)
azimuth angle (°)

(e)

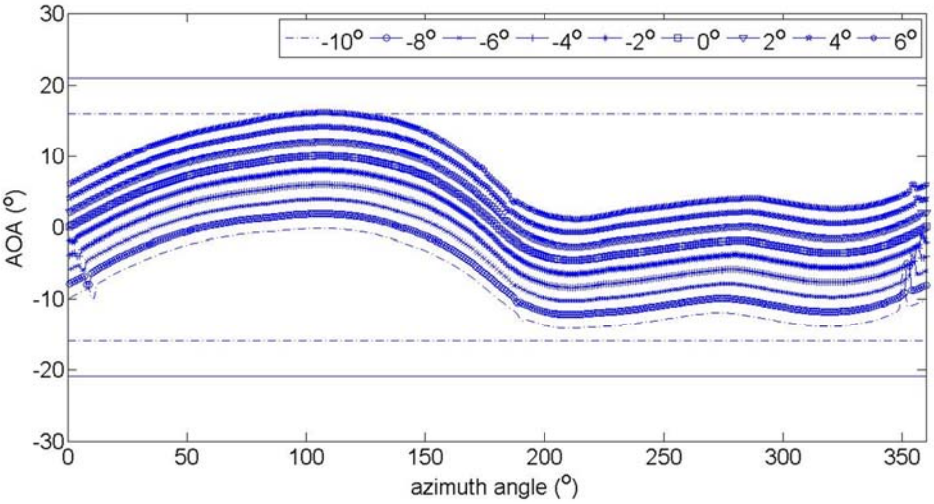

-10° -8° -6° -4° -2° 0° 2° 4° 6°
AOA (°)
azimuth angle (°)

(f)

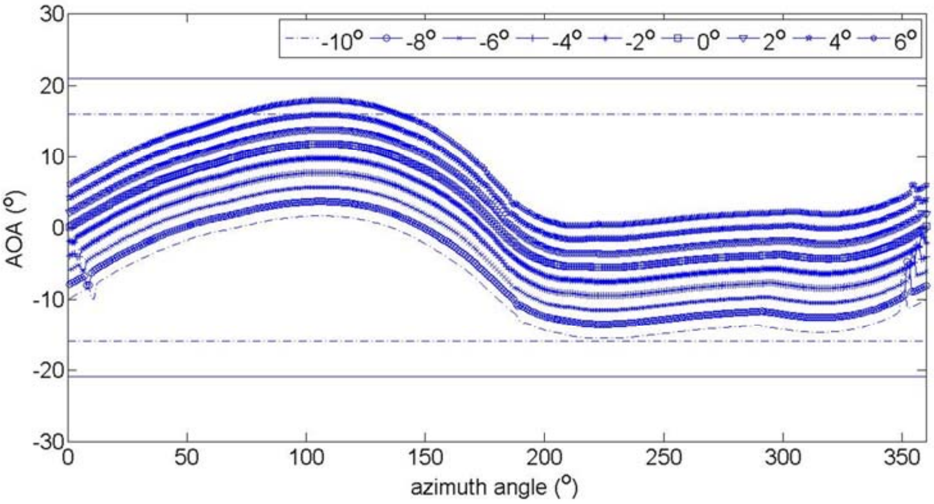

-10° -8° -6° -4° -2° 0° 2° 4° 6°
AOA (°)
azimuth angle (°)

(g)

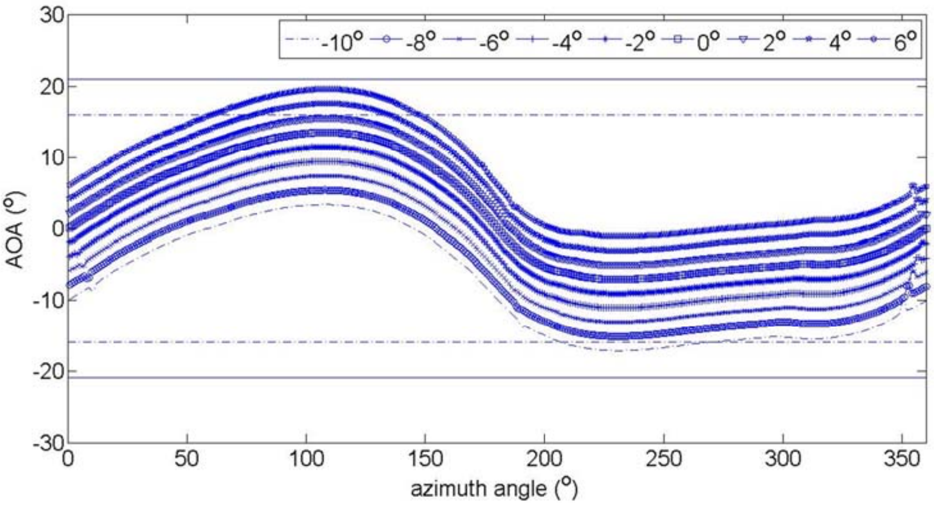

-10° -8° -6° -4° -2° 0° 2° 4° 6°
AOA (°)
azimuth angle (°)

(h)

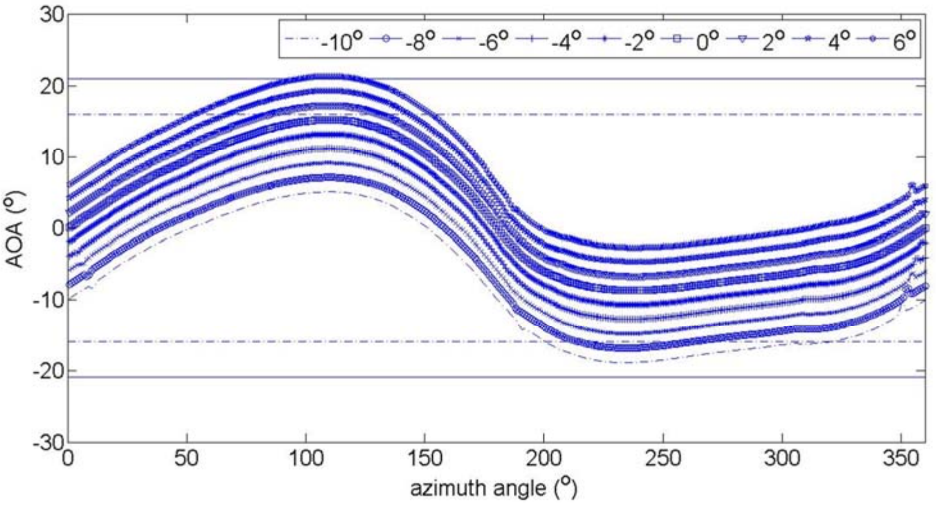

(i)

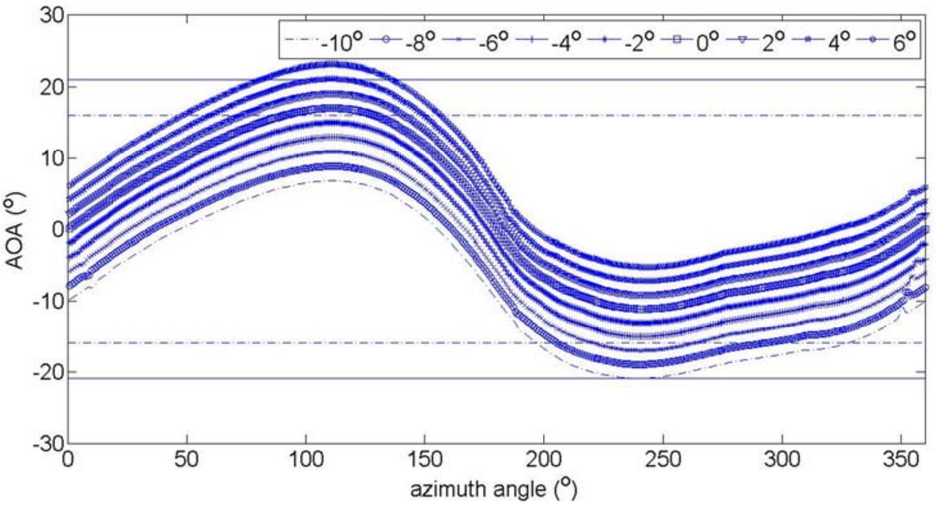

(j)

Fig. G.1 the AOA versus azimuth angle for the variable pitch cases at different wind speeds. (a) 5m/s; (b) 6m/s; (c) 7m/s; (d) 8m/s; (e) 9m/s; (f) 10m/s; (g) 11m/s; (h) 12m/s; (i) 13m/s; (j) 14m/s.

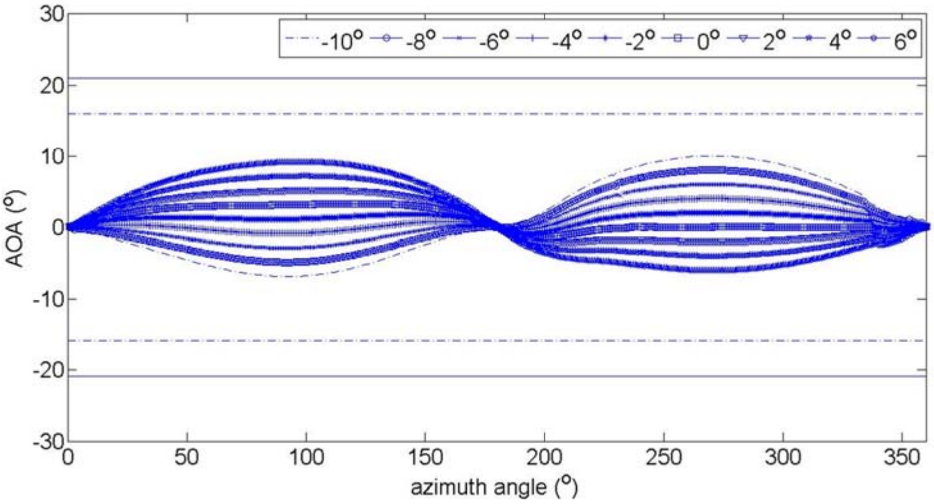

-10°
-8°
-6°
-4°
-2°
0°
2°
4°
6°
AOA (°)
azimuth angle (°)

(a)

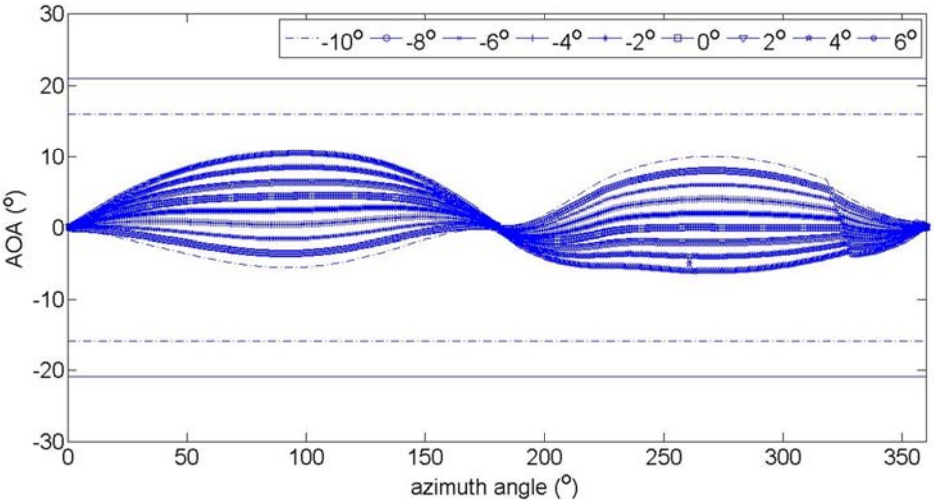

-10°
-8°
-6°
-4°
-2°
0°
2°
4°
6°
AOA (°)
azimuth angle (°)

(b)

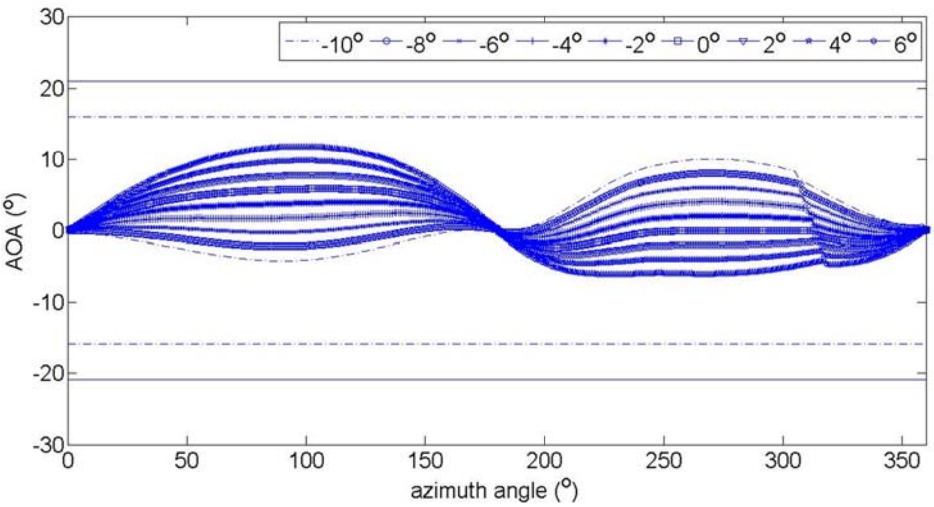

-10°
-8°
-6°
-4°
-2°
0°
2°
4°
6°
AOA (°)
azimuth angle (°)

(c)

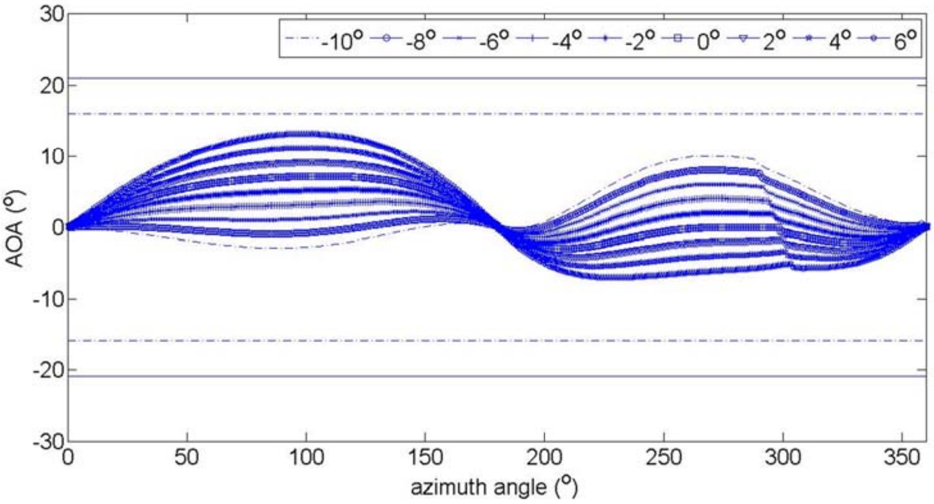
-10° -8° -6° -4° -2° 0° 2° 4° 6°
AOA (°)
azimuth angle (°)
30
20
10
0
-10
-20
-30
0
50
100
150
200
250
300
350

(d)

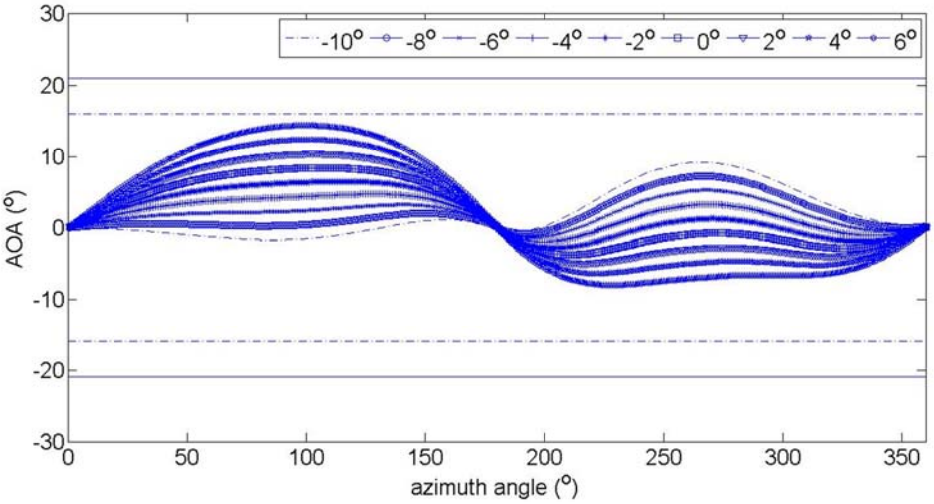
-10° -8° -6° -4° -2° 0° 2° 4° 6°
AOA (°)
azimuth angle (°)
30
20
10
0
-10
-20
-30
0
50
100
150
200
250
300
350

(e)

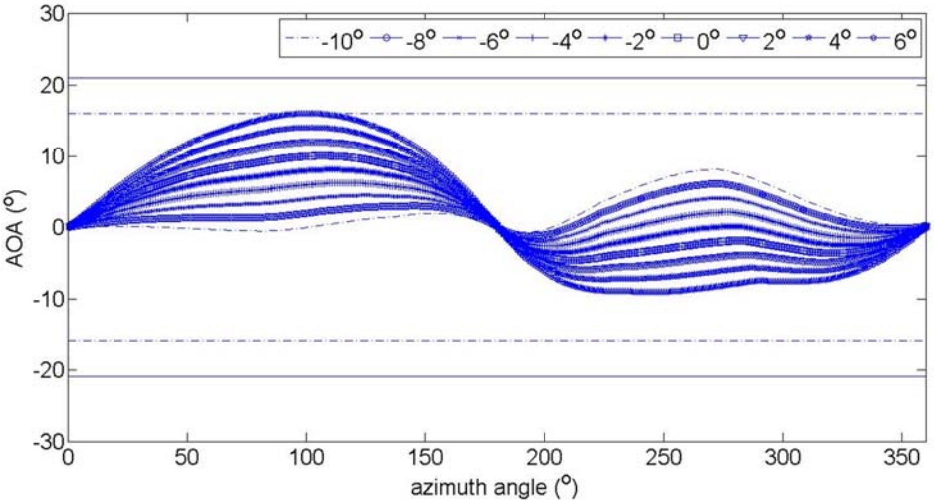
-10° -8° -6° -4° -2° 0° 2° 4° 6°
AOA (°)
azimuth angle (°)
30
20
10
0
-10
-20
-30
0
50
100
150
200
250
300
350

(f)

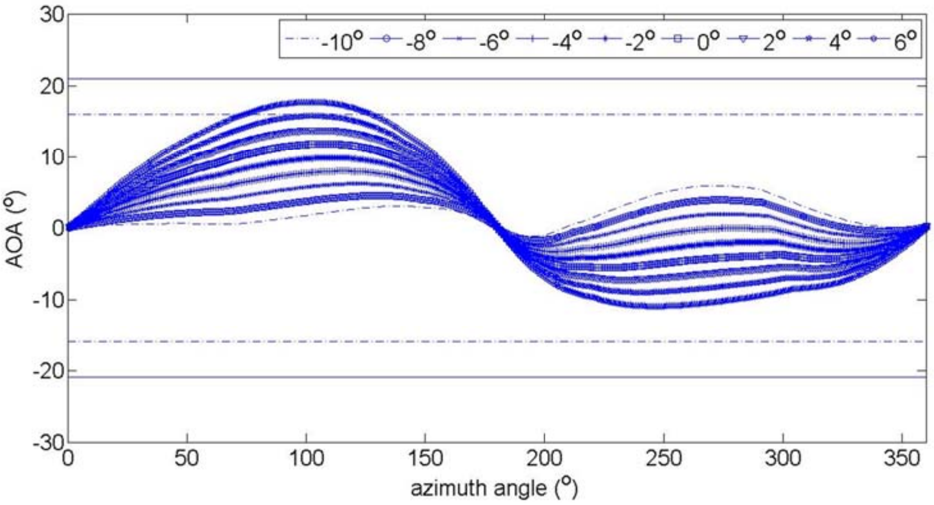
-10° -8° -6° -4° -2° 0° 2° 4° 6°
AOA (°)
azimuth angle (°)

(g)

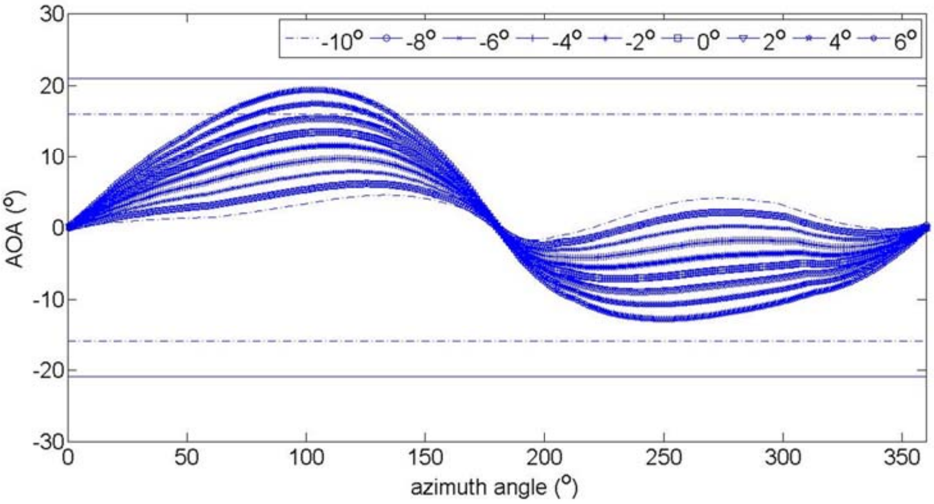
-10° -8° -6° -4° -2° 0° 2° 4° 6°
AOA (°)
azimuth angle (°)

(h)

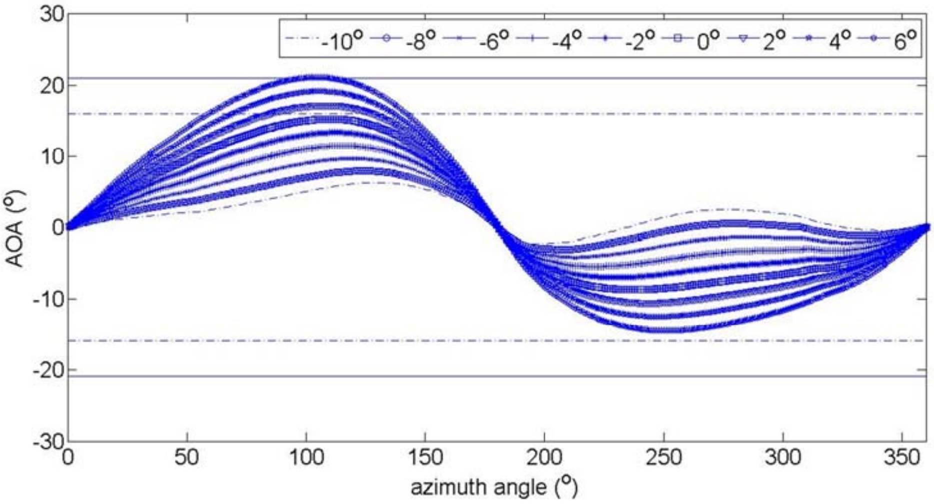
-10° -8° -6° -4° -2° 0° 2° 4° 6°
AOA (°)
azimuth angle (°)

(i)

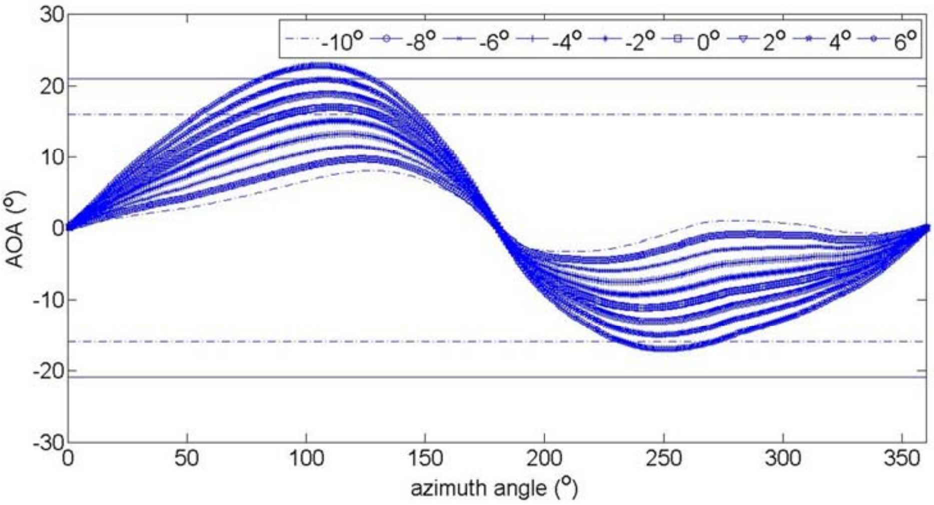

(j)

Fig. G.2 the amplitude of AOA versus azimuth angle for the variable pitch cases at different wind speeds. (a) 5m/s; (b) 6m/s; (c) 7m/s; (d) 8m/s; (e) 9m/s; (f) 10m/s; (g) 11m/s; (h) 12m/s; (i) 13m/s; (j) 14m/s.

APPENDIX H

TORQUE AND AOA IN THE OPERATION STATE UNDER RATED WIND SPEED

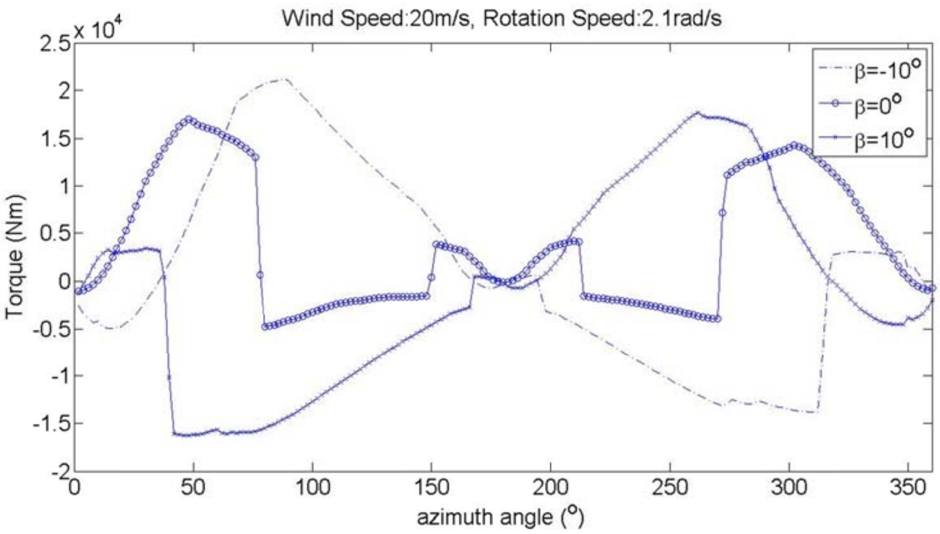

(a)

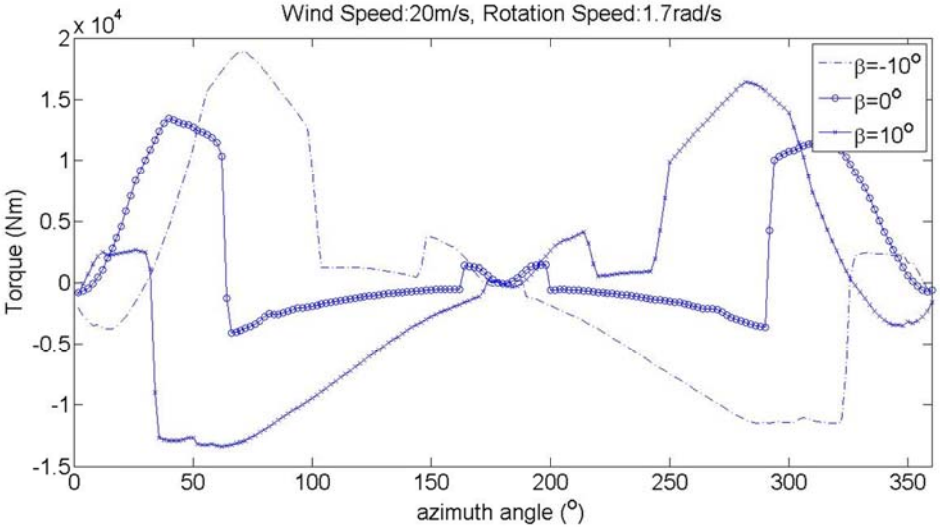

(b)

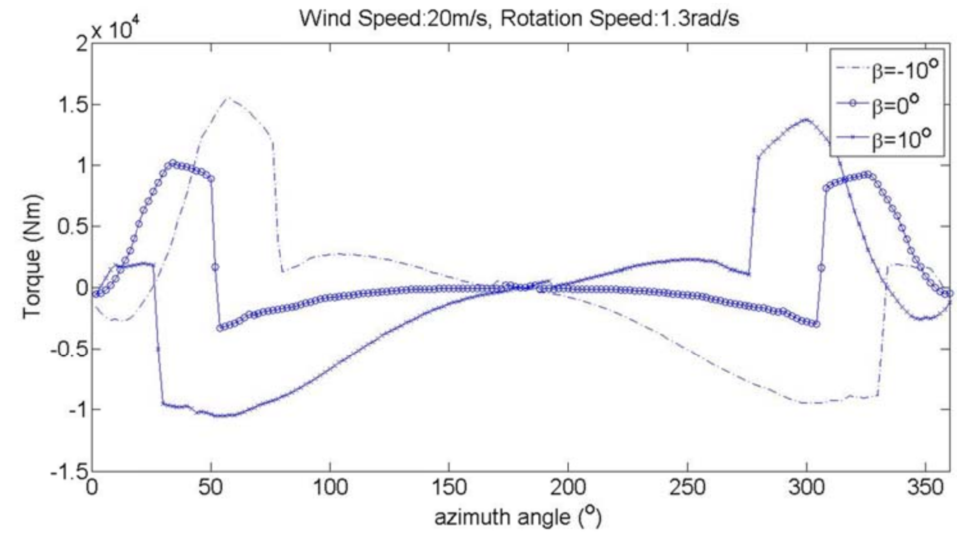

Wind Speed:20m/s, Rotation Speed:1.3rad/s
x 10^4
β=-10°
β=0°
β=10°
Torque (Nm)
azimuth angle (°)

(c)

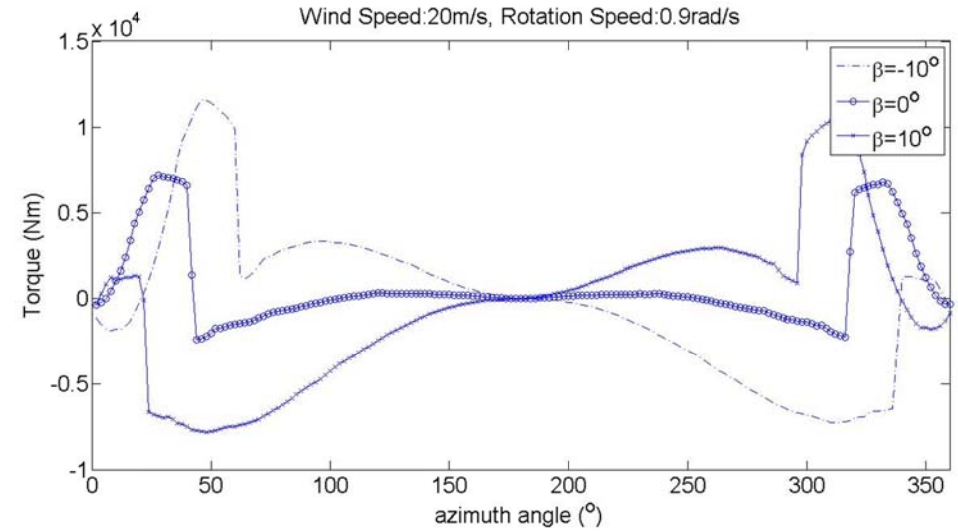

Wind Speed:20m/s, Rotation Speed:0.9rad/s
x 10^4
β=-10°
β=0°
β=10°
Torque (Nm)
azimuth angle (°)

(d)

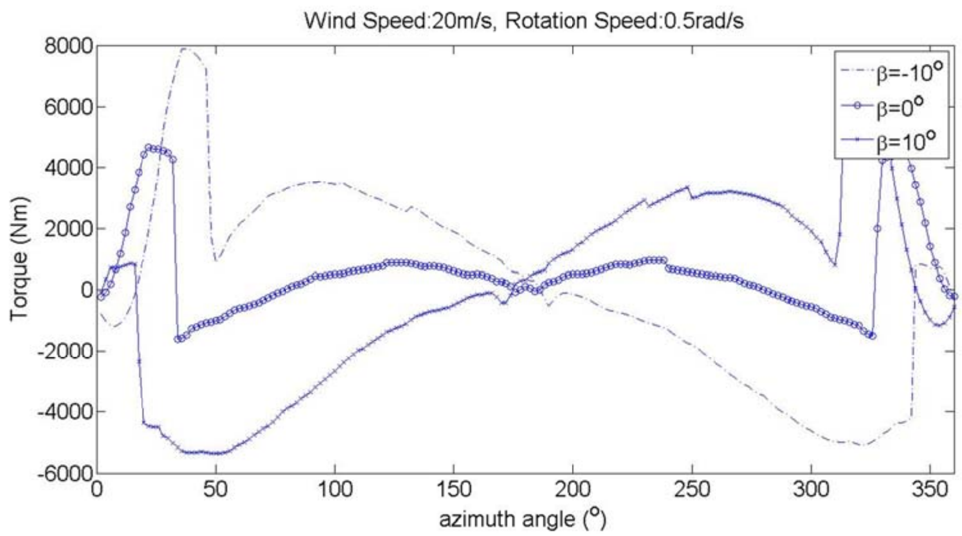

Wind Speed:20m/s, Rotation Speed:0.5rad/s
β=-10°
β=0°
β=10°
Torque (Nm)
azimuth angle (°)

(e)

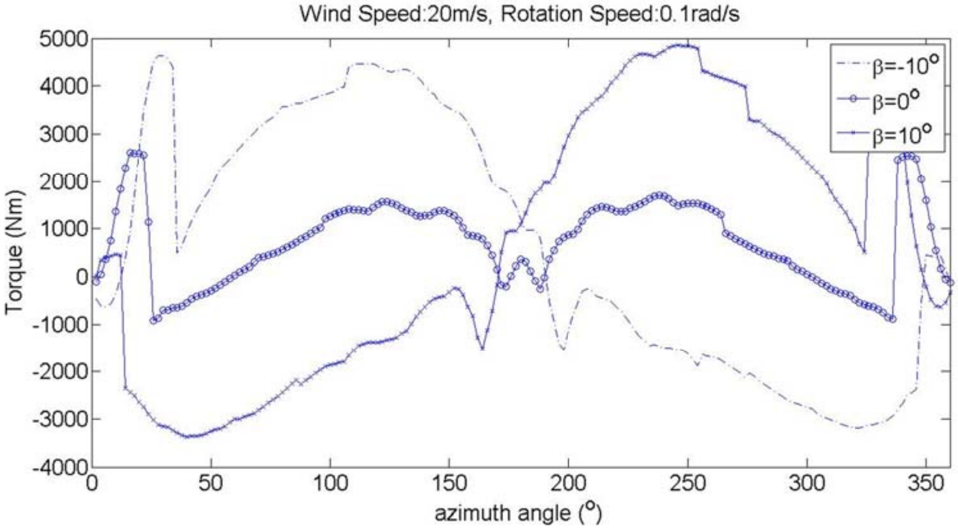

(f)

Fig. H.1 the aerodynamic torques T per length for the fixed pitch cases. (a) $\omega = 2.1\,rad/s$; (b) $\omega = 1.7\,rad/s$; (c) $\omega = 1.3\,rad/s$; (d) $\omega = 0.9\,rad/s$; (e) $\omega = 0.5\,rad/s$; (f) $\omega = 0.1\,rad/s$;

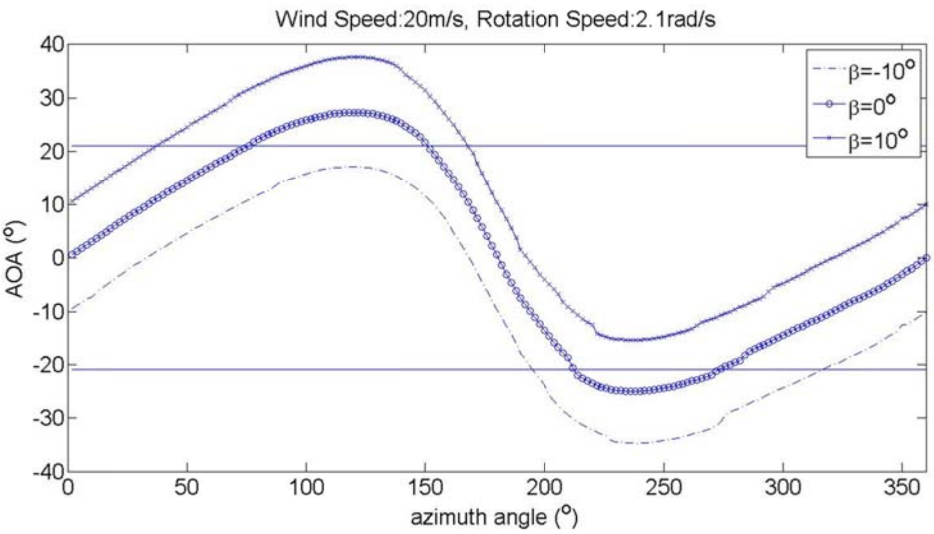

(a)

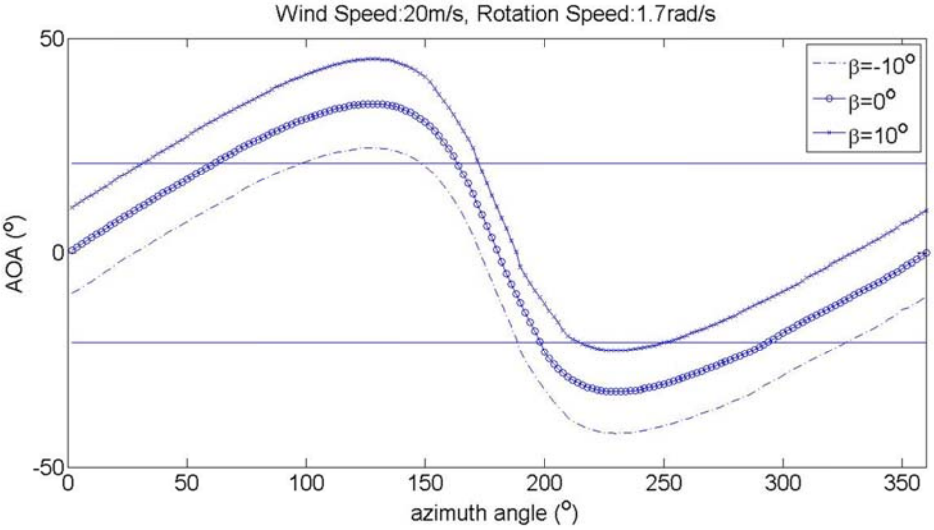
Wind Speed:20m/s, Rotation Speed:1.7rad/s
β=-10°
β=0°
β=10°
AOA (°)
azimuth angle (°)
50
0
-50
0
50
100
150
200
250
300
350

(b)

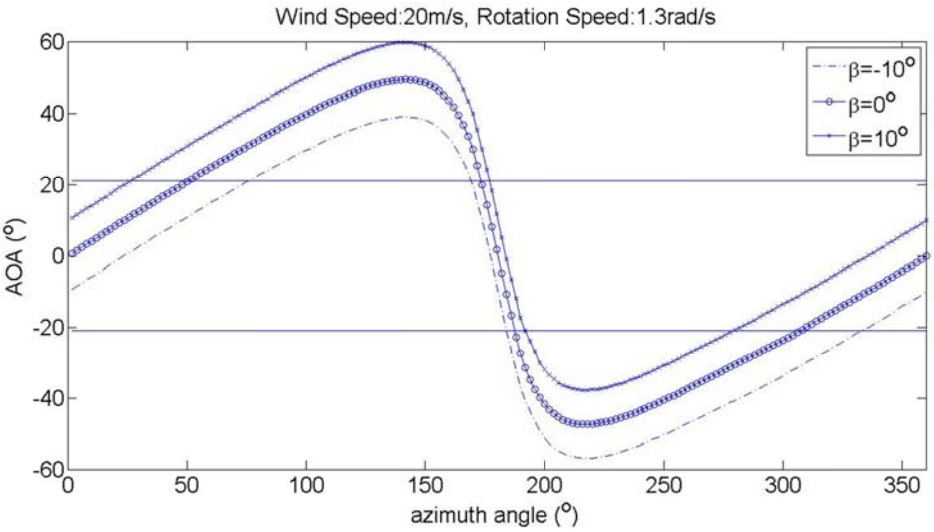
Wind Speed:20m/s, Rotation Speed:1.3rad/s
β=-10°
β=0°
β=10°
AOA (°)
azimuth angle (°)
60
40
20
0
-20
-40
-60
0
50
100
150
200
250
300
350

(c)

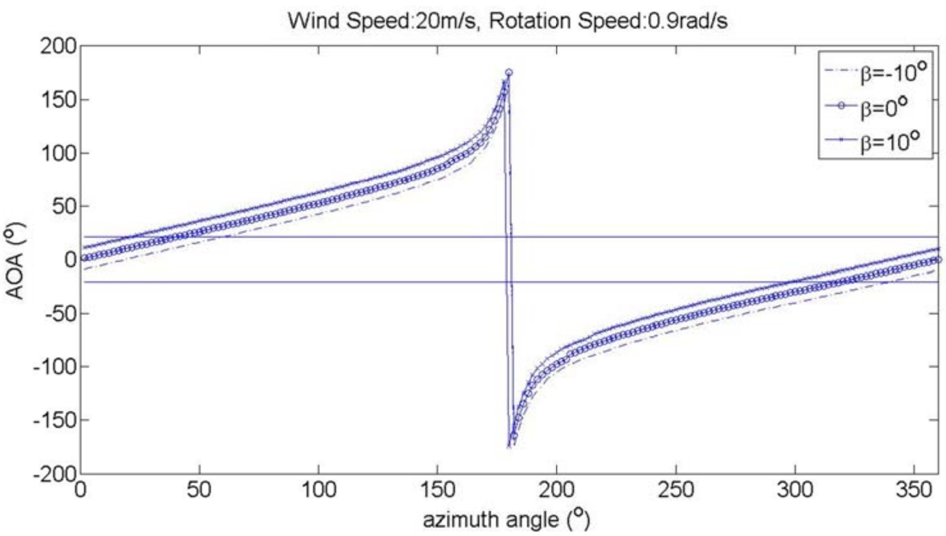
Wind Speed:20m/s, Rotation Speed:0.9rad/s
β=-10°
β=0°
β=10°
AOA (°)
azimuth angle (°)
200
150
100
50
0
-50
-100
-150
-200
0
50
100
150
200
250
300
350

(d)

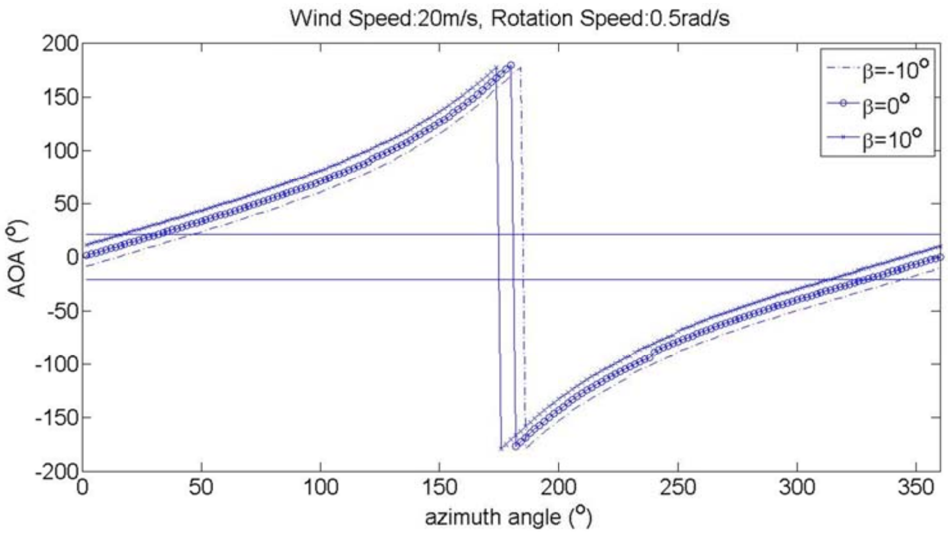

(e)

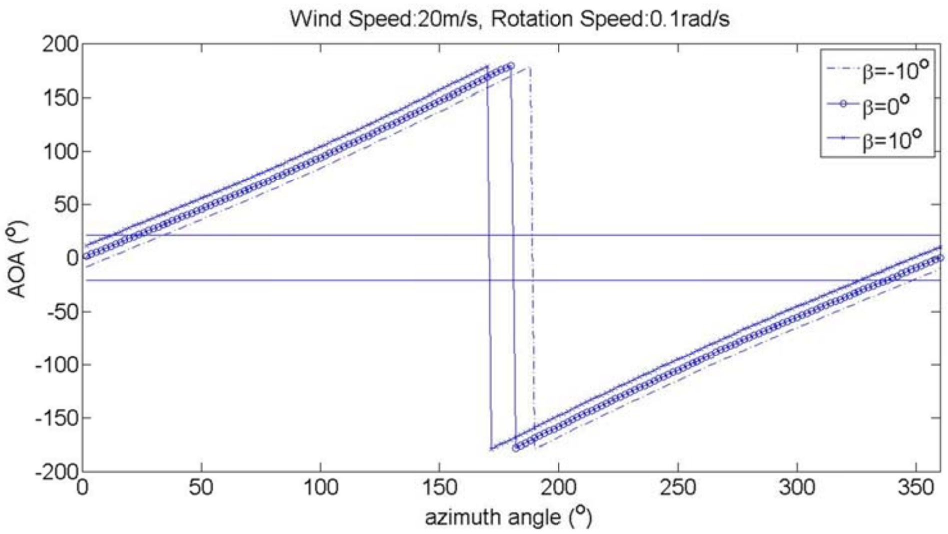

(f)

Fig. H.2 The AOA versus azimuth angle for the fixed pitch cases. (a) $\omega = 2.1\, rad/s$; (b) $\omega = 1.7\, rad/s$; (c) $\omega = 1.3\, rad/s$; (d) $\omega = 0.9\, rad/s$; (e) $\omega = 0.5\, rad/s$; (f) $\omega = 0.1\, rad/s$;

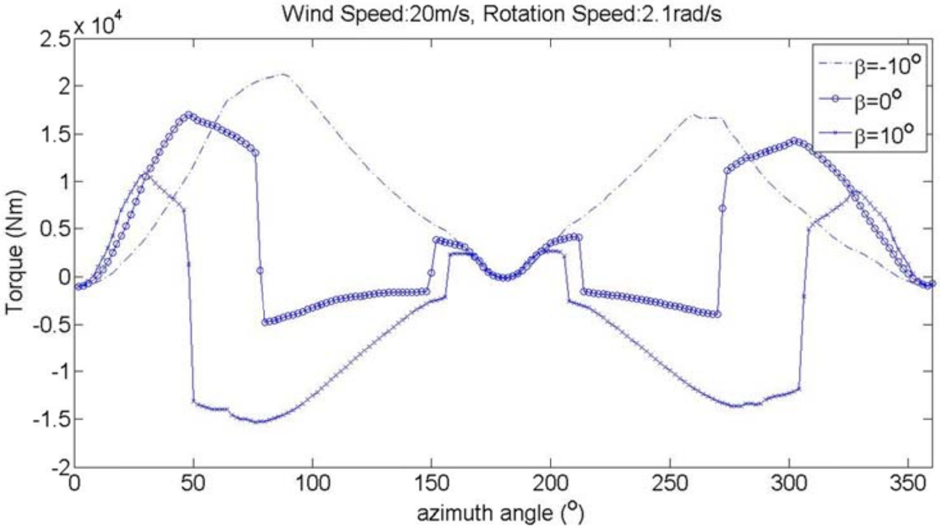
Wind Speed:20m/s, Rotation Speed:2.1rad/s
x 10^4
Torque (Nm)
azimuth angle (°)
β=-10°
β=0°
β=10°

(a)

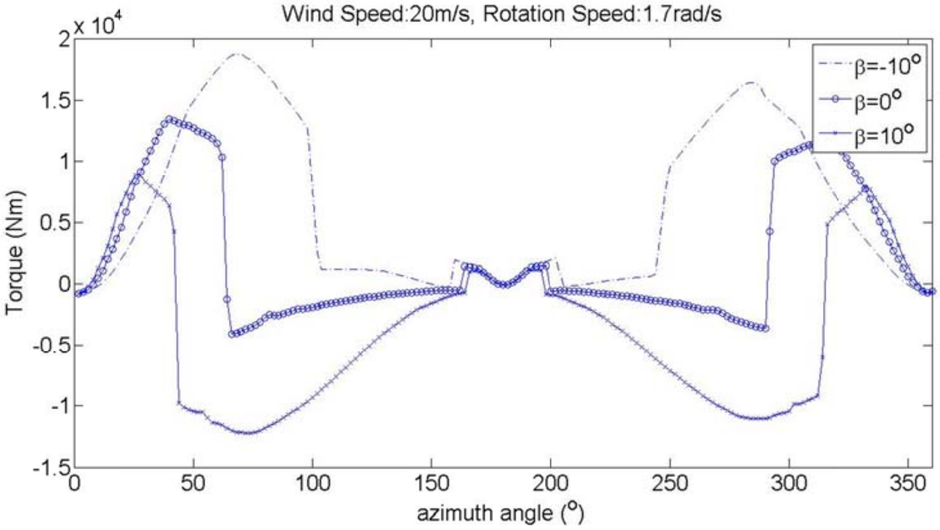
Wind Speed:20m/s, Rotation Speed:1.7rad/s
x 10^4
Torque (Nm)
azimuth angle (°)
β=-10°
β=0°
β=10°

(b)

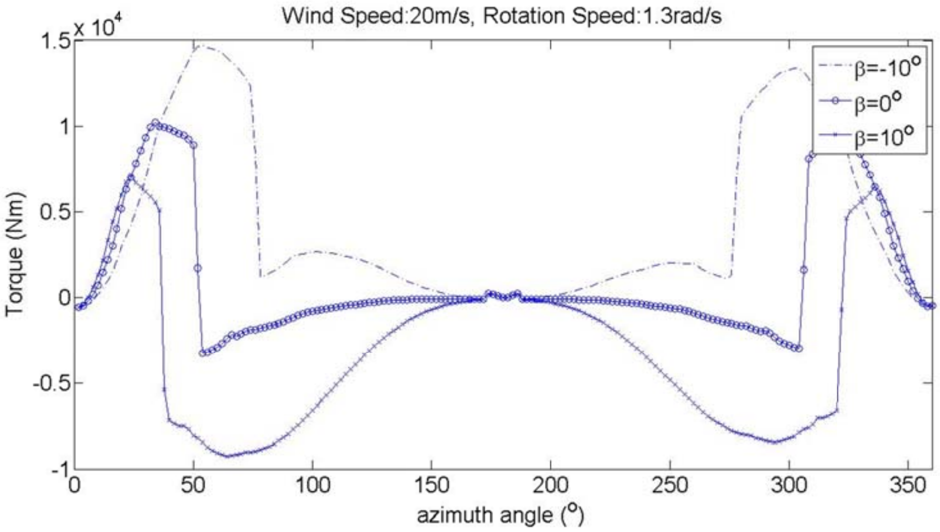
Wind Speed:20m/s, Rotation Speed:1.3rad/s
x 10^4
Torque (Nm)
azimuth angle (°)
β=-10°
β=0°
β=10°

(c)

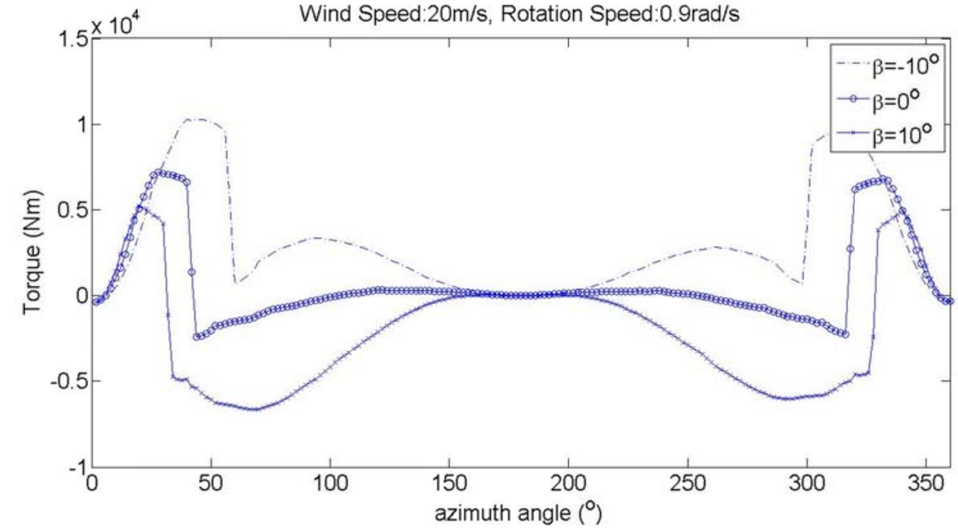

(d)

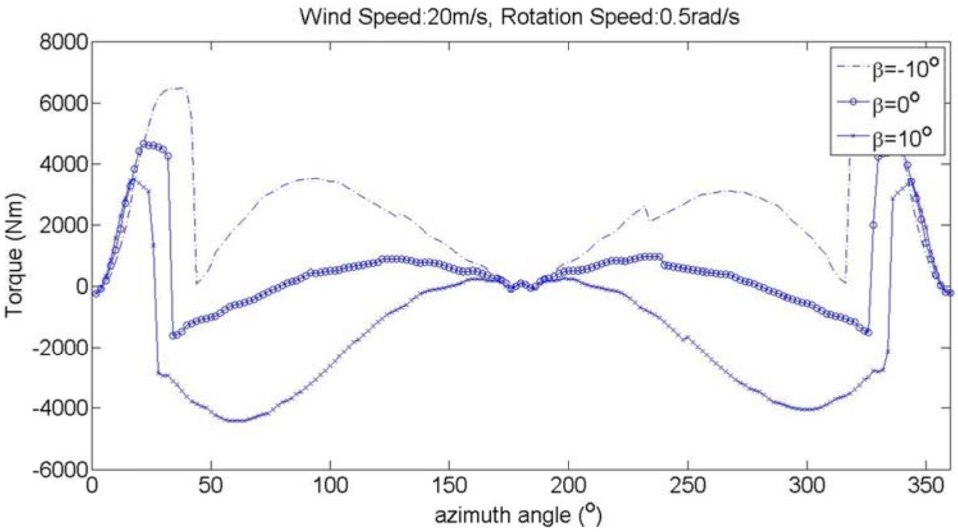

(e)

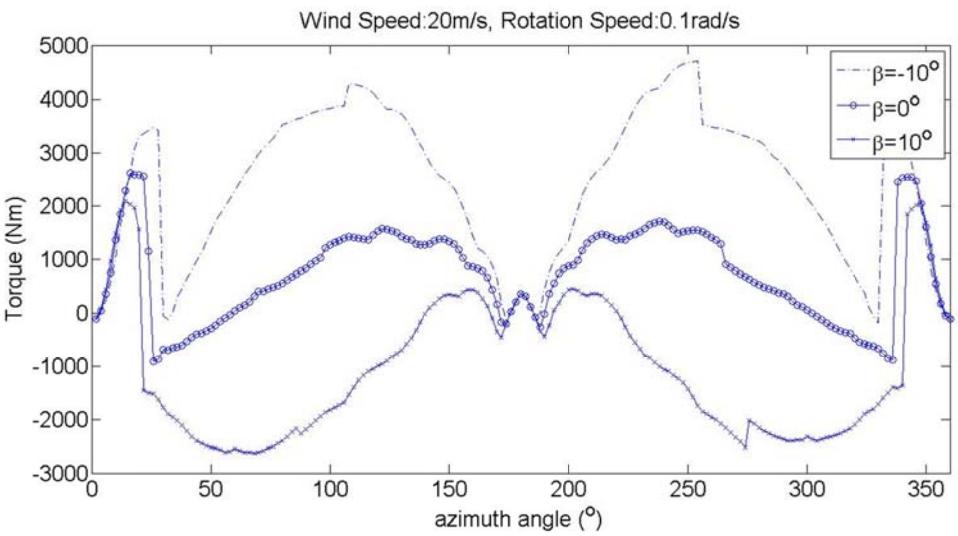

(f)

Fig. H.3 The aerodynamic torques T per length for the sinusoidal variation pitch cases. (a) $\omega = 2.1\,rad/s$; (b) $\omega = 1.7\,rad/s$; (c) $\omega = 1.3\,rad/s$; (d) $\omega = 0.9\,rad/s$; (e) $\omega = 0.5\,rad/s$; (f) $\omega = 0.1\,rad/s$;

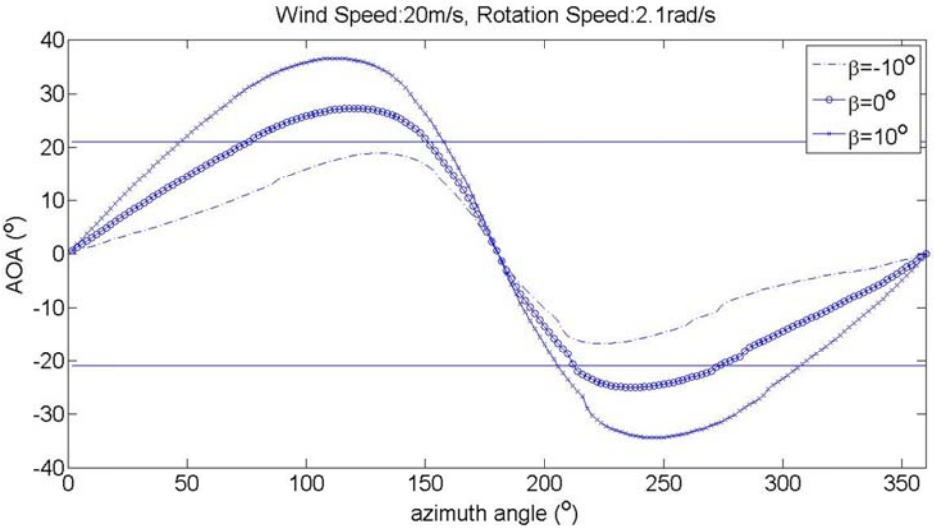

(a)

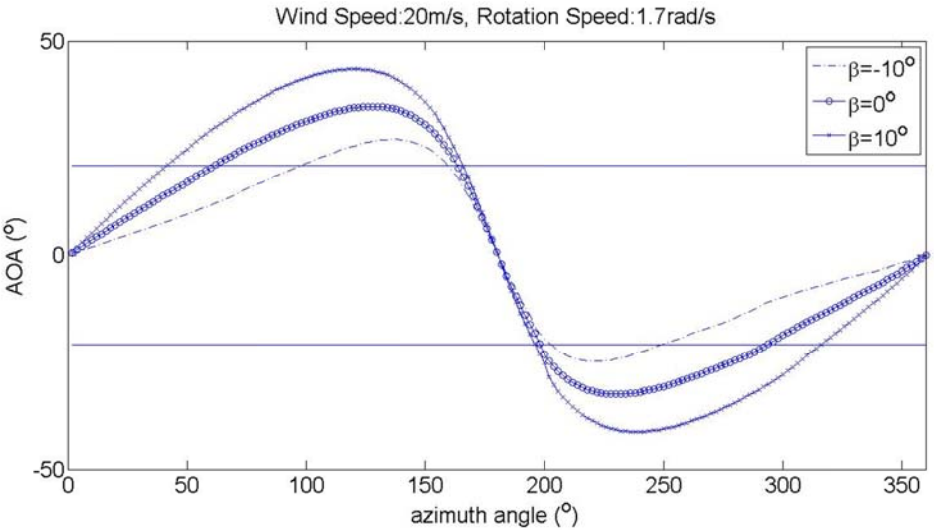

(b)

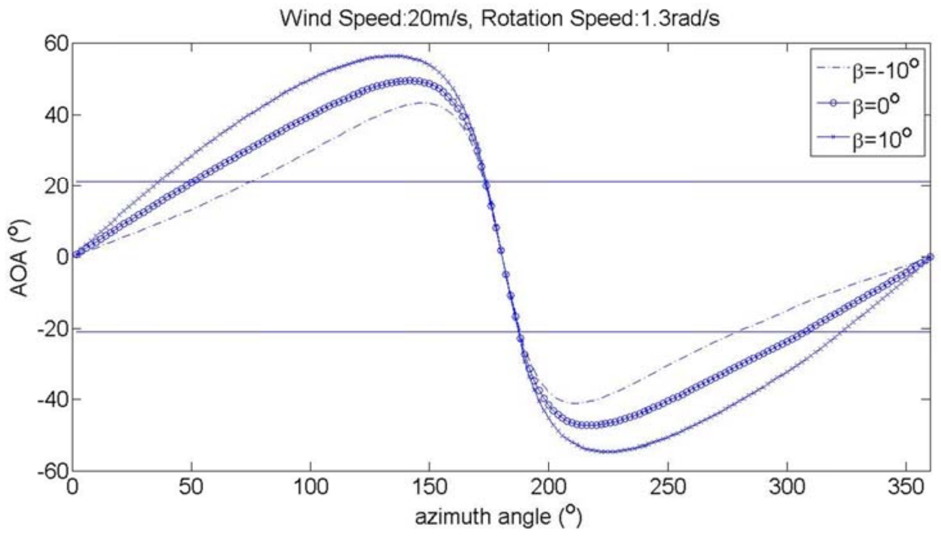

Wind Speed:20m/s, Rotation Speed:1.3rad/s
β=-10°
β=0°
β=10°
AOA (°)
azimuth angle (°)

(c)

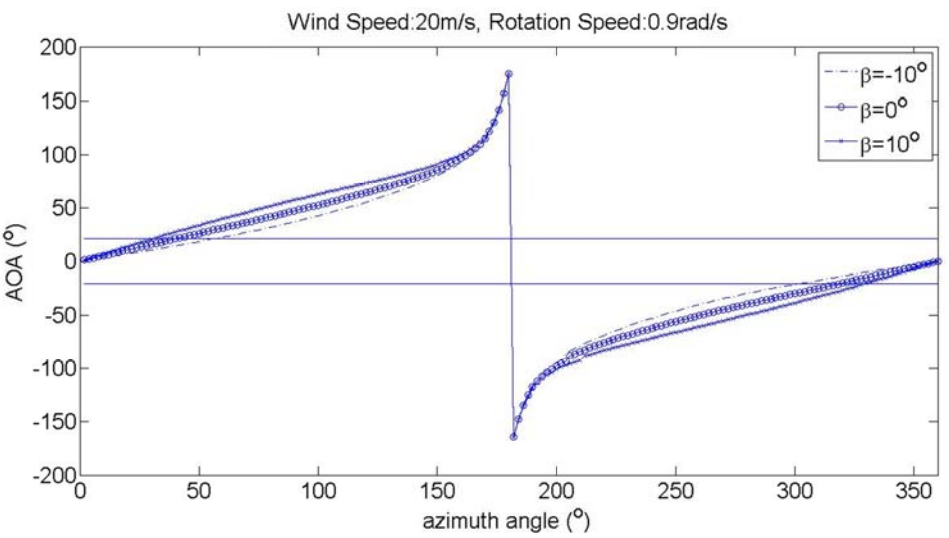

Wind Speed:20m/s, Rotation Speed:0.9rad/s
β=-10°
β=0°
β=10°
AOA (°)
azimuth angle (°)

(d)

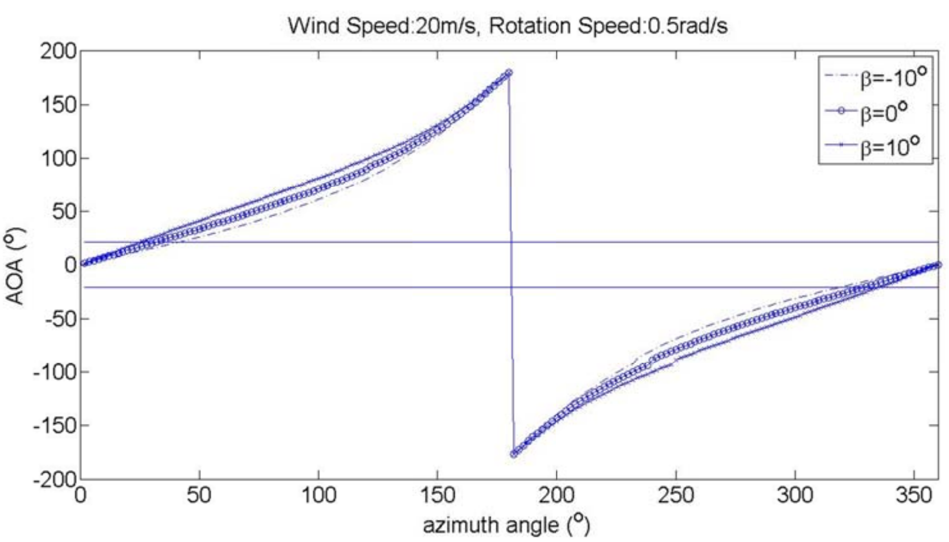

Wind Speed:20m/s, Rotation Speed:0.5rad/s
β=-10°
β=0°
β=10°
AOA (°)
azimuth angle (°)

(e)

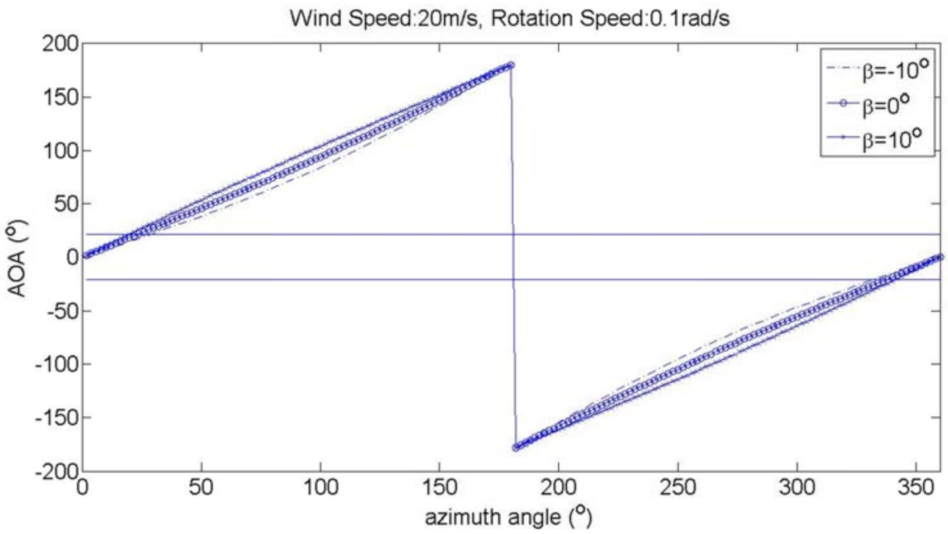

(f)

Fig. H.4 The AOA versus azimuth angle for the sinusoidal variation pitch cases. (a) $\omega = 2.1\,rad/s$; (b) $\omega = 1.7\,rad/s$; (c) $\omega = 1.3\,rad/s$; (d) $\omega = 0.9\,rad/s$; (e) $\omega = 0.5\,rad/s$; (f) $\omega = 0.1\,rad/s$;

REFERENCES

AGMA/AWEA 921-A97 (1997) Recommended Practices for Design and Specification of Gearboxes for Wind Turbine Generator Systems, *American Gear Manufacturers Association, Alexandria*, VA.

Ahlström, A. (2005). *Aerolastic simulation of wind turbine dynamics*. Doctoral Thesis. Royal Institute of Technology, Sweden.

Allix, O., & Ladevèze, P. (1992). Interlaminar interface modelling for the prediction of delamination. *Composite structures, 22*(4), 235-242.

Almohammadi, K. M., Ingham, D. B., Ma, L., & Pourkashan, M. (2013). Computational fluid dynamics (CFD) mesh independency techniques for a straight blade vertical axis wind turbine. *Energy, 58*, 483-493.

Amet, E., MaÃŽtre, T., Pellone, C., & Achard, J. L. (2009). 2D numerical simulations of blade-vortex interaction in a darrieus turbine. *Journal of fluids engineering, 131*(11), 111103.

Amirat, Y., Benbouzid, M. E. H., Al-Ahmar, E., Bensaker, B., & Turri, S. (2009). A brief status on condition monitoring and fault diagnosis in wind energy conversion systems. *Renewable and Sustainable Energy Reviews*,*13*(9), 2629-2636.

Armstrong, S., Fiedler, A., & Tullis, S. (2012). Flow separation on a high Reynolds number, high solidity vertical axis wind turbine with straight and canted blades and canted blades with fences. *Renewable Energy*, *41*, 13-22.

Angioni, S. L., Meo, M., & Foreman, A. (2011). A comparison of homogenization methods for 2-D woven composites. *Composites Part B: Engineering, 42*(2), 181-189.

ANSYS, A. F. (2009). 12.0 user's guide. *Ansys Inc*.

Ashwill, T. D. (1992). *Measured data for the Sandia 34-meter vertical axis wind turbine*: Sandia National Laboratories.

Avril S., Bonnet M., Bretelle A., Grédiac M., Hild F., Ienny P., Latourte F., Lemosse D., Pagano S., Pagnacco E., Pierron F. (2008). Overview of identification methods of mechanical parameters based on full-field measurements. *Experimental Mechanics, 48*(4), 381-402.

Azzi, V., & Tsai, S. (1965). Anisotropic strength of composites. *Experimental Mechanics, 5*(9), 283-288.

Bathe, K.-J. (2006). *Finite element procedures*: Klaus-Jurgen Bathe.

Baumgart, A. (2002). A mathematical model for wind turbine blades. *Journal of Sound and Vibration, 251*(1), 1-12.

Bazeos, N., Hatzigeorgiou, G. D., Hondros, I. D., Karamaneas, H., Karabalis, D. L., & Beskos, D. E. (2002). Static, seismic and stability analyses of a prototype wind turbine steel tower. *Engineering Structures, 24*(8), 1015-1025.

Bazilevs, Y., Hsu, M. C., Kiendl, J., Wüchner, R., & Bletzinger, K. U. (2011). 3D simulation of wind turbine rotors at full scale. Part II: Fluid–structure interaction modeling with composite blades. *International Journal for*

Numerical Methods in Fluids, 65(1 - 3), 236-253.
Bednarcyk, B. A., & Arnold, S. M. (2003). Micromechanics-based modeling of woven polymer matrix composites. *AIAA journal, 41*(9), 1788-1796.
Behmanesh, I., Moaveni, B., Lombaert, G., & Papadimitriou, C. (2015). Hierarchical Bayesian model updating for structural identification.*Mechanical Systems and Signal Processing*, *64*, 360-376.
Benesty, J. (1982). The committee on fatigue and fracture relia-bility of the committee on structural safety and reliabilityof the structural division fatigue reliability. *Journal ofthe Structural Division, 108*(1), 3-88.
Berg, D. E. (1983). Improved double-multiple streamtube model for the Darrieus-type vertical-axis wind turbine: Sandia National Labs., Albuquerque, NM (USA).
Berg, D. E. (1985). *Structural design of the Sandia 34-meter vertical-axis wind turbine*: Citeseer.
Bhatta, P., Paluszek, M. A., & Mueller, J. B. (2008, June). Individual blade pitch and camber control for vertical axis wind turbines. In *Proc. World Wind Energy Conference, Kingston, Canada*.
BP (2016). BP Statistical Review of World Energy. "www.bp.com/statisticalreview."
Biadgo, M. A., Simonović, A., Komarov, D., & Stupar, S. (2013). Numerical and analytical investigation of vertical axis wind turbine. *FME Transactions*,*41*(1), 49-58.
Biswas, S., Sreedhard, B. N., & Singh, Y. P. (1997). Dynamic analysis of a vertical axis wind turbine using a new wind load estimation technique. *Computers & structures*, *65*(6), 903-916.
Blanch, M. J., & Dutton, A. G. (2003, July). Acoustic emission monitoring of field tests of an operating wind turbine. In *Key Engineering Materials* (Vol. 245, pp. 475-482). Trans Tech Publications.
Boston, G. (2000), *Development of a Novel Wind Turbine*, Undergraduate BE (Mechanical) Thesis, University of Wollongong.
Brøndsted, P., Lilholt, H., & Lystrup, A. (2005). Composite materials for wind power turbine blades. *Annu. Rev. Mater. Res.*, *35*, 505-538.
Bravo, R., Tullis, S., & Ziada, S. (2007, June). Performance testing of a small vertical-axis wind turbine. In *Proceedings of the 21st Canadian Congress of Applied Mechanics (CANCAM07), Toronto, Canada, June* (pp. 3-7).
Brownjohn, J. M. (2007). Structural health monitoring of civil infrastructure. *Philosophical Transactions of the Royal Society of London A: Mathematical, Physical and Engineering Sciences, 365*(1851), 589-622.
Brownjohn, J. M., & Xia, P.-Q. (2000). Dynamic assessment of curved cable-stayed bridge by model updating. *Journal of Structural Engineering, 126*(2), 252-260.
Budiansky, B., & Fleck, N. A. (1993). Compressive failure of fibre composites. *Journal of the Mechanics and Physics of Solids, 41*(1), 183-211.
Burton, T., Sharpe, D., Jenkins, N., & Bossanyi, E. (2001). *Wind energy handbook*. John Wiley & Sons.
Byström, J., Jekabsons, N., & Varna, J. (2000). An evaluation of different models for prediction of elastic properties of woven composites. *Composites Part B:*

Engineering, *31*(1), 7-20.
Carne TG, Lobitz DW, Nord AR, Watson RA. Finite element analysis and modal testing of a rotating wind turbine, *Proceedings of the AIAA 23rd Structures, Structural Dynamics and Materials Conference*, New Orleans, Louisiana, USA, 1982.
Carne TG, Lauffer JP, Gomez AJ. Modal testing of a very flexible 110 m wind turbine structure, *Proceedings of the 6th International Modal Analysis Conference*, Kissimmee, Florida, USA, 1988.
Carne, T. G., Lauffer, J. P., Gomez, A. J., & Ashwill, T. D. (1989). *Model validation of the Sandia 34-Meter Test Bed Turbine using substructure modal-testing* (No. SAND-88-1774C; CONF-890102-11). Sandia National Labs., Albuquerque, NM (USA).
Cárdenas, D., Elizalde, H., Marzocca, P., Gallegos, S., & Probst, O. (2012). A coupled aeroelastic damage progression model for wind turbine blades.*Composite Structures*, *94*(10), 3072-3081.
Carvelli, V., & Poggi, C. (2001). A homogenization procedure for the numerical analysis of woven fabric composites. *Composites Part A: Applied Science and Manufacturing, 32*(10), 1425-1432.
Castelli, M. R., Dal Monte, A., Quaresimin, M., & Benini, E. (2013). Numerical evaluation of aerodynamic and inertial contributions to Darrieus wind turbine blade deformation. *Renewable energy*, *51*, 101-112.
Castelli, M. R., Englaro, A., & Benini, E. (2011). The Darrieus wind turbine: Proposal for a new performance prediction model based on CFD. *Energy*,*36*(8), 4919-4934.
Caselitz, P., & Giebhardt, J. (2005). Rotor condition monitoring for improved operational safety of offshore wind energy converters. *Journal of Solar Energy Engineering*, *127*(2), 253-261.
Cesnik, C. E., & Hodges, D. H. (1997). VABS: A New Concept for Composite Rotor Blade Cross‐Sectional Modeling. *Journal of the American helicopter society, 42*(1), 27-38.
Chalasani, S., & Conrad, J. M. (2008). *A survey of energy harvesting sources for embedded systems.* Paper presented at the Southeastcon, 2008. IEEE.
Chattot, J., & Hafez, M. Theoretical and Applied Aerodynamics.
Chattot, J., & Hafez, M. (2015). Wind Turbine and Propeller Aerodynamics—Analysis and Design *Theoretical and Applied Aerodynamics* (pp. 327-372): Springer.
Chawla, K. K. (2012). *Composite materials: science and engineering*: Springer Science & Business Media.
Chen, X., & Kareem, A. (2004). Equivalent static wind loads on buildings: New model. *Journal of Structural Engineering, 130*(10), 1425-1435.
Cheung, M., & Li, W. (2003). Probabilistic fatigue and fracture analyses of steel bridges. *Structural Safety, 25*(3), 245-262.
Chin, E. B., English, S. A., & Briggs, T. M. (2015). Criteria for initiation of delamination in quasi-static punch-shear tests of a carbon-fiber composite material. *Sandia National Laboratories, Livermore, CA SAND2015-8886*.

Choi, H., Choi, S., & Cha, H. (2008). Structural health monitoring system based on strain gauge enabled wireless sensor nodes. In *Networked Sensing Systems, 2008. INSS 2008. 5th International Conference on* (pp. 211-214). IEEE.

Chou, J. S., Chiu, C. K., Huang, I. K., & Chi, K. N. (2013). Failure analysis of wind turbine blade under critical wind loads. *Engineering Failure Analysis*,*27*, 99-118.

Christensen, R., & Lo, K. (1979). Solutions for effective shear properties in three phase sphere and cylinder models. *Journal of the Mechanics and Physics of Solids, 27*(4), 315-330.

Ciang, C. C., Lee, J. R., & Bang, H. J. (2008). Structural health monitoring for a wind turbine system: a review of damage detection methods.*Measurement Science and Technology*, *19*(12), 122001.

Commission, I. E. (2005). IEC 61400-1: Wind turbines part 1: Design requirements. *International Electrotechnical Commission*.

Crisfield, M. A. (1990). A consistent co-rotational formulation for non-linear, three-dimensional, beam-elements. *Computer methods in applied mechanics and engineering, 81*(2), 131-150.

Cugnoni, J., Gmür, T., & Schorderet, A. (2007). Inverse method based on modal analysis for characterizing the constitutive properties of thick composite plates. *Computers & Structures*, *85*(17), 1310-1320.

Cunha, J., & Piranda, J. (1999). Application of model updating techniques in dynamics for the identification of elastic constants of composite materials. *Composites Part B: Engineering, 30*(1), 79-85.

Danao, L. A., Eboibi, O., & Howell, R. (2013). An experimental investigation into the influence of unsteady wind on the performance of a vertical axis wind turbine. *Applied Energy*, *107*, 403-411.

Danao, L. A., Edwards, J., Eboibi, O., & Howell, R. (2014). A numerical investigation into the influence of unsteady wind on the performance and aerodynamics of a vertical axis wind turbine. *Applied Energy*, *116*, 111-124.

Davenport, A. G., King, J. P. C., & Larose, G. L. (1992). Taut strip model tests. *Proceedings of the First International Symposium on Aerodynamics of Large Bridges*, Copenhagen, Denmark.

de Normalisation, C. E. (1991). *Eurocode 2: Design of Concrete Structures: Part 1: General Rules and Rules for Buildings*: European Committee for Standardization.

De Wilde, W. P., Narmon, B., Sol, H., & Roovers, M (1984). *Determination of the material constants of an anisotropic lamina by free vibration analysis.* Paper presented at the Proceedings of the 2nd International Modal Analysis Conference.

Deobald, L. R., & Gibson, R. F. (1988). Determination of elastic constants of orthotropic plates by a modal analysis/Rayleigh-Ritz technique. *Journal of Sound and Vibration, 124*(2), 269-283.

Do, T. Q., Mahmoud, H., & van de Lindt, J. W. (2014). Fatigue Life of Wind Turbine Tower Bases throughout Colorado. *Journal of Performance of Constructed*

Facilities, *29*(4), 04014109.

Dodd, H. M., Ashwill, T. D., Berg, D. E., Ralph, M. E., Stephenson, W. A., & Veers, P. S. (1989). *Test results and status of the DOE/Sandia 34-M VAWT test bed* (No. SAND-89-1535C; CONF-8909217--1). Sandia National Labs., Albuquerque, NM (USA).

Edwards, J., Durrani, N., Howell, R., & Qin, N. (2007). Wind tunnel and numerical study of a small vertical axis wind turbine. In *45th AIAA Aerospace Sciences Meeting and Exhibit, Reno, Nevada*.

Elkhoury, M., Kiwata, T., & Aoun, E. (2015). Experimental and numerical investigation of a three-dimensional vertical-axis wind turbine with variable-pitch. *Journal of Wind Engineering and Industrial Aerodynamics*, *139*, 111-123.

Farrar, C. R., & Worden, K. (2007). An introduction to structural health monitoring. *Philosophical Transactions of the Royal Society of London A: Mathematical, Physical and Engineering Sciences, 365*(1851), 303-315.

Fatemi, A., & Yang, L. (1998). Cumulative fatigue damage and life prediction theories: a survey of the state of the art for homogeneous materials. *International Journal of Fatigue, 20*(1), 9-34.

Fazio, P. (1992). Annual Book of ASTM Standards , vol. 03.01 ASTM. *Philadelphia, PA*, 130.

Fereidooni, A. (2013). *Numerical Study of Aeroelastic Behaviour of a Troposkien Shape Vertical Axis Wind Turbine.* Carleton University.

Ferrari, G. M. (2012). *Development of an aeroelastic simulation for the analysis of vertical-axis wind turbines.* ResearchSpace@ Auckland.

Ferreira, C. S., Bijl, H., Van Bussel, G., & Van Kuik, G. (2007). Simulating dynamic stall in a 2D VAWT: modeling strategy, verification and validation with particle image velocimetry data. In *Journal of physics: conference series* (Vol. 75, No. 1, p. 012023). IOP Publishing.

Ferreira, C. S., van Kuik, G., van Bussel, G., & Scarano, F. (2009). Visualization by PIV of dynamic stall on a vertical axis wind turbine.*Experiments in Fluids*, *46*(1), 97-108.

Fiedler, A., & Tullis, S. (2009). Blade offset and pitch effects on a high solidity vertical axis wind turbine. *Wind engineering, 33*(3), 237-246.

Fingersh, L. J., Hand, M. M., & Laxson, A. S. (2006). *Wind turbine design cost and scaling model*. National Renewable Energy Laboratory Golden, Colo, USA.

Fleming, I., & Luscher, D. (2014). A model for the structural dynamic response of the CX - 100 wind turbine blade. *Wind Energy, 17*(6), 877-900.

Friswell, M., & Mottershead, J. E. (1995). *Finite element model updating in structural dynamics* (Vol. 38): Springer Science & Business Media.

Garrad, A., & Quarton, D. (1986). Symbolic computing as a tool in wind turbine dynamics. *Journal of Sound and Vibration, 109*(1), 65-78.

Genovese, K., Lamberti, L., & Pappalettere, C. (2004). A new hybrid technique for in-plane characterization of orthotropic materials. *Experimental Mechanics*, *44*(6), 584-592.

Germanischer, L. (2010). Guideline for the Certification of Wind Turbines Edition 2010 [G]: Germany.

Gipe, P. (2005). Wind energy—the breath of life or the kiss of death: contemporary wind mortality rates. *Online at http://www. wind-works. org/articles/BreathLife. html*.

Gipe, P. (2009). *Wind Energy Basics: A Guide to Home and Community-Scale Wind-Energy Systems*: Chelsea Green Publishing.

Gohari, S., Sharifi, S., Vrcelj, Z., & Yahya, M. Y. (2015). First-ply failure prediction of an unsymmetrical laminated ellipsoidal woven GFRP composite shell with incorporated surface-bounded sensors and internally pressurized.*Composites Part B: Engineering*, *77*, 502-518.

Gol'denblat, I., & Kopnov, V. (1965). Strength of glass-reinforced plastics in the complex stress state. *Polymer Mechanics, 1*(2), 54-59.

Gorban, A. N., Gorlov, A. M., & Silantyev, V. M. (2001). Limits of the turbine efficiency for free fluid flow. *Journal of energy resources technology*, *123*(4), 311-317.

Gorlov, A. M. (1998). Helical turbines for the gulf stream: conceptual approach to design of a large-scale floating power farm. *Marine Technology and Sname News, 35*(3), 175.

Grédiac, M., & Paris, P. (1996). Direct identification of elastic constants of anisotropic plates by modal analysis: theoretical and numerical aspects. *Journal of Sound and Vibration, 195*(3), 401-415.

Gras, R., Leclerc, H., Roux, S., Otin, S., Schneider, J., & Périé, J. N. (2013). Identification of the out-of-plane shear modulus of a 3D woven composite. *Experimental Mechanics*, *53*(5), 719-730.

Greenblatt, D., Schulman, M., & Ben-Harav, A. (2012). Vertical axis wind turbine performance enhancement using plasma actuators. *Renewable Energy*, *37*(1), 345-354.

Griffith DT, Mayes RL, Hunter PS. Excitation methods for a 60 kW vertical axis wind turbine, *Proceedings of the 28th International Modal Analysis Conference*, Jacksonville, Florida, USA, 2010; 329–338.

Hahn, H. T., & Tsai, S. W. (1980). *Introduction to composite materials*: CRC Press.

Ham, N. D., Soohoo, P., Noll, R. B., & Drees, H. M. (1979, June). Analytical and experimental evaluation of Cycloturbine aerodynamic performance. In *American Institute of Aeronautics and Astronautics, Terrestrial Energy Systems Conference, Orlando, Fla., June 4-6, 1979, 7 p. Research supported by the US Department of Energy.* (Vol. 1).

Hand, M., Jackson, M., & Ong, S. (2009). *Land-use requirements of modern wind power plants in the United States*. Golden, CO: National Renewable Energy Laboratory.

Hansen, M. O. (2015). *Aerodynamics of wind turbines*: Routledge.

Hansen, M. O. L., Sørensen, J. N., Voutsinas, S., Sørensen, N., & Madsen, H. A. (2006). State of the art in wind turbine aerodynamics and aeroelasticity. *Progress in aerospace sciences*, *42*(4), 285-330.

Hart-Smith, L. (1998a). Predictions of a generalized maximum-shear-stress failure criterion for certain fibrous composite laminates. *Composites science and technology, 58*(7), 1179-1208.

Hart-Smith, L. (1998b). Predictions of the original and truncated maximum-strain failure models for certain fibrous composite laminates. *Composites science and technology, 58*(7), 1151-1178.

Hashin, Z. (1965). On elastic behaviour of fibre reinforced materials of arbitrary transverse phase geometry. *Journal of the Mechanics and Physics of Solids, 13*(3), 119-134.

Hashin, Z. (1980). Failure criteria for unidirectional fiber composites. *Journal of applied mechanics, 47*(2), 329-334.

Hashin, Z., & Rosen, B. W. (1964). The elastic moduli of fiber-reinforced materials. *Journal of applied mechanics, 31*(2), 223-232.

Hashin, Z., & Rotem, A. (1973). A fatigue failure criterion for fiber reinforced materials. *Journal of Composite Materials, 7*(4), 448-464.

Hassan, G. E., Hassan, A., & Youssef, M. E. (2015). Numerical Investigation of medium range Re numbers Aerodynamics Characteristics for NACA0018 Airfoil. *CFD Letters*, *6*(4), 175-187.

He, J., Huang, Q., & Xu, Y. L. (2014). Synthesis of vibration control and health monitoring of building structures under unknown excitation. *Smart Materials and Structures*, *23*(10), 105025.

Hill, R. (1964). Theory of mechanical properties of fibre-strengthened materials: I. Elastic behaviour. *Journal of the Mechanics and Physics of Solids, 12*(4), 199-212.

Hill, R. (1965). A self-consistent mechanics of composite materials. *Journal of the Mechanics and Physics of Solids, 13*(4), 213-222.

Hill, R. (1998). *The mathematical theory of plasticity* (Vol. 11): Oxford university press.

Hou, S. Q., Cai, X. J., & Xu, J. Q. (2015). A life evaluation formula for high cycle fatigue under uniaxial and multiaxial loadings with mean stresses.*International Journal of Mechanical Sciences*, *93*, 229-239.

Howell, R., Qin, N., Edwards, J., & Durrani, N. (2010). Wind tunnel and numerical study of a small vertical axis wind turbine. *Renewable energy*,*35*(2), 412-422.

Huang, Z.-M. (2001). Simulation of the mechanical properties of fibrous composites by the bridging micromechanics model. *Composites Part A: Applied Science and Manufacturing, 32*(2), 143-172.

Huang, Z.M. (2000). The mechanical properties of composites reinforced with woven and braided fabrics. *Composites science and technology, 60*(4), 479-498.

Huston, D. (2010). *Structural sensing, health monitoring, and performance evaluation*: CRC Press.

Hwang, I. S., Hwang, C. S., Min, S. Y., Jeong, I. O., Lee, Y. H., & Kim, S. J. (2005, October). Efficiency improvement of cycloidal wind turbine by active control of blade motion. In *16th International Conference on Adaptive Structures and Technologies, Paris, France* (pp. 9-12).

Hwang, I. S., Min, S. Y., Jeong, I. O., Lee, Y. H., & Kim, S. J. (2006, March). Efficiency improvement of a new vertical axis wind turbine by individual active control of blade motion. In *Smart Structures and Materials*(pp. 617311-617311). International Society for Optics and Photonics.

Hwu, C., Kao, C. J., & Chang, L. E. (1995). Delamination fracture criteria for composite laminates. *Journal of Composite materials*, *29*(15), 1962-1987.

Ishikawa, T., & Chou, T.-W. (1982). Stiffness and strength behaviour of woven fabric composites. *Journal of Materials Science, 17*(11), 3211-3220.

Islam, M., Ting, D. S. K., & Fartaj, A. (2008). Aerodynamic models for Darrieus-type straight-bladed vertical axis wind turbines. *Renewable and Sustainable Energy Reviews*, *12*(4), 1087-1109.

Islam, M., Ting, D. S. K., & Fartaj, A. (2008). Aerodynamic models for Darrieus-type straight-bladed vertical axis wind turbines. *Renewable and Sustainable Energy Reviews*, *12*(4), 1087-1109.

Ismail, M. F., & Vijayaraghavan, K. (2015). The effects of aerofoil profile modification on a vertical axis wind turbine performance. *Energy, 80*, 20-31.

Ivanov, I., & Tabiei, A. (2001). Three-dimensional computational micro-mechanical model for woven fabric composites. *Composite structures, 54*(4), 489-496.

Jørgensen, E. R., Borum, K. K., McGugan, M., Thomsen, C. L., Jensen, F. M., Debel, C. P., & Sørensen, B. F. (2004). *Full scale testing of wind turbine blade to failure-flapwise loading*. Risø National Laboratory, Roskilde

Jaishi, B., & Ren, W. X. (2005). Structural finite element model updating using ambient vibration test results. *Journal of Structural Engineering, 131*(4), 617-628.

Jardine, A. K., Lin, D., & Banjevic, D. (2006). A review on machinery diagnostics and prognostics implementing condition-based maintenance.*Mechanical systems and signal processing*, *20*(7), 1483-1510.

Jensen, F. M., Falzon, B. G., Ankersen, J., & Stang, H. (2006). Structural testing and numerical simulation of a 34m composite wind turbine blade.*Composite structures*, *76*(1), 52-61.

Jha, A. R. (2010). *Wind turbine technology*: CRC press.

Jiang, L., Wang, C., Huang, Y., Pei, Z., Xin, S., Wang, W., Ma S. & Brown, T. (2015). Growth in Wind and Sun: Integrating Variable Generation in China.Power and Energy Magazine, IEEE, 13(6), 40-49.

Jones, R. M. (1975). *Mechanics of composite materials* (Vol. 193): Scripta Book Company Washington, DC.

Joosse, P. A., Blanch, M. J., Dutton, A. G., Kouroussis, D. A., Philippidis, T. P., & Vionis, P. S. (2002). Acoustic emission monitoring of small wind turbine blades. *Journal of solar energy engineering*, *124*(4), 446-454.

Jung, S. N., Dhadwal, M. K., Kim, Y. W., Kim, J. H., & Riemenschneider, J. (2015). Cross-sectional constants of composite blades using computed tomography technique and finite element analysis. *Composite Structures*,*129*, 132-142.

Jureczko, M. E. Z. Y. K., Pawlak, M., & Mężyk, A. (2005). Optimisation of wind turbine blades. *Journal of materials processing technology*, *167*(2), 463-471.

Kang, N., Park, S. C., Park, J., & Atluri, S. N. (2016). Dynamics of flexible tower-blade and rigid nacelle system: dynamic instability due to their interactions in wind turbine. *Journal of Vibration and Control*, *22*(3), 826-836.

Kardos, J. (1976). The Halpin‐Tsai equations: a review. *Polymer Engineering & Science, 16*(5), 344-352.

Kelley, N. D. (1995). A comparison of measured wind park load histories with the WISPER and WISPERX load spectra: National Renewable Energy Lab., Golden, CO (United States).

Kessentini, S., Choura, S., Najar, F., & Franchek, M. A. (2010). Modeling and dynamics of a horizontal axis wind turbine. *Journal of Vibration and Control*.

Khan, M. J., Bhuyan, G., Iqbal, M. T., & Quaicoe, J. E. (2009). Hydrokinetic energy conversion systems and assessment of horizontal and vertical axis turbines for river and tidal applications: A technology status review. *Applied Energy*, *86*(10), 1823-1835.

Khandan, R., Noroozi, S., Sewell, P., & Vinney, J. (2012). The development of laminated composite plate theories: a review. *Journal of Materials Science*, *47*(16), 5901-5910.

Kirikera, G. R., Shinde, V., Schulz, M. J., Sundaresan, M. J., Hughes, S., van Dam, J., ... & Ghoshal, A. (2008). Monitoring multi-site damage growth during quasi-static testing of a wind turbine blade using a structural neural system. *Structural Health Monitoring*, *7*(2), 157-173.

Kirke, B. (2011). Tests on ducted and bare helical and straight blade Darrieus hydrokinetic turbines. *Renewable Energy, 36*(11), 3013-3022.

Kong, C., Bang, J., & Sugiyama, Y. (2005). Structural investigation of composite wind turbine blade considering various load cases and fatigue life.*Energy*, *30*(11), 2101-2114.

Kosaku, T., Sano, M., & Nakatani, K. (2002, October). Optimum pitch control for variable-pitch vertical-axis wind turbines by a single stage model on the momentum theory. In *Systems, Man and Cybernetics, 2002 IEEE International Conference on* (Vol. 5, pp. 6-pp). IEEE.

Kubiak, T., & Kaczmarek, L. (2015). Estimation of load-carrying capacity for thin-walled composite beams. *Composite structures, 119*, 749-756.

Kujawski, D., & Ellyin, F. (1988). On the concept of cumulative fatigue damage. *International journal of fracture, 37*(4), 263-278.

Lanzafame, R., Mauro, S., & Messina, M. (2013). Wind turbine CFD modeling using a correlation-based transitional model. *Renewable Energy*,*52*, 31-39.

Lanzafame, R., Mauro, S., & Messina, M. (2014). 2D CFD modeling of H-Darrieus wind turbines using a transition turbulence model. *Energy Procedia*,*45*, 131-140.

Larsen, H. (1975). *Summary of a vortex theory for the cyclogiro.* Paper presented at the Proceedings of the 2nd US National conference on Wind Engineering Research.(1975-8), Colorad State University.

Larsen, J. W., & Nielsen, S. R. (2006). Non-linear dynamics of wind turbine wings. *International Journal of Non-Linear Mechanics, 41*(5), 629-643.

Larsen, J. W., & Nielsen, S. R. (2007). Nonlinear parametric instability of wind turbine wings. *Journal of Sound and Vibration, 299*(1), 64-82.

Larsson, D. (1997). Using modal analysis for estimation of anisotropic material constants. *Journal of engineering mechanics, 123*(3), 222-229.

Lavassas, I., Nikolaidis, G., Zervas, P., Efthimiou, E., Doudoumis, I. N., & Baniotopoulos, C. C. (2003). Analysis and design of the prototype of a steel 1-MW wind turbine tower. *Engineering structures*, *25*(8), 1097-1106.

Lazauskas, L. (1992). Three pitch control systems for vertical axis wind turbines compared. *Wind engineering, 16*(5), 269-282.

Lanzafame, R., Mauro, S., & Messina, M. (2014). 2D CFD modeling of H-Darrieus wind turbines using a transition turbulence model. *Energy Procedia*,*45*, 131-140.

Lee, D., Hodges, D. H., & Patil, M. J. (2002). Multi - flexible - body Dynamic Analysis of Horizontal Axis Wind Turbines. *Wind Energy*, *5*(4), 281-300.

Lewis, R. M., & Torczon, V. (2000). Pattern search methods for linearly constrained minimization. *SIAM Journal on optimization, 10*(3), 917-941.

Li, C., Zhu, S., Xu, Y. L., & Xiao, Y. (2013). 2.5 D large eddy simulation of vertical axis wind turbine in consideration of high angle of attack flow.*Renewable energy*, *51*, 317-330.

Li, Q. A., Maeda, T., Kamada, Y., Murata, J., Kawabata, T., & Kogaki, T. (2014). Study on flow around straight-bladed vertical axis wind turbine under low tip speed ratio. *Journal of Fluid Science and Technology*, *9*(3), JFST0051-JFST0051.

Li, Q. A., Maeda, T., Kamada, Y., Murata, J., Furukawa, K., & Yamamoto, M. (2015). Effect of number of blades on aerodynamic forces on a straight-bladed vertical axis wind turbine. *Energy*, *90*, 784-795.

Li, Q. A., Maeda, T., Kamada, Y., Murata, J., Yamamoto, M., Ogasawara, T., Kogaki, T. (2016). Study on power performance for straight-bladed vertical axis wind turbine by field and wind tunnel test. *Renewable Energy*,*90*, 291-300.

Lian, D., Lee, J. H., & Kim, Y. C (2008) Power prediction of darrieus type wind turbine considering real air velocity on the wind turbine blade. *The 2008 European Wind Energy Conference and Exhibition, Brussels*

Lin, H. H., Shih, M. J., Wei, H. Y., & Vannithamby, R. (2015). DeepSleep: IEEE 802.11 enhancement for energy-harvesting machine-to-machine communications. *Wireless Networks*, *21*(2), 357-370.

Liu, K.S., & Tsai, S. W. (1998). A progressive quadratic failure criterion for a laminate. *Composites science and technology, 58*(7), 1023-1032.

Liu, Y., & Ishihara, T. (2015) Fatigue Failure Accident of wind turbine tower in Taikoyama Wind Power Plant. *measurement*, *15*, 20.

Liu, L., Liu, C., & Zheng, X. (2015). Modeling, Simulation, Hardware Implementation of a Novel Variable Pitch Control for H-Type Vertical Axis Wind Turbine. *Journal of Electrical Engineering*, *66*(5), 264-269.

Lobitz, D., & Sullivan, W. (1980). VAWTDYN: a numerical package for the dynamic analysis of vertical axis wind turbines: Sandia Labs., Albuquerque, NM (USA).

Lobitz, D. W., & Ashwill, T. (1986). Aeroelastic effects in the structural dynamic analysis of vertical axis wind turbines: Sandia National Labs., Albuquerque, NM (USA).

Márquez, F. P. G., Tobias, A. M., Pérez, J. M. P., & Papaelias, M. (2012). Condition monitoring of wind turbines: Techniques and methods. *Renewable Energy*, *46*, 169-178.

Mandell, J. F., Reed, R. M., & Samborsky, D. D. (1992). *Fatigue of fiberglass wind turbine blade materials*. Sandia National Laboratories.

Mandell, J. F., Reed, R. M., & Samborsky, D. D. (1993). Fatigue performance of wind turbine blade composite materials. *Wind Energy, 14*, 191-198.

Mandell, J. F., & Samborsky, D. D. (1997). DOE/MSU composite material fatigue database: test methods, materials, and analysis: Sandia National Labs., Albuquerque, NM (United States).

Mandell, J. F., & Samborsky, D. D. (2009). DOE/MSU composite material fatigue database. *Montana State University, Bozeman, MT, Version, 18*.

Marat-Mendes, R. M., & Freitas, M. M. (2010). Failure criteria for mixed mode delamination in glass fibre epoxy composites. *Composite structures, 92*(9), 2292-2298.

Marco, S., & Starkey, W. (1954). A concept of fatigue damage. *Trans. ASME, 76*(4), 627-632.

Marin, J. C., Barroso, A., Paris, F., & Canas, J. (2009). Study of fatigue damage in wind turbine blades. *Engineering failure analysis*, *16*(2), 656-668.

McCormick, B. W. (1995). *Aerodynamics, aeronautics, and flight mechanics* (Vol. 2): Wiley New York.

Mcintosh, S. C., Babinsky, H., & Bertenyi, T. (2007, January). Optimizing the energy output of vertical axis wind turbines for fluctuating wind conditions. In *45th AIAA aerospace sciences meeting and exhibit, Reno, Nevada*.

Mcintosh, S. C., Babinsky, H., & Bertenyi, T. (2008). *Unsteady power output of vertical axis wind turbines operating within a fluctuating free-stream.* Paper presented at the 46th AIAA aerospace sciences meeting and exhibit, Reno, Nevada.

McIntosh, S. C., & Babinsky, H. (2012). Aerodynamic modeling of swept-bladed vertical axis wind turbines. *Journal of Propulsion and Power, 29*(1), 227-237.

McLaren, K., Tullis, S., & Ziada, S. (2012). Computational fluid dynamics simulation of the aerodynamics of a high solidity, small - scale vertical axis wind turbine. *Wind Energy*, *15*(3), 349-361.

McLaren, K., Tullis, S., & Ziada, S. (2012b). Measurement of high solidity vertical axis wind turbine aerodynamic loads under high vibration response conditions. *Journal of Fluids and Structures, 32*, 12-26.

McLaren, K. W. (2011). A numerical and experimental study of unsteady loading of high solidity vertical axis wind turbines.

McNiff, B.P., W.D. Musial, and R. Errichello, "Variations in Gear Fatigue Life for Different Wind Turbine Braking Strategies," *Proceedings of Windpower '90*, AWEA, Washington, DC, 1990, p. 131.

Menet, J. L., & Bourabaa, N. (2004). Increase in the Savonius rotors efficiency via a parametric investigation. *European Wind Energy*.

Menter, F. R., Kuntz, M., & Langtry, R. (2003). Ten years of industrial experience with the SST turbulence model. *Turbulence, heat and mass transfer*, *4*(1).

Miner, M. A. (1945). Cumulative damage in fatigue. *Journal of applied mechanics, 12*(3), 159-164.

Mishra, A., & Chakraborty, S. (2015). Determination of Material Parameters of FRP Plates With Rotational Flexibility at Boundaries Using Experimental Modal Testing and Model Updating. *Experimental Mechanics, 55*(5), 803-815.

Mishra, A. K., & Chakraborty, S. (2015). Development of a finite element model updating technique for estimation of constituent level elastic parameters of FRP plates. *Applied Mathematics and Computation, 258*, 84-94.

Molimard, J., Le Riche, R., Vautrin, A., & Lee, J. R. (2005). Identification of the four orthotropic plate stiffnesses using a single open-hole tensile test.*Experimental Mechanics*, *45*(5), 404-411.

Mollineaux, M. G., Van Buren, K. L., Hemez, F. M., & Atamturktur, S. (2013). Simulating the dynamics of wind turbine blades: part I, model development and verification. *Wind Energy*, *16*(5), 694-710.

Moran, W. A. (1977). *Giromill wind tunnel test and analysis*: Department of Energy.

Moussu, F., & Nivoit, M. (1993). Determination of elastic constants of orthotropic plates by a modal analysis/method of superposition. *Journal of Sound and Vibration, 165*(1), 149-163.

Mukinović, M., Brenner, G., & Rahimi, A. (2010). Analysis of vertical axis wind turbines. In *New Results in Numerical and Experimental Fluid Mechanics VII* (pp. 587-594). Springer Berlin Heidelberg.

Natarajan, B., Lee, J., Lim, J., & Shin, S. (2012). Structural analysis of composite wind turbine blade using advanced beam model approach.*International Journal of Precision Engineering and Manufacturing*, *13*(12), 2245-2250.

Negm, H. M., & Maalawi, K. Y. (2000). Structural design optimization of wind turbine towers. *Computers & structures, 74*(6), 649-666.

Nejad, A. R., Gao, Z., & Moan, T. (2013). Long-term analysis of gear loads in fixed offshore wind turbines considering ultimate operational loadings.Energy Procedia, 35, 187-197.

Nelson, V. (2013). *Wind energy: renewable energy and the environment*: CRC press.

Nijssen, R. P. L. (2006). *Fatigue life prediction and strength degradation of wind turbine rotor blade composites*: TU Delft, Delft University of Technology.

Nini, M., Motta, V., Bindolino, G., & Guardone, A. (2014). Three-dimensional simulation of a complete vertical axis wind turbine using overlapping grids.*Journal of Computational and Applied Mathematics*, *270*, 78-87.

Normung, D. A. f. S. D. I. f. (2003). *Erläuterungen zu DIN 1045-1*: Beuth.

O'Brien, T. K. (1982). Characterization of delamination onset and growth in a composite laminate *Damage in Composite Materials: Basic Mechanisms, Accumulation, Tolerance, and Characterization*: ASTM International.

Overgaard, L. C., Lund, E., & Thomsen, O. T. (2010). Structural collapse of a wind turbine blade. Part A: Static test and equivalent single layered models. *Composites Part A: Applied Science and Manufacturing*, *41*(2), 257-270.

Pagano, N., & Pipes, R. B. (1973). Some observations on the interlaminar strength of composite laminates. *International Journal of Mechanical Sciences, 15*(8), 679-688.

Panigrahi, S., & Pradhan, B. (2009). Through-the-width delamination damage propagation characteristics in single-lap laminated FRP composite joints. *International Journal of Adhesion and Adhesives, 29*(2), 114-124.

Paraschivoiu, I. (2002). *Wind turbine design: with emphasis on Darrieus concept*: Presses inter Polytechnique.

Paraschivoiu, I., Trifu, O., & Saeed, F. (2009). H-Darrieus wind turbine with blade pitch control. *International Journal of Rotating Machinery*, *2009*.

Pawsey, N. C. K. (2002). *Development and evaluation of passive variable-pitch vertical axis wind turbines*. University of New South Wales.

Pettersson, L., Andersson, J., Orbert, C., & Skagerman, S. (2010). *RAMS-database for Wind Turbines*. Elforsk

Polyzois, D. J., Raftoyiannis, I. G., & Ungkurapinan, N. (2009). Static and dynamic characteristics of multi-cell jointed GFRP wind turbine towers.Composite structures, 90(1), 34-42.

Popelka, D. (1982). *Aeroelastic stability analysis of a Darrieus wind turbine*: Sandia National Laboratories.

Puck, A., & Schürmann, H. (1998). Failure analysis of FRP laminates by means of physically based phenomenological models. *Composites science and technology, 58*(7), 1045-1067.

Quaresimin, M. (2015). 50th Anniversary Article: Multiaxial Fatigue Testing of Composites: From the Pioneers to Future Directions. *Strain, 51*(1), 16-29.

Quaresimin, M., Susmel, L., & Talreja, R. (2010). Fatigue behaviour and life assessment of composite laminates under multiaxial loadings. *International Journal of Fatigue*, *32*(1), 2-16.

Quilligan, A., O'Connor, A., & Pakrashi, V. (2012). Fragility analysis of steel and concrete wind turbine towers. *Engineering Structures*, *36*, 270-282.

Rahmani, B., Mortazavi, F., Villemure, I., & Levesque, M. (2013). A new approach to inverse identification of mechanical properties of composite materials: Regularized model updating. *Composite Structures*, *105*, 116-125.

Reddy, J., & Pandey, A. (1987). A first-ply failure analysis of composite laminates. *Computers & structures, 25*(3), 371-393.

Reeder, J. (1992). An Evaluation of Mixed-Mode Delamination Failure Criteria.

Ren, W. X., & De Roeck, G. (2002). Structural damage identification using modal data. I: Simulation verification. *Journal of Structural Engineering, 128*(1), 87-95.

Reuter, R. C., & Worstell, M. H. (1978). *Torque ripple in a vertical axis wind turbine*: Sandia Laboratories, Department of Energy.

Ribrant, J., & Bertling, L. (2007). *Survey of failures in wind power systems with focus on Swedish wind power plants during 1997-2005.* Paper presented at the Power Engineering Society General Meeting, 2007. IEEE.

Rumsey, M. A., & Paquette, J. A. (2008). *Structural health monitoring of wind turbine blades*. Paper presented at the The 15th International Symposium on: Smart Structures and Materials & Nondestructive Evaluation and Health Monitoring.

Rumsey, M. A., & Musial, W. (2001). Application of acoustic emission nondestructive testing during wind turbine blade tests. *Journal of Solar Energy Engineering*, *123*(4), 270-270.

Salençon, J. (2012). *Handbook of Continuum Mechanics: General Concepts Thermoelasticity*: Springer Science & Business Media.

Sanayei, M., Imbaro, G. R., McClain, J. A., & Brown, L. C. (1997). Structural model updating using experimental static measurements. *Journal of structural engineering*, *123*(6), 792-798.

Sanayei, M., Phelps, J. E., Sipple, J. D., Bell, E. S., & Brenner, B. R. (2011). Instrumentation, nondestructive testing, and finite-element model updating for bridge evaluation using strain measurements. *Journal of bridge engineering*, *17*(1), 130-138.

Saravia, C. M., Machado, S. P., & Cortínez, V. H. (2013). A composite beam finite element for multibody dynamics: Application to large wind turbine modeling. *Engineering Structures*, *56*, 1164-1176.

Sawin, J. L. , Seyboth K., Sverrisson F.. (2016). Renewables 2016 global status report.

Sawyer, S., & Rave, K. (2016). Global Wind Report–Annual Market Update 2015. *GWEC, Global Wind Energy Council*.

Scheurich, F., & Brown, R. E. (2013). Modelling the aerodynamics of vertical - axis wind turbines in unsteady wind conditions. *Wind Energy, 16*(1), 91-107.

Scheurich, F., Fletcher, T. M., & Brown, R. E. (2010, January). The influence of blade curvature and helical blade twist on the performance of a vertical-axis wind turbine. In *29th ASME wind energy symposium, Orlando*.

Schwaar, M., Gmür, T., & Frieden, J. (2012). Modal numerical–experimental identification method for characterising the elastic and damping properties in sandwich structures with a relatively stiff core. *Composite Structures*, *94*(7), 2227-2236. Schroeder, K., Ecke, W., Apitz, J., Lembke, E., & Lenschow, G. (2006). A fibre Bragg grating sensor system monitors operational load in a wind turbine rotor blade. *Measurement Science and Technology*, *17*(5), 1167.

Schwaar, M., Gmür, T., & Frieden, J. (2012). Modal numerical–experimental identification method for characterising the elastic and damping properties in sandwich structures with a relatively stiff core. *Composite Structures*, *94*(7), 2227-2236.

Shen, W. A., Zhu, S., & Xu, Y. L. (2012). An experimental study on self-powered vibration control and monitoring system using electromagnetic TMD and wireless sensors. *Sensors and Actuators A: Physical*, *180*, 166-176.

Shinozuka, M., & Deodatis, G. (1991). Simulation of stochastic processes by spectral representation. *Applied Mechanics Reviews, 44*(4), 191-204.

Shinozuka, M., & Jan, C.-M. (1972). Digital simulation of random processes and its applications. *Journal of Sound and Vibration, 25*(1), 111-128.

Shokrieh, M. M., & Rafiee, R. (2006). Simulation of fatigue failure in a full composite wind turbine blade. *Composite structures, 74*(3), 332-342.

Siddiqui, M. S., Durrani, N., & Akhtar, I. (2015). Quantification of the effects of geometric approximations on the performance of a vertical axis wind turbine. *Renewable Energy*, *74*, 661-670.

Simiu, E., & Scanlan, R. H. (1986). *Wind effects on structures: an introduction to wind engineering*: John Wiley.

Snel, H., & Schepers, J. G. (1995). *Joint investigation of dynamic inflow effects and implementation of an engineering method*. Netherlands Energy Research Foundation ECN.

Song, S. H., Kang, S. I., & Hahm, N. K. (2003, February). Implementation and control of grid connected AC-DC-AC power converter for variable speed wind energy conversion system. In *Applied Power Electronics Conference and Exposition, 2003. APEC'03. Eighteenth Annual IEEE* (Vol. 1, pp. 154-158). IEEE.

Song, F., Ni, Y., & Tan, Z. (2011). Optimization design, modeling and dynamic analysis for composite wind turbine blade. *Procedia Engineering*,*16*, 369-375.

South, P., & Rangi, R. (1975). *An Experimental Investigation of a 12 Ft. Diameter High Speed Vertical Axis Wind Turbine*: National Research Council Canada, National Aeronautical Establishment.

Spagnoli, A. (2001). A new high-cycle fatigue criterion applied to out-of-phase biaxial stress state. *International Journal of Mechanical Sciences, 43*(11), 2581-2595.

Spera, D. A. (1994). Wind turbine technology.

Staelens, Y., Saeed, F., & Paraschivoiu, I. (2003, January). A straight-bladed variable-pitch VAWT concept for improved power generation. In*ASME 2003 wind energy symposium* (pp. 146-154). American Society of Mechanical Engineers.

Stanton, S. C., McGehee, C. C., & Mann, B. P. (2010). Nonlinear dynamics for broadband energy harvesting: investigation of a bistable piezoelectric inertial generator. *Physica D: Nonlinear Phenomena*, *239*(10), 640-653.

Strickland, J. H., Webster, B. T., & Nguyen, T. (1979). A vortex model of the Darrieus turbine: an analytical and experimental study. *Journal of Fluids Engineering*, *101*(4), 500-505.

Strickland, J. H. (1975). Darrieus turbine: a performance prediction model using multiple streamtubes: Sandia Labs., Albuquerque, N. Mex.(USA).

SUN, C.-T. (1996). COMPARATIVE EVALUATION OF FAILURE ANALYSIS METHODS FOR COMPOSITE LAMINATES.

Sutherland, H. (1999). On the fatigue analysis of wind turbines.

Sutherland, H. J., Berg, D. E., & Ashwill, T. D. (2012). A retrospective of VAWT technology. *Sandia Report No. SAND2012-0304*.

Tanov, R., & Tabiei, A. (2001). Computationally efficient micromechanical models for woven fabric composite elastic moduli. *Journal of applied mechanics, 68*(4), 553-560.

Templin, R. (1974). Aerodynamic performance theory for the NRC vertical-axis wind turbine: National Aeronautical Establishment, Ottawa, Ontario (Canada).

Templin, R. (1985). The nrc double multiple stream tube theory for vertical axis wind

turbines. *National Research Council Canada, Tech. Rep. TM WE, 23*.
Thomas G. Carne, D. W. L., Arlo R. Nerd, Robert A. Watson. (1982). Finite element analysis and modal testing of a rotating wind turbine.
Thomsen, K. and S.M. Petersen. (1992) Experimental Investigation of Gear Box Duration Loadings on Stall and Pitch Controlled Wind Turbines, *Riso-R-653(EN)*, RISO, Roskilde, Denmark.
Thresher, R. W., Mirandy, L. P., Carne, T. G., Lobitz, D. W., & James, G. H. (2009). Structural dynamic behavior of wind turbines. In *Wind Turbine Technology: Fundamental Concepts in Wind Turbine Engineering, Second Edition*. ASME Press.
Torczon, V. (1997). On the convergence of pattern search algorithms. *SIAM Journal on optimization, 7*(1), 1-25.
Torresi, M., Camporeale, S. M., Strippoli, P. D., & Pascazio, G. (2008). Accurate numerical simulation of a high solidity Wells turbine. *Renewable Energy*, *33*(4), 735-747.
Tsai, S. W. (1992). *Theory of composites design*: Think composites Dayton.
Tullis, S., Fiedler, A., McLaren, K., & Ziada, S. (2008). Medium-solidity vertical axis wind turbines for use in urban environments.
Van Buren, K. L., Mollineaux, M. G., Hemez, F. M., & Atamturktur, S. (2013). Simulating the dynamics of wind turbine blades: part II, model validation and uncertainty quantification. *Wind Energy*, *16*(5), 741-758.
Vandenbereghe, D., & Dick, E. (1986). A theoretical and experimental investigation into the straight bladed vertical axis wind turbine with second order harmonic pitch control. *Wind engineering, 10*, 122-138.
Vassberg, J. C. (2005). Revisiting the Vertical-Axis Wind-Turbine Design using Advanced Computational Fluid Dynamics John C. Vassberg* Hydro-Aero Consulting Group Long Beach, CA 90803, USA.
Veers, P. S. (1983). *A general method for fatigue analysis of vertical axis wind turbine blades*: Sandia National Laboratories.
Velazquez, A., & Swartz, R. A. (2015). Operational model updating of low-order horizontal axis wind turbine models for structural health monitoring applications. *Journal of Intelligent Material Systems and Structures*, *26*(13), 1739-1752.
Walford, C. A. (2006). *Wind turbine reliability: understanding and minimizing wind turbine operation and maintenance costs*: United States. Department of Energy.
Wang, J., Qin, D., & Lim, T. C. (2010). Dynamic analysis of horizontal axis wind turbine by thin-walled beam theory. *Journal of Sound and Vibration*,*329*(17), 3565-3586.
Wang, J., Qin, D., & Zhang, Q. (2008). Mathematical model for predicting the blade behaviour of horizontal axis wind turbine. *Proceedings of the Institution of Mechanical Engineers, Part C: Journal of Mechanical Engineering Science*, *222*(9), 1681-1694.
Wang, S., Ingham, D. B., Ma, L., Pourkashanian, M., & Tao, Z. (2010). Numerical investigations on dynamic stall of low Reynolds number flow around

oscillating airfoils. *Computers & Fluids*, *39*(9), 1529-1541.

Wekesa, D. W., Wang, C., Wei, Y., Kamau, J. N., & Danao, L. A. M. (2015). A numerical analysis of unsteady inflow wind for site specific vertical axis wind turbine: A case study for Marsabit and Garissa in Kenya. *Renewable Energy*, *76*, 648-661.

Whitcomb, J., & Tang, X. (2001). Effective moduli of woven composites. *Journal of Composite Materials, 35*(23), 2127-2144.

Xiao, X., Xu, Y. L., & Zhu, Q. (2014). Multiscale modeling and model updating of a cable-stayed bridge. II: Model updating using modal frequencies and influence lines. *Journal of Bridge Engineering*, *20*(10), 04014113.

Xu, Y. L. (2013). *Wind effects on cable-supported bridges*: John Wiley & Sons.

Xu, Y. L., Huang, Q., Xia, Y., & Liu, H. J. (2015). Integration of health monitoring and vibration control for smart building structures with time-varying structural parameters and unknown excitations. *Smart Structures and Systems*, *15*(3), 807-830.

Xu, Y. L., & Xia, Y. (2011). *Structural health monitoring of long-span suspension bridges*: CRC Press.

Younsi, R., El-Batanony, I., Tritsch, J. B., Naji, H., & Landjerit, B. (2001). Dynamic study of a wind turbine blade with horizontal axis. *European Journal of Mechanics-A/Solids*, *20*(2), 241-252.

Zhang, J., Zhengjun, L., & Xiaoxia, S. (2009). Changing landscape in the Three Gorges Reservoir Area of Yangtze River from 1977 to 2005: Land use/land cover, vegetation cover changes estimated using multi-source satellite data. *International Journal of applied earth observation and geoinformation*, *11*(6), 403-412.

Zhang, L., Pei, Y., Liang, Y., Zhang, F., Wang, Y., Meng, J., & Wang, H. (2015, August). Design and implementation of straight-bladed vertical axis wind turbine with collective pitch control. In *Mechatronics and Automation (ICMA), 2015 IEEE International Conference on* (pp. 1258-1263). IEEE.

Zhu, S., Shen, W. A., & Xu, Y. L. (2012). Linear electromagnetic devices for vibration damping and energy harvesting: modeling and testing. *Engineering Structures*, *34*, 198-212.

Zhang, Z., Yin, Z., Han, T., & Tan, A. C. (2013). Fracture analysis of wind turbine main shaft. *Engineering Failure Analysis*, *34*, 129-139.